frontiers | Research Topics

Recent development in energy conversion systems

Edited by
Sunday Olayinka Oyedepo, Fidelis Ibiang Abam,
Olusegun David Samuel, Oluseyi Olanrewaju Ajayi,
Abimbola Patricia Popoola and Diana-Andra Borca-Tasciuc

Published in
Frontiers in Energy Research

ISSN 1664-8714
ISBN 978-2-8325-4636-9
DOI 10.3389/978-2-8325-4636-9

About Frontiers

Frontiers is more than just an open access publisher of scholarly articles: it is a pioneering approach to the world of academia, radically improving the way scholarly research is managed. The grand vision of Frontiers is a world where all people have an equal opportunity to seek, share and generate knowledge. Frontiers provides immediate and permanent online open access to all its publications, but this alone is not enough to realize our grand goals.

Frontiers journal series

The Frontiers journal series is a multi-tier and interdisciplinary set of open-access, online journals, promising a paradigm shift from the current review, selection and dissemination processes in academic publishing. All Frontiers journals are driven by researchers for researchers; therefore, they constitute a service to the scholarly community. At the same time, the *Frontiers journal series* operates on a revolutionary invention, the tiered publishing system, initially addressing specific communities of scholars, and gradually climbing up to broader public understanding, thus serving the interests of the lay society, too.

Dedication to quality

Each Frontiers article is a landmark of the highest quality, thanks to genuinely collaborative interactions between authors and review editors, who include some of the world's best academicians. Research must be certified by peers before entering a stream of knowledge that may eventually reach the public - and shape society; therefore, Frontiers only applies the most rigorous and unbiased reviews. Frontiers revolutionizes research publishing by freely delivering the most outstanding research, evaluated with no bias from both the academic and social point of view. By applying the most advanced information technologies, Frontiers is catapulting scholarly publishing into a new generation.

What are Frontiers Research Topics?

Frontiers Research Topics are very popular trademarks of the *Frontiers journals series*: they are collections of at least ten articles, all centered on a particular subject. With their unique mix of varied contributions from Original Research to Review Articles, Frontiers Research Topics unify the most influential researchers, the latest key findings and historical advances in a hot research area.

Find out more on how to host your own Frontiers Research Topic or contribute to one as an author by contacting the Frontiers editorial office: frontiersin.org/about/contact

Recent development in energy conversion systems

Topic editors

Sunday Olayinka Oyedepo — Bells University of Technology, Nigeria
Fidelis Ibiang Abam — University of Calabar, Nigeria
Olusegun David Samuel — Federal University of Petroleum Resource Effurun, Nigeria
Oluseyi Olanrewaju Ajayi — Covenant University, Nigeria
Abimbola Patricia Popoola — Tshwane University of Technology, South Africa
Diana-Andra Borca-Tasciuc — Rensselaer Polytechnic Institute, United States

Citation

Oyedepo, S. O., Abam, F. I., Samuel, O. D., Ajayi, O. O., Popoola, A. P., Borca-Tasciuc, D.-A., eds. (2024). *Recent development in energy conversion systems*. Lausanne: Frontiers Media SA. doi: 10.3389/978-2-8325-4636-9

Table of contents

frontiers | Frontiers in Energy Research

TYPE Editorial
PUBLISHED 08 March 2024
DOI 10.3389/fenrg.2024.1385470

OPEN ACCESS

EDITED AND REVIEWED BY
Ellen B. Stechel,
Arizona State University, United States

*CORRESPONDENCE
Sunday O. Oyedepo,
sooyedepo@bellsuniversity.edu.ng

RECEIVED 12 February 2024
ACCEPTED 29 February 2024
PUBLISHED 08 March 2024

CITATION
Oyedepo SO, Abam FI, Ajayi OO, Samuel OD, Borca-Tasciuc D-A and Popoola API (2024), Editorial: Recent development in energy conversion systems.
Front. Energy Res. 12:1385470.
doi: 10.3389/fenrg.2024.1385470

Editorial: Recent development in energy conversion systems

Sunday O. Oyedepo[1]*, Fidelis I. Abam[2], Oluseyi O. Ajayi[3], Olusegun D. Samuel[4,5], Diana-Andra Borca-Tasciuc[6] and Abimbola P. I. Popoola[7]

[1]Department of Mechanical/Biomedical Engineering, Bells University of Technology, Ota, Nigeria, [2]Department of Mechanical Engineering, University of Calabar, Calabar, Nigeria, [3]Department of Mechanical Engineering, Covenant University, Ota, Nigeria, [4]Department of Mechanical Engineering, Federal University of Petroleum Resources, Effurun, Nigeria, [5]Department of Mechanical Engineering, University of South Africa, Pretoria, South Africa, [6]Mechanical, Aerospace and Nuclear Engineering Department, Rensselaer Polytechnic Institute, Troy, NY, United States, [7]Department of Chemical and Metallurgical Engineering, Tshwane University of Technology, Pretoria, South Africa

KEYWORDS

energy systems, energy optimization, design, thermodynamic analysis, sustainability

Editorial on the Research Topic
Recent development in energy conversion systems

In this industrial and technological age, energy plays a principal role in sustainable development. This is connected to Research Topic regarding availability, production processes, utilization and environmental impact. Due to the increasing population growth rate, the global energy demand will get to an unsustain level shortly if serious measures are not initiated to address the situation, especially from research and development perspectives. "None of the millennium development goals (MDGs) can be completed without considerable improvements in the quality and quantity of energy services in developing countries," according to the United Nations Development Programme (UNDP). Based on this fact, UNDP is making efforts, especially in developing countries, to ensure people have access to sustainable sources of clean, reliable, and affordable energy since this vital resource impacts every aspect of human development.

The available energy conversion systems have limited efficiencies, high operating costs, and environmental effects. Sustainable energy systems are expected to minimize the environmental impact during their design and operation, to provide economically affordable energy to maximize their benefits to a large population and help mitigate emissions to the environment. Based on the above, the Frontiers in Energy Research Journal agreed to host a Research Topic about Recent Developments in Energy Conversion Systems. This Research Topic collects articles that examine research and development towards achieving sustainable energy conversion systems. Nearly 29 papers have been submitted to this Research Topic, and 10 have been finally accepted, including 4 original research papers and 6 review papers. This Research Topic received very positive and supportive responses from various stakeholders globally. Since it began in 2022, there were 22,020 total views; 21,001 article views; 4,428 article downloads, 1,019 Research Topic views as of 30 January 2024. Ten articles published within this Research Topic can be found at: https://www.frontiersin.org/research-topics/39922/recent-development-in-energy-conversion-systems.

The first paper on this Research Topic was by Ogbonna et al. The review study centres on piezoelectric materials to better understand the properties of different piezoelectric materials (ceramic) when placed under mechanical stress or vibration and electrical field during energy harvesting using transducer devices. The study concludes that lead-free piezoelectric materials, such as zinc oxide and barium titanate, remain the best conducive piezoelectric material over lead zirconate titanate, which affects the human environment due to its toxicity.

The second paper on this Research Topic by Alao et al. carries out a comprehensive review on the utilization of green inhibitors as a sustainable corrosion control method for steel in the energy (oil and gas) industries. This study elaborates on the inhibitory mechanism of organic inhibitors, mainly plant extracts, amino acids, drugs, and biomass waste. The study reveals that the phytochemicals generated from plant derivatives, the amino group (NH_2) present in the molecular structure of amino groups and drugs' molecular weights, and the shielding effect of biomass wastes are the major inhibitory properties of these organic inhibitors against corrosion. It was observed that some organic inhibitors could thrive under any circumstances (temperatures, pressure, and other parameters), whereas others may not sustain their inhibition at specific parameters. Therefore, the study concludes that judicious parameters should be considered before selecting and using any organic inhibitor as a corrosion inhibitor for different pipeline steel.

The third paper is by (Awelewa et al.). The authors present a hybrid estimator that combines the extended Kalman filter (EKF) and sliding mode observer (SMO) via a switching function and tracking closed loop to achieve the qualities of noise cancellation and disturbance rejection. The study demonstrates the quality of the hybrid technique in estimating multi-cell lithium-ion batteries. It offers more research opportunities to design adaptive estimators for complex disturbances from other battery types.

The fourth paper on this Research Topic by Babayomi et al. reviews renewable off-grid mini-grids in Sub-Saharan Africa. The study evaluates the current status of the level of deployment of off-grid mini-grids. Multi-criteria decision-making models were considered for optimizing engineering, economics, and management interests in mini-grid siting and design in Sub-Saharan Africa (SSA). It covers current research and technological developments, policy tariffs, design techniques, and energy justice in SSA's off-grid mini-grids. The review indicates that solar PV is the most common and easiest renewable to deploy for mini-grids in SSA.

Alabi et al. review "Materials for Electrocatalysts in Proton Exchange Membrane Fuel Cell". This review study highlights recent research efforts to replace platinum and carbon support with other cost-effective and durable materials in proton exchange membrane fuel cell electrocatalysts. Overview of promising materials such as alloy-based (binary, ternary, quaternary and high-entropy alloys), single atom and metal-free electrocatalysts were discussed, as the research areas are still in their infancy and have many open questions that need to be answered to gain insight into their intrinsic requirements that will inform the recommendation for outlook in selecting them as electrocatalysts for oxygen reduction reaction in proton exchange membrane fuel cell.

"Flexible Dielectric Polymer Nanocomposites with Improved Thermal Energy Management for Energy-Power Applications" is authored by Uyor et al. The study investigates the poor thermal energy management and low energy density of poly (vinylidene fluoride) (PVDF) while maintaining its flexible property using low content of hybrid carbon nanotubes (CNTs–0.05wt%, 0.1wt%) and boron nitride (BN–5wt%, 10wt %) nano-reinforcements. It was noted that adding the CNTs and BN to the PVDF matrix improved its melting and crystallization temperatures, enhancing thermal properties. This was attributed to the high thermal energy required to decompose the bond between the polymer matrix and the nanoparticles. Therefore, the polymer dielectric nanocomposites developed in this study can find advanced applications in the energy-power sector owing to their enhanced performances.

In "Functional Materials for Solar Thermophotovoltaic Devices in Energy Conversion Applications: A Review", Dada et al. conduct a thorough investigation of solar thermophotovoltaic devices and the high-tech materials used in solar thermophotovoltaic systems as a solution to the conversion challenges encountered in conventional conversion methods. The study reveals that nanomaterials as advanced functional materials can enhance the efficiency of solar thermophotovoltaic devices.

The eighth paper on this Research Topic by Dada and Popoola is on high-entropy nanomaterials for energy storage and catalysis applications. The paper discusses the production of high entropy alloy nanoparticles (HE-NPs) and the impact of synthesis on the structure of the resulting nanomaterial for newly emerging components like HEA-NPs. The study reveals that the linkages between synthesis, structure, and property are essential for creating HEA-NP-based applications for energy storage applications, requiring the creation of a fundamental protocol to enable their mass manufacture and efficiency in service. Moreover, the study presents a straightforward review of high entropy alloys, recent advances in high entropy nanoparticles and their various syntheses for energy and catalysis applications.

Attabo et al. present "Assessment of the Wind Energy Potential and Economic Viability of Selected Sites Along Nigeria's Coastal and Offshore Locations". The wind energy potential and the economic viability of using wind turbines to generate electricity in some selected sites along Nigeria's coastline and offshore locations were evaluated. Using the statistical two-parameter Weibull probability density function method, wind speed data retrieved from an indigenous oceanography company and global information system (GIS) were analyzed for wind energy harvest. The energy output, unit cost of electricity generated by three commercially available wind turbine models (3 MW, 4 MW, and 6 MW), net present value (NPV), and payback period were evaluated. Levelized cost of electricity (LCOE) sensitivity to the discount rate, foundation cost, and turbine lifespan were also examined. The study reveals that the offshore sites have four times greater wind power potential than the coastal sites. It is also noted that discount rates and foundation cost reductions positively affect the LCOE.

The last article on this Research Topic, "Optimal design and control of permanent magnet assisted dual rotor motor" is authored by Kong et al. They examine a method to reduce the cogging torque

of the permanent magnet rotor of the permanent magnet-assisted double rotor motor. By analyzing the motor power equation, it is concluded that the pole arc coefficient, the magnetic steel's thickness, the air gap's length, and the stator's slot width have four influences on the teeth's rotor. For the parameters of the slot torque, the upper and lower limits of the parameter value are obtained according to the size of the motor. The study further designs a fuzzy controller based on granular functions, and the fuzzy rules of the fuzzy controller are to perform feature sampling and fit the response function, eliminating fuzzification and defuzzification, improve the response speed of fuzzy control, and simplifying the control system.

In summary, the collective knowledge and research on this Research Topic provide valuable insights and motivation for ongoing endeavours toward a more sustainable and energy-efficient future.

Author contributions

SO: Conceptualization, Methodology, Supervision, Writing–original draft, Writing–review and editing. FA: Investigation, Project administration, Writing–original draft, Writing–review and editing. OA: Investigation, Methodology, Writing–original draft, Writing–review and editing. OS: Investigation, Methodology, Writing–original draft. D-AB-T: Methodology, Writing–original draft, Writing–review and editing. AP: Investigation, Supervision, Writing–original draft, Writing–review and editing.

Funding

The author(s) declare that no financial support was received for the research, authorship, and/or publication of this article.

Conflict of interest

The authors declare that the research was conducted in the absence of any commercial or financial relationships that could be construed as a potential conflict of interest.

Publisher's note

frontiers | Frontiers in Energy Research

TYPE Review
PUBLISHED 22 December 2022
DOI 10.3389/fenrg.2022.1051081

OPEN ACCESS

EDITED BY
Iskander Tlili,
National School of Engineers of Monastir, Tunisia

REVIEWED BY
Hitesh Panchal,
Government Engineering College, India
Sami Ullah Khan,
COMSATS University Islamabad, Pakistan

*CORRESPONDENCE
V. E. Ogbonna,
ogbonnavictor87@gmail.com

SPECIALTY SECTION
This article was submitted to Process and Energy Systems Engineering, a section of the journal Frontiers in Energy Research

RECEIVED 22 September 2022
ACCEPTED 30 November 2022
PUBLISHED 22 December 2022

CITATION
Ogbonna VE, Popoola API and Popoola OM (2022), Piezoelectric ceramic materials on transducer technology for energy harvesting: A review.
Front. Energy Res. 10:1051081.
doi: 10.3389/fenrg.2022.1051081

Piezoelectric ceramic materials on transducer technology for energy harvesting: A review

V. E. Ogbonna[1]*, A. P. I. Popoola[1] and O. M. Popoola[2]

[1]Chemical Metallurgical and Materials Engineering, Faculty of Engineering and the Built Environment, Tshwane University of Technology, Pretoria, South Africa, [2]Center for Energy and Power, Electrical Engineering, Faculty of Engineering and the Built Environment, Tshwane University of Technology, Pretoria, South Africa

Recently, energy harvesting through the means of piezoelectric transducer technology has increasingly attracted the attention of engineers and scientists in producing/generating electricity for human consumption. However, understanding of piezoelectric materials for application in piezoelectric transducer devices in energy harvesting remains important in today's energy systems engineering. Thus, the present review study is centered on piezoelectric materials for a better understanding of the properties of different piezoelectric materials (ceramic) when placed under mechanical stress or vibration and electrical field during energy harvesting using transducer devices. With the available literature, lead zirconate titanate materials showed to be the most common piezoelectric material with a high energy-generating performance but possessed more mechanical failure and also compromised in a harsh environment compared to lead-free piezoelectric materials. As such, the authors conclude that lead-free piezoelectric materials, such as zinc oxide and barium titanate, remain the best conducive piezoelectric material over lead zirconate titanate, which basically affects the human environment due to its toxicity. Thus, to widen the use of lead-free piezoelectric materials in energy harvesting, owing to their improved properties and environment-friendly nature, the authors recommend further enhancement of the lead-free piezoelectric material properties *via* nanodielectric filler incorporations using the spark plasma sintering technique.

KEYWORDS

transducer, energy harvesting, lead zirconate titanate (piezoelectric ceramic), lead-free piezoelectric materials, electromechanical coupling characteristics

Introduction

In the recent era, electricity has become a major need in almost all activities worldwide, owing to its increasing rate and demand for use in operating certain types of electrical devices. This occurs with respect to the growth of the human population, and as such, the means of energy presently has become inadequate for the demand of the users. Furthermore, energy consumption is increasing as a result of modernization, with natural resources being present at the site of extinction (Ramkrishna et al., 2016). However, to

harness this problem, renewable energy harvesting has been adopted *via* proper means of storing energy for future use as micro energy harvesting is basically in search of conventional battery alternatives (Singh and Datta, 2011). The advances in renewable energy and sustainability have opened many doors for energy harvesting systems and research in real-world applications. Piezoelectricity is one such area under energy harvesting where electric charge is accumulated in certain solid materials in response to applied pressure. However, the word "Energy harvesting" can further be described as the process of capturing energy or obtaining energy from a source in accumulation and storing for future use (Elham, Noor, and Balbir, 2017; Adhithan, Vignesh, and Manikandan, 2015). Thus, in capturing this energy, electricity can be generated without any negative effect on human life and its surroundings. Accordingly, it was reported that using the human footprint, useful energy can be harvested and used to generate electricity, and this type of renewable energy does not depend on weather conditions (Mohd Asry et al., 2019). Hence, to achieve this, transducer technology is reportedly adopted as a means to address the high cost of energy and exponential reduction in the supply of fossil fuels and nuclear power instability in the current era. The type of transducer applied here is known as the piezoelectric transducer (Mohd Asry et al., 2019). Piezoelectric/piezoelectricity for transducers can be defined as the property potential of a certain material to generate electric voltage when they are subjected or exposed to mechanical stress and vibration, or vibrate when affected by an AC voltage, or both (Curie and Curie, 1880; Mitcheson et al., 2008; Kanani, 2014). The piezoelectric energy harvester on a sub-micron scale has limitless scope for research and application in the near future technology (Beeby, Tudor, and White, 2006). However, using the piezoelectric properties of some materials remains an inspiring means of alternative energy harvesting techniques (Kumar and Kim, 2012; Chennault et al., 2008), owing to the fact that piezoelectric materials could be employed as a means of converting ambient vibrations into electrical energy, which can be stored and utilized to power other devices. Therefore, the aim of this review paper was to focus on piezoelectric materials, which will offer an insight into today's energy harvesting procedure using the piezoelectric transducer mechanism as a reference point in selecting the piezoelectric material for piezo-transducer devices in energy storage/energy harvesting applications without causing any side effects on human health.

Piezoelectric material for energy storage/harvesting

In 1880, Pierre and Jacques Curie discovered the direct piezoelectric effect in crystal quartz, which generated electrical charge and/or voltage under pressure. The word piezo stands for pressure in Greek; thus, the original meaning of the word piezoelectricity means pressure electricity; in other words, materials exhibiting this phenomenon depict a geometric strain proportional to the applied electric field known as the converse piezoelectric performance, as revealed by Gabriel Lippmann in 1880 (Uchino, 2010). After these studies on quartz material for energy harvesting that produces electricity when subjected to a mechanical stress, low outcome was reported for quartz as a result of its brittleness and poor electrical conductivity. However, observing the drawbacks of quartz as a piezoelectric material in energy scavenging, another piezoelectric material known as lead zirconate titanate (PZT) was developed, which has become the most commonly used material for energy harvesting (Raghu, Sastry, and Mohammed, 2015). Piezoelectric ceramic material, used in the design of transducer devices for energy harvesting, has been adopted for the mechanism of transferring ambient vibration (mechanical energy) into electrical energy that could be stored in energy devices and later utilized in powering other devices. Today, lead zirconate titanate power generation is used as a conventional alternative over traditional power sources used in the operation of some kinds of sensors or micro electro–mechanical system devices. The processes of self-power generation using the vibration loads of structures and human motions have all received attention. Therefore, the importance of this technology being used as the power supply for electrodevices and as sensors for monitoring the vibration status of buildings, bridges, and machine equipment has been a welcome development for researchers (Shohei et al., 2013). Moreover, studies on the analysis of vibration power generation using piezoelectric elements as a power supply to drive micro devices have greatly been reported in the literature (Glynne-Jones, Beeby, and White, 2001; Arms et al., 2005). However, the outcome of the studies on vibration power generation was found in different ways, for example, the human motion (Gorlatova et al., 2014), ocean wave (Lewis, 2011), and the gathering of strain from beam particles in structures (Pfeifer, Leming, and Rumpf, 2001). Also, energy captured from mechanical loading generated from the ground in the form of compressive forces as human beings move toward the floor of a building is noted to be another sustainable means to generate electrical energy (Bischur and Schwesinger, 2012). However, along this line, Umeda et al. (1996) developed an electrical model of lead zirconate titanate in converting mechanical impact energy to electrical power. Furthermore, another experiment was carried out on generating electricity using piezoelectric materials by Dayou et al. (2009). In their finding, it was reported that lead zirconate titanate as a piezoelectric material showed a better outcome adopting the Euler–Bernoulli method. Hailu et al. (2018), on the other hand, carried out a study on the highway piezoelectric power supply system. In their study, a piezoelectric energy harvester was manufactured in advance and embedded in the pavement along the roadway of the test site, considering the contact

point of vehicle tires. However, it was reported that the PZT–5H piezoelectric material used exhibited a better result in terms of excellent power-generating performance. The open circuit voltage generated from the piezoelectric energy harvester in the actual road traffic conditions was higher than 250 V. The output voltage was reportedly sensitive to the vehicle speed and increased with the increase in speed. The study deduced that energy generated by the piezoelectric energy harvester would be supplied to the light-emitting diode (LED) lamp, which could solve the challenge of the high cost of the power supply system for the mountain highway in line with the notion of sustainable energy development. Paradiso et al. (2005) also reported that PZT piezoelectric material has been the most commonly used piezoelectric material for vibration energy harvesting. However, lead zirconate titanate as a piezoelectric material for a transducer in terms of energy capturing has been recommended over the years but still faces some limitations like brittleness. This remains a major issue that was discovered in quartz as a piezoelectric material during application, although PZT still remains more efficient than quartz (Adnan, Mahmoud, and Mohamed (2017). Apart from PZT brittleness, other imperfections have also been reported by many researchers, such as the toxicity effect, greenhouse effect, and contamination of seas and rivers. With respect to this observation, the European community pointed out the restrictions over the utilization of hazardous substances, and this clearly reduced the application of lead (Pb)-based piezoelectric material in electronic devices. Furthermore, another drawback of conventional piezoelectric PZT ceramics was as a result of incessant behavior in hysteresis and aging effects when it comes to huge electric fields (Uchino, 2010). All these aforementioned imperfections of PZT, however, lead to the development of lead-free piezoelectric materials in designing piezoelectric transducers for energy harvesting. The effectiveness and potential of any energy conversion depend on the size, material properties, load or pressure, and vibration, affecting the piezoelectric material. It was also noted that high thickness and higher forces do generate suitable surface charge (Elham et al., 2017a). In enhancing the potential of PZT after its restriction, other studies were carried out on PZT for improving its performance. However, PZT as an inorganic ceramic was found to be brittle with low expansion characteristics. Again, a study revealed that PZT required maximum protection in a harsh environment (Bischur and Schesinger, 2012), such as salt water, moisture, noxious gases, mechanical stress, and even an acidic environment, hence resulting in more limitations to its application. In addition, it is worth noting that this brittleness, which is characteristic of PZT material, actually contributes to the rapid failure of a piezoelectric transducer made of PZT in service when a load or vibration is applied in the cyclic form. Yao et al. (2014) provided evidence about the presence of internal stress on the domain of lead zirconate titanate piezoelectric material after mechanical cyclic loading during their study on the fatigue

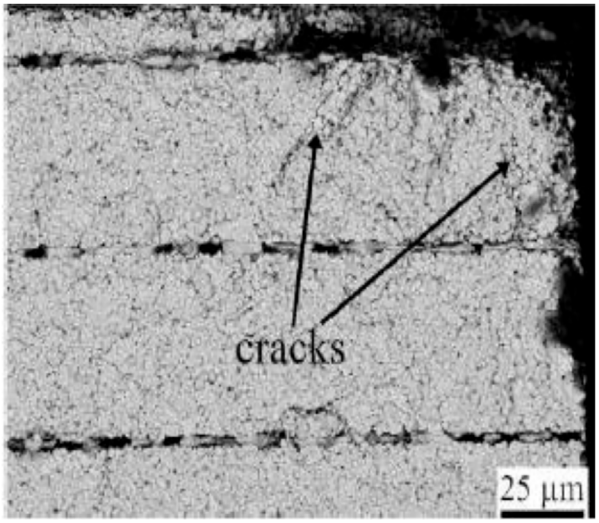

FIGURE 1
Scanning electron microscopic view of the fractured surface of the poled multilayer PZT ceramic composite reproduced from the study by Bermejo et al. (2012).

behavior of PZT material. This internal stress in the structure of the PZT material results in inhomogeneity strain and, as such, reduces the property potential of the piezoelectric transducer in energy harvesting when it comes to the piezoelectric strain coefficient, as noted by the author. Another problem of a PZT material is that when a pressure load greater than 50 kbar is applied to PZT, a rapid decrease in output current occurs (Sastry, Mohammed, and Raghu, 2015). This makes the electromechanical coupling of PZT material low because Kumar et al. (2013) stated that for a higher output voltage to occur, there must be a high coupling coefficient of piezoelectric material. Again, considering heel-strike generators using piezoelectric material as a result of high impact forces generated during walking (Starner and Paradisco, 2004), the benefits of piezoelectric materials are mostly used for heel-strike devices, based on little effort of incorporating them into shoes, meaning that a material with a superior power to weight ratio is needed (Riemer, 2011). Herein, PZT as a piezoelectric material might not be accepted as a result of its density. Furthermore, another issue with PZT is the volatility of lead oxide (PbO) during sintering at about 800°C (Jordan and Ounaies, 2001). With this volatility, there might be hazardous effects of lead on human health within such an environment, and it was also reported that PZT elastic properties can vary as much as 5%, and dielectric properties, 20% within the same batch of production. This is as a result of the rapid volatility of lead oxide (Jordan and Ounaies, 2001). In addition, it was noted that PZT-0 with a high lead content cracked during sintering due to large spontaneous strains and thermal expansion anisotropy accompanied with lead titanate materials at the point of cooling

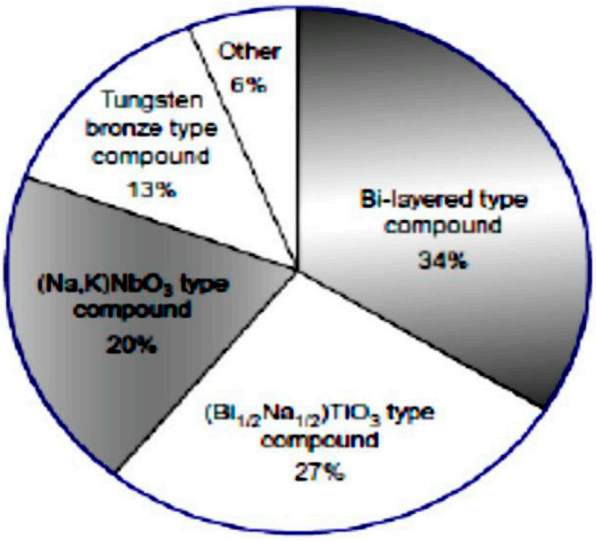

FIGURE 2
Patent statistics for the lead-free piezoelectric (Uchino, 2010).

TABLE 1 Chemical composition of PZT using EDAX analysis reproduced from the study by Praveen et al. (2018).

Element	Weight %
Lead	52.9
Oxygen	14.5
Zirconium	13.1
Barium	4.2
Titanium	3.7
Lanthanum	2.7

from the sintering temperature (Karapuzha et al., 2016). According to Bermejo et al. (2012), in the mechanical characterization of PZT ceramics for the multilayer piezoelectric, it was observed that during poling, a crack occurred in the pole multilayer metal PZT ceramic composite, as can be seen in Figure 1, hence its limitation.

With all these limitations to PZT piezoelectric material, lead-free piezoelectric material was found to be a promising material and was employed in order to meet up in energy harvesting using a piezoelectric transducer. Lead-free piezoceramics were actually developed after 1999 (Uchino, 2010). Figure 2 shows the statistics of lead-free piezoelectric ceramic materials, and this came into existence after a patent statistical study. Although the application of lead-free piezoelectric material was not actually adopted until more percentage of lead on PZT was noticed in creating hazards during processing, it is greatly toxic to the environment when disposed; however, this outcome of PZT material as a hazardous material led to the attention of regulatory agencies worldwide in putting strict restrictions on the use of lead (Elena and Jacob, 2010). Table 1 lists the chemical composition of bulk PZT, as revealed in EDAX analysis, during characterization of porous PZT piezoelectric ceramics. The results of the EDAX analysis showed that there was a reduction in the weight concentration of the elements, and this could be from lead and oxygen as a result of their volatile behavior, hence causing a problem with lead (Pb) side effects on human health.

In a nutshell, the piezoelectricity of any material can be determined by its piezoelectric coefficient and/or piezoelectric modulus (G). The piezoelectric modulus can be described as a change in volume that occurs in a piezoelectric material when subjected to an electric field (Indrani and Nitin, 2013), and it has been reported in the literature that the piezoelectric coefficient depends on crystal orientation (Damjanovic, 1998). With this, piezoelectricity in zinc oxide (ZnO) was noted because of its versatility as a metal oxide semiconductor material. In addition, zinc oxide nanostructures depict anisotropic piezoelectric properties as a result of their structural non-central symmetry (Kong and Wang, 2003; Kwon et al., 2008). In noticing the properties of zinc metal oxide, which happened to be lead-free, Lee et al. (2011) examined ZnO nanowires as a piezoelectric material for energy harvesting, and results showed that a higher output voltage suitable for driving small commercial electronic devices was generated. In addition, in previous research works on zinc oxide, better properties were recorded compared to PZT; for example, the density of zinc oxide was found to be lower than that of lead zirconate titanate. Another lead-free piezoelectric material developed was barium titanate ($BaTiO_3$). Barium titanate ($BaTiO_3$) was the first discovered ferroelectric oxide with a perovskite structure (Robert, 1947). This ceramic material was found to exhibit a relatively high electromechanical coupling factor of about 0.50 and a good piezoelectric strain constant mode, which is incompletely adopted for piezoelectric applications, for example, sonars. Although, the working temperature range of barium titanate was reported to be small for real applications because barium titanate has a low Curie temperature of about 120–135°C (Takahashi et al., 2006). Therefore, to enhance the Curie temperature of barium titanate, the doping process was adopted, and potassium as the doping agent, hence the bismuth potassium titanate, which happened to be a typical lead-free ferroelectric with a perovskite structure of tetragonal symmetry at ambient temperature and a higher temperature of about 380°C (Buhrer, 1962). Seeing the properties of some lead-free piezoelectric materials, like barium titanate, it is a welcome development in using it to produce piezoelectric transducers for energy harvesting when doped. However, in doing so, it results in the reduction of environmental damage when disposing piezoelectric product waste (Tadashi, 2013) than lead zirconate titanate (PZT) mentioned previously in this review paper. In addition, barium titanate as a piezoelectric material continues to serve as a model system for more fundamental

TABLE 2 Power generation in floor building techniques for energy harvesting.

Piezoelectric material	Generated power	Company technology	Reference
Barium titanate ($BaTiO_3$)	7 mW/cm^3	$BaTiO_3$ technology	Adnan et al. (2017)
Zinc oxide (ZnO)	5 pW, 11, 2.7 mW/cm^3	ZnO nanowire	
Lead zirconate titanate (PZT)	8.4 mW	PZT ceramic	Ariel (2016)

investigations for technological applications (Rogan et al., 2003). Thus, as lead-free piezoelectric materials are reportedly an alternative to piezoelectric materials, owing to the growing environmental concerns about the toxicity of lead-based piezoelectric materials, Zhao et al. (2018) investigated the high piezoelectricity in $BaTiO_3$ using multiphase convergence with broad structural flexibility. In their study, an ultrahigh piezoelectric constant of 700 pC/N in $BaTiO_3$ ceramic over a wide composition range was recorded. It was deduced that the lead-free piezoelectric material exceeds the performance of the majority of lead-based piezoelectric systems, including PZT-5H, in the temperature range of 10–40°C. Moreover, Dogrusoz et al. (2021) reported on the PZT-5H and PZT-8 type piezoelectric effects on the cycling stability of multiwall carbon nanotubes containing anode materials. In characterizing the resultant composites, results show that the addition of the PZT material in the composites improved its capacity value (420 mA/hg), which is about a 300% improvement in comparison with the pure composite without PZT. In another study, Yang et al. (2021) improved the piezoelectric output capability of a piezoelectric mechanical energy harvester *via* the development of a 3D porous structure of polyvinylidene fluoride/$BaTiO_3$ by the assisted selective laser sintering process. From the experimental results under the synergistic influence of $BaTiO_3$, a high output with an output voltage of 20.9 V and a current density of about 0.371 nA/mm2 were recorded. In the study, it was concluded that the developed piezoelectric energy harvester can directly light up 11 green LEDs and charge a 1-μF commercial capacitor to 4.9 V within 180 s, establishing that the $BaTiO_3$ solid solution with the pseudo-cubic phase has received much attention based on their large strains for potential piezoelectric multilayer actuator applications. Yuan et al. (2021), on the other hand, examined the strain and electrical properties of Li_2CO_3 sintering aid modified $0.64BiFeO_3$–$0.36BaTiO_3$ ceramics produced by the high-temperature sintering method. The experimental results indicate that the dielectric loss and strain hysteresis of $BiFeO_3$–$BaTiO_3$ were reduced by 40% and 47%, respectively, with a large strain of 0.3% (dielectric strength of 60 kV/cm). The reduced dielectric loss and strain hysteresis attributed from the improved relative density decreased the concentration of defects and partial phase transition from partial pseudo-cubic to rhombohedral symmetry by Li_2CO_3 incorporations. The observed low dielectric loss and reduced strain hysteresis of the ceramics demonstrate that they are promising candidate materials for high-temperature and lead-free piezoelectric actuator applications. Wang et al. (2018) also reported on the piezoelectric property enhancement of BiFeO3–BaTiO3 on calcium-doped BiFeO3–BaTiO3 ceramics fabricated by the solid-state reaction process. The results revealed that calcium doping has little effect on the crystal structure of the resultant ceramic material, while notable grain growth occurred. Enhanced piezoelectric characteristics with a piezoelectric coefficient of 168 pC/N, a planar electromechanical coupling factor of 0.28, a maximum strain of 0.146%, and high thermal stability are recorded at 0.75% calcium-doped ceramics. The mechanism, which attributes to the improved piezoelectric properties, could be the stability of the long-range ferroelectric state at the high-temperature and high-degree poling-induced domain structure of the doped ceramic. The results, in other words, evidence the use of lead-free piezoceramics for energy applications.

Energy generation by different piezoelectric materials

Piezoelectric material in generating electricity has been a major material used in the design and fabrication of piezoelectric transducer devices for energy capturing. However, Table 2 shows generated power values by different company technology methods using a transducer device manufactured with piezoelectric material. In addition, there are other technologies or models in energy harvesting apart from the floor which can be found in Zhang, Li, and Yu (2016).

Conclusion

In this review article, an attempt has been made to discuss piezoelectric material on transducer technology for energy harvesting. This was actually achieved with little available literature. In the review study, it was noted that lead zirconate titanate was commonly used for piezoelectric transducers, but because of its shortcomings, such as mechanical failure, the aging effect when subjected to an electric field, and the hazardous effect within the human environment during disposal resulted in its restriction. However, lead-free piezoelectric material was developed and started being used in the fabrication of transducer devices. From the literature reviewed, it was noted that better properties were observed in lead-free piezoelectric material without hazardous effects than in lead zirconate titanate

(PZT). This review article also demonstrated that electricity could be generated with no negative impact on human life and surroundings when a lead-free piezoelectric material is employed fully in the design and manufacturing of piezoelectric transducer devices for energy harvesting. However, there is a need for future study in the improvement of piezoelectric properties of lead-free piezoelectric materials, for example, $BaTiO_3$, for better performance during service. As such, the authors recommend the incorporation of nanoparticles with a high strain output, high strain (charge) constant and permittivity, low mechanical quality factor, and excellent thermal stability in lead-free piezoceramics in the design of piezoelectric transducer components using the Taguchi design of experiment and spark plasma sintering processing methods.

Author contributions

Study conception and design: VO and AP; draft manuscript preparation: VO, OM, and AP. All authors proofread the manuscript and approved the final version of the manuscript.

Acknowledgments

The authors appreciate the Tshwane University of Technology for granting access to their e-library.

Conflict of interest

The authors declare that the research was conducted in the absence of any commercial or financial relationships that could be construed as a potential conflict of interest.

Publisher's note

All claims expressed in this article are solely those of the authors and do not necessarily represent those of their affiliated organizations, or those of the publisher, the editors, and the reviewers. Any product that may be evaluated in this article, or claim that may be made by its manufacturer, is not guaranteed or endorsed by the publisher.

References

Adhithan, A., Vignesh, K., and Manikandan, M. (2015). Proposed method of foot step power generation using piezo electric sensor. *Int. Adv. Res. J. Sci. Eng. Technol.* 2, 25–29. doi:10.17148/1ARJSET.2015.2406

Adnan, M. E., Mahmoud, Y. M. G., and Mohamed, E. (2017). Feasibility study for using piezoelectric energy harvesting floor in buildings' interior space. *Energy Procedia* 115, 114–126. doi:10.1016/j.egypro.2017.05.012

Ariel, S. (2016). Electricity generating dance floors and other miracles of piezoelectricity. https://www.good.is/articles/electricty-generating-dance-floors-and-other miracles-of-piezoelectricity.

Arms, S. W., Townsend, C. P., Churchill, D. L., Galberath, J. H., and Mundll, S. W. (2005). "Power management for energy harvesting wireless sensor," in *Smart structures and meterials, smart electronics, MEMS, bio-MEMS and nanotechnology*. Editor V. K. Varadan (Proc. SPIE), 5763, 267. New York.

Beeby, S. P., Tudor, M. J., and White, N. M. (2006). Energy harvesting vibration sources for microsystems applications. *Meas. Sci. Technol.* 17, 175–195. doi:10.1088/0957-0233/17/12/r01

Bermejo, R., and Deluca, M. (2012). Mechanical characterization of PZT ceramics for multilayer piezoelectric actuators. *J. Ceram. Sci. Technol.* 3 (4), 159–168.

Bischur, E., and Schwesinger, N. (2012a). "Energy harvesting from floor using organic piezoelectric modules," in Power Engineering and Automation Conference (PEAM) (IEEE). Wuhan, China.

Buhrer, C. F. (1962). Some properties of bismuth perovskites. *J. Chem. Phys.* 36 (3), 798–803. doi:10.1063/1.1732613

Chennault, K. A. C., Thambi, N., and Sastry, A. M. (2008). Powering micro electromechanical system (MEMS) portable devices - a review of non regenerative and regenerative power supply systems with special emphasis on piezoelectric energy. *Smart Mater. Struct.* 17 (4), 1–33. doi:10.1088/0964-1726/17/4/043001

Curie, J., and Curie, P. (1880). Development via compression of electric polarization in hemihedral crystals with inclined faces. *bulmi.* 3, 90–93. doi:10.3406/bulmi.1880.1564

Dayou, J., Man-Sang, C., Dalimin, M. N., and Wang, S. (2009). Generating electricity using piezoelectric material. *Borneo Sci.* 24, 47–51.

Damjanovic, D. (1998). Ferroelectric, dielectric and piezoelectric properties of ferroelectric thin films and ceramics. *Rep. Prog. Phys.* 61 (9), 1267–1324. doi:10.1088/0034-4885/61/9/002

Doğrusöz, M., Demirkan, M. T., and Çakan, R. D. (2021). Investigation of PZT-5H and PZT-8 type piezoelectric effect on cycling stability on Si-MWCNT containing anode materials. *Turk. J. Chem.* 45 (5), 1551–1558. doi:10.3906/kim-2102-62

Elena, A., and Jacob, L. J. (2010). Advances in lead-free piezoelectric materials for sensors and actuators. *Sensors* 10, 1935–1954. doi:10.3390/s100301935

Elham, M. N., Noor Amila, W. Z., and Balbir Singh, M. (2017b). A review of walking energy harvesting using piezoelectric materials. *IOP Conf. Ser. Mat. Sci. Eng.* 291, 012026–012028. doi:10.1088/1757-899x/291/1/012026

Elham, M. N., ZawawiAmila Wan Abdullah, N., and Singh Mahinder Singh, B. (2017a). A review of walking energy harvesting using piezoelectric materials. *IOP Conf. Ser. Mat. Sci. Eng.* 291 (1), 012026. doi:10.1088/1757-899x/291/1/012026

Glynne-Jones, P., Beeby, S. P., and White, N. M. (2001). Towards a piezoelectric vibration-powered microgenerator. *IEE Proc. Sci. Meas. Technol.* 148 (2), 68. doi:10.1049/ip-smt:20010323

Gorlatova, M., Sarik, J., Grebla, G., Cong, M., Kymissis, I., and Zussman, G. (2014). Movers and shakers: Kinetic energy harvesting for the internet of things. *SIGMETRICS Perform. Eval. Rev.* 42, 407–419. doi:10.1145/2637364.2591986

Hailu, Y., Linbing, W., Bin, Z., Ya, W., and Qian, Z. (2018). A preliminary study on the highway piezoelectric power supply system. *Int. J. Pavement Res. Technol.* 11, 168–175. doi:10.1016/j.ijprt.2017.08.006

Indrani, D., and Nitin, A. (2013). Piezoelectric energy generation and harvesting at the nano-scale: Materials and devices. *Nanomater. Nanotechnol.* 3, 21. doi:10.5772/56941

Jordan, T. L., and Ounaies, Z. (2001). *Piezoelectric ceramics characterisation*. Virginia, VA, USA: ICASE, NASA Langley research center hampton.

Kanani, B. D. (2015). *Electrical measurements and measuring instruments*. Vasan Gandhinagar: Institute of engineering and technology.

Karapuzha, A. S., James, N. K., Khanbareh, H., Van der Zwaag, S., and Groen, W. A. (2016). Structure, dielectric and piezoelectric properties of donor doped pzt ceramics across the phase diagram. *Ferroelectrics* 504 (1), 160–171. doi:10.1080/00150193.2016.1240571

Kim, H. S., Kim, J. H., and Kim, J. (2011). A review of piezoelectric energy harvesting based on vibration. *Int. J. Precis. Eng. Manuf.* 12 (6), 1129–1141. doi:10.1007/s12541-011-0151-3

Kong, X. Y., and Wang, Z. L. (2003). Spontaneous polarization-induced nanohelixes, nanosprings, and nanorings of piezoelectric nanobelts. *Nano Lett.* 3 (12), 1625–1631. doi:10.1021/nl034463p

Kumar, B., and Kim, S. (2012). Energy harvesting based on semiconducting piezoelectric ZnO nanostructures. *Nano Energy*. Kanpur, India 1 (3), 342–355. doi:10.1016/j.nanoen.2012.02.001

Kumar, D., and Chaturvedi, P. (2013). IIT Kanpur.Piezoelectric energy harvesting from vibration induced deformation of floor tilesSixth National Power Electronics Conference (NPEC). 2013, Kanpur, India.

Kwon, S., Hong, W., Jo, G., Maeng, J., Kim, T., Song, S., et al. (2008). Piezoelectric effect on the electronic transport characteristics of ZnO nanowire field-effect transistors on bent flexible substrates. *Adv. Mat.* 20 (23), 4557–4562. doi:10.1002/adma.200800691

Lee, M., Lee, J., Lee, C. S., Hong, S., and Wang, Z. L. (2011). Self-powered environmental sensor system driven by nanogenerators. *Energy Environ. Sci.* 4, 3359–3363. doi:10.1039/c1ee01558c

Lewis, A. (2011). "Ocean energy," in *IPCC special report on renewable energy sources and climate change mitigation*. Editors O. Edenhofer, R. Pichs-Madruga, Y. Sokona, K. Seyboth, P. Matschoss, S. Kadner, et al. (Cambridge, United Kingdom and New York, NY, USA.

Mitcheson, P. D., Yeatman, E. M., Rao, G. K., Holmes, A. S., and Green, T. C. (2008). Energy harvesting from human and machine motion for wireless electronic devices. *Proc. IEEE* 96 (9), 1457–1486. doi:10.1109/jproc.2008.927494

Mohd Asry, A. M., Mustafa, F., Ishak, M., and Ahmad, A. (2019). Power generation by using piezoelectric transducer with bending mechanism support. *Int. J. Power Electron. Drive Syst. (IJPEDS)* 10, 562–567. doi:10.11591/ijpeds.v10.i1.pp562-567

Paradiso, J. A., and Starner, T. (2005). Energy scavenging for mobile and wireless electronics. *IEEE Pervasive Comput.* 4, 18–27. doi:10.1109/mprv.2005.9

Pfeifer, K. B., Leming, S., and Rumpf, A. (2001). Embedded self-powered micro sensors for monitoring the surety of critical buildings and infrastructures. *SAND2001-3619 Unltd. Release Print.* 3, 3–6.

Praveen, K. B., Bhupender, R., and Rajan, K. M. (2018). Characterization of high porous PZT piezoelectric ceramics by different techniques. *Def. Sci. J.* 68 (5), 500–504. doi:10.14429/dsj.68.12315

Raghu, C. G., Sastry, V. R., and Mohammed, S. M. (2015). Piezo-gen - an approach to generate electricity from vibrations. *Procedia earth Planet. Sci.* 11, 445–456. doi:10.1016/j.proeps.2015.06.044

Ramkrishnaa, S. N., Nikesha, C., Allamrajub, V. K., and Korlac, S. (2016). *Comparative study between tapping and straining for effective energy harvesting using piezoelectirc disc actuators. National conference on MEMS, smart materials, structures and systems*. Kanpur, India: IIT Kanpur.

Riemer, R., and Shapiro, A. (2011). Biomechanical energy harvesting from human motion: Theory, state of the art, design guidelines, and future directions. *J. Neuroengineering Rehabilitation* 8 (1), 22–13. doi:10.1186/1743-0003-8-22

Robert, S. (1947). Dielectric and piezoelectric properties of barium titanate. *Phys. Rev.* 71, 890–895. doi:10.1103/physrev.71.890

Rogan, R. C., Tamura, N., Swift, G. A., and Ustundag, E. (2003). Direct measurement of triaxial strain fields around ferroelectric domains using X-ray microdiffraction. *Nat. Mat.* 2, 379–381. doi:10.1038/nmat901

Sastry, V. R., Mohammed, S. M., and Raghu, C. G. (2015). Piezo-gen - an approach to generate electricity from vibrations. *Procedia Earth Planet. Sci.* 11, 445–456. doi:10.1016/j.proeps.2015.06.044

Shohei, Y., Shigeru, F., Masaaki, I., Tokio, K., and Takeshi, M. (2013). *Characterization of the piezoelectric power generation of pzt ceramics under mechanical force DTIP*. 2013 Symposium on Design, Test, Integration and Packaging of MEMS/MOEMS (DTIP), Barcelona, Spain.

Starner, T., and Paradiso, J. A. (2004). Human generated power for mobile electronics. *Low. Power Electron. Des.* 45, 1–35. doi:10.1201/9781420039559.ch45

Tadashi, T. (2013). "Lead-free piezoelectric ceramics," in *Handbook of advanced ceramics applications processing, and properties*. Elsevier, 429–446.

Takahashi, H., Numamoto, Y., Tani, J., and Tsurekawa, S. (2006). Piezoelectric properties of BaTiO3 ceramics with high performance fabricated by microwave sintering. *Jpn. J. Appl. Phys. (2008).* 45, 7405–7408. doi:10.1143/jjap.45.7405

Uchino, K. (2010). *Development of piezoelectric materials and the new perspective"*. State College, PA, USA, Pennsylvania State University, 1–39.

Umeda, M., Nakamura, K., and Ueha, S. (1996). Analysis of the transformation of mechanical impact energy to electric energy using piezoelectric vibrator. *Jpn. J. Appl. Phys. (2008).* 35 (1), 3267–3273. doi:10.1143/jjap.35.3267

Wang, J., Zhou, C., Li, Q., Yang, L., Xu, J., Chen, Q., et al. (2018). Simultaneously enhanced piezoelectric properties and depolarization temperature in calcium doped BiFeO3-BaTiO3 ceramics. *J. Alloys Compd.* 748, 758–765. doi:10.1016/j.jallcom.2018.03.174

Yang, C., Chen, F., Sun, J., and Chen, N. (2021). Boosted mechanical piezoelectric energy harvesting of polyvinylidene fluoride/barium titanate composite porous foam based on three-dimensional printing and foaming technology. *ACS omega* 6 (45), 30769–30778. doi:10.1021/acsomega.1c04998

Yao, Y., Xu-Sheng, W., Yan-Xia, L., and Xi, Y. (2014). Fatigue behaviors in PZT ceramics induced by mechanical cyclic load. *Ferroelectr. Lett. Sect.* 41 (4-6), 123–128. doi:10.1080/07315171.2014.956021

Yuan, H., Li, L., Hong, H., Ying, Z., Zheng, X., Zhang, L., et al. (2021). Low sintering temperature, large strain and reduced strain hysteresis of BiFeO3–BaTiO3 ceramics for piezoelectric multilayer actuator applications. *Ceram. Int.* 47, 31349–31356. doi:10.1016/j.ceramint.2021.08.008

Zhang, S. J., Li, F., and Yu, F. P. (2016). "Piezoelectric materials for cryogenic and high-temperature applications," in In *structural health monitoring (SHM) in Aerospace Structures*. Woodhead Publishing, 59–93. doi:10.1016/B978-0-08-100148-6.00003-2

Zhao, C., Wu, H., Li, F., Cai, Y., Zhang, Y., Song, D., et al. (2018). Practical high piezoelectricity in barium titanate ceramics utilizing multiphase convergence with broad structural flexibility. *J. Am. Chem. Soc.* 140 (45), 15252–15260. doi:10.1021/jacs.8b07844

frontiers | Frontiers in Energy Research

TYPE Review
PUBLISHED 09 January 2023
DOI 10.3389/fenrg.2022.1063315

OPEN ACCESS

EDITED BY
Chandrabhan Verma,
King Fahd University of Petroleum and Minerals, Saudi Arabia

REVIEWED BY
Ashish Kumar,
Government of Bihar, India
Tolutope Oluwasegun Siyanbola,
Covenant University, Nigeria

*CORRESPONDENCE
Alice Osheiza Alao,
sweetdamsel08@gmail.com

SPECIALTY SECTION
This article was submitted to Process and Energy Systems Engineering, a section of the journal Frontiers in Energy Research

RECEIVED 06 October 2022
ACCEPTED 09 December 2022
PUBLISHED 09 January 2023

CITATION
Alao AO, Popoola AP, Dada MO and Sanni O (2023), Utilization of green inhibitors as a sustainable corrosion control method for steel in petrochemical industries: A review. *Front. Energy Res.* 10:1063315. doi: 10.3389/fenrg.2022.1063315

Utilization of green inhibitors as a sustainable corrosion control method for steel in petrochemical industries: A review

Alice Osheiza Alao*, Abimbola Patricia Popoola, Modupeola Oluwaseun Dada and Omotayo Sanni

Department of Chemical, Metallurgical and Materials Engineering, Tshwane University of Technology, Pretoria, South Africa

Infrastructure upgrades in the energy sector are encouraged to satisfy the expanding world's energy needs, including innovation, consumption, production, and transportation. Thus, steel has been an extensively used construction material, particularly for pipelines and oil wells. However, in their application, every step of the production cycle results in the corrosion of metal parts. One of the simplest and most active ways to inhibit steel from corroding, especially in acidic situations, is to use a corrosion inhibitor. Synthetic organic compounds have been used successfully as corrosion inhibitors in the gas and oil industry. However, their use is today restricted and controlled due to their toxicity, environmental harm, and growing concern about the preservation of ecosystems. This has necessitated the present trend of searching for and developing green inhibitors that are environmentally benign, non-toxic, biodegradable, and low in cost. Corrosion inhibitor develops a shielding layer on the metal surface. Corrosion is avoided by a thin coating that has been adsorbed on the metal surface, which keeps the metal isolated from its surroundings. Several researchers have reported on the success of green inhibitors for steel corrosion protection, particularly in acidic environments. However, the use of green inhibitors still leaves several questions about inhibitor formulation, content, and adsorption mechanisms to be answered. Therefore, based on provided experimental results and an explanation of their inhibitory action, the use of green inhibitors (especially organic inhibitors) for the prevention of pipeline steel corrosion in various grades is studied in this review. Both the identified drawback and the projected future trend have also been highlighted.

KEYWORDS

corrosion, green inhibitors, environmentally friendly, sustainability, pipeline steel, adsorption

1 Introduction

Corrosion is a gradual deterioration of components caused by various environmental conditions. This scenario potentially damages the manufacturing and transportation of oil and gas facilities. Practically any environment with an aqueous solution can initiate corrosion, which happens under various difficult situations during the processing and production of oil and gas in pipeline systems. This mechanism entails three factors: an electrolyte, an anode, and a cathode (Dehghani et al., 2019a; Mobin et al., 2019a). The electrolyte is the corrosive medium that initiates the electron movement from the anode to the cathode, the anode is the area where the corroding metal is situated, and the cathode in the cell that produces the electrical conductor is herewith not used in the corrosion mechanism. Natural gas and crude oil can convey different high-impure substances which are intrinsically corrosive, and one of the vital materials used for industrial purposes is steel and its alloys. However, these materials experience huge corrosion deterioration when encountered by acidic media. In the case of gas and oil wells and pipelines, some extremely corrosive media, such as hydrogen sulfide (H_2S), carbon dioxide (CO_2), and water, can initiate corrosion (Oguntuyi et al., 2021a). The continuous flow of H_2S, CO_2, and water *via* gas and oil material can induce the internal surface of the material to be corroded. Hence, the lines and the material fittings would experience deterioration with the different situations of the well because of overtime well souring, alteration in fluid contents, and changes in operating temperatures and pressures. The material's deterioration produces a decline in mechanical features such as impact strength, density, ductility, and hardness. Thus, the material reduces in thickness and sometimes causes total material failure during service. A stage will be attained where the material will entirely break down, and the assemblage will be required to be changed while the manufacturing is ceased (Villamizar et al., 2006; Subasree and Selvi, 2020).

Universally, the corrosion mechanism is a serious challenge to the energy industries. Therefore, industries have considered the impact of corrosion on the design and fabrication of their equipment. History shows that industries have lost billions of dollars due to corrosion (Shukla and Quraishi, 2009; Eliyan et al., 2013; Oguntuyi et al., 2021b; Oguntuyi et al., 2022a). Some reports in the world stated that some oil pipeline industries had their equipment destroyed because of corrosion, which consequently led to oil leakages that developed environmental contamination (ecological damage). Moreover, much capital is being consumed in rectifying the environmental nuisance. The occurrence of corrosion in an industrial plant has developed many challenges for chemical, mechanical, and petroleum engineers. Corrosion can influence a material's procedural chemistry and the purity of the substance being conveyed (Quraishi et al., 2007; Raja and Sethuraman, 2008). The existence of oxidizing acids, such as HNO_3, in reacting with steel forms a layer of oxide [Fe $(NO_3)_3$] on a metal surface. This formation (layer) first inhibits the contact metal acid to prevent further occurrence. Afterward, the brittle oxide layer continuously experiences exfoliation, thus redeveloping the contacted metal acid, prompting adverse metal surface dissolution and material corrosion. The contact of the non-oxidizing acids (HCl) with steel produces iron salts ($FeCl_2$) in the aftermath of corrosion. Synonymously, the contact of strong sulphuric acid (H_2SO_4) with steel produces $FeSO_4$.

There are diverse methods to shield steel from the attack of corrosion, such as changes in the environment, cathodic protection, material modification, and application of corrosion inhibitors. Some techniques depend on the elimination of oxygen moisture, while others apply permanent coating on the metal surface. Various mechanisms depend on the changes to a cathode from the anodic components. However, the present applied techniques are constrained by diverse restrictions. For example, the modification of materials is always difficult or expensive. Moreover, the process of environmental replacement is not the possible answer in various industrial practices because the metal may undergo a specific reactive solution. Applying some techniques, such as coating, could erupt CO_2 above the standard levels. Likewise, some techniques, such as cathodic protection, need expensive devices, consequently increasing the general cost. However, the corrosion inhibitors are a user-friendly and less expensive solution as an alternative to the above challenges encountered by the other methods (Kiefner and Kolovich, 2007; Cheng, 2013; Tawancy et al., 2013; Oguntuyi et al., 2022b).

When introduced in minute quantity in a corrosive media, an inhibitor is intended to inhibit corrosion reaction by developing a shielding film. These inhibitors have various uses in many steel pipeline industries because they are active agents that prevent some in-service steel materials (heat exchangers, boilers and gas, oil containers, or pipelines) from corrosion. Usually, before performing coating or welding, metals and steels are opened to an acidic solution. Furthermore, to inhibit corrosion products, corroded structures (e.g., heat exchangers, oil wells, pipelines, and oil tankers) are made to undergo acidification. The application of these inhibitors for structural treatments has depicted capable outcomes in restricting the corrosion reactions and the resulting metal deterioration. Diverse important factors influence inhibitor selection. The major factor is inhibitor toxicity. Overall, harmful traditional inhibitors of high volatility, such as phosphates, chromates, and nitrates and toxic gases in the products, negatively influence the environment. Alternative green methods have emerged owing to the strict legislation on the environment over the past years for toxic inhibitors. This inhibitor operates on a green chemistry mechanism, which entails the importance of the atomic economy, waste prevention, derivatives minimization, energy efficiency, decrement in hazard chemical synthesis, pollution prevention, safer solvent development, and

safer chemistry for accident prevention (Kiefner and Kolovich, 2007; Marc, 2013).

The green inhibitor is an effective eco-friendly method that has had more recognition in past years. Many prevalent bases of green inhibitors comprise ionic liquids, pharmaceutical drugs, plant extracts, and synthetic inhibitors, which are roots of ecological benign corrosion inhibitors. The important origin of green corrosion inhibitors is plants (e.g., oils and their derivatives). They can operate in diverse acidic solutions because they possess versatile chemical, physical, and biological features. Low cost, biodegradability, and availability are the other importance of plants being applied as the bases of corrosion inhibitors. Plants are considered a high natural origin of chemical compounds, which can be easily hauled out with less cost and low ecosystem pollution. Also known as green solvents are ionic liquids containing ions that can dissociate various organic and inorganic compounds. Ionic liquid application in practically all chemical engineering fields is due to their promising features, which have recognized them as environmentally friendly chemicals.

Furthermore, green corrosion inhibitor drugs have comparatively huge structures comprising synthetic or natural compositions. Drugs produced from natural bases have engrossed more interest in past years. Furthermore, outdated drugs can be applied as corrosion inhibitors, thus minimizing environmental pollution and disposal expenses. Gece (2011) studied the efficiency of drugs as corrosion shielding. Various eco-friendly inhibitors have been discovered and are being studied often time. Mobin et al. (2019a) examined the applicability of drugs (bronopol) on aluminum metal as a corrosion inhibitor in HCl media. The magnitude of its inhibition mechanism and shielding capacity was determined by an electrochemical test and weight loss. The outcome indicated that optimum inhibition of 93.89% was achieved at an inhibitor concentration of 4,000 ppm in 0.5 M HCl. Two other studies published in 2011 stated the significance of surfactants and biopolymers in diverse solutions (Mobin and Rizvi, 2017; Fawzy et al., 2018; Oguntuyi et al., 2021c). Rani and Basu (2012) successfully introduced natural substances as green corrosion shields in various media. Verma et al. (2018) highlighted the behavior of ionic liquids as corrosion protectors. Thakur et al. (2022a) revealed the capability of a weed known as *Cnicus benedictus* extract as a corrosion restrictor on mild steel. An inhibition efficiency (IE) of 92.45% was attained. Moreover, the increment in the inhibitor concentration in the solution significantly decreased the corrosion rate. The IE of 91.24% was attained at 298 K when a weed regarded as *Vicia sativa* was examined as an inhibitor in 0.5 M HCl for mild steel (Thakur et al., 2022b), hence demonstrating the protective ability of the inhibitor extract. Therefore, huge success has been recorded in different green inhibitor categories in the last 10 years.

This review emphasizes the formulation, content, and adsorption mechanisms of green inhibitors (especially organic inhibitors) as a prevention technique from corrosion for all grades of pipeline steel. Moreover, the identified drawbacks and the projected future trend have been highlighted. In addition, the effort aims to provide useful insight into future research in this area for precise measurement of inhibitory efficiency and the development of industrial applications.

1.1 The mechanisms of pipeline corrosion

One of the huge impacts of failures in the pipeline of gas and oil manufacturing systems due to corrosion is that it influences about one-quarter to two-thirds of the overall breakdown of service in the industry [25] (Da Rocha et al., 2010; Eduok et al., 2012). A massive amount of money is consumed each year on diverse categories of corrosion regulation to sustain pipeline integrity. However, challenges associated with acquiring, monitoring, specific designs and mitigation approaches employed portrays high huge sums of money consumed around the world to corrosion related with pipelines and other structural damage in the oil and gas industries (Bedairi et al., 2012; Ashassi-Sorkhabi et al., 2015). Studies have indicated that above 80% of pipeline failures due to corrosion are regulated from one system to the other (Al-Turkustani et al., 2011; Abdelaziz et al., 2021; Alao et al., 2022). In contrast, the total amount, especially 20%–65%, consumed on corrosion impairment could only be kept if there is an availability of outstanding knowledge on corrosion inhibitors, control methods, and protection (Brown, 2014). Pipeline corrosion can be related to different influences, which could be chemical or physical factors, environmental circumstances, or material features. Figure 1 displays the factors that influence pipeline corrosion.

The occurrence of inorganic and organic acids, CO_2, and H_2S in an operating pipeline surrounding may produce corrosion effects of diverse categories (Ossai et al., 2015). Li et al. (2014) observed the influence of the concentrated H_2S on grade X60 pipe in a coexisting medium of CO_2 and H_2S. The corrosion rate of CO_2 declined below 0.05 mmol/L of H_2S, and at the concentration of H_2S between 0.05 and 2 mmol/L, the CO_2 corrosion rate revealed negligible variation. However, it rises at a concentration beyond 2 mmol/L. The development of sulfide layers on the steel surfaces produces some forms of crystal structures (e.g., pyrite, mackinawite, greigite, troilite, and pyrrhotite), which can be ascribed to the coexisting CO_2 and H_2S (Yin et al., 2008; Davoodi et al., 2011). Water slugs or splashes and the water-oil interface can influence corrosion propagation on pipelines. This corrosion propagation occurs when fluid flows in a multiphase from scattered flow to a constant water-in-oil movement. This only occurs when there is intense turbulence in the oil phase to produce water breakage to droplets. This droplet breakage flows to the pipeline's walls when it reaches above a specific critical diameter and thus causes

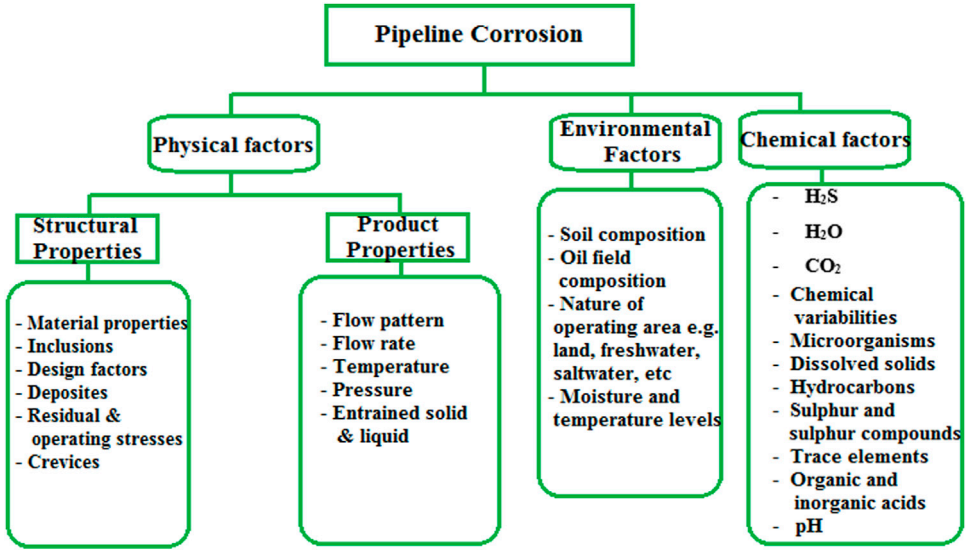

FIGURE 1
Factors that influence corrosion on pipelines.

corrosion speedup. The effect of inclination angles on the pipeline interior with the multiphase flow was performed by Khaksarfard et al. (2013) using computational fluid dynamics. There was a wet-water surface in the pipeline when there was upward flow compared to when it was downward. This signifies that with the upward flow, more surfaces are susceptible to corrosion than in the situation where it is a downward flow. Thus, the application of corrosion-resistant alloys for making flexible pipes is highly needed for some energy (oil and gas) distribution operations, especially in gas lift lines, well tubing, and subsea risers, because they possess high resistance to corrosion (Guo et al., 2005).

A uniform corroded pipeline devoid of defects may be predicted directly with linear and non-linear models about the projected corrosion damage. However, the present defects, such as cracks, dents, buckles, and gouges around the corroded pipeline surfaces, could produce a more difficult estimation because these defects will have a greater stress load on the pipeline, leading to pressure burst at the corroded surfaces. The crack-in-corrosion defect is one of the defects that researchers have focused on. This defect is a hybrid one whose cracks are equally incident in a corroded surface, and the pipe wall thickness is consumed by 10% of this defect. To depict the influence of hybrid defects, Bedairi et al. (2012) examined corrosion, crack-in-corrosion, and cracking defects of pipelines with the aid of finite element analysis subjected to elastic–plastic fracture mechanics. This research was practically confirmed on 5.7 mm thickness and 508 mm diameter pipe. It was concluded that the corrosion defect was highly projected with 3.2% differences between FEA data and the practical outcome after examining the corroded depth percentages of 200 mm elongated defect and cracked wall thickness. This was tracked by crack-in-corrosion and crack defects, which have 17.4% and 12.4% differences between the practical outcome and FEA data, respectively. These results depict that the prediction accuracy of crack-in-corrosion defects should be enhanced so that the aging pipeline's integrity can be well managed. Diverse research has shown that flow configuration can impact pipeline corrosion (Hernandez-Rodriguez et al., 2007; Ilman, 2014). Biomorgi et al. (2012) experimentally analyzed the differential impact of operating parameters on energy (oil and gas) pipeline corrosion. It was revealed that after 4 months of experimentation, the impacts of iron carbonate, sand, flow pattern, and sulfide scales were hugely produced under deposits in the examined 102 and 154 mm diameter pipelines. Furthermore, the flow of the slug and pipe configurationcontributed to the corrosion mechanism more than the gas bubbles in the pipeline, and pitting corrosion was affected by the interior diameter of the pipeline. Papavinasam et al. (2010) synonymously established that subcutaneous materials, such as sand, were added to pitting corrosion development in energy pipelines. Pitting corrosion rates differ from phase to phase because of the flow velocities and configuration. However, Mazumder et al. (2008) ascribed these differences to particle-to-fluid, particle-to-particle, and particle-to-wall relationships at such phases. Production techniques have likewise been discovered to influence pipelines' vulnerability to corrosion, as revealed by Zhang et al. (2009) after examining the hydrostatic pressure impact on Fe-20Cr components. The outcome showed palpable pit

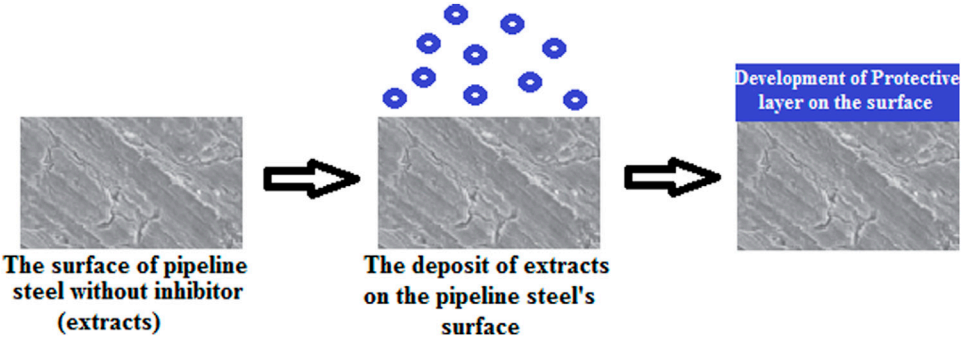

FIGURE 2
The adsorption of the protective layer (extracts) on a pipeline steel's surface.

development and growth rates and metastable pits enlargement into cavities.

1.2 The mechanism of corrosion inhibitor

The corrosion inhibitor operating system depends on the indirect or direct inhibitor molecules adsorbed on the metal surface, consequently shielding the contact of the harsh or corrosive medium from the metal surface. Common metallic substances are unstable naturally. For example, they are inclined to electrochemically react with destructive constituents of the medium (e.g., H^+ and Cl^-) to develop a steady corrosion product. Introducing corrosion inhibitors in the corrosive solution will yield adsorption on the metal surface in its active sites after protective film development, thus shielding it from corrosion. When inhibited by organic substances, metal surface passivation is highly important in contrast to inorganic inhibitors. For example, there is uniform passivation on the surface when organic inhibitors are applied, thus producing optimal feasible shielding. However, when inorganic inhibitors are applied, the passive film is very brittle, thus creating a metal surface liable to local corrosion occurrence (crevice, pitting) (Chadli et al., 2017).

Chemical or physical adsorption or the mixed mode of the two are the ways by which inhibitor adsorption may occur. The correlation between the inhibitor substances and a metal surface in any of the two methods described above relies on the substrate surface charge. The electrostatic relationship between the oppositely charged metal surface and the charged inhibitors produces inhibitor adsorption directly on the metal surface. However, the electrostatic correlation of previously adsorbed ions (e.g., ions of halide in amino acids) is the surface that is negatively charged, thus enhancing its efficiency to adsorbed proton inhibitors. This mechanism could particularly happen in acidic solutions. Hence,in the situation where the metal surface is of null charged, or no anions or cations which could undergo adsorption on the surface, inhibitor adsorption will happen via a chemical reaction between the inhibitor substance and the metal surface. Inhibitor adsorption will happen *via* a chemical reaction betwixt the inhibitor substances and the metal surface. Inhibitors are considered donor–acceptor reactants because they are electron donators in such a way that unpaired electrons of heteroatoms (e.g., S, N, and O) or the aromatic ring inhibitors of p-electrons react with a metal surface substrate of d-orbital to produce shielding layer. Some reactions of functional groups ($-NH_2$, $-OH$) with metallic ions can also configure a defensive film (insoluble complexes) that shields the surface of the metal from corrosion. Through molecular adsorption by a shielding film formation, organic inhibitors can inhibit corrosion when adsorbed on the metal surface (Amitha and Bharathi, 2012; Popoola, 2019a; Popoola, 2019b). The existence of phytochemicals, especially in plant derivatives, is applied to corrosion restrictors because their protective influence is owed to the inhibitor molecule adsorption on the metal surface, thus initiating a shielding layer on the metal surface *via* active site blockage (as shown in Figure 2 and Figure 3). Therefore, this protection is less reactive than the surface without an inhibitor. The substitution of π electrons and aromatic rings with heteroatoms is applied to initiate the corrosion inhibitor. Moreover, the inhibitor's solubility in a prevalent corrosive solution is due to the polar functional groups, which behave as the adsorption region for the inhibitor molecules (Anadebe et al., 2019; Abdelaziz et al., 2021).

1.3 Categories of green corrosion inhibitors/green inhibitors

Green corrosion inhibitors are hugely applied to regulate the various corrosion categories in diverse steel grades, especially in acidic mediums. These steel pipelines are needed to convey gas and oil in the energy industry. Green inhibitors can be categorized into two phases: organic and inorganic. High deliberation will only be channeled to organic green inhibitors

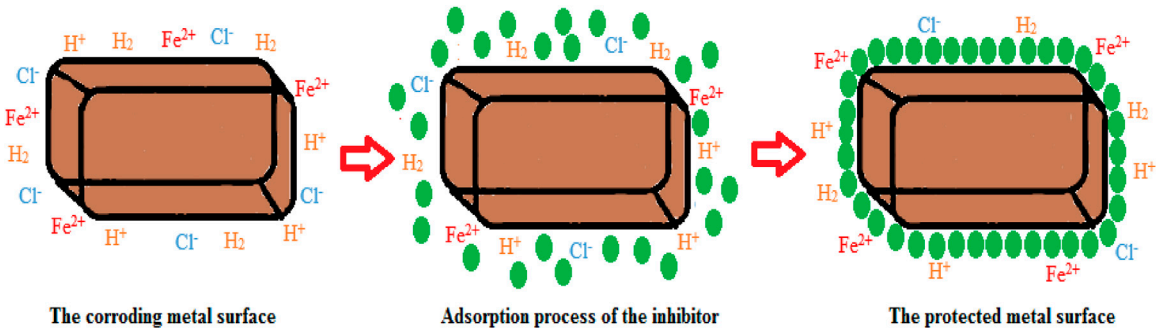

FIGURE 3
Illustrative diagram of how phytochemicals develop defensive layers on the metal surface.

for this research. Some diverse organic green inhibitors comprise ionic liquids, plants (oil and other derivatives), natural polymers, drugs, and biomass wastes. All these substances possess heteroatoms comprising elements with electron density, such as S, O, and N, acting as active phases for which they will be adsorbed on the metal area. Overall, organic inhibitors are more appropriate in an acidic solution; they have anodic or cathodic behavior and the two may coexist together. In contrast to inorganic inhibitors, organic green inhibitors display higher efficiency in corrosion inhibition. A huge amount of research in the past 6 years has concentrated on plant derivatives. Their outcomes depicted an outstanding capacity to inhibit steel corrosion in acidic environments. Synonymous results as regards amino acids and ionic liquids have been published (Nair, 2017; Rathi et al., 2017; Asmara et al., 2018; Verma et al., 2018; Popoola, 2019b; El Ibrahimi et al., 2020). Diverse organic inhibitors, such as drugs and natural polymers, have likewise revealed encouraging outcomes (Gece, 2011; Macedo et al., 2019; Shongwe, 2020). These organic inhibitors have functional groups in which heteroatoms are embedded (e.g., $-NH_2$, $-OH$, $-COOH$, and $-NO_2$) and/or molecular structures of aromatic rings, making them interact with metallic parts electrostatically or chemically. Therefore, this leads to the protective film development on the metal parts. Contrastingly, inorganic inhibitors are usually anodic, and thus, their bounded metal atoms' layer can enhance substrate corrosion shielding. Due to their unfriendliness to the ecosystem, their research and work for corrosion protection in materials have begun to decline.

1.3.1 The inhibitory performance of green inhibitors (plant extracts) for the prevention of pipeline steel (various grades) corrosion

There has been some substantial recognition of eco-friendly green inhibitors as corrosion resistance due to the harmful influence of conventional corrosion inhibitors. The plant extracts or derivatives have depicted excellent outcomes. Owing to the high polarity of these derivatives prompted as a consequence of unshared electrons in their functional groups, they made excellent adsorption mechanism for the steelcomponents. The other importance comprises biocompatibility, reliability, less cost, ease of application, and renewable nature. The following post-work emphasizes how "plant derivatives" have been applied as corrosion inhibition for different categories of steel, which can be used for energy distribution in pipelines.

Haldhar et al. (2018) used a theoretical and empirical approach for mild steel's IE with derivatives' root of *Valeriana wallichii* as a green inhibitor. Due to the several existing phytochemicals comprising iridoid and naphthoic acid. Observation revealed that iridoid derivatives gave the optimal inhibition efficacy for mild steel in an environment comprising acid. Figure 4 reveals the SEM image of the mild steel surface when dipped in 0.5 M of sulphuric acid for 24 h at 298 K in the existence of an inhibitor and without an inhibitor. The sample without the inhibitor in the corrosive medium was detected to develop a porous surface of wide tracks and deep holes from metal surface dissociation. However, the solution with inhibitor has its surface quality improved. In the HCl solution, the leaf plant derivative of *Aquilaria subintegra* has been discovered as the most effective inhibitor, with an optimum 94% inhibition for mild steel. The inhibition method of this derivative was analyzed as physisorption aligning to Langmuir adsorption isotherm.

Singh et al. (2013) introduced a theoretical route to examine plant derivatives such as *Murraya koenigii*, *Andrographis paniculata*, *Terminalia arjuna*, *Citrus aurantium*, *Strychnos nux-vomica*, *Aegle marmelos*, and *Moringa oleifera*, to ease the mild steel corrosion in the HCl solution. The abovementioned derivatives possess a set of effective phytochemical contents, such as brucine, andrographolide, mahabinine, sitosterol, arginine, pyrayafoline, skimmianine, brucine, and threonine. Diverse factors were examined in the experimental setup, such as dipole moment, lowest unoccupied molecular orbital, highest occupied molecular orbital, Mulliken charges on molecular

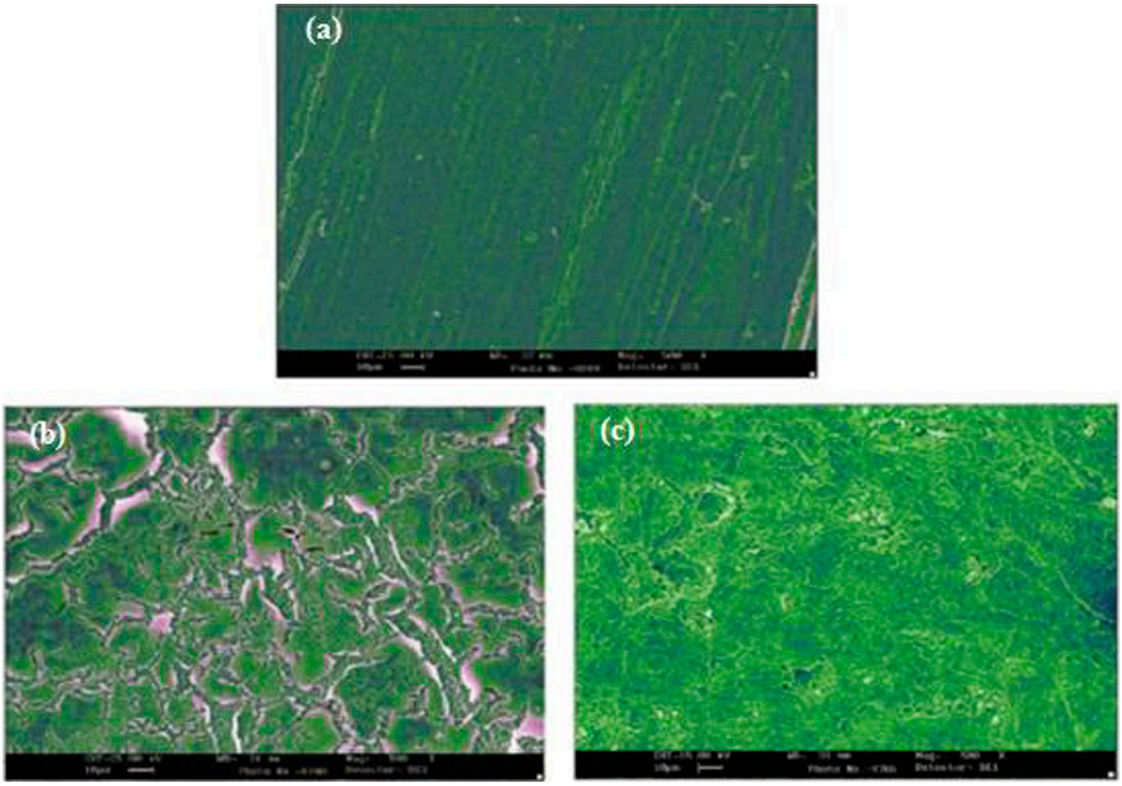

FIGURE 4
SEM image of a mild steel surface when submerged in 0.5 M of sulphuric acid for 24 h at 298 K, **(A)** polished sample **(B)** sample without inhibitor and **(C)** sample in presence of inhibitor.

capacity, and heteroatoms. The diverse plant derivatives showed suitable shielding efficiency because of the adherent inhibitor molecule adsorption on the mild steel surface. The outcomes demonstrated that the inhibitor adsorption features rely on diverse factors, such as molecular size, the number of adsorption phases, the development of metallic complexes, and interface nature.

Al-Turkustani et al. (2011) examined the protective behavior of alcohol derivatives of *Medicago sativa* plant and water to regulate the mild steel corrosion in a 2 M medium of sulphuric acid. Two chemical analysis methods were applied: the mass-loss technique and hydrogen evolution. The analysis behavior was performed in two processes: electrochemical impedance spectroscopy (EIS) and potentiodynamic polarization (PDP). It was discovered that the derivatives behave as a mixed inhibitor following the Langmuir adsorption isotherm. Moreover, the main corrosion defensive system was credited to the chemical adsorption *via* charge transference between the mild steel substrate and the inhibitor's molecules.

Dehghani et al. (2019b) conducted a theoretical and experimental investigation on the fruit derivatives of aqueous *Citrullus lanatus* (CL) in HCl media for inhibition against corrosion of mild steel. The functional groups of O-H and C=C in the phytochemicals, especially riboflavin, citrulline, resveratrol, and hesperetin, were found to be the reason why the 91% IE was attained. The synchronized reaction was likewise discovered to be a fundamental protective factor. Figure 5 describes the shielding behavior of CL derivatives on mild steel. The achieved outcome from SEM (Figure 6) revealed that a smoother surface on mild steel was attained as the CL concentration was increased.

Wei et al. (2020) estimated various plant extract parts comprising *Cassia occidentalis*, *Poinciana pulcherrima*, *papaya*, *Azadirachta indica*, *Calotropis Procera* B, *Cassia occidentalis*, and *Auforpio turkiale*. In all the abovementioned derivatives, *Poinciana pulcherrima Cassia* and *Azadirachta indica* revealed the optimum efficiency of 96% and 98%, respectively. Regarding polarization curves, these derivatives behaved as mixed inhibitors, hence decreasing iron anodic reaction dissolution and the hydrogen cathodic reaction change. Because the major parts for photosynthesis are plant leaves, these parts possess huge phytochemicals. This reason gives "leaves" a special selection for effectual green corrosion inhibition. The behavior of plant leaves derivatives of *Eriobotrya japonica* Lin. in an aqueous sulphuric

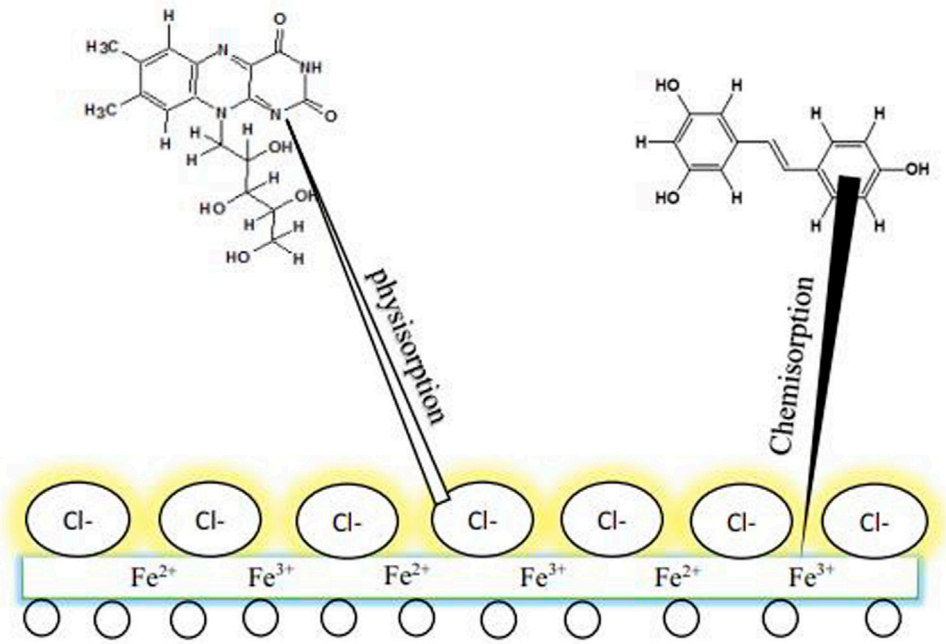

FIGURE 5
The adsorption system of CL extracts on mild steel in 1 M HCl medium (Dehghani et al., 2019b).

solution is worth stating. The outcome depicted that 96% efficiency could be attained for mild steel (Acharya et al., 2013). The evaluation, such as electrochemical measurements, weight-loss technique, and SEM, depicted that these derivatives were hugely cathodic inhibitors, thus satisfying the Langmuir adsorption isotherm. The combined influence of diverse phytochemicals in the derivatives was stated to be a major cause of their optimum IE.

Oguzie (2007) researched the shielding behavior of plant substances containing leaf derivatives such as *Azadirachta indica* (AI), *Ocimum viridis* (OV), *Garcinia kola* (GK), *Hibiscus sabdariffa* (HS), *Telfairia occidentalis* (TO), for mild steel in 1 M sulphuric acid and 2 M HCl. This experiment discovered that the plant derivatives possess adequate IE. The combined chemical adsorption with the halide ion's reaction of protonated organic substances for physical adsorption produces the optimal behavior of these constituents as an effective corrosion protector in the arrangement $Cl^- < Br^- < I^-$. Generally, peak inhibition efficiencies of 92.9% and 95% were achieved for GK and HS in 2 M HCl and 1 M sulphuric solutions, respectively.

Okafor et al. (2008) inspected the protective behavior of seeds (SD), leaves (LV), and the combined leave and seeds (LVSD) of *Phyllanthus amarus* (Pa) extracts in sulphuric and HCl media on mild steel corrosion. The behavior of the inhibition was examined with gasometric techniques and weight loss. The outcome revealed that the derivatives performed excellently as an excellent shield in both media, and the inhibition capacity improved with an upsurge in the extracts' concentration (Figure 7). The temperature examinations exhibited that the rise in IE resulted from the temperature rise. However, this led to the activation energy decrement in the extract existence. The inhibition performance is due to the extracts' chemical adsorption system on the metal surface. The adsorption inhibitor features were conformed to Temkin isotherm.

Another research examined rubber leaf derivatives as corrosion protective in HCl medium for mild steel (Okewale and Olaitan, 2017). FTIR and the gravimetric system were applied to analyze the shielding behavior. The derivatives' phytochemicals, such as flavonoids, saponins, tannins, and anthraquinone, produced 86% inhibition capacity. Moreover, the impulsive inhibitive adsorption conformed to the Langmuir isotherm. The plant IE relies on the quantity and the sorts of phytochemical changes in phases.

Eduok et al. (2012) assessed the inhibition capacity of *Sida acuta* plant stem and leaves for mild steel in a 1 M medium of sulphuric acid. Iodide ions were included in the medium to enhance their inhibition capacity. Weight loss and hydrogen evaluation measurements (HEMs) were the inhibition mechanism used at 30°C–60°C to determine shielding capacity. Although the inhibition followed similarly (Freundlich adsorption isotherm), the leaves were detected to possess a peak inhibition of 85.25%, which was attributed to the greater phytochemical percentage in the leaves.

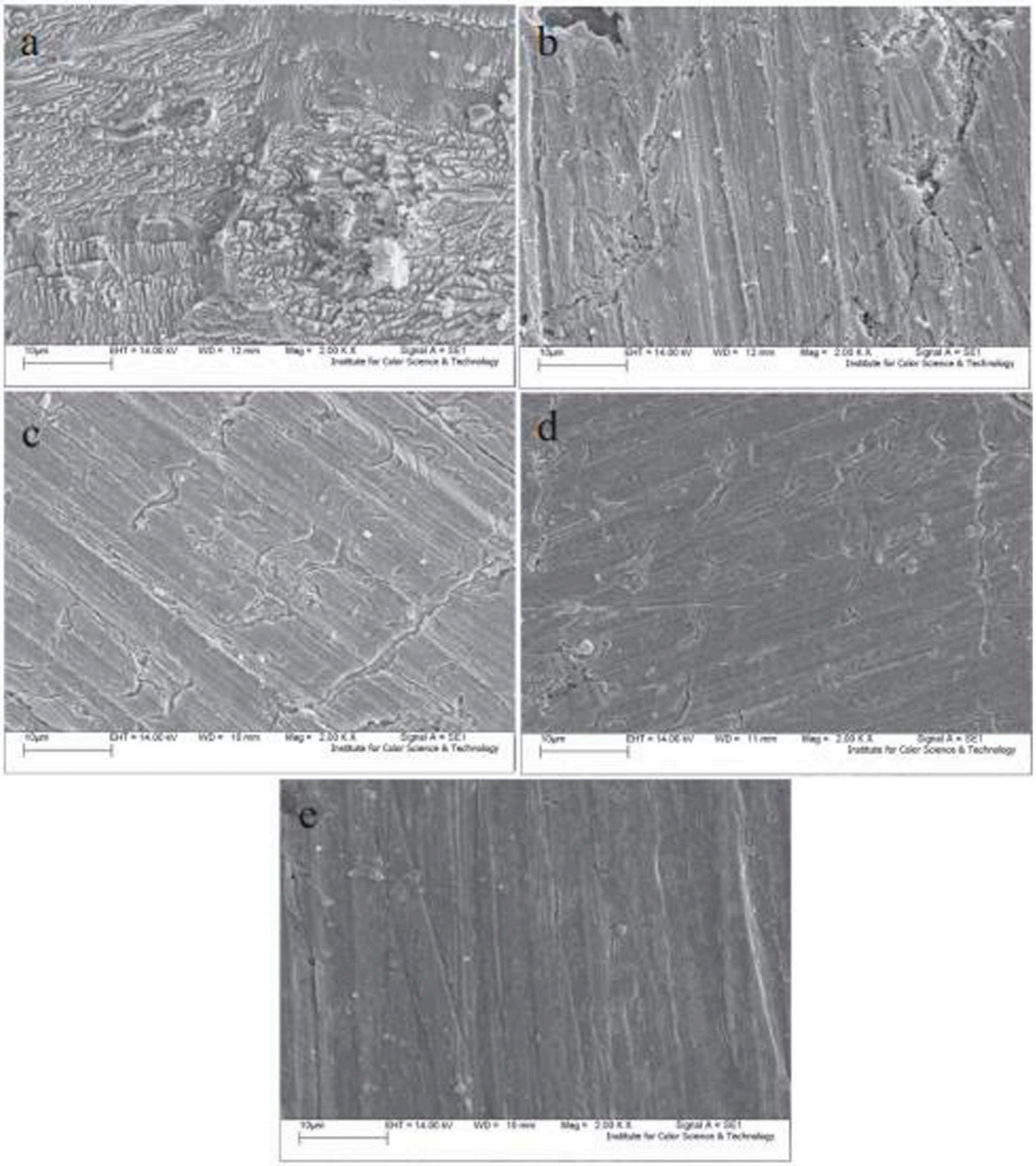

FIGURE 6
SEM image of mild steel for different concentration of Cl in 1M HCL—0 ppm **(A)** 200 ppm **(B)** 400 ppm **(C)** 600 ppm **(D)** and 800 ppm **(E)**.

Okafor and Ebenso (2007) juxtaposed the inhibitive behavior of diverse *Carica papaya* plant parts. They regarded leaves, bark (BK), seeds (SD), considered leaves (LV), and heartwood (HW) for the examination of mild steel in sulphuric acid. The plant derivatives are supplemented with organic compounds and nitrogenous substances such as saponins, choline, cardenolides, prunasin, anthraquinones, dehydrocarpaines, and pseudocarpaine. Gasometric and gravimetric systems were applied to determine the inhibition mechanism of the diverse components. All the derivatives were detected to restrict mild steel corrosion. Hence, the plant derivatives conform to the following arrangement with regard to the IE BK (85%) < HW (86%) < SD (94%) < LV (97.3%). The IE was detected proportionate to the concentration and inversely proportional to the temperature. Regarding the inhibition system, all the concerned derivatives involved phytochemicals' physical

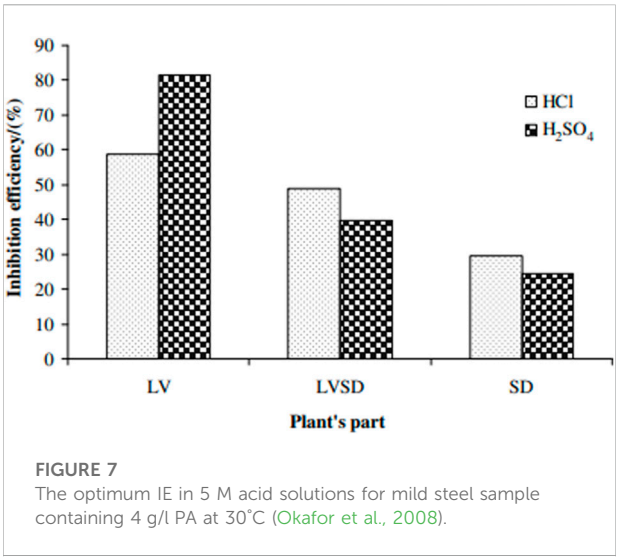

FIGURE 7
The optimum IE in 5 M acid solutions for mild steel sample containing 4 g/l PA at 30°C (Okafor et al., 2008).

adsorption on the metal surface. Furthermore, the Temkin and Langmuir isotherms aligned with the inhibitors.

Kumar and Mohana (2013) demonstrated that *Achyranthes aspera* L. plant derivatives could regulate mild steel corrosion in 1.0 M of HCl at normal temperature with 82.3% IE. Negative adsorption energy contributed to the instant adsorption actions, hence enhancing IE. The outcomes fitted perfectly with Flory–Huggins, Langmuir, and Frumkin adsorption isotherms. Furthermore, a spontaneous reaction was discovered between the molecules of the inhibitors, thus specifying an appreciable stability inhibitor in the acidic solution.

There are various findings on inhibitors, especially from a natural source that has appreciable efficiency for mild steel. They comprise pomegranate peel extract (Li et al., 2015), *Psidium guajava* seed extract (Kumar et al., 2011), *Neolamarckia cadamba* crude extract (bark, leaves) (Raja et al., 2013), panacea (*Flacourtia jangomas*) (Hasan and Sisodia, 2011), and *Salvia officinalis* oil (Chetouani and Hammouti, 2014). Some of these inhibitor mechanisms and efficiency are itemized in Table 1. These inhibitors align with chemical or physical adsorption. The main adsorption focus in organic compounds based on their reaction with steel surface is the oxygen-comprising hetero atoms in various derivatives phytoconstituents, such as phenolic compounds (specifically flavonoids). Derivatives such as fatty acids (linolenic acid), amino acids (methionine), tannins, steroids, antioxidant materials, and carbonyl groups are effective substances for the inhibition behavior of these derivatives.

Researchers have given plant oil derivatives huge recognition. Some important oils, which are also regarded as ethereal or volatile oils, are aggregated hydrophobic liquids that comprise sesquiterpene, monoterpene hydrocarbons, and oxygen-doped groups, such as acids, esters, ethers, alcohols, oxides, phenols, ketones, aldehydes, and lactones. Over the past ten years, various works have been conducted to determine IE for diverse metallic alloys using natural oils in alkaline, neutral, and acidic solutions. In the 1960s, the foremost effort to apply oil as a protective shield for the material was developed by Faraj and Khan (2015). They fruitfully applied molasses with vegetable oil in the acid pickling technique to prevent steel corrosion. Then, the utilization of natural oils as a material shield became common, hence providing other fruitful innovations, such as henna, ginger, artemisia, and jojoba oil (Buchweishaija, 2009; Azeiteiro et al., 2015; Nair, 2017). The adsorption on a metal surface by the mechanism of oil was simplified by Lahhit et al. (2011). *Foeniculum vulgare* was applied in this work as the examined oil, with steel applied as a substrate in an electrolyte of 1 M HCl. The Tafel polarization techniques, EIS, and weight loss characterizations were engaged to examine the protective mechanism. As vindicated *via* hydro-distillation, the oil comprised 17.8% pinene and 20.8% limonene. Through the reaction with the vacant iron atoms "d-orbitals," the two molecules (pinene and limonene) are adsorbed on the steel surface, thus producing a combined impact. As the oil concentration got risen, the adsorption rate was detected (*via* EIS analysis) to rise with the charge-transmission resistance. The polarization curves depicted that the incorporated natural oil changes the anodic and cathodic branches to the lesser currents, hence showing that the inhibitor oil was a mixed category.

Velázquez-González et al. (2014) investigated the protective performance of methanol, hexane, and acetone derivatives from the oil of *Rosmarinus officinalis*. Their behavior was examined in 0.5 M sulphuric acid for 1,018 steel. Every one of the derivatives depicted considerable optimum corrosion inhibitive features, though the 96% IE was depicted by the hexane derivative. The flavonoids in the derivatives are the attributing feature to the inhibitive performance. The derivative conforms to the isotherm of Frumkin adsorption, and its inhibitive attributes were controlled by the chemisorption system established by the adsorption free-energy value ($-37.4\ kJ.mol^{-1}$).

Different modern green capacity oil-based inhibitors have been applied in the past years. Some discoveries entail red pepper seed oil, *Nigella sativa* L. seed oil, palm oil, and *Artemisia mesatlantica* essential oil (Da Rocha et al., 2010; Machado et al., 2019). These inhibitors have depicted exceptional efficiency in acidic media with above 90%, hence revealing their capacity for industrial use. Some other important plant derivatives and oil-based inhibitors are presented in Table 1.

1.3.2 The inhibitory performance of green inhibitors (drugs) for the prevention of pipeline steel (various grades) corrosion

In the exploration of environmentally friendly corrosion protectors, drugs epitomize another invention that sprung from wide research and efforts produced over a decade. Drugs possess an appropriate potential for inhibitive features against corrosion similar to other inhibitors with similar molecular structures. For

TABLE 1 Some plant extracts and essential oil inhibitors for steel against corrosion in an acidic medium.

Category of inhibitors (plant extracts and oil inhibitors)	Corrosive media	Type of inhibitor	Category of steel	Type of adsorption mechanism or test methods	Inhibitor concentration	Parameters	IE	References
Cissus quadrangularis plant extract	1 M HCl	Mixed	Mild steel	Both chemical and physical adsorption	1,100 ppm	—	—	Mobin et al. (2019b)
Elaeis guineensis leaves extract	1 M HCl	Mixed	Mild steel	Physical adsorption	10% v/v	—	73.81%	Asaad et al. (2018)
Tragia involucrate L. (*T. involucrate* L.)	1 M HCl	Mixed	Low carbon steel	Both chemical and physical adsorption	0.25 g/L	—	87.54%	Chung et al. (2019)
Rosa canina fruit extract	1 M HCl	Mixed	Mild steel	Chemical adsorption	800 ppm	—	86%	Sanaei et al. (2019)
Extracts of *Chenopodium ambrosioides*	0.5 M sulphuric acid	Cathodic	Carbon steel	Chemical adsorption	4 g/L	—	94%	Bammou et al. (2014)
Extract of *Eucalyptus globulus* leaves	1 M sulphuric acid	Mixed	Carbon steel	Both chemical and physical adsorption	1.5 g/L	—	84%	Tezeghdenti et al. (2015)
Glycolipid biosurfactant	CH_3COOH	Mixed	Carbon steel	Physical adsorption	—	—	87%	Parthipan et al. (2018)
Lagerstroemia speciosa leaf extract	1 M HCl	Mixed	Mild steel	Both chemical and physical adsorption	500 ppm	—	94%	Mobin et al. (2019a)
Diospyros kaki (Persimmon) leaves	0.1 M HCl	Mixed	St37 steel	Both chemical and physical adsorption	200 mg/L	—	91%	Gerengi et al. (2016)
Adenopus breviflorus seed oil	0.5 M HCl	—	Mild steel	SEM, NMR, FTIR	0.5 mg/L	25 C, 35 C, 45 C	94.22%	Adewuyi et al. (2014)
Artemisia herba-alba oil	0.5 M sulphuric acid	—	Mild steel	GC, GC/MS	3 g/L	30 C, 40 C, 50 C, 60 C	88%	Hechiche et al. (2019)
The essential oil of *Salvia aucheri mesatlantica*	0.5 M sulphuric acid	—	Mild steel	GC, PDP, GC/MS, WLM, EIS	2 g/L	25 C	86.12%	Znini et al. (2012)
Red pepper seed oil	1 M HCl	—	304 stainless steel	FTIR, EIS, PDP	—	25 C, 35 C, 45 C, 55 C, 65 C	92.32%	Kurniawan and Madurani (2015)
Artemisia mesatlantica essential oil	1 M HCl	—	Carbon steel	PDP, XPS, SEM, EIS	2.76 g/L	25 C	92%	Boumhara et al. (2014)
Clove seed aqueous extract	1 M HCl	—	Carbon steel	EIS, DFT SEM, PP, AFM, MD	—	25 C	93%	Rathi et al. (2017)

instance, heterocyclic systems (e.g., isoxazoles, imidazoles, and furans) and carboxylic are numerously available in different categories of drugs and other various inhibitors. Synonymously, 5 or 6 participant rings with largely pseudo-aromatic or aromatic structures (e.g., benzene rings) are another similarity (Gece, 2011; Fouda et al., 2017; Singh et al., 2019a). Antibacterial drugs are among the various drug categories that have depicted excellent behavior in shielding steel corrosion in acidic environments. Various drugs, such as aminoglycosides, cephalosporins, and penicillin, have been stated to possess significant efficiency as green inhibitors. In the medicine industry, the highly applied drug is penicillin. It consists of heteroatoms in heterocycles regarded as b-lactam, which behave as an operative region for the adsorption mechanism. Moreover, adsorption happens because of the

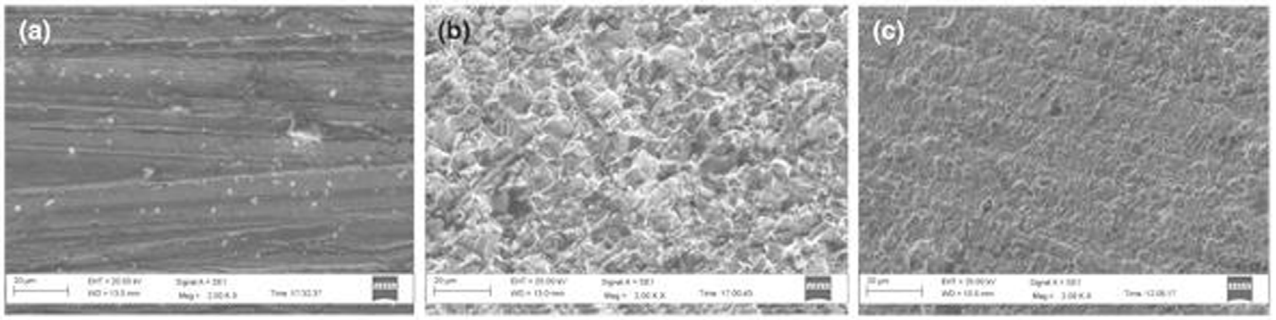

FIGURE 8
The SEM images of **(A)** polished sample, **(B)** sample submerged in a blank medium. and **(C)** sample submerged in an inhibited medium (Oguntuyi et al., 2021a).

p-electrons interaction in the drugs with metal surface "d-electron" valency, thus producing protective layer formation. Cephalosporins are similar to penicillin in action system and molecular structure (e.g., the fungus *Cephalosporin acremonium* derivative). Cephalosporins can be applied in situations where prohibition is ascribed to the use of penicillin. However, their inhibitive capacity is relatively less because they have lower solubility.

Liang et al. (2015) scrutinized the capacity of three sorts of penicillin (i.e., amoxicillin, ampicillin, and penicillin G) for carbon steel corrosion protection in 1 M HCl. The behavior was examined *via* EIS, PDP, and electrochemical noise checks. The outcomes showed that the active region needed for drug adsorption on the steel surface is the b-lactam rings' oxygen atom. Moreover, the measured drugs had high solubility, hence providing a good adsorption rate and inhibition capacity. In all the drugs, a chemisorption system was observed for penicillin G, whereas the physisorption mechanism followed the other two, thus producing 96% optimum efficiency for penicillin against 74.2% ampicillin and 61.2% amoxicillin.

Oguntuyi et al. (2021a) evaluated the drug (acarbose), with the molecular name of dideoxy-4-4,5,6-trihydroxy-3-(hydroxymethyl)cyclohexane-2-en-1-yl C7 cyclitol moiety, as a protective substance against corrosion for mild steel. Langmuir adsorption isotherm was confirmed owing to the inhibitor adsorption on the mild steel surface. The comprehensive theoretical study of the corrosion and inhibitor mechanism was achieved by computational evaluation, such as density functional theory and molecular dynamic simulations. From all the collective outcomes, significant IE was achieved. At the concentration of 4,000 ppm, optimum IE of 96% was noted. The microstructural evaluation *via* SEM (Figure 8B) revealed that the sample without acarbose as the inhibitor displayed a huge rough surface, which can be ascribed to the metal disintegration by the acidic media. However, a minute rough surface (Figure 8C) can be noticed for the sample immersed in the inhibited media (Marsoul et al., 2020), revealing the establishment of an efficient defensive layer on the sample's surface.

Talari et al. (2019) demonstrated the behavior of twin imidazole-based drugs (namely, 2-methyl-1, 3-thiazole-4-carboxylic acid and thiazole-4-carboxylic acid) by applying HCl solution as an electrolyte for the electrochemical examinations. A higher IE of 90% was depicted by the drug: thiazole-4-carboxylic acid of 150 ppm concentration at 25°C. It was concluded that the adsorption rate of the two inhibitors conforms to the Langmuir isotherm with a quickened adsorption mechanism. The charges of the dipole moment revealed effective adherence of the inhibitors on the metal surface.

Singh et al. (2019a) suggested that an outdated drug can likewise be applied efficiently as corrosion shielding. Two outdated drugs (i.e., dapsone-salicylaldehyde and dapsone-benzaldehyde) were examined to determine their inhibitive capacity. Examinations showed that outdated drugs could produce high efficiency of 94.23%–95.67% between the two. Potassium iodide ions were included in the HCl media to corroborate the drug's inhibitive capacity. They discovered that drug efficiency was enhanced to 97.98% and 99.03%, respectively.

In the area of green inhibitors when using drugs, the urispas drug is highly regarded as one of the efficient inhibitors. PDP, gravimetric measurements, and EIS tests were applied to determine the inhibitive performance. The drug was investigated on sulphuric acid using soft steel as the specimen. The IE reaches the optimal value of 97.85% when the inhibitor concentration rises to 1,000 ppm. The capacity of urispas to inhibit steel corrosion was deduced from its effective performance even at a lower concentration of 150 ppm (Anaee et al., 2019). Some other important drugs as green inhibitors are presented in Table 2.

TABLE 2 Some drug inhibitors for steel against corrosion in an acidic medium.

Category of inhibitors (drug inhibitor)	Corrosive media	Category of steel	Test methods	Type of adsorption mechanism	Inhibitor concentration	IE	References
Thiazole-4-carboxylic acid	0.1 mol/L HCl	Mild steel	MCS, QCC	Langmuir	150 ppm	~90%	Talari et al. (2019)
Carbamazepine	0.1 mol/L sulphuric acid	Carbon steel	Electrochemical	Langmuir	—	90%	(Vaszilcsin, Ordodi, Borza)
Chloramphenicol	0.1 M HCl	A315 mild steel	Electrochemical, WLM	Langmuir	10%	85.321%	Ayoola et al. (2018)
Melatonin	0.5 M HCl/ sulphuric acid	Mild steel	Electrochemical	Langmuir	500 ppm	94.76%	Al-Fahemi et al. (2016)
Expired etoricoxib	0.5 M H_3PO_4	Carbon steel	X-ray, SEM	Langmuir	225 ppm	80.627%	Anaee et al. (2019)
diethylenetriamine	1 M HCl	Mild steel	SFG, RSM	Langmuir	25 mg/L	92.67%	Baig et al. (2019)
Clopidogrel	1 M HCl	Carbon steel	DFT, electrochemical	Langmuir	800 ppm	95%	Naseri et al. (2018)
Penicillin G	1 M HCl	Carbon steel	Electrochemical	Langmuir	1 mM	75.4%	Liang et al. (2015)
Chemically modified expired dapsone	Sulphuric acid	Mild steel	DFT	Langmuir	0.219 mM	95.67%–94.23%	Singh et al. (2019a)
Ondansetron hydrochloride	1 M HCl	Mild steel	FTIR, electrochemical, AFM, EDX, SEM	Langmuir	300 ppm	90.4%	Vengatesh et al. (2017)
Expired antituberculosis drug isoniazid	1 M HCl	Mild steel	SEM, electrochemical, AFM, EDX, XPS	Langmuir	—	—	Singh et al. (2019b)

*MCS, Monte Carlo simulation; QCC, quantum chemical calculation; RSM, response surface method; SFG, sum frequency generation spectroscopy.

1.3.3 The inhibitory performance of green inhibitors (biomass waste) for the prevention of pipeline steel (various grades) corrosion

Biomass waste is one of the organic inhibitors applied to inhibit corrosion. Numerous works have been conducted on organic inhibitors (plant derivatives, amino, and drugs). However, little research has been conducted to determine biomass waste's efficiency as a corrosion inhibitor. Some studies experimenting with the inhibitive features of biomass waste are stated below.

Gapsari et al. (2019) applied the derivatives from the honeycomb waste as an inhibitor for stainless steel in the sulphuric medium. The inhibitor's concentration (about 2,000 mg/L) initiated the increase in the stainless corrosion rate. However, it declined when the concentration was 3,000–4,000 mg/L. Hence, the 97.29% IE was attained when the 2,000 mg/L inhibitor concentration was used in 0.5 M sulphuric acid. The inhibitive feature is connected to the adsorption performance of the honeycomb derivative because it contains vitexin, pinobanksin, luteolin, apigenin, fisetin, isoferulic, quercetin, and isorhamnetin.

Cruz-Zabalegui et al. (2019) used a gemini surfactant extracted from avocado oil on API X-52 steel as a CO_2 inhibitor. The examination depicted that at the inhibitor's concentration of 10–50 ppm, for 24 h at the temperature of 50°C, the compound shielded the steel because of the physical adsorption. Liao et al. (2018) revealed that the waste achieved from peel and seed (lychee) is realistic to undergo recycling and applied as an ecologically friendly inhibitor in 0.5 M HCl media on mild steel, with the inhibitor's concentration getting to 600 mg/L to attain the highest protection. The waste materials derived from eggshell was examined to hugely change the austenitic stainless steel corrosion inhibition (Sanni et al., 2018). It was further revealed that the inhibitor concentration increment restricted the passive film development, and the optimal shielding capacity of 94.74% was attained *via* weight loss scrutiny.

Montoya et al. (2019) applied the *Pinus radiata* bark as organic corrosion on 1020 steel. The biomass was extracted from the wastepaper and timber industries. The development of tannin-Fe acted as the shielding coatings.

One of the constant diets for humans is *Prunus dulcis* (almond), though its peel is regarded as waste. Pal et al. (2019) applied this waste substance for corrosion protection for mild steel. The inhibition capacities of 85% and

93% were attained, respectively, when aqueous and methanolic almond extracts shielded the mild steel. AFM and SEM examination revealed this greater efficiency of methanolic extract. It was vindicated that methanol comprises higher phytochemicals than water, such as chlorogenic acid, isorhamnetin-3-O-rutinoside, and catechin, which are accountable for mild steel protection. The extracts are categorized as a mixed type, where the adsorption is impure chemical or physical.

Munawaroh et al. (2022) evaluated the inhibitive behavior of protoporphyrin. A biomass waste derived from animal blood hemin was applied to carbon steel in 0.5 M HCl. The protoporphyrin quantity was evaluated as 40–200 ppm at a temperature variation of 298–318 K. The IE of 46.2% was attained with a concentration of the inhibitor at 160 ppm in the acidic solution at 298 K. However, with further increment in the temperature, the IE declined, thus indicating the exothermic nature of the reaction that consequently weakened the adsorption of the inhibitors on the carbon steel surface. A mixed-type inhibition was observed for the inhibitor as detected by the potentiodynamic polarization test. Furthermore, Langmuir adsorption isotherm was obeyed due to inhibitor adsorption on the steel surface.

Dehghani et al. (2019a) investigated that the fruit shell of Chinese gooseberry contains maltose, sucrose, and folate aqueous derivatives. These derivatives were examined as corrosion inhibitors in HCl media on carbon steel. The steel insertion in 1,000 ppm concentration of the inhibitors developed 92% shielding capacity. The achieved outcome *via* EIS collaborates with molecular simulation discoveries, which revealed that amidst the three main organic compositions, folate has an optimum inhibition mechanism over maltose and sucrose. Furthermore, amine groups, carbonyl, hydroxyl, and imine, with nitrogen and oxygen centers, are liable for the folate's higher inhibition system in contrast to the other two.

Fiori-Bimbi et al. (2015) discovered the derivation of pectin from the citrus peel as a corrosion inhibitor in HCl media for mild steel. The inhibitor concentration of about 2.0 g/L at 45°C produced 94.2% inhibition capacity *via* anodic and cathodic metallic surface shielding. Furthermore, Grassino et al. (2016) and Ninčević Grassino et al. (2020) depicted that pectin achieved from the waste of tomato peel can be applied as an environmental corrosion shield for tin. The corrosion examination mechanized in a citric acid/NaCl/acetic acid indicated that pectin produced 65.8% and 73% inhibition capacity for EIS and PDP, respectively, at less concentration of 4 g/L.

Adewuyi and Oderinde (2018) evaluated the inhibition capacity of *Khaya senegalensis* fatty hydroxylamine (KSFA) in an HCl solution for aluminum. The unused seed oil and its breakdowns, such as hydroxylation, esterification, amidation, and transesterification, were applied to create KSFA. The inhibition capacity of 90.43% was attained with 0.001 mg/L inhibitor concentration. This efficiency was associated with heteroatoms' presence in the KSFA.

Tiwari et al. (2018) examined the *Musa paradisiaca* peels in sulphuric and HCl acids for corrosion protection on mild steel. Ethyl acetate was derived from the peel, and the electrochemical tests indicated that the peel derivatives prevent the mild steel from corrosion in both acidic solutions, owing to aromatic rings and heteroatoms abundance (nitrogen and oxygen), which are adsorbed on the surface *via* an electrostatic or chemical interface with iron atoms. However, the derivative of banana peel consists of various bioactive compounds. Hence, they could influence the overall protective behavior of the derivatives. The inhibition mechanism is ruled by the gallocatechin molecule.

Generally, the inhibitive capability of beneficial-added compounds from underused and abundant materials paves the way for manufacturing modern categories of inhibitors, which could be applied as a shield against corrosion after general quantitative and qualitative examinations. Some biomass wastes and their extracts for corrosion inhibitors are tabulated in Table 3.

1.3.4 The inhibitory performance of green inhibitors (amino acids) for the prevention of pipeline steel (various grades) corrosion

The biodegradability and non-toxicity of amino acids have made them good corrosion inhibitors. Amino acids have molecules with at least an amino group (-NH_2) and carbonyl group (-COOH) attached with a single carbon atom in their structure. Moreover, amino acids have good solubility in aqueous solutions. They can be produced easily with high purity and are comparatively cheap. Amino acids can be categorized into various classes depending on their molecular structure, such as sulfur-containing cationic/anionic, W-amides, linear aliphatic, aromatics, and heterocyclic. (El Ibrahimi et al., 2020). The appearance of heteroatoms (e.g., O, N, and S) and associated p-electrons in their structure make the acids possess excellent inhibitive capacity against corrosion.

Some green inhibitors, such as tryptophan, imidazolium zwitterions, and konjac glucomannan, are excellent among diverse amino acid-based agents because they have outstanding shielding properties (Abdel-Fatah et al., 2017; Srivastava et al., 2017). In the inhibitors mentioned earlier, imidazolium zwitterions have depicted 96.08% inhibition, whereas the others have also been examined to have above 90% inhibition. The effective inhibitor adsorption on the steel surface is attained *via* mixed adsorption, which obeys the Langmuir isotherm.

Gong et al. (2019a) evaluated the protective capacity of amino acids against corrosion. Three halogen-alternated extracts [2-amino-4-(4-chlorophenyl)-thiazole (CPT), 2-amino-4-(4-fluorophenyl)-thiazole (FPT), and 2-amino-(4-bromophenyl)-thiazole (BPT)] were examined by temperature variation of 30°C–60°C. The electrochemical analysis depicted that BPT and CPT produced 95.45% and 95.16%, respectively. However, these efficiencies were sustained at elevated

TABLE 3 Some biomass wastes and their extracts for corrosion inhibitors.

Category of inhibitors (biomass wastes and their extracts)	Corrosive media	Category of steel	Concentration of inhibitor	Inhibition efficiency	References
Pectin from citrus peel	1 M HCl	Mild steel	2 g/L	94.2%	Fiori-Bimbi et al. (2015)
Peel and seed of lychee	0.5 M HCl	Mild steel	600 mg/L	97.95%	Liao et al. (2018)
Eggshell	0.5 M sulphuric acid	Stainless steel (316)	2—10 g	94.74%	Sanni et al. (2018)
Gallocatechin from *Musa paradisiaca* peel	0.5 M sulphuric acid	Mild steel	400 mg/L	85%	Tiwari et al. (2018)
Gallocatechin from *Musa paradisiaca* peel	1 M HCl	Mild steel	400 mg/L	91%	Tiwari et al. (2018)
Quercetin from honeycomb	0.5 M sulphuric acid	Stainless steel (304)	2,000 mg/L	97.29%	Gapsari et al. (2019)
Maltose, sucrose, and folate from gooseberry fruit shell	1 M HCl	Carbon steel	1,000 ppm	91.9%	Dehghani et al. (2019a)
Chitosan from shrimp shell	1 M HCl	Carbon steel	0.00001 M	88.50%	Hussein et al. (2013)
Spirulina maxima	1 M HCl	Carbon steel	100 m/L	96.40	Rodrigues et al. (2018)

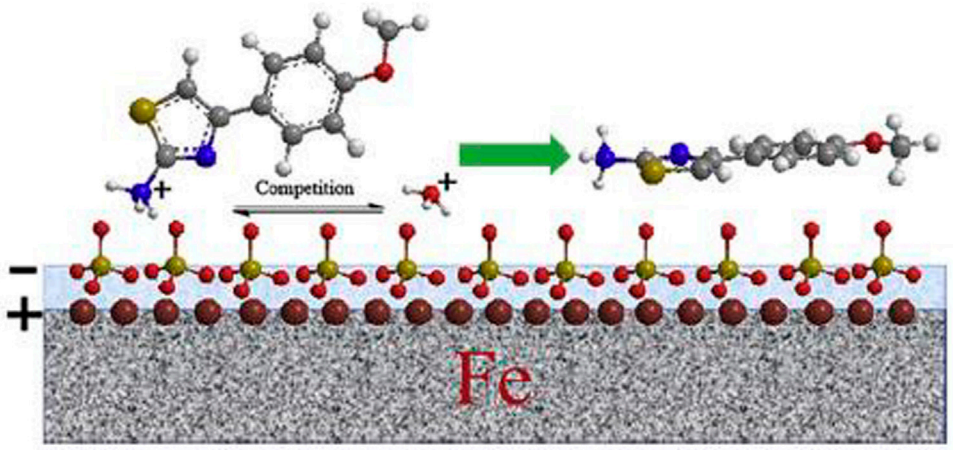

FIGURE 9
MPT adsorption system in a sulphuric solution on a mild steel surface (Gong et al., 2019a).

temperatures up to 60°C. Hence, this was attributed to the elevated stability behavior in the binding energy between the metal surface and inhibitors. FPT has 95% inhibition, although it decreased at 60°C by 22.62%. Furthermore, the authors examined the IE of 2-amino-4-(4-methoxyphenyl)-thiazole (MPT) in 0.5 sulphuric acids for mild steel against corrosion. Figure 9 reveals the diagrammatical representation of the adsorption system. Synonymous properties of this corrosion inhibition system were also observed in other categories of inhibitors. The introduction of the mild steel specimen into the corrosive solution caused a positive charge to form on the metal surface. However, the adsorption in the next stage of the mechanism happened in a way that the electrostatic energy in the acid medium produced negatively charged sulfate ion adsorption on the metal surface. Hence protonated H + and MPT were adsorbed on the steel surface (negatively charged), and the hydrogen evolution decreased because of the adsorption opposition. After that, the adsorption process stability developed chemical adsorption *via* covalent bond formation between Fe atoms and MPT molecules. Furthermore, the

TABLE 4 Some amino acid inhibitors for steel against corrosion in an acidic medium.

Category of inhibitors (amino acid inhibitors)	Corrosive media	Category of steel	Test methods	Parameters	IE (%)	References
2-Amino-4-(4-methoxyphenyl)-7,7-dimethyl-5-oxo-5,6,7,8-tetrahydro-4hchromene-3-carbonitrile (ap-1)	15% HCl	N80 steel	AFM, SEM	35 C	97.7	Singh et al. (2018)
2-((1h-Indol-2-yl)thio)-6-amino 4-phenylpyridine-3,5 dicarbonitriles	1 M HCl	Mild steel	EIS, WLM, AFM, OCP, EDX	35 C–65 C	96.6	Gong et al. (2019a)
Tetra-n-butyl ammonium methionine-nate	1 M HCl	Mild steel	EDX, SEM, EN	25 C	95.1	Kowsari et al. (2016)
Tryptophan	0.6 M HSO_3NH_2/ 0.6 M HCl	Low alloy steel	EIS	25 C–60 C	94.46	Abdel-Fatah et al. (2017)
Cysteamine modified PASP (PASP-s)	0.5 M H_2SO_4	Mild steel	XPS, WLM, OCP, SEM	35 C	91.8	Ghareba and Omanovic (2010)
(S)-6-Phenyl-2,3,5,6-tetrahydroimidazo [2,1-b] thiazole hydrochloride	0.5 M HCl	N80 steel	AFM, SEM, FTIR	30 C–60 C	96.4	Dehghani et al. (2019c)
2-nh2-Sulfamerazine	1.0 M HCl	Mild steel	DFT, SEM	30 C–60 C	90.55	Gece and Bilgiç (2010)
2-Amino-4-(4-fluorophenyl)-thiazole	0.5 M H_2SO_4	Mild steel	SEM, EIS	30 C	95.45	Gong et al. (2019b)
2-(3-(1-Carboxy-2-phenylethyl)-1himidazol-3-ium-1-yl)-3-phenylpropanoate (aiz-3)	1 M HCl	Mild steel	AFM, EDX, SEM	30 C	96.08	Srivastava et al. (2017)
2-Amino-4-methylpentanoic Acid (lcn)	1 M HCl	High carbon steel	OMI, WLM	30 C	85.88	Loto (2019)

*FTIR, Fourier-transform infrared spectroscopy; OCP, open circuit potential; EDX, energy dispersive X-ray; OMI, ozone monitoring instrument; EN, electrochemical noise.

relationship between chemical and physical adsorption produces defensive layers on the surface, thus shielding the mild steel in an acidic medium.

Verma and Ma (2014) demonstrated inhibitive extracts feature of 2-[(1H-indol-2-yl)thio]-6-amino-4-phenyl pyridine-3,5-dicarbonitriles (TAPD) in 1 M HCl for mild steel. Computational evaluation and diverse experimental analysis (PDP, WLM, EDX, and SEM) were all conducted. At least minimum efficiency of 90% was attained, showing that all extracts behaved well even at low concentrations of the inhibitors. It was observed that when the amino acid TAPD-III was substituted with –OH compound, a higher efficiency was developed than when replaced with NO_2 compound. Furthermore, the mechanism behaves as mixed inhibitors, which align with the Langmuir adsorption isotherm.

Loto (2019) evaluated the corrosion inhibition of 2-amino-4-methylpentanoic acid on carbon steel in 1 M acid solution (HCl). The outcomes obtained from the electrochemical examination revealed that the compound produced 85.88% and 87.46% inhibition efficiencies at 1.88% and 0% of the inhibitor concentration, respectively. Thermodynamic evaluations *via* Frumkin isotherm and Langmuir models depicted the adsorption and interaction of chemisorption molecules on the carbon steel surface.

Amino acids often conform to a synergism mechanism, similar to other inhibitors. This synergism mechanism occurs when surfactants are introduced into amino acids, which consequently enhances their protective efficiency to a high level. The synergistic influence of L-cysteine (CYS) and imidazoline derivative (IM) on carbon steel was investigated by Zhang et al. (2018). Similarly, Srivastava et al. (2017) discovered that increase in efficiency up to 84.66% was observed when the surfactant of cetyltrimethylammonium bromide and surfactant sodium dodecyl sulfate (SDS) were included in amino acid L-methionine. Some other worthwhile inhibitive capacities of amino acids are presented in Table 4.

2 Limitations of green inhibitors and their future outlook

Green inhibitors have been employed extensively in managing the corrosion problems of steels, particularly in acidic conditions, according to the research articles listed here. Plants extracts (e.g., peel, root, flower, wood, fruit, seed, and bark) and oils are discovered to be the most numerous sources of green inhibitors among the various groups of inhibitors. They are widely available and comparatively inexpensive in contrast to other forms of green inhibitors. Additionally, they contain several active ingredients and can be obtained using straightforward extraction procedures. However, items extracted from naturally occurring consumable sources (e.g.,

fruits and vegetables) must be gathered over a long period because they are seasonal and takes time to harvest. This could decrease their large-scale manufacture and industrial applicability. Furthermore, some of the important resources that have been evaluated for the creation of green inhibitors have competitive uses in the pharmaceutical and medical industries, as well as in other human requirements. According to the literature review, researchers do not place a high value on biowaste extracts. As a result, a thorough study procedure that investigates the extract characterization and the key corrosion inhibition elements, as well as theoretical investigations, from widely available waste sources, could significantly contribute to this sector.

The efficiency of corrosion inhibition is governed by active compounds contained in green inhibitors, such as phenols, flavonoids, pectin, and aldehydes. The amount of such a chemical in a certain extract is expected to change depending on the weather and location of such material sources. Additionally, these have restricted the rationalization of laboratory findings for various inhibitors to justify their industrial implementation. Therefore, the recognition of this feature during characterization can result in inhibitor consistency in an industrial setting. Furthermore, a good understanding (insight) of molecular structure and its impact on corrosion inhibition might help with inhibition performance enhancement.

Despite the extensive experimental effort and several research articles published in the field, there remains a gap in the scientific method, with the results frequently phenomenological and not often theoretical and mechanistic. Corrosion inhibitor evaluation is typically done through electrochemical studies to directly determine its efficiency in the ultimate use as corrosion protecting substance instead of focusing on the precise adsorption process and associated mechanisms. Another significant limitation is the poor identification of the effective ingredient in the green extract, which is frequently a combination of unidentified compounds. The inability to correctly identify the inhibitive substances, whether they inhibit alone or synergistically, is the other adsorption mechanism that needs further clarification. The inhibitory effect could be due to a single molecule or a synergistic impact of the complete extract. This inefficient identification is an issue that is frequently overlooked in the literature, thus restricting the reproducibility of outcomes in this area.

Another weak point worth of note in utilizing green inhibitors is their inability to endure high temperatures and storage concerns. When it comes to extracting natural compounds, the temperature has a significant impact. At low temperatures, the solubility of phytochemical compounds in extraction solvents is diminished, although, at elevated temperatures, the phytochemicals may decompose. The ideal temperature for a successful extraction is 60°C–80°C. Oven drying is somewhat advised because drying at normal temperature can consume a huge duration. Additionally, the efficiency of green inhibitors declines as the operational temperature rises for industrial applications, and trying to store them for an extended period causes them to degrade. More studies are needed to understand the impacts and use of additives such as iron control agents, anti-sludge agents, surfactants, and stabilizers to green inhibitors, as well as the formulation of composites with high refractoriness. These elements may not be inhibitory, but they may add to the corrosion inhibition properties of green inhibitors and enhance the temperature challenges.

Green inhibitors are generally efficient corrosion inhibitors in a variety of corrosive conditions. The main benefits of these inhibitors are their non-toxicity and biodegradability. Future research should be conducted under the guiding principle of a huge economic perspective with a clear evaluation of the obtainability and price of the green inhibitor source and the manufacturing procedure for huge-scale usage. The use of green inhibitors is an advanced practice that is environmentally benign, long-lasting, and cost-effective for steel protection. These days, corrosion prevention applications from nanoparticles are being researched. The usage of green inhibitors, however, continues to be a far safer and more environmentally friendly choice. The application of green inhibitors is possibly going to expand in the future as constant additional discoveries are made in this area.

3 Conclusion

The challenges of corrosion in the energy (oil and gas) industry are an unavoidable experience. Thus, full inhibition of this scenario is not feasible. However, proffering a preventive mechanism is more proficient and economical. This can be actualized by inhibiting the surface of the metal from the corrosion medium. The system of conventional (organic) inhibitors against corrosion has been prominent in use for a long time. In contrast, commercial inhibitors (usually inorganic) have been limited over time because of their toxic nature, which contributes to environmental (habitat) annihilation. Hence, organic inhibitors are highly preferred to other inhibitors because of their availability, low cost, environmentally benign and renewable nature, biodegradability, optimal efficiency, and natural compatibility. Therefore, this review has elaborated on the inhibitory mechanism of organic inhibitors, especially plant extracts, amino acids, drugs, and biomass waste. The phytochemicals generated from plant derivatives, the amino group (NH_2) present in the molecular structure of amino groups and drugs' molecular weights, and the shielding effect

of biomass wastes are the major inhibitory properties of these organic inhibitors against corrosion. From the various literature, it is well understood that the increment in the inhibitor concentration consequently enhances the sample's resistivity to corrosion. Although some situations were observed where irrespective of the increment in the inhibitor's concentration at some high temperature, there was no improvement in the samples' IE. Hence, this evaluation revealed that some organic inhibitors could thrive under any circumstances (temperatures, pressure, and other parameters), whereas others may not sustain their inhibition at certain parameters. Therefore, judicious parameters should be considered before the selection and use of any organic inhibitor as a corrosion inhibitor for different pipeline steel.

Author contributions

AA: data curation, methodology, and original draft. AP: proofreading, editing, and supervision. DM: data analysis. OS: data analysis.

Acknowledgments

The authors would like to thank the Surface Engineering Research Laboratory (SERL), Tshwane University of Technology, Pretoria, South Africa for their assistance.

Conflict of interest

The authors declare that the research was conducted in the absence of any commercial or financial relationships that could be construed as a potential conflict of interest.

Publisher's note

All claims expressed in this article are solely those of the authors and do not necessarily represent those of their affiliated organizations or those of the publisher, the editors, and the reviewers. Any product that may be evaluated in this article, or claim that may be made by its manufacturer, is not guaranteed or endorsed by the publisher.

References

Abdel-Fatah, H. T. M., Kamel, M. M., Hassan, A. A., Rashwan, S. A., Abd El Wahaab, S. M., and El-Sehiety, H. E. (2017). Adsorption and inhibitive properties of Tryptophan on low alloy steel corrosion in acidic media. *Arabian J. Chem.* 10, S1164–S1171. doi:10.1016/j.arabjc.2013.02.010

Abdelaziz, S., Benamira, M., Messaadia, L., Boughoues, Y., Lahmar, H., and Boudjerda, A. (2021). Green corrosion inhibition of mild steel in HCl medium using leaves extract of Arbutus unedo L. plant: An experimental and computational approach. *Colloids Surfaces A Physicochem. Eng. Aspects* 619, 126496. doi:10.1016/j.colsurfa.2021.126496

Acharya, M., Chouhan, J. S., Dixit, A., and Gupta, D. K. (2013). Green inhibitors for prevention of metal and alloys corrosion: An overview. *Chem. Mater. Res.* 3 (6), 16–24.

Adewuyi, A., Göpfert, A., and Wolff, T. (2014). Succinyl amide gemini surfactant from adenopus breviflorus seed oil: A potential corrosion inhibitor of mild steel in acidic medium. *Industrial Crops Prod.* 52, 439–449. doi:10.1016/j.indcrop.2013.10.045

Adewuyi, A., and Oderinde, R. A. (2018). Synthesis of hydroxylated fatty amide from underutilized seed oil of Khaya senegalensis: A potential green inhibitor of corrosion in aluminum. *J. Anal. Sci. Technol.* 9 (1), 26–13. doi:10.1186/s40543-018-0158-9

Al-Fahemi, J. H., Abdallah, M., Gad, E. A., and Jahdaly, B. (2016). Experimental and theoretical approach studies for melatonin drug as safely corrosion inhibitors for carbon steel using DFT. *J. Mol. Liq.* 222, 1157–1163. doi:10.1016/j.molliq.2016.07.085

Al-Turkustani, A. M., Arab, S. T., and Al-Qarni, L. S. S. (2011). Medicago Sative plant as safe inhibitor on the corrosion of steel in 2.0 M H2SO4 solution. *J. Saudi Chem. Soc.* 15 (1), 73–82. doi:10.1016/j.jscs.2010.10.008

Alao, A. O., Popoola, A. P., and Sanni, O. (2022). The influence of nanoparticle inhibitors on the corrosion protection of some industrial metals: A review. *J. Bio-and Tribo-Corrosion* 8 (3), 68–16. doi:10.1007/s40735-022-00665-1

Amitha, B. E., and Bharathi, B. J. (2012). Green inhibitors for corrosion protection of metals and alloys: An overview. *Inter. J. Corros.* 2012, 380217. doi:10.1155/2012/380217

Anadebe, V. C., Onukwuli, O., Omotioma, M., and Okafor, N. (2019). Experimental, theoretical modeling and optimization of inhibition efficiency of pigeon pea leaf extract as anti-corrosion agent of mild steel in acid environment. *Mater. Chem. Phys.* 233, 120–132. doi:10.1016/j.matchemphys.2019.05.033

Anaee, R. A., Tomi, I. H. R., Abdulmajeed, M. H., Naser, S. A., and Kathem, M. M. (2019). Expired Etoricoxib as a corrosion inhibitor for steel in acidic solution. *J. Mol. Liq.* 279, 594–602. doi:10.1016/j.molliq.2019.01.169

Asaad, M. A., Ismail, M., A. Khalid, N. H., Huseien, G. F., and Bothi Raja, P. (2018). Elaeis guineensis leaves extracts as eco-friendly corrosion inhibitor for mild steel in hydrochloric acid. *J. Teknol.* 80 (6). doi:10.11113/jt.v80.11191

Ashassi-Sorkhabi, H., Mirzaee, S., Rostamikia, T., and Bagheri, R. (2015). Pomegranate (Punica granatum) peel extract as a green corrosion inhibitor for mild steel in hydrochloric acid solution. *Int. J. Corros.* 2015, 1–6. doi:10.1155/2015/197587

Asmara, Y. P., Kurniawan, T., Sutjipto, A. G. E., and Jafar, J. (2018). Application of plants extracts as green corrosion inhibitors for steel in concrete-A review. *Indonesian J. Sci. Technol.* 3 (2), 158–170. doi:10.17509/ijost.v3i2.12760

Ayoola, A. A., Fayomi, O. S. I., and Ogunkanmbi, S. O. (2018). Data on inhibitive performance of chloraphenicol drug on A315 mild steel in acidic medium. *Data Brief* 19, 804–809. doi:10.1016/j.dib.2018.05.108

Azeiteiro, U. M., Bacelar-Nicolau, P., Caetano, F. J., and Caeiro, S. (2015). Education for sustainable development through e-learning in higher education: Experiences from Portugal. *J. Clean. Prod.* 106, 308–319. doi:10.1016/j.jclepro.2014.11.056

Baig, N., Chauhan, D. S., Saleh, T. A., and Quraishi, M. A. (2019). Diethylenetriamine functionalized graphene oxide as a novel corrosion inhibitor for mild steel in hydrochloric acid solutions. *New J. Chem.* 43 (5), 2328–2337. doi:10.1039/c8nj04771e

Bammou, L., Belkhaouda, M., Salghi, R., Benali, O., Zarrouk, A., Zarrok, H., et al. (2014). Corrosion inhibition of steel in sulfuric acidic solution by the Chenopodium Ambrosioides Extracts. *J. Assoc. Arab Univ. Basic Appl. Sci.* 16, 83–90. doi:10.1016/j.jaubas.2013.11.001

Bedairi, B., Cronin, D., Hosseini, A., and Plumtree, A. (2012). Failure prediction for Crack-in-Corrosion defects in natural gas transmission pipelines. *Int. J. Press. vessels Pip.* 96, 90–99. doi:10.1016/j.ijpvp.2012.06.002

Biomorgi, J., Hernandez, S., Marin, J., Rodriguez, E., Lara, M., and Viloria, A. (2012). Internal corrosion studies in hydrocarbons production pipelines located at Venezuelan Northeastern. *Chem. Eng. Res. Des.* 90 (9), 1159–1167. doi:10.1016/j.cherd.2011.12.013

Boumhara, K., Bentiss, F., Tabyaoui, M. H., Costa, J., Desjobert, J. M., Bellaouchou, A., et al. (2014). Use of Artemisia mesatlantica essential oil as green corrosion inhibitor for mild steel in 1 M hydrochloric acid solution. *Int. J. Electrochem. Sci.* 9, 1187–1206.

Brown, G. K. (2014). Appendix–internal corrosion monitoring techniques for pipeline systems. *Pipeline integrity handbook*. Boston: Gulf Professional Publishing, 255–292.

Buchweishaija, J. (2009). Phytochemicals as green corrosion inhibitors in various corrosive media: A review. *Tanzan. J. Sci.* 35. doi:10.4314/tjs.v29i1.18370

Chadli, R., Elherri, A., Elmsellem, H., Elazzouzi, M., Merad, N., Aouniti, A., et al. (2017). Synthesis of aza-pseudopeptides and the evaluation of their inhibiting efficacy of mild steel corrosion in 1.0 M HCl. *Prot. Metals Phys. Chem. Surfaces* 53 (5), 928–936. doi:10.1134/s2070205117050033

Cheng, Y. F. (2013). *Stress corrosion cracking of pipelines*. Hoboken, New Jersey: John Wiley & Sons.

Chetouani, A., and Hammouti, B. (2014). Salvia officinalis essential oil and the extract as green corrosion inhibitor of mild steel in hydrochloric acid. *J. Chem. Pharm. Res.* 6 (7), 1401–1416.

Chung, I.-M., Kim, S. H., Hemapriya, V., Kalaiselvi, K., and Prabakaran, M. (2019). Inhibition behavior of Tragia involucrata L. phenolic compounds against acidic medium corrosion in low carbon steel surface. *Chin. J. Chem. Eng.* 27 (3), 717–725. doi:10.1016/j.cjche.2018.10.008

Cruz-Zabalegui, A., Vazquez-Velez, E., Galicia-Aguilar, G., Casales-Diaz, M., Lopez-Sesenes, R., Gonzalez-Rodriguez, J., et al. (2019). Use of a non-ionic gemini-surfactant synthesized from the wasted avocado oil as a CO2-corrosion inhibitor for X-52 steel. *Industrial Crops Prod.* 133, 203–211. doi:10.1016/j.indcrop.2019.03.011

Da Rocha, J. C., Gomes, J. A. d. C. P., and D'Elia, E. (2010). Corrosion inhibition of carbon steel in hydrochloric acid solution by fruit peel aqueous extracts. *Corros. Sci.* 52 (7), 2341–2348. doi:10.1016/j.corsci.2010.03.033

Davoodi, A., Pakshir, M., Babaiee, M., and Ebrahimi, G. (2011). A comparative H2S corrosion study of 304L and 316L stainless steels in acidic media. *Corros. Sci.* 53 (1), 399–408. doi:10.1016/j.corsci.2010.09.050

Dehghani, A., Bahlakeh, G., and Ramezanzadeh, B. (2019). A detailed electrochemical/theoretical exploration of the aqueous Chinese gooseberry fruit shell extract as a green and cheap corrosion inhibitor for mild steel in acidic solution. *J. Mol. Liq.* 282, 366–384. doi:10.1016/j.molliq.2019.03.011

Dehghani, A., Bahlakeh, G., Ramezanzadeh, B., and Ramezanzadeh, M. (2019). A combined experimental and theoretical study of green corrosion inhibition of mild steel in HCl solution by aqueous *Citrullus lanatus* fruit (CLF) extract. *J. Mol. Liq.* 279, 603–624. doi:10.1016/j.molliq.2019.02.010

Dehghani, A., Bahlakeh, G., Ramezanzadeh, B., and Ramezanzadeh, M. (2019). Electronic/atomic level fundamental theoretical evaluations combined with electrochemical/surface examinations of Tamarindus indiaca aqueous extract as a new green inhibitor for mild steel in acidic solution (HCl 1 M). *J. Taiwan Inst. Chem. Eng.* 102, 349–377. doi:10.1016/j.jtice.2019.05.006

Eduok, U. M., Umoren, S. A., and Udoh, A. P. (2012). Synergistic inhibition effects between leaves and stem extracts of Sida acuta and iodide ion for mild steel corrosion in 1 M H2SO4 solutions. *Arabian J. Chem.* 5 (3), 325–337. doi:10.1016/j.arabjc.2010.09.006

El Ibrahimi, B., Jmiai, A., Bazzi, L., and El Issami, S. (2020). Amino acids and their derivatives as corrosion inhibitors for metals and alloys. *Arabian J. Chem.* 13 (1), 740–771. doi:10.1016/j.arabjc.2017.07.013

Eliyan, F. F., Mahdi, E., Farhat, Z., and Alfantazi, A. (2013). Interpreting the passivation of HSLA steel from electrochemical corrosion investigations in bicarbonate-oil aqueous emulsions. *Int. J. Electrochem. Sci.* 8, 3026–3038.

Faraj, L., and Khan, G. M. (2015). Application of natural product extracts as green corrosion inhibitors for metals and alloys in acid pickling processes-A. *Int. J. Electrochem. Sci.* 10, 6120–6134.

Fawzy, A., Abdallah, M., Zaafarany, I., Ahmed, S., and Althagafi, I. (2018). Thermodynamic, kinetic and mechanistic approach to the corrosion inhibition of carbon steel by new synthesized amino acids-based surfactants as green inhibitors in neutral and alkaline aqueous media. *J. Mol. Liq.* 265, 276–291. doi:10.1016/j.molliq.2018.05.140

Fiori-Bimbi, M. V., Alvarez, P. E., Vaca, H., and Gervasi, C. A. (2015). Corrosion inhibition of mild steel in HCL solution by pectin. *Corros. Sci.* 92, 192–199. doi:10.1016/j.corsci.2014.12.002

Fouda, A. S., El Morsi, M. A., and El Mogy, T. (2017). Studies on the inhibition of carbon steel corrosion in hydrochloric acid solution by expired Carvedilol drug. *Green Chem. Lett. Rev.* 10 (4), 336–345. doi:10.1080/17518253.2017.1380236

Gapsari, F., Madurani, K. A., Simanjuntak, F. M., Andoko, A., Wijaya, H., and Kurniawan, F. (2019). Corrosion inhibition of honeycomb waste extracts for 304 stainless steel in sulfuric acid solution. *Materials* 12 (13), 2120. doi:10.3390/ma12132120

Gece, G., and Bilgiç, S. (2010). A theoretical study on the inhibition efficiencies of some amino acids as corrosion inhibitors of nickel. *Corros. Sci.* 52 (10), 3435–3443. doi:10.1016/j.corsci.2010.06.015

Gece, G. (2011). Drugs: A review of promising novel corrosion inhibitors. *Corros. Sci.* 53 (12), 3873–3898. doi:10.1016/j.corsci.2011.08.006

Gerengi, H., Uygur, I., Solomon, M., Yildiz, M., and Goksu, H. (2016). Evaluation of the inhibitive effect of Diospyros kaki (Persimmon) leaves extract on St37 steel corrosion in acid medium. *Sustain. Chem. Pharm.* 4, 57–66. doi:10.1016/j.scp.2016.10.003

Ghareba, S., and Omanovic, S. (2010). Interaction of 12-aminododecanoic acid with a carbon steel surface: Towards the development of 'green'corrosion inhibitors. *Corros. Sci.* 52 (6), 2104–2113. doi:10.1016/j.corsci.2010.02.019

Gong, W., Xu, B., Yin, X., Liu, Y., Chen, Y., and Yang, W. (2019). Halogen-substituted thiazole derivatives as corrosion inhibitors for mild steel in 0.5 M sulfuric acid at high temperature. *J. Taiwan Inst. Chem. Eng.* 97, 466–479. doi:10.1016/j.jtice.2019.02.018

Gong, W., Yin, X., Liu, Y., Chen, Y., and Yang, W. (2019). 2-Amino-4-(4-methoxyphenyl)-thiazole as a novel corrosion inhibitor for mild steel in acidic medium. *Prog. Org. Coatings* 126, 150–161. doi:10.1016/j.porgcoat.2018.10.001

Grassino, A. N., Halambek, J., Djakovic, S., Rimac Brncic, S., Dent, M., and Grabaric, Z. (2016). Utilization of tomato peel waste from canning factory as a potential source for pectin production and application as tin corrosion inhibitor. *Food Hydrocoll.* 52, 265–274. doi:10.1016/j.foodhyd.2015.06.020

Guo, B., Song, S., Ghalambor, A., Lin, T., and Chacko, J. (2005). *Offshore pipelines*. Amsterdam, Netherlands: Elsevier.

Haldhar, R., Prasad, D., Saxena, A., and Singh, P. (2018). Valeriana wallichii root extract as a green & sustainable corrosion inhibitor for mild steel in acidic environments: Experimental and theoretical study. *Mater. Chem. Front.* 2 (6), 1225–1237. doi:10.1039/c8qm00120k

Hasan, S. K., and Sisodia, P. (2011). Paniala (Flacourtia Jangomas) plant extract as eco friendly inhibitor on the corrosion of mild steel in acidic media. *Rasayan J. Chem.* 4 (3), 548–553.

Hechiche, N., Kadri, A., and Boughrara, D. (2019). Artemisia herba alba essential oil as green corrosion inhibitor for aluminum in hydrochloric acid solution. *Anal. Bioanal. Electrochem.* 11, 1129–1147.

Hernandez-Rodriguez, M. A. L., Martinez-Delgado, D., Gonzalez, R., Perez Unzueta, A., Mercado-Solis, R., and Rodriguez, J. (2007). Corrosive wear failure analysis in a natural gas pipeline. *Wear* 263 (1-6), 567–571. doi:10.1016/j.wear.2007.01.123

Hussein, M. H. M., El-Hady, M. F., Shehata, H. A. H., Hegazy, M. A., and Hefni, H. H. H. (2013). Preparation of some eco-friendly corrosion inhibitors having antibacterial activity from sea food waste. *J. surfactants Deterg.* 16 (2), 233–242. doi:10.1007/s11743-012-1395-3

Ilman, M. N. (2014). Analysis of internal corrosion in subsea oil pipeline. *Case Stud. Eng. Fail. Analysis* 2 (1), 1–8. doi:10.1016/j.csefa.2013.12.003

Khaksarfard, R., Paraschivoiu, M., Zhu, Z., Tajallipour, N., and Teevens, P. J. (2013). *CFD based analysis of multiphase flows in bends of large diameter pipelines*. In CORROSION 2013.

Kiefner, J. F., and Kolovich, K. M. (2007). *Calculation of a corrosion rate using Monte Carlo simulation*. OnePetro. www.onepetro.org.

Kowsari, E., Arman, S., Shahini, M., Zandi, H., Ehsani, A., Naderi, R., et al. (2016). *In situ* synthesis, electrochemical and quantum chemical analysis of an amino acid-derived ionic liquid inhibitor for corrosion protection of mild steel in 1M HCl solution. *Corros. Sci.* 112, 73–85. doi:10.1016/j.corsci.2016.07.015

Kumar, C. B. P., and Mohana, K. N. (2013). The effect of *Achyranthes aspera* extracts on mild steel corrosion in industrial water medium. *Int. Sch. Res. Notices* 2013 (4), 261847. doi:10.1155/2013/261847

Kumar, K. P. V., Pillai, M. S. N., and Thusnavis, G. R. (2011). Seed extract of Psidium guajava as ecofriendly corrosion inhibitor for carbon steel in hydrochloric acid medium. *J. Mater. Sci. Technol.* 27 (12), 1143–1149. doi:10.1016/s1005-0302(12)60010-3

Kurniawan, F., and Madurani, K. A. (2015). Electrochemical and optical microscopy study of red pepper seed oil corrosion inhibition by self-assembled monolayers (SAM) on 304 SS. *Prog. Org. Coatings* 88, 256–262. doi:10.1016/j.porgcoat.2015.07.010

Lahhit, N., Bouyanzer, A., Desjobert, J. M., Hammouti, B., Salghi, R., Costa, J., et al. (2011). Fennel (Foeniculum vulgare) essential oil as green corrosion inhibitor

of carbon steel in hydrochloric acid solution. *Port. Electrochimica Acta* 29 (2), 127–138. doi:10.4152/pea.201102127

Li, D.-p., Zhang, L., Yang, J. w., Lu, M. x., Ding, J. h., and Liu, M. l. (2014). Effect of H2S concentration on the corrosion behavior of pipeline steel under the coexistence of H2S and CO2. *Int. J. Minerals, Metallurgy, Mater.* 21 (4), 388–394. doi:10.1007/s12613-014-0920-y

Li, Y., Fan, J., Hu, Z., Shao, Q., Zhang, L., and Yu, H. (2015). Influence of land use patterns on evapotranspiration and its components in a temperate grassland ecosystem. *Adv. Meteorology* 2015, 1–12. doi:10.1155/2015/452603

Liang, Y., Wang, C., Li, J., and Wang, L. (2015). The penicillin derivatives as corrosion inhibitors for mild steel in hydrochloric acid solution: Experimental and theoretical studies. *Int. J. Electrochem. Sci.* 10, 8072–8086.

Liao, L. L., Mo, S., Luo, H. Q., and Li, N. B. (2018). Corrosion protection for mild steel by extract from the waste of lychee fruit in HCl solution: Experimental and theoretical studies. *J. colloid interface Sci.* 520, 41–49. doi:10.1016/j.jcis.2018.02.071

Loto, R. T. (2019). Corrosion inhibition effect of non-toxic α-amino acid compound on high carbon steel in low molar concentration of hydrochloric acid. *J. Mater. Res. Technol.* 8 (1), 484–493. doi:10.1016/j.jmrt.2017.09.005

Macedo, R. G. M. d. A., Marques, N. d. N., Paulucci, L. C., Cunha, J. V. M., Villetti, M. A., Castro, B. B., et al. (2019). Water-soluble carboxymethylchitosan as green scale inhibitor in oil wells. *Carbohydr. Polym.* 215, 137–142. doi:10.1016/j.carbpol.2019.03.082

Machado, C., Ferreira Fagundes, T. d. S., Escarpini dos Santos, N., Shewry de M. Rocha, T., Garrett, R., Borges, R. M., et al. (2019). Ircinia strobilina crude extract as corrosion inhibitor for mild steel in acid medium. *Electrochim. Acta* 312, 137–148. doi:10.1016/j.electacta.2019.04.148

Marc, A. M. (2013). *Corrosion growth models and ILI-based estimation procedures for reliability-based and deterministic pipeline integrity assessments*. Houston, TX, United States: Pipeline Research Council International.

Marsoul, A., Ijjaali, M., Elhajjaji, F., Taleb, M., Salim, R., and Boukir, A. (2020). Phytochemical screening, total phenolic and flavonoid methanolic extract of pomegranate bark (Punica granatum L): Evaluation of the inhibitory effect in acidic medium 1 M HCl. *Mater. Today Proc.* 27, 3193–3198. doi:10.1016/j.matpr.2020.04.202

Mazumder, Q. H., Shirazi, S. A., and McLaury, B. (2008). Experimental investigation of the location of maximum erosive wear damage in elbows. *J. Press. Vessel Technol.* 130 (1). doi:10.1115/1.2826426

Mobin, M., Basik, M., and El Aoufir, Y. (2019). Corrosion mitigation of mild steel in acidic medium using lagerstroemia speciosa leaf extract: A combined experimental and theoretical approach. *J. Mol. Liq.* 286, 110890. doi:10.1016/j.molliq.2019.110890

Mobin, M., Basik, M., and Shoeb, M. (2019). A novel organic-inorganic hybrid complex based on Cissus quadrangularis plant extract and zirconium acetate as a green inhibitor for mild steel in 1 M HCl solution. *Appl. Surf. Sci.* 469, 387–403. doi:10.1016/j.apsusc.2018.11.008

Mobin, M., and Rizvi, M. (2017). Polysaccharide from Plantago as a green corrosion inhibitor for carbon steel in 1 M HCl solution. *Carbohydr. Polym.* 160, 172–183. doi:10.1016/j.carbpol.2016.12.056

Montoya, L. F., Contreras, D., Jaramillo, A., Carrasco, C., Fernandez, K., Schwederski, B., et al. (2019). Study of anticorrosive coatings based on high and low molecular weight polyphenols extracted from the Pine radiata bark. *Prog. Org. Coatings* 127, 100–109. doi:10.1016/j.porgcoat.2018.11.010

Munawaroh, H. S. H., Sunarya, Y., Anwar, B., Priatna, E., Risa, H., Koyande, A. K., et al. (2022). Protoporphyrin extracted from biomass waste as sustainable corrosion inhibitors of T22 carbon steel in acidic environments. *Sustainability* 14 (6), 3622. doi:10.3390/su14063622

Nair, R. N. (2017). Green Corrosion Inhibitors for mild steel in acidic medium. *Int. J. Mod. trends Eng. Res.* 4 (12), 216–221.

Naseri, E., Hajisafari, M., Kosari, A., Talari, M., Hosseinpour, S., and Davoodi, A. (2018). Inhibitive effect of Clopidogrel as a green corrosion inhibitor for mild steel; statistical modeling and quantum Monte Carlo simulation studies. *J. Mol. Liq.* 269, 193–202. doi:10.1016/j.molliq.2018.08.050

Ninčević Grassino, A., Djakovic, S., Bosiljkov, T., Halambek, J., Zoric, Z., Dragovic-Uzelac, V., et al. (2020). Valorisation of tomato peel waste as a sustainable source for pectin, polyphenols and fatty acids recovery using sequential extraction. *Waste Biomass Valorization* 11 (9), 4593–4611. doi:10.1007/s12649-019-00814-7

Oguntuyi, S. D., Johnson, O. T., and Shongwe, M. B. (2021). Spark plasma sintering of ceramic matrix composite of TiC: Microstructure, densification, and mechanical properties: A review. *Int. J. Adv. Manuf. Technol.* 116, 69–82. doi:10.1007/s00170-021-07471-y

Oguntuyi, S. D., Johnson, O. T., Shongwe, M. B., Jeje, S. O., and Rominiyi, A. L. (2021). The effects of sintering additives on the ceramic matrix composite of ZrO2: Microstructure, densification, and mechanical properties–a review. *Adv. Appl. Ceram.* 120 (5-8), 319–335. doi:10.1080/17436753.2021.1953845

Oguntuyi, S. D., Johnson, O. T., and Shongwe, M. B. (2021). Spark plasma sintering of ceramic matrix composite of ZrB2 and TiB2: Microstructure, densification, and mechanical properties—a review. *Metals Mater. Int.* 27 (7), 2146–2159. doi:10.1007/s12540-020-00874-8

Oguntuyi, S. D., Malatji, N., Shongwe, M., Johnson, O., Khoathane, C., and Tshabalala, L. (2022). The influence of Si3N4 on the microstructure, mechanical properties and the wear performance of TiB2–SiC synthesized via spark plasma sintering. *Int. J. Lightweight Mater. Manuf.* 5 (3), 326–338. doi:10.1016/j.ijlmm.2022.04.004

Oguntuyi, S. D., Shongwe, M. B., Tshabalala, L., Johnson, O. T., and Malatji, N. (2022). Effects of SiC on the microstructure, densification, hardness and wear performance of TiB2 ceramic matrix composite consolidated via spark plasma sintering. *Arabian J. Sci. Eng.* 2022, 1–15. doi:10.1007/s13369-022-07026-7

Oguzie, E. E. (2007). Corrosion inhibition of aluminium in acidic and alkaline media by Sansevieria trifasciata extract. *Corros. Sci.* 49 (3), 1527–1539. doi:10.1016/j.corsci.2006.08.009

Okafor, P. C., and Ebenso, E. E. (2007). Inhibitive action of Carica papaya extracts on the corrosion of mild steel in acidic media and their adsorption characteristics. *Pigment Resin Technol.* 36, 134–140. doi:10.1108/03699420710748992

Okafor, P. C., Ikpi, M., Uwah, I., Ebenso, E., Ekpe, U., and Umoren, S. (2008). Inhibitory action of Phyllanthus amarus extracts on the corrosion of mild steel in acidic media. *Corros. Sci.* 50 (8), 2310–2317. doi:10.1016/j.corsci.2008.05.009

Okewale, A. O., and Olaitan, A. (2017). The use of rubber leaf extract as a corrosion inhibitor for mild steel in acidic solution. *Int. J. Mater. Chem.* 7 (1), 5–13.

Ossai, C. I., Boswell, B., and Davies, I. J. (2015). Pipeline failures in corrosive environments–A conceptual analysis of trends and effects. *Eng. Fail. Anal.* 53, 36–58. doi:10.1016/j.engfailanal.2015.03.004

Pal, S., Lgaz, H., Tiwari, P., Chung, I. M., Ji, G., and Prakash, R. (2019). Experimental and theoretical investigation of aqueous and methanolic extracts of Prunus dulcis peels as green corrosion inhibitors of mild steel in aggressive chloride media. *J. Mol. Liq.* 276, 347–361. doi:10.1016/j.molliq.2018.11.099

Papavinasam, S., Doiron, A., and Revie, R. W. (2010). Model to predict internal pitting corrosion of oil and gas pipelines. *Corrosion* 66 (3), 35006–35011. doi:10.5006/1.3359623

Parthipan, P., Sabarinathan, D., Angaiah, S., and Rajasekar, A. (2018). Glycolipid biosurfactant as an eco-friendly microbial inhibitor for the corrosion of carbon steel in vulnerable corrosive bacterial strains. *J. Mol. Liq.* 261, 473–479. doi:10.1016/j.molliq.2018.04.045

Popoola, L. T. (2019). Organic green corrosion inhibitors (OGCIs): A critical review. *Corros. Rev.* 37 (2), 71–102. doi:10.1515/corrrev-2018-0058

Popoola, L. T. (2019). Progress on pharmaceutical drugs, plant extracts and ionic liquids as corrosion inhibitors. *Heliyon* 5 (2), e01143. doi:10.1016/j.heliyon.2019.e01143

Quraishi, M. A., Rafiquee, M. Z. A., Khan, S., and Saxena, N. (2007). Corrosion inhibition of aluminium in acid solutions by some imidazoline derivatives. *J. Appl. Electrochem.* 37 (10), 1153–1162. doi:10.1007/s10800-007-9379-0

Raja, P. B., Qureshi, A. K., Abdul Rahim, A., Osman, H., and Awang, K. (2013). Neolamarckia cadamba alkaloids as eco-friendly corrosion inhibitors for mild steel in 1 M HCl media. *Corros. Sci.* 69, 292–301. doi:10.1016/j.corsci.2012.11.042

Raja, P. B., and Sethuraman, M. G. (2008). Inhibitive effect of black pepper extract on the sulphuric acid corrosion of mild steel. *Mater. Lett.* 62 (17-18), 2977–2979. doi:10.1016/j.matlet.2008.01.087

Rani, B. E., and Basu, B. B. J. (2012). Green inhibitors for corrosion protection of metals and alloys: An overview. *Int. J. Corros.* 2012, 1–15. doi:10.1155/2012/380217

Rathi, P., Trikha, S., and Kumar, S. (2017). Plant extracts as green corrosion inhibitors in various corrosive media-a review. *World J. Pharm. Pharm. Sci.* 6 (4), 482–514. doi:10.20959/wjpps20174-8903

Rodrigues, L. S., do Valle, A. F., and D'Elia, E. (2018). Biomass of microalgae spirulina maxima as a corrosion inhibitor for 1020 carbon steel in acidic solution. *Int. J. Electrochem. Sci.* 13, 6169–6189. doi:10.20964/2018.07.11

Sanaei, Z., Ramezanzadeh, M., Bahlakeh, G., and Ramezanzadeh, B. (2019). Use of rosa canina fruit extract as a green corrosion inhibitor for mild steel in 1 M HCl solution: A complementary experimental, molecular dynamics and quantum mechanics investigation. *J. industrial Eng. Chem.* 69, 18–31. doi:10.1016/j.jiec.2018.09.013

Sanni, O., Popoola, A. P. I., and Fayomi, O. S. I. (2018). Enhanced corrosion resistance of stainless steel type 316 in sulphuric acid solution using eco-friendly waste product. *Results Phys.* 9, 225–230. doi:10.1016/j.rinp.2018.02.001

Shongwe, M. B. (2020). Spark plasma sintering of ceramic matrix composite of TiC: Microstructure, densification, and mechanical properties: A review. *Adv. Material Sci. Eng. Sel. Articles ICMMPE* 2020, 93.

Shukla, S. K., and Quraishi, M. A. (2009). 4-Substituted anilinomethylpropionate: New and efficient corrosion inhibitors for mild steel in hydrochloric acid solution. *Corros. Sci.* 51 (9), 1990–1997. doi:10.1016/j.corsci.2009.05.020

Singh, A., Adrianzen Herrera, D., Zhang, Y., Perez-Soler, R., and Cheng, H. (2018). Mouse models in squamous cell lung cancer: Impact for drug discovery. *J. Alloys Compd.* 762, 347–358. doi:10.1080/17460441.2018.1437137

Singh, A. K., Pandey, A. K., Banerjee, P., Saha, S. K., Chugh, B., Thakur, S., et al. (2019). Eco-friendly disposal of expired anti-tuberculosis drug isoniazid and its role in the protection of metal. *J. Environ. Chem. Eng.* 7 (2), 102971. doi:10.1016/j.jece.2019.102971

Singh, A., Kumar, A., and Pramanik, T. (2013). A theoretical approach to the study of some plant extracts as green corrosion inhibitor for mild steel in HCl solution. *Orient. J. Chem.* 29 (1), 277–283. doi:10.13005/ojc/290144

Singh, P., Chauhan, D., Chauhan, S., Singh, G., and Quraishi, M. (2019). Chemically modified expired Dapsone drug as environmentally benign corrosion inhibitor for mild steel in sulphuric acid useful for industrial pickling process. *J. Mol. Liq.* 286, 110903. doi:10.1016/j.molliq.2019.110903

Srivastava, V., Haque, J., Verma, C., Singh, P., Lgaz, H., Salghi, R., et al. (2017). Amino acid based imidazolium zwitterions as novel and green corrosion inhibitors for mild steel: Experimental, DFT and MD studies. *J. Mol. Liq.* 244, 340–352. doi:10.1016/j.molliq.2017.08.049

Subasree, N., and Selvi, J. A. (2020). Imidazolium based ionic liquid derivatives; synthesis and evaluation of inhibitory effect on mild steel corrosion in hydrochloric acid solution. *Heliyon* 6 (2), e03498. doi:10.1016/j.heliyon.2020.e03498

Talari, M., Mozafari Nezhad, S., Alavi, S. J., Mohtashamipour, M., Davoodi, A., and Hosseinpour, S. (2019). Experimental and computational chemistry studies of two imidazole-based compounds as corrosion inhibitors for mild steel in HCl solution. *J. Mol. Liq.* 286, 110915. doi:10.1016/j.molliq.2019.110915

Tawancy, H. M., Al-Hadhrami, L. M., and Al-Yousef, F. K. (2013). Analysis of corroded elbow section of carbon steel piping system of an oil–gas separator vessel. *Case Stud. Eng. Fail. Analysis* 1 (1), 6–14. doi:10.1016/j.csefa.2012.11.001

Tezeghdenti, M., Dhouibi, L., and Etteyeb, N. (2015). Corrosion inhibition of carbon steel in 1 M sulphuric acid solution by extract of eucalyptus globulus leaves cultivated in Tunisia arid zones. *J. Bio-and Tribo-Corrosion* 1 (3), 16–19. doi:10.1007/s40735-015-0016-x

Thakur, A., Kaya, S., Abousalem, A., Sharma, S., Ganjoo, R., Assad, H., et al. (2022). Computational and experimental studies on the corrosion inhibition performance of an aerial extract of Cnicus Benedictus weed on the acidic corrosion of mild steel. *Process Saf. Environ. Prot.* 161, 801–818. doi:10.1016/j.psep.2022.03.082

Thakur, A., Kaya, S., Abousalem, A. S., and Kumar, A. (2022). Experimental, DFT and MC simulation analysis of Vicia Sativa weed aerial extract as sustainable and eco-benign corrosion inhibitor for mild steel in acidic environment. *Sustain. Chem. Pharm.* 29, 100785. doi:10.1016/j.scp.2022.100785

Tiwari, P., Srivastava, M., Mishra, R., Ji, G., and Prakash, R. (2018). Economic use of waste Musa paradisica peels for effective control of mild steel loss in aggressive acid solutions. *J. Environ. Chem. Eng.* 6 (4), 4773–4783. doi:10.1016/j.jece.2018.07.016

Vaszilcsin, N., Ordodi, V., and Borza, A. (2012). Corrosion inhibitors from expired drugs. *Int. J. Pharm.* 431 (1-2), 241–244. doi:10.1016/j.ijpharm.2012.04.015

Velázquez-González, M. A., Gonzalez-Rodriguez, J. G., Valladares-Cisneros, M. G., and Hermoso-Diaz, I. A. (2014). Use of Rosmarinus officinalis as green corrosion inhibitor for carbon steel in acid medium. *Am. J. Anal. Chem.* 2014.

Vengatesh, G., Karthik, G., and Sundaravadivelu, M. (2017). A comprehensive study of ondansetron hydrochloride drug as a green corrosion inhibitor for mild steel in 1 M HCl medium. *Egypt. J. petroleum* 26 (3), 705–719. doi:10.1016/j.ejpe.2016.10.011

Verma, C. B., and Ma, Q. (2014). Schiff's bases of glutamic acid and aldehydes as green corrosion inhibitor for mild steel: Weight-loss, electrochemical and surface analysis. *Int. J. Innov. Res. Sci. Eng. Technol.* 3, 14601–14613.

Verma, C., Ebenso, E. E., Bahadur, I., and Quraishi, M. (2018). An overview on plant extracts as environmental sustainable and green corrosion inhibitors for metals and alloys in aggressive corrosive media. *J. Mol. Liq.* 266, 577–590. doi:10.1016/j.molliq.2018.06.110

Villamizar, W., Casales, M., Gonzales-Rodriguez, J. G., and Martinez, L. (2006). An EIS study of the effect of the pedant group in imidazolines as corrosion inhibitors for carbon steel in CO2 environments. *Mater. Corros.* 57 (9), 696–704. doi:10.1002/maco.200503957

Wei, H., Heidarshenas, B., Zhou, L., Hussain, G., Li, Q., and Ostrikov, K. K. (2020). Green inhibitors for steel corrosion in acidic environment: State of art. *Mater. Today Sustain.* 10, 100044. doi:10.1016/j.mtsust.2020.100044

Yin, Z. F., Zhao, W., Bai, Z., Feng, Y., and Zhou, W. (2008). Corrosion behavior of SM 80SS tube steel in stimulant solution containing H2S and CO2. *Electrochimica Acta* 53 (10), 3690–3700. doi:10.1016/j.electacta.2007.12.039

Zhang, K., Yang, W., Yin, X., Chen, Y., Liu, Y., Le, J., et al. (2018). Amino acids modified konjac glucomannan as green corrosion inhibitors for mild steel in HCl solution. *Carbohydr. Polym.* 181, 191–199. doi:10.1016/j.carbpol.2017.10.069

Zhang, T., Yang, Y., Shao, Y., Meng, G., and Wang, F. (2009). A stochastic analysis of the effect of hydrostatic pressure on the pit corrosion of Fe–20Cr alloy. *Electrochimica Acta* 54 (15), 3915–3922. doi:10.1016/j.electacta.2009.02.010

Znini, M., Majidi, L., Bouyanzer, A., Paolini, J., Desjobert, J. M., Costa, J., et al. (2012). Essential oil of Salvia aucheri mesatlantica as a green inhibitor for the corrosion of steel in 0.5 M H2SO4. *Arabian J. Chem.* 5 (4), 467–474. doi:10.1016/j.arabjc.2010.09.017

frontiers | Frontiers in Energy Research

TYPE Review
PUBLISHED 16 January 2023
DOI 10.3389/fenrg.2022.1089025

OPEN ACCESS

EDITED BY
Fidelis Ibiang Abam,
Michael Okpara University of Agriculture, Nigeria

REVIEWED BY
Macmanus Ndukwu,
Michael Okpara University of Agriculture, Nigeria
Ogheneruona E. Diemuodeke,
University of Port Harcourt, Nigeria

*CORRESPONDENCE
Tobiloba E. Somefun,
tobi.somefun@covenantuniversity.edu.ng

SPECIALTY SECTION
This article was submitted to Process and Energy Systems Engineering, a section of the journal Frontiers in Energy Research

RECEIVED 03 November 2022
ACCEPTED 15 December 2022
PUBLISHED 16 January 2023

CITATION
Babayomi OO, Olubayo B, Denwigwe IH, Somefun TE, Adedoja OS, Somefun CT, Olukayode K and Attah A (2023), A review of renewable off-grid mini-grids in Sub-Saharan Africa.
Front. Energy Res. 10:1089025.
doi: 10.3389/fenrg.2022.1089025

A review of renewable off-grid mini-grids in Sub-Saharan Africa

Oluleke O. Babayomi[1,2], Babatunde Olubayo[3], Iheanacho H. Denwigwe[4], Tobiloba E. Somefun[5]*, Oluwaseye Samson Adedoja[2,6], Comfort T. Somefun[5], Kevwe Olukayode[5] and Amarachi Attah[5]

[1]School of Electrical Engineering, Shandong University, Jinan, China, [2]National Space Research and Development Agency, Abuja, Nigeria, [3]Department of Electrical Engineering, Tshwane University of Technology, Pretoria, South Africa, [4]Department of Electrical and Electronics Engineering, University of Lagos, Lagos, Nigeria, [5]Department of Electrical and Information Engineering, Covenant University, Ota, Nigeria, [6]Centre for Atmospheric Research, National Space Research and Development Agency (NASRDA), Kogi State University Campus, Anyigba, Nigeria

Sub-Saharan Africa (SSA) is home to 75% of the world's unelectrified population, and approximately 500 million of these live in rural areas. Off-grid mini-grids are being deployed on a large scale to address the region's electrification inequalities. This study aims to provide a comprehensive review of the research on the off-grid renewable mini-grids in SSA. The study covers the current status of the level of deployment of off-grid mini-grids. It also reviews multi-criteria decision-making models for optimizing engineering, economics, and management interests in mini-grid siting and design in SSA. The statuses of financing, policy, and tariffs for mini-grids in SSA are also studied. Finally, the current status of energy justice research in respect of mini-grids in SSA is reviewed. The study shows the important role of decentralized renewable technologies in the electrification of SSA's rural population. Within a decade since 2010, the rural electrification rate of SSA has increased from 17% to 28%, and 11 million mini-grid connections are currently operational. Despite these gains, the literature points to several injustices related to the present model by which SSA's renewable mini-grids are funded, deployed, and operated. Hence, several recommendations are provided for the effective application of the energy justice framework (EJF) for just and equitable mini-grids in SSA.

KEYWORDS

off-grid mini-grids, renewable mini-grids, energy access, rural electrification, energy poverty, energy justice, Sub-Saharan Africa

1 Introduction

In September 2015, World Leaders ratified the United Nations Sustainable Development Goals (SDG). Among these, SDG7 has a target to "achieve universal access to affordable, reliable and modern energy services by 2030." This target has a unique alignment with the needs of Sub-Saharan Africa (SSA), where 60% of the population reside in rural areas. According to the SDG7 Tracking Report (Results, 2020), as of 2020, although the global electrification rate is 91%, SSA's electrification rate is 48% (up from 33% in 2010), which is the lowest among all other regions in the world. SSA's 2020 rural electrification rate is 28% (up from 17% in 2010), and the urban electrification rate is 78% (up from 86% in 2010). (The SDG7 Tracking Report data are a joint output of the International Energy Agency (IEA), International Renewable Energy Agency (IRENA), United Nations Statistics Division, the World Bank, and World Health Organization.) Apart from the low rural electrification rate, SSA also has a high youth population who form the core of the region's future human resources. Thus, fair attention

needs to be provided to the rural and urban populations. In this regard, mini-grids can help achieve SDG7.

Mini-grids have the potential to electrify off-grid communities while avoiding the high economic burdens associated with extending the grid to locations with low-population density and relatively low electrical energy demand (Come Zebra et al., 2021). Mini-grids are independent electrical networks of electrical loads which are powered by independent electrical sources. They have power ratings up to 10 MW and can flexibly operate in stand-alone and grid-connected modes. Three forms of mini-grids can be identified in the literature: fossil-based mini-grids, renewable-based mini-grids, and hybrid renewable mini-grids (BloombergNEF and SEforALL, 2020). Fossil-based mini-grids are powered by generators fueled mainly by diesel. Renewable-based mini-grids are powered by renewable sources of energy such as solar PV, wind, and small hydro. Hybrid renewable mini-grids are powered by a combination of fossil-fuels and renewable sources as a means to improve their reliability and cost-effectiveness.

In the past decade, significant efforts have been made to electrify rural areas, and 11 million mini-grid connections are now available in SSA (Domegni and Azouma, 2022). As of 2020, an estimated 2,200 mini-grids were operational in SSA, and the majority of these are powered by solar PV (Domegni and Azouma, 2022; USAID, 2022). A total of 32% of globally installed mini-grids operate on diesel, heavy oil, and hydropower (Domegni and Azouma, 2022). Due to the intermittency of generation, solar mini-grids require energy storage. Lead–acid batteries account for 66% of installed mini-grids due to lower capital and installation costs, whereas 32% use lithium–ion batteries (Domegni and Azouma, 2022). The mini-grid market is projected to impact 111 million households by 2030 (Domegni and Azouma, 2022). This requires the appropriate policies to overcome existing challenges with accessing performance and upfront subsidies, lengthy bureaucratic procedures to secure operational licenses, non-cost reflective tariffs, and uncertain grid-arrival regulations.

It is estimated that nearly 60% of Africans reside in rural communities, and approximately 5% of these people have access to clean electricity. One of the major causes of low electrification rates in rural African communities is the proximity to the existing grid infrastructure, sparsely distributed settlements and low population density, and the presence of low socio-economic activities. Critical to extending electricity access to these remote communities is the deployment of mini-grid technologies. As such, electrification policies in Africa are now redirecting focus to the proliferation of mini-grid facilities not only for the rural communities but also for the peri-urban and urban areas that are underserved (Akinyele et al., 2022). Governments, private sectors, and researchers at various levels are now dedicating efforts to unlocking the potentials embedded in mini-grid technologies to accomplish the attainment of SDG7. This is made possible because of the cost-effectiveness of various renewable energy (RE) technologies and the increase in the efficiency of these technologies (Magenta Global, 2021).

It is said that Africa is home to a large number of planned mini-grid initiatives globally. Data available from World Bank indicate that over 4,000 mini-grid facilities are currently in the planning stage on the African continent (Schwerhoff and Sy, 2019). Based on a market survey, the energy sectors of Nigeria and Senegal were identified as the most promising because they account for 40% of the planned mini-grid initiatives on the continent (Schwerhoff and Sy, 2019). Enabling policies and frameworks that can support the integration of mini-grids into the energy sectors in Africa have also been developed in Ghana, Nigeria, Uganda, Kenya, and Tanzania (Schwerhoff and Sy, 2019). This is expected to create an enabling environment for financiers to participate in emerging development.

The literature is replete with studies on techno-economic performance (Feron, 2016; Morstyn et al., 2018) and size optimization of the mini-grid systems (Gambino et al., 2019; Azimoh et al., 2016). Details on these studies are summarized in Table A1. Countries covered include South Africa, Tanzania, Mali, Burkina Faso, Togo, Uganda, Kenya, Namibia, Cameroon, and Ghana. The viability assessment of hybrid mini-grids for the electrification and development of two rural South African communities (Odarno et al., 2017; (Azimoh et al., 2017) provides insights into the cost frameworks of PV/hybrid mini-grid facilities for SSA. Eder et al. (2015) explored the contribution of mini-grids to electricity access in West Africa. Antonanzas-Torres et al. (2021a) analyzed the elements that impact the adoption of renewable electricity in Ugandan households. Pillot et al. (2019) explored the environmental life cycle impact assessment of mini-grids in West Africa. A review of hybrid renewable mini-grids for developing countries was reported by BloombergNEF and SEforALL (2020). Due to its broad global scope, several details on the specific status of mini-grids, challenges, solutions, and policies that affect SSA were left out. A historical review of solar PV systems in SSA was done by Antonanzas-Torres et al. (2021b). However, it focused on the impact of world-energy policy on the failure and successes of mini-grid projects in SSA. In addition, funding agencies have commissioned reports on the global state of mini-grids (Domegni and Azouma, 2022). Nonetheless, these focus on providing investors and funders with insights into the potential profitability of the min-grid market. These studies do not clarify policy status, optimal multi-criteria decision-making, or the recent energy-justice framework for off-grid mini-grids in SSA.

Motivated by these research gaps, this study provides a comprehensive review of the literature on renewable off-grid mini-grids in SSA. The key research questions answered in this study include the following:

- What is the status of the actual deployment of renewable off-grid mini-grids in SSA?
- What multi-criteria decision-making models can be used to optimize engineering, economics, and management interests in mini-grid siting and design in SSA?
- What are the financing and tariff trends for off-grid mini-grids in SSA?
- How is energy justice applied to off-grid mini-grids in SSA?

The current study is organized as follows: Section 2 discusses renewable mini-grid technologies in SSA. Section 3 reviews multi-criteria decision-making models for mini-grids. Section 4 discusses the challenges associated with mini-grid projects in SSA. Section 5 reviews finance and tariff with respect to SSA mini-grids. Section 6 discusses the progress made with policy for off-grid mini-grids across SSA. Section 7 presents cases of mini-grid progress in West, East, and Southern Africa. Section 8 discusses energy-justice themes with respect to SSA's mini-grids, and Section 9 concludes the article.

2 Renewable Energy sources and technologies for mini-grids in SSA

The local availability of renewable energy sources in SSA has a significant influence on the energy sources deployed in an off-grid

community. At present, solar energy is the dominant renewable energy source for off-grid mini-grids in SSA (Paliwal et al., 2014). Among more than 7,000 mini-grids in Asia and Africa, 63% were solar or solar hybrid systems, 21% hydro, 11% diesel/heavy fuel oil, and 3% biomass (Domegni and Azouma, 2022). Hybridization of different energy sources with respect to techno-economical and available resources is essential for sustainable electrification of SSA to attain energy access goals.

Figure 1 shows various RES technologies in different categories (Korkovelos et al., 2020). The electrical-based storages are not generation sources; they provide efficient and continuous utilization of power generated when energy sources are temporarily unavailable. The principles of operation of these technologies are given in Table 1. Energy stored in any storage technology is mainly used when energy sources are unavailable or during high tariff rates. The differences in these storage technologies are their sizes, storage methods, and types of stored energy.

The size of the mini-grid system is dependent on the amount of demanded energy. It usually combines multiple energy sources, including gas, water, solar, biomass, tidal, and geothermal. The renewable types of energy sources often make use of storage systems that are usually incorporated (e.g., batteries, flywheels, and capacitors) to guard against intermittent energy supply associated with renewable energy sources (RES) and also aid the reliable supply of electricity (Pedersen and Nygaard, 2018; Bhattacharyya, 2018; Shrestha et al., 2020). Mini-grid systems can stand alone to supply electricity to rural dwellers or be integrated into national grid systems to serve either as an additional generating unit (hybrid mode of operation) to supply electric power to the national grids or as distribution franchise reselling electric power from national grids to the rural dwellers due to the increase in their load demand. This type of configuration has been explained in several open studies (BloombergNEF and SEforALL, 2020; Korkovelos et al., 2020) but not properly captured, as depicted in Figure 2. By this integration, the power system operation becomes more complex as the mini-grid system should be able to be isolated from the national grid system (which is usually referred to as island mode) in case of faults from any of the systems or networks.

The mini-grid system can serve as a building block for several modern decentralized electricity systems in SSA (Duran and Sahinyazan, 2021). It can serve diverse electricity consumers, including homes, commercial buildings, farms, and industries. The mini-grid's operation and control are much easier and more flexible than those of the main grid due to lesser interconnectivity. Faults in the system and network can be attended to more easily, and energy theft can easily be identified and curbed. With the present era of power generation company deregulation, different persons or groups can own and manage mini-grid systems (Bhattacharyya, 2018). They can be owned by individuals, state utilities, private companies, or communities.

Mini-grid system technologies are becoming more advanced in terms of reliability and control, making the integration of mini-grids into national grids possible. Likewise, the improvement achieved by manufacturers of these technologies has led to the general acceptance of renewable energy sources for electric power generation by most countries (including SSA) because they are practical, cost-effective, and environmentally pollution-free (Moner-Girona et al., 2016). With these technologies, rural electrification can be easier to implement compared to the main grid extension because extending the main grid system will be more expensive than setting up a mini-grid system (Pedersen, 2016). Moreover, it is important to note that the grid extension approach is a long-term project that spans several decades, considering the level of development in the major towns and cities. This means that without the off-grid power

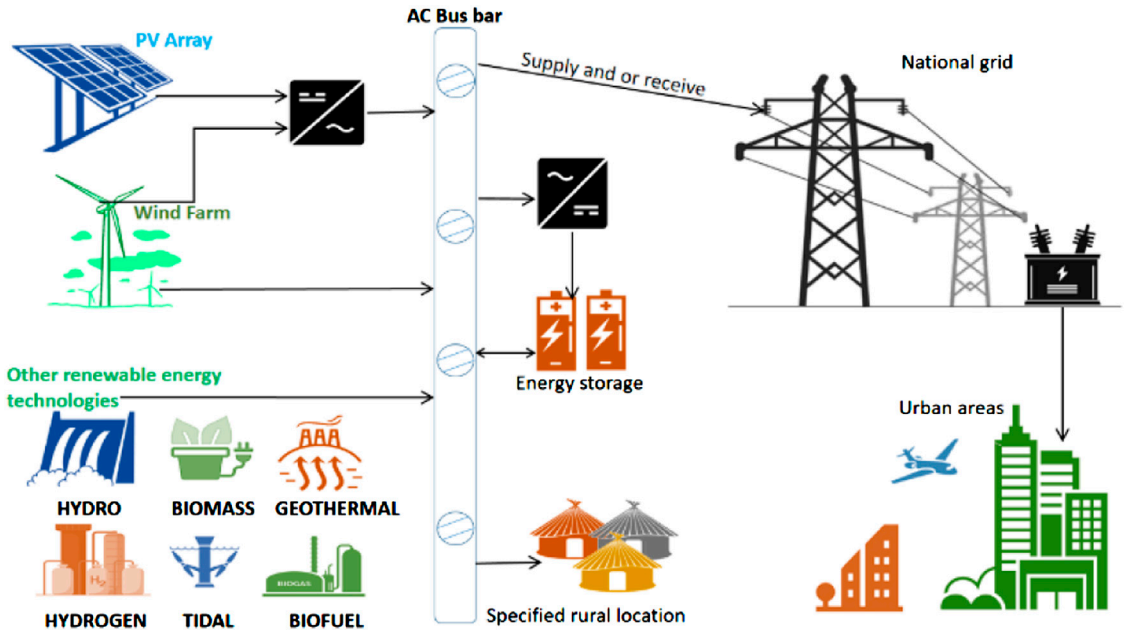

FIGURE 1
Renewable energy technologies of mini-grid systems.

TABLE 1 Renewable energy sources for SSA mini-grids.

Energy source	Technology	Operation principle	Remarks
Renewable energy source			
Water (river or lake)	Hydro turbine	It uses water potential energy, which can be manually achieved through dam creation across a river for a suitable water head. By releasing the water from the dam at the potential created to fall on the water turbine, the turbine changes the kinetic energy of the falling water into mechanical by causing shaft rotation which in turn drives the alternator that is coupled to it and generates electricity	Three processes of conversion are carried out before electrical energy is obtained. From water head energy potential to water kinetic energy to mechanical energy and lastly to electrical energy
			This technology is very reliable. It has a low operating cost (no fuel cost attached) and a high production rate capacity and is pollution-free. However, it has a high capital cost, and output power depends upon the availability of water
Sun (solar energy)	Photovoltaic solar power system	It works based on the principle of the photoelectric effect (i.e., absorption of photons and release of electrons). When sunlight strikes the photovoltaic cells, it releases electrons; the magnitude of which depends on the incident light. The movement of electrons causes the flow of direct current as the output of the PV module. The direct current is then passed to the chargeable batteries through the charge controller. The charge controller is meant to regulate the current flow to the battery. The DC output of the battery is then connected to an inverter for DC to AC conversion of electricity. The battery is essential because	To receive sufficient energy from the sunlight, several photovoltaic modules are connected to form a PV array
		- It serves as a storage - Its output is stable compared to that of the intermittent PV module	This technology comprises solar panel arrays, charge controllers, storage batteries and inverters
Sun (solar energy)	Concentrated solar power systems	It works by concentrating or focusing rays of sunlight through mirrors (heliostats) to the point that causes so much heat to be generated in the focused area. The heat is then absorbed by the heat exchanger (molten salt) and stored in a thermal storage tank (until needed). The stored heat is then passed through a steam generator, the output of which is used to drive a steam turbine, which in turn drives an alternator coupled to it to generate electricity	This type of renewable power generation also uses energy from the sun to generate electricity *via* a steam turbine. Unlike the conventional steam turbine powered by fossil fuel (gas, coal, and nuclear), this technology is powered by solar energy
			This technology gives high-quality superheated steam and maximum efficiency to generate reliable non-intermittent electricity
Wind	Wind turbine	It works based on the conversion of wind kinetic energy hitting the turbine wind vane to the mechanical energy of the rotor. As the rotor continues to rotate through the imparting of the wind kinetic energy, EMF is built up in the stator winding. The production of energy here is dependent on the speed of the blade spin, which in turn depends on the strength of the airflow	In wind turbine technology, we talk about rotors and stators, just like DC or AC generators
			The blade is first connected to the gearbox because the wind turbine blades turn at a very low RPM rate. The gearbox is meant to increase the speed ratio. A brake is also incorporated in case of excessive windy conditions
			The output of a wind turbine is AC, and it is usually converted to DC for storage purposes
Hot water under the earth (Magma)	Geothermal	It works based on the heat from the earth's crust that warms water under the ground. This water breaks out of the ground to the surface as steam or hot water when the temperature rises to a certain point. This hot water is then collected (in a steam separator) to drive a steam turbine, which in turn spines the coupled alternator to generate electricity	This type of renewable technology is strictly location-based. The location must be inspected against unforeseen natural disasters. The gases escaping from the ground may be hazardous
Biomass	Biomass gasification Direct combustion Co-firing anaerobic digestion	This method is based on steam generation to drive a steam turbine, which in turn drives an alternator to generate electricity. Biomass (plant-based materials such as energy crop, wood, and agricultural residues) are the fuel	Biomass gasification technology is trying to balance nature by giving back to the atmosphere energy absorbed from the environment by biomass
Tide or wave	Water turbine	It works based on the differences in the water head of sea tide and basin tide separated by a dam. The kinetic energy of the falling water from the higher tide is used to drive a water turbine which is used to generate electricity	Tide is a periodic rise and fall of the water level of the sea. It has a high level of potential energy, which is used for power generation
			There will be no electricity generated when both the sea and basin have the same water head level

(Continued on following page)

TABLE 1 (*Continued*) Renewable energy sources for SSA mini-grids.

Energy source	Technology	Operation principle	Remarks
Storage			
Electrical	Double layer capacitor	During charging conditions, current flows through the double-layer capacitor (DLC). The positive charge at the positive electrode attracts the negative charge present in the electrolyte of DLC to form a layer and *vice versa* for the negative electrode. The force of attraction between the electrode and electrolyte in each layer is electrostatic force. Hence, the alignment of positive and negative charges across the boundaries of the electrodes and the electrolytic solution is the double-layer capacitor that is responsible for storing charges	This is a specially designed capacitor for storing large electrical charges. It can be charged very quickly and discharge a large amount of power
Chemical	Hydrogen electrolyzer	It works by extracting hydrogen from a water molecule through electrolysis	The technology employs a redox reaction to store streams of hydrogen gas in an electrolyzer in the form of a direct current
Thermal	Sensible heat storage	It works on the principle of natural stratification of chilled water in a tank. It has four operational modes: i. Charging operation without load ii. Charging operation with load iii. Discharging operation without a chiller iv. Discharging operation with chiller	This technology is a sensible heat system. It utilizes sensible heat of the water for cooling energy storage in a tank
Electro-chemical	Secondary batteries	It works based on a chemical reaction taking place among the basic components of the battery, which are the positive electrode (lead peroxide), the negative electrode (pure lead), and the sulphuric acid and water solution	This technology uses sponge lead and lead peroxide for the conversion of chemical energy into electrical power. It has high cell voltage at a lower cost
Mechanical: flywheel	Flywheel energy storage	It works by absorbing mechanical energy in the rotational mass of a flywheel and then storing it as kinetic energy, which is then released to generate electricity or do useful work	This technology is a mechanical battery that acts as an energy reservoir by storing and supplying mechanical energy when required. It finds applications in electrical grids, reciprocating engines, toy cars, gyroscopes, *etc.*

interventions, most communities would remain in the dark even with gas-fired power additions to the central grid.

3 Optimal planning, sizing, and technology selection for mini-grids

In many cases, stakeholders in developing countries adopt top-bottom and bottom-top approaches for electrification purposes. While electrifying the urban and semi-urban through grid extension, mini-grid energy services are being proposed and deployed for rural and remote electricity consumers. However, many of these mini-grids have not been able to attain the standard and scale required to increase electrification considerably due to various reasons related to sustainability. Mini-grids designed for electrification purposes must be reliable (technical), cost-effective (economic), environmentally viable, and socially acceptable, with relevant policies to back them up (Babatunde et al., 2019a). As such, the design, operations, and planning of mini-grids are a multi-criteria problem in which a balance must be attained between conflicting objectives related to engineering, economics, and management (Somefun et al., 2022). To mitigate the multi-criteria challenges related to mini-grid proliferation, stakeholders must choose the right sizing and implementation tools; they must have a robust understanding of the energy needs. Moreover, it is expected that designers should know the optimal location of mini-grids based on the availability of resources and analyze the affordability of the technologies; this is the focus of this section.

3.1 Mini-grid planning tools

The design and sizing of a mini-grid largely depend on the adopted tools and methodologies. If not properly designed and optimally sized, it may lead to oversizing, which would eventually place an economic burden on the consumers, or undersizing, which would precipitate reliability challenges. Therefore, the choice of the right tools or methodologies for the design and sizing of mini-grids is essential (Denwigwe et al., 2021). Traditionally, the pen and paper approach (rule of thumb method) to the sizing and design of mini-grids may be sufficient for a single source system. However, as the complexity of the system increases, this method may produce a sub-optimal result considering various sustainability factors. Therefore, various computer-aided simulation tools have been developed for the design and optimal sizing of mini-grids. Mobile phone applications are also being developed for the sizing of mini-grids (Turcotte et al., 2001). Based on the literature, these sizing and simulation tools have been classified as open architecture research tools, pre-feasibility, simulation, and sizing (Kemausuor et al., 2018). Kemausuor et al. (2018) attempted to classify mini-grid planning tools into the design of production, network design, and territorial planning tools. However, based on another classification, energy system and sizing tools are classified as universal and global sizing tools, island energy-system tools, a single project or local community-based sizing tools, national energy-system tools, and tools that can handle all scales; examples of tools in these categories are given in Table 2 (Ajeigbe et al., 2020).

According to the explanation offered by Turcotte et al. (2001), prefeasibility modeling tools are used for the business case and initial

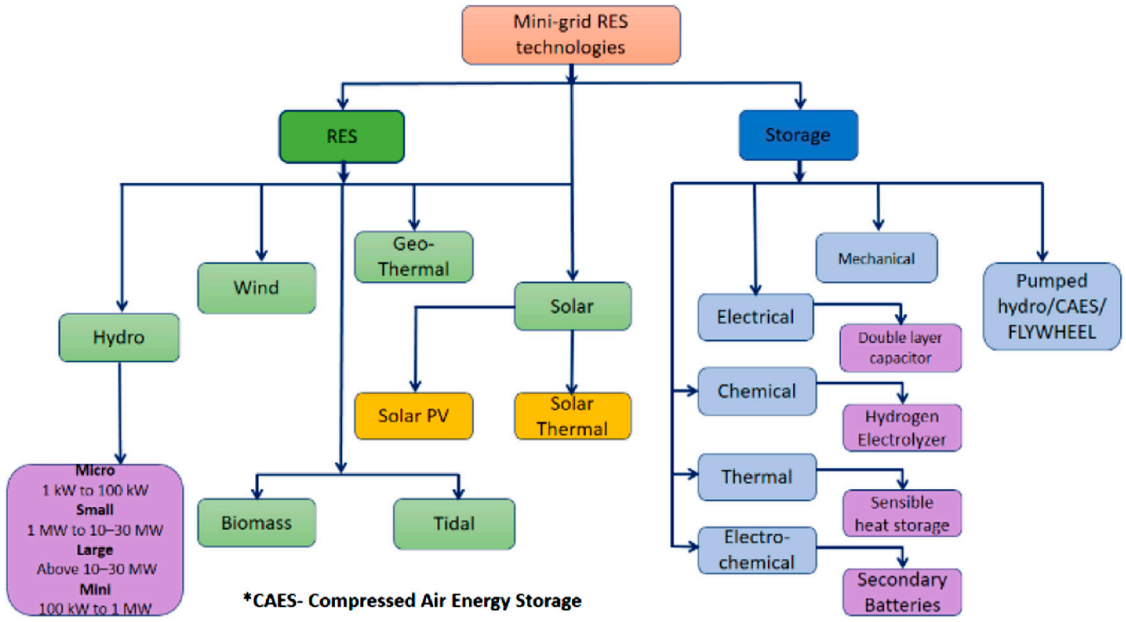

FIGURE 2
Integration of renewable mini-grids into the main grid.

assessment of mini-grids. These include technical and financial evaluations. As for the sizing tools, they provide the optimal combination of the sizes of each system component that satisfies the load. They also provide comprehensive information about the energy flow of viable energy systems. While open architecture research software enables users to adjust the communications and algorithms of the individual components of the energy system, simulation tools provide the option of specifying the features of the components to obtain the technical characteristics of the entire system. A summary of some of the prominent tools used for mini-grid design and planning is presented in Table 3. Both classical and meta-heuristic techniques have also been extensively explored for the sizing of mini-grids; more details are discussed in the literature (Dawoud et al., 2018; Baring-Gould et al., 1996).

3.2 Community needs assessment

During the conceptual stages of mini-grid projects, planners and other stakeholders are tasked with the responsibility of identifying the various needs of the communities. These needs are essential to the sustainability of such projects. Community needs appraisal is important to mini-grid developers because it helps them understand the technical, capacity, and energy needs of the community. Based on the role paid by a community, these needs usually vary from one community to another. For instance, ownership can play a role in the needs of a community; a community that does not wish to take ownership or maintain or operate a mini-grid would not need investments in local technical expertise.

3.3 Energy needs assessment

In order to determine the energy needs of a community, stakeholders are typically faced with questions related to the quality of electricity consumed, electricity use, electricity use pattern, and future growth of energy demand. Obtaining the present and expected load growth for the host community is an essential part of energy needs assessment and helps reduce uncertainties (Nsafon et al., 2020). Uncertainty with regard to energy needs can lead to over- or undersizing of the mini-grid, which may eventually lead to dissatisfaction on the part of the customers (Katre et al., 2019). Developers are expected to estimate the amount of energy the community would consume, what the energy would be used for, the pattern of consumption, and the anticipated growth in energy demand. These figures usually depend on the socio-economic status of the residents in the host community (Babatunde et al., 2019a; Ighravwe and Babatunde, 2018a). In cases where grid expansion is expected to reach the host community in the future, the mini-grid facility is cited at the closest proximity to the central grid. Besides elucidating the need for mini-grid or otherwise, energy needs assessment helps developers identify the best power generation technologies, the optimal sizes of the components, the cost of electricity, and the best revenue collection method (N R E C Association and others, 2019). With energy needs assessments, consumers can be classified according to the type of load, which helps in the development of a reflective tariff system.

While developing energy needs assessments, it is important to identify potential economically intensive activities and productive use of electricity that is present or may be put in place in the future. Thus, if the dynamics of the energy demand is known over the planning period, developers and utilities in mini-grid business would be able to set realistic economic and technical targets for the future of the business. A summary of the outputs offered by energy needs assessment is provided in Figure 3.

3.3.1 Energy demand estimation and projection

Typically, apart from residential needs, mini-grids may serve factory loads, commercial loads, schools, agricultural loads, municipal loads,

TABLE 2 Classification based on global sizing tools, island energy-system tools, single-project or local community-based sizing tools, national energy-system tools, and tools that can handle all scales (Ajeigbe et al., 2020).

Global and international energy-system tools	National energy-system tools
WILMAR Planning Tool	WASP
RAMSES	UniSyD3.0
PERSEUS	STREAM
National energy-system tools	SIVAEL
MiniCAM	SimREN
MESSAGE	ProdRisk
EMPS	PRIMES
BALMOREL	ORCED
Local community or single-project energy-system tools	NEMS
TRNSYS	MODEST
MODEST	Mesap PlaNet
HYDROGEMS	MARKAL/TIMES
HOMER	LEAP
ETEM	Invert
EnergyPRO	INFORSE
COMPOSE	IKARUS
BCHP Screening Tool	GTMax
All Scales	ENPEP-BALANCE
RETScreen	EnergyPLAN
Island energy-system tools	EMINENT
H2RES	EMCAS
	E4Cast
	AEOLIUS
	4see

hospitals, and any projected investments in those classifications. To project future demand, developers must access historical data related to population growth, the number of consumers, and the electricity use per consumer. To access future needs, it is also important to project future energy-consuming businesses, emerging technologies that can accelerate energy demand, and the state of infrastructure.

In estimating demand, the first step is to categorize the various consumers, followed by predicting the growth of the consumers based on their classification (Nkiriki and Ustun, 2017). Growth can either be in the form of energy consumption or the number of consumers. Municipal loads, such as public street lighting, are also included in the analysis. In remote communities without electricity access, the energy needs of residential consumers are carried out based on the willingness of the consumers to pay. The willingness to pay is a survey that estimates the present energy consumption (non-electric and electric) (Nkiriki and Ustun, 2017). The two components are then added to arrive at an equivalent electricity consumption. When the categories of consumers and the various energy-consuming equipment are known, the energy demand can be obtained using the following equation (Babatunde et al., 2019a):

$$E_{demand} = \sum_{a \in b} N_c \times \left(\sum_{d \in D} N_{da} P_{da} t_{da} \right), \quad (1)$$

where c is the category of the appliance to be connected, the class of the energy demand is denoted by a (this is either agricultural, commercial, educational, or agricultural), N_c is the number of users within class c, N_{da} is the number of appliances in each class, P_{da} is the nominal electric power rating of an appliance c in class a, and t_{da} is the period in which the appliance belonging to class a is used.

3.4 Capacity needs assessment

As for the capacity needs, developers must identify the administrative-related needs, technical expertise, financial needs, and institutional requirements that may hamper the construction

TABLE 3 Comparison of prominent mini-grid design tools.

Tool	Input	Output	Main energy components	Types of evaluation	Advantage	Limitations
Hybrid2 (Lambert et al., 2006)	Load data, economic data, technical details of components, resource data	Techno-economic results	Wind turbines, photovoltaic, diesel generator, energy storage	Techno-economic sizing and optimization	Dump load, supervisory control	Dynamic simulations not available, non-availability of nuclear plants
HOMER (Psomopoulos et al., 2015)	Energy demand, renewable energy resources data, economic and technical details of components, system constraints, penalties, emission data, system control	Optimal size of components, levelized cost of energy, net present cost, fuel consumption, emissions quantity, electricity production, excess energy, capacity shortage	Wind, solar PV, conventional generators, storage, boiler, electrolyzer, hydrogen tank, hydrokinetic, grid, converter, biomass, thermal system	Techno-economic analysis, emission assessment, sensitivity analysis	User-friendly, linked to MATLAB, multiple component performance results, and meteorological data can be imported from the NASA website	Dynamic simulations unavailable, non-availability of nuclear plants, single-objective optimization, unable to model system stability concerning voltage and frequency control, language limitation
RETScreen (Schwarzbözl et al., 2006)	Energy demand, economic details, component technical details, meteorological data, hydrology data	The optimal size of systems, economic details of the system	Solar PV, wind turbine, battery energy storage, cogeneration	Techno-economic, sensitivity and risk evaluation, performance analysis, benchmarking, portfolio assessment, cogeneration, energy savings emission analysis	Available in multiple languages	Time series cannot be imported, absence of temperature effect, complex evaluation not supported, data sharing issues, visualization, search, and retrieval options are limited
TRNSYS (LLC EnergySoft, 2017)	Climatic data and models from its library	Dynamic simulation results, operational features of the system, the energy output of the system	Thermal systems, wind turbines, solar thermal and PV, battery energy storage, conventional generator	Techno-economic analysis	Open-source code and dynamic simulations can be customized	Cannot model hydro, nuclear, tidal, and wave energy
EnergyPRO (Sinha and Chandel, 2014)	Techno-economic design, analysis, and optimization	Technical and economic details of the feasible systems	Battery storage, biogas fuelled CHP plants, biomass, cogeneration plants, fuel storage, geothermal, heat pumps, photovoltaic wind energy, solar thermal, tri-generation plants	Calculation and optimization of energy generation and operational economics of the optimal generators	Compressed-air energy storage, district-heating	Cannot perform dynamic simulations
COMPOSE (Ajeigbe et al., 2020)	Climate, technical, and economic details	Technical and financial results	Renewable energy, storage, and conversion, thermal- generation. Transport technologies	Techno-economic appraisal, uncertainty analysis, intermittency analysis	Users can define system methodology, compatibility with other tools, such as RETScreen and EnegyPlan	Dynamic simulations unavailable, non-availability of nuclear plants
iHOGA (Inversin, 2017)	Economic, technical, and meteorological data, constraints	Emission quantity	Solar PV, wind turbine, storage facility	Techno-economic analysis	Probability analysis, multi-objective optimization, multi-period simulation	Non-availability of nuclear plants

and smooth operation of the mini-grid facility in the host community. This would help in the sustainability of the project with regard to tariff collection, conflict resolution, facility vandalization, and technical expertise (Niyonteze et al., 2019; Hartvigsson et al., 2021). Other capacity needs that developers must identify are the ones related to the various ways residents use electricity. Some of these include demand-side activities and specific productive use of electricity (Ramakumar et al., 1986). The creation of awareness and sensitization of the community through education workshops are also some of the ways to build community capacity.

3.5 Mini-grid sizing

The sizing of a mini-grid system is typically an optimization problem. It involves sizing various components of the system so that the power generated by the entire system meets the load connected to the system. The mini-grid energy generated by the energy sources must be dispatched such that the reliability of the energy system is not compromised. Depending on the motivation, the sizing of a mini-grid system involves maximizing or minimizing a multi- or single-objective function subject to various constraints (optional or compulsory):

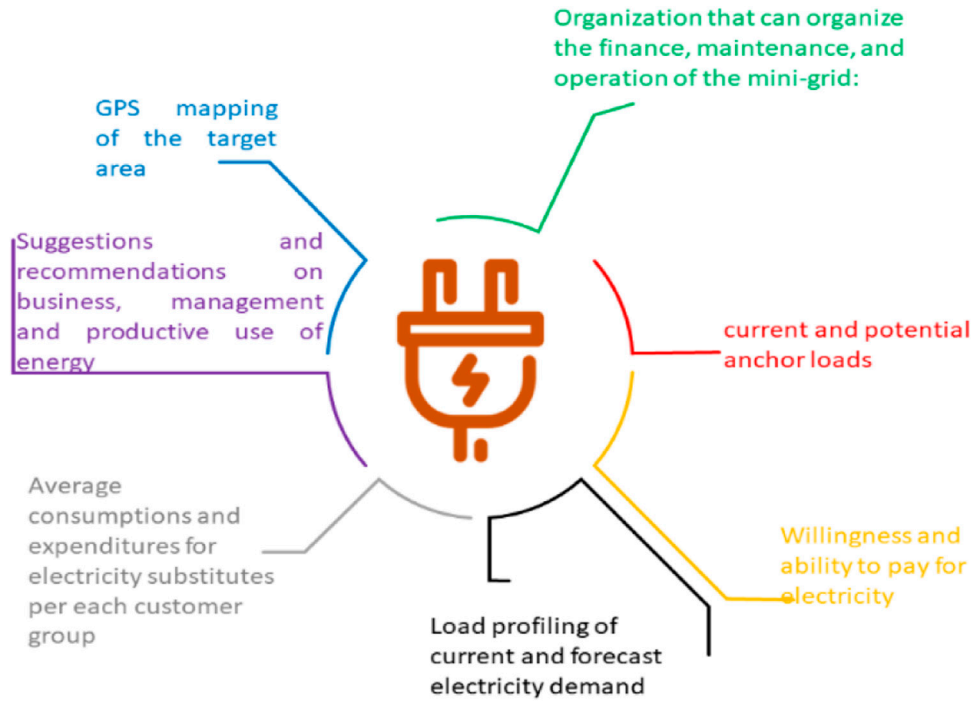

FIGURE 3
A summary of the outputs offered by energy needs assessment (Nsafon et al., 2020).

$$min\ or\ max\ Z$$
$$subject\ to \begin{cases} \text{compulsory constraints} \\ \text{optional constraints} \end{cases}$$

Some of the objective functions, constraints, and types of energy sources adopted in the literature are presented in Table 4. It could be inferred that the most common objective revolves around the economic/financial aspect of the project.

3.6 Multi-criteria perspectives in mini-grid planning

When planning for mini-grid development, certain evaluation metrics are considered. These are meant to ensure the sustainability of the projects. As earlier stated, these metrics assist the stakeholders involved in the planning and implementation of the project to make informed decisions. Depending on the objective of the mini-grid project, performance metrics are usually economic, technical (most especially reliability), environmental, social, policy, and legal (Greco et al., 2016). The economic metrics are related to the profitability and affordability of the project. The social metrics measure how bearable the proposed system is, whereas the environmental metrics measure the influence of the system on the host community. Examples of performance indicators are presented in Table 5.

The boundaries of these indicators usually overlap, thereby making decisions as regards the best mini-grid alternative complex. For instance, it could be cheap to install a fossil-powered generator because of its lower initial cost compared to solar PV. However, from the environmental perspective, more emissions are attributed to the operations of the fossil-powered generator, while none is attributed to that of the PV. Choosing between the two mini-grid options becomes a complex decision. Moreover, in the selection of the most preferred mini-grid alternative, decision-makers are usually faced with quantitative and qualitative indicators. While it is easy to measure the quantitative indicators, defining the extent of the qualitative indicators is usually complex. Since renewable energy-powered mini-grids are typically dependent on meteorological parameters and their availability at any time, decision-makers are faced with the dilemma of identifying the best sites. Mini-grid site locations also depend on proximity to existing infrastructures and land use.

Various multi-criteria decision-making (MCDM) frameworks have been developed to address these types of challenges, including TOPSIS, AHP, VIKOR, PROMETHEE, ARAS, EDAS, SAASPAS, MOORA, COPRAS, DEMATEL, and SWARA (Ighravwe and Babatunde, 2018b). For instance, to improve the sustainability of mini-grids, researchers have explored the use of MCDM in addressing various issues. Researchers have applied CRITIC-TOPSIS with interval type-2 fuzzy sets to prioritize the mini-grid business model that is applicable to the Nigerian energy sector (Pohekar and Ramachandran, 2004). The result from the study indicates that the most preferred model based on the 12 criteria identified by the authors is the private business model. In order to improve the planning process of mini-grids, another study used AHP-VIKOR with a Plan-Do-Check-Act cycle to rank hybrid renewable energy alternatives (Azimoh et al., 2016). A detailed review of the applications of MCDM in mini-grid developments, energy policy, and energy planning has been presented in the literature.

TABLE 4 Objective functions in the implementation of mini-grids.

Ref.	Objective function	Constraints	Energy sources considered
Balamurugan et al. (2009)	Minimization of total annualized cost $c = \sum_{i=1}^{M} R_i \left\{ \sum_{j=1}^{N} a_{ij} x_{ij} \right\}$	Total energy supplied, sum of the resources, non-negative constraint, rate of energy use	Wind turbine, solar PV, micro-hydro, biogas
Hennet and Samarakou (1986)	Maximization of energy supply and minimization of dumped load $\sum_{t=1}^{24} \left\{ \sum_{i} P_i I_i(t) - Q_{dump}(t) \right\}$	PV array constraints, load, gasifier module constraints, wind system constraints, dumped load, battery constraints	Solar PV, battery, wind turbine, biogas
Iniyan and Sumathy (2000)	Minimization of the system's entire life cycle cost $z = E\left\{ \sum_{i=1}^{n} C(X_i) \right\} + C_1(Q) + C_2(R) + C_3(B_{max})$	Operational constraints, electricity production	Solar PV, wind turbine, and storage
Nagabhushana et al. (2011)	Cost/efficiency ratio minimization $\sum_{j=1}^{6} \sum_{i=1}^{I} \left(\frac{C_{ij}}{\eta_{ij}}\right) \times X_{ij}$	Reliability, social acceptance, potential limit, demand	Solar PV, biogas, biomass, wind turbine
Li et al. (2019)	Equipment cost minimization $z = \sum_{i} C_{pv_i} N_{pv_i} + \sum_{j} C_{wd_j} N_{wd_j} + \sum_{k} C_{batt_k} N_{batt_k} + \sum_{l} C_{in_l} N_{in_l}$	Maximum power wattage, PV maximum power, annual load	PV, wind, battery
Zeng et al. (2010)	Maximization of daily net cash flow $z_1 = (\sum_{t=0}^{23} (revenue_t - VC_t) - FC$	Energy balance, resource limit, system operation boundaries	PV, wind, bioenergy, energy storage
	Minimization of emission $z_2 = (\sum_{k} \sum_{t=0}^{23} q_{GHG,k} \times P_{k,t}) - (\sum_{p} \sum_{t=0}^{23} W_{CO2/c} \times M(C)_{p,t})$		
Lee and Chen, (2009)	Minimization of cost and maximization of power quality $z = \sum_{i=1}^{n} \sum_{j=1} (\beta_1 C_i + \beta_2 Perf_{ij}) P_{ij}$	Power demand, capacity constraint	Wind, PV, battery
Katsigiannis et al. (2012)	Maximization of benefit-cost ratio $BCR = \frac{\sum_{m=1}^{12} E_m}{CC_w + AF_w + CC_p + AF_p + AOM}$	Contract capacity limits, wind, and PV installed capacity	Wind, PV
Hakimi and Moghaddas-Tafreshi (2009)	Cost of energy minimization $COE = \frac{C_{anntot}}{E_{anloadserved}}$	Components' size, capacity shortage, unmet load, fuel consumption, initial cost	Wind turbines, PV, diesel generators, biodiesel, fuel cells, batteries
Siddaiah and Saini (2016)	Minimization of the total net present cost $NPC_{tot} = NPC_{wd} + NPC_{el} + NPC_{\text{refreactor}} + NPC_{tank} + NPC_{converter} + NPC_{fc}$	Energy demand, over demand, over generation	Wind turbine, fuel cell, biomass

3.7 Mini-grid siting using geospatial analysis

The hybridization of the MCDM and GIS has been identified as a very valuable method to analytically harness available geographical information or meteorological data and to employ criteria importance in specifying the optimal sites for mini-grid implementation. As such, because of its visualization capabilities and high spatial resolution, more recently, the geographical information system (GIS) has been hybridized with MCDM approaches to select the best site for the location of mini-grid projects. Although potential sites for the implementation of mini-grids can be anchored on the factors discussed in Table 5 (social, technical, economic, environmental, and policy), geographical attributes, such as slope and proximity to major infrastructure, are also important factors that must be considered. Consequently, the integration of GIS MCDM tools has become effective in proposing solutions to the multifaceted dilemma of optimal site selection for mini-grid projects. The GIS-MCDM approach has found application in the wind and solar form siting. For instance, Ayodele et al. (2018) proposed a GIS-MCDM approach based on interval type-2 fuzzy analytic hierarchy to assess the most preferred site for the implementation of wind farms across Nigeria. Moreover, Al Garni and Awasthi (2017) applied the GIS-AHP approach to the selection of the best site for a solar PV power plant in Saudi Arabia. Other examples of cases where GIS and MCDM approaches have been deployed for energy planning in Africa are given in Table 6.

4 Challenges with off-grid mini-grid projects in SSA

In this section, challenges associated with mini-grid projects are discussed, as well as solutions proposed in the literature.

4.1 Poor community participation

When a community cannot buy into a social project, such a social venture is set up for failure *ab initio*. In situations such as this, there will be conflict over issues such as siting of the project, security of the project, and community part-financing the project *via* contributing free/minimized manual labor for stages such as site clearing. It is vital to engage the support of the entire community as much as possible through agencies of mediation and consultation that can facilitate communal interactions, including community leaders, traditional rulers, community

TABLE 5 Examples of performance indicators.

Criterion	Attribute	Description	Status
Technical	Reliability	The reliability of the power supply from the mini-grid is very important, and decision-makers usually ensure that the outage of supply is minimal. When designing mini-grids, the reliability of supply can be improved by hybridizing power sources. The reliability of mini-grids does not only improve the availability of power supply, but it reduces the net costs over the lifetime of the facility (Babatunde et al., 2019a). Therefore, there must be an optimum reliability level for the generating system based on the system's operational attributes. Some of the indicators used in measuring reliability in mini-grids include loss of power supply probability, equivalent loss factor, loss of load expected, total energy lost, level of autonomy (Somefun et al., 2022)	Beneficial
	Risk	Mini-grid risks can be related to various aspects of the business. According to van Bracht et al. (2016), mini-grid risks in rural communities include risks of resource price variability, political risks, and risks related to payments	Non-beneficial
	Unmet load	Unmet load occurs as a result of the imbalance between supply and demand (Babatunde et al., 2019a)	Non-beneficial
	Feasibility	This is related to the viability of project implementation (BloombergNEF and SEforALL, 2020)	Beneficial
	Uncertainty	When planners do not have access to quality information, various levels of uncertainty may occur, and this may affect service delivery. Decision-makers must integrate a certain level of certainty into their designs during the planning stage. One major technical uncertainty that a multi-source mini-grid face dispatch decision, which usually affects investment choices (Upadhyay and Sharma, 2014)	Non-beneficial
	Duration of implementation	According to Bhattacharyya (2015), this indicator is used to estimate the accessibility of availability in the host community and reach the minimum cost and is an alternative to decreasing the financial assets. During the implementation phase, the years or months it takes to implement the project is taken as an indicator	Non-beneficial
Economic	Capital cost	The capital cost is the economic investment used in implementing the proposed project. The indicator examines the total costs needed to make the mini-grid totally operational (Yusuf and Mustafi, 2018)	Non-beneficial
	Net present cost/life cycle cost	The total net present cost of a mini-grid is the present value of all the costs that it incurs over its lifespan, excluding the present value of all the income that it receives over its existence. This indicator is extensively used in the literature for selecting optimal mini-grid (Hansen, 2019)	Non-beneficial
	Levelized cost of energy	The levelized cost of energy is the ratio of the cumulative cost of the mini-grid to the energy served by the system over its lifetime (Babatunde et al., 2019b)	Non-beneficial
	Profitability	This indicator assesses the economic viability of the system from the business perspective. Some of the profitability indices used for assessing mini-grid include present worth, discounted payback, annual worth, simple payback, internal rate of return, and return on investment (Eales and Unyolo, 2018)	Beneficial
	Funds availability	This indicator explores the avenues by which economic support can be harnessed for the implementation of the mini-grid. Some of these include government, private, charity, and international agencies	Beneficial
Environment	Emission	These include the quantity of a pollutant released from the implementation and operations of the mini-grid	Non-beneficial
	Life cycle assessment	Life cycle assessment is an evaluation of "cradle-to-grave" or "cradle-to-cradle" to obtain the environmental effects related to all the phases of all the components of the mini-grid (Micangeli et al., 2017)	
	Land requirement	What is the quantity of land needed for the implementation of the mini-grid? It is one of the most important factors that must be considered by all stakeholders because if the host communities are not properly considered, they may become hostile to the facility (Ortega-Arriaga et al., 2021)	Non-beneficial
	Environmental impact	When mini-grid projects are implemented, they usually have an impact on the environment. This must be considered during the planning stages of the project (Babatunde et al., 2019c)	Non-beneficial
Social	Employment opportunities	This measures the number of jobs created by the implementation of the mini-grid; this could be direct or indirect. What impact does the mini-grid project have on the labor market (Wolsink, 2020)?	Beneficial
	Social acceptance	The criterion accounts for the avoidance of backlash from all stakeholders with respect to renewable energy alternatives (Pillot et al., 2019)	
	Political acceptance	Political acceptability is a strategic choice-limiting factor for investments in mini-grid projects (Akinyele et al., 2018)	

development associations (CDAs), and local government and town hall meetings (Peters et al., 2019).

The question of who owns the mini-grid project must be settled from the point of conception. The research has indicated that the method used by donors and donor agencies to simply install energy generation systems without plans for long-term sustainability does not work in the end. For instance, solar installations that have the potential to last for 20 years do not survive after the third year after installation and commissioning (Babayomi and Okharedia, 2019). Some other challenges associated with community participation include a lack of clearly defined commercial/community ownership structure, infrastructural insecurity, and community illiteracy on sustainable energy practices. Hence, solutions to these challenges include effective community participation, clearly defined commercial/community ownership structure, collaborating with community security groups, and public energy literacy and advocacy campaigns (Peters et al., 2019; AMDA and ECA, 2020).

TABLE 6 Application of GIS in energy panning and mini-grid site location.

Methods	Application	Location	Ref.
GIS-type-2 fuzzy analytic hierarchy	Wind farm	Nigeria	Al Garni and Awasthi (2017)
Best Worst Method, TOPSIS and VIKOR	Solar PV, wind, and hybrid solar/wind	Kenya	Diemuodeke et al. (2016)
TOPSIS	Diesel, solar PV, wind energy systems	Nigeria	Odoi-Yorke et al. (2022)
15 unique MCDM algorithms and Spearman rank correlation	PV, wind, battery, and natural gas	Ghana	Rezk et al. (2021)
HOMER, no priority, CRITIC, entropy, pairwise comparisons, TOPSIS, COPRAS, SAW, GRAY	PV, battery, diesel	Egypt	Messaoudi et al. (2019)
GIS-AHP	Solar hydrogen production sites	Algeria	Wagemann and Manetsgruber (2016)

4.2 Economic challenges

This relates to subsisting poverty in spite of electricity access. The average monthly energy consumed by each connected off-grid mini-grid user in SSA is only 6.1 kWh (Nygaard et al., 2015). To put this in context, this amount of energy can only power a 65 W laptop charger for only 3 h daily. When residents do not have a compelling reason to subscribe to electricity plans, it can limit its impact and even sustainability in the rural area supplied. Other challenges include revenue generation problems, macroeconomic economic instability, exchange rate fluctuations, and high operational and maintenance costs. A lack of government cash guarantees and high import taxes also hamper mini-grid development. Their policy even supports developers with insurance in case of political instability. A tax-free import regime on PV panels, like the practice in Kenya, is more favorable to mini-grid businesses (Ohunakin et al., 2014). Furthermore, for components that government is unwilling to give tax-free classification (probably due to their use by non-mini-grid entities too), lower taxes will be a boon (Peters et al., 2019; AMDA and ECA, 2020).

4.3 Technical challenges

Several remote communities had no prior data on electricity consumption. It is sometimes difficult to carry out energy forecasts, for instance, the village size, prior adoption of mobile phones, how much the mobile phone is used, and the nature of commercial activities in the community. There is a paucity of skilled technical workers and a void of standardization and certifications in the mini-grid and hybrid renewable energy sectors (Peters et al., 2019). A lack of feasibility studies prior to the commencement of the project also leaves the project vulnerable to circumstances and factors that could result in premature failure. These challenges can be overcome by leveraging technology to improve energy forecast accuracies and engage engineers and technologists with a track record of professionalism, bespoke feasibility surveys, regular maintenance procedures, government-led oversight and standardization, and use of quality-certified equipment and components (Peters et al., 2019; AMDA and ECA, 2020).

4.4 Environmental challenges

The lack of detailed mapping of local renewable energy resources that form inputs to the mini-grid system makes cost-minimization difficult. A resource map available at a country level and spread across all the remote communities will enable a correct mapping of energy resources to mini-grid projects. The International Renewable Energy Agency (IRENA) has published data from Geographic Information Systems (GIS) data to prepare a country-by-country mapping of renewable energy technology resources for solar energy, wind energy, and bioenergy production (Morstyn et al., 2018). There is a lack of impact assessment reports on how renewable energy technology sources affect the local environment. For instance, wind energy turbines impact the skyline, and when there are many of them, they cause noise pollution. Furthermore, there could be a need to clear vegetation or a forest to accommodate a large amount of energy equipment such as solar panels or wind turbine farms. The details in the energy impact assessment at each location should form a significant determinant of the type of renewable energy system deployed there (Peters et al., 2019; AMDA and ECA, 2020).

4.5 Policy and political challenges

Traditionally, power investments and developments in SSA have been the prerogative of government electricity agencies or parastatals. Therefore, in climes where there is still heavy government involvement, the focus on traditional large-scale electrification projects to the exclusion of decentralized electrification is rampant. Some of this stems from skills and knowledge gaps at the top echelon of government. The weak political will of the government (Monyei and Akpeji, 2020) stems largely from the poor quality of energy advisers in the government. For instance, due to bureaucratic inefficiencies, it takes an average of 17 months to secure regulatory license approvals to operate mini-grids in SSA (Nygaard et al., 2015). Moreover, a lack of a grid-creep protection policy causes uncertainties about the future fate of rural mini-grids. This apprehension makes major private investments in the industry high risk and, hence, high cost. Policies, including mini-grid or renewable feed-in tariffs, can help in such situations (Pedersen, 2016). Additional related challenges include a lack of tariff-subsidy regulations and ineffective quality control implementation. Some tariff-subsidy policies required to boost the penetration and proliferation of mini-grids in SSA include feed-in tariffs and feed-in premiums (Babayomi and Okharedia, 2019). These also

TABLE 7 Challenges to mini-grid developments in Sub-Saharan Africa and corresponding solutions (Peters et al., 2019; Boait, 2014).

Title	Solutions
Community ownership *vs.* commercial ownership	• Effective community participation
	• Clearly defined commercial/community ownership
	• Security for energy infrastructure
	• Public energy literacy and advocacy
Economics	• Microfinance and business capacity development
	• Viable commercial mini-grid model
	• Political and economic instability guarantee and incentives
	• Government cash guarantees and low-tax import
Technical considerations	• Leverage technology to improve energy forecast accuracies
	• Engage engineers and technologists with a track record of professionalism
	• Bespoke feasibility surveys
	• Regular maintenance procedures
	• Government-led oversight and standardization
	• Government-subsidized capacity-building
	• Use of quality certified equipment and components
Environmental considerations	• Local energy resource mapping data
	• Energy impact assessment reports
Policy and political factors	• Better skilled and up-to-date power and energy technocrats
	• Grid-creep protection policy
	• Tariff-subsidy regulations
	• Invigorated and empowered quality control task force

provide mini-grid operators additional income and security when the grid is later extended to their remote locations.

Table 7 summarizes the sustainable mini-grid framework to combat the problem of failed mini-grids in SSA.

5 Finance and tariffs for SSA mini-grids

This section discusses the finance and tariffs of mini-grids in SSA.

5.1 Finance

Mini-grid projects are funded through loans, equities, grants, and subsidies (Aziz et al., 2016). These funds are sourced from corporate entities, foundations, and government agencies.

Selecting financial means and types of investment for funding mini-grids depends on the mini-grid type and the development stage of the project. The earlier the stage, the riskier the project, and the later the stage, the less risky the project (Zhang et al., 2020).

Most mini-grids in SSA heavily rely on grants and subsidies for at least 30% of the cost used for investment. The grants and subsidies are majorly used for piloting the mini-grid project, the initial operational needs of the projects, and investing in capital and technical engagements. They are usually sourced from local agencies, private individuals, international agencies, trust funds, and foundations (von Breitenstein, 1999).

Equity is another means by which mini-grids in SSA are financed. Equity investors are a very good means of financing mini-grid investments. Equity investors include Angel investors and venture capitalists (who provide initial capital for the development and implementation of mini-grid projects), private equity (for expansion of capital investments), impact investors (who decide to provide initial or final capital investment depending on the investor, and the social and financial return of the project), and development financing institutions (DFIs) that provide equity investments directly or through third-party funding streams. DFIs look for potentials in the form of development impact and project viability before making financial commitments (Jonker Klunne, 1020; Nuru et al., 2021; Bukari et al., 2021; Antonanzas-Torres et al., 2021c).

Loans become necessary when grants, subsidies, and equities are unavailable. DFIs are the most common sources of loan provision in SSA. They offer loans that are concessional and lower-priced than other commercial lenders. However, the high transaction cost for DFIs does not suit the operations of small mini-grids. Local commercial banks categorize the business models of mini-grids as very high risks; they either do not lend at all or offer prohibitive lending rate terms and conditions (Jonker Klunne, 1020; Nuru et al., 2021). International

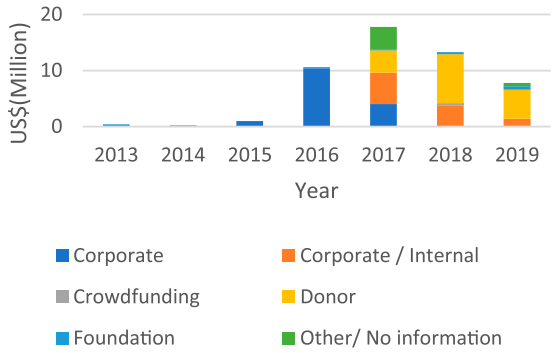

FIGURE 4
Comparison of funding obtained from different funding types (Eales and Unyolo, 2018).

lenders avoid mini-grid transactions, too, owing to their relatively small value and foreign exchange risks (Jonker Klunne, 1020; Nuru et al., 2021; Bukari et al., 2021; Antonanzas-Torres et al., 2021c).

Guarantees are used to ensure that financing mini-grids are successful by improving the debit or credit worthiness of the mini-grid project. This serves as an assurance to investors that mini-grids can meet their profit expectations. Two types of financial guarantee exist; loan guarantee, which covers repayment of loans in full and in due time, and risk guarantee, which covers the full or part repayment of loans (Jonker Klunne, 1020; Nuru et al., 2021; Bukari et al., 2021; Antonanzas-Torres et al., 2021c).

Foreign exchange risk is a major challenge faced by developers of mini-grids in SSA. The capital cost of mini-grid projects is usually in foreign currency, whereas the revenues are in local currency. There is usually a currency mismatch between capital investments and revenue whenever the local currency loses its value against the foreign currency. Projects funded in foreign currency, such as dollars, pounds, and euros, are usually affected by this currency mismatch (Pillot et al., 2019; Ihirwe et al., 2021).

In 2008, the Tanzanian government developed a framework to encourage investments in decentralized electrification. This led to an increase in the number of mini-grid investments in the country. Since that period, private businesses and local communities now conduct their activities using mini-grid systems (Booth et al., 2018). The framework of small power producers (SPP) designed by the Tanzanian government in 2008 allowed facilities generating electricity of less than 10 MW from renewable sources to sell power to the country's main grid as retailers and wholesalers as a means of funding the operations of the facilities. In order to support the development of mini-grids, the Tanzania Rural Electrification Agency (REA) created the Tanzania Energy Development and Access Project (TEDAP) supported by the World Bank, offering grants to develop mini-grid projects in Tanzania. The World Bank also came up with a $23 million loan scheme to support the government-owned Tanzania Investment Bank for the delivery of 15-year loan facilities to local commercial banks, which was to be used for the development of mini-grid projects in Tanzania (Booth et al., 2018). Although the loan scheme has benefited mini-grid projects, many developers have had trouble accessing the funds. Despite funding support received by the Tanzanian government from other international donors in support of activities for the development of mini-grid projects, developers remain concerned about the unknown risks involved in mini-grid investment (Nfah and Ngundam, 2012).

Figure 4 and Table 8 show the number of funds obtained from result-based financing schemes to support mini-grid development in East Africa since 2013.

Figure 4 shows that the year 2017 experienced the highest amount of funds (with more than $17 million) distributed for financing mini-grid projects. Funding for that year came from foundations, donor agencies, crowdfunding sources, and corporate organizations. The years 2013 and 2014 experienced the lowest amounts of funding, which came only from corporate organizations and foundations. Figure 4 shows that funding increased from 2014 to 2017 before experiencing a decrease in 2018. The increase can be linked to good returns on investment, which increases the confidence of funders, whereas the decrease can be linked to poor returns on investment, which could be caused by mismanagement or unfavorable government policies leading to a decrease in the confidence of funders.

In Table 8, grant capital expenditure (CAPEX) refers to grants in the form of capital expenditures (in the form of building sites, provision and installation of panels, generators, meters, and batteries), whereas grant operating expenditure (OPEX) refers to grants in the form of operating costs and expenses (research and development, consultancy, capacity building, and marketing). It can be observed that corporate organizations provide grants only in the form of capital expenditures, whereas donor agencies and foundations provide grants in the form of capital expenditures and operating costs. In terms of capital expenditure, donor agencies provide the highest amount.

Figure 4 and Table 8 show the importance of funding in the development of mini-grid projects and initiatives.

Figure 5 shows the amount of funding received by the different regions in the African continent.

From Figure 5, Western and Central Africa received no funding from 2013 to 2016 while receiving a small amount of

TABLE 8 Funding support received through corporate expenditures and operation expenses (Nygaard et al., 2015).

	Grants—CAPEX	Grants—OPEX	Debt.
Corporate	$4.2 million	—	—
Corporate/internal	$0.4 million	—	$10.0 million
Crowdfunding	—	—	$0.3 million
Donor	$27.0 million	$3.0 million	—
Foundation	$1.4 million	$0.2 million	—

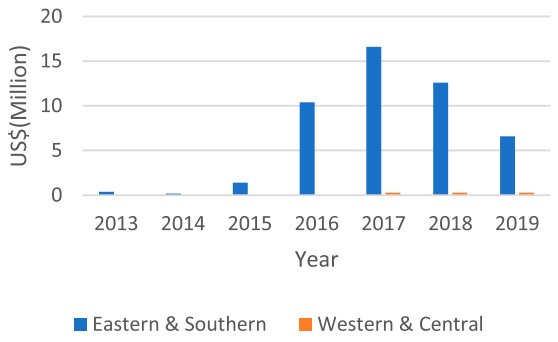

FIGURE 5
Funding obtained by different regions in Africa (Nygaard et al., 2015).

funding below $1 million from 2017 to 2019. East and Southern Africa received funding support from 2013 to 2019. Funding for East and Southern Africa increased from 2014 to 2017 and experienced a decrease in 2018 and 2019. The year 2017 showed the highest amount of funding support to regions in Africa.

5.2 Tariffs

Some key drivers influence tariff plans for mini-grids in SSA. For effectiveness and sustainability, any tariff structure must adequately balance the needs of three key groups of stakeholders: governments, developers, and customers (Allee, 2021).

- Government: Composed of ministries of energy, government regulatory agencies, and banks who are responsible for the creation and implementation of energy policy, enforcement of regulations, and provision of financial and funding instruments for implementation of mini-grid projects.
- Developers: Oversee all activities regarding planning, construction, commissioning, operation, management, and revenue collection for the mini-grid project. They are held responsible by financial donors for all expenses made during project implementation. They ensure that all financial requirements put in place by donor agencies are met during project implementation.
- Customers: Typically do not have direct control over tariffs, but their concerns and subsequent decisions influence the considerations of both governments and developers. For example, their perceptions of and willingness to pay tariffs and fees can have political impacts on governments and real impacts on system design, customer connection rates, load growth, and financing considerations.

Creation and regulation of tariff plans can be achieved with the use of different approaches. Some of these approaches include the following:

i) Uniform tariff: In this type of structure, all mini-grid consumers are billed the same way without consideration of the utility type of the grid (which could be rural utility, urban utility, or isolated type of grid) they are connected to. This type of tariff plan ensures fairness and equity in utility distribution amongst customers. The government subsidizes electricity rates to ensure that electricity prices are cheap and affordable (Korzhenevych and Owusu, 2021; Reber and Booth, 2018).

ii) Cost-reflective tariff: In this tariff plan, mini-grid developers freely set their own tariff and payment plans at high levels that enable them to recover their capital and operational expenses directly from the consumers. In several situations, the tariff plans may also be subject to approval by a regulatory body or the government. Cost-reflective tariffs are usually higher than the rates that existing grid customers are charged; however, these charges are decided *via* negotiations between customers and micro-grid operators where both parties agree on a rate suitable for the customers while allowing the operators to recover all expenses and incurred cost (if this arrangement does not exist, this could lead to a potential failure in the micro-grid development). Most times, the micro-grid developers charge cost-reflective rates, which are lower than the price unconnected customers would pay for energy generation in the form of kerosene, candles, batteries, or other fuels (Antonanzas-Torres et al., 2021c; Akpan et al., 2013; U.S. Agency et al., 2020).

iii) Bid Tariff: In this tariff plan, prices are set at the lowest price by mini-grid developers in a competitive and efficient bidding process involving retailers who push down prices to consumers (Léautier, 2001). Prices generated from bids provide good solutions to the problem of defining the prudent cost of electricity that would be passed to consumers. This is a good strategy that could be used in procurement policies aimed at reforming the power sector of any country (Kalathil et al., 2019).

iv) Willing buyer, willing seller: In this scheme, tariffs are created *via* an agreement involving mini-grid developers and customers or a network of customers (customers could be retailers or direct consumers). In this type of plan, middlemen can be bypassed, and consumers can directly access the developers (Manetsgruber, 2015).

v) Hybrid approaches: In this tariff plan, elements of the cost-reflective and uniform tariff structures are combined. Using this approach, the government allows the use of cost-reflective tariffs while providing grants or subsidies to offset micro-grid costs to ensure that micro-grid tariffs consistently match those charged to grid-tied customers. In this situation, subsidies are directly provided to micro-grid developers or consumers. However, it is very risky for investors and developers to rely on subsidies from governments that have a reputation for lacking creditworthiness. Investors might require a guarantee that any form of government subsidies will be valid for a long time (at least 7 years and above) to recover their costs and become profit-oriented eventually (Antonanzas-Torres et al., 2021c; Akpan et al., 2013).

Table 9 summarizes the tariff strategies used by different countries in SSA.

All governments consider equity and fairness when determining tariff plans for public use. Many African governments have put in place electricity tariffs, which are uniform across their country, and they have ensured that these plans are low and affordable for public consumption based on economic realities. In most cases, the national tariffs are set lower than the charges that must be set by the mini-grid

TABLE 9 Tariff strategies in Sub-Saharan Africa (Léautier, 2001).

Tariff approach	Countries
Uniform tariff	Ghana, Kenya
Bid tariff	Uganda
Cost-reflective	Ethiopia, Kenya, Nigeria, Ghana, Rwanda, Tanzania, Zambia, Uganda
Hybrid	Namibia, Ghana
Willing buyer, willing seller	Nigeria, Ghana, Rwanda, Tanzania, Zambia, Uganda

utilities to make up for their cost of operations and capital. While this is favorable for consumers, this is unfavorable for micro-grid developers. In a recent survey conducted for stakeholders in the African power industry, two-thirds of respondents expressed concerns over the difficulties involved in recovering from the high costs of implementing power projects under current tariff schemes. According to them, this is the biggest barrier to rapid power development in SSA (Akpan et al., 2013).

As a result, national governments have created subsidy schemes to make up for the gaps and ensure a continuous supply of utility services. As attractive as the arrangement of subsidy may be, it is potentially able to drain the financial resources of the country and distort capital market operations. Subsidy shortfalls arising from subsidy schemes can discourage utilities from expanding their energy service because their operations have become overly dependent on funding coming from government subsidies. This can lead to utilities losing profits and bring a premature end to their operations. For instance, in 2016, the Tanzania Electric Supply Company Limited (TANESCO) made a request to the Tanzanian government for a hike in the rate of electricity supply by 18.9% to make up for ongoing losses. The government regulator responded by granting a hike of 8.5% rather than the 18.9% requested. The 8.5% hike was later blocked by the Tanzanian president, which led to continuous losses in utility, thereby affecting grid expansion and long-term financial liabilities (Akpan et al., 2013). The provision of subsidies to mini-grid utilities should only be explored in critical times. It is very important to make these utilities economically viable with little support from the government by expanding their capacity to meet growing energy demand and support economic development. To forestall the effects of changing domestic responsibilities and global trends, the governments in SSA avoid signing long-term power purchase agreements (PPAs) that can cause barriers to short-term restructuring, which are immediate responses to unforeseen circumstances.

6 Policy status for off-grid electrification in SSA

Despite the global attention that energy access has received in recent years, at least since the launch of the "Energy for All" in 2012 and the Sustainable Development Goals 2015 (Goal 7), the pace of growth has failed to match the projected level of delivery to the society, especially in rural areas, which has remained slow compared to the population growth. Access to electricity is more problematic and evident in the SSA region and demands an active-driven approach from the national government of each country to enact workable and sustainable energy policies that will attract investors. Such policies will encourage patronage of off-grid mini-grid electrification, which will improve access to electricity in the region, thereby reducing poverty and improving the standard of living. Despite the enormous potential offered by off-grid electrification as alternative access to electricity, some technical and environmental limitations affect it. These challenges include weak regulatory and policy environmental instability, business practicability, affordability, and financial obstacles. In all of these and according to Aglina et al. (2016), who categorized the challenges related to off-grid electrification, their study identified weak regulatory and policy frameworks as the main challenge. Therefore, this section presents the policy status for off-grid electrification in SSA countries.

6.1 Policy status of off-grid electrification in Ghana

In 2016, Ghana's Ministry of Energy (MoEn) issued a policy statement to regulate the deployment of mini-grid electrification in Ghana. The policy incorporated the public sector model of ownership and installation of mini-grids. The policy highlighted that electricity generation would be the responsibility of the public utility generation and the Volta River Authority (VRA). While the responsibility to distribute power to customers is vested in the distribution utilities: the Electricity Company of Ghana (ECG) and the Northern Electricity Distribution Company of Ghana (NEDCo) (Bukari et al., 2021). Thereafter, Safdar (2017) reported that all utilities have permission to generate and distribute power to customers. He asserted that VRA is allowed to generate and distribute power on the island, whereas NEDCo and ECG shall provide for lakeside communities within their territories. The policy statement further includes the incorporation of mini-grid electrification into the National Electrification Scheme (NES) and the safeguarding of the investment by the government. In addition, the proposition to develop an inclusive investment plan for mini-grids by the Ministry of Energy (MoEn) and the procurement of all mini-grids that allow competitiveness are part of the policy. Furthermore, the application of uniform tariffs to all customers as it is relevant to the central grid and the provision of renewable energy funds that will support the expansion of mini-grids are stated in the regulation. Based on these established facts, all businesses relating to electricity generation in Ghana are expected to acquire licenses that will guide their activities, including mini-grid operations. Currently, there is no record of a sole regulatory policy apart from the incorporated one, which will partially regulate the mini-grid operations in Ghana. Notwithstanding, the authors proclaimed to

have sighted a revised version of regulations being drafted by the Energy Commission in 2017, which will address: the scope of applicability, conditions of award of licenses, and technical and commercial regulations.

6.2 Policy status of off-grid electrification in Nigeria

As many African countries are seriously developing interest in the deployment of mini-grid electrification, Nigeria is not exempted. In 2017, the country's electricity regulatory commission approved inclusive guidelines to encourage mini-grids for both off and grid connections with a cap to regulate tariffs for grids with a distribution capacity of more than 100 kW. In a situation of stand-alone mini-grid energy generation with a capacity ranging from 100 kW to 1 MW, developers are required to obtain permits, whereas those with capabilities to generate up to 100 kW are required to register with the country's electricity regulatory commission. The provision of subsidized capital cost by the Nigerian regulatory commission has significantly contributed to the attendant of the mini-grid electrification projects the country has recently enjoyed. In some cases, there are hybrid ownerships of the system in which the federal government offers financial resources for the project, whereas the local communities make available land and security of the projects.

6.3 Policy status of off-grid electrification in Mali, Kenya, and Senegal

Over time, diesel-based mini-grid electrification is mostly embraced in Mali, and the establishment of a rural electrification fund for mini-grid development has enhanced the involvement of private investors and developers. The rural electrification fund set aside to offset the feasibility studies and the capital cost of the projects make it more pronounced. Even then, the associated negative consequences of diesel-based mini-grid electrification, such as global warming, have motivated the Malian Agency for the Development of Domestic Energy and Rural Electrification to provide financial aid by relieving the value-added tax (VAT) on all renewable energy equipment imported. The financial aid is to inspire the deployment and incorporation of renewable energy into the existing mini-grid systems, which are more sustainable (Tenenbaum et al., 2018). Like Mali, Kenya's earlier mini-grid electrification is diesel-based. Thereafter, some non-government organizations, faith-based organizations, and research institutions introduced the deployment of renewable energy mini-grid to the country. This prompted Kenya's government to institute a program incorporating renewable energy into the diesel-based mini-grid system, which has improved the number of mini-grid systems in the country. Presently, the Kenya Power and Lighting Company is responsible for the operation and maintenance of the systems. With this policy arrangement, the non-government organizations support the community-based mini-grids, whereas the private organizations are free to operate under various business models. To ensure an effective operation, Kenya's government signed an agreement with the Kenya Power and Lighting Company to keep all profits generated from mini-grids for the operation and maintenance of the system, and it will be responsible for the emanated losses. This arrangement has improved the feasibility of the system in the country (Niyonteze et al., 2019; Tenenbaum et al., 2018).

6.4 Policy status of off-grid electrification in Rwanda, Mozambique, and Tanzania

The first set of mini-grid electrification in Rwanda was for powering a set of rural healthcare clinics funded by international partners (Energy Sector Management Assistance Program, 2017). Recently, in 2015, the Rwanda Utility Regulatory Agency publicized an enthusiastic mini-grid regulation framework that excuses electricity generation below 50 kW from procuring an operating license, but the generation of 50–100 kW needs a simple license. The policy extends olive oil to private operators of mini-grid electrification to have access to grant support of 40%–70% and capital expenditure subsidies up to 100 kW. Further, the suppliers of mini-grids where there is the attendance of the main grid electrification are allowed to either transfer its asset to the utility company or sell electricity based on a fixed tariff as a small electricity generator (Safdar, 2017; Euei, 2014; Walters et al., 2015; Stiles and Murove, 2015). In Mozambique, the earliest mini-grid electrification, mostly installed by the Energy Fund (FUNAE) created by the government, are not functional due to the lack of maintenance (SEI, 2016). Although FUNAE is responsible for the operation of the existing off-grid mini-grids, it handed the management of small electricity generation below 10 kW to the local management committees, which shows that a regulatory framework for an effective operation of mini-grid electrification is needed. Interestingly, the Tanzania government has a mini-grid regulatory framework that exempts payment of VAT and import duty, which are motivations for the deployment of mini-grid electrification (Moner-Girona et al., 2016). Furthermore, the small power producers' framework released by the Energy and Water Utilities Regulatory Authority (EWURA) has motivated private investors to invest in off-grid and mini-grid electrifications. These have contributed to the rapid growth of the mini-grid electrification in Tanzania, amounting to 0.2 MW (Pedersen, 2016; Bukari et al., 2021; Bank, 2017a). Presently, in Tanzania, private organizations install mini-grids, but the Rural Electrification Agency (REA) provides technical support (Tenenbaum et al., 2018; Euei, 2014).

6.5 Policy status of off-grid electrification in South Africa

There is vast potential for off-grid electrification in South Africa. However, this potential is yet to be fully explored due to the limited and unclear policy framework (Nasir et al., 2018). The success of off-grid electrification in South Africa depends on the right regulation and policy framework, which is lacking. Although the South Africa Government and those of other SSA countries are giving significant attention and encouraging investors to support mini-grid electrification in their regions through the development of environmentally friendly policymaking (Pegels, 2010), the current energy policy in South Africa is primarily intended for grid electrification, which is unhealthy for the utilization of mini-grid applications. This current energy policy is monopolistic in nature, unaligned with mini-grid investment, and limiting its usage. This has driven countries to review their energy policies to accommodate different key energy players who will attract investors and eventually promote the usage of mini-grid electrifications. The adoption and effective utilization of mini-grid electrification are vital for South Africa, particularly the rural

settlers, where the lack of grid electrification is more pronounced. Therefore, an environmentally friendly policy framework is essential to provide and improve access to electricity for rural dwellers (Nikolina, 2016).

South Africa has a prospect to enact an effective energy policy framework because of its affiliation with a reputable global institution, the International Renewable Energy Agency (IRENA), which advocates for the use of renewable energy policies as one of its key objectives for its member countries (Winkler et al., 2009). There are three energy policies in South Africa: the white paper on energy policy in 1998, the white paper on renewable energy policy in 2003, and the National Climate Change Response Policy white paper in 2011. These energy policy documents aim to enhance access to low-cost energy services and facilitate operational energy governance. In addition, they aim to secure energy resource diversity, handle the environmental consequences that may ensue, and promote economic growth. Other related existing strategic policy documents are the Integrated Energy Plan (IEP) and Integrated Resources Plan (IRP) for mediating and determining the future of renewable energy usage in South Africa (Boait, 2014; Babatunde et al., 2019c; AMDA and ECA, 2020). The 2016 IEP provides an imperative framework for a sustainable energy environment supporting impending investment in the energy sector (Motjoadi et al., 2020). Unfortunately, this document was not approved, just like those of 2010, 2013, and 2018. Furthermore, the most recent IRP 2019 is yet to be approved. All of these have posited a negative viewpoint on renewable energy policy in South Africa and have eventually held back investment to secure the system's flexibility and productivity (Pegels, 2010; Justo et al., 2013; Renné et al., 2006).

Table 10 shows the capacity thresholds of mini-grid operation with license exemption by some countries in the Sub-Sahara region. (Domegni and Azouma, 2022).

7 Rural off-grid mini-grid case studies in SSA

There are three main classes of decentralized solutions in SSA: mini-grids, energy kiosks, and individual systems. Mini-grids are managed by independent developers, usually with hybrid designs composed of renewable energy and storage sources combined together, supplying electricity to end users (small- and medium-scale businesses and households). Energy kiosks provide community-based services, for example, mobile phone charging and on-demand refrigeration in shared commercial refrigerators. Individual systems (solar kits, solar torches, and outdoor solar lanterns) meet basic needs such as lighting and phone charging.

These solutions, which are mostly distributed commercially by external stakeholders and industry players, constitute an autonomous model that provides a pathway to actualizing a vision of an independent and self-sufficient supply of off-grid electricity to solve the problems of energy poverty. In this section, we study off-grid scenarios of mini-grid adoption in East, West, and Southern African countries. Case studies from countries from SSA will be considered to get an in-depth understanding of off-grid solutions for improving access to electricity to reduce energy poverty.

At present, more than 50 mini-grid developers (both non-profit and for-profit organizations) operate across Africa, with the majority of them locally owned. Africa Minigrid Developers Association (AMDA) reports that more than 40 active for-profit developers spread across 19 countries in Africa (Nygaard et al., 2015). Several of these operators are not only focused on rural electrification but also provide renewable electrification solutions to urban entities. It is also reported that most operators do not share details of their projects in the public domain (Nygaard et al., 2015). Therefore, it is difficult to ascertain their market shares based on publicly available data. Table 11 provides a list of for-profit companies that have at least one operational mini-grid that provides 600 h or more of monthly electricity supply.

7.1 East Africa

During 2010–2018, an approximate value of $1.28 billion in equity and debt from venture capital and bonds was invested in SSA companies to improve access to energy in SSA. More than half of the investment was given to off-grid renewable energy companies in East Africa whose mode of operation was the sale of small-scale photovoltaic systems and renewable energy-powered appliances (Acker and Kammen, 1996).

The use of decentralized or off-grid solar energy is now very popular in rural communities across East Africa in the 21st century. It is very common to find solar panels on rooftops of schools, homes, and health centers across rural communities in Tanzania, Kenya, and Uganda. Before the advent of the 21st century, the implementation of solar energy projects in East Africa was undertaken to support the development of national grids. Extensive public programs organized by East African governments (supported by multinational financial organizations such as the World Bank) for national development through rural electrification were majorly focused on building energy infrastructures for the generation of electricity in regional power grids (Sheya and Mushi, 2000; Jacobson, 2007). Before the 21st century, only Kenya had a flourishing market for off-grid solar systems in rural communities, which was fully spearheaded by the efforts of a small number of entrepreneurs (Allela, 2022). In the last 20 years, business operations involving the use of off-grid solar energy systems have become very fruitful across East Africa, largely due to the commitment of privately owned, for-profit companies. Currently, off-grid solar photovoltaics are used as portable lighting and charging systems.

As of 2015, approximately 8.4 million households in Kenya, nearly 32% of the population, were connected to the nation's electricity grid. While the connected urban population was 60%, the percentage of rural households connected to the grid was only 7% (Bhatia and Angelou, 2015). When there is no electricity supply, most households in rural communities depend on kerosene lamps and devices powered by dry cell batteries for lighting purposes (Wagner et al., 2021). The Kenyan government has made commitments toward ensuring that access to universal energy in rural locations is achieved by 2022; the government accepts the fact that it is important that the use of alternative energy be encouraged in locations with dispersed patterns of settlements requiring huge investments in building infrastructure and connection to the national grid (Hagumimana et al., 2021). The option of using solar energy as a means of generating alternative energy is very prominent as insolation in Kenya occurs all year round. Generally, the Kenyan government supports the use off-grid solutions and has put in place policies such as waivers for VAT and tariffs on solar PV products (Antonanzas-Torres et al., 2021c). Kenya has now become a leading market for off-grid solar products in Africa due to support

TABLE 10 Capacity thresholds of mini-grid operation with license exemption (Domegni and Azouma, 2022).

S/N	Country	Set capacity threshold for license exemptions (kW)
1	Uganda	2,000
2	Ghana	100
3	Tanzania	100
4	Nigeria	100
5	Senegal	50
6	Rwanda	50
7	Mali	20
8	Mozambique	10

TABLE 11 For-profit mini-grid developers in SSA.

Company	Country
Access SA	Mali
ANKA Madagascar	Madagascar
Ashipa Electric Corp.	Nigeria
Bboxx	Nigeria
Community Research and Development Centre (CREDC)	Nigeria
Havenhill Synergy	Nigeria
Rubitec Solar	Nigeria
Ensol	Nigeria
Guinea Energy	Guinea
Rift Valley Energy	Tanzania
Engie Power Corner	Tanzania
Jumeme	Tanzania
Kya Energy	Togo
Nal Offgrid	Kenya
RVE.Sol/Kudura Power	Kenya
PowerHive	Kenya
Redavia	Kenya
Virunga Power	Kenya
Renewable Energy Innovators	Cameroon
Standard Microgrid	Zambia
Equatorial Power	Uganda
Standard Microgrid	Zambia

from favorable government policies and key stakeholders. During 2009–2013, there was an increase in the sale of solar lanterns by over 200% (Hagumimana et al., 2021). Between January 2009 and June 2018, Kenya witnessed the sale of 4.7 million high-powered solar products, and almost 10 million people (approximately 20% of Kenya's population) used high-powered solar products to meet their basic electricity needs (Antonanzas-Torres et al., 2021c). This prominent growth attributed to sales in the country is largely based on sales in densely populated parts of the country. These solar products are sold using distribution models such as direct sales to customers, pay-as-you-go (PAYG) systems, and loan-based sales through credit systems. Portable solar lights represent 90% of solar products sold in Kenya, thereby dominating its off-grid solar market (Antonanzas-Torres et al., 2021c).

In Rwanda, the off-grid solar electrification strategy encourages the use of solar water pumps, solar lanterns, solar mini-grids, solar water heaters, and SHS (Grimm et al., 2020). Therefore, much progress has been made in Rwanda in improving access to energy, with an increase from 6% in on-grid access in 2000 to 37% in on-grid access in 2019 (Eustache et al., 2019). Despite the progress in on-grid access to electricity, the low percentage of on-grid access is an opportunity for the off-grid sector to experience a boom. Presently, off-grid access to electricity in Rwanda covers 14% of the population. Currently, energy generated from renewable sources makes up 52.4% (113.14 MW) of the total energy generated in Rwanda; 218 MW is the total installed energy capacity from all energy sources in Rwanda (Chang et al., 2021). The Rwandan government has committed to the off-grid sector by targeting 48% of its population for off-grid electricity supply by 2024 (Niyonteze et al., 2020). Currently, SHS, sold using a pay-as-you-go (PAYG) model, continues to dominate the off-grid sector. This situation is very similar to other off-grid markets in East Africa (Bishoge et al., 2019). However, according to results from a survey conducted by the Fifth Integrated Household Living Conditions (EICV5), the consumer's ability to pay for the off-grid solar product in Rwanda is discouraging. According to the survey, 75% of off-grid households spend less than $1.67 per month on lighting and charging electric devices (Bishoge et al., 2019). Therefore, the Rwandan government has recognized this constraint and is working with development partners to develop an effective subsidy scheme.

In Tanzania, rural electrification is a serious challenge, as only 2% of the rural population can access electricity. Most rural communities are forced to depend on low-quality fuels (such as kerosene for lighting and charcoal) for cooking, which are hazardous and expensive (Marcel et al., 2021). In 2013, Tanzania had a *per capita* electricity consumption of 89 kWh. At the time, this was one of the lowest rates in the world and only one-quarter of the average rate of electricity consumption in SSA (Kadri et al., 2019). Some of the main challenges faced by the energy sector in Tanzania include rising rural electrification demand and unreliable electric utilities. The high cost of grid extension and grid unreliability in remote

areas with dense populations in Tanzania provide an opportunity for off-grid electrification (Kadri et al., 2019). Tanzania is blessed with immense, high-quality renewable energy resources, which are yet to be explored to their full potential. Tanzania has an abundance of sunlight, experiencing a range of 2,800–3,500 h of solar radiation yearly and an average radiation of 4–7 kWh per square meter every day. There is a wealth of solar energy resources in the central region of Tanzania. Tanzania is also known for its high wind power potential averaging 15–23 feet per second. More than 10% of Tanzania, equaling the landmass of Malawi, have high wind power potential. The overall wind potential of Tanzania also exceeds the wind speed potential and coverage of the entire state of California (Marcel et al., 2021). According to an estimation performed by the Rural Electrification Investment Prospectus in 2012, half of the rural populace in Tanzania might have a better experience combining mini-grids and off-grid options rather than using the conventional grid connection (Pillot et al., 2019). It is cheaper to generate off-grid electricity using renewable energy compared to the conventional diesel option. Integrating multiple renewable energy sources, which are highly accessible, ensures that residents of rural communities have renewable energy systems that provide a clean and reliable supply of electricity for rural residents. The optimal configuration and sizing of an integrated system would be specific to a site for the minimization of energy generation costs (Pedersen, 2016).

7.2 West Africa

The status of electrification in West African nations is currently presented to be below 40%, losses in the national grid above 39% with regular disruptions, and electricity prices averaging between $0.35/kWh and $0.66/kWh (Pillot et al., 2019). Accordingly, in the last decade, great attention has been given to off-grid systems (SHS and mini-grids) as an alternative to conventional energy solutions. Currently, over 385 mini-grids operate with a power of approximately 30 MW in West Africa, and 95% of these mini-grids are based on PV (USAID, 2022). Since 2019, different projects aiming to install at least 317 new mini-grids in Togo, 250 in Nigeria, 100 in Burkina Faso, and 2 in Mali using funding obtained from international aid have been implemented. Moreover, the market involving start-ups dealing with mini-grid energy has grown from $19 million in 2013 to $339 million in 2018 (Bamisile et al., 2017).

Nigeria is rich in conventional and renewable energy sources. The economic potential of renewable energy in Nigeria is twice higher than that of oil and natural gas reserves. Solar, biomass, hydro, and wind energy are notable sources of renewable energy in Nigeria. The daily solar radiation capacity of Nigeria is 3.5–7.0 kWm^{-2} solar radiation, and the wind speed capacity is 2.0–4.0 m^{-1}. An estimated hydro potential of 14,750 MW, including 144 million tons per year of biomass resources, also exists in Nigeria (Liu et al., 2019). Although Nigeria is rich in vast energy resources, there is surprisingly poor coverage in terms of access to electricity. As of 2020, only 55.4% of the entire Nigerian population have access to electricity, and only 24.6% of the rural population have access to electricity (Liu et al., 2019). The nature of the power sector has led to problems and challenges undermining access to a reliable and constant power supply in Nigeria. The national grid is mostly unsuitable for the electrification of several rural populations in Nigeria due to long rural distances from the grid and bad topography, making it uneconomical or difficult to extend such rural populations to the national grid. The Rural Electrification Agency (REA) of Nigeria estimates an annual market opportunity of $10 Bn/year from the use of mini-grids and solar home systems in Nigeria, with a saving potential of $6 Bn/year. The mini-grid market in Nigeria can be increased to 10,000 sites by 2023, covering 14% of the Nigerian population with a capacity of up to 3,000 MW. This will create an estimated investment potential of ~$20 Bn and an annual revenue opportunity exceeding $3 Bn. Most mini-grid projects in Nigeria can be found in densely populated agrarian communities, with a population of 2,500 people distributed among 300–500 households. Before the advent of mini-grids in Nigeria, people in rural communities used torchlights, kerosene lamps, candles, and generators as lighting sources (Liu et al., 2019). According to the Rural Electrification Agency (REA) of Nigeria, there is an enabling environment for the growth of mini-grid markets. There is developer protection in the form of mini-grid regulations, effective site-selection processes, and procedures to de-risk projects (Bamisile et al., 2017). Some proposals for the use of educational tools in the form of digital applications to improve consumer knowledge of renewable energy opportunities exist in Nigeria. For instance, Turcotte et al. (2001) designed an android application that uses a framework that gives information to consumers about a chosen PV system architecture and provides cost implications of continuing with the investment. The application aims to enlighten household owners about the viability of utilizing solar energy systems for residential energy needs, especially in rural areas.

In Togo, the use of energy systems is a balance between centralized and distributed energy systems. This is a current trend aimed at improving the reliability and independence of energy by ensuring that the electricity supply is stable (Kansongue et al., 2018). Togo depends on the following composition for the generation of energy: biomass energy of 71% (vegetable waste, firewood, charcoal, *etc.*), petroleum products of 26%, and electric power of 3% (Kansongue et al., 2018). Electricity is currently the main source of energy in Togo. Access to electricity in Togo has increased from 17% in 2000 to 45% in 2018. However, there is a large difference between urban and rural access to electricity, where urban access is 88% and rural access is 8% (Kansongue et al., 2022). The total production of electricity in Togo in 2018 was 385.62 GWh, with losses in transmission and distribution activities accounting for 15.85% of the generated units of electricity (Kitegi et al., 2022). Togo has significant resources of renewable energy such as solar, wind, and hydroelectric power. The renewable energy potential of the country could be developed effectively for a sustainable nationwide energy system. The Togolese government is conscious of this fact and is trying to improve off-grid access to electricity *via* mini-grids (Kitegi et al., 2022). The Government of Togo aims to deploy more than 300 mini-grids worth $251 million in investments by 2030. The Togolese government is currently focused on mobilizing investments in the private sector by facilitating Public Private Partnerships (PPP). The government is also leveraging the use of digital tools for the rapid and effective increase in rural energy access through the implementation of off-grid energy services. It aims to expand the extension of energy services in rural areas to improve rural access to electricity (Monyei et al., 2018a). Therefore, it has developed a strategy for electrification that uses geospatial modeling to determine the most efficient means of electrifying households in rural communities. Between 2018 and 2030, this strategy aims to cover the deployment of 555,000 SHS, 300 mini-grids (with 55,000 connections), and 400,000 on-grid connections, with the goal of achieving universal electrification by 2030 (Kitegi et al., 2022).

In Mali, there has been a considerable shift in the mix of energy over the years from power generation dominated by hydro sources to a generation nearly split equally between hydro and thermal (fossil) power. Averagely, installed power capacity has increased by 8.1% on a yearly basis during 2005–2015. Despite this growth, an electricity supply deficit of 150 MW remains owing to the rising demand for electricity. Despite uncertainties in the sector, progress has significantly been made in terms of increasing access to electricity in Mali. As of 2017, over 40.5% of Malians had access to modern energy services, with 83% of that access being in urban areas and 17% in rural areas. However, the interaction between on-grid and off-grid access to electricity remains very unclear and actively hinders future electrification plans by preventing the involvement of donors, operators, and government institutions alike. The price difference between mini-grids in urban and rural areas remains very high, with the price charge in rural areas estimated to be $0.44–$0.49/kWh and that charged by the national utility in the urban areas being $0.23/kWh. The electricity system is composed of a national grid owned and operated by Energie du Mali SA (EDM SA). The national grid supplies 35 towns, including the city of Bamako. The Malian Agency for Domestic Energy and Rural Electrification (AMADER) is responsible for the implementation and regulation of rural electrification schemes below 250 kW in accordance with the rural electrification reference framework adopted in the year 2003. Hydro and thermal power stations are the main sources of energy in Mali. Although there has been an increase in the installation of hybrid systems (solar/diesel) and small-scale decentralized photovoltaic (PV) systems since 2011, the use of renewable energy with the exclusion of large hydropower remains low. Mali continues to face major challenges in the power sector. Due to the high costs of energy generation from thermal power stations and excessive losses from technical and non-technical networks, there exist high tariffs in charges when consumption is below 50 kWh per month. According to IRENA, in 2015, using only 2% of the country's solar PV potential was sufficient to cover the total supply of electricity (Moner-Girona et al., 2016). The Malian National Renewable Energy Action Plan (NREAP) has set ambitious objectives for both on-grid and off-grid systems. A target of 1,416 MW in installed capacity for on-grid renewable energy sources has been set for connected systems to achieve by 2030. For off-grid renewables, installed capacity is targeted to increase from 20 MW in 2010 to over 600 MW by 2030.

7.3 Southern Africa

Southern Africa, just like every other region, has great prospects as regards the potential of renewable energy for achieving complete access to electricity. However, several challenges hindering the exploration of these prospects also exist and are quite similar to those faced by East and West Africa.

In South Africa, non-renewable fossil fuel, which generates more than 95% of the nation's electricity, has peaked and is now experiencing a decline. This has led to an increase in the cost of electricity generation in the presence of an irreversible increase in electricity demand (Monyei and Adewumi, 2017). Incidentally, the domestic housing sector accounts for 20% of this demand (Nhamo and Mukonza, 2016). The national grid of South Africa provides electricity access to 85% of South Africans. However, it is greatly challenged by capacity and connection constraints, which hinder the development of renewable energy in the country. Some of the capacity constraints faced by the national grid include aging infrastructure and vast geography, leading to grid congestion. This hinders potential consumers, especially in rural areas, from connecting to the national grid. As of 2013, the rate of access to electricity in rural areas of South Africa was 77%. However, the need to improve the off-grid generation of electricity remains, as the South African National Energy Development Institute (SANEDI) estimated that an excess of three million people still live without electricity in rural areas of South Africa (Winkler, 2005). In addition, kerosene and paraffin are still dominantly used for lighting in rural areas amongst the poorest populations, as 17–20 million South Africans (accounting for 40% of the population) use kerosene daily (Oyewo et al., 2019). To improve rural electrification in South Africa, the Government of South Africa, through the Department of Energy, came up with New Household Electrification Strategy in 2011. The strategy aims to reach 90% on-grid electrification and 10% off-grid electrification (Temudo et al., 2019).

In Angola, access to clean, modern, and reliable energy remains low: 33% nationwide, 69% in urban areas, and 6% in rural areas (Puati Zau and Daniel Chowdhury B, 2018). The Government of Angola aims to increase access to electricity by 60% by 2025 as part of its long-term development strategy. It also aims to make renewable energy (RE) contribute 70% of the country's installed capacity by 2025. The potential of hydropower is huge, with a current estimation of 18.2 GW, out of which only 20% is currently exploited (Garcia and Raji, 2021). So far, the Government of Angola has identified 100 locations with the potential to cumulatively generate 600 MW from mini-hydropower resources. Angola has an annual global horizontal radiation of 1.350–2.070 kWh/m^2/year (Temudo et al., 2020). The Angolan government has also targeted the installation of 100 MW of solar resources by 2025, with 30 MW planned for off-grid electricity generation. In addition to solar energy, a substantial opportunity also exists to develop wind energy with the presence of wind farms in Southern Angola (Lyambai, 2018). Exploring the renewable energy potential in Angola needs significant investments from the private sector in collaboration with technical assistance from relevant institutions in charge of promoting the implementation of renewable energy projects. Putting in place effective regulatory frameworks to bring in credible independent power producers (IPPs) is very important in meeting the targets of the Angolan Government. The Government of Angola has already begun conducting reforms to improve the country's investment climate in the renewable energy sector. They have a) adopted a new renewable energy strategy, b) revised the electricity tariff regime and enacted a reform on energy subsidy, and c) adopted new laws on procurement and distribution of electricity to support independent power generation. To support its achievements and challenges, the Government of Angola has formally requested the assistance of The Sustainable Energy Fund for Africa (SEFA) to develop and implement a regulatory and institutional framework to encourage private sector investment in renewable energy generation aimed at reducing the dependence of the country on fossil fuel resources that are depleting. The support from SEFA will assist the Angolan Government in achieving commitments in the form of investments in the renewable energy project. A one-stop shop unit called the Energy Project Implementation Support Unit (EPISU) was established to achieve this. The technical assistance provided by SEFA includes a) providing legal frameworks, policy statements, and fiscal incentives for renewable energy to ensure an enabling environment for IPP/PPP projects and improve the economic viability of renewable energy projects and b) resolving issues related to

capacity building, procurement, implementation, and monitoring of projects (Temudo et al., 2020).

In Zambia, a wide range of energy resources exist, including coal, woodlands, hydropower, sand forests, and renewable sources of energy. However, the electrification rate remains low because only 31.2% of the Zambian population are connected to the grid (Stritzke and Jain, 2021). As of 2019, 69% (accounting for approximately 11 million Zambians) are without access to electricity. Nearly 67% of the access to electricity is in urban areas, whereas only 4% is in rural areas. As of 2016, the installed electricity generation capacity was 2,800 MW, with 2,380 MW (85%) generated by hydropower plants and 405 MW (15%) generated by non-hydropower plants. Independent power producers exist to support the generation of electricity across the country (Heffron and McCauley, 2017). Although the Zambian Government aims to reach 90% urban electrification and 51% rural electrification by 2030, it has slowly invested in the solar and hydro energy sector, not up to 30% of the available 6,000 MW potential of hydro resources in Zambia has been used, and the installation of solar PV only exists in approximately 400 households, few schools, and Chief's Palaces across the country (Stritzke and Jain, 2021). At least five mini-grids exist in Zambia, and the government has put in place frameworks and strategies to ensure that the development of the off-grid generation of electricity is effective.

8 Energy justice in off-grid mini-grids in SSA

Energy justice is a framework that addresses the energy trilemma of politics, economics, and the environment, with a just and equitable approach (Villavicencio Calzadilla and Mauger, 2017). It comprises three key tenets: distributional justice, recognition justice, and procedural justice. Distributive justice is concerned with the fair distribution of the burdens and gains of energy production to all social and spatial strata. Recognition justice identifies those affected by injustices and pays attention to fair representation of all socio-political groups. Procedural justice ensures that energy-related decision-making processes are performed transparently and impartially (Sovacool et al., 2017). Figure 6 shows that these tenets can be applied to the entire energy life cycle through principles including availability, affordability, due process, transparency/accountability, sustainability, intra- and inter-generational equity, and responsibility (Villavicencio Calzadilla and Mauger, 2017).

Researchers consider decentralized renewable universal energy access as a just means of closing the energy gap in developing countries because "they can provide safe, reliable, affordable and sustainable energy to local communities in developing countries" (Sovacool et al., 2017). Nonetheless, without the application of the energy justice framework (EJF) tenets and principles, it will be unclear where influential stakeholders have taken advantage of the poor and marginalized people and communities they were meant to assist. EJF also helps assess the intentions and activities of the global community under the lenses of justice and equity, providing guidelines for restorative justice where necessary. The implementation of energy justice in SSA's off-grid micro-grid development will facilitate a paradigm shift from the prevalent norm (i.e., rural electrification for the mere sake of participating in the clean transition or mainly as a means of only improving human development by universal energy access). Under the EJF, rural off-grid electrification should achieve affordability, energy reliability, sufficiency, environmental sustainability, economic growth, human development, intra- and inter-generational equity, and freedom to call out and resist perceived energy injustices (Monyei et al., 2018b).

Researchers from the Global South have pointed out the gap in understanding that some Global North researchers have in respect of the needs of the Global South, resulting in models and policies that cause failed projects (Monyei and Adewumi, 2017; Lacey-Barnacle et al., 2020; Gladkykh et al., 2021). This poor understanding is reflected by Boamah (2020), who applied "energy justice" to SSA's energy access. The developed model is intended to achieve energy sufficiency for households with 100%-renewables as a priority. It resulted in a levelized cost of energy (LCOE) six times higher than the 25%-renewable scenario. Several limitations can be observed within the work. First, it ignored the place of economic activities that will enable the energy-poor communities to fund the proposed high-cost sustainable electricity without perpetual recourse to grants and charity donations. Second, it defines energy sufficiency from the viewpoint of having electricity to meet "basic" household needs (i.e., lighting, charging mobile phones, fan-based cooling, and radio). These household devices are insufficient to facilitate skilling up and active social participation in the information age. The researchers ignore the low utility of the proposed solar PV electricity for heating and cooling, cooking, and medium-scale commercial activities. Thus, residents still have to pay for additional solid biomass for cooking and heating. Hence, for the EJF to be effective for SSA's off-grid mini-grids, it is important for researchers to deeply understand the peculiarities and practical needs of the region.

8.1 Identified challenges with solar energy-focused policy

- Solar PV provides restrictive utility because SHS and solar mini-grids are unaffordable for heating, cooking, heavy machine/motor operation, and medium/large-scale agro-processing (Monyei and Adewumi, 2017).
- Solar PV systems require energy storage due to the intermittency of solar energy availability. This necessitates battery storage technologies, and the literature has a consensus on their unaffordability for rural communities in developing SSA. For instance, battery storage accounts for 40% or more (depending on the kind of battery technology) of total capital expenditure for installing decentralized building solar systems in SSA. Declining solar PV prices are yet to be matched by a commensurate fall in energy storage technologies (Babayomi and Dahoro, 2021).
- Local innovation and maintenance are difficult, leading the bulk of indirect economic impacts of solar electrification systems to be directed to already-developed and prosperous countries. The key technologies in solar systems, including solar panels, inverters, and battery storage, are relatively new and advanced, which increases dependence on foreign expertise (Babayomi et al., 2020).
- AC mini-grids are relatively inefficient and increase energy losses due to higher conversion stages from DC/AC along the path from generation to consumption. Solar energy is

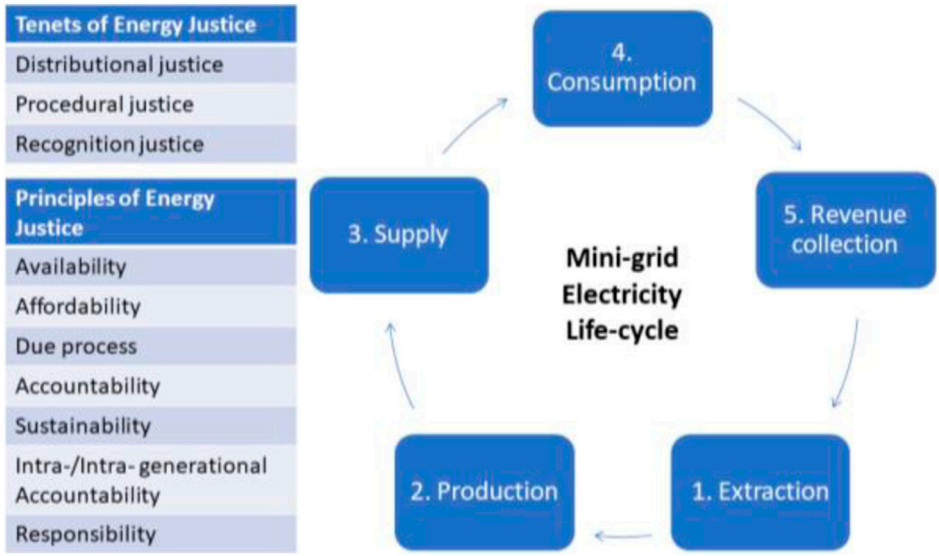

FIGURE 6
The energy justice framework applied to mini-grid electricity life-cycle (Villavicencio Calzadilla and Mauger, 2017).

generated directly in DC form, whereas most rural electrical appliances and equipment utilize a form of AC power. If DC appliances are sold to rural SSA communities, inverters will become unnecessary, and the capital cost and (financial and technical) inconveniences caused by faulty inverters can be eliminated. This will further improve equity in rural electrification. Thus, DC mini-grids need to be better promoted (Kyriakarakos et al., 2020).

8.2 Recommendations for just and equitable mini-grids in SSA

- Several studies advocate for the adoption of hybrid energy systems which accommodate renewable and fossil-based (particularly diesel and gasoline) energy sources. Hybrid electricity systems provide lower LCOE and energy sufficiency, enabling households to meet diverse energy needs from lighting to cooking and heating (Akpan et al., 2013; Lacey-Barnacle et al., 2020). Hybrid systems also provide energy mobility, easing the ability of users to increase energy asset acquisition as their demand increases without incurring financial losses (Allela, 2022). Energy resilience, as measured *via* sufficiency and mobility, should be given a prime place in the planning and deployment of off-grid electricity projects. Moreover, hybrid electricity systems permit a paced transition for SSA rather than the immediate clean transition, which widens the energy poverty gap, and exacerbates energy injustice.
- Productive use of energy is an oft-overlooked form of energy justice. When mini-grid suppliers provide affordable electricity to power profitable commercial ventures in rural agricultural/pastoral settlements, they further empower the consumers to pay for electricity to improve their economic activities and standard of living (USAID, 2022; Reber et al., 2018). Catering to commercial energy needs also spreads energy use throughout the day (instead of only at night-time for households), leading to a higher load factor and a lower tariff (Akpan et al., 2013; Reber and Booth, 2018). Therefore, metrics that facilitate the productive use of energy, including affordable tariff (that facilitates competitive production of goods and services), quantity, quality, and reliability of electricity, must be integrated into off-grid mini-grid planning, financing, and business models (USAID, 2022). Customized solutions to catalyze commercial agriculture and livestock and the agro-processing industry should be provided by mini-grid developers.
- Babayomi et al. (2020) explored the theme of renewable energy access for economic growth in developing countries, advocating for balancing rural policies between human development and economic growth. Interventions that do not prioritize local economic growth will be unsustainable in the long term and will remain ever dependent on grants and hand-outs from charities. The study pointed out that the present technologies and market models of decentralized rural electrification result in tariffs up to 37 times the main grid tariff (most SSA grid tariffs are not cost-reflective). As a result, rural agro-industries and allied industries in SSA struggle to sell produce in the cities due to cheaper imported alternatives, which, paradoxically, are produced in developed countries operating on mainly fossil-powered grids. Therefore, the entire solar PV off-grid mini-grid value chain, from the promoted technologies in SSA to the market models in its present form, does not support low-cost rural energy access. Until these challenges are solved, SSA policymakers may need to adopt hybrid forms of decentralized electrification, which are more affordable, and catalyze competitive rural markets.
- Off-grid mini-grids should be designed beyond only providing basic, reliable access to catalyzing community members to

realize multi-faceted personal potentials and impact the larger society politically (Lacey-Barnacle et al., 2020).

- Improved funding for the competitiveness of decentralized solar PV systems over the centralized grid and financing mechanisms that substantially reduce the prices of battery storage systems where utilizing PV is unavoidable are recommended (Boamah, 2020).
- Special agreements can be made with mini-grid equipment vendors for more affordable and reliable off-grid DC-based technologies. As earlier explained, the prevalent AC-based inverter systems are more expensive and less efficient and suffer lower reliability than DC systems (Babayomi and Dahoro, 2021; Babayomi et al., 2020).
- Policy uncertainties about the grid extension to the off-grid locations where mini-grid projects will be sited discourage private participation. As grid tariffs are usually better subsidized than mini-grid tariffs, electricity users are likely to prefer grid supply over the prior existing mini-grid, causing a loss of income for investors. Therefore, clear policies that protect mini-grid investments can further improve private investment in off-grid mini-grids in SSA.

9 Conclusion

This study reviewed the developments in the renewable off-grid mini-grids of SSA over the past 2 decades. This work covered the present state of research and developments in technologies, policy tariffs, design techniques, and energy justice in SSA's off-grid mini-grids. The review indicates that solar PV is the most common and easiest renewable to deploy for mini-grids in SSA. In order to reduce the spate of oversized mini-grids installed across SSA, modern multi-criteria design techniques need to be better engaged during the feasibility study and design stages. This would also lead to the efficient deployment of financial and social resources toward the goal of providing electricity access for all. Key challenges include weak regulatory and policy frameworks, which increase the time for approvals, and financial requirements to operate off-grid mini-grids. The energy justice body of work asserts that enabling the ease of deploying hybrid mini-grids and catalyzing the profitability and growth of rural agro-markets will improve energy justice in off-grid mini-grid developments of SSA (EnergyPLAN, 2022; Long and Steinberger, 2018; Elkadeem et al., 2021).

Author contributions

OB: conceptualization, introduction, and conclusion. BO: optimal planning, sizing, and technology selection for mini-grids. ID: rural off-grid mini-grid case studies in SSA. TS: review of different renewable technologies. OA: challenges with off-grid mini-grid projects in SSA. CS: policy states for off-grid electrification in SSA. KO: rural off-grid mini-grid case studies in SSA. AA: energy justice in off-grid mini-grids in SSA.

Acknowledgments

The authors would like to express special thanks to Covenant University Management for financial support through CUCRID.

Conflict of interest

The authors declare that the research was conducted in the absence of any commercial or financial relationships that could be construed as a potential conflict of interest.

Publisher's note

References

Acker, R. H., and Kammen, D. M. (1996). The quiet (energy) revolution: Analysing the dissemination of photovoltaic power systems in Kenya. *Energy Policy* 24 (1), 81–111. doi:10.1016/0301-4215(95)00112-3

Aglina, M. K., Agbejule, A., and Nyamuame, G. Y. (2016). Policy framework on energy access and key development indicators: ECOWAS interventions and the case of Ghana. *Energy Policy* 97, 332–342. doi:10.1016/j.enpol.2016.07.012

Ajeigbe, O. A., Munda, J. L., and Hamam, Y. (2020). Towards maximising the integration of renewable energy hybrid distributed generations for small signal stability enhancement: A review. *Int. J. Energy Res.* 44 (4), 2379–2425. doi:10.1002/er.4864

Akinyele, D., Belikov, J., and Levron, Y. (2018). Challenges of microgrids in remote communities: A steep model application. *Energies* 11, 432. doi:10.3390/EN11020432

Akinyele, D., Okakwu, I., Olabode, E., Blanchard, R., Ajewole, T., and Monyei, C. (2022). Integrated TEEP approach to microgrid design and planning with small hydro/solar/diesel resources for standalone application. *e-Prime-Advances Electr. Eng. Electron. Energy*, 100091.

Akpan, U. S., Isihak, S. R., and Udoakah, Y. O. N. (2013). "Electricity access in Nigeria: Viability of off-grid photovoltaic system," in Proceeding of the IEEE AFRICON Conf, Pointe aux Piments, Mauritius, September 2013 (IEEE). doi:10.1109/AFRCON.2013.6757778

Al Garni, H. Z., and Awasthi, A. (2017). Solar PV power plant site selection using a GIS-AHP based approach with application in Saudi Arabia. *Appl. Energy* 206, 1225–1240. doi:10.1016/j.apenergy.2017.10.024

Allee, A. (2021). *Bioenergy and minigrids for sustainable human development*.

Allela, T. (2022). A 2020 desk review of Power Africa. *J. Int. Dev.* 34, 334–348. doi:10.1002/jid.3595

Aly, A., Jensen, S. S., and Pedersen, A. B. (2017). Solar power potential of Tanzania: Identifying CSP and PV hot spots through a GIS multicriteria decision making analysis. *Renew. energy* 113, 159–175. doi:10.1016/j.renene.2017.05.077

AMDA and ECA (2020). *Benchmarking africa's minigrids*, 1–59. Africa Minigrid Developers Association and Economic Consulting Associates.

Antonanzas-Torres, F., Antonanzas, J., and Blanco-Fernandez, J. (2021). State-of-the-art of mini grids for rural electrification in West Africa. *Energies* 14 (4), 990. doi:10.3390/en14040990

Antonanzas-Torres, F., Antonanzas, J., and Blanco-Fernandez, J. (2021). State-of-the-Art of mini grids for rural electrification in West Africa. *Energies* 14, 990. doi:10.3390/EN14040990

Antonanzas-Torres, F., Antonanzas, J., and Blanco-Fernandez, J. (2021). Environmental life cycle impact of off-grid rural electrification with mini grids in West Africa. *Sustain. Energy Technol. Assessments* 47, 101471. doi:10.1016/j.seta.2021.101471

Aydin, N. Y., Kentel, E., and Duzgun, H. S. (2013). GIS-based site selection methodology for hybrid renewable energy systems: A case study from Western Turkey. *Energy Convers. Manag.* 70, 90–106. doi:10.1016/j.enconman.2013.02.004

Ayodele, T. R., Ogunjuyigbe, A. S. O., Odigie, O., and Munda, J. L. (2018). A multi-criteria GIS based model for wind farm site selection using interval type-2 fuzzy analytic hierarchy process: The case study of Nigeria. *Appl. Energy* 228, 1853–1869. doi:10.1016/j.apenergy.2018.07.051

Azimoh, C. L., Klintenberg, P., Wallin, F., Karlsson, B., and Mbohwa, C. (2016). Electricity for development: Mini-grid solution for rural electrification in South Africa. *Energy Convers. Manag.* 110, 268–277. doi:10.1016/j.enconman.2015.12.015

Azimoh, C. L., Klintenberg, P., Mbohwa, C., and Wallin, F. (2017). Replicability and scalability of mini-grid solution to rural electrification programs in sub-Saharan Africa. *Renew. energy* 106, 222–231. doi:10.1016/j.renene.2017.01.017

Aziz, S., Chowdhury, S. A., and Groh, S. (2016). The success of solar diesel minigrids in Bangladesh: A case study of sandwip island. *Energy Procedia* 103, 316–321. doi:10.1016/J.EGYPRO.2016.11.292

Babatunde, O. M., Munda, J. L., and Hamam, Y. (2019). A comprehensive state-of-the-art survey on power generation expansion planning with intermittent renewable energy source and energy storage. *Int. J. Energy Res.* 43, 6078–6107. doi:10.1002/er.4388

Babatunde, O. M., Munda, J. L., and Hamam, Y. (2019). How can a low-income household procure small-scale hybrid renewable energy system? A techno-economic and acquisition analysis. *Int. J. Energy Sect. Manag.* 13, 1149–1172. doi:10.1108/IJESM-03-2019-0003

Babatunde, O. M., Munda, J. L., and Hamam, Y. (2019). Selection of a hybrid renewable energy systems for a low-income household. *Sustainability* 11 (16), 4282. doi:10.3390/su11164282

Babatunde, O. M., Munda, J. L., and Hamam, Y. (2020). A comprehensive state-of-the-art survey on hybrid renewable energy system operations and planning. *IEEE Access* 8, 75313–75346. doi:10.1109/access.2020.2988397

Babayomi, O., and Dahoro, D. (2021). "Energy access vs. Energy for prosperity: A reassessment of africa's strategies and priorities," in Proceeding of the 2021 IEEE PES/IAS PowerAfrica, Nairobi, Kenya, August 2021 (IEEE), 1–5. doi:10.1109/PowerAfrica52236.2021.9543177

Babayomi, O. O., Dahoro, D. A., and Zhang, Z. (2022). Affordable clean energy transition in developing countries: Pathways and technologies. *iScience* 25 (5), 104178. doi:10.1016/J.ISCI.2022.104178

Babayomi, O., and Okharedia, T. (2019). "Challenges to sub-saharan africa's renewable microgrid expansion - a cetep solution model," in Proceeding of the 2019 IEEE PES/IAS PowerAfrica, Abuja, Nigeria, August 2019 (IEEE). doi:10.1109/PowerAfrica.2019.8928865

Babayomi, O., Shomefun, T., and Zhang, Z. (2020). "Energy efficiency of sustainable renewable microgrids for off-grid electrification," in Proceeding of the 2020 IEEE PES/IAS PowerAfrica, Nairobi, Kenya, August 2020 (IEEE). doi:10.1109/PowerAfrica49420.2020.9219958

Balamurugan, P., Ashok, S., and Jose, T. L. (2009). Optimal operation of biomass/wind/PV hybrid energy system for rural areas. *Int. Jouran Green Energy* 6 (1), 104–116. doi:10.1080/15435070802701892

Bamisile, O., Dagbasi, M., Babatunde, A., and Ayodele, O. (2017). A review of renewable energy potential in Nigeria; solar power development over the years. *Eng. Appl. Sci. Res.* 44 (4), 242–248. Accessed: Jun. 25, 2022. [Online]. Available: https://ph01-ohno.tci-thaijo.org/index.php/easr/article/view/77226.

Bank, W. (2017). *State of electricity access report 2017*. Washington, DC, United States: World Bank.

Bank, W. (2017). *State of electricity access report*. Washingt. DC, USA: World Bank Group.

Baring-Gould, E. I., Green, H. J., van Dijk, V. A. P., and Manwell, J. F. (1996). *Hybrid2: The hybrid power system simulation model*. Golden, Colorado, United States: National Renewable Energy Laboratory.

Bhatia, M., and Angelou, N. (2015). *Beyond connections : Energy access redefined*. ESMAP Technical Report;008/15. Available: https://openknowledge.worldbank.org/handle/10986/24368 (accessed Jan. 17, 2022).

Bhattacharyya, S. C. (2015). Mini-grid based electrification in Bangladesh: Technical configuration and business analysis. *Renew. Energy* 75, 745–761. doi:10.1016/j.renene.2014.10.034

Bhattacharyya, S. C. (2018). Mini-grids for the base of the pyramid market: A critical review. *Energies* 11, 813. doi:10.3390/EN11040813

Bishoge, O. K., Zhang, L., and Mushi, W. G. (2019). The potential renewable energy for sustainable development in Tanzania: A review. *Clean. Technol.* 1, 70–88. doi:10.3390/CLEANTECHNOL1010006

BloombergNEF and SEforALL (2020). *State of the global mini-grids market report 2020: Trends of renewable energy hybrid mini-grids in sub-saharan africa, asia and island nations*. United Kingdom: BloombergNEF and Sustainable Energy for All. [Online]. Available: https://www.seforall.org/system/files/2020-06/MGP-2020-SEforALL.pdf.

Boait, P. J. (2014). *Mini-grids for rural electrification of developing countries: Technical aspects of mini-grids for rural electrification*. Springer Cham. doi:10.1007/978-3-319-04816-1

Boamah, F. (2020). Desirable or debatable? Putting africa's decentralised solar energy futures in context. *Energy Res. Soc. Sci.* 62, 101390. doi:10.1016/J.ERSS.2019.101390

Booth, S., Li, X., Baring-Gould, I., Kollanyi, D., Bharadwaj, A., and Weston, P. (2018). *Productive use of energy in african micro-grids: Technical and business considerations*. doi:10.2172/1465661

Bukari, D., Kemausuor, F., Quansah, D. A., and Adaramola, M. S. (2021). Towards accelerating the deployment of decentralised renewable energy mini-grids in Ghana: Review and analysis of barriers. *Renew. Sustain. Energy Rev.* 135, 110408. doi:10.1016/J.RSER.2020.110408

Bukari, D., Quansah, D. A., Kemausuor, F., and Adaramola, M. S. (2022). Ex-post design, operations and financial cost-benefit analysis of mini-grids in Ghana: What can we learn? *Energy sustain. Dev.* 68, 390–409. doi:10.1016/j.esd.2022.04.009

Bullich-Massagué, E., D\'\iaz-González, F., Aragüés-Peñalba, M., Girbau-Llistuella, F., Olivella-Rosell, P., and Sumper, A. (2018). Microgrid clustering architectures. *Appl. Energy* 212, 340–361. doi:10.1016/j.apenergy.2017.12.048

Chang, K. C., Hagumimana, N., Zheng, J., Asemota, G. N. O., Niyonteze, J. D. D., Nsengiyumva, W., et al. (2021). Standalone and minigrid-connected solar energy systems for rural application in Rwanda: An *in situ* study. *Int. J. Photoenergy* 2021, 2021–2022. doi:10.1155/2021/1211953

Come Zebra, E. I., van der Windt, H. J., Nhumaio, G., and Faaij, A. P. C. (2021). A review of hybrid renewable energy systems in mini-grids for off-grid electrification in developing countries. *Renew. Sustain. Energy Rev.* 144, 111036. doi:10.1016/j.rser.2021.111036

Dawoud, S. M., Lin, X., and Okba, M. I. (2018). Hybrid renewable microgrid optimization techniques: A review. *Renew. Sustain. Energy Rev.* 82, 2039–2052. doi:10.1016/j.rser.2017.08.007

de Energia, F., and Funae, M. (2015). *Solar photovoltaic systems for social infrastructure and village electrification in Mozambique: Study of existing systems in two provinces*.

Denwigwe, I. H., Akinde-Peters, J. D., Babatunde, O. M., Samson Adedoja, O., Taiwo, I. A., and Adedoja, T. B. (2021). An Android-based mobile platform for understanding Residential PV system sizing. *Afr. J. Sci. Technol. Innov. Dev.*, 1–14. doi:10.1080/20421338.2021.1959280

Department of Energy (2015). Department of energy south Africa. *Energy Advocacy Newsl.* Accessed, no. 29th April 2022.

Diemuodeke, E. O., Hamilton, S., and Addo, A. (2016). Multi-criteria assessment of hybrid renewable energy systems for Nigeria's coastline communities. *Energy. sustain. Soc.* 6 (1), 26. doi:10.1186/s13705-016-0092-x

Domegni, K. M. S., and Azouma, Y. O. (2022). Productive uses of energy: A solution for promoting energy justice in rural areas in West Africa. *Renew. Sustain. Energy Rev.* 160, 112298. doi:10.1016/J.RSER.2022.112298

Duran, A. S., and Sahinyazan, F. G. (2021). An analysis of renewable mini-grid projects for rural electrification. *Socioecon. Plann. Sci.* 77, 100999. doi:10.1016/J.SEPS.2020.100999

Eales, A., and Unyolo, B. (2018). *Renewable energy mini-grids in Malawi: Status, barriers and opportunities*. Scottish: University of Strathclyde.

Eder, J. M., Mutsaerts, C. F., and Sriwannawit, P. (2015). Mini-grids and renewable energy in rural Africa: How diffusion theory explains adoption of electricity in Uganda. *Energy Res. Soc. Sci.* 5, 45–54. doi:10.1016/j.erss.2014.12.014

Elkadeem, M. R., Younes, A., Sharshir, S. W., Campana, P. E., and Wang, S. (2021). Sustainable siting and design optimization of hybrid renewable energy system: A geospatial multi-criteria analysis. *Appl. Energy* 295, 117071. doi:10.1016/j.apenergy.2021.117071

Energy Sector Management Assistance Program (2017). *Mini grids in Kenya: A case study of a market at a turning point*. Kenya: World Bank.

EnergyPLAN (2022). *Advanced energy system analysis computer model*. Denmark: EnergyPLAN.

Euei (2014). Mini-grid policy toolkit. Rep. From: Http//Www.Euei-Pdf.Org.

Eustache, H., Sandoval, D., Wali, U. G., and Venant, K. (2019). Current status of renewable energy technologies for electricity generation in Rwanda and their estimated potentials. *Energy Environ. Eng.* 6 (1), 8–15. doi:10.13189/eee.2019.060102

Feron, S. (2016). Sustainability of off-grid photovoltaic systems for rural electrification in developing countries: A review. *Sustain* 8, 1326. doi:10.3390/SU8121326

Fowlie, M., Khaitan, Y., Wolfram, C., and Wolfson, D. (2018). *Solar microgrids and remote energy access: How weak incentives can undermine smart technology*. California: Energy Institute AT HAAS.

Franz, M., Peterschmidt, N., Rohrer, M., and Kondev, B. (2014). "Mini-grid policy toolkit," in *Alliance rural electrif. Eschborn, tech. Rep*.

Gambino, V., Del Citto, R., Cherubini, P., Tacconelli, C., Micangeli, A., and Giglioli, R. (2019). Methodology for the energy need assessment to effectively design and deploy mini-grids for rural electrification. *Energies* 12 (3), 574. doi:10.3390/en12030574

Garcia, F. P. K., and Raji, A. K. (2021). "Potential and reliability assessment of renewable power: The case of Angola," in Proceeding of the 2021 IEEE PES/IAS PowerAfrica, PowerAfrica, Nairobi, Kenya, August 2021 (IEEE). doi:10.1109/POWERAFRICA52236.2021.9543099

Gladkykh, G., Davíðsdóttir, B., and Diemer, A. (2021). When justice narratives meet energy system models: Exploring energy sufficiency, sustainability, and universal access in Sub-Saharan Africa. *Energy Res. Soc. Sci.* 79, 102075. doi:10.1016/J.ERSS.2021.102075

Graber, S., Narayanan, T., Alfaro, J., and Palit, D. (2018). Solar microgrids in rural India: Consumers' willingness to pay for attributes of electricity. *Energy sustain. Dev.* 42, 32–43. doi:10.1016/j.esd.2017.10.002

Greco, S., Figueira, J., and Ehrgott, M. (2016). *Multiple criteria decision analysis*, 37. Springer.

Grimm, M., Lenz, L., Peters, J., and Sievert, M. (2020). Demand for off-grid solar electricity: Experimental evidence from Rwanda. *J. Assoc. Environ. Resour. Econ.* 7 (3), 417–454. doi:10.1086/707384

Hagumimana, N., Zheng, J., Asemota, G. N. O., Niyonteze, J. D. D., Nsengiyumva, W., Nduwamungu, A., et al. (2021). Concentrated solar power and photovoltaic systems: A new approach to boost sustainable energy for all (Se4all) in Rwanda. *Int. J. Photoenergy* 2021, 1–32. doi:10.1155/2021/5515513

Hakimi, S. M., and Moghaddas-Tafreshi, S. M. (2009). Optimal sizing of a stand-alone hybrid power system via particle swarm optimization for Kahnouj area in south-east of Iran. *Renew. energy* 34 (7), 1855–1862. doi:10.1016/j.renene.2008.11.022

Hansen, K. (2019). Decision-making based on energy costs: Comparing levelized cost of energy and energy system costs. *Energy Strateg. Rev.* 24, 68–82. doi:10.1016/j.esr.2019.02.003

Hartvigsson, E., Ehnberg, J., Ahlgren, E. O., and Molander, S. (2021). Linking household and productive use of electricity with mini-grid dimensioning and operation. *Energy sustain. Dev.* 60, 82–89. doi:10.1016/j.esd.2020.12.004

Heffron, R. J., and McCauley, D. (2017). The concept of energy justice across the disciplines. *Energy Policy* 105, 658–667. doi:10.1016/J.ENPOL.2017.03.018

Hennet, J. C., and Samarakou, M. T. (1986). Optimization of a combined wind and solar power plant. *Int. J. energy Res.* 10 (2), 181–188. doi:10.1002/er.4440100208

Ighravwe, D., and Babatunde, M. (2018). Selection of a mini-grid business model for developing countries using CRITIC-TOPSIS with interval type-2 fuzzy sets. *Decis. Sci. Lett.* 7 (4), 427–442. doi:10.5267/j.dsl.2018.1.004

Ighravwe, D. E., and Babatunde, M. O. (2018). Determination of a suitable renewable energy source for mini-grid business: A risk-based multicriteria approach. *J. Renew. Energy* 2018, 1–20. doi:10.1155/2018/2163262

Ihirwe, J. P., Li, Z., Sun, K., Bimenyimana, S., Wang, C., Asemota, G. N. O., et al. (2021). Solar PV minigrid technology: Peak shaving analysis in the East African community countries. *Int. J. Photoenergy* 2021, 1–40. doi:10.1155/2021/5580264

Iniyan, S., and Sumathy, K. (2000). An optimal renewable energy model for various end-uses. *Energy* 25 (6), 563–575. doi:10.1016/s0360-5442(99)00090-0

Inversin, A. R. (2017). "Mini-grid design manual-ESMAP technical paper 007," in *Energy sect. Manag. Assist. Program.* (Washington, DC: ESMAP), 17. viewed.

Irena, I. (2018). *Renewable power generation costs in 2017. Report*. Abu Dhabi: Int. Renew. Energy Agency.

Jacobson, A. (2007). Connective power: Solar electrification and social change in Kenya. *World Dev.* 35 (1), 144–162. doi:10.1016/J.WORLDDEV.2006.10.001

Jonker Klunne, W. *Current status and future developments of small and micro hydro in southern Africa*. Wroclaw, Poland: Hydroenergia. Available: http://researchspace.csir.co.za/dspace/handle/10204/6032 (accessed Jun. 25, 2022).

Justo, J. J., Mwasilu, F., Lee, J., and Jung, J.-W. (2013). AC-microgrids versus DC-microgrids with distributed energy resources: A review. *Renew. Sustain. energy Rev.* 24, 387–405. doi:10.1016/j.rser.2013.03.067

Kadri, S. M., Bagre, A. O., Camara, M. B., Dakyo, B., and Coulibaly, Y. (2019). "Electrical power distribution status in West Africa: Assessment and perspective overview," in Proceeding of the 8th Int. Conf. Renew. Energy Res. Appl. ICRERA, Brasov, Romania, Nov. 2019 (IEEE), 511–515. doi:10.1109/ICRERA47325.2019.8997112

Kalathil, D., Wu, C., Poolla, K., and Varaiya, P. (2019). The sharing economy for the electricity storage. *IEEE Trans. Smart Grid* 10 (1), 556–567. doi:10.1109/TSG.2017.2748519

Kansongue, N., Njuguna, J., and Vertigans, S. (2022). An assessment of renewable energy development in energy mix for Togo. *Int. J. Sustain. Energy* 41. doi:10.1080/14786451.2021.2023150

Kansongue, N., Njuguna, J., and Vertigans, S. (2018). "Sustainable energy for emerging nations development-A case study on Togo renewable energy," in Proceeding of the 2018 IEEE PES/IAS PowerAfrica, PowerAfrica, Cape Town, South Africa, June 2018 (IEEE), 137–141. doi:10.1109/POWERAFRICA.2018.8521054

Katre, A., Tozzi, A., and Bhattacharyya, S. (2019). Sustainability of community-owned mini-grids: Evidence from India. *Energy. sustain. Soc.* 9 (1), 2–17. doi:10.1186/s13705-018-0185-9

Katsigiannis, Y. A., Georgilakis, P. S., and Karapidakis, E. S. (2012). Hybrid simulated annealing--tabu search method for optimal sizing of autonomous power systems with renewables. *IEEE Trans. Sustain. Energy* 3 (3), 330–338. doi:10.1109/tste.2012.2184840

Kaya, I., Çolak, M., and Terzi, F. (2018). Use of MCDM techniques for energy policy and decision-making problems: A review. *Int. J. Energy Res.* 42 (7), 2344–2372. doi:10.1002/er.4016

Kemausuor, F., Sedzro, M. D., and Osei, I. (2018). Decentralised energy systems in africa: Coordination and integration of off-grid and grid power systems—review of planning tools to identify renewable energy deployment options for rural electrification in africa. *Curr. Sustain. Energy Rep.* 5 (4), 214–223. doi:10.1007/s40518-018-0118-4

Kempener, R., Lavagne, O., Saygin, D., Skeer, J., Vinci, S., and Gielen, D. (2015). *Off-grid renewable energy systems: Status and methodological issues*. Abu Dhabi, United Arab Emirates: Int. Renew. Energy Agency.

Kitegi, M. S. P., Lare, Y., Coulibaly, O., Kitegi, M. S. P., Lare, Y., and Coulibaly, O. (2022). Potential for green hydrogen production from biomass, solar and wind in Togo. *Smart Grid Renew. Energy* 13 (2), 17–27. doi:10.4236/SGRE.2022.132002

Korkovelos, A., Zerri, H., Howells, M., Bazilian, M., Rogner, H. H., and Nerini, F. F. (2020). A retrospective analysis of energy access with a focus on the role of mini-grids. *Sustain* 12, 1793. doi:10.3390/SU12051793

Korzhenevych, A., and Owusu, C. K. (2021). Renewable minigrid electrification in off-grid rural Ghana: Exploring households willingness to pay. *Sustain* 13 (21), 11711. doi:10.3390/SU132111711

Kumar, A., Sah, B., Singh, A. R., Deng, Y., He, X., Kumar, P., et al. (2017). A review of multi criteria decision making (MCDM) towards sustainable renewable energy development. *Renew. Sustain. Energy Rev.* 69, 596–609. doi:10.1016/j.rser.2016.11.191

Kyriakarakos, G., Balafoutis, A. T., and Bochtis, D. (2020). Proposing a paradigm shift in rural electrification investments in sub-saharan africa through agriculture. *Sustain* 12 (8), 3096. doi:10.3390/SU12083096

Lacey-Barnacle, M., Robison, R., and Foulds, C. (2020). Energy justice in the developing world: A review of theoretical frameworks, key research themes and policy implications. *Energy sustain. Dev.* 55, 122–138. doi:10.1016/J.ESD.2020.01.010

Lambert, T., Gilman, P., and Lilienthal, P. (2006). "Micropower system modeling with HOMER," in *Integration of alternative sources of energy*, 379–418.

Léautier, T. O. (2001). Electricity auctions. *J. Econ. Manag. Strategy* 10 (3), 331–358. doi:10.1111/j.1430-9134.2001.00331.x

Lee, T.-Y., and Chen, C.-L. (2009). Wind-photovoltaic capacity coordination for a time-of-use rate industrial user. *IET Renew. Power Gener.* 3 (2), 152–167. doi:10.1049/iet-rpg:20070068

Lena, G. (2013). "Rural electrification with PV hybrid systems: Overview and recommendations for further deployment," in *Int. Energy agency photovolt. Power syst. Program. Club african natl. Agencies struct. Charg. Rural electrif.*

Li, L., Yao, Z., You, S., Wang, C.-H., Chong, C., and Wang, X. (2019). Optimal design of negative emission hybrid renewable energy systems with biochar production. *Appl. Energy* 243, 233–249. doi:10.1016/j.apenergy.2019.03.183

Liu, W. H., Ho, W. S., Lee, M. Y., Hashim, H., Lim, J. S., Klemes, J. J., et al. (2019). Development and optimization of an integrated energy network with centralized and decentralized energy systems using mathematical modelling approach. *Energy* 183, 617–629. doi:10.1016/J.ENERGY.2019.06.158

LLC EnergySoft (2017). *User's manual EnergyPro version 7*.

Lloyd, P. J. D. (2012). *Restructuring South Africa's electricity supply industry*.

Long, N., and Steinberger, K. (2018). Renewable energy is key to fighting climate change. *Nat. Resour. Def. Counc.* Accessed, no. 29th April 2022.

Lyambai, M. (2018). *Accelerating energy access through public-private partnership investment in Zambia*. Tlemcen Algeria: SSRN Electron. J. doi:10.2139/SSRN.3211256

Magenta Global (2021). *Advancing successful mini grid & solar home systems in africa*.

Manetsgruber, D. (2015). *Risk management for mini-grids: A new approach to guide mini-grid deployment*.

Marcel, E. T., Mutale, J., and Mushi, A. T. (2021). Optimal design of hybrid renewable energy for Tanzania rural communities. *Tanzan. J. Sci.* 47 (5), 1716–1727. doi:10.4314/tjs.v47i5.19

Messaoudi, D., Settou, N., Negrou, B., and Settou, B. (2019). GIS based multi-criteria decision making for solar hydrogen production sites selection in Algeria. *Int. J. Hydrogen Energy* 44 (60), 31808–31831. doi:10.1016/j.ijhydene.2019.10.099

Micangeli, A., Del Citto, R., Kiva, I., Santori, S., Gambino, V., Kiplagat, J., et al. (2017). Energy production analysis and optimization of mini-grid in remote areas: The case study of habaswein, Kenya. *Energies* 10 (12), 2041. doi:10.3390/en10122041

Mokveld, K., and Von Eije, S. (2018). *Final energy report Mozambique*. Netherlands: Netherlands Enterp. Agency Hague.

Moner-Girona, M., Ghanadan, R., Solano-Peralta, M., Kougias, I., Bodis, K., Huld, T., et al. (2016). Adaptation of feed-in tariff for remote mini-grids: Tanzania as an illustrative case. *Renew. Sustain. Energy Rev.* 53, 306–318. doi:10.1016/j.rser.2015.08.055

Moner-Girona, M., Solano-Peralta, M., Lazopoulou, M., Ackom, E. K., Vallve, X., and Szabó, S. (2018). Electrification of Sub-Saharan Africa through PV/hybrid mini-grids: Reducing the gap between current business models and on-site experience. *Renew. Sustain. Energy Rev.* 91, 1148–1161. doi:10.1016/J.RSER.2018.04.018

Monyei, C. G., and Adewumi, A. O. (2017). Demand Side Management potentials for mitigating energy poverty in South Africa. *Energy Policy* 111, 298–311. doi:10.1016/J.ENPOL.2017.09.039

Monyei, C. G., and Akpeji, K. O. (2020). Repurposing electricity access research for the Global South: A tale of many disconnects. *Joule* 4 (2), 278–281. doi:10.1016/J.JOULE.2019.11.013

Monyei, C. G., Adewumi, A. O., and Jenkins, K. E. H. (2018). Energy (in)justice in off-grid rural electrification policy: South Africa in focus. *Energy Res. Soc. Sci.* 44, 152–171. doi:10.1016/J.ERSS.2018.05.002

Monyei, C. G., Jenkins, K., Serestina, V., and Adewumi, A. O. (2018). Examining energy sufficiency and energy mobility in the global south through the energy justice framework. *Energy Policy* 119, 68–76. doi:10.1016/J.ENPOL.2018.04.026

Morstyn, T., Savkin, A. V., Hredzak, B., and Tuan, H. D. (2018). Scalable energy management for low voltage microgrids using multi-agent storage system aggregation. *IEEE Trans. Power Syst.* 33 (2), 1614–1623. doi:10.1109/TPWRS.2017.2734850

Motjoadi, V., Bokoro, P. N., and Onibonoje, M. O. (2020). A review of microgrid-based approach to rural electrification in South Africa: Architecture and policy framework. *Energies* 13 (9), 2193. doi:10.3390/en13092193

N R E C Association and others (2019). *Guides for electric cooperative development and rural electrification*. United States: NRECA Int. Ltd., Arlingt.

Nagabhushana, A. C., Jyoti, R., and Raju, A. B. (2011). "Economic analysis and comparison of proposed HRES for stand-alone applications at various places in Karnataka state," in Proceeding of the ISGT2011-India, Kollam, India, December 2011 (IEEE), 380–385.

Nasir, M., Jin, Z., Khan, H. A., Zaffar, N. A., Vasquez, J. C., and Guerrero, J. M. (2018). A decentralized control architecture applied to DC nanogrid clusters for rural electrification in developing regions. *IEEE Trans. Power Electron.* 34 (2), 1773–1785. doi:10.1109/tpel.2018.2828538

Nfah, E. M., and Ngundam, J. M. (2012). Identification of stakeholders for sustainable renewable energy applications in Cameroon. *Renew. Sustain. Energy Rev.* 16 (7), 4661–4666. doi:10.1016/J.RSER.2012.05.019

Nhamo, G., and Mukonza, C. (2016). Policy, institutional and programme readiness for solar energy uptake in South Africa. *Afr. Insight* 45 (4), 69–90. doi:10.4314/ai.v45i4

Nikolina, S. (2016). *International renewable energy agency (IRENA)*.

Niyonteze, J. D. D., Zou, F., Asemota, G. N. O., and Bimenyimana, S. (2019). Solar-powered mini-grids and smart metering systems, the solution to Rwanda energy crisis. *J. Phys. Conf. Ser.* 1311 (1), 012002. doi:10.1088/1742-6596/1311/1/012002

Niyonteze, J. D. D., Zou, F., Norense Osarumwense Asemota, G., Bimenyimana, S., and Shyirambere, G. (2020). Key technology development needs and applicability analysis of renewable energy hybrid technologies in off-grid areas for the Rwanda power sector. *Heliyon* 6 (1), e03300. doi:10.1016/J.HELIYON.2020.E03300

Nkiriki, J., and Ustun, T. S. (2017). "Mini-grid policy directions for decentralized smart energy models in Sub-Saharan Africa," in Proceeding of the 2017 IEEE PES innovative smart grid technologies conference europe (ISGT-Europe), Turin, Italy, September 2017 (IEEE), 1–6.

Nsafon, B. E. K., Butu, H. M., Owolabi, A. B., Roh, J. W., Suh, D., and Huh, J.-S. (2020). Integrating multi-criteria analysis with PDCA cycle for sustainable energy planning in Africa: Application to hybrid mini-grid system in Cameroon. *Sustain. energy Technol. assessments* 37, 100628. doi:10.1016/j.seta.2020.100628

Nuru, J. T., Rhoades, J. L., and Gruber, J. S. (2021). The socio-technical barriers and strategies for overcoming the barriers to deploying solar mini-grids in rural islands: Evidence from Ghana. *Technol. Soc.* 65, 101586. doi:10.1016/J.TECHSOC.2021.101586

Nygaard, I., Hansen, U. E., Mackenzie, G., and Pedersen, M. B. (2015). Measures for diffusion of solar PV in selected African countries. *Int. J. Sustain. Energy* 36 (7), 707–721. doi:10.1080/14786451.2015.1086768

Odarno, L., Sawe, E., Swai, M., Katyega, M. J. J., and Lee, A. (2017). *Accelerating mini-grid deployment in sub-Saharan Africa: Lessons from Tanzania*. United States: World Resources Institute.

Odoi-Yorke, F., Owusu, J. J., and Atepor, L. (2022). Composite decision-making algorithms for optimisation of hybrid renewable energy systems: Port of Takoradi as a case study. *Energy Rep.* 8, 2131–2150. doi:10.1016/j.egyr.2022.01.118

Ohunakin, O. S., Adaramola, M. S., Oyewola, O. M., and Fagbenle, R. O. (2014). Solar energy applications and development in Nigeria: Drivers and barriers. *Renew. Sustain. Energy Rev.* 32, 294–301. doi:10.1016/J.RSER.2014.01.014

Ortega-Arriaga, P., Babacan, O., Nelson, J., and Gambhir, A. (2021). Grid versus off-grid electricity access options: A review on the economic and environmental impacts. *Renew. Sustain. Energy Rev.* 143, 110864. doi:10.1016/j.rser.2021.110864

Oyewo, A. S., Aghahosseini, A., Ram, M., Lohrmann, A., and Breyer, C. (2019). Pathway towards achieving 100% renewable electricity by 2050 for South Africa. *Sol. Energy* 191, 549–565. doi:10.1016/J.SOLENER.2019.09.039

Paliwal, P., Patidar, N. P., and Nema, R. K. (2014). Planning of grid integrated distributed generators: A review of technology, objectives and techniques. *Renew. Sustain. Energy Rev.* 40, 557–570. doi:10.1016/J.RSER.2014.07.200

Patel, H., and Chowdhury, S. (2015). "Review of technical and economic challenges for implementing rural microgrids in South Africa," in Proceeding of the 2015 IEEE Eindhoven PowerTech, Eindhoven, Netherlands, September 2015 (IEEE), 1–6.

Pedersen, M. B. (2016). Deconstructing the concept of renewable energy-based mini-grids for rural electrification in East Africa. *Wiley Interdiscip. Rev. Energy Environ.* 5 (5), 570–587. doi:10.1002/wene.205

Pedersen, M. B., and Nygaard, I. (2018). System building in the Kenyan electrification regime: The case of private solar mini-grid development. *Energy Res. Soc. Sci.* 42, 211–223. doi:10.1016/J.ERSS.2018.03.010

Pegels, A. (2010). Renewable energy in South Africa: Potentials, barriers and options for support. *Energy Policy* 38 (9), 4945–4954. doi:10.1016/j.enpol.2010.03.077

Peters, J., Sievert, M., and Toman, M. A. (2019). Rural electrification through mini-grids: Challenges ahead. *Energy Policy* 132, 27–31. doi:10.1016/J.ENPOL.2019.05.016

Pillot, B., Muselli, M., Poggi, P., and Dias, J. B. (2019). Historical trends in global energy policy and renewable power system issues in Sub-Saharan Africa: The case of solar PV. *Energy Policy* 127, 113–124. doi:10.1016/J.ENPOL.2018.11.049

Pohekar, S. D., and Ramachandran, M. (2004). Application of multi-criteria decision making to sustainable energy planning-a review. *Renew. Sustain. energy Rev.* 8 (4), 365–381. doi:10.1016/j.rser.2003.12.007

Psomopoulos, C. S., Ioannidis, G. C., Kaminaris, S. D., Mardikis, K. D., and Katsikas, N. G. (2015). A comparative evaluation of photovoltaic electricity production assessment software (PVGIS, PVWatts and RETScreen). *Environ. Process.* 2 (1), 175–189. doi:10.1007/s40710-015-0092-4

Puati Zau, A. T., and Daniel Chowdhury B, S. P. (2018). "Design of photo voltaic (PV) solar power plant to supply electricity and to pump water to chele community," in Proceeding of the 2018 IEEE PES/IAS PowerAfrica, PowerAfrica, Cape Town, South Africa, June 2018 (IEEE), 821–826. doi:10.1109/POWERAFRICA.2018.8521177

Pueyo, A., and DeMartino, S. (2018). The impact of solar mini-grids on Kenya's rural enterprises. *Energy sustain. Dev.* 45, 28–37. doi:10.1016/j.esd.2018.04.002

Ramakumar, R., Shetty, P. S., and Ashenayi, K. (1986). A linear programming approach to the design of integrated renewable energy systems for developing countries. *IEEE Trans. Energy Convers.* 4, 18–24. doi:10.1109/tec.1986.4765768

Raturi, A. K. (2019). *Renewables 2019 global status report*.

Reber, T., Booth, S., Cutler, D., Li, X., and Salasovich, J. (2018). *Tariff considerations for micro-grids IN SUB-saharan africa*. Accessed: Jun. 25, 2022. [Online]. Available: www.nrel.gov/publications.

Reber, T., and Booth, S. (2018). Tariff structures to encourage micro-grid deployment in sub-saharan africa: Review and recent trends. *Curr. Sustain. Energy Rep.* 53 (3), 199–204. doi:10.1007/S40518-018-0115-7

Renné, D., Kelly, M., Lilienthal, P., Gilman, P., Baring-Gould, I., Heimiller, D., et al. (2006). A strategic approach for promoting access to clean energy development. *Int. Sol. Energy Conf.* 2006.

Results (2020). *Results | tracking SDG 7*. Available at: https://trackingsdg7.esmap.org/results?p=Access_to_Electricity&i=Electricity_access_rate,_Total_(%25). accessed Jun. 25, 2022.

Rezk, H., Mukhametzyanov, I. Z., Al-Dhaifallah, M., and Zeiden, H. A. (2021). Optimal selection of hybrid renewable energy system using multi-criteria decision-making algorithms. *Comput. Mat. \& Contin.* 68 (2), 2001–2027. doi:10.32604/cmc.2021.015895

Safdar, T. (2017). *Business models for mini-grids: Technical report 9. 2017*. Cambridge, UK: Smart Villages Initiat. c/o Trinity Coll.

Scholtz, L., Muluadzi, K., Kritzinger, K., Mabaso, M., and Forder, S. (2017). *Renewable Energy: Facts and Futures the energy future we want*. Cape Town: Cape T.

Schwarzbözl, P., Eiden, U., Pitz-Paal, R., Zentrum, D., and Jones, S. (2006). *A TRNSYS model library for solar thermal electric components (STEC) reference manual release 3.0*.

Schwerhoff, G., and Sy, M. (2019). Developing Africa's energy mix. *Clim. Policy* 19 (1), 108–124. doi:10.1080/14693062.2018.1459293

SEI (2016). *Renewable energy mini-grids: An alternative approach to energy access in southern africa*. Accessed, no. 28th April 2022.

Shao, M., Han, Z., Sun, J., Zhang, S., Zhao, Y., and Shao, Z. (2020). "A GIS-MCDM combination for the site assessment of wave energy power station in qingdao, eastern China," in Preoceeding of the 30th International Ocean and Polar Engineering Conference, Virtual, October 2020 (IEEE).

Sheya, M. S., and Mushi, S. J. S. (2000). The state of renewable energy harnessing in Tanzania. *Appl. Energy* 65 (1–4), 257–271. doi:10.1016/S0306-2619(99)00116-6

Shimray, B. A., Singh, K. M., and Mehta, R. K. (2017). A survey of multi-criteria decision making technique used in renewable energy planning. *Int. J. Comput.* 4523, 124–140.

Shrestha, P., Shrestha, A., Shrestha, N. T., Papadakis, A., and Maskey, R. K. (2020). Assessment on scaling-up of mini-grid initiative: Case study of mini-grid in rural Nepal. *Int. J. Precis. Eng. Manuf. Technol.* 8 (1), 217–231. doi:10.1007/S40684-020-00190-X

Siddaiah, R., and Saini, R. P. (2016). A review on planning, configurations, modeling and optimization techniques of hybrid renewable energy systems for off grid applications. *Renew. Sustain. Energy Rev.* 58, 376–396. doi:10.1016/j.rser.2015.12.281

Sinha, S., and Chandel, S. S. (2014). Review of software tools for hybrid renewable energy systems. *Renew. Sustain. Energy Rev.* 32, 192–205. doi:10.1016/j.rser.2014.01.035

Somefun, T., Popoola, O., Abdulkareem, A., and Awelewa, A. (2022). Review of different methods for siting and sizing distributed generator. *Int. J. Energy Econ. Policy* 12 (3), 16–31. doi:10.32479/ijeep.12803

Sovacool, B. K., Burke, M., Baker, L., Kotikalapudi, C. K., and Wlokas, H. (2017). New frontiers and conceptual frameworks for energy justice. *Energy Policy* 105, 677–691. doi:10.1016/J.ENPOL.2017.03.005

Stiles, G., and Murove, C. (2015). *SADC renewable energy and energy efficiency status report*.

Stritzke, S., and Jain, P. (2021). The sustainability of decentralised renewable energy projects in developing countries: Learning lessons from Zambia. *Energies* 14 (13), 3757. doi:10.3390/EN14133757

Temudo, M. P., Cabral, A. I. R., and Talhinhas, P. (2019). Petro-Landscapes: Urban expansion and energy consumption in mbanza kongo city, northern Angola. *Hum. Ecol.* 47 (4), 565–575. doi:10.1007/S10745-019-00088-6

Temudo, M. P., Cabral, A. I. R., and Talhinhas, P. (2020). Urban and rural household energy consumption and deforestation patterns in zaire province, northern Angola: A landscape approach. *Appl. Geogr.* 119, 102207. doi:10.1016/J.APGEOG.2020.102207

Tenenbaum, B., Greacen, C., Siyambalapitiya, T., and Knuckles, J. (2014). *From the bottom up: How small power producers and mini-grids can deliver electrification and renewable energy in africa*. Washington, DC: World Bank Publications.

Tenenbaum, B., Greacen, C., and Vaghela, D. (2018). *Mini-grids and arrival of the main grid*.

Turcotte, D., Ross, M., and Sheriff, F. (2001). "Photovoltaic hybrid system sizing and simulation tools: Status and needs," in *PV horizon: Workshop on photovoltaic hybrid systems*, 1–10.

Unwin, J. (2020). Solar power in South Africa: A look at the country's solar Plants.2020. *Sol. Energy Newsl. S. Afr.* vol. Accessed, no. 28th April 2022.

Upadhyay, S., and Sharma, M. P. (2014). A review on configurations, control and sizing methodologies of hybrid energy systems. *Renew. Sustain. Energy Rev.* 38, 47–63. doi:10.1016/j.rser.2014.05.057

U. S. Agency, I. Development, and R. U. Commissioners (2020). *Exploring africa ' S mini-grid tariff exploring africa ' S mini-grid tariff*.

USAID (2022). *Unlocking africa's mini-grid market*.

van Bracht, N., Grote, F., Fehler, A., and Moser, A. (2016). "Incorporating long-term uncertainties in generation expansion planning," in Preoceeding of the 2016 13th International Conference on the European Energy Market (EEM), Porto, Portugal, June 2016 (IEEE), 1–5.

Villavicencio Calzadilla, P., and Mauger, R. (2017). The UN's new sustainable development agenda and renewable energy: The challenge to reach SDG7 while achieving energy justice. *J. Energy & Nat. Resour. Law* 36 (2), 233–254. doi:10.1080/02646811.2017.1377951

von Breitenstein, A. (1999). 'Enterprises of trust' - sustainable development through local utilities for renewable energies in rural areas of Tanzania. *Sustain. Dev. through Renew. Energies Tanzan.*

Wagemann, B., and Manetsgruber, D. (2016). Risk management for mini-grid deployment in rural areas. *Energy Procedia* 103, 106–110. doi:10.1016/j.egypro.2016.11.257

Wagner, N., Rieger, M., Bedi, A. S., Vermeulen, J., and Demena, B. A. (2021). The impact of off-grid solar home systems in Kenya on energy consumption and expenditures. *Energy Econ.* 99, 105314. doi:10.1016/J.ENECO.2021.105314

Walters, T., Rai, N., Esterly, S., Cox, S., Reber, T., Muzammil, M., et al. (2015). *Policies to spur energy access. Executive summary; volume 1, engaging the private sector in expanding access to electricity; volume 2, case studies to public-private models to finance decentralized electricity access*. United States.

Winkler, H., Hughes, A., and Haw, M. (2009). Technology learning for renewable energy: Implications for South Africa's long-term mitigation scenarios. *Energy Policy* 37 (11), 4987–4996. doi:10.1016/j.enpol.2009.06.062

Winkler, H. (2005). Renewable energy policy in South Africa: Policy options for renewable electricity. *Energy Policy* 33 (1), 27–38. doi:10.1016/S0301-4215(03)00195-2

Wolsink, M. (2020). Distributed energy systems as common goods: Socio-political acceptance of renewables in intelligent microgrids. *Renew. Sustain. Energy Rev.* 127, 109841. doi:10.1016/j.rser.2020.109841

Yusuf, S. S., and Mustafi, N. N. (2018). Design and simulation of an optimal mini-grid solar-diesel hybrid power generation system in a remote Bangladesh. *Int. J. Smart Grids, ijSmartGrid* 2 (1), 27–33.

Zeng, J., Li, M., Liu, J. F., Wu, J., and Ngan, H. W. (2010). "Operational optimization of a stand-alone hybrid renewable energy generation system based on an improved genetic algorithm," in Proceeding of the IEEE PES general meeting, Minneapolis, MN, USA, July 2010 (IEEE), 1–6.

Zerhouni, F. Z., Zerhouni, M. H., Zegrar, M., Benmessaoud, M. T., Stambouli, A. B., and Midoun, A. (2010). Proposed methods to increase the output efficiency of a photovoltaic (PV) system. *Acta Polytech. Hung.* 7 (2), 55–70.

Zhang, X., Yang, J., Wang, W., Jing, T., and Zhang, M. (2020). Construction and application of evaluation indexes for rural micro-energy-grid. *Nongye Gongcheng Xuebao/Transactions Chin. Soc. Agric. Eng.* 36 (6). doi:10.11975/j.issn.1002-6819.2020.06.023

10.3389/fenrg.2022.1089025

Glossary

R_i annual energy of the ith resources in kWh/m^2

x_{ij} part of ith resources used for the Jth task

I_i fraction of time t that the load i is supplied energy

E energy demand

$C_2(R)$ prospective yearly costs of wind turbine(s)

C_{ij} the unit cost of the system

X_{ij} quantum of renewable energy

$N_{pv_i}, N_{wd_j}, N_{batt_k}, N_{in_l}$ number of PV, wind turbine, battery bank, and inverter, respectively

VC_t variable costs

$q_{GHG,k}$ unit amount of greenhouse gas emission of component k

$W_{CO2/c}$ carbon stability factor

β_1, β_2 the weights for the economic and quality index

P_{ij} the real power output of each power supplier

CC_w, CC_p investment cost of wind turbine and PV, respectively

AOM annual operating and maintenance cost

$E_{anloadserved}$ energy served annually

a_{ij} cost in dollars in kWh when ith resources used for Jth task

P_i load demand i at t time in kW

Q_{dump} dumped energy

$C_1(Q)$ prospective yearly costs of the solar system and the battery storage system as functions of their size

$C_3(B_{max})$ prospective yearly costs of the battery storage system as functions of their size

η_{ij} the efficiency of the system

$C_{pv_i}, C_{wd_j}, C_{batt_k}, C_{in_l}$ cost of the wind turbine, photovoltaic, battery bank, inverter, and controller, respectively

$revenue_t$ hourly revenue from the sales of the products

FC daily fixed cost

$P_{k,t}$ amount of power produced from component k

$M(C)_{p,t}$ amount of fixed carbon generated by process p at time t

$Perf_{ij}$ assessment value of power quality for each generator

E_m electricity saving at the m_{th} month

AF_w, AF_p annualization factor for wind turbine and PV, respectively

C_{antot} annualized total cost

$NPC_{wd}, NPC_{el}, NPC_{\text{refreactor}}, NPC_{tank}, NPC_{converter}, NPC_{fc}$ the net present cost of the wind turbine, electrolyzer, reformer and reactor, tank, converter, and fuel cell, respectively.

Appendix

TABLE A1 Literature on the state of mini-grids in SSA.

Ref	Location	Objective	Outcome
Odarno et al. (2017)	South Africa	Viability assessment of hybrid mini-grids for the electrification and development of two rural communities	Hybrid hydro-mini-grid is the most viable energy system for the communities
Moner-Girona et al. (2018)	East Africa	Presented a critical analysis using mini-grid to electrify rural communities	Integration of existing utility-owned electricity infrastructure for powering communities does not translate to electrification
Antonanzas-Torres et al. (2021c)	Sub-Saharan Africa	Provides superior insight into the cost frameworks of PV/hybrid mini-grid facilities	Minimization of the data quality gap between the contemporary business model and those successfully implemented in the past is essential
Azimoh et al. (2017)	Tanzania	A review of the mini-grid sector	Based on the power plant mix, fossil fuel sources accounts for the majority of the power produced
Pillot et al. (2019)	Nigeria, Mali, Burkina Faso, Togo	Explored the contribution of mini-grid to electricity access in West Africa	Based on a 2018 analysis, the value of the mini-grid market in the surveyed countries is worth about $339 million
Eder et al. (2015)	Namibia	Investigated the scalability and replicability of mini-grid facilities in the electrification of rural communities in Sub-Saharan Africa	Sustainability was achieved because the current model is developed from an existing framework with possibilities for growth
Azimoh et al. (2016)	Cameroon	Proposed the hybridization of AHP-VIKOR and "Plan-Do-Check-Act" to continually enhance the panning process in mini-grid development	Optimal system is technically reliable and economically viable
Antonanzas-Torres et al. (2021a)	Uganda	Analyzed the elements that impact the adoption of renewable electricity at the household level	Social, economic, and technical factors are the most critical factors that influence the adoption
Micangeli et al. (2017)	15 ECOWAS countries	Environmental life cycle impact assessment of mini-grids in West Africa	PV mini-grids outperformed PV-diesel
Bukari et al. (2022)	Kenya	Investigated the effect of mini-grids on the development of a typical rural community	Although its tariffs were higher than national rates, the mini-grid had a positive impact on the background development and paid back a part of its cost
Babatunde et al. (2020)	Ghana	Examined the financial feasibility, challenges with power supply, as well as design accuracy in existing mini-grids	Adoption of existing tariff regulation with a well-designed tariff regime tends to considerably enhance economic indicators to ensure sustainability

frontiers | Frontiers in Energy Research

TYPE Original Research
PUBLISHED 19 January 2023
DOI 10.3389/fenrg.2022.1069364

OPEN ACCESS

EDITED BY
Olusegun David Samuel,
Federal University of Petroleum Resource Effurun, Nigeria

REVIEWED BY
Jichao Hong,
University of Science and Technology Beijing, China
Alireza Alfi,
Shahrood University of Technology, Iran

*CORRESPONDENCE
Ayokunle Awelewa,
ayokunle.awelewa@covenantuniversity.edu.ng

†These authors have contributed equally to this work and share first authorship

SPECIALTY SECTION
This article was submitted to Process and Energy Systems Engineering, a section of the journal Frontiers in Energy Research

RECEIVED 13 October 2022
ACCEPTED 28 December 2022
PUBLISHED 19 January 2023

CITATION
Awelewa A, Omiloli K, Samuel I, Olajube A and Popoola O (2023), Robust hybrid estimator for the state of charge of a lithium-ion battery.
Front. Energy Res. 10:1069364.
doi: 10.3389/fenrg.2022.1069364

Robust hybrid estimator for the state of charge of a lithium-ion battery

Ayokunle Awelewa[1*†], Koto Omiloli[1†], Isaac Samuel[1], Ayobami Olajube[2] and Olawale Popoola[3]

[1]Department of Electrical and Information Engineering, Covenant University, Ota, Nigeria, [2]Department of Electrical and Computer Engineering, Florida State University, Tallahassee, FL, United States, [3]Department of Electrical Engineering, Centre for Energy and Electric Power, Tshwane University of Technology, Pretoria, South Africa

The use of batteries for diverse energy storage applications is increasing, primarily because of their high energy density, and lithium-ion batteries (LiBs) are of particular significance in this regard. However, designing estimators that are robust to compute the state of charge (SOC) of these batteries in the presence of disturbance signals arising from different battery types remains a challenge. Hence, this paper presents a hybrid estimator that combines the extended Kalman filter (EKF) and sliding mode observer (SMO) *via* a switching function and tracking closed loop to achieve the qualities of noise cancellation and disturbance rejection. Hybridization was carried out in such a way that the inactive observer tracks the output of the used observer, simultaneously feeding back a zero-sum signal to the input gain of the used observer. The results obtained show that noise filtering is preserved at a convergence time of .01 s. Also, the state of charge estimation interval improves greatly from a range of [1, .93] and [.94, .84] obtained from the extended Kalman filter and sliding mode observer, respectively, to a range of [1, 0], in spite of the added disturbance signals from a lithium–nickel (INR 18650) battery type.

KEYWORDS

extended Kalman filter, lithium-ion battery, Sliding mode observer, state of charge, hybrid, state

1 Introduction

So far, lithium-ion batteries (LiBs) have been increasingly used in energy repository systems, power backups, and electronics (Orovwode et al., 2021) due to their inherent properties of dense energy, lower self-discharge, and prolonged cycle life (Guangzhong et al., 2016), more than conventional lead–acid batteries. LiBs constitute an essential energy repository system (Adeyemi et al., 2022) used in electrical vehicles and smart grids, hence the need for a battery management system (BMS). The BMS plays a significant role in monitoring the battery states, which include the state of charge (SOC) for the purpose of ensuring efficient and safe operation (ShichunYang et al., 2021; Zhang et al., 2017).

The SOC indicates the available battery capacity relative to the maximum capacity and lies in the range of 100 to 0 per cent. A typical challenge is that there is no known measuring instrument to determine the SOC. Thus, there is a continuous quest for developing state observers that can accurately estimate the SOC based on models that capture the internal dynamics of the LiB. One of the most popular models used in the SOC estimation task is the equivalent circuit model (ECM) composed of components such as resistors, capacitors, voltage sources, and, in some cases, hysteresis elements (Yujie et al., 2020). The attractiveness of the ECM is based on the less mathematical complexity in developing it and its fewer tuning

parameters unlike the electrochemical models, which contain complex partial differential equations (Simin et al., 2017) and a significant number of tuning parameters.

SOC estimation methods are based on open-loop, model-free, and closed-loop techniques. The coulomb counting (CC) and open-circuit voltage (OCV) methods are examples of open-loop techniques. The former makes use of the current integration technique for SOC estimation, but it is prone to inaccuracies due to the initial current measurement error, which accumulates (Liu et al., 2021) and, in addition, requires the initial SOC to be known. The OCV method uses a non-linear fitting function to map the relationship between the SOC and OCV in order to set up a look-up table from which the SOC of the battery at any step time is obtained (Xu et al., 2020). In real time, carrying out OCV experiments usually requires a large amount of time for electrolytes in the battery to become uniformly distributed before the battery terminal voltage can be accurately measured (Peng et al., 2017). Model-free techniques include artificial neural networks (ANNs) (Samuel et al., 2021) and fuzzy logic (FL), which are developed as a black box, and by studying the trained dataset (Surajudeen et al., 2021) such as the terminal voltage, temperature, charge–discharge current, and cycle, the look-up table function that describes the relationship between the SOC and battery parameters can be determined (Liu et al., 2021). A major drawback is that the estimation accuracy of these models is dependent on the size of the trained data and quality of the dataset (Ng et al., 2009).

Closed-loop SOC estimation techniques include the Kalman filter (KF), particle filter (PF), unscented particle filter (UPF), and sliding mode observer (SMO). The superior advantage they have over other methods is the ability of handling real-time disturbance and uncertainties of the battery system by correction in the feedback non-open-loop structure, leading to high accuracies in SOC estimation (Yidan, 2020). The PF and UPF produce good estimate results when used in non-linear systems, but they are restricted to non-Gaussian noise distribution. However, the KF is best used for uncertainties represented as Gaussian distributions, but its shortcoming is that its accuracy decreases when applied to non-linear systems, i.e., it generates accurate estimates for linear processes only. To this end, various extensions of the Kalman filter, namely, the extended Kalman filter (EKF), dual extended Kalman Filter (DEKF), and dual Kalman Filter (DKF), have been developed to further improve the SOC accuracy for non-linear systems affected with Gaussian noise distribution. The SMO is seen as a paradigm shift from the traditional Luenberger observers and Urtink observers, in which they do not require the system to be observable before the sliding motion can be implemented. In traditional observers, the error between the plant and model output, decreases to zero in infinite time. However, SMOs guarantee the error is exactly zero, and the model state is exactly that of the plant, beginning from the instant the sliding motion takes place. They also offer high robustness to measurement uncertainties and disturbances (Bouchareb et al., 2020). A major drawback in these observers is that the sliding motion is majorly composed of chattering caused by the high switching gain present in the SMO feedback loop.

Over the years, several works have been carried out by researchers in estimating the battery SOC. The KF was implemented by Guangzhong et al. (2016) for onboard SOC applications. The performance results under experiment conditions, namely, the dynamic current, direct power, and discharge capability tests, showed estimation errors of about 4 percent. The method is limited to linear system applications, and the complexity of the algorithm also limits its practical implementation. Benedikt et al. (2021) proposed an EKF with a hysteresis-coupled battery model for multiple cell SOC determination. The method showed a 300 percent decrease in maximum error and high stability from an EKF with no hysteresis present in its battery model. The shortfall was that the EKF parameters were highly sensitive on the variations of the process noise, which had effect on its accuracy and convergence. To solve this problem, an improved EKF (IEKF) was proposed in Shichun et al. (2021) by developing noise filtering and adaptation methods as augments to an existing EKF. The results showed an under temperature disturbance and dynamic stress conditions (DSCs); the maximum errors were three percent and one per cent, respectively. However, the SOC response due to complex coupling effects of the battery was not considered.

By Wenhui et al. (2019), the SOC estimation for power LiB using a fuzzy logic sliding mode observer (FLSMO) was proposed. The work improved the performance of SMOs through the use of the fuzzy logic control (Atayero et al., 2012). The discharging test results showed that the FLSMO algorithm had a higher SOC estimation accuracy, with a considerable convergence rate. Compared with the sliding mode observer and extended Kalman filter, the FLSMO algorithm shows better performance regarding the robustness against the measurement noise and parameter disturbance. Sassi et al. (2018) carried out a comparison of the KF and SMO and noted the competitive nature of both methods with regards to the precision but concluded on the superiority of the SMO over KF in terms of handling parameter changes to uncertainties in the battery model.

To obtain desired qualities associated with two or more SOC estimation strategies, hybridization is required. The unique difference between a hybrid state estimator and existing state estimators is that it offers an approach for combining the strength of noise filtration, a characteristic of the EKF, and robustness, an attribute of SMO, in predicting the SOC of batteries, thus producing a better adaptive system to the uncertainties that arise from the environment and measurement instruments. In addition, the hybrid system consists of a well-posed dynamic system and draws both discrete time and continuous time behaviors of EKF and SMO state estimation algorithms to improve the accuracy of individual methods.

One of the challenges present in the SOC estimation subject is the problem of designing accurate state observers that can be adaptive to disturbances influencing the signal characteristics of lithium-ion batteries. A state observer designed for one battery type loses its estimation reliability when subjected to a different battery type due to variation of chemistry. In fact, the model sees the new input signals as a form of disturbance, and hence, the question that arises is how one can redesign the system to become insensitive to alien data in a way it maintains precise parameter predictions. This paper aims to address this issue by proposing the design and implementation of a hybrid estimator combining EKF and SMO state estimation strategies to improve the performance accuracy of the EKF and the robustness quality of both estimators in the face of complex LiB parameter disturbances due to the change of the battery type.

Beginning with this introductory section, the organization of this paper starts with data collection description in Section 2. The equivalent circuit model of the batteries derived in the discrete state space is presented in Section 3. The battery model parameter identification technique is discussed in Section 4. In Sections 5 and 6, developments of EKF and SMO state estimators are presented, respectively. Section 7 explains the hybridization procedure, while Section 8 presents the results and evaluation of estimators. The conclusion of this paper is given in Section 9.

TABLE 1 Experiment material specifications.

Name of equipment	Specification
Coulomb counter	12 V
18650 Panasonic	4 no. 4 V; 2 Ah
Battery charger	19 V; 3 A
BMS	4S; 40 A
Current transformer	110/3 A
DC–DC converter	15 V

2 Data collection

A charge and discharge experiment was carried out on 4 No. 4-V and 2-Ah Panasonic's lithium-ion batteries connected in a series at room temperature. The materials used and the experimental setup are shown in Table 1 and Figure 1, respectively. The charge experiment was made possible through the DC–DC converter passing the charging current at the 1 C rate to flow into the batteries. The current transformer (CT) rated 3-A measures the current and passes the signal to the 12-V digital Coulomb counter for the measurement of the capacity, voltage, and current information on the batteries. The BMS helps regulate the batteries from overcharging and discharging and monitors the maximum cut-off voltage of 4 V and minimum cut-off voltage of 2.7 V for each cell set by the manufacturer. The cut-off voltage set was required to protect the batteries from overcharging and discharging by disconnecting the load from the batteries whenever the limits were reached. This is crucial in ensuring the batteries maintain maximum capacity, increased life, and are not damaged in an excessive charge or discharge process. For the discharge readings, a 3.8-V, 2.35-Ah mobile device was used as the load connected across the batteries in parallel and to the Coulomb counter for the measurement readings to be displayed. The current and voltage profiles for the discharge and charge experiment are shown in Figures 2A–D, respectively. The positive and negative values of the current profile in Figures 2A, C show the batteries were charged and discharged, respectively.

TThe step-by-step procedures used in carrying out the experiment are outlined as follows:

Step 1: Connection of the batteries in a series.

Step 2: Connection of the battery terminals to the BMS.

Step 3: Connection of the BMS output to the CT.

Step 4: CT connected to the coulomb counter.

Step 5: The negative terminal of the CT passed to the negative terminal of the BMS, and positive terminal of the CT passed through the CT to the positive terminal of the BMS.

Step 6: The DC–DC converter is connected to the power pack.

Step 7: The converter voltage output is adjusted to 12 V.

Step 8: The converter is connected to the CT and BMS.

Step 9: The measurement reading is taken at the display interface of the coulomb counter.

3 Battery modeling

The choice of the model in representing the LiB internal states is the equivalent circuit model (ECM) due to its merits of simplicity, few parameters, and faster implementation in carrying out the SOC estimation. To carry out battery modeling with a reasonable level of accuracy and with less parameters, a first-order ECM choice is required. As shown in Figure 3, the first-order ECM can be regarded as an RC (resistor and capacitor) model. It consists of an open-circuit voltage (OCV), two internal resistors, and a single capacitor. The internal resistance, R_0, is responsible for the drop and rise of the measurement voltage profile, while the R_1C_1 term describes the transient behavior of the measurement voltage response.

At node A, applying Kirchhoff's current law (KCL), we obtain the following:

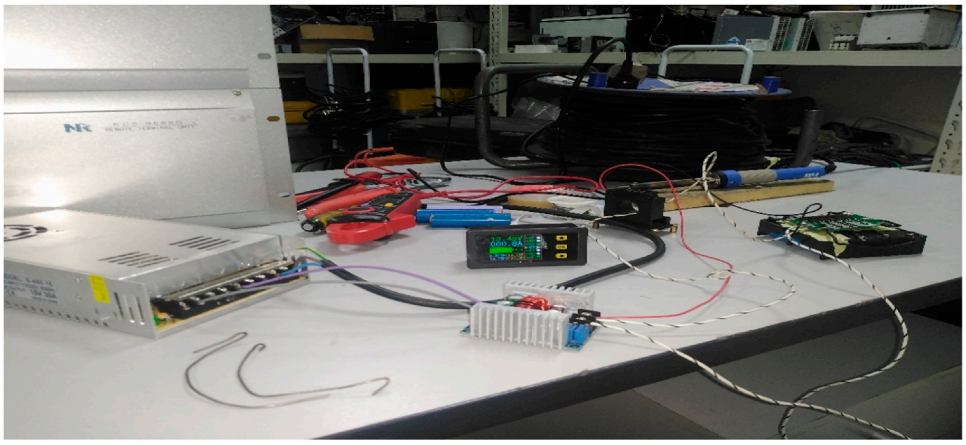

FIGURE 1
Experimental setup.

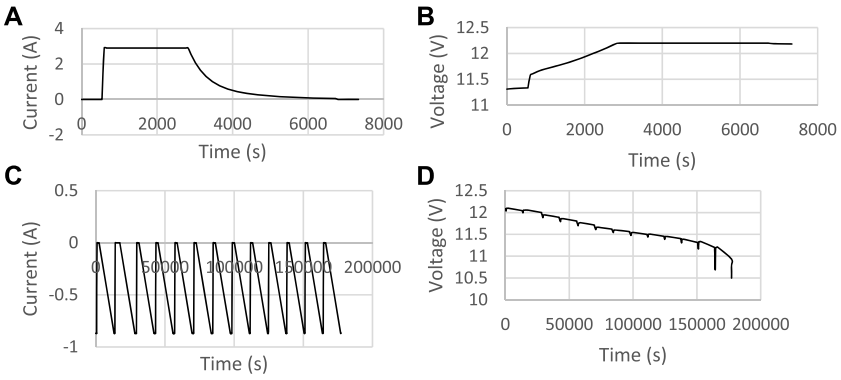

FIGURE 2
(A) Primary data charge current plot. **(B)** Primary data charge voltage plot. **(C)** Primary data discharge current plot. **(D)** Primary data discharge voltage plot.

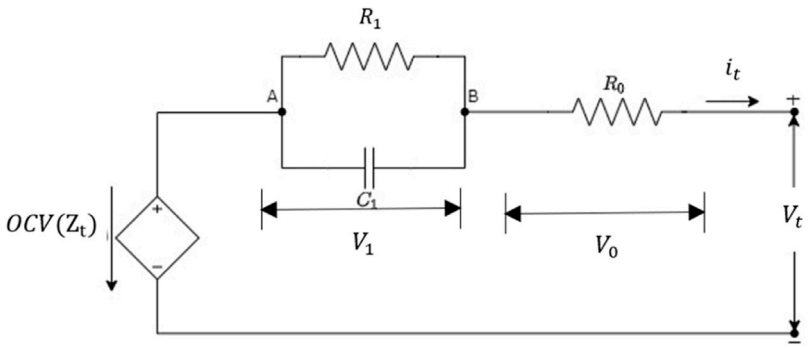

FIGURE 3
First-order ECM model.

$$i_t = i_{R_1} + i_{C_1} = \frac{V_1}{R_1} + C_1\dot{V}_1. \tag{1}$$

Making the derivative of V_1 the subject of the formula, we obtain the following:

$$\dot{V}_1 = -\frac{V_1}{R_1C_1} + \frac{1}{C_1}i_t. \tag{2}$$

Taking Kirchhoff's voltage law (KVL) across the full loop results, we obtain

$$V_t = OCV(Z_t) - V_0 - V_1 = OCV - R_0 i_t - V_1. \tag{3}$$

The SOC equation is given as follows:

$$Z_t = Z_0 - \frac{\eta_k}{Q_{batt}}\int_0^t i dt, \tag{4}$$

where Z_t refers to the state of charge at time t, Z_0, the initial state of charge (=100%), Q_{batt}, the maximum battery capacity, η_k, the Coulombic efficiency, OCV, the open circuit voltage, and i, the input current.

The following sign convention was used for the current:

$$\text{sgn}(i_t) = \begin{cases} +, & \text{for discharging,} \\ -, & \text{for charging.} \end{cases} \tag{5}$$

The coulombic efficiency describes the efficiency of a charging process due to the number of electrons transferred into the cell. It can be estimated from the OCV charge and discharge curves (Benedikt et al., 2021), which is expressed as follows:

$$\eta_k = \begin{cases} 1, & i_k > 0 \text{ for discharging,} \\ \eta^*, & i_k < 0 \text{ for charging.} \end{cases} \tag{6}$$

The next step is to discretize Eqs 2–4 using the sample time k + 1 as the present value and k as the previous value. To discretize Eq. 2, the difference ratio is approximated as follows:

$$\dot{V}_1 \cong \frac{V_{1,k+1} - V_{1,k}}{\delta t} = -\frac{V_{1,k}}{R_1C_1} + \frac{1}{C_1}i_k, \tag{7}$$

so that

$$V_{1,k+1} = V_{1,k}\left(1 - \frac{\delta t}{R_1C_1}\right) + \frac{\delta t}{C_1}i_k. \tag{8}$$

The discretization of Eqs 3, 4 is straightforward. Therefore, the battery model is represented in the state space form as follows:

$$\begin{bmatrix} V_{1,k+1} \\ Z_{k+1} \end{bmatrix} = \begin{bmatrix} 1 - \frac{\delta t}{\tau_1} & 0 \\ 0 & 1 \end{bmatrix}\begin{bmatrix} V_{1,k} \\ Z_k \end{bmatrix} + \begin{bmatrix} \frac{\delta t}{C_1} \\ -\frac{\eta \delta t}{Q} \end{bmatrix}[i_k] \tag{9}$$
$$V_k = OCV(Z_k) - R_0 i_k - V_{1,k},$$

TABLE 2 First order ECM parameters.

SOC	Fitting functions
.1	11.38–.3166*exp(-.2093t)
.2	10.114–.74exp(-.392t)
.3	11.83–.277exp(-.046t)
.4	10.672–.95exp(-.03445t)
.5	10.596–.18exp(-.48t)
.6	11.541–.276exp(-.6797t)
.7	11.459–.956exp(-.34t)
.8	11.336–.506exp(-.6991t)
.9	11.544–.301exp(-.587t)
1.0	10.758–.402exp(-.672t)

where Z_k is the state of charge, OCV is the open circuit voltage of the battery at no load, Q is the battery-rated capacity, and R_0 is the battery ohmic resistance. The product R_1C_1 represents the polarization time constant τ_1; $V_{1,k}$ represents the current state of voltage across the capacitor C_1 and resistor R_1. The model's output V_k represents the terminal or observed voltage, and the input is the measured current i_k; η_k represents the battery coulombic efficiency assumed as 1 in this paper.

4 Model parameter identification

A global pattern search algorithm (GPSA) available in the Simulink parameter optimization toolbox is used for the offline battery parameter identification to obtain the optimum values of the internal parameters, $\{OCV, R_0, \tau_1\}$. The algorithm generates these parameters by searching sets of points called the mesh around a current point determined to have had the least objective function, $\sum_k^n (V_t - \hat{V}_t)$ value. The step-by-step implementation is presented as follows:

Step 1: The number of independent N variables for the objective function is set.

Step 2: The initial point v_0 is set along with upper and lower boundaries of model parameters.

Step 3: Pattern vectors are generated depending on N. By default, for a 2N maximal base, where N = 2 for the pattern vector, v_i is represented as follows:

$$v_1 = [1 \;\; 0]; \quad v_2 = [0 \;\; 1]; \quad v_3 = [-1 \;\; 0]; \; v_4 = [0 \;\; -1]. \tag{10}$$

Step 4: The current mesh size Δ^m is set.

Step 5: The mesh is computed as follows:

$$m = v_0 + \Delta^m \cdot v_i. \tag{11}$$

Step 6: The process of polling is initiated, following the direction produced by the pattern vector that generates a mesh point.

4.1 Parameter initialization

Proper parameter initialization of the battery model is essential for obtaining an accurate fitting relationship between the measured and estimated voltage input. Hence, the voltage discharge curve is partitioned into 10 pulses corresponding to an SOC value in the range [.1, 1.0] with a step value of .1. To compute the initial parameters (OCV, R_0; R_1), a mathematical comparison between the fitting functions in Table 2 described by the transient pulses and the transient terminal voltage in Eq. 12a, 12b, 12c is carried out as follows:

$$V_L = OCV - R_0 I_t - R_1 I_t e^{\frac{-t}{\tau_1}} \tag{12a}$$

The transient terminal voltage V_L describes the dynamic exponential behavior of the battery terminal voltage profile shown in Figure 2D after each rise and drop in the pulse and is derived from the transient solution of Eq. 2 by first recalling from basic principles; the general solution of a first-order non-homogenous linear differential Eq. 2 is given as follows:

$$V_1 = e^{\frac{-t}{\tau_1}} \left[\int \frac{i_t}{c_1} \cdot e^{\frac{-t}{\tau_1}} \cdot dt + k \right] \tag{12b}$$

Carrying out the integration in Eq. 12b and applying the initial condition, $V_1(0) = 0$. This implies $k = -R_1 i_t$ so that

$$V_1 = R_1 i_t - R_1 i_t e^{\frac{-t}{\tau_1}} \tag{12c}$$

Taking the transient portion of Eq. 12c, i.e., the term with the exponential function for the discharge case and then substituting it in Eq. 3, the transient terminal voltage equation $V_t = V_L$ in Eq. 12a is obtained.

5 The extended Kalman filter algorithm

The non-linear dynamic state representation of the battery is expressed as follows:

$$\begin{aligned} x_{k+1} &= f(x_k, u_k) + w_k \\ y_k &= g(x_k, u_k) + v_k \end{aligned} \tag{13}$$

where $f(x_k, u_k)$ represents the process of non-linear dynamics and $g(x_k, u_k)$ represents the measurement of non-linear dynamics. The matrices, w_k and v_k, represent the noise present in the process and measurement part of the system, respectively (Rui et al., 2017). A step-by-step implementation of the first-order EKF algorithm is given as follows using a hat (^) notation to identify the state estimates:

Step 1: Setting the internal state $x_{k+1}[0] = \begin{bmatrix} 1 \\ 0 \end{bmatrix}$ and system state error $P_{k+1}[0] = [0]_{2\times 2}$.

Step 2: Calculating the priori estimates

$$\begin{aligned} \hat{x}_{k+1|k} &= A_k \hat{x}_{k|k} + B_k u_k \\ P_{k+1} &= A_k P_{k|k} A_k^T + Q_k. \end{aligned} \tag{14}$$

Step 3: Linearizing the system model (Awelewa et al. 2013) about $x_{k+1|k}$ such that

$$A_k = \left(\frac{\partial f(x_k, u_k)}{\partial x_k}\right)_{x_{k+1|k}, u_k} = \mathrm{diag}\left(1,\ e^{\frac{-\Delta t}{\tau_1}}\right);\ B_k = \begin{pmatrix} \frac{-\eta_k \Delta t}{Q_{batt}} \\ R_1\left(1 - e^{\frac{-\Delta t}{\tau_1}}\right) \end{pmatrix}, \tag{15}$$

$$C_k = \left(\frac{\partial g(x_k, u_k)}{\partial x_k}\right)_{x_{k+1|k}, u_k} = \left[\frac{\partial V_0}{\partial Z_k}, -1\right]. \tag{16}$$

The Jacobean matrices A_k, B_k, and C_k were derived from the first-order Taylor series approximation (Awelewa et al., 2021) of (13); V_0 is the OCV; Z_k is the SOC, and the state vector is $x_k = \begin{bmatrix} Z_k \\ V_{1,k} \end{bmatrix}$.

Step 4: Calculating the Kalman gain K_{k+1}

$$K_{k+1} = P_{k+1|k} C^T \left(C P_{k+1|k} C^T + R_{k+1}\right)^{-1}. \tag{17}$$

Step 5: Calculating the a posteriori (Mohammed, 2013) estimates

$$\hat{x}_{k+1|k+1} = \hat{x}_{k+1|k} + K_{k+1}\left(y_k - \hat{y}_k\right). \tag{18}$$

Step 6: Calculating the system state error

$$P_{k+1|k+1} = (1 - K_{k+1} C_{k+1}) P_{k+1|k}. \tag{19}$$

6 The sliding mode observer

From the first-order ECM in Figure 3, the equations representing the state dynamics of the LiB is deduced as follows:

$$V_t = V_{oc}(SOC) - R_0 I_b - V_1, \tag{20a}$$

$$\dot{V}_1 = \left(\frac{-1}{R_1 C_1}\right) V_1 + \left(\frac{1}{C_1}\right) I_b, \tag{20b}$$

$$\dot{SOC} = \frac{-I_b}{C_b}, \tag{20c}$$

where V_{oc} is the open-circuit voltage (OCV); I_b is the battery current; V_1 is the voltage across the RC pair; C_b is the nominal battery capacity. The SOC derivative equation in Eq. 20c is deduced from the relationship $SOC_t = SOC_0 - \frac{1}{C_b}\int i dt$, which represents the current integration SOC technique.

From the terminal voltage equation, V_t in Eq. 20a, we get the following equation:

$$-I_b = \frac{V_t - V_{oc} + V_1}{R_0}. \tag{21}$$

Substituting Eq. 21 into Eq. 20c results in the following equation:

$$\dot{SOC} = \left(\frac{1}{R_0 C_b}\right)(V_t - V_{oc} + V_1). \tag{22}$$

Differentiating V_t in Eq. 20a gives the following equation:

$$\dot{V}_t = \frac{dV_{oc}}{dSOC} \cdot \frac{dSOC}{dt} - \frac{dV_1}{dt}. \tag{23}$$

Since $\frac{dV_{oc}}{dSOC} \approx 0$, substituting Eq. 20b gives the following:

$$\dot{V}_t = -\dot{V}_1 = \frac{V_1}{R_1 C_1} + \frac{I_b}{C_b}. \tag{24}$$

Making V_1 the subject in Eq. 20a and substituting it in Eq. 24, we get the following expression:

$$\dot{V}_t = \frac{-1}{R_1 C_1} V_t + \frac{1}{R_1 C_1} V_{oc} - \left(\frac{R_0}{R_1 C_1} + \frac{1}{C_1}\right) I_b. \tag{25}$$

Combining $\dot{V}_t$, $\dot{V}_1$, and $\dot{SOC}$ equations, the state dynamics of the battery becomes the following:

$$\begin{aligned} \dot{V}_t &= \frac{-1}{R_1 C_1} V_t + \frac{1}{R_1 C_1} V_{oc} - \left(\frac{R_0}{R_1 C_1} + \frac{1}{C_1}\right) I_b + \Delta f_1 \\ \dot{V}_1 &= \left(\frac{-1}{R_1 C_1}\right) V_1 + \left(\frac{1}{C_1}\right) I_b + \Delta f_2, \\ \dot{SOC} &= \left(\frac{1}{R_0 C_b}\right)(V_t - V_{oc} + V_1) + \Delta f_3, \end{aligned} \tag{26}$$

where Δf_1, Δf_2, and Δf_3 represent non-linear disturbances (uncertainties) added to the real system in Eq. 24, satisfying the Lipschitz boundary criterion $\|\Delta f(x) - \Delta f(\hat{x})\|_2 \le \gamma \|x - \hat{x}\|_2$. Here, $1 \le \gamma$. The SMO equations are then proposed as follows:

$$\begin{aligned} \dot{\hat{V}}_t &= \frac{-1}{R_1 C_1} \hat{V}_t + \frac{1}{R_1 C_1} \hat{V}_{oc} - \left(\frac{R_0}{R_1 C_1} + \frac{1}{C_1}\right) I_b + \lambda_1 \mathrm{sgn}\left(e_{V_t}\right), \\ \dot{\hat{V}}_1 &= \frac{-1}{R_1 C_1} \hat{V}_1 + \left(\frac{1}{C_1}\right) I_b + \lambda_2 \mathrm{sgn}\left(e_{V_{oc}}\right), \\ \widehat{\dot{SOC}} &= \left(\frac{1}{R_0 C_b}\right)\left(\hat{V}_t - \hat{V}_{oc} + \hat{V}_1\right) + \lambda_3 \mathrm{sgn}\left(e_{V_{R_1 C_1}}\right). \end{aligned} \tag{27}$$

Subtracting Eq. 27 from Eq. 26 gives the following error dynamics:

$$\dot{e}_{V_t} = \frac{-1}{RC} e_{V_t} + \frac{1}{RC} e_{V_{oc}} + \Delta f_1 - \lambda_1 \mathrm{sgn}\left(e_{V_t}\right), \tag{28a}$$

$$\dot{e}_{V_1} = \left(\frac{-1}{R_1 C_1}\right) e_{V_1} + \Delta f_2 - \lambda_2 \mathrm{sgn}\left(e_{V_{oc}}\right), \tag{28b}$$

$$\dot{e}_{SOC} = \left(\frac{1}{R_0 C_b}\right)\left(e_{V_t} + e_{V_{oc}} + e_{V_1}\right) + \Delta f_3 - \lambda_3 \mathrm{sgn}\left(e_{V_1}\right), \tag{28c}$$

where the switching signal $\mathrm{sgn}(e) = \begin{cases} +1, & e > 0 \\ -1, & e < 0 \end{cases}$ and state errors are defined as follows:

$$\begin{aligned} &e_{V_t} = V_t - \hat{V}_t;\ e_{V_1} = V_1 - \hat{V}_1;\ e_{V_{OC}} = V_{OC} - \hat{V}_{OC} = k\left(SOC - \widehat{SOC}\right) \\ &= k e_{SOC}. \end{aligned} \tag{29}$$

To achieve stability (quadratic) of the terminal voltage error (e_{V_t}), the following Lyapunov function is chosen for a symmetric error:

$$V_{vt} = \frac{1}{2} {e_{V_t}}^2 = {e_{V_t}}^T \frac{1}{2} e_{V_t}. \tag{30}$$

To achieve an ideal sliding motion, i.e., ($e_{V_t} = 0$), then $\dot{V}_{vt} < 0$.
The sliding surface $S_0 = \{(e_{state}, e_{V_t}):\ e_{V_t} = 0\}$.
Differentiating Eq. 30 gives the following:

$$\dot{V}_{vt} = e_{V_t} \times \dot{e}_{V_t}. \tag{31}$$

For the Lyapunov stability condition to be satisfied $\lambda \gg \Delta f$ so that $\dot{V}_{vt} < 0$, which implies $\dot{e}_{V_t} = e_{V_t} = 0$.

By replacing $\dot{e}_{V_t} = e_{V_t} = 0$ in Eq. 28a and recalling $e_{V_{oc}} = k e_{SOC}$, the equivalent injection signal is deduced as follows:

$$e_{SOC} = \frac{\lambda_1}{k b_1} \mathrm{sgn}\left(e_{V_t}\right). \tag{32}$$

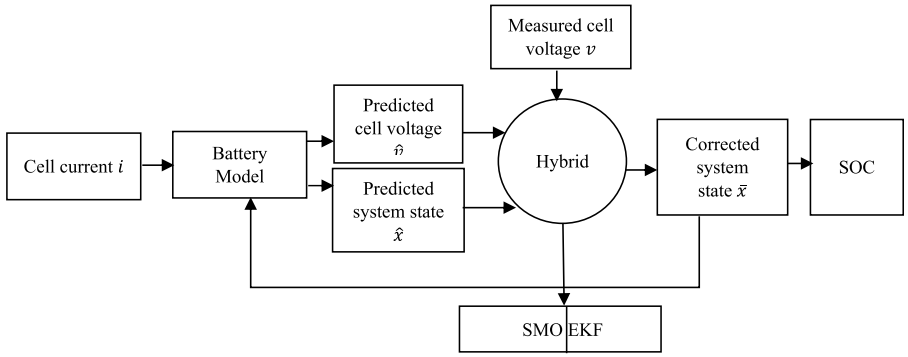

FIGURE 4
Block diagram of the hybrid SOC estimator.

Similarly, by replacing $\dot{e}_{SOC} = e_{SOC} = 0$ and $e_{V_t} = 0$ in Eq. 28c and substituting them in Eq. 32, we obtain the following equation:

$$e_{V_1} = \frac{\lambda_2}{b_2}\mathrm{sgn}\left(\frac{\lambda_1}{kb_1}\right)\mathrm{sgn}\left(e_{V_t}\right). \tag{33}$$

The state vector $\begin{bmatrix} SOC \\ V_1 \end{bmatrix}$ can then be obtained by substituting the aforementioned injection signals into the error dynamics equations.

7 Hybridized estimator

Among the estimators developed, this work observes certain intervals, in which the first-order EKF has poor performance. This means that there are regions where there is the presence of a mismatch between the EKF and Ah (referred to as the real SOC), typically at the SOC error bound [−.05, .05] and [−.1, .1]. In addition, the SMO has a slow convergence time when subjected to complex disturbances. To solve these problems, a hybrid EKF–SMO observer is designed, as shown in the block diagram of Figure 4 such that the inactive observer tracks the output of the used observer, simultaneously feeding back a zero-sum signal to the input gain of the used observer. The following steps are carried out in achieving the hybrid estimation:

Step 1: Determination of intervals for switching to take place

Step 2: Connection of the current input source to both observers

Step 3: Back feeding the error obtained from the outputs of the two observers *via* a gain to the input of the currently used observer.

Step 4: Finally, tuning the observer gain to improve the response of hybridization.

In brevity, switching is performed as follows:

$$H_{switch} = \begin{cases} SMO\,(SOC), & -0.05 \le SOC \le 0.05 \text{ and } -0.1 \le SOC \le 0.1, \\ EKF\,(SOC), & \text{otherwise.} \end{cases} \tag{34}$$

8 Results and discussion

The performance of the first-order ECM based on discharge measurement data obtained from the experiment is presented in this section, followed by the response analysis of individual estimators and the robust hybrid estimator designed.

8.1 Parameter estimation performance

The optimum parameters (OCV, R_0, R_1, and τ_1) of the battery model are shown in Table 3 from the GPSA results. With these parameter values, the model response is simulated *via* the discharge data voltage and current input obtained from the experiment to derive the model states (V_1 and Z_t) and output terminal voltage (V_t) of the batteries, as shown in Figure 5. This was carried out in order to validate the model developed and further visualize the real SOC, which will be used as a benchmark to test the performance of the EKF and SMO. The voltage plots in Figure 6 represent the measurement from the experiment and the estimation from the model parameter identification. Evidently, the extremely close fit verifies the accuracy of the model developed in this work, which is dependent on good parameter initialization discussed in Section 4.1.

8.2 Validation of the EKF and SMO estimator

The response of the first-order EKF and SMO is shown in Figures 7, 8 respectively, with the root mean square error (RMSE) and maximum absolute error (MAE) values presented in Table 4. The benchmark used is the coulomb counting technique to compare the performance of both estimators. From the plots, it is evident that the SMO converges faster with a higher SOC estimation accuracy than the EKF. The SMO drove the error between the real and estimated SOC to zero, as shown by its RMSE and MAE values in Table 4. Both estimators show high quality in filtering the random white noise that is added to the input current and voltage measurement. However, it is observed beginning from $t = 2.6 \times 10^4$ that the EKF diverges from the ideal value in contrast to the SMO, which maintains a high matching behavior. The RMSE and MAE metrics of the EKF are approximately zero in Table 4 due to the large time range of matching between the real and estimated SOC, overwhelmingly exceeding the short time range of the mismatch, as shown in Figure 7.

To test for robustness of the estimators designed, the current and voltage measurement inputs of the Panasonic 18650 batteries are interchanged with that of a 5 A h, 4V, lithium–nickel rechargeable (INR 18650) battery to see how far the stability behavior could be met

TABLE 3 Optimized parameter values for the first-order ECM.

SOC	.1	.2	.3	.4	.5	.6	.7	.8	.9	1
R_0	.00297	.00228	.00234	.002253	.002265	.002226	.002209	.002120	.001968	.001901
R_1	.00200	.00069	.00076	.00083	.000702	.000651	.000741	.000814	.000814	.000769
τ_1	27.9060	18.7730	38.6630	35.1800	28.0850	24.3610	29.6090	29.8280	21.7490	16.2450
OCV	11.3849	11.4595	11.5455	11.944	11.6297	11.6805	11.7733	11.8280	10.9828	11.1093

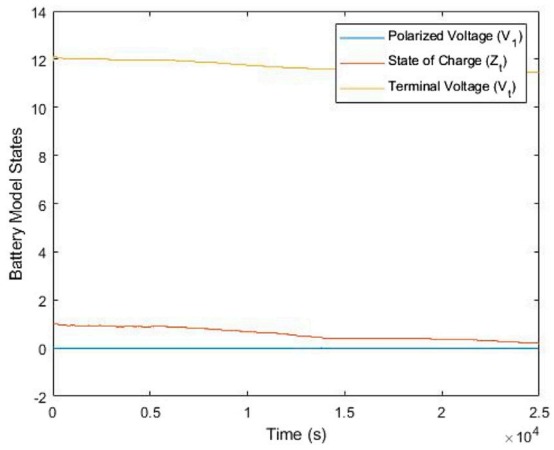

FIGURE 5
Model response of the first-order ECM.

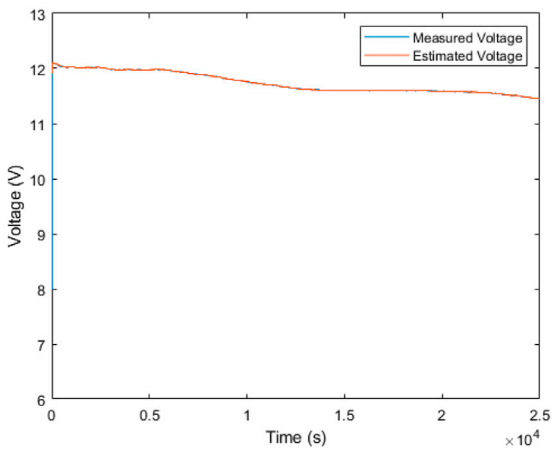

FIGURE 6
Measured *vs.* the estimated voltage response of the first-order ECM.

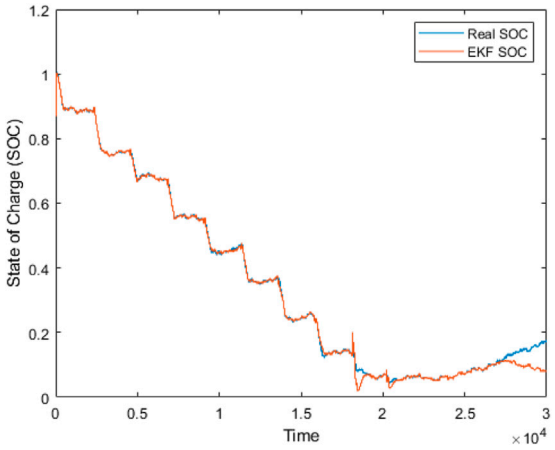

FIGURE 7
Extended Kalman filter response.

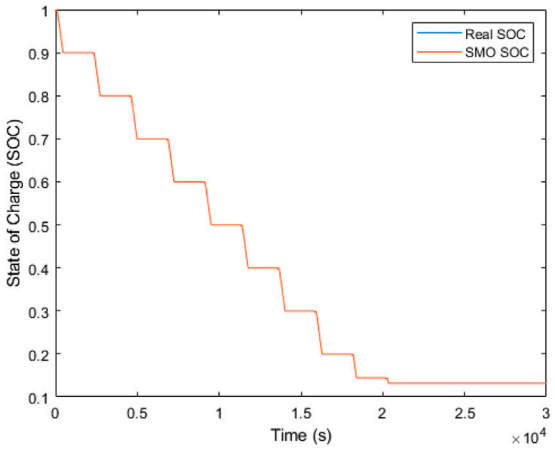

FIGURE 8
Sliding mode observer response.

in the face of complex disturbances. Figures 9, 10 show the performance of the EKF and SMO subjected to the disturbance. As seen, the SMO diverges from the initial SOC of 100% to begin at an initial SOC of 94% and later maintains an estimation of about 90% SOC. The EKF, on the other hand, maintains a sustained estimation in

TABLE 4 Estimator performance metrics.

	EKF	SMO
RMSE	.000170	0
MAE	.00733	0

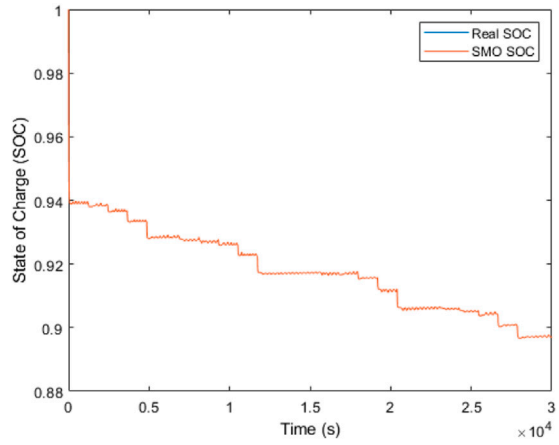

FIGURE 9
Response of the SMO under INR 18650.

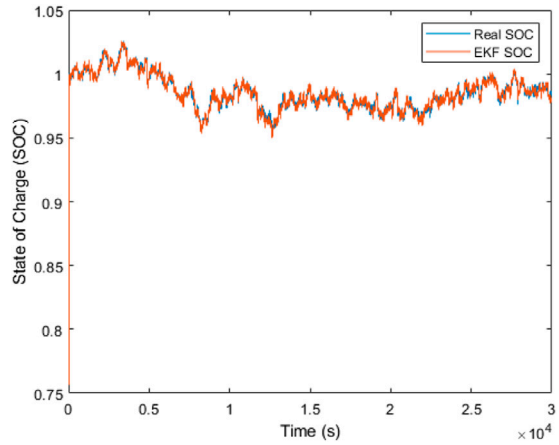

FIGURE 10
Response of the EKF under INR 18650.

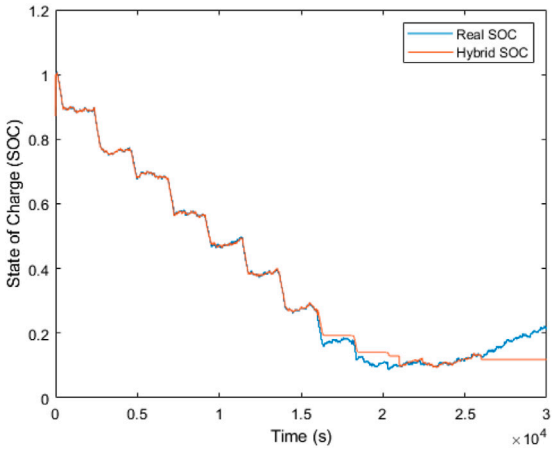

FIGURE 11
Hybrid estimator performance under noisy measurements.

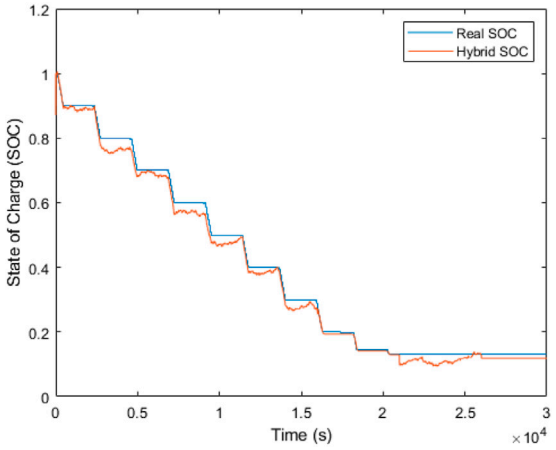

FIGURE 12
Hybrid estimator performance without the noise.

the SOC range of [1, .93]. This shows that the EKF experienced the greatest impact on its behavior compared to the SMO due to the complex disturbance. However, the filtering properties of both estimators are still preserved during the course of estimation.

8.3 Hybrid estimator performance

The hybrid estimator performance is shown in Figures 11, 12 for noise and with no noise additions to measurement inputs, respectively. The hybrid estimation goal in this work is to improve the response of the EKF and provide improved robustness to complex disturbances originating from other battery types. As Table 5 reveals, the improvement goal is met as the hybrid performance is seen to have two (2) decimal places of accuracy compared to the EKF estimation having an accuracy of a single decimal place. Furthermore, the hybrid estimation shows that the convergence starts at the initial SOC of 100% with an impressive error bound of 12.9%. It is observed that starting at time $t = 2.5 \times 10^4$, the hybrid estimator is seen not following the real SOC in Figure 11 due to the non-adaptive filtering addition. However, upon removing the noise, as shown in Figure 12, the hybrid estimator is seen to draw closer to the real SOC from that time onwards.

TABLE 5 Performance metrics of the hybrid estimation performance.

	Hybrid	EKF	SMO
RMSE	.0262	.3826	0
MAE	.0136	.3508	0

The hybrid estimator has also shown the ability to adjust its response to the measurement data on the INR 18650 used as the replica complex disturbance in Figure 13. It can be seen that unlike the EKF and SMO individual poor stability for parameter changes influenced by the chemistry of INR 18650, the hybrid estimator is observed to closely match the real SOC with the starting convergency time at nearly the initial time period, thereby supporting the merit of combining both estimators. Another observation from the result of hybridization is that the SOC estimation range has impressively improved from a range of [1, .93] to an

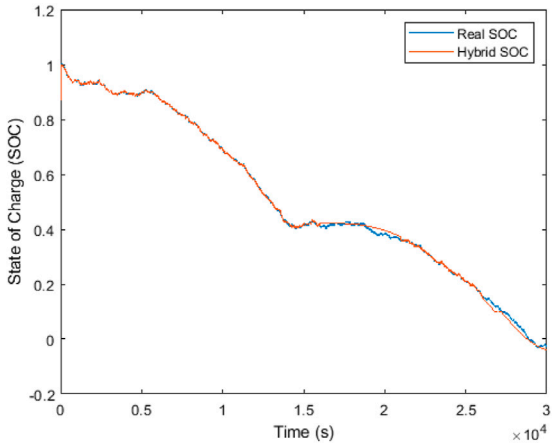

FIGURE 13
Hybrid estimator performance under INR 18650.

estimation range of [1, 0], in spite of the disturbance addition. Varying the tracking gain of the SMO could increase the accuracy further but reduce the SOC estimation range. The hybrid improvement can be explained due to the role the tuning parameters of the EKF have in ensuring faster convergency and noise cancellation, and the role the SMO gains have in ensuring robustness.

9 Conclusion

This paper has demonstrated the use of a first-order equivalent circuit model in the implementation *via* the simulation of the extended Kalman filter (EKF) and sliding mode observer (SMO) for estimating the SOC of multi-cell LiB batteries under discharge measurement data. The response of the individual estimators and their hybridized form has been shown. Following the existing works carried out for the SOC estimation being reviewed, the hybrid method having an MAE value of 1.36 percent is seen to outperform both the onboard SOC estimation technique in Guangzhong et al. (2016) and the improved EKF technique developed in Shichun et al. (2021), having both MAE values of 4 percent and 3 percent, respectively. However, Benedikt et al. (2021) proposed that the work had an accuracy difference of roughly one-quarter compared to that of the hybrid MAE performance. This is because of the addition of a hysteresis element, which accounted for a more accurate battery model than that used in this paper. The traditional method such as the curve fitting-based SOC estimation has shown divergent characteristics (Yujie et al., 2020), especially during the starting phase due to the difficulty in deducing the parameters of suitable fitting functions describing the battery terminal voltage profile, making model identification parameters less accurate in the consequent outputting poor estimation results. Furthermore, the hybrid technique performance is not affected by a variation of the initial state estimates, a challenge commonly used for SOC estimation techniques including the coulomb counting integration method (Ng et al., 2009) we still face.

It is true that various hybrid estimation strategies have been developed in the literature such as by Alfi et al. (2014), where the radial bias neural network was used to obtain the output equation (linearized battery terminal voltage) so as to form a full state equation with the SOC variable in combination with the extended H_{∞} filter, which was used for estimating the SOC. A contrast between the proposed model developed in this paper and similar hybrid works is that this work combines discrete and continuous form representations of the model equations for the EKF and SMO, respectively, in order to improve accuracy. Furthermore, in comparison to the work introduced by Alfi et al. (2014), the accuracy of the estimation carried out in this paper does not depend on large discharge data required for neural network training since the algorithms used here are procedure-based. The estimation accuracy in this work showed that the RMSE using the hybrid neural technique performed better with a negligible error difference of .12 percent. However, matching accuracy between both methods can be achieved by proper tuning of the EKF gain in contrast to the hybrid neural technique, which depends on the trial and error method for selecting a number of hidden neurons and learning rates. With a convergence time of about 1 s, the proposed method surpasses the 4 min time it took for the extended H_{∞} filter to approach the real SOC, giving the former a significant advantage. These faster convergence characteristics can be attributed to accurate modeling of the battery in its non-linear form, as opposed to linearization carried out using the radial bias function.

In summary, the hybridized estimator shows an impressive SOC estimation range, convergence rate, and high matching results *via* the results discussed; these are the properties traditional SOC estimation methods lack. This demonstrates the quality of the hybrid technique in estimating multi-cell lithium-ion batteries and offers more research opportunities in designing estimators that are adaptive to complex disturbances arising from other battery types.

Data availability statement

The raw data supporting the conclusion of this article will be made available by the authors, without undue reservation.

Author contributions

All authors have contributed in designing an estimator that is robust and accurately sufficient to determine the state of charge (SOC) of LiBs in the presence of disturbance signals arising from other battery types.

Acknowledgments

The authors deeply recognize the assistance given by Covenant University in all aspects of this research, especially the payment of the publication charges.

Conflict of interest

The authors declare that the research was conducted in the absence of any commercial or financial relationships that could be construed as a potential conflict of interest.

Publisher's note

References

Adeyemi, K. T., Misra, S., Orovwode, H., and Adoghe, A. J. E. (2022). Modeling the Next Decade of Energy Sustainability: A Case of a Developing Country. *Energies* 15 (14), 5083.

Alfi, A., Charkhgard, M., and Haddad Zarif, M. (2014). Hybrid state of charge estimation for lithium-ion batteries: Design and implementation. *IET Power Electron.* 7 (11), 2758–2764. doi:10.1049/iet-pel.2013.0746

Atayero, A. A., Luka, M. K., and Alatishe, A. A. (2012). Neural-encoded fuzzy models for load balancing in 3GPP LTE. *Int. J. Appl. Inf. Syst.* 4. doi:10.5120/ijais12-450628

Awelewa, A. A., Samuel, I. A., Ademola, A., and Iyiola, S. O. (2013). An undergraduate control tutorial on root locus-based magnetic levitation system stabilization. *Int. J. Eng. Comput. Sci.* 13 (1), 14–22.

Awelewa, A., Omiloli, K., Olajube, A., and Samuel, I. (2021). "Design and optimization of an intelligent fuzzy logic controller for a nonlinear dynamic system," in Proceedings of the 2021 International Conference on Decision Aid Sciences and Application (DASA), Sakheer, Bahrain, December, 2021, 687–694.

Bouchareb, H., Saqli, K., M'sirdi, N. K., Bentaie, M. O., and Naamane, A. (2020). "Sliding mode observer design for battery state of charge estimation," in Proceedings of the 2020 5th International Conference on Renewable Energies for Developing Countries (REDEC), Marrakech, Morocco, June, 2020, 1–5.

Dong, Guangzhong, Wei, Jingwen, and Chen, Zonghai (2016). Kalman filter for onboard state of charge estimation and peak power capability analysis of lithium-ion batteries. *J. Power Sources* 328, 615–626. doi:10.1016/j.jpowsour.2016.08.065

Mohammed, Farag. (2013). *Lithium-ion batteries: Modelling and state of charge estimation.* PhD thesis (Toronto, ON, Canada: University of Toronto).

Ng, K. S., Moo, C. S., Chen, Y. P., and Hsieh, Y. C. (2009). Enhanced coulomb counting method for estimating state-of-charge and state-of-health of lithium-ion batteries. *Appl. energy* 86 (9), 1506–1511. doi:10.1016/j.apenergy.2008.11.021

Orovwode, H. E., Matthew, S., Amuta, E., Agbetuyi, F. A., and Odun-Ayo, I. (2021). Carbon footprint evaluation and environmental sustainability improvement through capacity optimization. *International Journal of Energy Economics and Policy* 11 (3), 454–459.

Peng, S., Chen, C., Shi, H., and Yao, Z. (2017a). State of charge estimation of battery energy storage systems based on adaptive unscented Kalman filter with a noise statistics estimator. *Ieee Access* 5, 13202–13212. doi:10.1109/access.2017.2725301

Peng, Simin, Chen, Chong, Shi, Hongbing, and Yao, Zhilei (2017b). State of charge estimation of battery energy storage systems based on adaptive unscented kalman filter with a noise statistics estimator. *IEEE Access* 5, 13202–13212. doi:10.1109/access.2017.2725301

Rzepka, Benedikt, Simon, Bischof, and Blank, Thomas (2021). Implementing an extended kalman filter for soc estimation of a li-ion battery with hysteresis" A step-by-step guide. *Energies* 14 (13), 3733. doi:10.3390/en14133733

Samuel, I., Soyemi, A., Awelewa, A., and Adekitan, A. (2021). Artificial neural network based load flow analysis for power system networks. *IAENG Int. J. Comput. Sci.* 48 (4).

Sassi, H. B., Errahimi, F., and Najia, E. S. (2020). State of charge estimation by multi-innovation unscented Kalman filter for vehicular applications. *J. Energy Storage* 32, 101978. doi:10.1016/j.est.2020.101978

Shichun, Y., Zhou, S., Hua, Y., Zhou, X., Liu, X., Pan, Y., et al. (2021). A parameter adaptive method for state of charge estimation of lithium-ion batteries with an improved extended Kalman filter. *Sci. Rep.* 11 (1), 1–15.

Surajudeen-Bakinde, N., Faruk, N., Oloyede, A., Abdulkarim, A., Olawoyin, L., Popoola, S., et al. (2021). Effect of membership functions and data size on the performance of ANFIS-based model for predicting path losses in the VHF and UHF bands. *J. Eng. Res.* 10, 203–226. doi:10.36909/jer.10457

Wang, Yujie, Tian, Jiaqiang, Sun, Zhendong, Wang, Li, Xu, Ruilong, Li, Mince, et al. (2020). A comprehensive review of battery modeling and state estimation approaches for advanced battery management systems. *Renew. Sustain. Energy Rev.* 131, 110015. doi:10.1016/j.rser.2020.110015

Xiong, R., Cao, J., Yu, Q., He, H., and Sun, F. (2017). Critical review on the battery state of charge estimation methods for electric vehicles. *Ieee Access* 6, 1832–1843. doi:10.1109/access.2017.2780258

Xu, Y., Hu, M., Zhou, A., Li, Y., Li, S., Fu, C., et al. (2020a). State of charge estimation for lithium-ion batteries based on adaptive dual Kalman filter. *Appl. Math. Model.* 77, 1255–1272. doi:10.1016/j.apm.2019.09.011

Xu, Yidan, Hu, Minghui, Zhou, Anjian, Li, Yunxiao, Li, Shuxian, Fu, Chunyun, et al. (2020b). State of charge estimation for lithium-ion batteries based on adaptive dual kalman filter. *Appl. Math. Model.* 77, 1255–1272. doi:10.1016/j.apm.2019.09.011

Yang, Shichun, Zhou, Sida, Yang, Hua, Zhou, Xinan, Liu, Xinhua, Pan, Yuwei, et al. (2021). A parameter adaptive method for state of charge estimation of lithium-ion batteries with an improved extended kalman filter. *Sci. Rep.* 11 (1), 5805–5815. doi:10.1038/s41598-021-84729-1

Zheng, Wenhui, Xia, Bizhong, Wang, Wei, Lai, Yongzhi, Wang, Mingwang, and Wang, Huawen (2019). State of charge estimation for power lithium-ion battery using a fuzzy logic sliding mode observer. *Energies* 12 (13), 2491. doi:10.3390/en12132491

Zheng, Liu, Yuan, Qiu, Yang, Chunshan, Ji, Jianbo, and Zhao, Zhenhua (2021). A state of charge estimation method for lithium-ion battery using pid compensator-based adaptive extended kalman filter. *Complexity* 2021. doi:10.1155/2021/6665509

frontiers | Frontiers in Energy Research

TYPE Original Research
PUBLISHED 07 February 2023
DOI 10.3389/fenrg.2023.1114512

OPEN ACCESS

EDITED BY
Chuanchang Li,
Changsha University of Science and Technology, China

REVIEWED BY
Solomon Giwa,
Olabisi Onabanjo University, Nigeria
Collins Nwaokocha,
Olabisi Onabanjo University, Nigeria

*CORRESPONDENCE
U. O. Uyor,
UyorUO@tut.ac.za

SPECIALTY SECTION
This article was submitted to Process and Energy Systems Engineering, a section of the journal Frontiers in Energy Research

RECEIVED 02 December 2022
ACCEPTED 27 January 2023
PUBLISHED 07 February 2023

CITATION
Uyor UO, Popoola API and Popoola OM (2023), Flexible dielectric polymer nanocomposites with improved thermal energy management for energy-power applications.
Front. Energy Res. 11:1114512.
doi: 10.3389/fenrg.2023.1114512

Flexible dielectric polymer nanocomposites with improved thermal energy management for energy-power applications

U. O. Uyor[1,2]*, A. P. I. Popoola[1] and O. M. Popoola[2,3]

[1]Department of Chemical, Metallurgical and Materials Engineering, Tshwane University of Technology, Pretoria, South Africa, [2]Center for Energy and Electric Power, Tshwane University of Technology, Pretoria, South Africa, [3]Department of Electrical Engineering, Tshwane University of Technology, Pretoria, South Africa

Most polymer materials are thermal and electrical insulators, which have wide potential in advanced energy-power applications including energy conversion. However, polymers get softened when in contact with heat, which causes their molecular chains to flow as the temperature increases. Although polymer dielectrics exhibit high power density, they face challenges of low energy density which is due to the low dielectric permittivity associated with them. Therefore, this study tried to address the poor thermal energy management and low energy density of poly (vinylidene fluoride) (PVDF) while maintaining its flexible property using low content of hybrid carbon nanotubes (CNTs–0.05wt%, 0.1wt%) and boron nitride (BN–5wt%, 10wt%) nano-reinforcements. The nanocomposites were developed through solvent mixing and hot compression processes. The dielectric constant increased from 9.1 for the pure PVDF to 42.8 with a low loss of about 0.1 at 100 Hz for PVDF-0.1wt%CNTs-10wt%BN. The thermal stability of the nanocomposites was enhanced by 55°C compared to the pure PVDF. The nanocomposites also showed improved melting and crystallization temperatures. The developed PVDF-CNTs-BN nanocomposites showed significant enhancements in thermal energy management, stability, and dielectric properties. The significantly improved properties are credited to the synergetic effects between CNTs and BN in the PVDF matrix in promoting homogeneous dispersion, thermal barrier, interfacial polarization/bonding, insulative and conductive properties. Therefore, the developed nanomaterials in this study can find advanced applications in the energy-power sector owing to their enhanced performances.

KEYWORDS

boron nitride, dielectric properties, thermal stability, PVDF (polyvinyliden fluoride), CNTS (carbon nanotube)

1 Introduction

Polymer materials are constantly developing and appealing issue in a variety of scientific fields, including material engineering, electro-technology, and even biomedical applications. Polymer-based nanocomposites have gained increasing attention due to their improved thermal properties, mechanical flexibility, fatigue reliability, and ease of production. Fluoropolymers such as poly (vinylidene fluoride) (PVDF) has gained attention as dielectric energy storage material in recent years (Wang et al., 2018a; Karaphun et al., 2021; Adaval et al., 2022a; Adaval et al., 2022b). PVDF is widely used as dielectric energy storage because of its good mechanical strength, thermal stability, strong dielectric strength, higher dielectric constant compared to other polymers. Polymer dielectrics possess the advantages of excellent flexibility, high dielectric

breakdown strength and good processability. Due to the desired power density and charging-discharging rate capabilities of dielectric materials (Xihong, 2013), they are commonly used in design of capacitors which convert electrostatic charges and store as electrical energy. They have found wide application in electronics and electric power systems. In comparison to other types of energy storage devices such as batteries, the dielectric capacitor is currently one of the most promising options due to its fast charge/discharge speed and high power density. The dielectric constant, loss and breakdown strength are intrinsic material parameters that describe the dielectric properties of a dielectric substance (Ye et al., 2018).

In addition, thermal conversation/dissipation and thermal stability are also required features of dielectric materials for advanced electric power application. However, polymer dielectric materials get softened when in contact with heat, which causes their molecular chains to flow as the temperature increases due to their poor thermal management (Uyor et al., 2019a). Although polymer dielectrics exhibit high power density, they face challenges of low energy density which is due to the low dielectric permittivity associated with them. However, there have been various efforts by different studies to address these challenges by incorporating large dielectric constant and high thermal property materials into the matrix of various polymer (Wang et al., 2018b; Jiang et al., 2018; Jin et al., 2019). For instance, Zhang et al. (2015) significantly enhanced thermal properties of a PVDF/CNTs by the addition of graphene oxide. Also, Maity et al. (2016) developed percolative polymer-graphene nanocomposites with improved dielectric properties.

Percolative polymer-based nanocomposites through experimental studies have shown characteristic of high dielectric constant materials up to 1×10^6 (Weng et al., 2017). This range of dielectric constant can be used to achieve significantly large energy density that can compete with electrochemical capacitors (Cortes and Phillips, 2015). High dielectric loss, energy dissipation, and poor breakdown strength, however, are the main obstacles preventing this class of polymer nanocomposites from being used in practical applications (Han et al., 2013). This is explained by significant current leakage, free electron mobility, and -orbital electrons. Additionally, pure polymers often have a poor thermal management (Jang et al., 2021), low dielectric constant and energy storage density (Uyor et al., 2019b). It is well known that a polymer film with a low dielectric constant restricts high energy storage capacity (Ye et al., 2019). However, various studies have tried to address these challenges using percolative conductive (such as graphene and carbon nanotubes) and insulative ceramic nanoparticles (Li et al., 2015; Du et al., 2016; Lakshmi et al., 2018). This high volume of ceramic nanoparticles often leads to deterioration of the flexibility and other mechanical properties of such polymer composites with difficulty in processing.

Therefore, utilizing modest concentrations of hybrid carbon nanotubes (CNTs) and boron nitride (BN), this study enhanced the thermal energy management, stability, and dielectric permittivity of PVDF while keeping its flexibility. PVDF is a semi crystalline material with good mechanical property, chemical resistance and ferroelectric properties (Wang et al., 2012). The CNTs is a 1D carbon-based nanomaterials with excellent mechanical, electrical and thermal properties. On the other hand, BN has a good thermal conductivity, insulative property, and breakdown strength. Although it has a low dielectric permittivity, it is preferred for this study due to its proximity in dielectric properties with the polymer to reduce localized electric field accumulation and sudden breakdown on the application of electric field. The generation of micro-capacitors by CNTs and BN in the PVDF matrix was the cause of the increased dielectric permittivity attained in this work. The increased thermal stability was a result of the uniform dispersion and good thermal properties of CNTs and BN, which were aided by the nanoparticles' various dimensional configurations. The fabricated nanocomposites provide the necessary characteristics for advanced dielectric energy-power applications and superior thermal management.

TABLE 1 Nanocomposites preparation concentrations.

S/N	CNTs (wt%)	BN (wt%)	Nanocomposites Denotation
1	0.00	0.00	Pure PVDF
2	0.05	5.00	PVDF-0.05wt%CNTs-5wt%BN
3	0.05	10.00	PVDF-0.05wt%CNTs-10wt%BN
4	0.10	5.00	PVDF-0.1wt%CNTs-5wt%BN
5	0.10	10.00	PVDF-0.1wt%CNTs-10wt%BN

2 Experimental section

2.1 Materials

Poly (vinylidene fluoride) (PVDF) (average molecular weight 534,000, density 1.74 g/mL at 25 C) and N, N-dimethyl formamide (DMF) (assay ≥99%) were purchased from Sigma-Aldrich, South Africa. Hexagonal boron nitride (BN) (assay >99.5%, particles size 100 nm, and density 2.2 g/mL at 25°C) and multi-walled carbon nanotubes (MWCNTs) (purity - >98%, diameter - 10–30 nm, length - 5–20 μm) were sourced from Hongwu International Group, China. All materials were used as received without any modification.

2.2 Nanocomposites fabrication

Solution mixing technique was used to produce the polymer nanocomposites. The various concentrations of CNTs and BN as shown in Table 1 were randomly mixed in beakers containing DMF to exfoliate the nanoparticles. The mixtures were ultrasonicated for 5 h (at high frequency, power of 300 W and temperature of 80°C). PVDF was mixed with DMF for 10 min while being magnetically stirred (at speed of 300 rpm and temperature of 80°C). The pre-dispersed PVDF was then added to the dispersed mixtures of CNTs and BN, which were then homogeneously mixed using stirrer for 3 h. Later, the nanocomposites were cast onto a clean glass plate and dried in an oven until the weights were constant. Using a carver press moulder, the nanocomposites were hot pressed to desired shape and size at temperature of 200°C and pressure of 10 MPa for 10 min. The nanocomposites developed in this study with different amounts of CNTs and BN are denoted as displaced in Table 1. Also, pure PVDF was also fabricated following similar steps as described above for comparison.

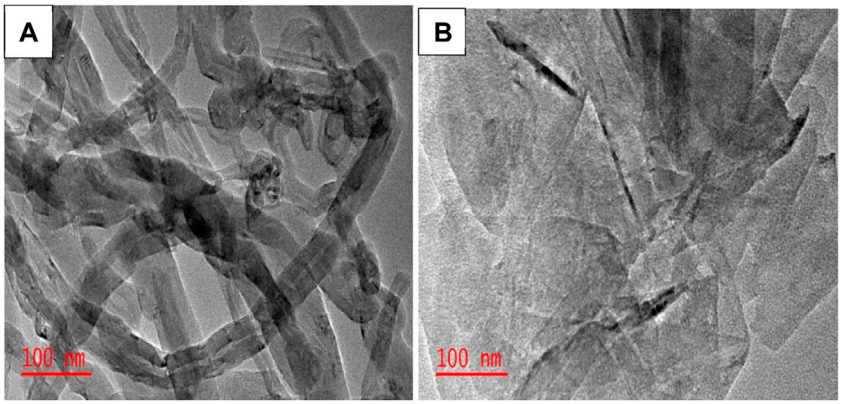

FIGURE 1
TEM micrographs of the **(A)** CNTs and **(B)** BN nanoparticles.

2.3 Nanocomposites characterization

A high-performance Scanning Electron Microscope (SEM) (VEGA 3 TESCAN) operating at accelerated voltage of 20 kV was used to evaluate the dispersion and morphology of the nanocomposites. The Transmission Electron Microscope (TEM) (JEM-2100) was used to examine the structures of the CNTs and BN at acceleration voltage 200 kV and beam current of 110 μA. X'pert PRO PANalytical diffractometer at 30 kV and 40 mA was used to study the diffraction patterns of the nanoparticles and nanocomposite materials. Utilizing a differential scanning calorimeter (DSC Q2000 with accuracy of ± 0.01°C), the melting and crystallization properties of the nanocomposites were studied in a nitrogen-filled atmosphere at a 10 C/min heating and cooling rate. The thermal stability of the nanocomposites was obtained using Thermogravimetry Analyzer (TGA) (TA instrument Q500 with accuracy of ± 1°C) at a heating rate of 10 C/min in a nitrogen environment. Capacitance and resistance of the nanocomposites were measured using an LCR meter (B&K 891 with accuracy of ± 0.05%) through a frequency range of 100 Hz to 10 kHz, from which the electrical conductivity, dielectric constant and loss of the nanocomposites were obtained. To prevent contact resistance, the nanocomposites films were coated with silver paste. By utilizing a high voltage transformer (Conelectric BS 3941 with accuracy of ± 1 V) at an applied rate of 50 V/min until failure, the dielectric breakdown strength of the nanocomposites was measured.

3 Results and discussion

3.1 Microstructural analysis

The microstructures of the CNTs and BN were examined using TEM as displayed in Figure 1. The CNTs has long in-plane dimension (Figure 1A), while the BN shows few stackings of nanoparticles' layers (Figure 1B). Interpenetration of CNTs and BN results in 3D dense network configurations in the polymer matrix since they are respectively 1D and 2D structural nanomaterials (Schmidt et al., 2002; Yu et al., 2016). Such 3D structures facilitate the enhancement of i) dielectric constant *via* micro-capacitors formation and ii) thermal properties *via* formation of conductive network structures. The presence of the plate-like structure of the insulative BN nanoparticles led to the reduction of the conductive network structures formation in the polymer matrix. The combination of different conductive and insulative nanoparticles enhances dielectric properties through formation of micro-capacitors in the polymer matrix. In addition, their different dimensional structures assisted each other in promoting dispersion in the polymer matrix. Both nanoparticles have good synergy and compatibility with each other since they are uniformly distributed in the polymer matrix as presented by the SEM micrographs in Figure 2.

Morphological structures of the developed PVDF-CNTs-BN nanocomposites are shown in Figure 2. Addition of foreign bodies in a polymer matrix often changes its microstructure and gives it new properties. This was noted in this study when CNTs and BN were incorporated into the PVDF matrix as compared to its pure state (Figure 2A). The morphologies of PVDF-CNTs-BN nanocomposites revealed good interaction and dispersion of the nanoparticles. All the nanocomposites showed dense microstructure due to the presence of the BN nanoparticles as displayed in Figures 2B–E. However, PVDF-0.1wt%CNTs-5wt%BN showed some visible CNTs due to the increase in content of CNTs from 0.05wt% to 0.1wt% with only 5wt% BN (Figure 2D). This can also be attributed to the high driving force in bringing the CNTs together at high content. In general, good dispersion of the CNTs and BN in the PVDF matrix was achieved. None of the nanocomposites generally displayed substantial microcracking or debonding of the nanoparticles from the matrix, indicating good compatibility with their constituents. The different dimensional structures of CNTs (1D) and BN (2D) assist each other in obtaining uniform dispersion in the PVDF matrix (Min et al., 2018). Where BN may have minimized the wall-to-wall interactions of CNTs and CNTs minimized the layers-layers interactions of BN nanoparticles. Although CNTs has high tendency of showing agglomeration in the polymer matrix due to its entanglement nature (see Figure 1A) and BN may show difficulty to intercalate with polymer molecular chain due to its layered structure, this was supressed by using them at relative low quantities as shown with SEM micrographs in Figure 2.

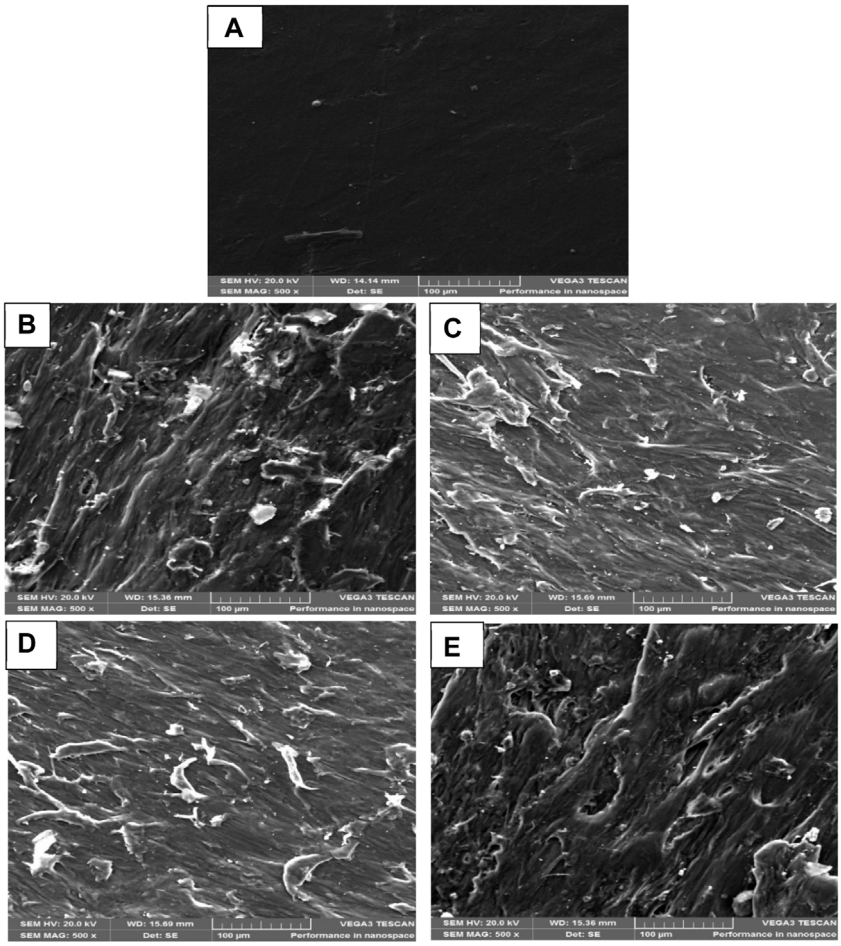

FIGURE 2
SEM Micrographs of the **(A)** pure PVDF **(B)** PVDF-0.05wt%CNTs-5wt%BN **(C)** PVDF-0.05wt%CNTs-10wt%BN **(D)** PVDF-0.1wt%CNTs-5wt%BN and **(E)** PVDF-0.1wt%CNTs-10wt%BN nanocomposites.

3.2 XRD analysis

This study further examined the crystal phases of the CNTs and BN using XRD after employing TEM analysis in determining their structural dimensions. The CNTs and BN have similar diffraction patterns as shown in Figure 3A, since they are both hexagonally organized nanoparticles. They typically have significant diffraction peaks at $2\theta = 26.4^{\circ}$ and 44.3°, which correspond to the crystal planes of (002) and (100), indicating graphitic crystal plane (Ouyang et al., 2014) and hexagonal BN (Ansaloni and de Sousa, 2013; Huang et al., 2013) respectively. While the diffraction peak at $2\theta = 54.5^{\circ}$ with crystal plane of (004) suggests a limited number of CNTs walls and BN stacking layers. The nanocomposites' XRD diffraction patterns were also examined as shown in Figure 3B. PVDF showed strong - phase intensity at $2\theta = 17.5^{\circ}$, 19.1°, 26.4° and a broad peak at $2\theta = 38^{\circ}$, corresponding to crystal plane of (100) (020) (021) and (040) respectively. The PVDF matrix showed predomination of α-phase. However, the broad peak significantly decreased upon inclusion of the CNTs and BN nanoparticles into the PVDF matrix. This can be attributed to the good interfacial bond and interaction between the PVDF and the nanoparticles. Comparing the diffraction patterns of the pure PVDF and the nanocomposites, no new diffraction peak was found. This indicates absence of new phase formation, but the phases predominated by the PVDF matrix. The reduction in the broad peak of the nanocomposites indicates increase in crystalline phase, which is caused by the addition of the nanoparticle. This indicates reduction in the amorphous phase of the PVDF with the addition of the CNTs and BN, which is vital for improvement of dielectric and piezoelectric properties (Fan et al., 2012).

3.3 DSC properties and thermal stability

The melting (T_m) and crystallization (T_c) Temperature of the nanocomposites from the DSC results are represented in Figure 4. The figure shows that all the nanocomposites required higher thermal energy to be melted compared to the pure PVDF. The larger T_m of the nanocomposites is an indicative of higher energy required in thermal breaking of the bonds between the PVDF matrix and the nanoparticles (He et al., 2014). This is due to the good interfacial interaction between the matrix and CNTs-BN, which gave the nanocomposites higher T_m. Therefore, T_m in the range of 160.73°C for the pure PVDF to optimal of about 169.6°C for PVDF-0.05wt%CNTs-10wt%BN were obtained

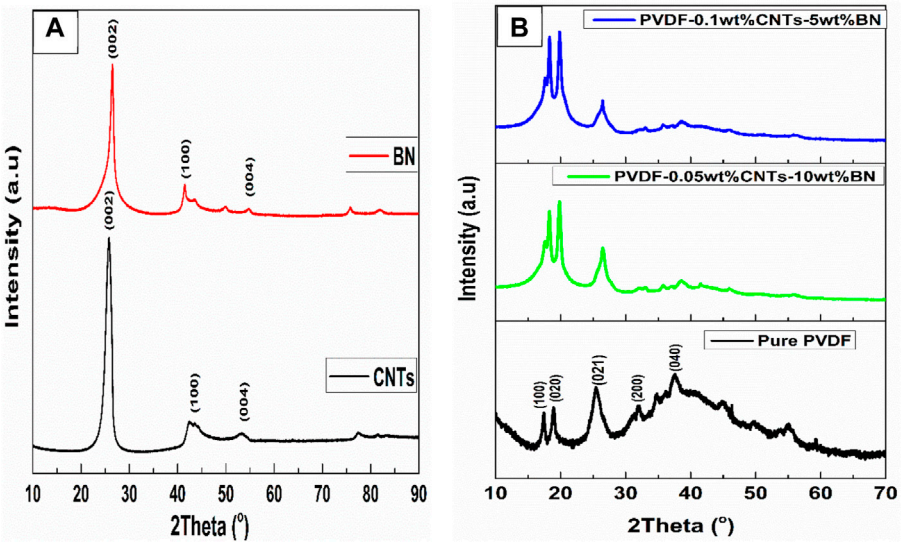

FIGURE 3
XRD diffraction patterns of the **(A)** nanoparticles and **(B)** nanocomposites.

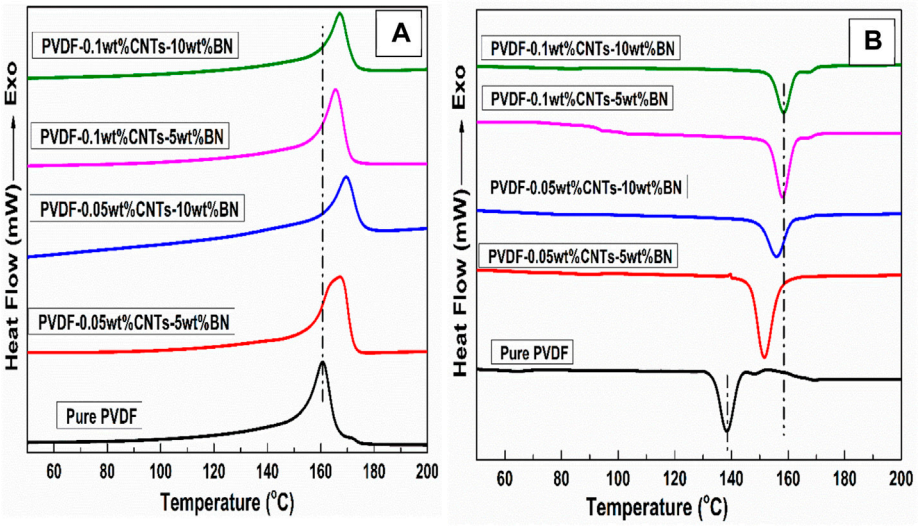

FIGURE 4
(A) Melting and **(B)** crystallization temperature of the nanocomposites.

as displayed in Figure 4A, which is about 8.87°C increase. Since there was no decrease in the T_m of the nanocomposites relative to the pure PVDF, the nanocomposites have no significant formation of small bundles or aggregate by the nanoparticles in the PVDF matrix which could have results to decrease in the T_m (Li et al., 2017). Also, all the nanocomposites had higher T_c compared to the pure PVDF. The T_c increased from 138.34°C for the pure PVDF to the range of 151.59°C–158.49°C depending on the nanocomposites as presented Figure 4B. This shows that crystallization of the nanocomposites started at higher temperature when compared with the pure PVDF due to the presence of the CNTs-BN which promoted heterogeneous nucleation. Although the introduction of CNTs-BN nanoparticles into the PVDF matrix increased its T_m more than its T_c, this indicates the effect of undercooling for crystallization to take place.

The degree of the undercooling ($\triangle T$) and percentage crystallinity (X_c) of the nanocomposites are presented in Table 2. Due to the heterogenous nucleation of the nanocomposites and increase in T_c, the $\triangle T$ is lower for all the nanocomposites compared to the pure PVDF. According to Li et al. (2017), the reduction in the $\triangle T$ is an indication of narrow distribution of crystallite size in the nanocomposites, while the pure polymer could have wide distribution of the crystallite size. This often results to lower driving energy for crystallization of the polymer matrix with addition of nanoparticles (Thomas and Zaikov, 2008; Jun et al., 2018), which is the major reason for the start of

TABLE 2 DSC properties of the nanocomposites.

Samples	Melting temperature T_m (°C)	Crystallization temperature T_c (°C)	Undercooling △T (T_m-T_c)	Percentage crystallinity X_c (%)
Pure PVDF	160.73	138.34	22.39	35.00
PVDF-0.05wt%CNTs-5wt %BN	167.19	151.59	15.60	36.77
PVDF-0.05wt%CNTs-10wt %BN	169.60	155.95	13.65	37.05
PVDF-0.1wt%CNTs-5wt %BN	165.55	158.03	7.52	36.86
PVDF-0.1wt%CNTs-10wt %BN	167.24	158.49	8.75	39.24

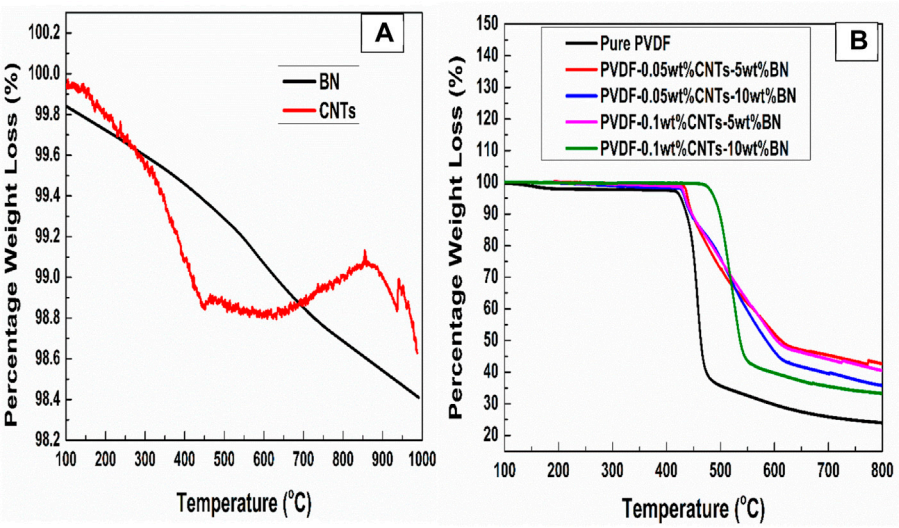

FIGURE 5
TGA curves of the **(A)** nanoparticles and **(B)** nanocomposites.

crystallization at higher temperature compared to the pure PVDF. This study recorded decreased in the △T from 22.39°C for the pure PVDF to the range of 15.60°C–7.52°C for various nanocomposites as depicted in Table 2. Although, the addition of CNTs and BN in the PVDF matrix could impede the regional growth of polymer chains (Mertens and Senthilvelan, 2018), the formation of many nucleation sites in the liquid matrix results to enhance crystalline phase and increase in X_c. Therefore, in this study, X_c increased from 35% for the pure PVDF to optimal of 39.24% for PVDF-0.05wt%CNTs-10wt%BN. Similar observation of the increment of X_c relative to that of pure polymer have been previously reported (Miltner et al., 2008; Kazemi et al., 2017).

The TGA curves of the BN and CNTs nanoparticles is presented in Figure 5A. The BN exhibits excellent thermal stability with only about 1.3 wt% loss up to 900°C. Other studies have also shown that up to that temperature range, BN has relatively little weight loss (Sudeep et al., 2015; Wu et al., 2019). On the other hand, CNTs typically have great thermal stability (Trakakis et al., 2013). In this study, CNTs also demonstrated its high thermal stability and good thermal resistance to disintegration. The thermal decomposition of the CNTs began around 88.3°C, which is attributed to the material's loss of water. The CNTs having oxygen functional groups demonstrated pyrolytic breakdown at 450°C with a weight loss of roughly 1.2 wt%. It only lost about 1 wt% of its weight at 900°C, which shows very excellent thermal stability. The thermal stability of the nanocomposites is represented in Figure 5B, which shows that all the nanocomposites moved to the high temperature compared to the pure PVDF. This was because of the larger amount of energy needed to break the interfacial bonds between the matrix and nanoparticles and cause the PVDF chains degrade (He et al., 2014).

The pure PVDF showed first thermal decomposition around 150°C and second major decomposition around 420°C. The nanocomposites showed major thermal decomposition above 440°C with optimal of about 475°C for PVDF-0.1wt%CNTs-10wt %BN nanocomposite, which is about 55°C increase in thermal stability. This implies that the degradation of the PVDF molecular chains at lower applied thermal energy was prevented by the CNTs and BN in the matrix. Hence, more thermal energy was absorbed by the nanocomposites before degradation. The pure PVDF also showed sharper slope of thermal decomposition

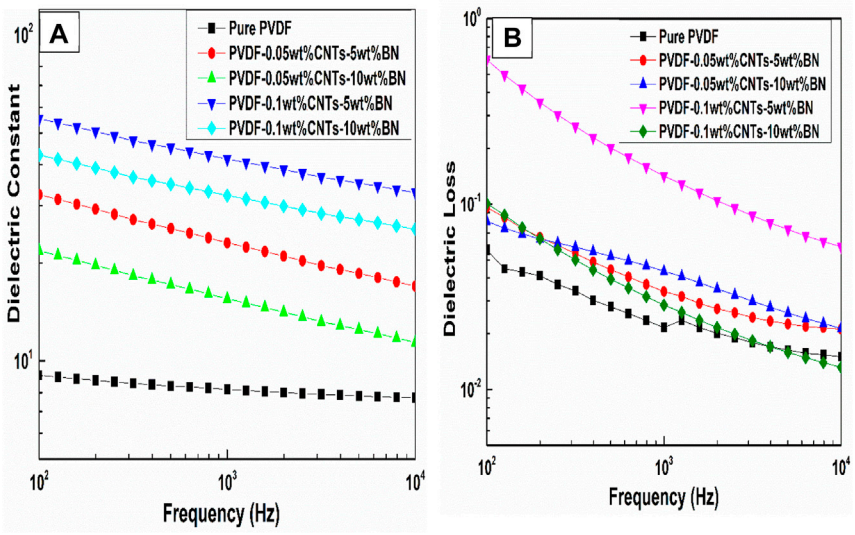

FIGURE 6
(A) Dielectric constant and **(B)** dielectric loss of the nanocomposites.

relative to the nanocomposites except the PVDF-0.1wt%CNTs-10wt%BN. Although this nanocomposite formulation shows higher starting of major thermal decomposition, it also revealed fast decomposition slope. This can be attributed to the higher content of the reinforcing phase compared to the other nanocomposites, which could have led to little formation of aggregates in the PVDF matrix. However, the general enhancement in thermal stability of the of nanocomposites can be credited to the good dispersion and interaction between the polymer matrix and the reinforcement phases as represented by the SEM micrograph in Figure 3 (Li et al., 2017). Since the BN and CNTs nanoparticles have good thermal stability as shown in Figure 5A, they offered thermal barriers in the matrix of the polymer, which slowed down the degradation of the nanocomposites (Nurul and Mariatti, 2013). In addition, the CNTs and BN have good capability of mechanically interlocking of the PVDF chains and restrict the flow of the chains on the application of heat, leading to improved thermal stability of the nanocomposites (Chu et al., 2012).

3.4 Dielectric constant and loss

The dielectric constant (ε^{I}) and dielectric loss (ε^{II}) of the nanocomposites are shown in Figure 6. A polymer matrix's characteristics such as dielectric properties are often modified by changing the microstructure of the matrix using reinforcement phase(s). The developed nanocomposites in this study showed significant rise in the ε^{I} due to the conductive nature of CNTs. As a result, when CNTs enter a polymer matrix, it significantly increases the ε^{I} of that polymer close to the percolative threshold (Ameli et al., 2013). On the other hand, various studies have also used BN to enhance the ε^{I} of polymeric materials (Wu et al., 2019; Zou et al., 2019). However, compared to CNTs, the ε^{I} enhancing potential of BN is often lesser due to its lower aspect ratio and insulative nature. To considerably improve the ε^{I} of the polymer in which such ceramic particles are incorporated, they need a high proportion (over 40 vol%) (Yoon et al., 2009), which has negative effect on mechanical properties of such polymer composites such as poor strength and flexibility. Hence, addition of small amount of conductive CNTs into the PVDF-BN system significantly improved the ε^{I} of the nanocomposites at a low fraction of BN.

For instance, ε^{I} at 100 Hz increased from about 9.1 for the pure PVDF to the range of 21.8 for PVDF-0.05wt%CNTs-10wt%BN and optimal of 55.4 for PVDF-0.1wt%CNTs-5wt%BN as shown in Figure 6A. This is a large range of improvement with the optimal of about 508.8% increase compared to the pure PVDF. There have been several theories linking the development of micro-capacitors in the polymer matrix to such increase in ε^{I} of the nanocomposites (Fan et al., 2012; Chu et al., 2013). This type of micro-capacitor is created in the polymer matrix by separating adjacent fillers with thin polymer layers to create sandwich structures that consist of conductor - insulator - conductor. Therefore, in the polymer matrix, several of these micro-capacitors can be created when the CNTs content increases with a larger increase in ε^{I}. This is most likely the cause of the high ε^{I} of the PVDF-0.1wt%CNTs-5wt%BN nanocomposite compared to others as the content of CNTs increase from 0.05wt% to 0.1wt% and BN decreased from 10wt% to 5wt%. At all the tested frequency range, the developed nanocomposites revealed higher ε^{I} than the pure PVDF. However, all the nanocomposites exhibited greater frequency dependence than the pure PVDF. This is because of the PVDF matrix and the nanoparticles having different polarization effects and dipole relaxation while achieving equilibrium at high frequency (Alhusaiki-Alghamdi, 2017).

The ε^{II} of the nanocomposites is shown Figure 6B, which reveals that the addition of the CNTs and BN to the polymer matrix caused an increase in the ε^{II}. However, the ε^{II} of the nanocomposites is relatively low (less than 1 for all the developed nanocomposites). For instance, the ε^{II} of about 0.06 was recorded for the pure PVDF, while 0.09, 0.08 and 0.1 at 100 Hz were measured for PVDF-0.05wt%CNTs-5wt%

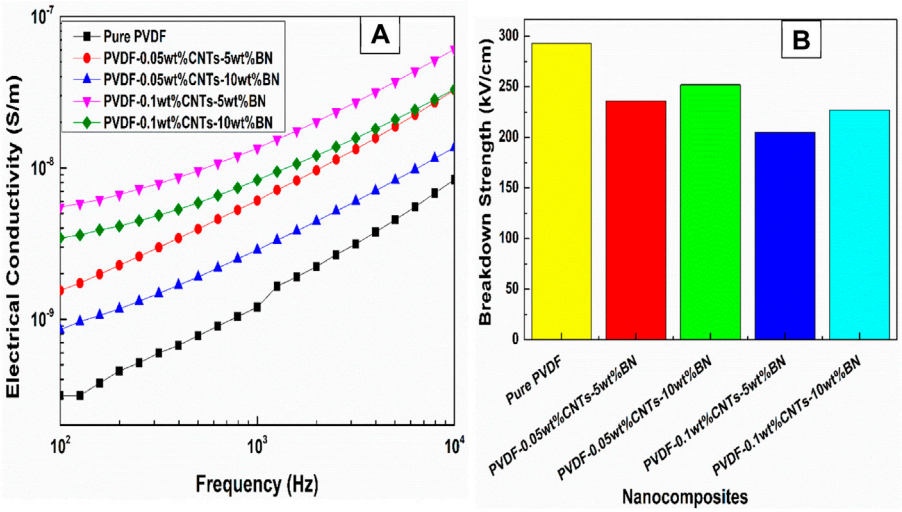

FIGURE 7
(A) Electrical conductivity and **(B)** breakdown strength of the nanocomposites.

BN, PVDF-0.05wt%CNTs-10wt%BN and PVDF-0.1wt%CNTs-10wt %BN respectively. The low ε^{II} of the nanocomposites can be credited to the incorporation of the insulation BN nanoparticles in the polymer matrix. This reduced the current leakage, fast mobility of charge carriers, trapping of charges at the interface of CNTs-BN, minimizing the migration of charge carriers from one CNTs to another, reduction of direct contact of CNTs, low formation conductive networks and increase in insulative barrier by the presence of BN in the PVDF matrix (Wan et al., 2017; Lakshmi et al., 2018). Among all the nanocomposites developed in this study, the ε^{II} was more pronounced for the PVDF-0.1wt%CNTs-5wt%BN nanocomposite due the higher conductive CNTs and low insulative BN content. This indicates that there was more interconnection among CNTs and 5wt% BN could not provide optimal insulative barrier for the 0.1wt% CNTs content. However, the ε^{II} of the developed nanocomposites is still relatively low, which can also be attributed to the use of the conductive CNTs at low concentration and the presence of BN. Hence, the nanocomposites exhibit improved ε^{I} and low ε^{II}, which indicate their energy storage and loss capabilities respectively. In general, while CNTs enhanced the energy storage capacity of PVDF, the BN lowered the energy loss capacity of the nanocomposites.

3.5 Electrical conductivity and breakdown strength

The measured electrical conductivity σ) of the nanocomposites is presented in Figure 7A. The addition of CNTs into polymer matrix often formed conductive network structures *via* interconnection of the nanoparticles (Szentes et al., 2012). This facilitates the movement of free electrons from one nanoparticle to another with significant increase in the σ. Once percolative threshold of such nanocomposites is reached, they show significant increase in the σ (Panwar et al., 2007; Deepa et al., 2013). In this study, it was observed that CNTs and BN in the PVDF matrix slight increased the σ of the nanocomposites to approximately one-fold compared to the pure PVDF. This can be credited to the good insulative property of BN, which relatively maintained the low σ of the PVDF that is required for dielectric materials. As stated earlier the BN minimized direct contact of CNTs, reduced formation of conductive network configurations and provided insulative barriers on the surfaces of the CNTs in the PVDF matrix. Hence, it is believed that the main contribution to the little increase in the σ of the nanocomposites is non-ohmic conduction (where charge carriers migrate from one CNTs to another through bulk insulative barrier). Therefore, increase in the σ from about 3.13×10^{-10} S/m for the pure PVDF to the range of 8.5×10^{-10} S/m to 5.5×10^{-9} S/m at 100 Hz for the nanocomposites were measured as shown in Figure 7A. The σ increased with increasing frequency due to the development of conductive grain boundaries at high frequency (Elashmawi et al., 2017). The dielectric breakdown strength (E_b) of the nanocomposites, which slight decreased with addition of CNTs and BN compared to the pure PVDF is shown in Figure 7B. This was expected since the CNTs is a conductive nanoparticles capable of forming conductive network structures in the matrix with increase in the flow of charge carriers. Although the presence of BN could supressed this effect, foreign bodies in a polymer matrix often lead to electric field distortion and enhancement with reduction in the E_b (Xiao and Du, 2016). In addition, due to the difference in surface energy and ε^{I} between the PVDF matrix and the nanoparticles, there is large chances of localized electric field accumulation and reduction in the E_b on the application of electric field (Huang et al., 2011). However, the reduction in E_b of the nanocomposites relative to the pure PVDF is small, which indicates that the nanocomposites maintained appreciably the good E_b of the PVDF. For instance, the E_b only reduced from 293 kV/cm for the pure PVDF to the range of 252 kV/cm for PVDF-0.05wt%CNTs-10wt%BN. The nanocomposites containing 0.1wt% CNTs and 5wt% BN has the lowest E_b of about 205 kV/cm as shown in Figure 7B.

4 Conclusion

Polymer nanocomposites reinforced with CNTs and BN were developed and characterized in this study. SEM analysis of the nanocomposites showed that the nanoparticles were homogeneously dispersed in the polymer matrix, which contributed to the enhanced properties. It was noted that the addition of the CNTs and BN in the PVDF matrix improved its T_m and T_c, indicating enhancement in thermal properties. This was attributed to the high thermal energy required to decompose the bond between the polymer matrix and the nanoparticles. The calculated X_c of the nanocomposites showed that the CNTs and BN could improve the X_c of the PVDF matrix due to the increase in their T_c resulting from heterogeneous nucleation. The TGA analysis revealed that the decomposition temperature of the nanocomposites shifted to the higher temperature compared to the pure PVDF. About 55°C increase in the thermal stability was achieved. The residual materials at the elevated temperature were higher for the nanocomposites compared to the pure PVDF. The developed PVDF-CNTs-BN nanocomposites showed increased ε^{l} of about 508.8 when related to the pure PVDF. The nanocomposites showed low ε^{ll} and appreciable E_b, which were close to that of the pure PVDF. The developed polymer dielectric nanocomposites exhibit good potentials for energy-power application.

Data availability statement

The original contributions presented in the study are included in the article/supplementary material, further inquiries can be directed to the corresponding author.

Author contributions

UU: Conceptualization, Methodology, Investigation, Formal analysis and Writing Original Draft AP: Supervision, Funding Acquisition, Review, Editing and Validation and Methodology OP: Supervision, Funding Acquisition and Resources and Project Administration.

Acknowledgments

We appreciate the Faculty of Engineering and the Built Environment and the Centre for Energy and Electric Power, Tshwane University of Technology, South Africa for their supports.

Conflict of interest

The authors declare that the research was conducted in the absence of any commercial or financial relationships that could be construed as a potential conflict of interest.

Publisher's note

All claims expressed in this article are solely those of the authors and do not necessarily represent those of their affiliated organizations, or those of the publisher, the editors and the reviewers. Any product that may be evaluated in this article, or claim that may be made by its manufacturer, is not guaranteed or endorsed by the publisher.

References

Adaval, A., Chinya, I., Bhatt, B. B., Kumar, S., Gupta, D., Samajdar, I., et al. (2022). Poly (vinylidene fluoride)/graphene oxide nanocomposites for piezoelectric applications: Processing, structure, dielectric and ferroelectric properties. *Nano-Structures Nano-Objects* 31, 100899. doi:10.1016/j.nanoso.2022.100899

Adaval, A., Subash, C., Shafeeq, V., Aslam, M., Turney, T. W., Simon, G. P., et al. (2022). A comprehensive investigation on the influence of processing techniques on the morphology, structure, dielectric and piezoelectric properties of poly (vinylidene fluoride)/Graphene oxide nanocomposites. *Polymer* 256, 125239. doi:10.1016/j.polymer.2022.125239

Alhusaiki-Alghamdi, H. M. (2017). Thermal and electrical properties of graphene incorporated into polyvinylidene fluoride/polymethyl methacrylate nanocomposites. *Polym. Compos.* 38, E246–E253. doi:10.1002/pc.23997

Ameli, A., Jung, P., and Park, C. (2013). Electrical properties and electromagnetic interference shielding effectiveness of polypropylene/carbon fiber composite foams. *Carbon* 60, 379–391. doi:10.1016/j.carbon.2013.04.050

Ansaloni, L. M. S., and de Sousa, E. M. B. (2013). Boron nitride nanostructured: Synthesis, characterization and potential use in cosmetics. *Mater. Sci. Appl.* 4 (1), 22–28. doi:10.4236/msa.2013.41004

Chu, C-C., White, K. L., Liu, P., Zhang, X., and Sue, H-J. (2012). Electrical conductivity and thermal stability of polypropylene containing well-dispersed multi-walled carbon nanotubes disentangled with exfoliated nanoplatelets. *Carbon* 50 (12), 4711–4721. doi:10.1016/j.carbon.2012.05.063

Chu, L., Xue, Q., Sun, J., Xia, F., Xing, W., Xia, D., et al. (2013). Porous graphene sandwich/poly(vinylidene fluoride) composites with high dielectric properties. *Compos. Sci. Technol.* 86, 70–75. doi:10.1016/j.compscitech.2013.07.001

Cortes, F. J. Q., and Phillips, J. (2015). Tube-super dielectric materials: Electrostatic capacitors with energy density greater than 200 J.cm(-3). *Mater. (Basel)* 8 (9), 6208–6227. doi:10.3390/ma8095301

Deepa, K. S., Gopika, M. S., and James, J. (2013). Influence of matrix conductivity and coulomb blockade effect on the percolation threshold of insulator–conductor composites. *Compos. Sci. Technol.* 78, 18–23. doi:10.1016/j.compscitech.2013.01.012

Du, M., Wang, W., Chen, L., Xu, Z., Fu, H., and Ma, M. (2016). Enhancing dielectric properties of poly(vinylidene fluoride)-based hybrid nanocomposites by synergic employment of hydroxylated BaTiO3and silanized graphene. *Polymer-Plastics Technol. Eng.* 55 (15), 1595–1603. doi:10.1080/03602559.2016.1163595

Elashmawi, I. S., Alatawi, N. S., and Elsayed, N. H. (2017). Preparation and characterization of polymer nanocomposites based on PVDF/PVC doped with graphene nanoparticles. *Results Phys.* 7, 636–640. doi:10.1016/j.rinp.2017.01.022

Fan, P., Wang, L., Yang, J., Chen, F., and Zhong, M. (2012). Graphene/poly(vinylidene fluoride) composites with high dielectric constant and low percolation threshold. *Nanotechnology* 23 (36), 365702–365708. doi:10.1088/0957-4484/23/36/365702

Han, K., Li, Q., Chen, Z., Gadinski, M. R., Dong, L., Xiong, C., et al. (2013). Suppression of energy dissipation and enhancement of breakdown strength in ferroelectric polymer–graphene percolative composites. *J. Mater. Chem. C* 1 (42), 7034–7042. doi:10.1039/c3tc31556h

He, Q., Yuan, T., Yan, X., Ding, D., Wang, Q., Luo, Z., et al. (2014). Flame-retardant polypropylene/multiwall carbon nanotube nanocomposites: Effects of surface functionalization and surfactant molecular weight. *Macromol. Chem. Phys.* 215 (4), 327–340. doi:10.1002/macp.201300608

Huang, C., Chen, C., Ye, X., Ye, W., Hu, J., Xu, C., et al. (2013). Stable colloidal boron nitride nanosheet dispersion and its potential application in catalysis. *J. Mater. Chem. A* 1 (39), 12192–12197. doi:10.1039/c3ta12231j

Huang, X., Jiang, P., and Tanaka, T. (2011). A review of dielectric polymer composites with high thermal conductivity. *IEEE Electr. Insul. Mag.* 27 (4), 8–16. doi:10.1109/mei.2011.5954064

Jang, J-U., Lee, S. H., Kim, J., Kim, S. Y., and Kim, S. H. (2021). Nano-bridge effect on thermal conductivity of hybrid polymer composites incorporating 1D and 2D nanocarbon fillers. *Compos. Part B Eng.* 222, 109072. doi:10.1016/j.compositesb.2021.109072

Jiang, Y., Shi, X., Feng, Y., Li, S., Zhou, X., and Xie, X. (2018). Enhanced thermal conductivity and ideal dielectric properties of epoxy composites containing polymer modified hexagonal boron nitride. *Compos. Part A Appl. Sci. Manuf.* 107, 657–664. doi:10.1016/j.compositesa.2018.02.016

Jin, X., Wang, J., Dai, L., Wang, W., and Wu, H. (2019). Largely enhanced thermal conductive, dielectric, mechanical and anti-dripping performance in polycarbonate/boron nitride composites with graphene nanoplatelet and carbon nanotube. *Compos. Sci. Technol.* 184, 107862. doi:10.1016/j.compscitech.2019.107862

Jun, Y-S., Um, J. G., Jiang, G., Lui, G., and Yu, A. (2018). Ultra-large sized graphene nano-platelets (GnPs) incorporated polypropylene (PP)/GnPs composites engineered by melt compounding and its thermal, mechanical, and electrical properties. *Compos. Part B Eng.* 133, 218–225. doi:10.1016/j.compositesb.2017.09.028

Karaphun, A., Tuichai, W., Chanlek, N., Sriwong, C., and Ruttanapun, C. (2021). Dielectric and electrochemical properties of hybrid Pt nanoparticles deposited on reduced graphene oxide nanoparticles/poly (vinylidene fluoride) nanocomposites. *Mater. Today Commun.* 27, 102232. doi:10.1016/j.mtcomm.2021.102232

Kazemi, Y., Kakroodi, A. R., Wang, S., Ameli, A., Filleter, T., Pötschke, P., et al. (2017). Conductive network formation and destruction in polypropylene/carbon nanotube composites via crystal control using supercritical carbon dioxide. *Polymer* 129, 179–188. doi:10.1016/j.polymer.2017.09.056

Lakshmi, N., Tambe, P., and Sahu, N. K. (2018). Giant permittivity of three phase polymer nanocomposites obtained by modifying hybrid nanofillers with polyvinylpyrrolidone. *Compos. Interfaces* 25 (1), 47–67. doi:10.1080/09276440.2017.1338876

Li, C-Q., Zha, J-W., Long, H-Q., Wang, S-J., Zhang, D-L., and Dang, Z-M. (2017). Mechanical and dielectric properties of graphene incorporated polypropylene nanocomposites using polypropylene-graft-maleic anhydride as a compatibilizer. *Compos. Sci. Technol.* 153, 111–118. doi:10.1016/j.compscitech.2017.10.015

Li, Y., Yang, W., Gao, X., Sun, R., and Wong, C-P. (2015). "Dielectric properties of CVD graphene/$BaTiO_3$/polyvinylidene fluoride nanocomposites fabricated through powder metallurgy," in *16th international conference on electronic packaging technology*. Paper presented at the 2015.

Maity, N., Mandal, A., and Nandi, A. K. (2016). Hierarchical nanostructured polyaniline functionalized graphene/poly(vinylidene fluoride) composites for improved dielectric performances. *Polymer* 103, 83–97. doi:10.1016/j.polymer.2016.09.048

Mertens, A. J., and Senthilvelan, S. (2018). Mechanical and tribological properties of carbon nanotube reinforced polypropylene composites. *J. Mater. Des. Appl.* 232 (8), 669–680. doi:10.1177/1464420716642620

Miltner, H. E., Grossiord, N., Lu, K., Loos, J., Koning, C. E., and Van Mele, B. (2008). Isotactic polypropylene/carbon nanotube composites prepared by latex technology. Thermal analysis of carbon nanotube-induced nucleation. *Macromolecules* 41 (15), 5753–5762. doi:10.1021/ma800643j

Min, C., Liu, D., Shen, C., Zhang, Q., Song, H., Li, S., et al. (2018). Unique synergistic effects of graphene oxide and carbon nanotube hybrids on the tribological properties of polyimide nanocomposites. *Tribol. Int.* 117, 217–224. doi:10.1016/j.triboint.2017.09.006

Nurul, M., and Mariatti, M. (2013). Effect of thermal conductive fillers on the properties of polypropylene composites. *J. Thermoplast. Compos. Mater.* 26 (5), 627–639. doi:10.1177/0892705711427345

Ouyang, W., Zeng, D., Yu, X., Xie, F., Zhang, W., Chen, J., et al. (2014). Exploring the active sites of nitrogen-doped graphene as catalysts for the oxygen reduction reaction. *Int. J. hydrogen energy* 39 (28), 15996–16005. doi:10.1016/j.ijhydene.2014.01.045

Panwar, V., Sachdev, V. K., and Mehra, R. M. (2007). Insulator conductor transition in low-density polyethylene–graphite composites. *Eur. Polym. J.* 43 (2), 573–585. doi:10.1016/j.eurpolymj.2006.11.017

Schmidt, D., Shah, D., and Giannelis, E. P. (2002). New advances in polymer/layered silicate nanocomposites. *Curr. Opin. Solid State Mater. Sci.* 6 (3), 205–212. doi:10.1016/s1359-0286(02)00049-9

Sudeep, P. M., Vinod, S., Ozden, S., Sruthi, R., Kukovecz, A., Konya, Z., et al. (2015). Functionalized boron nitride porous solids. *RSC Adv.* 5 (114), 93964–93968. doi:10.1039/c5ra19091f

Szentes, A., Varga, C., Horvath, G., Bartha, L., Kónya, Z., Haspel, H., et al. (2012). Electrical resistivity and thermal properties of compatibilized multi-walled carbon nanotube/polypropylene composites. *Express Polym. Lett.* 6 (6), 494–502. doi:10.3144/expresspolymlett.2012.52

Thomas, S., and Zaikov, G. E. (2008). *Polymer nanocomposite research advances*. New York, USA: Nova Science Publishers.

Trakakis, G., Tasis, D., Parthenios, J., Galiotis, C., and Papagelis, K. (2013). Structural properties of chemically functionalized carbon nanotube thin films. *Materials* 6 (6), 2360–2371. doi:10.3390/ma6062360

Uyor, U., Popoola, A., Popoola, O., and Aigbodion, V. (2019). Advancement on suppression of energy dissipation of percolative polymer nanocomposites: A review on graphene based. *J. Mater. Sci. Mater. Electron.* 30, 16966–16982. doi:10.1007/s10854-019-02079-1

Uyor, U. O., Popoola, A. P. I., Popoola, O. M., and Aigbodion, V. S. (2019). Enhanced thermal and mechanical properties of polymer reinforced with slightly functionalized graphene nanoplatelets. *J. Test. Eval.* 47 (4), 0336–2692. doi:10.1520/JTE20180336

Wan, Y-J., Zhu, P-L., Yu, S-H., Yang, W-H., Sun, R., Wong, C-P., et al. (2017). Barium titanate coated and thermally reduced graphene oxide towards high dielectric constant and low loss of polymeric composites. *Compos. Sci. Technol.* 141, 48–55. doi:10.1016/j.compscitech.2017.01.010

Wang, D., Bao, Y., Zha, J-W., Zhao, J., Dang, Z-M., and Hu, G-H. (2012). Improved dielectric properties of nanocomposites based on poly (vinylidene fluoride) and poly (vinyl alcohol)-functionalized graphene. *ACS Appl. Mater. interfaces* 4 (11), 6273–6279. doi:10.1021/am3018652

Wang, J., Shi, Z., Wang, X., Mai, X., Fan, R., Liu, H., et al. (2018). Enhancing dielectric performance of poly (vinylidene fluoride) nanocomposites via controlled distribution of carbon nanotubes and barium titanate nanoparticle. *Eng. Sci.* 4 (24), 79–86.

Wang, M., Jiao, Z., Chen, Y., Hou, X., Fu, L., Wu, Y., et al. (2018). Enhanced thermal conductivity of poly (vinylidene fluoride)/boron nitride nanosheet composites at low filler content. *Compos. Part A Appl. Sci. Manuf.* 109, 321–329. doi:10.1016/j.compositesa.2018.03.023

Weng, L., Wang, T., and Liu, L. (2017). A study on the structure and properties of poly(vinylidene fluoride)/graphite micro-sheet composite films. *J. Compos. Mater.* 51 (27), 3769–3778. doi:10.1177/0021998317693675

Wu, L., Wu, K., Lei, C., Liu, D., Du, R., Chen, F., et al. (2019). Surface modifications of boron nitride nanosheets for poly (vinylidene fluoride) based film capacitors: Advantages of edge-hydroxylation. *J. Mater. Chem. A* 7 (13), 7664–7674. doi:10.1039/c9ta00616h

Xiao, M., and Du, B. X. (2016). Review of high thermal conductivity polymer dielectrics for electrical insulation. *High. Volt.* 1 (1), 34–42. doi:10.1049/hve.2016.0008

Xihong, H. (2013). A review on the dielectric materials for high energy-storage application. *J. Adv. Dielectr.* 3 (1), 1330001–1330014. doi:10.1142/S2010135X13300016

Ye, H., Meng, N., Xu, C., Meng, Z., and Xu, L. (2018). High dielectric constant and low loss in poly (fluorovinylidene-co-hexafluoropropylene) nanocomposite incorporated with liquid-exfoliated oriented graphene with assistance of hyperbranched polyethylene. *Polymer* 145, 391–401. doi:10.1016/j.polymer.2018.05.002

Ye, H., Zhang, X., Xu, C., and Xu, L. (2019). Few-layer boron nitride nanosheets exfoliated with assistance of fluoro hyperbranched copolymer for poly (vinylidene fluoride-trifluoroethylene) nanocomposite film capacitor. *Colloids Surfaces A Physicochem. Eng. Aspects* 580, 123735. doi:10.1016/j.colsurfa.2019.123735

Yoon, J-R., Han, J-W., and Lee, K-M. (2009). Dielectric properties of polymer-ceramic composites for embedded capacitors. *Trans. Electr. Electron. Mater.* 10 (4), 116–120. doi:10.4313/teem.2009.10.4.116

Yu, J., Choi, H. K., Kim, H. S., and Kim, S. Y. (2016). Synergistic effect of hybrid graphene nanoplatelet and multi-walled carbon nanotube fillers on the thermal conductivity of polymer composites and theoretical modeling of the synergistic effect. *Compos. Part A Appl. Sci. Manuf.* 88, 79–85. doi:10.1016/j.compositesa.2016.05.022

Zhang, W-B., Zhang, Z-X., Yang, J-H., Huang, T., Zhang, N., Zheng, X-T., et al. (2015). Largely enhanced thermal conductivity of poly(vinylidene fluoride)/carbon nanotube composites achieved by adding graphene oxide. *Carbon* 90, 242–254. doi:10.1016/j.carbon.2015.04.040

Zou, D., Huang, X., Zhu, Y., Chen, J., and Jiang, P. (2019). Boron nitride nanosheets endow the traditional dielectric polymer composites with advanced thermal management capability. *Compos. Sci. Technol.* 177, 88–95. doi:10.1016/j.compscitech.2019.04.027

frontiers | Frontiers in Energy Research

TYPE Review
PUBLISHED 14 February 2023
DOI 10.3389/fenrg.2023.1091105

OPEN ACCESS

EDITED BY
Xiaohu Yang,
Xi'an Jiaotong University, China

REVIEWED BY
Gouse Peera Shaik,
Keimyung University, Republic of Korea
Lindiwe Eudora Khotseng,
University of the Western Cape, South Africa

*CORRESPONDENCE
A. S. Alabi,
ayo.alabi@ymail.com

SPECIALTY SECTION
This article was submitted to Process and Energy Systems Engineering, a section of the journal Frontiers in Energy Research

RECEIVED 06 November 2022
ACCEPTED 03 February 2023
PUBLISHED 14 February 2023

CITATION
Alabi AS, Popoola API, Popoola OM, Mathe NR and Abdulwahab M (2023), Materials for electrocatalysts in proton exchange membrane fuel cell: A brief review.
Front. Energy Res. 11:1091105.
doi: 10.3389/fenrg.2023.1091105

Materials for electrocatalysts in proton exchange membrane fuel cell: A brief review

A. S. Alabi[1]*, A. P. I. Popoola[1], O. M. Popoola[2], N. R. Mathe[3] and M. Abdulwahab[4]

[1]Chemical, Metallurgical and Materials Engineering, Faculty of Engineering and Built Environment, Tshwane University of Technology, Pretoria, South Africa, [2]Center for Energy and Electric power, Electrical Engineering, Faculty of Engineering and Built Environment, Tshwane University of Technology, Pretoria, South Africa, [3]National Laser Center, Council for Scientific and Industrial Research, Pretoria, South Africa, [4]Metallurgical and Materials Engineering, Faculty of Engineering, Air Force Institute of Technology, Kaduna, Nigeria

Energy is a requisite factor for technological advancement and the economic development of any society. Currently, global energy demand and supply largely rely on fossil fuels. The use of fossil fuels as a source of energy has caused severe environmental pollution and global warming. To salvage the dire situation, research effort is geared toward the utilization of clean, renewable and sustainable energy sources and the hydrogen energy economy is among the most preferred choices. Hydrogen energy economy, which includes hydrogen production, storage and conversion has gained wide consideration as an ecofriendly future energy solution with a fuel cell as its conversion device. Fuel cells, especially, the proton exchange membrane category, present a promising technology that converts hydrogen directly into electricity with great efficiency and no hazardous emissions. Unfortunately, the current generation of proton exchange membrane fuel cells faces some drawbacks that prevent them from large-scale market adoption. These challenges include the high costs and durability concerns of catalyst materials. The main source of high cost in fuel cells is the platinum catalyst used in the electrodes, particularly at the cathode where the sluggish oxygen reduction reaction kinetics require high loading of precious metals. Many research efforts on proton exchange membrane fuel cells are directed to reduce the device cost by reducing or completely replacing the platinum metal loading using alternative low-cost materials with "platinum-like" catalytic behaviour while maintaining high power performance and durability. Consequently, this review attempts to highlight recent research efforts to replace platinum and carbon support with other cost-effective and durable materials in proton exchange membrane fuel cell electrocatalysts. Overview of promising materials such as alloy-based (binary, ternary, quaternary and high-entropy alloys), single atom and metal-free electrocatalysts were discussed, as the research areas are still in their infancy and have many open questions that need to be answered to gain insight into their intrinsic requirements that will inform the recommendation for outlook in selecting them as electrocatalysts for oxygen reduction reaction in proton exchange membrane fuel cell.

KEYWORDS

proton exchange membrane fuel cell, oxygen reduction reaction, platinum-based electrocatalysts, platinum-free electrocatalysts, alloy-based electrocatalysts, single atom electrocatalysts, metal-free electrocatalysts

1 Introduction

The ability of any society to evolve technologically and develop economically depends on the availability and effective utilisation of energy. The current global energy consumption mainly relies on fossil fuels (Abbasi et al., 2022; Shamoon et al., 2022). This state of global energy demand and supply is not sustainable considering the growth in global population, fast exhaustion of fossil fuel deposits and the environmental effects of using fossil fuels on the fragile ecosystem (Bogdanov et al., 2021; Schwanitz and Wierling, 2022). In addition, the increasing rate of fossil fuel utilization threatens to destabilise the environment because of the worsening greenhouse gas emissions and global warming that might result in unprecedented changes to human lives if nothing is done to prevent it (Chen et al., 2022a; Icaza-Alvarez et al., 2022). To address the situation, research effort is focused on utilising clean, renewable and sustainable energy sources and the hydrogen energy economy is among the most preferred choices.

The idea of a hydrogen economy was initiated by John Bockris in the 1970s. It was a dream to generate hydrogen *via* water electrolysis and channel it through pipelines to factories, homes, and fuelling stations where it would be harnessed and converted to other forms of energy (Oliveira et al., 2021). However, many challenges still need to be overcome in hydrogen production, storage and conversion to realise Bockris' dream of a global transition to a hydrogen economy. Such challenges include the high cost and poor reliability of the hydrogen energy conversion device known as the fuel cell. A fuel cell is an electrochemical device that converts chemical energy directly into electricity with great efficiency and no hazardous emissions (Wang and Jiang, 2017; Ioroi et al., 2019). It is a thermodynamic system that operates based on electrochemical reactions, which consumes reactants from external source (Rahaman and Islam, 2019). The fuel cell combines the best features of combustion engines and batteries. It can work continuously without any intermediate mechanical energy conversion if fuel is supplied constantly and also shows the characteristics of battery under load condition (Manoharan et al., 2019). Fuel cells are usually classified according to the electrolyte, fuel used, operating conditions, required load or the application for which they are used (Abdelkareem et al., 2021b). Diverse kinds of fuel cells are presented in Table 1 Although these fuel cells use different electrolytes and fuels, they all operate on a similar redox reaction principle and platinum (Pt) is the catalyst widely used for the cathodic and anodic redox reaction in proton exchange membrane fuel cell (PEMFC).

The PEMFC is promising for large-scale commercialisation because of its dynamic response, high efficiency, low operating temperature (60°C—80°C), high power density and quick start-up when compared with other fuel cells (Lucia, 2014; Jiao et al., 2021).

Despite the potential of PEMFC for widespread commercialisation, it needs to meet certain criteria about cost and reliability to gain end-user acceptance and compete favourably with other commercial energy conversion devices such as internal combustion engines and batteries (Wang et al., 2018a). The high cost of active electrocatalyst materials and their poor durability at PEMFC operation conditions are the major challenges facing the large-scale commercialisation of PEMFC (Borup et al., 2020). In addition, it has been reported that the membrane electrode assembly parameters have significant impact on the efficiency of the PEMFC stack (Majlan et al., 2018; Madheswaran and Jayakumar, 2021). Hence, improving the efficiency of PEMFC by rational selection of cost-effective materials is essential to achieve the hydrogen economy potential as an alternative to fossil fuel in electricity generation, fuel for vehicles and industrial processes (Egeland-Eriksen et al., 2021).

These could be achieved by deliberate attempt to improve the state-of-the-art electrocatalysts in PEMFC. The electrocatalyst is a vital component that performs a significant role in reaction kinetics involved in the effective functioning of PEMFC. It has to do with the surface adsorption of reactants, breaking the reactants bonds and formation of new bonds of intermediates and desorption of products (Figure 1) (Wacławek et al., 2018; Madheswaran and Jayakumar, 2021). The electrocatalyst in the PEMFC works as the cathode and anode, which conventionally uses Pt particles on carbon support (Wang et al., 2020b). Unfortunately, Pt-based electrocatalysts account for about half of the cost of the PEMFC stack and suffer degradation during prolonged PEMFC operation (Xie et al., 2020; Fan et al., 2022). The main degradation mechanisms have been identified as dissolution, migration and agglomeration of metal particles and carbon support corrosion that results in a loss in the electrochemical surface area (ECSA) (Wei et al., 2021b). In addition, Pt-based electrocatalysts are susceptible to carbon monoxide poisoning and requires highly active material loading at the cathode because of the cathodic sluggish oxygen reduction reaction kinetics. To address these challenges, two routes have been widely investigated to achieve low-cost electrocatalysts; which are lowering the loading of Pt and looking for substitutes (Ding et al., 2020b).

PEMFC energy conversion is achieved through hydrogen oxidation reaction (HOR) and oxygen reduction reaction (ORR) (Figure 2) (Cruz-Martínez et al., 2021). These reactions involve the transfer of charge (electrons) between an electrocatalyst and a chemical species. During the HOR, an external circuit transports electrons to the cathode while protons are transferred across the polymer exchange membrane. Meanwhile, ORR involves oxygen reduction with electrons and hydrogen protons at the cathode, leaving only water and heat as by-products (Cruz-Martínez et al., 2019). Research interest focus more on ORR because of its sluggish kinetics that is 4–6 times slower in order of magnitude when compared with HOR (Wang et al., 2018b; Wan et al., 2020).

The slow rate of ORR remains a major challenge in PEMFC (Kong et al., 2023). Significant progress has been made globally towards improving the-state-of-the-art electrocatalysts for ORR. As a result of these research efforts, commercial Pt/C remains the most widely used electrocatalyst among others because of its comprehensive evaluation and the superior activity of the Pt surface to other oxygen reducing surfaces (Ma et al., 2020a; Liu et al., 2022; Li et al., 2023). However, Pt high cost, scarcity and poor durability during prolong PEMFC operation hinder the widespread commercialisation of PEMFC, as the frequent cost of the replacement of the electrocatalyst significantly affects the overall cost of the fuel cell (Lv et al., 2019b; Meng et al., 2021; Xia, 2021). To this end, addressing the stability challenges, particularly at the cathode where the sluggish ORR kinetics require high loading of precious metal is imperative for its practical employment in PEMFC (Zhao et al., 2022). To overcome these challenges, research efforts

TABLE 1 Types of fuel cells.

Type of fuel cell	Advantages	Disadvantages	References
Proton exchange membrane fuel cell	o Promising for large scale commercialisation	o Sluggish oxygen reduction kinetics	Abdelkareem et al. (2021a)
	o High efficiency	o Carbon monoxide poisoning	
	o Dynamic response	o Poor heat and water management	
	o Low operating temperature 40°C – 80 °C	o Costly catalysts	
	o Quick start-up		
	o High energy density		
Alkaline fuel cell	o Operates at low temperature 27°C – 70 °C	o Carbon dioxide intolerance	Ferriday and Middleton (2021)
	o Quick start-up		
	o High efficiency		
	o Low cost		
	o Good heat management		
	o Fast oxygen reduction kinetics		
	o High activity		
	o Can resist carbon monoxide poisoning		
Direct methanol fuel cell	o Quick start-up	o Fuel crossover that causes cathode poisoning	Alias et al. (2020)
	o Fuel can be obtained from wastes		
	o Cost effective	o Costly catalysts	
	o High energy density		
Phosphoric acid fuel cell	o High tolerance to carbon monoxide poisoning	o High cost of Pt catalysts	Stonehart and Wheeler (2005)
	o Comparatively lower Pt catalyst demand	o Sluggish start-up	
	o High activity	o Low ionic conductivity	
	o Good heat management		
Molten carbonate fuel cell	o High efficiency	o Susceptible to high temperature corrosion	Antolini (2011)
	o Can use carbon dioxide as oxidant	o Sluggish start-up	
	o Cost effective as its does not require precious metal catalyst	o Difficulty in handling molten carbonate	
Solid oxide fuel cell	o High efficiency	o Requires high temperature materials for effective functioning	Yang et al. (2020)
	o Good heat management		
	o Can function without precious metal catalysts		
	o Has long operational time		
	o Can use different types of fuels		
Reversible fuel cell	o Can operate both as fuel cell and water electrolyser	o Comparatively not cost effective	Wang et al. (2016), Lim et al. (2021)
	o High specific energy	o Relatively low efficiency	
	o Has energy storage capacity		
Direct ammonia fuel cell	o Runs at lower temperature	o Susceptible to ammonia crossover	Jeerh et al. (2021)
	o Cost effective	o Has low cell efficiency and power density	
	o Requires low-cost electrolyte and electrocatalyst		

(Continued on following page)

TABLE 1 (*Continued*) **Types of fuel cells.**

Type of fuel cell	Advantages	Disadvantages	References
Direct propane fuel cell	o Low-cost	o Generates carbon dioxide as reaction product	Mohammed et al. (2019)
	o Can be easily handle		
	o Requires simple infrastructure		
	o Has relatively higher power density		
	o Has the potential to work with low-cost membrane		
Microbial fuel cell	o Converts wastes to electricity	o Low power density	Do et al. (2018)
	o Can be used in wastewater treatment	o Current instability	
	oCan be used as biosensor	o Uses costly materials	
		o High internal resistance	

are on-going to develop durable electrocatalysts that are highly active and cheap (Batchelor et al., 2019).

1.1 Pt/C electrocatalyst degradation mechanism

Pt particles dispersed on carbon support remain the most widely used commercial electrocatalyst for PEMFC (He et al., 2022). This is due to the advance conductivity, flexibility and wide range of operable potentials that Pt offers for PEMFC application (Abbas et al., 2020). Unfortunately, under PEMFC operation conditions, Pt dissolves and breaks up and the carbon support also corrodes leading to the deterioration of the performance of the fuel cell (Kregar et al., 2020). The major degradation mechanisms were identified as dissolution, migration and agglomeration of metal particles and carbon support corrosion that results in a loss in the ECSA which causes overall decrease in the performance of PEMFC (Wang et al., 2021a; Wei et al., 2021b). Several studies have been conducted to investigate the degradation mechanism of Pt/C in PEMFC (Weber et al., 2018; Labata et al., 2021; Fan et al., 2022). The studies were aimed at understanding the degradation mechanism of Pt-based electrocatalyst to help researchers in developing mitigation strategies that could significantly reduce the cost of PEMFC (Lopes et al., 2020; Hersbach et al., 2021). Different perspectives exist in the literature on the cause of Pt-based electrocatalyst disintegration. Some researchers argued that Pt disintegrate due to change in cell potential, other researchers asserted that the discrepancy in anodic and cathodic charges is the cause of the disintegration (Okonkwo et al., 2021). With the disparity in the potential ranges at which Pt disintegration occurs in PEMFC operation, factors such as particles size and morphology play important role in the disintegration of Pt (Lopes et al., 2020; Hussain et al., 2022). To address these challenges, promising strategies (Figure 3) such as alloying Pt with transition metals has been suggested as an effective method to reduce the usage of the scarce and expensive

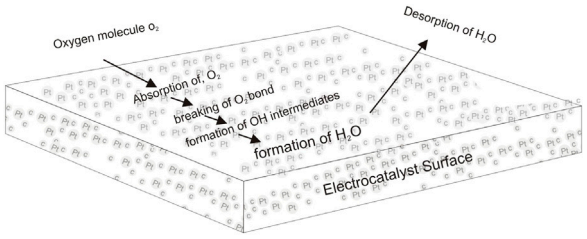

FIGURE 1
Schematic representation of electrocatalyst surface.

precious metal as electrocatalyst without loss in its performance (Bhoyate et al., 2023). In addition, the use of mixed phases has been recommended as an effective strategy to optimise electrocatalysts activity and stability, thereby encouraging the development of electrocatalysts from binary, ternary, quaternary and high entropy alloys (Li et al., 2020c; Prabhu et al., 2020; Li et al., 2021; Du et al., 2022). The desired electrocatalyst activity and stability optimisation in alloy electrocatalysts is achieved by alloy compositional, morphological and particles size control (Zhang et al., 2021a; Loffler et al., 2021).

It is noteworthy that other electrocatalyst design strategies such as Pt-free alloys, single atom and metal-free electrocatalysts have been investigated (Bhatt and Lee, 2020; Han et al., 2020; Zhang and Guan, 2020; Wei et al., 2021a; Muhyuddin et al., 2021). Efforts have also been directed toward the development of other durable catalyst-support materials. Consequently, this review summarises recent research efforts to enhance or replace Pt and carbon support with other cost-effective and durable materials in PEMFC electrocatalysts application (Table 2). Overview of design strategies in developing alternative electrocatalyst using other cost-effective and durable materials to replace platinum and carbon support are highlighted with the activity and stability of various electrocatalysts for oxygen reduction reaction in PEMFC.

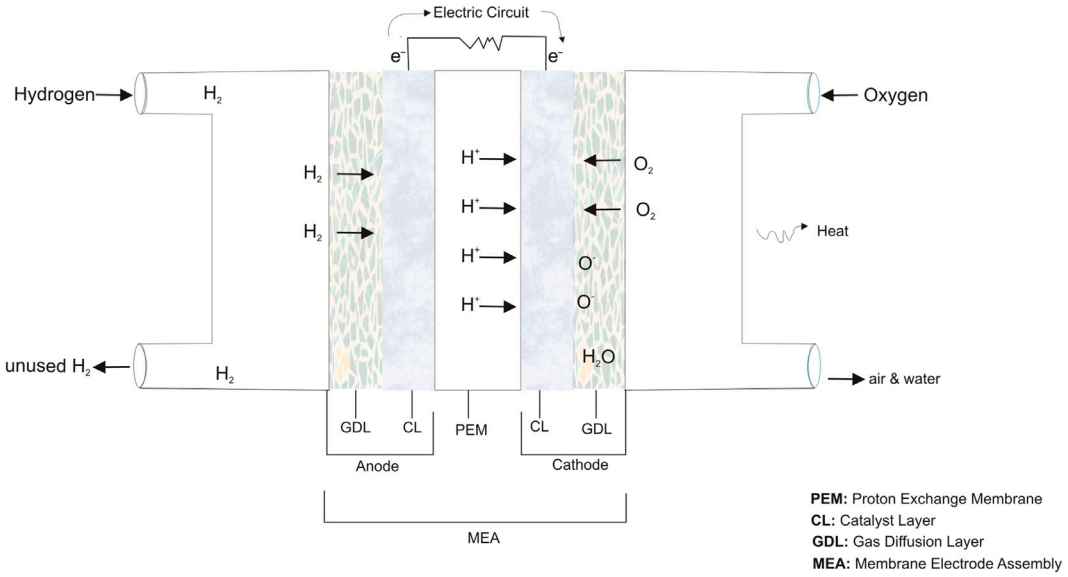

FIGURE 2
Representation of the role of electrocatalyst in HOR and ORR in PEMFC.

2 An overview of materials used as electrocatalysts in PEMFC

Herein research progress on electrocatalyst design strategies to address the drawbacks associated with the state-of-the-art Pt/C electrocatalyst for PEMFC were summarised. Pt-based electrocatalyst were discussed followed by alloy electrocatalysts. Emerging electrocatalysts such as high-entropy alloys, single atom and metal-free electrocatalysts were also highlighted.

2.1 Platinum-based electrocatalysts

Pt/C electrocatalyst remains the state-of-the-art catalyst for ORR in PEMFC because of its effectiveness in ORR kinetics (Tian et al., 2017; Huang et al., 2021; Kong et al., 2021). However, due to its high cost and durability concerns, research to enhance its performance and reduce its high Pt particle loading are on-going (Shao et al., 2018; Lopes et al., 2020; Kishida et al., 2021). According to Etesami et al. (2021), there are three major research areas for Pt-based catalysts, which are 1) reducing the particle size of Pt and increasing its dispersion in the carbon support in order to increase its active sites surface area 2) producing Pt-based catalysts with particles surface oriented in a specific direction and 3) dispersing Pt into other metals especially transition metals or modified carbon supports to form alloys or mixtures. Efforts have also been directed toward the development of other durable catalyst-support materials such as transition metal-based compounds (carbides, nitrides, oxides and chalcogenides) (Shang et al., 2020), carbon-based materials (carbon nanotube and graphene) (Liu et al., 2018), nitrogen doped carbon (Chen et al., 2021) and metal-organic-framework to address the carbon support corrosion challenge. On the other hand, Mukherjee et al. (2022) asserted that electrocatalysts that use only micro-sized Pt particles as their actives sites are no longer the state-of-the-art catalysts for fuel cell application. The authors claimed that high cost of electrocatalysts due to unrealistic Pt loading requirements and Pt particle susceptibility to carbon monoxide poisoning are the key reasons for the assertion. Along this line, research have evolved from using micro sized Pt on carbon supports to using Pt nanoparticles, Pt nanowires, introduction of porosity to increase catalysts surface area and bimetallic Pt electrocatalysts with other metals (Table 3) (Gilroy et al., 2016; Li and Sun, 2019; Shao et al., 2019; Xiao et al., 2021a).

2.2 Platinum-free electrocatalysts

To reduce the overall cost of PEMFC, researchers focus on the reduction or substitution of Pt in Pt-based electrocatalyst. Thus, research efforts have been directed towards the development of non-Pt-based electrocatalysts. Other Pt group metal-based electrocatalysts such as Pd-C, Ir-C, Rh-C electrocatalysts have been reported (Wang et al., 2022). Several Pt-free electrocatalysts have been developed using non-precious metals because of their low-cost, availability and abundance in nature (Etesami et al., 2021). Non-precious metal-based electrocatalysts have been widely investigated because of their excellent catalytic performance, durability and cost-effectiveness (Etesami et al., 2020). Such electrocatalysts include transition metal-nitrogen-carbon electrocatalysts, nitrides, carbides, chalcogenides and transition metal oxides (Gewirth et al., 2018; Xiao et al., 2021a). To achieve a Pt metal group-free electrocatalyst for PEMFC application Sanad et al. (2021) synthesised a non-precious metals Co-Cu metal organic framework bimetallic electrocatalyst by low-temperature hydrothermal strategy. The catalytic activity of the electrocatalyst was tuned by varying Co/Cu molar ratios. It was observed that the

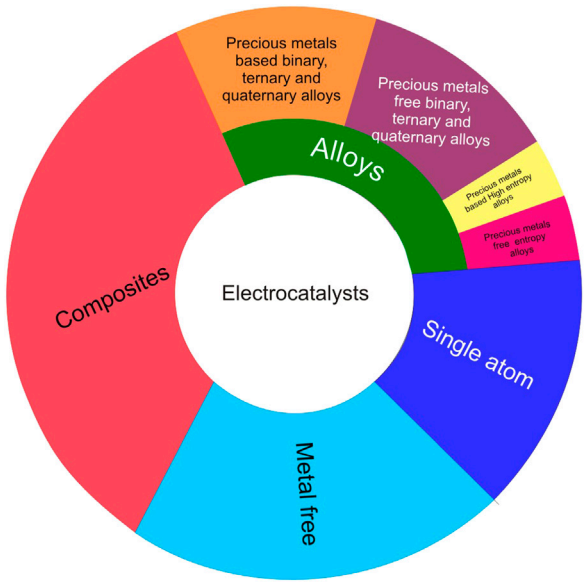

FIGURE 3
Electrocatalyst design strategies.

metal organic framework bimetallic electrocatalyst outperformed the electrocatalytic activity of commercial Pt–C catalyst for ORR in alkaline environment. It exhibited onset potential of 1.06V, half wave potential of 0.95 V and electrochemical stability of 30 mV after 1000 ORR cycles in 1.0 M sodium hydroxide solution. Chandran et al. (2018) adopted a single-step synthesis approach to develop Pd-Co alloy supported on reduced graphene oxide doped with nitrogen. The ORR activity of the electrocatalyst proceeded through the four-electron reaction pathway. The electrocatalyst showed 1.6 times enhanced mass activity when compared to the Pd-reduced graphene oxide doped with nitrogen. The electrocatalyst also recorded of power density of 68 $mWcm^{-2}$ with metal loading of 0.5 mg cm^{-2} at 60°C without any back pressure.

2.3 Alloy-based electrocatalysts

2.3.1 Bimetallic alloy electrocatalysts

Research findings have shown that alloying Pt with the d-block metals to form a bimetallic electrocatalyst could positively influence the stability and activity of Pt-C electrocatalyst in ORR of PEMFC (Seh et al., 2017; Sui et al., 2017). Literature also showed that the addition of a second metal to Pt-based electrocatalyst can prevent the adsorption of carbon-monoxide on the electrocatalyst's surface (Molochas and Tsiakaras, 2021; Lee et al., 2022b). In addition, such secondary metal addition could re-expose blocked sites on a poisoned Pt surface by oxidising the carbon monoxide thereby speeding up ORR kinetics (Zhang et al., 2021b; Lu and Elam, 2022). Owing to these characteristics, bimetallic electrocatalysts have been reported to exhibit comparatively better efficiency than Pt-C electrocatalyst due to their highly exposed surfaces (Bai, 2018; Huang et al., 2018; Wang and Spendelow, 2021). Guterman et al. (2018) prepared Cu_xPt-C electrocatalyst by successive deposition of copper and Pt on carbon support. The electrochemical performance of the Cu_xPt-C electrocatalyst was studied at ambient temperature in a three-electrode electrochemical cell with the help of CV using a rotating-disk as the working electrode. The results obtained were compared with that of commercial Pt-C catalyst. The study showed that the bimetallic electrocatalyst exhibited a combination of higher stability and mass activity values when compared with the commercial Pt-C catalyst with the same Pt loading. Ying et al. (2018) also developed a metal-organic framework Pt-Co bimetallic nanoparticles supported by hollow porous carbon capsules that were doped with nitrogen as highly active and durable electrocatalyst for ORR. The bimetallic catalyst was synthesised by wet chemistry method and was found to demonstrate outstanding ORR performance, with a mass activity that was 5.5 and 13.5 times better than those of commercial Pt/C and Pt/black catalysts respectively. Moreover, the catalyst exhibited better durability in terms of ECSA and mass activity when compared with commercial catalysts. The exceptional ORR performance of the catalyst was ascribed to the large surface area of bimetallic Pt-Co nanoparticles and hollow porous structure of nitrogen-doped carbon capsules. Although Pt has been widely alloyed with many transition metals and of recent lanthanides to form bimetallic electrocatalysts, they have not gain wide adoption for commercial application in fuel cell (Martínez-Hincapié and Čolić, 2022). However, it was reported that Pt-Co bimetallic electrocatalyst was recently use in commercial electric vehicle (Toyota Mirai) (Wang and Spendelow, 2021). The poor commercial patronage of Pt-based bimetallic electrocatalysts could be attributed to their susceptibility to poisoning by formic acid electrooxidation and dissolution into strong acids in working electrolytes, which lead to the loss of integrity of electrocatalysts and result in deterioration of catalytic performance. As a result, different electrochemical reaction pathways have different electronic structure requirements (Zhang et al., 2018; Mukherjee et al., 2022).

2.3.2 Trimetallic/ternary alloy electrocatalysts

To benefit from synergistic effect that can result from using three elements in trimetallic alloys, researchers have attempted to develop ternary alloy electrocatalysts for ORR in PEMFC (Wang et al., 2019c; Wang et al., 2020a; Zhu et al., 2020a). The introduction of a third element has proven to improve the lifespan of the parent bimetallic electrocatalyst at PEMFC operating conditions (Zhang et al., 2017). Hu et al. (2021) synthesised ternary platinum-based electrocatalyst using co-doping strategy. Cu and Co were co-doped into Pt-C to modulate the electronic structure of Pt in order to weaken the adsorption of deoxygenated species by Pt thereby enhancing the ORR kinetics. It was found that the trimetallic electrocatalyst exhibited better mass activity of 0.52 A mg_{pt}^{-1} and power density 1.15 Wcm^{-2}. Moreover, the mass activity of the ternary electrocatalyst only reduced by 8.3% after 30,000 cycles indicating comparatively good durability. Xiao et al. (2021b) reported a facile synthesis of carbon supported Pt-Cu-Fe nanoparticles trimetallic electrocatalyst for ORR in PEMFC. The authors found that the trimetallic electrocatalyst recorded a significant 0.99 A mg_{pt}^{-1} ORR activity at 0.9V potential and enhanced stability, losing only 7.6% of mass activity after 5000 durability cycles. Ma et al. (2022) developed a Pt-Ru-Te ternary electrocatalyst with only 11 at% of Pt for HOR in fuel cell. The electrocatalyst showed a current density of 30.6 $mAcm^{-2}$ at 50 mV and exchange current density of 0.426 $mAcm^{-2}$.

TABLE 2 Activities and durabilities of different electrocatalysts.

Electrocatalyst	Mass activity (A g^{-1})	Durability (Mass activity loss)	References
Commercial Pt/C	0.1	80% loss after 30,000 cycles	Liang et al. (2019)
Nanoparticle Pt/C	0.87	NA	Garlyyev et al. (2019)
$Pt_{26}Cu_{74}$ nanocrystals	0.74	21.2% after 1000 cycles	Huang et al. (2019)
Gallium-doped PtNi/C nanoparticles	1.24	12% after 15,000 cycles	Lim et al. (2018)
Pt supported on Mo-doped titanium nanotubes	0.10	No loss after 2000 cycles	Esfahani et al. (2018)
Nanoparticles Pt/TiO_2@CNT	0.36	No loss after 10,000 cycles	Kong et al. (2020)
$Ir_{23}Pd_{77}$/C	0.17	NA	Nguyen and Shim (2018)
Pt-Pd/C	0.15	Negligible loss after 10,000 cycles	Wu et al. (2019)
$Cu_{0.75}Fe_{0.25}$@Pt/C core-shell structure	0.91	11% loss after 10,000 cycles	Cao et al. (2020)
PtNiCo nanocage	1.03	NA	Ma et al. (2021)
PtNiRh nanowires	2.51	12.8% loss after 10,000 cycles	Li et al. (2018b)
AgCoCu oxides on reduced graphene oxide	0.04	No loss after 10,000 cycles	Madakannu et al. (2022)
$Pd_{59}Cu_{30}Co_{11}$ nanoalloy	1.01	No loss after 10,000 cycles	Li et al. (2018a)
Nanoparticle AlCuNiPtMn	3.47	No loss after 30,000 cycles	Li et al. (2020b)
Nanoparticle PtRuCuOsIr	0.86	50% loss after 15,000 cycles	Chen et al. (2015)
Nanoparticle PtPdCuNiCoAl	2.24	7.5% loss after 10,000 cycles	Qiu et al. (2019)

Furthermore, the electrocatalyst exhibited excellent stability with 5% loss in activity after 2000 durability circle.

The literature showed improvement in performance of ternary electrocatalysts in fuel cell application over their bimetallic counterparts, establishing the significance of ternary platinum based electrocatalyst in improving electrocatalytic performance. However, ternary electrocatalysts are also faced with the challenges of metal dissolution, agglomeration and carbon support corrosion. In addition, it is uncertain if the electrocatalyst will be able to replicate their excellent experimental activities in actual fuel cell operating conditions (Mukherjee et al., 2022).

2.3.3 Quaternary alloy electrocatalysts

Quaternary alloy has the potential to offer additional options that could improve electrocatalytic performance and durability than binary and ternary alloy electrocatalysts. However, it remains the least reported alloy-based electrocatalysts in literature (Du et al., 2022). Wang et al. (2019a) developed a quaternary structurally ordered Pt(Fe,Co,Ni) alloy electrocatalyst with equal proportion of constituent elements *via* a facile synthesis method that requires spray dehydration on a solid surface followed by annealing procedure. The electrocatalyst showed improved electrocatalytic performance towards ORR with mass activity 6.6 fold higher than that of commercial Pt/C with only 17% attenuation after 10,000 potential cycles at 0.9 V. Hornberger et al. (2022) synthesised an octahedral quaternary PtNi(RhMo) alloy electrocatalyst. The alloy electrocatalyst was prepared to control the shape of PtNi by co-doping it with Rh and Mo using solvothermal process. The electrocatalysts exhibited remarkable mass activity of 1.53 mg_{pt}^{-1}.

2.3.4 High-entropy alloy electrocatalysts

For centuries, alloying has been employed to impart desired material properties. It usually entails the addition of comparatively small quantities of secondary elements to the parent metal. However, for the past two decades, a new alloying approach has been in vogue that entails the combination of several key elements in high concentrations to create novel materials called high entropy alloys (HEAs) (George et al., 2019). HEAs have two definitions that are based on composition and configuration entropy, respectively. They are alloys that contain a minimum of five primary elements having respective atomic weight percentage between 5 and 35 based on composition. The entropic definition states that HEAs are alloys having configurational entropies at a random state greater than 1.5R, whether they are single or multiphase at ambient temperature; where R is gas constant (Yeh and Lin, 2018). HEAs have been recently used in catalysis because of their exceptional benefits, which include high tolerance, complex surface and adjustable composition (Li and Chen, 2021). They have gained wide acceptance as catalysts in electrochemical reactions due to their ability to catalyse different reactions. Such reactions include but are not limited to nitrogen reduction reaction (NRR), alcohol oxidation reaction (AOR), oxygen reduction reaction (ORR), hydrogen evolution reaction (HER), oxygen evolution reaction (OER) and carbon dioxide reduction reaction (CO_2 RR) (Zhang et al., 2022). HEA catalysts characteristics that distinguished them from other catalysts have been highlighted as their multiple combinations of elements located next to each other, which results in tailorable active sites. In addition, it was emphasised that their non-typical electrochemical behaviour made them a distinctive class of catalyst materials that are promising as a better alternative to other catalysts (Löffler et al., 2019). The application of HEAs in ORR is being researched to improve the

TABLE 3 Summary of recent works on Pt-based electrocatalysts for ORR.

Electrocatalyst	Research aim	Activity (A mg $^{-1}$)	Durability	Reference
Au@Pt nanoparticles	Development of nanoparticles Au@Pt core-shell structure to mitigate the instability of Pt nanoparticles electrocatalyst used in ORR.	0.35	Less than 5% loss after 10,000 potential cycles	Chung et al. (2020)
Pt/TiO_2@CNT nanoparticles	Synergistic combination of the high surface area of carbon nanotube, excellent conductivity and stability of TiO_2 nanoparticles and high activity of dispersed Pt nanoparticles for ORR.	0.36	No loss in activity after 10,000 potential cycles	Kong et al. (2020)
Pt/SnO_2-C nanocomposite	Modification of the electronic properties of Pt nanoparticles by selectively depositing it on SnO_2 nanoclusters formed on carbon surface	0.07	No loss after 2000 potential cycles	Hussain et al. (2019)
Pt@COF (covalent organic framework)	Development of Pt nanoparticles anchored on nitrogen-rich covalent organic framework for ORR.	Onset potential of 1.04V and half-wave potential of 0.89V	Current density drops by 4% of its initial values after 50 h of operation	Zhai et al. (2020)
Pt-N-S-pCNFs hybrid	Preparation of ultrafine Pt nanoparticles supported on sulphur and nitrogen codoped porous carbon nanonanofibers as electrocatalyst for ORR, OER and HER.	Recorded onset potential of 1.02 eV and half-wave potential of 0.83 eV	10.5% loss in current density after 10,000 s	Chen et al. (2022b)
PtM_3/C ordered intermetallic M = Fe, Co, Ni	Development of low-Pt ordered intermetallic on carbon support electrocatalyst	$PtCo_3$ exhibited mass activity of 0.74 A mg $^{-1}$	9% loss in mass activity after 10,000 potential cycles	Wang et al. (2019b)
Pt@CNT	Determination of effect of different particle sizes of Pt (1.5nm, 3nm and 6 nm) on the performance of Pt supported on carbon nanotubes electrocatalyst for HER and ORR.	The electrocatalyst with 3 nm particle size showed optimal ORR mass activity of 0.03 A g $^{-1}$	16% loss in initial value of current density after 15000s test	Ma et al. (2020b)
Pt/C nanoparticles	Investigation of effect of mesoporous carbon support on ORR activity and stability of nanosized Pt/C electrocatalyst	0.15	10.9% loss of ECSA in half cell test	Xie et al. (2022)
Pt/C nanoparticles	Study the effect of Pt(100) and Pt(111) orientations on the ORR properties of different nanosized Pt/C electrocatalyst (3 – 7 nm)	4.6 nm with Pt(100) crystallographic orientation exhibited the optimum ORR of 0.05 Ag $^{-1}$	NA	Erikson et al. (2022)
Pt_3Ni nanowires	Development of 1 nm thick bimetallic alloy nanowire as durable electrocatalyst for ORR.	0.55	67% mass activity loss after 50,000 potential cycles	Gong et al. (2019)
Pt_3Co-Mo nanowires	Preparation of Molybdenum doped Pt-cobalt bimetallic alloy nanowire as efficient electrocatalyst for ORR.	0.84	24% loss in mass activity after 50,000 potential cycles	Deng et al. (2022)

cathodic sluggish kinetics that limits the reliability of PEMFC. This is because HEAs emerged as materials that are capable of overcoming the limitation of Pt and Pt group metals (PGM) catalysts (Martínez-Hincapié and Čolić, 2022). Wu et al. (2020) studied the catalytic behaviour of the six PGM as self-supported HEA catalyst synthesised by wet chemistry method for ethanol oxidation reaction and found that the HEA exhibited variety of adsorption sites on its surface, which can catalyse many complex reactions. The PGM HEA catalyst's intrinsic mass activity was also compared with those of commercial palladium-C, palladium-black and Pt-C catalysts and found to be 2.5, 6.1 and 12.8 times higher than the intrinsic mass activity of the commercial catalysts, respectively. Lee et al. (2022a) synthesised IrPtPdRuRh HEA electrocatalyst by plasma ionic liquid reduction and showed excellent hydrogen evolution reaction catalytic performance with overpotential of 60 mV at a current density of 10 $mAcm^{-2}$. The electrocatalyst also recorded a Tafel slope of 42 mV dec^{-1} in alkaline electrolyte and demonstrated good stability for 6 h at a high constant current density of 100 $mAcm^{-2}$ without appreciable decay. The HEA nanoparticles were deposited on a carbon support. Qiu et al. (2019) synthesised senary AlNiCuPtPdAu octonary AlNiCuPtPdAuCoFe and senary all-non-noble metal AlNiCuMoCoFe nanoporous HEAs using a route that combined bulk melting and fast cooling followed by dealloying. The nanoporous HEA with low Pt loading exhibited 10 times mass activity when compared with commercial Pt-C catalyst for ORR and maintained 92.5% of its initial activity after 100,000 electrochemical cycles. It was also discovered that, unlike binary alloy system, HEAs exhibited high stability under electrochemical cycling conditions. An attribute that made them promising electrocatalysts for PEMFC. Furthermore, to explore catalytic potentials of PGM–free HEAs in ORR, Nandan et al. (2022) reported a facile method that combines wet chemistry and pyrolysis to synthesise FeCoNiMnCr HEA nanoparticles grafted on nitrogen-doped carbon nanotubes. The electrocatalyst designed for electrochemical ORR utilised the synergy between nitrogen-doped carbon nanotubes and HEA nanoparticles to promote improved performance in the ohmic polarization region of fuel cells when compared with commercial Pt-C electrocatalyst. Moreover, the FeCoNiMnCr-based catalysts exhibited better ORR performance compared to various newly reported transition metal-based conventional catalysts. In another research, Liu et al. (2021)

synthesised CoCrFeMnNi HEA nanoparticle-activated carbon nanocomposites electrocatalyst. The electrocatalyst was fabricated by impregnation–adsorption method of precursor salt solution followed by calcination. The HEA-activated carbon electrocatalyst performed excellently in the degradation of methylene blue at a comparable rate with those of other catalysts. The exceptional efficiency was because of the coupling effects of the solid-solution structure of HEA nanoparticles and the large specific surface area and considerable reaction channels of the activated carbon. In addition, HEA nanoparticles embedded in distinctive porous structure accelerated the mass transport and the electron transfer as nanoscale galvanic cells in the active bond splitting of methylene blue.

Most conventional alloys are made up of a single element with various alloying elements added to improve the properties of the principal element, forming an alloy family based on the principal element (Tsai and Yeh, 2014). HEAs were thought to be complex because they contained more than four primary elements and complex phase diagram systems that are often unavailable. As a result, the majority of HEAs earlier reported were created using the traditional trial-and-error method (Zhang et al., 2012). However, as the design of high entropy alloys progresses, several design routes have emerged which include the use of alloys design principles of materials science, building on promising binary or ternary alloy systems, the use of combinatorial material synthesis technique, Taguchi optimisation method and material science computational methods such as finite element, molecular dynamics, simulation, phase computation (PHACOMP) and calculation of phase diagram (CALPHAD) (Yeh, 2013). Wen et al. (2019) used material design strategy that combines machine learning model and experimental algorithms to determine high entropy alloys with high hardness in AlCoCrCuFeNi alloy system. Several alloys with hardness values that are 10% higher than the best original data set were fabricated using only seven experiments. In another study, Floriano et al. (2020) designed equiatomic TiZrNbFeNi and non-equiatomic $Ti_{20}Zr_{20}Nb_5Fe_{40}Ni_{15}$ high entropy alloys *via* thermodynamic calculations using CALPHAD. The alloys were fabricated by arc melting technique and showed small amount of cubic phases and C14 laves phases with $(Zr,Ti)_1$, $(Fe,Ni,Nb, Ti)_2$ constitution.

2.3.4.1 High-entropy alloy-based composites

HEA composites are emerging advanced materials that are produced by dispersing reinforcing phases (usually ceramics, whiskers or fibers) in multi-principal element metal matrix to improve their desired properties from the standpoint of dispersion strengthening mechanism (Liu et al., 2019; Zhu et al., 2020b; Wang et al., 2021b; Wang et al., 2021c). The reinforcing phase may be coated to prevent its chemical reaction with the matrix (Sharma et al., 2020). It is noteworthy that the use of HEAs as matrix in metal-based composites is still in the early stage (Sun et al., 2022). HEAs usually contain multi-principal elements in high concentration, thereby hindering their industrial application as bulk materials because of their higher cost compared to the conventional alloys (Fu et al., 2017; Wang et al., 2021b). However, their application as coatings have received considerable research interest because of the wide field of application and relatively cheaper cost of thin films (Li et al., 2018c). However, the hardness of HEAs coatings is usually relatively low, hence, their application as coatings requires enhanced hardness and wear resistance, which could be achieved by the addition of hard phases (Wang et al., 2021b; Guan et al., 2021). Wang et al. (2021b) prepared a HEA composite coating from titanium powder, C_3N_4 powder and $Cr_{20}Cu_{20}Fe_{20}Ni_{20}Al_{20}$ by plasma transfer arc cladding technique and studied the hardness, wear properties and microstructural features of the HEA composite coating using microhardness tester, dry wear test multifunctional tribometer, SEM, TEM and EDS. The results showed that the microhardness of the composite coating was 3.33 and 127.4 times higher than those of the Q235 steel substrate and the unreinforced HEA. The wear resistance of the composite coatings was 3.03 and 8.06 times greater than the monolithic HEA and the Q235 steel substrate. The coating exhibited good interfacial bonding with the substrate. Microstructural examination revealed that the coating contains body-centred cubic matrix grains with intergranular cuboidal nanoprecipitates that have face-centred cubic Ti(C, N) particles distributed along its grain boundary and a small quantity of face-centred cubic Cu–rich phase around the intergranular nanoprecipitate. A core-shell structure was observed in the nanoprecipitates, with the core rich in nitrogen and the shell found to be carbon-rich. Along the same line, Zhu et al. (2020b) developed TiN and Al_2O_3 reinforced CoCrFeNiMn HEA composite through the plasma cladding method. The reinforcements were prepared from high purity commercial Al, TiO_2 and BN precursors. The microstructure, chemical composition, hardness and wear properties were determined using field emission scanning electron microscopy, EDS, XRD, Vicker hardness tester and multi-functional tribometer. The microstructural examination revealed that the as-developed coating has a single face-centred cubic phase with TiN–Al_2O_3 as crystal dendrites associated with the Cr-B rich interdendritic phase. The hardness and wear resistance of the HEA composite coating were compared with those of the pure HEA and found to be 17.6% and 12.5% better. It was found that the reinforcing phases play significant roles in restricting the adhesive wear and encouraged the steady-state friction of the HEA composite coating throughout the sliding process. Cui et al. (2022) produced a corrosion resistance CeO_2 reinforced FeCoNiCrMo HEA composite coating by laser cladding technique. The composite coating was developed for TC4 titanium alloy surface coating. The morphology, microhardness and corrosion resistance of the composite coating were investigated using XRD, EDS, SEM, Vickers hardness tester and electrochemical workstation. The result revealed that the introduction of the CeO_2 powder to the HEA matrix reduced the coating sensitivity to crack. In addition, the introduction of the reinforcing phase to the HEA matrix did not change its body-centred cubic phase structure. Moreover, the microstructural examination showed that the CeO_2 was evenly distributed at the grain boundary, thereby refining the grains. This phenomenon improved the strength and toughness of the HEA composite coating. Due to this improvement, the microhardness of the coating increased 2.7 times than that of the TC4 titanium alloy substrate. The corrosion behaviour of the substrate, pure HEA and composite coating were examined, and

TABLE 4 Alloy-based electrocatalyst and their composites.

Electrocatalyst	Research aim	Fabrication method	Activity	Durability	Reference
CoNi@N-GCNT	Production of transition metal-based CoNi alloy supported on nitrogen-doped graphite carbon nanotube	Freeze drying	Onset potential of 0.9V and half-wave potential of 0.84V	No loss in current density after 10,000 potential cycles	Niu et al. (2021)
Ti_4O_7/Mxene	Development of non-precious metal-based nanocomposite electrocatalyst	Hydrothermal followed by carbothermal reaction	Onset potential of 0.91V and half-wave potential of 0.72V	35% loss in current density after 80,000 s	Wei et al. (2023)
PdNi nanowire	Synthesis of untrathin PdNi nanowire as electrocatalyst for ORR.	Hydrothermal reaction	Exhibited half-wave potential of 0.95V	29% ECSA loss after 200,000 potential cycles	Sahoo et al. (2022)
PdBP	Preparation of ternary alloy nanosphere as electrocatalyst for ORR.	Soft templating synthesis	Recorded mass activity of 1.45 mg_{pd}^{-1}	32.1% loss in mass activity after cycling for 5000s	Lv et al. (2019a)
MnO/CoMn@N-doped graphite composite	Fabrication of CoMn alloy coated with nitrogen doped carbon and MnO as composite electrocatalyst for OER and ORR.	Annealing of prusian blue analogue	Onset potential of 0.91V and half-wave potential of 0.76V	16% loss of its initial current density after continuous operation for 40000s	Deng et al. (2019)
$Fe_2Co_2Ni_2$/N-CNT	Development of ternary transition metal alloy embedded nitrogen doped carbon nanotube as electrocatalysts for ORR.	Solvothermal synthesis	0nset potential of 0.81V and half-wave 0.75V	4.5% loss in current density after 25000s cyclic test	Wang et al. (2021d)
Rh2.6Fe3Co2.6@NG	Synthesis of bifunctional rhodium, iron and cobalt alloy nanoparticles electrocatalyst anchored on nitrogen doped graphene for HER and ORR.	Sequential annealing and substitution reaction	Onset potential of 0.98V and half-wave potential of 0.82V	Positive shift in half-wave potential by 9 mV after 5000 cycles	Jiang et al. (2021)
$Pt(Fe,Co,Ni)_3$/C	Production of low Pt structurally ordered quaternary alloy electrocatalyst for ORR.	Spray dehydration and annealing process	Exhibited mass activity of 3.189 mA μg_{Pt}^{-1}	17% loss in mass activity after 10,000 potential cycles	Wang et al. (2019a)
PtNiRhMo nanoalloy	Preparation of octahedral shaped PtNi doped with rhodium and molybdenum as electrocatalyst for ORR.	Solvothermal synthesis	Recorded mass activity of 1.53 A g_{pt}^{-1}	NA	Hornberger et al. (2022)
PtFe/Pt intermetallic compound	Preparation of atomically ordered Pt-based intermetallic compound as electrocatalyst for ORR.	Wet impregnation method	Exhibited mass activity of 0.92 A mg_{pt}^{-1}	24% loss in mass activity after 10,000 potential cycles	Song et al. (2022)
$FeNi_3$@NC intermetallic compound	Development of intermetallic compound embedded in nitrogen doped carbon as bifunctional electrocatalyst for OER and ORR.	Freeze drying followed by annealing	Recorded 0.86V half-wave potential	Positive shift in half-wave potential by 6 mV after 3000 cycles	Chen et al. (2020)
Pt_5La intermetallic compound	Alloying Pt with early transition metal to produce intermetallic compound as durable electrocatalyst for ORR.	Solvothermal method	Exhibited mass activity of 0.49 A mg_{pt}^{-1}	Loss 6.1% of initial value of mass activity after 30,000 potential cycles	Zhu et al. (2022)
FeCoNiMnCr@N-CNT	Development of FeCoNiMnCr HEA nanoparticles grafted on nitrogen-doped carbon nanotubes as efficient electrocatalyst for ORR.	Solvothermal method	Onset potential of 0.95V and half-wave potential of 0.8V	10% loss in initial value of current density after 14 h of continuous operation	Nandan et al. (2022)
FeCoNiCuMn/NCNS	Utilization of the synergistic effect of HEA nanoparticles formed on nitrogen doped carbon nanosheet as bifunctional electrocatalyst of nitrite sensing and ORR.	Confinement growth method	Half-wave potential of 0.87V	Negligible loss in initial value of current density after 3000 potential cycles	Gao et al. (2022)
AlCuNiPtMn nanoparticles	Fabrication of self-supported AlCuNiPtMn nanoparticles HEA as durable electrocatalyst for ORR.	De-alloying method	Exhibited mass activity of 3.5 A mg^{-1}	No loss in mass activity after 30,000 potential cycles	Li et al. (2020b)

it was found that corrosion products were deposited on the TC4 titanium substrate. Pitting corrosion was observed in the pure HEA, however, the addition of CeO_2 enhanced the formation of higher density of stable passive film that significantly inhibited the pitting corrosion.

The use of HEA composites as coatings has been considerably explored, however, their application for catalytic purposes which are equally a surface phenomenon have not been well investigated. Hence, the authors of this review are currently investigating the potentials of HEA composites as self-supported electrocatalysts for ORR in PEMFC.

Table 4 summarises alloy-based electrocatalysts and their composites.

2.4 Single-atom electrocatalysts

This is a novel brand of electrocatalyst represented by the acronym M-N-C, where M is usually a transition metal and N-C is carbonaceous material doped with nitrogen (Xu et al., 2018). The electrocatalyst has shown promising optimum atomic efficiency, outstanding intrinsic activity, high electrical conductivity, large surface area, well-defined structure with composition and configuration that can serve as an alternative substitute to the pricy precious metal-based electrocatalyst for ORR in PEMFC (Han et al., 2020; Zhang et al., 2020; Zhang and Guan, 2020; Chen et al., 2021). Single-atom electrocatalyst is synthesised by the pyrolysis of transition metal with doped-carbonaceous materials, a process that covalently anchors well dispersed metal particles at an atomic scale on suitable support. The resulting electrocatalyst thereby exhibit exceptional activity and stability for specific reaction (Hou et al., 2020a). The multiscale tunability of a single atom electrocatalyst facilitates increasing active sites density with enhanced activity, stability, anti-poisoning properties and ultra-high affinity for oxygen (Zhu et al., 2018). (Yang et al., 2019) synthesised two-dimensional conjugated single atom electrocatalyst consisting of 10 wt% iron and 0.73 wt% cobalt atoms anchored on phthalocyanine macrocycles. The electrocatalyst was synthesised by pyrolysis-free one step ball milling of polyphthalocyanine and showed excellent ORR mass activity of 47 mAmg $^{-1}$ that was 6.4 times superior to that of commercial Pt/C with no appreciable loss in stability after 100 h of operation. Ding et al. (2020a) designed and synthesised an atomically dispersed Fe-N_4/C single atom electrocatalyst *via* an organic solution esterification process followed by melamine treatment to introduce nitrogen and restrict the migration of metal particles. ORR test was conducted on the single atom electrocatalyst and revealed a half-wave potential of 0.78 V. The electrocatalyst also showed a 17% loss in current density after 7 h of continuous polarization in acidic condition. (Xu et al., 2021). developed a single atom copper anchored on graphite foam doped with sulphur and nitrogen synthesised through underpotential deposition strategy. The single atom electrocatalyst showed outstanding ORR activity recording half wave potential of 0.862 V with calculated mass activity of 5.71 Amg_{Cu}^{-1}. The stability test revealed that the electrocatalyst retains 98% of its initial current density after 20,000s under continuous potential of 0.85 V. Chen et al. (2020) reported a single atom tungsten dispersed on nitrogen doped carbon nanosheet produced by modulated pyrolysis method. The electrocatalyst showed notable electrocatalytic activity with half wave potential of 0.88 V and mass activity of 0.63 Amg^{-1} at 0.9 V. The electrocatalyst only loss 13.9% of its mass activity after 10,000 sweeping cycles of cyclic voltammetry durability test. Wan et al. (2019) developed a concave Fe–N–C single-atom catalyst possessing an enhanced external surface area and porosity. The Concave-shaped Fe–N–C electrocatalyst was synthesised by preheating mesoporous SiO_2-coated ZIF-8 (Z8) metal-organic framework at 650°C under argon-controlled atmosphere, the silica layer was etched off to form a concave-shaped host having a negative zeta potential and larger micropores. The electrocatalysts displayed high current density of 0.047 A cm $^{-2}$ at 0.88 V under 1.0 bar H_2–O_2 that stems from the high density of active sites, which was achieved by exposing Fe–N_4 moieties and enhanced mass transportation of the mesoporous electrocatalyst. Furthermore, Zhu et al. (2021) reported a nitrogen doped carbon embedded rare-earth single-cerium-atom metal–organic framework electrocatalyst. The electrocatalyst was synthesised *via* hard–template approach and showed comparable ORR activity but inadequate stability to that of commercial Pt–C catalyst in PEMFC application. The result of the study revealed half-wave potential of 0.862 V in ORR and 0.525 W cm $^{-2}$ power density under 2.0 bar hydrogen–oxygen in fuel cell test.

2.5 Metal-free electrocatalysts

Heteroatom-doped carbon materials have demonstrated excellent ORR activity that is comparable or even better than that of commercial Pt-C electrocatalyst because of their extraordinary large specific surface area, good electrical conductivity and excellent durability under unfavourable conditions (Hu and Dai, 2019; Ma et al., 2019). Research progress have been made in developing highly stable and durable heteroatom-doped advanced carbon electrocatalysts such as iodine-doped graphene (Marinoiu et al., 2018), boron-doped carbon nanotube or graphene (Sawant et al., 2022), sulphur-doped graphene (Garino et al., 2021) and phosphorus-doped graphite layers (Shimoyama et al., 2015). It was also observed that doping advanced carbon materials with more than one heteroatom showed better ORR activity (Gao et al., 2019). For instance, Sun et al. (2018) co-doped carbon nanomaterial with boron and nitrogen to produce a very active, stable and inexpensive metal-free bifunctional electrocatalyst for ORR and OER. The catalyst was prepared by pyrolysis of precursors under ammonia atmosphere and exhibited excellent activity and stability for both ORR and OER. The catalyst showed an onset potential of 0.98 V for ORR in alkaline medium, which is similar to that of Pt-C catalysts. On the other hand, the onset potential recorded in acidic medium was 0.81 V for a 4–electron transfer process. The outstanding performance of the catalyst was attributed to the joint positive effect of rich carbon defects and the heteroatomic co-dopants. Duraisamy et al. (2022) synthesised a nitrogen-sulphur dual heteroatom doped mesoporous carbon electrocatalyst using 2D amorphous silica as support material and L-cysteine as nitrogen and sulphur precursor. The electrocatalyst showed high concentration of defective sites on the surface of the mesoporous carbon that favours improved ORR performance with onset potential of 0.78 V, half-wave potential of 0.68 V and current density of 2.8 $mAcm^{-2}$. Li et al. (2020a) co-doped porous carbon with nitrogen and sulphur for ORR and CO_2RR catalytic applications. The electrocatalyst was prepared by pyrolysis of glucosamine hydrochloride and thiocyanuric acid precursors using hard silica dioxide templates. The co-doped carbon electrocatalyst showed enhanced activity and selectivity with the porous structure exposing abundant active sites to reaction species which resulted in increased activity of the electrocatalyst. The authors reported that the electrocatalyst exhibited excellent ORR

activities in both acidic and alkaline media and is suitable for PEMFC application.

Despite the significant research progress in developing advanced carbon based electrocatalysts, the fundamental understanding of the doping effects and structural diversity of such catalysts remain unclear, particularly in terms of the molecular structures of active sites and the specific doping effects that control electrocatalytic reactions (Zhu et al., 2020c; Wu et al., 2021; Chattopadhyay et al., 2022). Many factors hinder the understanding of these phenomena, which include the sophistication of reactions at electrochemical interfaces; a lack of efficient strategies for precisely controlling the structures of active sites for directing catalytic reactions; and troubles inspecting and understanding the electrode-electrolyte interfaces through direct *in situ* observations. (Hu and Dai, 2019; Lai et al., 2022).

2.6 Catalyst supports

Most electrocatalysts used in fuel cell rely on support materials for mass transfer and water management (Ziv et al., 2018). Loading the electrocatalyst on high surface area support enhanced its catalytic activity and durability by increasing its electrochemical surface area (Hou et al., 2020b). Many carbon-based materials such as graphene, carbon nanotube, carbon black and mesoporous carbon have been used as catalyst supports due to their high surface area and electrical conductivity (Qiao et al., 2019). However, due to carbon corrosion that leads to the loss of ECSA, other electrocatalysts support materials such as transition metal oxides, carbides and nitrides have been adopted because of their excellent stability in harsh conditions (Samad et al., 2018). The presence of surface functional groups that promote catalyst support interaction, corrosion resistance, low surface poisoning, electrochemical stability, high electrical conductivity, a large surface area and a porous structure that improves the triple phase boundary are the characteristics of a good catalyst support material (Fashedemi et al., 2022). Asset et al. (2018) attempted to improve the ORR kinetics by investigating the effect of carbon supports' structure, texture and chemistry on the morphological properties, stability, and ORR activity of porous hollow Pt-Ni nanoparticles carbon black, carbon nanotubes, graphene nanosheets, and carbon xerogel. The nanomaterials had varying degrees of graphitisation, surface areas, and surface functionalisation. The inner and outer diameters of the supported porous hollow Pt-Ni/C nanoparticles were found to decrease as the surface area of the carbon mesopore increased. Despite their differences, the nanomaterials demonstrated comparable morphological properties and electrocatalytic activities for the ORR. The simulated electrochemical potential of PEMFC was used to evaluate the stability of the synthesised electrocatalysts. Identical location transition electron microscopy (IL-TEM) and electrochemical method showed that degradation in carbon nanotube, carbon xerogel and graphene nanosheet were by carbon corrosion to carbon dioxide while carbon black showed carbon surface oxidation to carbon monoxide. Souza et al. (2018) added niobium pentoxide (Nb_2O_5) and tungsten carbide (WC) separately to Pt/C electrocatalyst by impregnation method followed by heat treatment to modify its carbon content for improved stability. Both modified electrocatalysts were analysed by X-ray diffraction (XRD), energy dispersive X-ray spectroscopy (EDS), IL-TEM and cyclic voltammetry (CV). Results of the analyses were compared with those of commercial Pt/C electrocatalyst. The authors found two phenomena that led to ECSA loss in the electrocatalysts; which are Pt particle agglomeration and the loss of catalyst materials due to the degradation of carbon support. It was observed that WC addition increased the electrocatalyst particles' corrosion and detachment, however, the addition of Nb_2O_5 was more effective in improving the Pt/C electrocatalyst stability. More so, Yuan et al. (2022) synthesised a dandelion-like structured titanium nitride nanospheres as a non-carbon-based catalyst support for Pt nanoparticles, which were deposited on the dendritic structured titanium nitride by an electrochemical pulse deposition method. The catalyst recorded ORR mass and specific activity of 0.44 mA g^{-1} and 0.33 mA cm^{-2} at 0.9 V. At similar test conditions, the catalysts demonstrated superior stability to the commercial Pt/C catalysts recording 61% of the initial activity after 3000 repeated runs. In another study, Islam et al. (2019) attempted to address the carbon corrosion problem by developing a silica-coated carbon nanofibers catalyst support for Pt particles. Platelet-type carbon nanofibers were uniformly coated with silica using the hydrolysis method. Thereafter, the Pt was then deposited on the silica coating rather than carbon nanofibers. Accelerated degradation test was conducted on the silica-coated carbon nanofibers Pt catalyst and the result showed that the silica coated catalyst was more durable than Pt/C nanofibers catalyst under potential cycling. After 30,000 potential cycles, it was observed that silica coated carbon nanofiber catalyst lost 11% of its ECSA, while the loss of ECSA recorded by its uncoated Pt/C nanofiber counterpart was 21%.

3 Conclusion and recommendation

This review clearly showed that various authors asserted that the state-of-the-art Pt/C electrocatalyst typically impose cost ineffectiveness on PEMFC. In addition, Pt/C electrocatalyst suffers from rapid degradation during prolonged PEMFC operation, thereby, posing significant reliability challenge of the device. The rapid degradation is attributed to the dissolution, migration or aggregation of Pt as well as the carbon support corrosion leading to ECSA loss of the electrocatalysts and the eventual deterioration of electrocatalyst's activity during long-term operation. Many studies have been conducted to unveil other low-cost materials that can serve as active catalyst constituents to augment or replace the precious metal loading in the state-of-the-art electrocatalyst used in PEMFC. Efforts have also been made to modify or replace the carbon support with other corrosion resistance and highly stable materials. In the light of these, the following recommendations are made for further research in various emerging electrocatalysts:

1. Bimetallic, ternary and quarterly alloys electrocatalysts serve a pivotal role as emerging electrocatalysts for ORR in PEMFC. Significant progress has been made in the fabrication and characterisation of these alloys. However, the effective control of their composition, morphology and particle sizes could pave a

way for their commercial application in PEMFC. An understanding of the tunability of elemental composition, morphology and particles size could be used to control these alloys' microstructures thereby positively influencing their activity and stability towards ORR in PEMFC. Tuning alloy electrocatalyst composition has significant effect on its ORR activity and stability. Consequently, effect of elemental composition and ratios on various alloy electrocatalyst could be investigated. Some researchers have asserted that the ORR mass activity of alloy-based electrocatalyst is inversely proportional to its particle size, therefore, advancing design strategy to fabricate nanostructured alloy electrocatalysts could expose more active sites thereby improving catalytic mass activity. To investigate the assertion that alloy electrocatalyst activity has direct correlation to its particles shape, the effect of different particle shapes on various alloy electrocatalyst could be studied. In addition, considering a preferred crystallographic orientation for alloy particles in electrocatalyst can be a promising strategy for achieving its high performance for ORR in PEMFC.

2. HEA electrocatalysts have been suggested to be promising candidates that will address the existing limitations in the state-of-the-art electrocatalyst. However, their complex catalysts' structure-activity relationship still needs to be unravelled. In addition, only a small portion of the compositional space of HEAs has been investigated, therefore, there exist a vast possibility of HEA electrocatalysts to be explored. Understanding elemental interactions in HEAs is also necessary in order to predict suitable elemental combinations for PEMFC catalytic application. Research is required to determine the compositional limits of elemental choices needed for specific phase formation in HEA electrocatalysts. The effect of each element on the stability of HEA electrocatalysts need to be studied, as well as how to tune each element to achieve physical or chemical stability. Furthermore, the synergistic interactions between HEA and emerging electrocatalyst support materials can be investigated by developing their self-supported HEA-based composite electrocatalysts. More so, heteroatoms such as nitrogen, boron, sulphur and phosphorus could be introduced into the interstices of transition metals based high entropy alloys to offer the advantages of a self-supported electrocatalysts with surface that enhances accelerated electron transfer, high activity and stability that can meet PEMFC performance requirements at low cost.
3. Single atom electrocatalysts have the potential of offering high density of active sites that could speed up the sluggish kinetics of ORR in PEMFC. However, the research progress of this emerging electrocatalyst still needs to be consolidated in the areas of its synthesis and characterisation to achieve its commercial application in PEMFC. Synthesis of single atom electrocatalysts require expensive precursors and equipment, hence, there is a need to find alternative low-cost precursors and facile synthesis method for the large-scale commercialisation of the electrocatalyst. In addition, developing porous support materials that will enhance accessibility to single atom actives sites could greatly enhance the electrocatalysts activity and stability. More so, the support materials should possess high conductivity and corrosion resistance to address the undesired Fenton reaction that characterises single atom electrocatalyst in acidic medium. Designing and synthesising single atom electrocatalyst with dual adjacent metal atoms could result in synergistic effect that significantly improve the ORR activity and stability. Lastly, there is a need for *in situ* characterisation techniques for single atom electrocatalyst to identify and understand the central metal interactions with oxygen containing species at electrocatalyst working potential conditions.
4. The catalytic properties of metal-free electrocatalyst is based on doping carbonaceous materials with heteroatoms which serve as defects that enhance promising catalytic performance. Developing metal-free electrocatalyst with hierarchical porous structure could be beneficial in providing multiple active sites, however, there is a need for facile fabrication techniques for this structure due to the uncontrollability of the pyrolysis process currently used in its synthesis. Further research is required to understand the nature of the active sites in the emerging electrocatalyst to facilitate its future large-scale commercialisation and catalytic application in PEMFC. Sophisticated *operando* characterisation techniques such as the use of *in situ* equipment or on-line monitoring are required to unravel the nature of the active sites in this electrocatalyst in order to gain insight on the requirements for its structure-activity and stability correlations and the improvement strategies that will engender its commercial application in PEMFC.

Author contributions

AA contributed to the conceptualization and writing of the review draft. AP, OP, NM, and MA contributed to the writing of the review, editing and funding.

Acknowledgments

The authors acknowledge the funding support of the Department of Chemical, Metallurgical and Materials Engineering, Faculty of Engineering and Built Environment. Tshwane University of Technology, Pretoria. South Africa.

Conflict of interest

The authors declare that the research was conducted in the absence of any commercial or financial relationships that could be construed as a potential conflict of interest.

Publisher's note

References

Abbas, Q., Mirzaeian, M., Hunt, M. R., Hall, P., and Raza, R. (2020). Current state and future prospects for electrochemical energy storage and conversion systems. *Energies* 13, 5847. doi:10.3390/en13215847

Abbasi, K. R., Shahbaz, M., Zhang, J., Irfan, M., and Alvarado, R. (2022). Analyze the environmental sustainability factors of China: The role of fossil fuel energy and renewable energy. *Renew. Energy* 187, 390–402. doi:10.1016/j.renene.2022.01.066

Abdelkareem, M. A., Elsaid, K., Wilberforce, T., Kamil, M., Sayed, E. T., and Olabi, A. (2021a). Environmental aspects of fuel cells: A review. *Sci. Total Environ.* 752, 141803. doi:10.1016/j.scitotenv.2020.141803

Abdelkareem, M. A., Wilberforce, T., Elsaid, K., Sayed, E. T., Abdelghani, E. A. M., and Olabi, A. G. (2021b). Transition metal carbides and nitrides as oxygen reduction reaction catalyst or catalyst support in proton exchange membrane fuel cells (PEMFCs). *Int. J. Hydrogen Energy* 46, 23529–23547. doi:10.1016/j.ijhydene.2020.08.250

Alias, M., Kamarudin, S., Zainoodin, A., and Masdar, M. (2020). Active direct methanol fuel cell: An overview. *Int. J. Hydrogen Energy* 45, 19620–19641. doi:10.1016/j.ijhydene.2020.04.202

Antolini, E. (2011). The stability of molten carbonate fuel cell electrodes: A review of recent improvements. *Appl. energy* 88, 4274–4293. doi:10.1016/j.apenergy.2011.07.009

Asset, T., Job, N., Busby, Y., Crisci, A., Martin, V., Stergiopoulos, V., et al. (2018). Porous hollow PtNi/C electrocatalysts: Carbon support considerations to meet performance and stability requirements. *ACS Catal.* 8, 893–903. doi:10.1021/acscatal.7b03539

Bai, L. (2018). Synthesis of PtRu/Ru heterostructure for efficient methanol electrooxidation: The role of extra Ru. *Appl. Surf. Sci.* 433, 279–284. doi:10.1016/j.apsusc.2017.10.026

Batchelor, T. A., Pedersen, J. K., Winther, S. H., Castelli, I. E., Jacobsen, K. W., and Rossmeisl, J. (2019). High-entropy alloys as a discovery platform for electrocatalysis. *Joule* 3, 834–845. doi:10.1016/j.joule.2018.12.015

Bhatt, M. D., and Lee, J. Y. (2020). Advancement of platinum (Pt)-free (non-Pt precious metals) and/or metal-free (non-precious-metals) electrocatalysts in energy applications: A review and perspectives. *Energy & Fuels* 34, 6634–6695. doi:10.1021/acs.energyfuels.0c00953

Bhoyate, S. D., Kim, J., De Souza, F. M., Lin, J., Lee, E., Kumar, A., et al. (2023). Science and engineering for non-noble-metal-based electrocatalysts to boost their ORR performance: A critical review. *Coord. Chem. Rev.* 474, 214854. doi:10.1016/j.ccr.2022.214854

Bogdanov, D., Ram, M., Aghahosseini, A., Gulagi, A., Oyewo, A. S., Child, M., et al. (2021). Low-cost renewable electricity as the key driver of the global energy transition towards sustainability. *Energy* 227, 120467. doi:10.1016/j.energy.2021.120467

Borup, R. L., Kusoglu, A., Neyerlin, K. C., Mukundan, R., Ahluwalia, R. K., Cullen, D. A., et al. (2020). Recent developments in catalyst-related PEM fuel cell durability. *Curr. Opin. Electrochem.* 21, 192–200. doi:10.1016/j.coelec.2020.02.007

Cao, J., Cao, H., Shen, J., Wang, F., and Zhu, H. (2020). Impact of CuFe bimetallic core on the electrocatalytic activity and stability of Pt shell for oxygen reduction reaction. *Electrochimica Acta* 350, 136205. doi:10.1016/j.electacta.2020.136205

Chandran, P., Ghosh, A., and Ramaprabhu, S. (2018). High-performance Platinum-free oxygen reduction reaction and hydrogen oxidation reaction catalyst in polymer electrolyte membrane fuel cell. *Sci. Rep.* 8, 3591. doi:10.1038/s41598-018-22001-9

Chattopadhyay, J., Pathak, T. S., and Pak, D. (2022). Heteroatom-doped metal-free carbon nanomaterials as potential electrocatalysts. *Molecules* 27, 670. doi:10.3390/molecules27030670

Chen, X., Si, C., Gao, Y., Frenzel, J., Sun, J., Eggeler, G., et al. (2015). Multi-component nanoporous platinum–ruthenium–copper–osmium–iridium alloy with enhanced electrocatalytic activity towards methanol oxidation and oxygen reduction. *J. Power Sources* 273, 324–332. doi:10.1016/j.jpowsour.2014.09.076

Chen, Z., Gong, W., Liu, Z., Cong, S., Zheng, Z., Wang, Z., et al. (2019). Coordination-controlled single-atom tungsten as a non-3d-metal oxygen reduction reaction electrocatalyst with ultrahigh mass activity. *Nano Energy* 60, 394–403. doi:10.1016/j.nanoen.2019.03.045

Chen, D., Zhu, J., Mu, X., Cheng, R., Li, W., Liu, S., et al. (2020). Nitrogen-Doped carbon coupled FeNi3 intermetallic compound as advanced bifunctional electrocatalyst for OER, ORR and zn-air batteries. *Appl. Catal. B Environ.* 268, 118729. doi:10.1016/j.apcatb.2020.118729

Chen, M. X., Tong, L., and Liang, H. W. (2021). Understanding the catalytic sites of metal–nitrogen–carbon oxygen reduction electrocatalysts. *Chemistry–A Eur. J.* 27, 145–157. doi:10.1002/chem.202002427

Chen, L., Msigwa, G., Yang, M., Osman, A. I., Fawzy, S., Rooney, D. W., et al. (2022a). Strategies to achieve a carbon neutral society: A review. *Environ. Chem. Lett.* 20, 2277–2310. doi:10.1007/s10311-022-01435-8

Chen, X., Niu, K., Xue, Z., Liu, X., Liu, B., Zhang, B., et al. (2022b). Ultrafine platinum nanoparticles supported on N, S-codoped porous carbon nanofibers as efficient multifunctional materials for noticeable oxygen reduction reaction and water splitting performance. *Nanoscale Adv.* 4, 1639–1648. doi:10.1039/d2na00014h

Chung, D. Y., Park, S., Lee, H., Kim, H., Chung, Y.-H., Yoo, J. M., et al. (2020). Activity–stability relationship in Au@ Pt nanoparticles for electrocatalysis. *ACS Energy Lett.* 5, 2827–2834. doi:10.1021/acsenergylett.0c01507

Cruz-Martínez, H., Tellez-Cruz, M., Guerrero-Gutiérrez, O., Ramírez-Herrera, C., Salinas-Juárez, M., Velázquez-Osorio, A., et al. (2019). Mexican contributions for the improvement of electrocatalytic properties for the oxygen reduction reaction in PEM fuel cells. *Int. J. hydrogen energy* 44, 12477–12491. doi:10.1016/j.ijhydene.2018.05.168

Cruz-Martínez, H., Rojas-Chávez, H., Matadamas-Ortiz, P., Ortiz-Herrera, J., López-Chávez, E., Solorza-Feria, O., et al. (2021). Current progress of Pt-based ORR electrocatalysts for PEMFCs: An integrated view combining theory and experiment. *Mater. Today Phys.* 19, 100406. doi:10.1016/j.mtphys.2021.100406

Cui, C., Wu, M., Miao, X., Zhao, Z., and Gong, Y. (2022). Microstructure and corrosion behavior of CeO2/FeCoNiCrMo high-entropy alloy coating prepared by laser cladding. *J. Alloys Compd.* 890, 161826. doi:10.1016/j.jallcom.2021.161826

Deng, C., Wu, K.-H., Scott, J., Zhu, S., Amal, R., and Wang, D.-W. (2019). Ternary MnO/CoMn alloy@ N-doped graphitic composites derived from a bi-metallic pigment as bi-functional electrocatalysts. *J. Mater. Chem. A* 7, 20649–20657. doi:10.1039/c9ta08016c

Ding, R., Liu, Y., Rui, Z., Li, J., Liu, J., and Zou, Z. (2020a). Facile grafting strategy synthesis of single-atom electrocatalyst with enhanced ORR performance. *Nano Res.* 13, 1519–1526. doi:10.1007/s12274-020-2768-y

Ding, Z., Bian, J., Shuang, S., Liu, X., Hu, Y., Sun, C., et al. (2020b). High entropy intermetallic–oxide core–shell nanostructure as superb oxygen evolution reaction catalyst. *Adv. Sustain. Syst.* 4, 1900105. doi:10.1002/adsu.201900105

Deng, Z., Pang, W., Gong, M., Jin, Z., and Wang, X. (2022). Revealing the role of mo doping in promoting oxygen reduction reaction performance of Pt3Co nanowires. *J. Energy Chem.* 66, 16–23. doi:10.1016/j.jechem.2021.06.018

Do, M., Ngo, H., Guo, W., Liu, Y., Chang, S., Nguyen, D., et al. (2018). Challenges in the application of microbial fuel cells to wastewater treatment and energy production: A mini review. *Sci. Total Environ.* 639, 910–920. doi:10.1016/j.scitotenv.2018.05.136

Du, M., Li, X., Pang, H., and Xu, Q. (2022). Alloy electrocatalysts. *EnergyChem*, 100083. doi:10.1016/j.enchem.2022.100083

Duraisamy, V., Venkateshwaran, S., Thangamuthu, R., and Kumar, S. M. S. (2022). Hard template derived N, S dual heteroatom doped ordered mesoporous carbon as an efficient electrocatalyst for oxygen reduction reaction. *Int. J. Hydrogen Energy* 47, 40327–40339. doi:10.1016/j.ijhydene.2022.03.250

Egeland-Eriksen, T., Hajizadeh, A., and Sartori, S. (2021). Hydrogen-based systems for integration of renewable energy in power systems: Achievements and perspectives. *Int. J. hydrogen energy* 46, 31963–31983. doi:10.1016/j.ijhydene.2021.06.218

Erikson, H., Antoniassi, R. M., Solla-Gullón, J., Torresi, R. M., Tammeveski, K., and Feliu, J. M. (2022). Oxygen electroreduction on small (<10 nm) and {100}-oriented Pt nanoparticles. *Electrochimica Acta* 403, 139631. doi:10.1016/j.electacta.2021.139631

Esfahani, R. A. M., Gavidia, L. M. R., García, G., Pastor, E., and Specchia, S. (2018). Highly active platinum supported on Mo-doped titanium nanotubes suboxide (Pt/TNTS-Mo) electrocatalyst for oxygen reduction reaction in PEMFC. *Renew. Energy* 120, 209–219. doi:10.1016/j.renene.2017.12.077

Etesami, M., Oroujzadeh, M., and Mehdipour-Ataei, S. (2020). 3D nitrogen-doped carbon supported non-precious metals electrocatalyst for oxygen reduction reaction. *Mol. Catal.* 485, 110834. doi:10.1016/j.mcat.2020.110834

Etesami, M., Mehdipour-Ataei, S., Somwangthanaroj, A., and Kheawhom, S. (2021). Recent progress of electrocatalysts for hydrogen proton exchange membrane fuel cells. *Int. J. Hydrogen Energy* 47, 41956. doi:10.1016/j.ijhydene.2021.09.133

Fan, L., Zhao, J., Luo, X., and Tu, Z. (2022). Comparison of the performance and degradation mechanism of PEMFC with Pt/C and Pt black catalyst. *Int. J. Hydrogen Energy* 47, 5418–5428. doi:10.1016/j.ijhydene.2021.11.135

Fashedemi, O. O., Bello, A., Adebusuyi, T., and Bindir, S. (2022). Recent trends in Carbon support for improved performance of Alkaline Fuel cells. *Curr. Opin. Electrochem.* 36, 101132. doi:10.1016/j.coelec.2022.101132

Ferriday, T. B., and Middleton, P. H. (2021). Alkaline fuel cell technology-A review. *Int. J. hydrogen energy* 46, 18489–18510. doi:10.1016/j.ijhydene.2021.02.203

Floriano, R., Zepon, G., Edalati, K., Fontana, G. L., Mohammadi, A., Ma, Z., et al. (2020). Hydrogen storage in TiZrNbFeNi high entropy alloys, designed by thermodynamic calculations. *Int. J. Hydrogen Energy* 45, 33759–33770. doi:10.1016/j.ijhydene.2020.09.047

Fu, X., Schuh, C. A., and Olivetti, E. A. (2017). Materials selection considerations for high entropy alloys. *Scr. Mater.* 138, 145–150. doi:10.1016/j.scriptamat.2017.03.014

Gao, K., Wang, B., Tao, L., Cunning, B. V., Zhang, Z., Wang, S., et al. (2019). Efficient metal-free electrocatalysts from N-doped carbon nanomaterials: Mono-doping and co-doping. *Adv. Mater.* 31, 1805121. doi:10.1002/adma.201805121

Gao, P., Zhao, S., Qu, X., Qian, X., Duan, F., Lu, S., et al. (2022). Bifunctional high-entropy alloys for sensitive nitrite detection and oxygen reduction reaction. *Electrochimica Acta* 432, 141160. doi:10.1016/j.electacta.2022.141160

Garino, N., Sacco, A., Chiodoni, A., Pirri, C. F., and Castellino, M. (2021). Microwave-Assisted synthesis of nitrogen and sulphur doped graphene decorated with antimony oxide: An effective catalyst for oxygen reduction reaction. *Materials* 15, 10. doi:10.3390/ma15010010

Garlyyev, B., Kratzl, K., Rück, M., Michalička, J., Fichtner, J., Macak, J. M., et al. (2019). Optimizing the size of platinum nanoparticles for enhanced mass activity in the electrochemical oxygen reduction reaction. *Angew. Chem. Int. Ed.* 58, 9596–9600. doi:10.1002/anie.201904492

George, E. P., Raabe, D., and Ritchie, R. O. (2019). High-entropy alloys. *Nat. Rev. Mater.* 4, 515–534. doi:10.1038/s41578-019-0121-4

Gewirth, A. A., Varnell, J. A., and Diascro, A. M. (2018). Nonprecious metal catalysts for oxygen reduction in heterogeneous aqueous systems. *Chem. Rev.* 118, 2313–2339. doi:10.1021/acs.chemrev.7b00335

Gilroy, K. D., Ruditskiy, A., Peng, H.-C., Qin, D., and Xia, Y. (2016). Bimetallic nanocrystals: Syntheses, properties, and applications. *Chem. Rev.* 116, 10414–10472. doi:10.1021/acs.chemrev.6b00211

Gong, M., Deng, Z., Xiao, D., Han, L., Zhao, T., Lu, Y., et al. (2019). One-nanometer-thick Pt3Ni bimetallic alloy nanowires advanced oxygen reduction reaction: Integrating multiple advantages into one catalyst. *Acs Catal.* 9, 4488–4494. doi:10.1021/acscatal.9b00603

Guan, H., Chai, L., Wang, Y., Xiang, K., Wu, L., Pan, H., et al. (2021). Microstructure and hardness of NbTiZr and NbTaTiZr refractory medium-entropy alloy coatings on Zr alloy by laser cladding. *Appl. Surf. Sci.* 549, 149338. doi:10.1016/j.apsusc.2021.149338

Guterman, V. E., Belenov, S. V., Alekseenko, A. A., Lin, R., Tabachkova, N. Y., and Safronenko, O. I. (2018). Activity and stability of Pt/C and Pt-Cu/C electrocatalysts. *Electrocatalysis* 9, 550–562. doi:10.1007/s12678-017-0451-1

Han, J., Bian, J., and Sun, C. (2020). Recent advances in single-atom electrocatalysts for oxygen reduction reaction. *Research* 2020, 9512763. doi:10.34133/2020/9512763

He, W., Xiang, Y., Xin, M., Qiu, L., Dong, W., Zhao, W., et al. (2022). Investigation of multiple commercial electrocatalysts and electrocatalyst degradation for fuel cells in real vehicles. *RSC Adv.* 12, 32374–32382. doi:10.1039/d2ra05682h

Hersbach, T. J., Garcia, A. C., Kroll, T., Sokaras, D., Koper, M. T., and Garcia-Esparza, A. T. (2021). Base-accelerated degradation of nanosized platinum electrocatalysts. *ACS Catal.* 11, 9904–9915. doi:10.1021/acscatal.1c02468

Hornberger, E., Klingenhof, M., Polani, S., Paciok, P., Kormányos, A., Chattot, R., et al. (2022). On the electrocatalytical oxygen reduction reaction activity and stability of quaternary RhMo-doped PtNi/C octahedral nanocrystals. *Chem. Sci.* 13, 9295–9304. doi:10.1039/d2sc01585d

Hou, C.-C., Wang, H.-F., Li, C., and Xu, Q. (2020a). From metal–organic frameworks to single/dual-atom and cluster metal catalysts for energy applications. *Energy & Environ. Sci.* 13, 1658–1693. doi:10.1039/c9ee04040d

Hou, J., Yang, M., Ke, C., Wei, G., Priest, C., Qiao, Z., et al. (2020b). Platinum-group-metal catalysts for proton exchange membrane fuel cells: From catalyst design to electrode structure optimization. *EnergyChem* 2, 100023. doi:10.1016/j.enchem.2019.100023

Hu, B., Yuan, J., Zhang, J., Shu, Q., Guan, D., Yang, G., et al. (2021). High activity and durability of a Pt–Cu–Co ternary alloy electrocatalyst and its large-scale preparation for practical proton exchange membrane fuel cells. *Compos. Part B Eng.* 222, 109082. doi:10.1016/j.compositesb.2021.109082

Hu, C., and Dai, L. (2019). Doping of carbon materials for metal-free electrocatalysis. *Adv. Mater.* 31, 1804672. doi:10.1002/adma.201804672

Huang, L., Zhang, X., Wang, Q., Han, Y., Fang, Y., and Dong, S. (2018). Shape-control of Pt–Ru nanocrystals: Tuning surface structure for enhanced electrocatalytic methanol oxidation. *J. Am. Chem. Soc.* 140, 1142–1147. doi:10.1021/jacs.7b12353

Huang, X.-Y., You, L.-X., Zhang, X.-F., Feng, J.-J., Zhang, L., and Wang, A.-J. (2019). -proline assisted solvothermal preparation of Cu-rich rhombic dodecahedral PtCu nanoframes as advanced electrocatalysts for oxygen reduction and hydrogen evolution reactions. *Electrochimica Acta* 299, 89–97. doi:10.1016/j.electacta.2019.01.002

Huang, L., Zaman, S., Tian, X., Wang, Z., Fang, W., and Xia, B. Y. (2021). Advanced platinum-based oxygen reduction electrocatalysts for fuel cells. *Accounts Chem. Res.* 54, 311–322. doi:10.1021/acs.accounts.0c00488

Hussain, S., Kongi, N., Erikson, H., Rähn, M., Merisalu, M., Matisen, L., et al. (2019). Platinum nanoparticles photo-deposited on SnO2-C composites: An active and durable electrocatalyst for the oxygen reduction reaction. *Electrochimica Acta* 316, 162–172. doi:10.1016/j.electacta.2019.05.104

Hussain, I., Lamiel, C., Sahoo, S., Ahmad, M., Chen, X., Javed, M. S., et al. (2022). Factors affecting the growth formation of nanostructures and their impact on electrode materials: A systematic review. *Mater. Today Phys.* 27, 100844. doi:10.1016/j.mtphys.2022.100844

Icaza-Alvarez, D., Jurado, F., Tostado-Véliz, M., and Arevalo, P. (2022). Decarbonization of the Galapagos Islands. Proposal to transform the energy system into 100% renewable by 2050. *Renew. Energy* 189, 199–220. doi:10.1016/j.renene.2022.03.008

Ioroi, T., Siroma, Z., Yamazaki, S., and Yasuda, K. (2019). Electrocatalysts for PEM fuel cells. *Adv. Energy Mater.* 9, 1801284. doi:10.1002/aenm.201801284

Islam, J., Kim, S.-K., Lee, E., and Park, G.-G. (2019). Durability enhancement of a Pt/C electrocatalyst using silica-coated carbon nanofiber as a corrosion-resistant support. *Int. J. Hydrogen Energy* 44, 4177–4187. doi:10.1016/j.ijhydene.2018.12.138

Jeerh, G., Zhang, M., and Tao, S. (2021). Recent progress in ammonia fuel cells and their potential applications. *J. Mater. Chem. A* 9, 727–752. doi:10.1039/d0ta08810b

Jiang, A., Chen, J., Liu, S., Wang, Z., Li, Q., Xia, D., et al. (2021). Intermetallic rhodium alloy nanoparticles for electrocatalysis. *ACS Appl. Nano Mater.* 4, 13716–13723. doi:10.1021/acsanm.1c03128

Jiao, K., Xuan, J., Du, Q., Bao, Z., Xie, B., Wang, B., et al. (2021). Designing the next generation of proton-exchange membrane fuel cells. *Nature* 595, 361–369. doi:10.1038/s41586-021-03482-7

Kishida, K., Harigai, T., Takikawa, H., and Hashimoto, T. (2021). Performance improvement of platinum-based electrocatalyst layer for PEFC by mixing single walled carbon nanotubes. *Denki Gakkai Ronbunshi, B (Online)* 141, 316–321. doi:10.1541/ieejpes.141.316

Kong, J., Qin, Y.-H., Wang, T.-L., and Wang, C.-W. (2020). Photodeposition of Pt nanoparticles onto TiO2@ CNT as high-performance electrocatalyst for oxygen reduction reaction. *Int. J. Hydrogen Energy* 45, 1991–1997. doi:10.1016/j.ijhydene.2019.11.016

Kong, Z., Zhang, D., Lu, Y., Yang, C., Du, S., Li, W., et al. (2021). Advanced cathode electrocatalysts for fuel cells: Understanding, construction, and application of carbon-based and platinum-based nanomaterials. *ACS Mater. Lett.* 3, 1610–1634. doi:10.1021/acsmaterialslett.1c00450

Kong, F., Wang, M., Huang, Y., Meng, G., Chen, M., Tian, H., et al. (2023). Cu-N-bridged Fe-3d electron state regulations for boosted oxygen reduction in flexible battery and PEMFC. *Energy Storage Mater.* 54, 533–542. doi:10.1016/j.ensm.2022.11.003

Kregar, A., Tavčar, G., Kravos, A., and Katrašnik, T. (2020). Predictive system-level modeling framework for transient operation and cathode platinum degradation of high temperature proton exchange membrane fuel cells. *Appl. energy* 263, 114547. doi:10.1016/j.apenergy.2020.114547

Labata, M. F., Li, G., Ocon, J., and Chuang, P.-Y. A. (2021). Insights on platinum-carbon catalyst degradation mechanism for oxygen reduction reaction in acidic and alkaline media. *J. Power Sources* 487, 229356. doi:10.1016/j.jpowsour.2020.229356

Lai, W., Ma, Z., Zhang, J., Yuan, Y., Qiao, Y., and Huang, H. (2022). Dynamic evolution of active sites in electrocatalytic CO2 reduction reaction: Fundamental understanding and recent progress. *Adv. Funct. Mater.* 32, 2111193. doi:10.1002/adfm.202111193

Lee, G., Nguyen, N.-A., Nguyen, V.-T., Larina, L. L., Chuluunbat, E., Park, E., et al. (2022a). High entropy alloy electrocatalyst synthesized using plasma ionic liquid reduction. *J. Solid State Chem.* 314, 123388. doi:10.1016/j.jssc.2022.123388

Lee, S., Gwon, K., Kim, H., Park, B. J., and Shin, J. H. (2022b). High-performance amperometric carbon monoxide sensor based on a xerogel-modified PtCr/C microelectrode. *Sensors Actuators B Chem.* 369, 132275. doi:10.1016/j.snb.2022.132275

Li, J., and Sun, S. (2019). Intermetallic nanoparticles: Synthetic control and their enhanced electrocatalysis. *Accounts Chem. Res.* 52, 2015–2025. doi:10.1021/acs.accounts.9b00172

Li, K., and Chen, W. (2021). Recent progress in high-entropy alloys for catalysts: Synthesis, applications, and prospects. *Mater. Today Energy* 20, 100638. doi:10.1016/j.mtener.2021.100638

Li, C., Yuan, Q., Ni, B., He, T., Zhang, S., Long, Y., et al. (2018a). Dendritic defect-rich palladium-copper-cobalt nanoalloys as robust multifunctional non-platinum electrocatalysts for fuel cells. *Nat. Commun.* 9, 3702. doi:10.1038/s41467-018-06043-1

Li, K., Li, X., Huang, H., Luo, L., Li, X., Yan, X., et al. (2018b). One-nanometer-thick PtNiRh trimetallic nanowires with enhanced oxygen reduction electrocatalysis in acid media: Integrating multiple advantages into one catalyst. *J. Am. Chem. Soc.* 140, 16159–16167. doi:10.1021/jacs.8b08836

Li, W., Liu, P., and Liaw, P. K. (2018c). Microstructures and properties of high-entropy alloy films and coatings: A review. *Mater. Res. Lett.* 6, 199–229. doi:10.1080/21663831.2018.1434248

Li, R., Liu, F., Zhang, Y., Guo, M., and Liu, D. (2020a). Nitrogen, sulfur co-doped hierarchically porous carbon as a metal-free electrocatalyst for oxygen reduction and carbon dioxide reduction reaction. *ACS Appl. Mater. Interfaces* 12, 44578–44587. doi:10.1021/acsami.0c06506

Li, S., Tang, X., Jia, H., Li, H., Xie, G., Liu, X., et al. (2020b). Nanoporous high-entropy alloys with low Pt loadings for high-performance electrochemical oxygen reduction. *J. Catal.* 383, 164–171. doi:10.1016/j.jcat.2020.01.024

Li, Y., Sun, Y., Qin, Y., Zhang, W., Wang, L., Luo, M., et al. (2020c). Recent advances on water-splitting electrocatalysis mediated by noble-metal-based nanostructured materials. *Adv. Energy Mater.* 10, 1903120. doi:10.1002/aenm.201903120

Li, H., Lai, J., Li, Z., and Wang, L. (2021). Multi-sites electrocatalysis in high-entropy alloys. *Adv. Funct. Mater.* 31, 2106715. doi:10.1002/adfm.202106715

Li, W., Bhuvanendran, N., Liu, H., Xu, Q., Hooshyari, K., and Su, H. (2023). Ternary PtPdCo mesoporous nanospheres with superior electrocatalytic performance towards

methanol oxidation reaction. *J. Alloys Compd.* 933, 167706. doi:10.1016/j.jallcom.2022.167706

Liang, J., Li, N., Zhao, Z., Ma, L., Wang, X., Li, S., et al. (2019). Tungsten-doped L10-PtCo ultrasmall nanoparticles as a high-performance fuel cell cathode. *Angew. Chem. Int. Ed.* 58, 15617–15623. doi:10.1002/ange.201908824

Lim, J., Shin, H., Kim, M., Lee, H., Lee, K.-S., Kwon, Y., et al. (2018). Ga–doped Pt–Ni octahedral nanoparticles as a highly active and durable electrocatalyst for oxygen reduction reaction. *Nano Lett.* 18, 2450–2458. doi:10.1021/acs.nanolett.8b00028

Lim, A., Lee, J. S., Lee, S., Lee, S. Y., Kim, H.-J., Yoo, S. J., et al. (2021). Polymer electrolyte membrane unitized regenerative fuel cells: Operational considerations for achieving high round trip efficiency at low catalyst loading. *Appl. Catal. B Environ.* 297, 120458. doi:10.1016/j.apcatb.2021.120458

Liu, D., Tao, L., Yan, D., Zou, Y., and Wang, S. (2018). Recent advances on non-precious metal porous carbon-based electrocatalysts for oxygen reduction reaction. *ChemElectroChem* 5, 1775–1785. doi:10.1002/celc.201800086

Liu, H., Liu, J., Chen, P., and Yang, H. (2019). Microstructure and high temperature wear behaviour of *in-situ* TiC reinforced AlCoCrFeNi-based high-entropy alloy composite coatings fabricated by laser cladding. *Opt. Laser Technol.* 118, 140–150. doi:10.1016/j.optlastec.2019.05.006

Liu, Y., Chen, Z., Yang, X., Zhang, J., Sun, Z., Chen, Y., et al. (2021). A facile synthesis of high entropy alloy nanoparticle–activated carbon nanocomposites for synergetic degradation of methylene blue. *RSC Adv.* 11, 24636–24646. doi:10.1039/d1ra03661k

Liu, B., Feng, R., Busch, M., Wang, S., Wu, H., Liu, P., et al. (2022). Synergistic hybrid electrocatalysts of platinum alloy and single-atom platinum for an efficient and durable oxygen reduction reaction. *ACS Nano* 16, 14121–14133. doi:10.1021/acsnano.2c04077

Loffler, T., Ludwig, A., Rossmeisl, J., and Schuhmann, W. (2021). What makes high-entropy alloys exceptional electrocatalysts? *Angew. Chem. Int. Ed. Engl.* 60, 26894–26903. doi:10.1002/anie.202109212

Lopes, P. P., Li, D., Lv, H., Wang, C., Tripkovic, D., Zhu, Y., et al. (2020). Eliminating dissolution of platinum-based electrocatalysts at the atomic scale. *Nat. Mater.* 19, 1207–1214. doi:10.1038/s41563-020-0735-3

LoFfler, T., Savan, A., Garzón-Manjón, A., Meischein, M., Scheu, C., Ludwig, A., et al. (2019). Toward a paradigm shift in electrocatalysis using complex solid solution nanoparticles. *ACS Energy Lett.* 4, 1206–1214. doi:10.1021/acsenergylett.9b00531

Lu, Z., and Elam, J. W. (2022). Synthesis techniques for ultrathin oxide layers of heterogeneous catalysts. *Ultrathin Oxide Layers Sol. Electrocatalytic Syst.* 30, 210. doi:10.1039/9781839163708-00210

Lucia, U. (2014). Overview on fuel cells. *Renew. Sustain. Energy Rev.* 30, 164–169. doi:10.1016/j.rser.2013.09.025

Lv, H., Xu, D., Sun, L., Henzie, J., Suib, S. L., Yamauchi, Y., et al. (2019a). Ternary palladium–boron–phosphorus alloy mesoporous nanospheres for highly efficient electrocatalysis. *ACS Nano* 13, 12052–12061. doi:10.1021/acsnano.9b06339

Lv, Y., Yang, L., and Cao, D. (2019b). Sulfur, nitrogen and fluorine triple-doped metal-free carbon electrocatalysts for the oxygen reduction reaction. *ChemElectroChem* 6, 741–747. doi:10.1002/celc.201801433

Ma, R., Lin, G., Zhou, Y., Liu, Q., Zhang, T., Shan, G., et al. (2019). A review of oxygen reduction mechanisms for metal-free carbon-based electrocatalysts. *npj Comput. Mater.* 5, 78–15. doi:10.1038/s41524-019-0210-3

Ma, Z., Cano, Z. P., Yu, A., Chen, Z., Jiang, G., Fu, X., et al. (2020a). Enhancing oxygen reduction activity of Pt-based electrocatalysts: From theoretical mechanisms to practical methods. *Angew. Chem.* 132, 18490–18504. doi:10.1002/ange.202003654

Ma, Z., Tian, H., Meng, G., Peng, L., Chen, Y., Chen, C., et al. (2020b). Size effects of platinum particles@ CNT on HER and ORR performance. *Sci. China Mater.* 63, 2517–2529. doi:10.1007/s40843-020-1449-2

Ma, H., Zheng, Z., Zhao, H., Shen, C., Chen, H., Li, H., et al. (2021). Trimetallic PtNiCo branched nanocages as efficient and durable bifunctional electrocatalysts towards oxygen reduction and methanol oxidation reactions. *J. Mater. Chem. A* 9, 23444–23450. doi:10.1039/d1ta07488a

Ma, S.-Y., Ma, T., Hu, Q., Yang, H.-P., and He, C.-X. (2022). Ternary PtRuTe alloy nanofibers as an efficient and durable electrocatalyst for hydrogen oxidation reaction in alkaline media. *Sci. China Mater.* 65, 3462–3469. doi:10.1007/s40843-022-2089-6

Madakannu, I., Patil, I., Kakade, B., and Datta, K. K. R. (2022). Electrocatalytic oxygen reduction activity of AgCoCu oxides on reduced graphene oxide in alkaline media. *Beilstein J. Nanotechnol.* 13, 1020–1029. doi:10.3762/bjnano.13.89

Madheswaran, D. K., and Jayakumar, A. (2021). Recent advancements on non-platinum based catalyst electrode material for polymer electrolyte membrane fuel cells: A mini techno-economic review. *Bull. Mater. Sci.* 44, 1–12. doi:10.1007/s12034-021-02572-6

Majlan, E. H., Rohendi, D., Daud, W. R. W., Husaini, T., and Haque, M. A. (2018). Electrode for proton exchange membrane fuel cells: A review. *Renew. Sustain. Energy Rev.* 89, 117–134. doi:10.1016/j.rser.2018.03.007

Manoharan, Y., Hosseini, S. E., Butler, B., Alzhahrani, H., Senior, B. T. F., Ashuri, T., et al. (2019). Hydrogen fuel cell vehicles; current status and future prospect. *Appl. Sci.* 9, 2296. doi:10.3390/app9112296

Marinoiu, A., Raceanu, M., Carcadea, E., and Varlam, M. (2018). Iodine-doped graphene–Catalyst layer in PEM fuel cells. *Appl. Surf. Sci.* 456, 238–245. doi:10.1016/j.apsusc.2018.06.100

Martínez-Hincapié, R., and Čolić, V. (2022). Electrocatalysts for the oxygen reduction reaction: From bimetallic platinum alloys to complex solid solutions. *ChemEngineering* 6, 19. doi:10.3390/chemengineering6010019

Meng, H.-L., Lin, S.-Y., Cao, Y., Wang, A.-J., Zhang, L., and Feng, J.-J. (2021). CoFe alloy embedded in N-doped carbon nanotubes derived from triamterene as a highly efficient and durable electrocatalyst beyond commercial Pt/C for oxygen reduction. *J. Colloid Interface Sci.* 604, 856–865. doi:10.1016/j.jcis.2021.07.061

Mohammed, H., Al-Othman, A., Nancarrow, P., Tawalbeh, M., and Assad, M. E. H. (2019). Direct hydrocarbon fuel cells: A promising technology for improving energy efficiency. *Energy* 172, 207–219. doi:10.1016/j.energy.2019.01.105

Molochas, C., and Tsiakaras, P. (2021). Carbon monoxide tolerant Pt-based electrocatalysts for H2-PEMFC applications: Current progress and challenges. *Catalysts* 11, 1127. doi:10.3390/catal11091127

Muhyuddin, M., Mustarelli, P., and Santoro, C. (2021). Recent advances in waste plastic transformation into valuable platinum-group metal-free electrocatalysts for oxygen reduction reaction. *ChemSusChem* 14, 3785–3800. doi:10.1002/cssc.202101252

Mukherjee, P., Kakade, B., and Swami, A. (2022). Current trends in platinum-based ternary alloys as promising electrocatalysts for the oxygen reduction reaction: A mini review. *Energy & Fuels* 36, 2306–2322. doi:10.1021/acs.energyfuels.1c03667

Nandan, R., Raj, G., and Nanda, K. K. (2022). FeCoNiMnCr high-entropy alloy nanoparticle-grafted NCNTs with promising performance in the ohmic polarization region of fuel cells. *ACS Appl. Mater. Interfaces* 14, 16108–16116. doi:10.1021/acsami.1c21336

Nguyen, A. T. N., and Shim, J. H. (2018). Facile one-step synthesis of Ir-Pd bimetallic alloy networks as efficient bifunctional catalysts for oxygen reduction and oxygen evolution reactions. *J. Electroanal. Chem.* 827, 120–127. doi:10.1016/j.jelechem.2018.09.012

Niu, L., Liu, G., Li, Y., An, J., Zhao, B., Yang, J., et al. (2021). CoNi alloy nanoparticles encapsulated in N-doped graphite carbon nanotubes as an efficient electrocatalyst for oxygen reduction reaction in an alkaline medium. *ACS Sustain. Chem. Eng.* 9, 8207–8213. doi:10.1021/acssuschemeng.1c02098

Okonkwo, P. C., Ige, O. O., Uzoma, P. C., Emori, W., Benamor, A., Abdullah, A. M., et al. (2021). Platinum degradation mechanisms in proton exchange membrane fuel cell (PEMFC) system: A review. *Int. J. Hydrogen Energy* 46, 15850–15865. doi:10.1016/j.ijhydene.2021.02.078

Oliveira, A. M., Beswick, R. R., and Yan, Y. (2021). A green hydrogen economy for a renewable energy society. *Curr. Opin. Chem. Eng.* 33, 100701. doi:10.1016/j.coche.2021.100701

Prabhu, P., Jose, V., and Lee, J.-M. (2020). Design strategies for development of TMD-based heterostructures in electrochemical energy systems. *Matter* 2, 526–553. doi:10.1016/j.matt.2020.01.001

Qiao, Z., Hwang, S., Li, X., Wang, C., Samarakoon, W., Karakalos, S., et al. (2019). 3D porous graphitic nanocarbon for enhancing the performance and durability of Pt catalysts: A balance between graphitization and hierarchical porosity. *Energy & Environ. Sci.* 12, 2830–2841. doi:10.1039/c9ee01899a

Qiu, H.-J., Fang, G., Wen, Y., Liu, P., Xie, G., Liu, X., et al. (2019). Nanoporous high-entropy alloys for highly stable and efficient catalysts. *J. Mater. Chem. A* 7, 6499–6506. doi:10.1039/c9ta00505f

Rahaman, M. Z., and Islam, M. M. (2019). Comparative study of different fuel cell technologies. *Asian J. con. Sci. Technol.* 1, 29–32. doi:10.5281/zenodo.3384260

Sahoo, L., Garg, R., Kaur, K., Vinod, C., and Gautam, U. K. (2022). Ultrathin twisty PdNi alloy nanowires as highly active ORR electrocatalysts exhibiting morphology-induced durability over 200 K cycles. *Nano Lett.* 22, 246–254. doi:10.1021/acs.nanolett.1c03704

Samad, S., Loh, K. S., Wong, W. Y., Lee, T. K., Sunarso, J., Chong, S. T., et al. (2018). Carbon and non-carbon support materials for platinum-based catalysts in fuel cells. *Int. J. hydrogen energy* 43, 7823–7854. doi:10.1016/j.ijhydene.2018.02.154

Sanad, M. F., Puente Santiago, A. R., Tolba, S. A., Ahsan, M. A., Fernandez-Delgado, O., Shawky Adly, M., et al. (2021). Co–Cu bimetallic metal organic framework catalyst outperforms the Pt/C benchmark for oxygen reduction. *J. Am. Chem. Soc.* 143, 4064–4073. doi:10.1021/jacs.1c01096

Sawant, S. V., Patwardhan, A. W., Joshi, J. B., and Dasgupta, K. (2022). Boron doped carbon nanotubes: Synthesis, characterization and emerging applications–A review. *Chem. Eng. J.* 427, 131616. doi:10.1016/j.cej.2021.131616

Schwanitz, V. J., and Wierling, A. (2022). "Toward sustainable global energy production and consumption," in *Responsible consumption and production* (Springer).

Seh, Z. W., Kibsgaard, J., Dickens, C. F., Chorkendorff, I., Nørskov, J. K., and Jaramillo, T. F. (2017). Combining theory and experiment in electrocatalysis: Insights into materials design. *Science* 355, eaad4998. doi:10.1126/science.aad4998

Shamoon, A., Haleem, A., Bahl, S., Javaid, M., Garg, S. B., Sharma, R. C., et al. (2022). Environmental impact of energy production and extraction of materials-a review. *Mater. Today Proc.* 57, 936–941. doi:10.1016/j.matpr.2022.03.159

Shang, X., Tang, J.-H., Dong, B., and Sun, Y. (2020). Recent advances of nonprecious and bifunctional electrocatalysts for overall water splitting. *Sustain. Energy & Fuels* 4, 3211–3228. doi:10.1039/d0se00466a

Shao, Q., Li, F., Chen, Y., and Huang, X. (2018). The advanced designs of high-performance platinum-based electrocatalysts: Recent progresses and challenges. *Adv. Mater. Interfaces* 5, 1800486. doi:10.1002/admi.201800486

Shao, Q., Wang, P., Zhu, T., and Huang, X. (2019). Low dimensional platinum-based bimetallic nanostructures for advanced catalysis. *Accounts Chem. Res.* 52, 3384–3396. doi:10.1021/acs.accounts.9b00262

Sharma, D. K., Mahant, D., and Upadhyay, G. (2020). Manufacturing of metal matrix composites: A state of review. *Mater. Today Proc.* 26, 506–519. doi:10.1016/j.matpr.2019.12.128

Shimoyama, I., Hakoda, T., Shimada, A., and Baba, Y. (2015). Influence of configuration at dopant sites on catalytic activity of phosphorus-doped graphite. *Carbon* 81, 260–271. doi:10.1016/j.carbon.2014.09.057

Song, T. W., Chen, M. X., Yin, P., Tong, L., Zuo, M., Chu, S. Q., et al. (2022). Intermetallic PtFe electrocatalysts for the oxygen reduction reaction: Ordering degree-dependent performance. *Small* 18, 2202916. doi:10.1002/smll.202202916

Souza, N. E., Bott-Neto, J. L., Rocha, T. A., Da Silva, G. C., Teixeira-Neto, E., Gonzalez, E. R., et al. (2018). Support modification in Pt/C electrocatalysts for durability increase: A degradation study assisted by identical location transmission electron microscopy. *Electrochimica Acta* 265, 523–531. doi:10.1016/j.electacta.2018.01.180

Stonehart, P., and Wheeler, D. (2005). "Phosphoric acid fuel cells (PAFCs) for utilities: Electrocatalyst crystallite design, carbon support, and matrix materials challenges," in *Modern aspects of electrochemistry*. Editors B. E. Conway, C. G. Vayenas, R. E. White, and M. E. Gamboa-Adelco (Boston, MA: Springer) Vol. 38, 373–424. doi:10.1007/0-387-25838-8_4

Sui, S., Wang, X., Zhou, X., Su, Y., Riffat, S., and Liu, C.-J. (2017). A comprehensive review of Pt electrocatalysts for the oxygen reduction reaction: Nanostructure, activity, mechanism and carbon support in PEM fuel cells. *J. Mater. Chem. A* 5, 1808–1825. doi:10.1039/c6ta08580f

Sun, T., Wang, J., Qiu, C., Ling, X., Tian, B., Chen, W., et al. (2018). B, N codoped and defect-rich nanocarbon material as a metal-free bifunctional electrocatalyst for oxygen reduction and evolution reactions. *Adv. Sci.* 5, 1800036. doi:10.1002/advs.201800036

Sun, D., Cai, Y., Zhu, L., Gao, F., Shan, M., Manladan, S. M., et al. (2022). High-temperature oxidation and wear properties of TiC-reinforced CrMnFeCoNi high entropy alloy composite coatings produced by laser cladding. *Surf. Coatings Technol.* 438, 128407. doi:10.1016/j.surfcoat.2022.128407

Tian, X. L., Xu, Y. Y., Zhang, W., Wu, T., Xia, B. Y., and Wang, X. (2017). Unsupported platinum-based electrocatalysts for oxygen reduction reaction. *ACS Energy Lett.* 2, 2035–2043. doi:10.1021/acsenergylett.7b00593

Tsai, M.-H., and Yeh, J.-W. (2014). High-entropy alloys: A critical review. *Mater. Res. Lett.* 2, 107–123. doi:10.1080/21663831.2014.912690

Wacławek, S., Padil, V. V., and Černík, M. (2018). Major advances and challenges in heterogeneous catalysis for environmental applications: A review. *Ecol. Chem. Eng. S* 25, 9–34. doi:10.1515/eces-2018-0001

Wan, X., Liu, X., Li, Y., Yu, R., Zheng, L., Yan, W., et al. (2019). Fe–N–C electrocatalyst with dense active sites and efficient mass transport for high-performance proton exchange membrane fuel cells. *Nat. Catal.* 2, 259–268. doi:10.1038/s41929-019-0237-3

Wan, C., Duan, X., and Huang, Y. (2020). Molecular design of single-atom catalysts for oxygen reduction reaction. *Adv. Energy Mater.* 10, 1903815. doi:10.1002/aenm.201903815

Wang, C., and Spendelow, J. S. (2021). Recent developments in Pt–Co catalysts for proton-exchange membrane fuel cells. *Curr. Opin. Electrochem.* 28, 100715. doi:10.1016/j.coelec.2021.100715

Wang, S., and Jiang, S. P. (2017). Prospects of fuel cell technologies. *Natl. Sci. Rev.* 4, 163–166. doi:10.1093/nsr/nww099

Wang, Y., Leung, D. Y., Xuan, J., and Wang, H. (2016). A review on unitized regenerative fuel cell technologies, part-A: Unitized regenerative proton exchange membrane fuel cells. *Renew. Sustain. Energy Rev.* 65, 961–977. doi:10.1016/j.rser.2016.07.046

Wang, J., Wang, H., and Fan, Y. (2018a). Techno-economic challenges of fuel cell commercialization. *Engineering* 4, 352–360. doi:10.1016/j.eng.2018.05.007

Wang, Y.-J., Long, W., Wang, L., Yuan, R., Ignaszak, A., Fang, B., et al. (2018b). Unlocking the door to highly active ORR catalysts for PEMFC applications: Polyhedron-engineered Pt-based nanocrystals. *Energy & Environ. Sci.* 11, 258–275. doi:10.1039/c7ee02444d

Wang, S., Luo, Q., Zhu, Y., Tang, S., and Du, Y. (2019a). Facile synthesis of quaternary structurally ordered L12-Pt (Fe, Co, Ni) 3 nanoparticles with low content of platinum as efficient oxygen reduction reaction electrocatalysts. *ACS omega* 4, 17894–17902. doi:10.1021/acsomega.9b02918

Wang, Z., Yao, X., Kang, Y., Miao, L., Xia, D., and Gan, L. (2019b). Structurally ordered low-Pt intermetallic electrocatalysts toward durably high oxygen reduction reaction activity. *Adv. Funct. Mater.* 29, 1902987. doi:10.1002/adfm.201902987

Wang, Z., Yao, X., Kang, Y., Xia, D., and Gan, L. (2019c). Rational development of structurally ordered platinum ternary intermetallic electrocatalysts for oxygen reduction reaction. *Catalysts* 9, 569. doi:10.3390/catal9070569

Wang, X., Zhang, L., Wang, F., Yu, J., and Zhu, H. (2020a). Nickel-introduced structurally ordered PtCuNi/C as high performance electrocatalyst for oxygen reduction reaction. *Prog. Nat. Sci. Mater. Int.* 30, 905–911. doi:10.1016/j.pnsc.2020.10.017

Wang, Y., Ruiz Diaz, D. F., Chen, K. S., Wang, Z., and Adroher, X. C. (2020b). Materials, technological status, and fundamentals of PEM fuel cells – a review. *Mater. Today* 32, 178–203. doi:10.1016/j.mattod.2019.06.005

Wang, K., Li, N., Yang, Y., Ke, S., Zhang, Z., Dou, M., et al. (2021a). Effect of load-cycling amplitude on performance degradation for proton exchange membrane fuel cell. *Chin. Chem. Lett.* 32, 3159–3163. doi:10.1016/j.cclet.2021.02.045

Wang, M., Lu, Y., Zhang, G., Cui, H., Xu, D., Wei, N., et al. (2021b). A novel high-entropy alloy composite coating with core-shell structures prepared by plasma cladding. *Vacuum* 184, 109905. doi:10.1016/j.vacuum.2020.109905

Wang, Y., Zhao, L., Wan, D., Guan, S., and Chan, K. (2021c). Additive manufacturing of TiB2-containing CoCrFeMnNi high-entropy alloy matrix composites with high density and enhanced mechanical properties. *Mater. Sci. Eng. A* 825, 141871. doi:10.1016/j.msea.2021.141871

Wang, Z., Cheng, L., Zhang, R., Lv, W., and Wang, W. (2021d). Surface-oxidized Fe–Co–Ni alloys anchored to N-doped carbon nanotubes as efficient catalysts for oxygen reduction reaction. *J. Alloys Compd.* 857, 158249. doi:10.1016/j.jallcom.2020.158249

Wang, X., Li, X., Kong, D., Zhao, L., Cui, Y., Wang, Y., et al. (2022). Platinum-free electrocatalysts for hydrogen oxidation reaction in alkaline media. *Nano Energy* 104, 107877. doi:10.1016/j.nanoen.2022.107877

Weber, P., Werheid, M., Janssen, M., and Oezaslan, M. (2018). Fundamental insights in degradation mechanisms of Pt/C nanoparticles for the ORR. *ECS Trans.* 86, 433–445. doi:10.1149/08613.0433ecst

Wei, P., Li, X., He, Z., Sun, X., Liang, Q., Wang, Z., et al. (2021a). Porous N, B co-doped carbon nanotubes as efficient metal-free electrocatalysts for ORR and Zn-air batteries. *Chem. Eng. J.* 422, 130134. doi:10.1016/j.cej.2021.130134

Wei, X., Wang, R.-Z., Zhao, W., Chen, G., Chai, M.-R., Zhang, L., et al. (2021b). Recent research progress in PEM fuel cell electrocatalyst degradation and mitigation strategies. *EnergyChem* 3, 100061. doi:10.1016/j.enchem.2021.100061

Wei, Y., Wu, D., Yong, C., Wang, Z., Zhong, P., Qiu, J., et al. (2023). Robust and highly conductive Ti4O7/MXene nanocomposites as high-performance and long cyclic stability oxygen reduction electrocatalysts. *Appl. Surf. Sci.* 607, 154929. doi:10.1016/j.apsusc.2022.154929

Wen, C., Zhang, Y., Wang, C., Xue, D., Bai, Y., Antonov, S., et al. (2019). Machine learning assisted design of high entropy alloys with desired property. *Acta Mater.* 170, 109–117. doi:10.1016/j.actamat.2019.03.010

Wu, R., Li, Y., Gong, W., and Shen, P. K. (2019). One-pot synthesis of Pt–Pd bimetallic nanodendrites with enhanced electrocatalytic activity for oxygen reduction reaction. *ACS Sustain. Chem. Eng.* 7, 8419–8428. doi:10.1021/acssuschemeng.9b00056

Wu, D., Kusada, K., Yamamoto, T., Toriyama, T., Matsumura, S., Kawaguchi, S., et al. (2020). Platinum-group-metal high-entropy-alloy nanoparticles. *J. Am. Chem. Soc.* 142, 13833–13838. doi:10.1021/jacs.0c04807

Wu, Q., Yan, X., Jia, Y., and Yao, X. (2021). Defective carbon-based materials: Controllable synthesis and electrochemical applications. *EnergyChem* 3, 100059. doi:10.1016/j.enchem.2021.100059

Xia, B. (2021). *Progress and perspective on oxygen reduction electrocatalysts toward practical fuel cells*. Angewandte Chemie. (International ed. in English).

Xiao, F., Wang, Y. C., Wu, Z. P., Chen, G., Yang, F., Zhu, S., et al. (2021a). Recent advances in electrocatalysts for proton exchange membrane fuel cells and alkaline membrane fuel cells. *Adv. Mater.* 33, 2006292. doi:10.1002/adma.202006292

Xiao, Z., Jiang, Y., Wu, H., Zhong, H., Song, H., Abdelhafiz, A., et al. (2021b). De-alloyed ternary electrocatalysts with high activity and stability for oxygen reduction reaction. *J. Alloys Compd.* 877, 160221. doi:10.1016/j.jallcom.2021.160221

Xie, X., He, C., Li, B., He, Y., Cullen, D. A., Wegener, E. C., et al. (2020). Performance enhancement and degradation mechanism identification of a single-atom Co–N–C catalyst for proton exchange membrane fuel cells. *Nat. Catal.* 3, 1044–1054. doi:10.1038/s41929-020-00546-1

Xie, M., Chu, T., Wang, X., Li, B., Yang, D., Ming, P., et al. (2022). Effect of mesoporous carbon on oxygen reduction reaction activity as cathode catalyst support for proton exchange membrane fuel cell. *Int. J. Hydrogen Energy* 47, 28074–28085. doi:10.1016/j.ijhydene.2022.06.131

Xu, H., Cheng, D., Cao, D., and Zeng, X. C. (2018). A universal principle for a rational design of single-atom electrocatalysts. *Nat. Catal.* 1, 339–348. doi:10.1038/s41929-018-0063-z

Xu, J., Li, R., Xu, C.-Q., Zeng, R., Jiang, Z., Mei, B., et al. (2021). Underpotential-deposition synthesis and in-line electrochemical analysis of single-atom copper electrocatalysts. *Appl. Catal. B Environ.* 289, 120028. doi:10.1016/j.apcatb.2021.120028

Yang, S., Yu, Y., Dou, M., Zhang, Z., Dai, L., and Wang, F. (2019). Two-dimensional conjugated aromatic networks as high-site-density and single-atom electrocatalysts for the oxygen reduction reaction. *Angew. Chem. Int. Ed.* 58, 14866–14872. doi:10.1002/ange.201908023

Yang, B., Wang, J., Zhang, M., Shu, H., Yu, T., Zhang, X., et al. (2020). A state-of-the-art survey of solid oxide fuel cell parameter identification: Modelling, methodology, and perspectives. *Energy Convers. Manag.* 213, 112856. doi:10.1016/j.enconman.2020.112856

Yeh, J.-W. (2013). Alloy design strategies and future trends in high-entropy alloys. *Jom* 65, 1759–1771. doi:10.1007/s11837-013-0761-6

Yeh, J.-W., and Lin, S.-J. (2018). Breakthrough applications of high-entropy materials. *J. Mater. Res.* 33, 3129–3137. doi:10.1557/jmr.2018.283

Ying, J., Li, J., Jiang, G., Cano, Z. P., Ma, Z., Zhong, C., et al. (2018). Metal-organic frameworks derived platinum-cobalt bimetallic nanoparticles in nitrogen-doped hollow porous carbon capsules as a highly active and durable catalyst for oxygen reduction reaction. *Appl. Catal. B Environ.* 225, 496–503. doi:10.1016/j.apcatb.2017.11.077

Yuan, Z., Cao, Y., Zhang, Z., Fang, Y., Liu, Q., Dang, D., et al. (2022). Dandelion-like titanium nitride supported platinum as an efficient oxygen reduction catalyst in acidic media. *Int. J. Hydrogen Energy* 47, 15035–15043. doi:10.1016/j.ijhydene.2022.03.010

Zhai, L., Yang, S., Yang, X., Ye, W., Wang, J., Chen, W., et al. (2020). Conjugated covalent organic frameworks as platinum nanoparticle supports for catalyzing the oxygen reduction reaction. *Chem. Mater.* 32, 9747–9752. doi:10.1021/acs.chemmater.0c03614

Zhang, Q., and Guan, J. (2020). Single-atom catalysts for electrocatalytic applications. *Adv. Funct. Mater.* 30, 2000768. doi:10.1002/adfm.202000768

Zhang, Y., Yang, X., and Liaw, P. (2012). Alloy design and properties optimization of high-entropy alloys. *Jom* 64, 830–838. doi:10.1007/s11837-012-0366-5

Zhang, C., Shen, X., Pan, Y., and Peng, Z. (2017). A review of Pt-based electrocatalysts for oxygen reduction reaction. *Front. Energy* 11, 268–285. doi:10.1007/s11708-017-0466-6

Zhang, B. W., Yang, H. L., Wang, Y. X., Dou, S. X., and Liu, H. K. (2018). A comprehensive review on controlling surface composition of Pt-based bimetallic electrocatalysts. *Adv. Energy Mater.* 8, 1703597. doi:10.1002/aenm.201703597

Zhang, C., Wang, S., Li, J., Zhu, Y., Peng, T., and Yang, H. (2020). Additive manufacturing of products with functional fluid channels: A review. *Addit. Manuf.* 36, 101490. doi:10.1016/j.addma.2020.101490

Zhang, J., Yuan, Y., Gao, L., Zeng, G., Li, M., and Huang, H. (2021a). Stabilizing Pt-based electrocatalysts for oxygen reduction reaction: Fundamental understanding and design strategies. *Adv. Mater.* 33, 2006494. doi:10.1002/adma.202006494

Zhang, S., Xia, Z., Zhang, M., Zou, Y., Shen, H., Li, J., et al. (2021b). Boosting selective hydrogenation through hydrogen spillover on supported-metal catalysts at room temperature. *Appl. Catal. B Environ.* 297, 120418. doi:10.1016/j.apcatb.2021.120418

Zhang, Y., Wang, D., and Wang, S. (2022). High-entropy alloys for electrocatalysis: Design, characterization, and applications. *Small* 18, 2104339. doi:10.1002/smll.202104339

Zhao, L., Zhu, J., Zheng, Y., Xiao, M., Gao, R., Zhang, Z., et al. (2022). Materials engineering toward durable electrocatalysts for proton exchange membrane fuel cells. *Adv. Energy Mater.* 12, 2102665. doi:10.1002/aenm.202102665

Zhu, C., Shi, Q., Xu, B. Z., Fu, S., Wan, G., Yang, C., et al. (2018). Hierarchically porous M–N–C (M = Co and Fe) single-atom electrocatalysts with robust MN_x active moieties enable enhanced ORR performance. *Adv. Energy Mater.* 8, 1801956. doi:10.1002/aenm.201801956

Zhu, J., Xie, M., Chen, Z., Lyu, Z., Chi, M., Jin, W., et al. (2020a). Pt-Ir-Pd trimetallic nanocages as a dual catalyst for efficient oxygen reduction and evolution reactions in acidic media. *Adv. Energy Mater.* 10, 1904114. doi:10.1002/aenm.201904114

Zhu, S., Yu, Y., Zhang, B., Zhang, Z., Yan, X., and Wang, Z. (2020b). Microstructure and wear behaviour of *in-situ* TiN-Al2O3 reinforced CoCrFeNiMn high-entropy alloys composite coatings fabricated by plasma cladding. *Mater. Lett.* 272, 127870. doi:10.1016/j.matlet.2020.127870

Zhu, X., Hu, C., Amal, R., Dai, L., and Lu, X. (2020c). Heteroatom-doped carbon catalysts for zinc–air batteries: Progress, mechanism, and opportunities. *Energy & Environ. Sci.* 13, 4536–4563. doi:10.1039/d0ee02800b

Zhu, M., Zhao, C., Liu, X., Wang, X., Zhou, F., Wang, J., et al. (2021). Single atomic cerium sites with a high coordination number for efficient oxygen reduction in proton-exchange membrane fuel cells. *ACS Catal.* 11, 3923–3929. doi:10.1021/acscatal.0c05503

Zhu, S., Yang, L., Bai, J., Chu, Y., Liu, J., Jin, Z., et al. (2022). Ultra-stable Pt5La intermetallic compound towards highly efficient oxygen reduction reaction. *Nano Res.*, 1–6. doi:10.1007/s12274-022-4868-3

Ziv, N., Mustain, W. E., and Dekel, D. R. (2018). The effect of ambient carbon dioxide on anion-exchange membrane fuel cells. *ChemSusChem* 11, 1136–1150. doi:10.1002/cssc.201702330

frontiers | Frontiers in Energy Research

TYPE Review
PUBLISHED 20 March 2023
DOI 10.3389/fenrg.2023.1149446

OPEN ACCESS

EDITED BY
Sunday Olayinka Oyedepo,
Covenant University, Nigeria

REVIEWED BY
Huai-Jun Lin,
Jinan University, China
Tolutope Oluwasegun Siyanbola,
Covenant University, Nigeria

*CORRESPONDENCE
Dada Modupeola,
dadadupeola@gmail.com
Patricia Popoola,
poppolaAPI@tut.ac.za

SPECIALTY SECTION
This article was submitted to Process and Energy Systems Engineering, a section of the journal Frontiers in Energy Research

RECEIVED 21 January 2023
ACCEPTED 08 March 2023
PUBLISHED 20 March 2023

CITATION
Modupeola D and Popoola P (2023), High entropy nanomaterials for energy storage and catalysis applications. *Front. Energy Res.* 11:1149446. doi: 10.3389/fenrg.2023.1149446

High entropy nanomaterials for energy storage and catalysis applications

Dada Modupeola* and Patricia Popoola*

Department of Chemical, Metallurgical and Materials Engineering, Tshwane University of Technology, Pretoria, South Africa

In the past decade, high entropy alloys have been a research field of interest largely attributed to the enormous possibilities in alloy compositions, solid solution microstructures, and enhanced properties. The progress accomplished so far in the innovative growth and development of the mechanical, nanomechanical, chemical, electrochemical properties for energy storage systems using high entropy alloys on the nanoscale has limited reports in the literature. Mastering the synthesis of high entropy alloys is the deciding factor, if not the holy grail, when interested in a new material. For nanoparticles, in particular, this is true. Hence, the study on the production of high entropy alloy nanoparticles (HE-NPs) and the impact of synthesis on the structure of the resulting nanomaterial is valid for newly emerging components like HEA-NPs and the linkages between synthesis, structure, and property are essential for creating HEA-NP-based applications for energy storage applications, requiring the creation of a fundamental protocol to enable their mass manufacture and efficiency in service. In this study, we have presented a straightforward review of high entropy alloys, recent advances in high entropy nanoparticles and their various syntheses for energy and catalysis applications.

KEYWORDS

high entropy alloys, energy storage applications, nanomaterials, catalysis, energy

1 Introduction

The fundamental concept of alloying in material engineering was based on the tactic of sparingly combining a few minor elements with major elements for centuries (Dąbrowa et al., 2016; George et al., 2019; Marques et al., 2021). However, different alloys which are made from different primary elements like Iron, Aluminum. Nickel, Copper, and Zinc have increased the overall number of alloys, most of which have already been found and studied and are severely constrained in their use of principal elements (Li H. et al., 2021). As a result, innovative alloying ideas have been in high demand since they significantly expand the compositional possibilities for creating new materials both at the micro and nanoscale (Stepanov et al., 2018; Moghaddam et al., 2021). Traditional alloys have one or two primary components that are selected based on a specific property criterion, and other minor alloying components are included to further improve their properties. High-entropy alloys (HEAs), which Yeh et al. presented in 2004, constitute a revolutionary alloy idea design (Chen et al., 2018). Opening up a wide, uncharted arena of alloy compositions and the possibility of influencing solid solution phase stability through the management of configurational entropy are the two main novelties of this alloy design (George et al., 2020). HEAs are described as “those comprising five or more primary elements in equimolar ratios” (Jien-Wei, 2006). The following clause broadens the definition to include “principal elements with

the concentration of each element being between 35 and five atomic percentage," which circumscribes the criterion for equimolar concentrations. As a result, HEAs need not be equimolar to greatly expand the number of compositions (Sathiyamoorthi and Kim, 2022), or to change the features of the base HEA and create more HEAs.

HEAs may additionally contain minor elements. This definition based on composition merely specifies elemental concentrations and does not limit the amount of entropy in the system (Moghaddam et al., 2021). Additionally, this concept does not stipulate that there must be only a single-phase SS observed (Miracle and Senkov, 2017). The entropy definition based on the concept of "high entropy" is motivated by the size of the entropy. A different definition so distinguishes $S^{SS,ideal}$ and R, which is the total configurational molar entropy in an idyllic solid solution and gas constant, respectively. Low entropy alloys have their configurational molar entropy less than 0.69R while higher entropies' configurational molar entropy is greater than 1.61R. Using the Boltzmann equation, estimating the configurational molar entropy is made easy, yet it needs atoms to occupy many lattice configurations (Fu et al., 2021).

$$\Delta S_{mix} = RIn_{(n)} \quad (1)$$

Rarely does this happen in metallic solutions. Additionally, this definition suggests that an alloy has one value of configurational entropy. Entropy in an alloy, however, can vary as the temperature varies. The impact of temperature can be little, yet giving minute adjustments to the short-range atomic ordering, or it could be dramatic, resulting in a chemical separation between parent and product phases at a first-order phase transformation (Tomilin and Kaloshkin, 2015). The first two definitions are paradoxical in some situations. The common consensus is that a greater composition restriction is beneficial for developing innovative alloys; hence, there is no need to rigidly adhere to the specifications and innovative design of HEAs. It is generally agreed that HEAs have four primary characteristics that set them apart from other alloys: high entropy, severe lattice distortion, slow diffusion, and cocktail effect (Li et al., 2016). The thermodynamic perspective on high entropy involvement in influencing the formation of simple solid solutions in HEA is a positive characteristic feature. In particular, the Gibbs free energy of mixing determines whether it may triumph over other reactions (Cao et al., 2020). Most of the entropy for HEAs is configurational entropy. For a random quinary equimolar solution, intermetallic compounds that are stoichiometric; their configurational entropy is 1.61R (R 14 8.31 J/K mol). The equation $G = H - TS$, where G is the Gibbs free, states that enthalpy, T is temperature, S is entropy, and E is energy, suggesting that phases with more entropy have lower Gibbs free energies. Thus, the creation of HEAs is facilitated by their high mixing entropy. Intermetallic phases are not as common as random solid-solution phases. Nevertheless, the high entropy impact cannot ensure the emergence of an easy solid-solution phase in alloys with many components. Other essential factors such as mixing enthalpy (ΔH_{mix}), Valence Electron Concentration and atomic size difference (δ) should be considered (Schuh et al., 2015). According to Gibbs free energy, as the temperature is reduced, the high entropy effect's contribution to the stability of random solid-solution phases decreases. This indicates that, when HEAs are annealed at a very low temperature, the random solid solution phases may change into intermetallic phases (Schuh et al., 2015). For instance, after homogenization treatment, the refractory HEA HfNbTaTiZr exhibits a single BCC phase. However, following annealing at about 800 C, the HCP phase with Hf and Ta enrichment was discovered in the BCC matrix (Stepanov et al., 2018). It should be mentioned that occasionally, the intermetallic phase might enhance the characteristic properties of HEAs. The explanation for the exceptional high-temperature strength, impressive high-temperature structural stability, and formation of nanostructures was frequently attributed to the sluggish diffusion effect, which denotes that the diffusion in HEAs is lower than that in conventional alloys (Wang et al., 2014). The interdiffusion coefficients in the Co-Cr-Fe-Mn-Ni alloy system were studied by Tsai et al. (2013) utilizing a quasi-binary technique together with Sauer-Fraise analysis. They explained the slow diffusion effect in HEAs as being due to higher normalized activation energies brought on by a wider range of surrounding atoms than in typical alloys at each lattice site. According to Dąbrowa et al. (2016), the HEAs' crystalline structure has a greater influence on diffusion coefficients at high temperatures than the chemical environment their nearby atoms cause.

Kulkarni and Chauhan (2015) indicated that diffusional interactions should not be disregarded when describing diffusion in HEAs. According to Verma et al. (2017), the interdiffusion fluxes of different components in HEAs can be increased or decreased based on the diffusional interactions between diffusing components and the configuration of their concentration gradients. HEAs include the atomic sizes of numerous principal elements that can differ greatly, and seriously alter the lattice. X-ray diffraction and TEM with great resolution can intuitively demonstrate and quantify this distortion (Senkov et al., 2018). The HEAs' mechanical, optical, electrical, and chemical characteristics are all impacted by the distortion feature, and an irregular lattice restricts atom movement. Due to this strong barrier created by significant lattice distortion, stress corrosion cracking occurs *via* a separate process. Dislocation motion and deformation are thus strongly hindered (Han et al., 2020). The thermodynamic stability of HEAs is further decreased by substantial lattice distortion, which may impact the film's capacity to passivate alloy surfaces. Ranganathan (2003) was the one who first hypothesized the cocktail effect. The author thought that HEAs might exhibit unforeseen properties that are not the sum of their parts. Nonetheless, since HEAs first appeared at the beginning of the twenty-first century, their superior mechanical characteristics have led to extensive research into and application in numerous engineering fields. High Entropy Alloys have been extensively employed in a variety of technical fields, including high-strength construction materials, corrosion-resistant coating materials and energy storage applications as one of the three major material systems in the world (Li et al., 2019). For instance, HEAs are extremely durable and strong at higher temperatures. They can also sustain stability and a very long lifespan in a range of hostile conditions. The special functional characteristics of HEAs have drawn more attention in recent years, and their range of applications has increased. This study shall concentrate on using HEAs as advanced energy storage materials (Wang Q. et al., 2021).

2 High entropy nanomaterials

Nanomaterials and nanostructures play a critical role in the recent advancement of some key technologies (Liu et al., 2020). Nanomaterials differ from microsized and bulk materials not only on the scale of their characteristic dimensions but also because they may possess new physical properties and offer new possibilities for various technical applications (Huang and Liaw, 2019). When the characteristic dimensions of a semiconductor reduce to below a certain size, quantum confinement leads to an increased band gap (Okulov et al., 2020). The band gap can be controlled by simply varying the dimensions of the material, so the optical absorption and emission spectra can be tuned to meet the specific requirements of the desired applications.

Hence, the research and development of new technologies, as well as the improvement of current technologies, can benefit from smaller sizes or dimensions (Glasscott et al., 2019). For instance, nanoparticles are suitable medication delivery vehicles due to their small size. Furthermore, mobile phones can now perform a wide range of tasks due to the reduction in the size of electrical gadgets. There are fewer flaws in nanoparticles than in their bulk counterparts, and they have substantially better mechanical strength. However, some uses of nanomaterials may be negatively affected by their small size and high specific surface area, especially in applications for energy storage and conversion where nanomaterials have various benefits (Yan et al., 2022). The specific surface area, surface energy, and surface chemistry all play crucial roles in energy conversion and storage because these processes entail physical interaction and/or chemical reactions at the surface or interface. Surface effects can also affect the thermodynamics of heterogeneous reactions at the interface, the surface energy and surface chemistry, the nucleation and subsequent growth when phase transitions are present (Jiang et al., 2021). Surface effects are not just restricted to kinetics and rates. As well as accommodating dimensional changes brought on by some chemical reactions and phase transitions, nanomaterials' reduced dimensions may also provide more favorable mass, heat, and charge transfer (Hu et al., 2019). The fabrication of HEA nanoparticles (HEA-NPs) by carbothermal shock was described by Hu et al. (2019), which sparked research on nanoscale high-entropy materials (HEMs). High-entropy oxides (HEOs), high-entropy nitrides (HENs), high-entropy borides (HEBs), high-entropy silicides (HESs), high-entropy metallic glasses (HEMGs), high-entropy metal-organic frameworks (HE-MOFs), and other HEMs, which are now included in the broad definition of the "high entropy" concept, especially for energy storage applications (Hussain et al., 2021; Porodko et al., 2022). High entropy nanomaterials have chemical and physical properties that enable superior catalytic performances.

The catalytic performance in the hydrogen evolution reaction is influenced by the principal components at volcano plots, while the minor components slightly impact the adsorption-free energies. Hence, the catalytic performances of alloys are reported to be primarily determined by principal elements present in the alloying composition, while minor elements slightly influence the properties of the alloy. For high entropy materials on the nanoscale, the electrocatalytic performance is influenced by the interactions of multiple elements in the material composition (Li W. et al., 2021). Wang et al. (2020) reported that HEA nanoparticles are potential candidates for energy and electrocatalysis applications due to their high active sites per mass ratio. The authors fabricated HEA NPs using a continuous droplet-to-particle process as opposed the hollow structured fabrication method restricted to two or three elements. The decomposition of a gas-blowing agent, in which a significant amount of gas is produced *in situ* to "puff" the droplet during heating, is what allows the formation of the hollow HEA nanoparticles. This process is then followed by the decomposition of the metal salt precursors and the nucleation/growth of multimetallic particles. These hollow HEA nanoparticles are attractive candidates since they have a high active sites per mass ratio. These HEA NP materials, therefore, show superior electrocatalytic performance attributed to their active sites, enhanced synergetic transitions during metal interactions, the sluggish diffusion effect, the high entropy stabilization effect and random or irregular atom arrangements. High entropy stabilization effects result in a thermodynamically stable high entropy material for electrocatalysis, making high entropy materials potential materials for heterogeneous catalysis (Zhivulin et al., 2021).

2.1 Fabrication routes of high entropy nanomaterials (HE-NPs)

2.1.1 Physical vapour deposition method

A physical process, such as heat evaporation or an impact process, will transform the particles that are to be deposited in physical vapor deposition (PVD) operations from a solid to a gaseous state (Baptista et al., 2018a; Vu et al., 2019). Mostly, the substrate is deposited in a vacuum chamber with a gas pressure below approximately 10^{-1} mbar (Pinto et al., 2018). The techniques used in PVD deposition are shown in the flowchart of the PVD Process in Figure 1. Heating raises the kinetic energy of the atoms or molecules in a solid or liquid (Schneider et al., 2000; Baptista et al., 2018b). More atoms can overcome the energy of separation and can avoid evaporation as the temperature rises. According to the temperature at which the atoms evaporate, for example, for copper, the average kinetic energy of the evaporated atoms is about 0.2 eV (Reichelt and Jiang, 1990). The primary components of evaporated particles include atoms, molecules, and clusters of various sizes and compositions (Wang X. et al., 2021; Stuart and Stan, 2021). A laser beam or an arc discharge can heat the evaporator and cause it to evaporate. When compared to thermal evaporation, the composition and energy of the vapour particles are different. Surface particles and secondary electrons will detach from the target when it is bombarded with ions with energies of over 30 eV (Ali et al., 2019; Gupta et al., 2021). This action is known as sputtering. The ejected particles, which are primarily molecules and atoms, will deposit on the substrate and the vacuum chamber wall to form the film. High entropy alloy films can be easily deposited using physical vapor deposition *via* magnetron co-sputtering. High entropy nanomaterials can also be obtained in tuneable shape and size using ionic liquids in place of traditional solid substrates in the top-down technique (Sun et al., 2021). Ionic liquids serve as suspension mediums and stabilizers for low melting points and vapor pressure. For example, high entropy CrMnFeCoNi nanoparticles were fabricated using ionic liquids *via* vapor

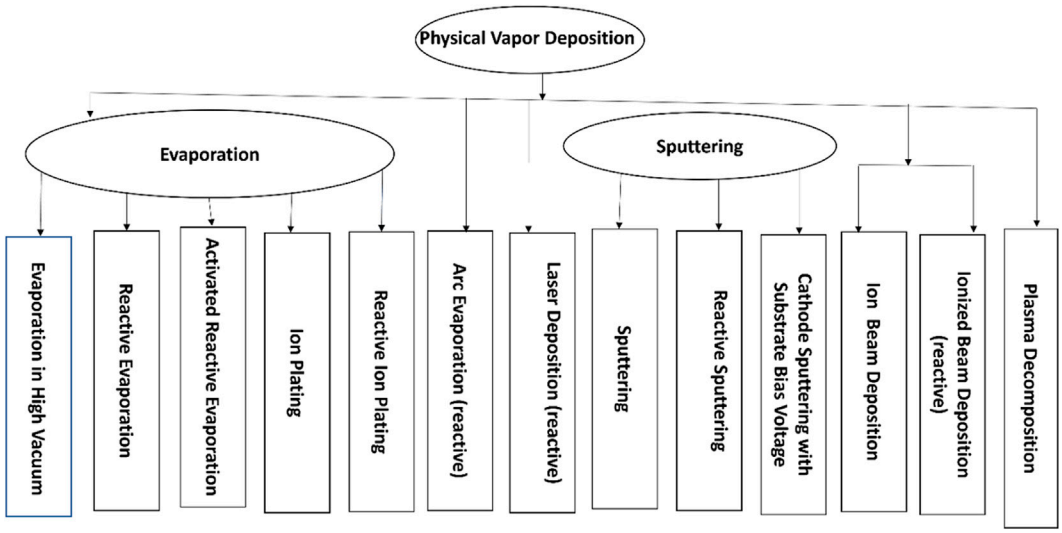

FIGURE 1
Chart of the PVD process.

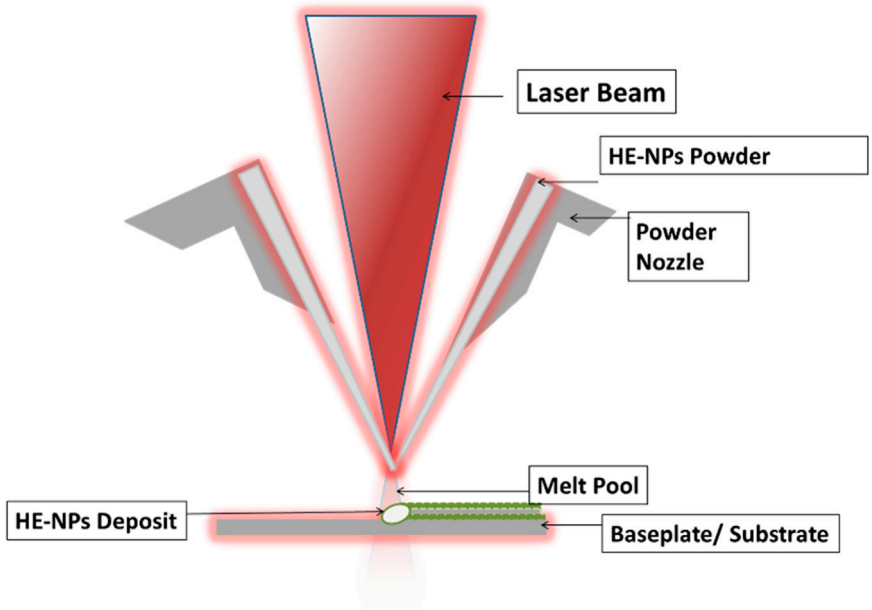

FIGURE 2
Schematic of the laser cladding process.

deposition technique with an extraordinary oxygen reduction reaction observed. The material, although amorphous in structure, showed complete compositional homogeneity (Garzón-Manjón et al., 2018).

Hence, crystalline high entropy materials on the nanoscale can be obtained by using the appropriate manufacturing routes, such as *ex situ* vacuum annealing, *in situ* electron beam irradiation, and vapour deposition techniques.

2.1.2 Laser deposition method

In the technique of "laser cladding," a heating source—a laser beam—is employed to melt the coating material onto the substrate (Boddu et al., 2001; Arif et al., 2021; Zhu et al., 2021). To create an alloy-clad layer, several metals and alloys can be placed on the substrate as shown in Figure 2. Due to the inherent characteristics of laser radiation, high input energy, low distortion, and the avoidance of unwanted phase change are all advantages of laser cladding in

addition to the ability to selectively clad small areas (Santo, 2008; Singh et al., 2020). These factors have led to its successful usage in the restoration of specific molds' metal components. Controlled shape, little diffusion of the substrate elements into the coating, fine microstructure, and low porosity in the deposited layer of the laser cladding technique were discussed by Wang et al. (1997) as the characteristic features of the laser cladding process. AlCoCrCuNi compositional system nanoparticles were fabricated by Mao et al. (2018). The authors investigated the influence of aluminum on the nanomaterial microstructure and properties. A single Cu-rich face-centered cubic (FCC) phase to FCC + M_3Al-type $L1_2$ phase structure was observed, followed by the FCC + body-centered cubic (BCC) phases as the Al content increased. The targets' nominal chemical compositions greatly differed from those of the nanoparticles, which were spherical and ranged in size from 110 nm to 180 nm on average.

When the microstructure changed from a pure FCC phase to an FCC + BCC phase, both the corrosion resistance and the soft magnetic behavior declined. In the technique of "laser cladding," a heating source—a laser beam—is employed to melt the coating material onto the substrate (Liu et al., 2017; Siddiqui and Dubey, 2021). To create an alloy-clad layer, several metals and alloys can be placed on the substrate. Due to the inherent characteristics of laser radiation, high input energy, low distortion, and the avoidance of unwanted phase change are all advantages of laser cladding in addition to the ability to selectively clad small areas (Santo, 2008; Tamanna et al., 2019). These factors have led to its successful usage in the restoration of specific molds' metal components. The M_3Al-type L12 phase contributed to the best corrosion resistance and the least amount of soft magnetic properties to the FCC matrix. The authors concluded that the laser cladding process makes it simple to create multicomponent nanoparticles with compositions and structures that can be adjusted (Weng et al., 2014; Liu et al., 2021).

2.1.3 Mechanical alloying and spark plasma sintering

Mechanical alloying (MA) followed by sintering (HEAs) is one of the most popular methods for creating nanocrystalline high-entropy alloys (Taha et al., 2019; Vaidya et al., 2019). As a well-known solid-state, nonequilibrium, top-down approach to producing nanocrystalline materials, mechanical alloying (MA) involves the milling of elemental powders on the micro or nanoscale to achieve alloying at an atomic scale (Suryanarayana, 2001; Suryanarayana, 2019). The MA process is described by the repeated fusing and splintering of powder particles entrapped between the milling media to an extent which depends on the mechanical attributes of powder constituents (Sundaresan and Froes, 1987; Benjamin, 1992). The main advantages of MA include improved solid solubility, room temperature processing, and homogeneous alloy production. High-density HEA pellets from milled powders have primarily been produced by spark plasma sintering (Sundaresan and Froes, 1987; Koch, 1998). The manufacturing of HEAs utilizing MA does, however, present several difficulties, including contamination during milling and high susceptibility to oxidation (Courtney, 1995; Murty and Ranganathan, 1998; Nagesha et al., 2013). A uniaxial press, punch electrodes, vacuum chamber, regulated atmosphere, DC pulse generator, and position, temperature, and pressure measurement devices support the sintering machine shown in Figure 3. Setting the holding time, ramp rate, pulse duration, pulse current and voltage allows for control of the sintering temperature. Spark plasma, spark impact pressure, joule heating, and an electrical field diffusion effect could all be produced by the DC pulse discharge. Compared to traditional hot pressing, SPS sintering is aided by the on-off DC pulse voltage. Pressure is applied to aid in the material's plastic flow (Kessel et al., 2010). Sintered samples are fabricated *via* SPS by taking a known quantity of dried, and milled powder samples in a cylindrical dye, lined with a graphite sheet which facilitates easy removal of the sintered compact (Munir et al., 2006; Mogale and Matizamhuka, 2020). The chiller is switched on the compressor and the machine and the die containing the powder sample are placed inside the SPS chamber. Then, set the specific pattern (time-temperature data) needed for the experiment to follow, and thereafter, the required atmospheres such as Vacuum, Argon, *etc.*, are maintained inside the chamber (Saheb et al., 2012; Yurlova et al., 2014). The power is set to the maximum in Auto mode and the required load to be applied on the die is also set. Also, the *z*-axis position is zero and then the timer is switched on and finally, the SINTER button is pressed to start the sintering process (Guillon et al., 2014; Matizamhuka, 2016). For measuring the temperature in SPS, two types of instruments are used: a thermocouple for sintering temperatures below 1,000°C and a pyrometer for sintering temperatures over 1,000°C. As the SPS process is characterized by high heating and cooling rates (Hungria et al., 2009; Hu et al., 2020). A high DC Pulse passed between graphite electrodes and axial pressure is simultaneously applied from the beginning of the sintering cycle. The sample is heated by Joules-heating, in which the sparking among the particles of sintered material leads to a faster heat and mass transfer instantaneously. After sintering, the power is switched off, and the sample is allowed to cool (Dudina et al., 2019; Abedi et al., 2021).

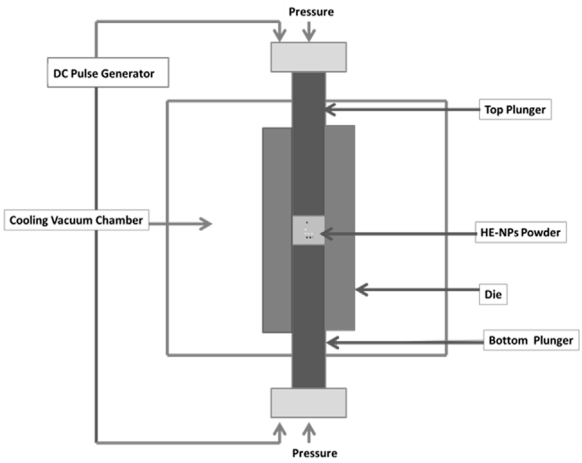

FIGURE 3
Schematic of the SPS process.

2.1.4 Other fabrication techniques

In the case of pure HE-NPs, the colloidal approach is frequently employed as a precise and efficient method to produce nano-objects

FIGURE 4
Schematic Diagram of droplet-to-particle evolution method of fabricating hollow high entropy alloy nanoparticles (Wang et al., 2020).

with regulated structure (size and shape). It is predicated on the presence of surfactants dissolved in an organic environment at a specific temperature and at the reduction of metallic precursors by a reducing agent. Equimolar CoCrFeNiMn HE-NPs have recently been produced using this colloidal method. The authors stated that the method in recent times has become a competitive method for synthesizing stable HE-NP colloids without the need for ligands to stabilize the process (Waag et al., 2019). To synthesize HE-NPs in the solid solution phase, without phase segregation like core-shell or Janus structures, the synthesis temperature specifically turned out to be important, according to Da Silva et al. (2022).

Kheradmandfard et al. (2021) studied the first high-entropy oxide (HEO) (Mg, Cu, Ni, Co, Zn) O nanoparticles using a novel ultrafast easy green microwave-assisted approach. The outcomes showed that the single-phase rocksalt structure of the HEO nanoparticles included equal amounts of all five metallic elements. The average particle size was 44 nm, while the range of particle sizes was 20–70 nm. The HEO nanoparticles showed outstanding lithium storage abilities with the impressive stability as was proved during 1,000 cycles at 1 A/g when utilized as anode materials for Li-ion batteries. With its amazing benefits, such as its ultrafast speed (few minutes), low temperature, nanoscale and high-purity products, and low cost, the approach suggested in this study is a superb synthesis methodology for use in newly developed high-entropy ceramics, especially for Li-ion batteries.

Li H. et al. (2020) effectively reviewed the various formation mechanisms and synthesis of HE-NPs with their accompanying challenges. The authors stated there are polymer-mediated methods comprising template synthetic strategies, scanning probe block copolymer lithography, and high entropy metal-organic frameworks (MOFs) while other fabrication routes are listed below.

2.1.4.1 Chemical technique

Chemical fabrication of high entropy nanomaterials includes Nanodroplet-Mediated Electrodeposition, Wet chemical technique, Dealloying and alloying process. High entropy alloys fabricated at the nanoscale using wet chemical methods are prepared in a special solution by reducing or mixing metal salts with some capping agents for the regulation of crystal aggregation and growth. Singh and Srivastava (2015) studied the fabrication and electron microscopy of HE-NPs using wet chemical synthesis. The average particle sizes of the nanomaterial were 26.7 ± 3.3 nm, and the results showed that the nanomaterial was fairly uniformly distributed with a solid solution FCC structure observed. Liu et al. (2019) also fabricated a PtAuPdRhRu HE-NPs using wet chemical synthesis with an average particle size of ~ 3 nm, and the authors reported that the nanoparticle had high electrocatalytic activities for hydrogen evolution reactions.

The incorporation of a gas-blowing agent and transient high-temperature heating enabled for the first time by Wang et al. (2020), is a continuous "droplet-to-particle" approach of producing hollow HEA nanoparticles with homogeneous mixing of up to eight different components as shown in Figure 4. Metal chloride salts homogeneously dissolved in ethanol, together with citric acid, which serves as a blowing agent, were used to create an aerosol stream with particles as tiny as 1 m in diameter. The droplets are then conveyed by argon at a flow rate of 5 L min1 across the heating zone of a tube furnace.

The nanodroplet-mediated Potentiostatic electrodeposition using electrolytes that are nonaqueous solvents for the fabrication of PtPdRhRuCe HE-NPs but similar to carbothermal-shock produces amorphous microstructures, according to Yao L. et al. (2018). The method comprises using shock metal salt, which is covered by carbon nanofibers and followed by rapid quenching to produce nanoparticles with applications in catalysis and energy storage. While dealloying and alloying chemical methods of synthesizing high entropy nanoporous materials with ligament sizes of about 3 nm contain polyelemental particle systems like Pd, Al, Co, Ni, Fe, Cu, Au and Mo (Chen et al., 2016). Chemical dealloying can also be used to fabricate High entropy nano oxides (Np-HEOs) (Qiu et al., 2019). The process adds reactants to small volumes where the size and composition can be controlled independently while forcing the reactant to form single particles comprising five or more transition metal ions using dip-pen lithography. This influences the HE-NPs to facilitate magnetic, hybrid chemical and electronic interactions for diverse applications such as plasmonic, catalysis and biological imaging (Song et al., 2021; Wang H. et al., 2022).

2.1.4.2 Nonequilibrium technique

The nonequilibrium techniques of fabricating HE-NPs include the strategies for fast-moving bed pyrolysis, electro-shock synthesis, and carbothermal shock. Carbothermal shock involves using high reaction temperature alongside fast cooling and heating rates for the formation of the HE-NPs on oxygenated carbon substances. The method is similar to vapor deposition and can create homogeneous

components. Quinary HEA-NPs were synthesized on the aligned electrospun carbon nanofibers (ACNFs) based on a carbothermal shock (CTS) method by Xu et al. (2020). CTS, a quick and controllable method, is worthy to be further promoted for HEA-NPs synthesis, other methods include sol-gel combustion, mechanical grinding and laser-synthesis. The authors stated that unstable nanoparticles/carbonaceousnanomaterial synthesis results in inhomogeneous mass and charge transfer across the electrode/electrolyte interface. High-entropy alloy nanoparticles (HEA-NPs) are rarely reported in supercapacitors. They used a self-designed collector for aligned CNFs in conjunction with an appropriate CTS current direction. The FeNiCoMnMg HEA-NPs/ACNFs electrodes with a 5 mM precursor concentration exhibited excellent electrochemical performance, with a high capacitance of 203 F/g and a specific energy density of 21.7 Wh/kg. These results suggest that carbonaceous nanomaterials, such as HEA-NPs, are interesting candidates for energy storage applications.

Asanova et al. (2021) developed HE-NP by using thermal decomposition of the metal salt precursor and the results showed that in methanol oxidation, the nanomaterial possessed excellent electrocatalytic activities. Yao Y. et al. (2018) created a method for fabricating HE-NPs by shock metal salt that is covered in carbon nanofibers by thermally shocking the precursor metal salt and loading the mixtures onto carbon supports to solve the cooling rate constraints and control the particle size, composition, phase and variety of physical and chemical properties the HE-NPs present. The authors concluded that using carbothermal shock synthesis completely mixes the synthesized high entropy alloy through the precursor with several metal salts. Therefore, the process involves the assembling of metal salt precursors into a dissolved mixture and then distributing the resulting droplets in hole grooves containing carbon support by a carbon injector. Then the decomposition of the metal salt precursors follows using high reaction temperature and fast cooling and heating rates (-10^5 K/s).

Fast-moving bed pyrolysis for synthesizing HE-NPs comprises about ten immiscible elements such as rhodium, manganese, gold, cobalt, platinum, nickel, iridium, copper, tin, and palladium. The process with fast cooling and heating rates, and low free energy under high reactive temperature is similar to the carbothermal shock; however, compared to the Carbothermal shock process, which is divided into two stages, the fast-moving bed pyrolysis method is divided into three stages. The first stage is moving the precursors to monomers, then the second stage is moving the monomers to nuclei and finally the nuclei to nanocrystals. Gao et al. (2020) reported on the synthesis of MnCoNiCuRhPdSnIrPtAu HE-NPs using fast-moving bed pyrolysis to immobilize the nanoparticles on three granular support systems, namely,; carbon black and graphene oxide, zeolite and γ-Al_2O_3 x with a 2 nm narrow size distribution at 923 K. The authors argued that this process of synthesis efficiently immobilizes HE-NPs on granular supports and prevents aggregation and rapid growth of the nanoparticles experienced using arc melting and laser cladding techniques (Zhang et al., 2011; Yang et al., 2018). The results showed that the fast-moving bed pyrolysis allowed metal precursors to reach a temperature of 923 k quickly and simultaneous pyrolysis of the mixed metal precursors was observed, resulting in smaller nuclei clusters and high supersaturated monomers. However, the method is only restricted to phase-separated alloy compositions and more studies are required on this aspect.

On the other hand, the electro-shock method, which was accomplished by reducing the number of metal salt precursors to water nanodroplets suspended in an organic solvent, including cobalt (II) chloride ($CoCl_2$), manganese (II) chloride ($MnCl_2$), chromium (III) chloride ($CrCl_3$), nickel (II) chloride ($NiCl_2$), and vanadium trichloride (VCl_3). In particular, the procedure can encourage the collision of nanodroplets with a biased electrode and facilitate the transfer of metal salt precursors to form nucleation. This procedure was utilized to demonstrate that metal salt precursors can quickly transform into HEAs with precisely controllable stoichiometric ratios using an electro-shock lasting in the range of 100 ms. For example, Glasscott et al. (2019) studied the electrosynthesis of HE-NPs. The authors used a typical nanodroplet filled with precursors of equal molar content, such as $CoCl_2$, $MnCl_2$, $CrCl_3$, $NiCl_2$, and VCl_3, (resulting in a total of 40 mM of metal salt) to hit the carbon fiber ultramicroelectrodes (UMEs, radium of 4 mm). Due to UME's microscale size, less background current was present, which made it simpler to see a nanodroplet collision. Additionally, as the metal salts in the nanodroplets were electrolyzed, the electrode's current decreased. The amount of charge that was transferred during the reduction phase, Q_{red}, was calculated by integrating the current vs. time curve for the blip-type response. This number is comparable to the initial charge of a nanodroplet, Q_{ini}, which was equal the total charge required to deplete every metal precursor ion.

2.2 Properties of high entropy nanomaterials (HE-NPs)

Energy storage materials and devices require conversion systems that are available when needed. These conversion systems depend on selecting the most suitable catalysts, which help increase reaction rates and storage efficiencies. Catalytic activity is not limited to the surface adsorption energy, d-band center theory, and the electronic structures for reaction intermediates and molecules, hence modifying the composition of the high entropy alloys can optimize the electronic structures and surface adsorption energy, which enhances the catalyst performance (Tomboc et al., 2020). The properties of HE-NPs for catalytic applications were experimentally characterized using different equipment, tools and software listed in Table 1.

Li H. et al. (2020) prepared a nanoporous high–performance Al96Cu1Ni1Pt1X1 high entropy where x was varied between V, Ti, Mn, Au, Co, Ir, and Mo (1 at%) using a melt-spinning technique. Composition and structural characterization were achieved using XRD, SEM, XPS, and TEM. The results of the analysis are displayed in Figure 5. The HE-NP has a bimodal porous structure with nano ligaments. A highly active Oxygen Reduction Reaction (ORR) np-AlCuNiPtMn catalyst was developed with a 0.945 V half-wave potential in an acidic media and mass activity of about 16 fold higher than benchmark Pt/C catalysts.

Qui et al. (2019) fabricated a nanoporous senary, octonary and senary all-non-noble HE-Np by dealloying the precursor alloys. The XRD, TEM and HER Polarization data presented in Figure 6 showed the HE-Np had uniformly distributed 3 nm nano-ligaments and enhanced catalytic activity with long-term durability for electrocatalysis and CO oxidation.

TABLE 1 Tabular Representation of Various Characterization Tools for Determining the Properties of HE-NPs for catalytic Applications.

Characterization	Objective
X-ray diffraction (XRD)	Investigates the phase analysis
Scanning Electron Microscopy (SEM) or Transmission electron microscopy (TEM)	Determines the particle shape and size distributions
Electron Probe Microanalysis (EPMA)	Quantifies each component
Inductively Coupled Plasma Mass Spectrometry (ICP-MS)	Detects the elements at milligram to nanogram and estimates the trace contamination level
X-Ray Photoelectron Spectroscopy (XPS), Atomic Emission Spectroscopy (AES), Operando X-Ray Absorption Near Edge Spectroscopy (XANES), Analysis of the Extended X-Ray Absorption Fine-Structure (EXFAS), and Surface Plasmon Resonance (SPR) Spectroscopic analysis	Investigates the surface chemistry, binding energy, and oxidation state
Density Functional Theory (DFT) Calculation and Molecular Dynamics Simulations	Determines the physical movements of molecules and atoms, energy barrier, ionic mobility and density of state
Cyclic Voltammetry	Probes the redox potential of the catalyst system and the oxidation reduction rates
Chronoamperometry	Examines the catalyst stability and the current changes during reaction

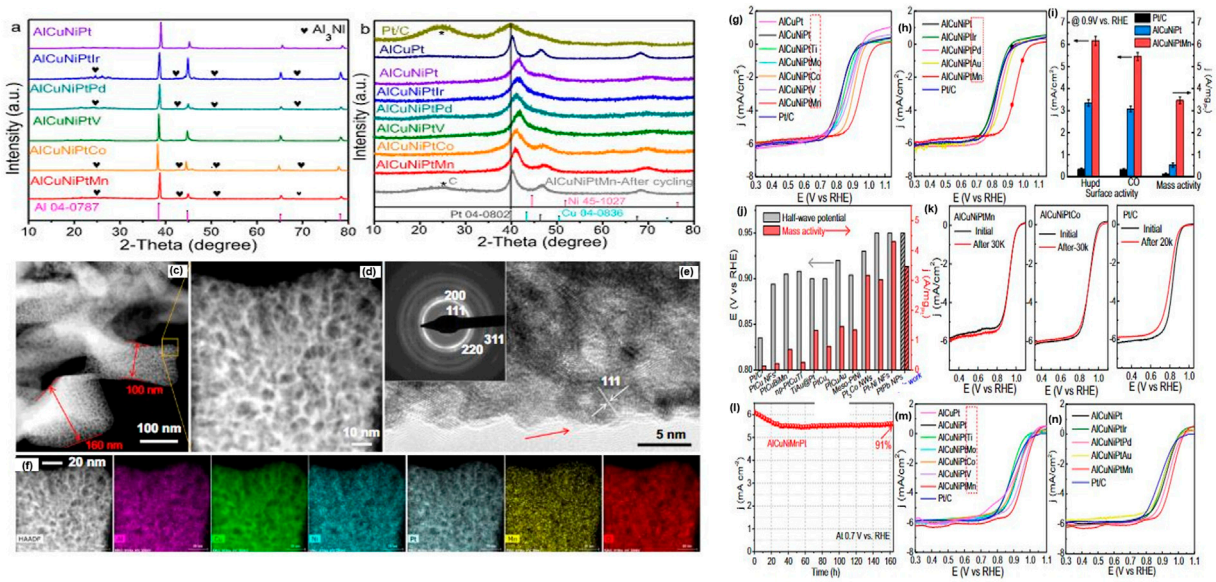

FIGURE 5
(A, B) XRD graphs of the precursor HE-NPs before and after etching in 0.5 M NaoH solution **(C–F)** SEM and TEM Micrographs of the np-AlCuNiPtMn HE-NP. **(G–N)** Oxygen Polarization curves of the HE-NPs (Li S. et al., 2020)

3 Application of high entropy nanomaterials

Although it is currently quite difficult, the creation of highly active and stable catalysts is important for the conversion of renewable energy, and the numerous elemental compositional combinations of HE-NPs offer several possibilities. Hence, due to their advantages in catalytic applications such as carbon dioxide reduction, water electrocatalysis and oxygen reduction, some newly developed catalysts based on HEAs with amazing catalytic activity, excellent product selectivity, and good durability have recently attracted a lot of research interest. To highlight the significant potentials of HEAs in the application of energy conversion, this study concentrates on discussing the catalytic conversion reactions of the hydrogen evolution reaction (HER) while just highlighting the oxygen reduction reaction (ORR), oxygen evolution reaction (OER), CO_2 reduction reaction (CO_2RR), and ammonia (NH_3) decomposition.

3.1 Electrocatalytic hydrogen evolution reaction

There is an immediate need for the development and effective use of renewable and clean energy resources due to the widely

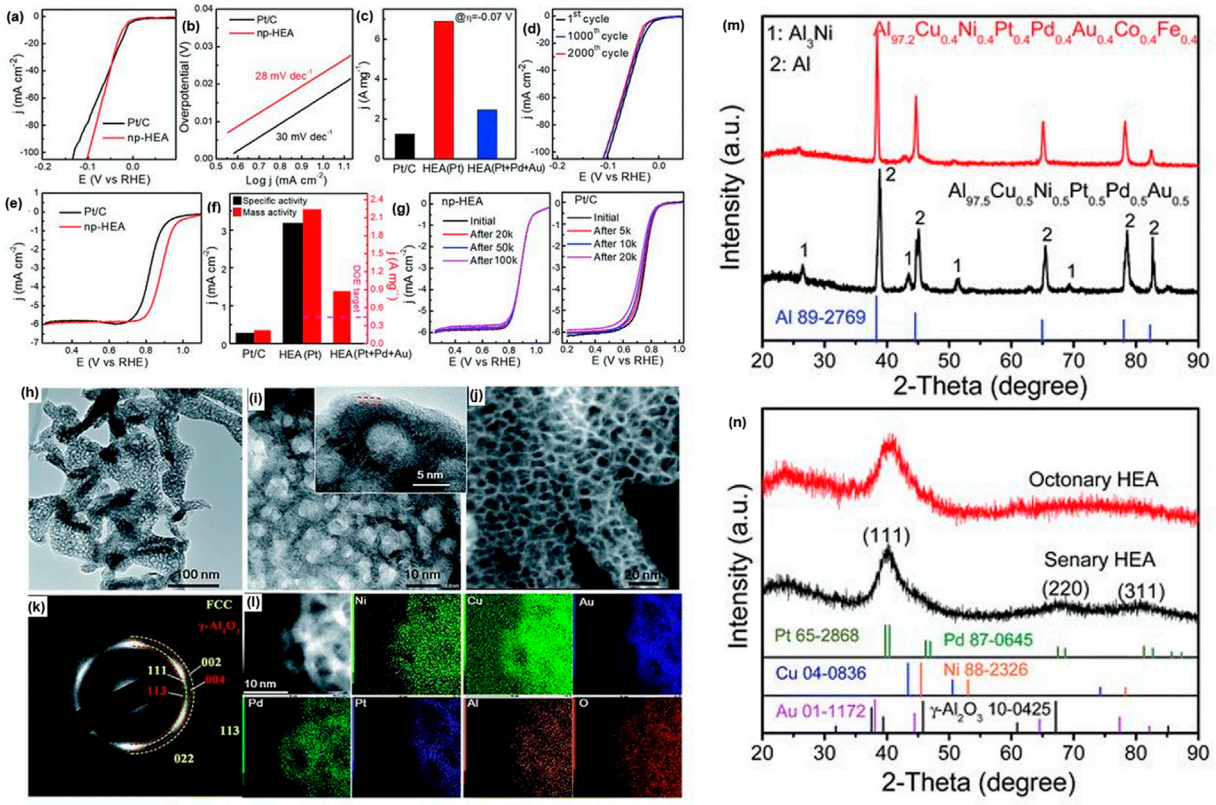

FIGURE 6
(A–G) HER Polarization curves, **(H–L)** TEM micrographs of the HEA-NP, **(M, N)** XRD graphs of the octonary and precursor senary alloy before and after dealloying in 0.5 M NaOH solution.

anticipated depletion of the world's fossil fuel reserves and the significant growth in greenhouse gas emissions and other environmental pollutions (Chen et al., 2020; Yao et al., 2021). Different approaches have been used to deal with the issues. Future changes to how we live could be influenced by one of them, the ability to store energy effectively, as well as the possibility of producing power and fuels like hydrogen using solar energy (Feng et al., 2021). Hydrogen (H2) as the most prevalent element in the Universe, is found in large quantities in water and organic substances (Zhang et al., 2021). It is a sustainable energy for solving the world's fossil fuel and environmental pollution challenges (Lin et al., 2022). The simplest and lower energy density by volume necessitates a larger storage tank. The very low ignition temperature of the flammable gas, hydrogen, is a major contributor to the risk connected with using it. Hydrogen has an atomic mass of 1.00794 due to its small molecular size and corrosive nature (Hydrogen Council, 2020; Yu et al., 2021).

Hydrogen with one proton and one electron make up the colorless, odorless, and flammable gas, which has an atomic mass of 1.008 (rounded up). The main safety issue is that if a leak goes unnoticed, and the gas builds up in a small area, it could eventually catch fire and explode (Abe et al., 2019; Andersson and Grönkvist, 2019). Compared to hydrocarbons, hydrogen gas has a better energy density by weight, which can cause mechanical failure and leakage in some materials; it can escape through materials (Andersson and Grönkvist, 2019; Howarth and Jacobson, 2021; Kovač et al., 2021). To illustrate the most cutting-edge hydrogen generation methods, various hydrogen production paths and technologies have been explored and contrasted. The four primary categories of hydrogen production pathways in the literature are electrolysis, photolysis, biolysis, and thermolysis (Abdin et al., 2020; Dawood et al., 2020; Yue et al., 2021).

The electrocatalytic hydrogen evolution reaction has received a lot of attention as one of the most promising methods of producing artificial hydrogen (Lu et al., 2022). Due to their distinct microstructures and unheard-of physicochemical features, HE-NPs have recently gained impressive scientific attention in the hydrogen evolution reaction process (HER) (Feng et al., 2022). It is generally known that catalysts made of noble metals, such as Ru and Pt, can increase the kinetics of the HER and lower electrochemical overpotentials for very effective water spitting (Ma et al., 2020). The HE-NPs with economic transition metals have received a lot of attention in the quest to create an effective catalyst that trades off low cost and efficiency (Fan et al., 2022). Furthermore, an efficient method for analyzing interfacial reactions and electrode dynamics in the HER is through electrochemical impedance spectroscopy (EIS) and one of the main elements influencing HER kinetics is rapid electron transport (Cai et al., 2021; Wang R. et al., 2022). Jia et al. (2020) stated that for the creation of hydrogen, electrochemical water splitting offers an

appealing method. However, its uses are greatly hampered by the lack of a high-performance, cost-effective electrocatalyst. In this article, a multinary high-entropy intermetallic (HEI) with multiple non-noble elements and an unusual regularly organized structure is described.

This material can act as a highly effective electrocatalyst for hydrogen evolution. With an overpotential of 88.2 mV at a current density of 10 mA cm^{-2} and a Tafel slope of 40.1 mV dec^{-1}, this HEI demonstrates exceptional alkalinity activities that are equivalent to those of noble catalysts. Theoretical studies show that startling atomic configurations and chemical complexity work in synergy to change the electrical structure. Additionally, a special site-isolation effect is made possible by the distinctive L12-type ordered structure to further stabilize the H2O/H* adsorption/desorption, which significantly lowers the energy barrier of hydrogen evolution.

A unique paradigm for creating innovative electrocatalysts with enhanced reaction activity is revealed by such an HEI method. Li and Chen (2021) described the dealloying and melt-spinning method for the fabrication of FeCoNiAlTi HE-NPs for electrocatalytic hydrogen evolution reactions. The results showed that there were no elemental changes but there was homogeneity with excellent activity as HER catalyst. The nanomaterial showed a Tafel slope of 40.1 mV/dec indicating that the material is a superior electrocatalyst, keeping adequate over potentials without amplifications showing that the nanomaterial has an excellent hydrogen evolution reaction stability. The authors concluded that the FeCoNiAlTi HE-NPs is a strong potential for HER electrocatalyst attributed to their environmental friendliness, low-cost and catalytic activities.

Gao et al. (2020) mentioned that for the creation of hydrogen, electrochemical water splitting offers an appealing method. However, its uses are greatly hampered by the lack of a high-performance, cost-effective electrocatalyst. In this article, a multinary high-entropy intermetallic (HEI) with multiple non-noble elements and an unusually regularly organized structure was developed. The authors stated that the material can act as a highly effective electrocatalyst for hydrogen evolution. With an overpotential of 88.2 mV at a current density of 10 mA cm^{2} and a Tafel slope of 40.1 mV dec^{-1}, this HEI demonstrates exceptional alkalinity activities that are equivalent to those of noble catalysts. Theoretical studies show that startling atomic configurations and chemical complexity work in synergy to change the electrical structure.

Zhang et al. (2018) detailed that transition metals and their alloys are projected to have significant catalytic activity for the hydrogen evolution reaction because of their partially filled d orbitals, which are suited for electron uptake and loss. However, their employment as electrocatalysts in both acidic and alkaline electrolytes is constrained by poor corrosion resistance. Here, we provide proof that the very corrosion-resistant high entropy alloy (HEA, $Ni_{20}Fe_{20}Mo_{10}Co_{35}Cr_{15}$) can behave as a very stable electrocatalyst for the hydrogen evolution reaction in both basic and acidic solutions. The HEA only requires an overpotential of 107 mV in acidic solutions and 172 mV in basic solutions at current densities of 100 mA cm^{-2}, which is significantly better than that of the dual-phase counterpart and even on par with that of the Pt sheet. The HEA only requires an overpotential of 107 mV in acidic solutions and 172 mV in basic solutions at current densities of 100 mA cm^{-2} for the hydrogen evolution reaction in both acidic and alkaline solutions. Which are much better than those of the dual-phase counterpart and even on par with those of Pt sheets and the majority of reported nanostructured noble-metal-free catalysts.

Intriguing electrochemical energy storage characteristics are anticipated for high entropy spinel oxides (HEO), a novel class of material stabilized by contributions from configurational entropy, according to Talluri et al. (2021). A reverse co-precipitation method was used to create the first spinel $(CrMnFeCoNi)_3O_4$ HEO nanoparticle-based supercapacitor electrode material. The phase-pure spinel structure was validated by the X-ray diffraction study. The oxidation states of the cations in spinel HEO were determined using X-ray photoelectron spectroscopy. HEO nanoparticles had a homogenous cation distribution and a smooth spherical shape, according to scanning electron microscopy and electron dispersive X-ray spectroscopy results. On the spinel HEO-based supercapacitor electrode material, electrochemical energy storage characteristics were further investigated with results showing that at a current density of 0.5 A g^{-1}, the HEO electrode had a capacitance of 239 F g^{-1} and a specific energy of 24.1 Wh kg^{-1}. From 0.5 to 25 A g^{-1}, a rate capability of 38% was seen. After 1,000 cycles, the retention of the capacitance was found to be 76%. For 1,000 cycles, the columbic efficiency remained at 86%, showing that HEO had strong charge-discharge reversibility. HEO electrodes were discovered to have solution resistance (Rs) and charge transfer (Rct) values of 0.96 and 1.56, respectively. The use of pure spinel-type HEO nanoparticles in supercapacitor was described for the first time, providing a starting point for subsequent research into other HEOs.

4 Summary and outlook

Attributed to their high surface area, which leads to parasitic interactions with the electrolyte, especially during the first cycle, known as the first cycle irreversibility, and their tendency to aggregate, the high entropy nanomaterials are limited in energy storage devices. Therefore, future initiatives seek to develop the intelligent assembly of nanomaterials into controlled-geometry architectures. Additionally, it is important to combine nanomaterials with complementary functions, such as graphene's high electronic conductivity or MXenes' high operating voltage and strong redox activity of oxides. Building complex electrode topologies involve innovative manufacturing techniques, including 3D printing, spray deposition, and other methods. Devices composed of nanomaterials should be produced using already known processes such as 3D printing, roll-to-roll manufacturing, self-assembly from solutions, atomic layer deposition, and other advanced techniques. Co-sputtering from elemental or alloy targets into ionic liquids allows for the fabrication of multinary NP libraries with adjustable compositional diversity. How to increase HEA-NPs yields and separate them from ionic liquids for intended uses, however, is still a mystery and should be further investigated. Despite the potential for applications in a wide range of industries, there are still significant gaps between laboratory research and real-world engineering applications of High entropy alloys on the micro and nanoscale. While actual applications must be justified by

considering a combination of several features, laboratory research concentrates on one or two fundamental properties that are important to a particular application. For instance, HE-NPs used for energy conversion applications must also have excellent strength and ductility to maintain structural integrity under difficult conditions. To close the gaps, additional application-driven or application-focused research that examines all-important qualities is needed. Benchmarking against commercial materials, if available, is another critical step in establishing the validity of HE-NPs in specific applications.

5 Conclusion

The development of high-performance high entropy nanomaterials is essential despite the advancement of current energy conversion and storage technologies and devices because it is challenging to simultaneously achieve high levels of energy conversion and adequate energy storage. To avoid the requirement for restacking, maintain a high surface area, and allow target molecules and ions to intercalate, the proper design of HE-NPs is very important. Additionally, it may be necessary to take into account the energy and environmental implications of the production of nanomaterials in addition to high entropy-based nanomaterials. Although these newly developed, HE-NPs show promise for the creation of high-performance electrocatalytic applications, there are still many obstacles to be solved.

Author contributions

DM: Conceptualization, Writing of Original draft, Review and Editing PP: Supervision, Writing of Original draft, Review and Editing.

Conflict of interest

The authors declare that the research was conducted in the absence of any commercial or financial relationships that could be construed as a potential conflict of interest.

Publisher's note

References

Abdin, Z., Zafaranloo, A., Rafiee, A., Merida, W., Lipinski, W., and Khalilpour, K. R. (2020). Hydrogen as an energy vector. *Renew. Sustain. energy Rev.* 120, 109620. doi:10.1016/j.rser.2019.109620

Abe, J. O., Popoola, A., Ajenifuja, E., and Popoola, O. M. (2019). Hydrogen energy, economy and storage: Review and recommendation. *Int. J. Hydrogen Energy* 44 (29), 15072–15086. doi:10.1016/j.ijhydene.2019.04.068

Abedi, M., Asadi, A., Vorotilo, S., and Mukasyan, A. S. (2021). A critical review on spark plasma sintering of copper and its alloys. *J. Mater. Sci.* 56 (36), 19739–19766. doi:10.1007/s10853-021-06556-z

Ali, N., Teixeira, J. A., Addali, A., Saeed, M., Al-Zubi, F., Sedaghat, A., et al. (2019). Deposition of stainless steel thin films: An electron beam physical vapour deposition approach. *Materials* 12 (4), 571. doi:10.3390/ma12040571

Andersson, J., and Grönkvist, S. (2019). Large-scale storage of hydrogen. *Int. J. Hydrogen Energy* 44 (23), 11901–11919. doi:10.1016/j.ijhydene.2019.03.063

Arif, Z. U., Khalid, M. Y., Ur Rehman, E., Ullah, S., Atif, M., and Tariq, A. (2021). A review on laser cladding of high-entropy alloys, their recent trends and potential applications. *J. Manuf. Process.* 68, 225–273. doi:10.1016/j.jmapro.2021.06.041

Asanova, T., Asanov, I., Yusenko, K., La Fontaine, C., Gerasimov, E., Zadesenets, A., et al. (2021). Time-resolved study of pd-os and pt-os nanoalloys formation through thermal decomposition of [pd (nh3) 4] [oscl6] and [pt (nh3) 4] [oscl6] complex salts. *Mater. Res. Bull.* 144, 111511. doi:10.1016/j.materresbull.2021.111511

Baptista, A., Silva, F., Porteiro, J., Miguez, J., Pinto, G., and Fernandes, L. (2018b). On the physical vapour deposition (pvd): Evolution of magnetron sputtering processes for industrial applications. *Procedia Manuf.* 17, 746–757. doi:10.1016/j.promfg.2018.10.125

Baptista, A., Silva, F., Porteiro, J., Miguez, J., and Pinto, G. (2018a). Sputtering physical vapour deposition (pvd) coatings: A critical review on process improvement and market trend demands. *Coatings* 8 (11), 402. doi:10.3390/coatings8110402

Benjamin, J. (1992). Fundamentals of mechanical alloying. *Mater. Sci. Forum* 88-90, 1–18. doi:10.4028/www.scientific.net/MSF.88-90.1

Boddu, M. R., Landers, R. G., and Liou, F. W. (2001). "Control of laser cladding for rapid prototyping--a review," in 2001 International Solid Freeform Fabrication Symposium, Austin, Texas, August 6-8, 2001.

Cai, Z-X., Goou, H., Ito, Y., Tokunaga, T., Miyauchi, M., Abe, H., et al. (2021). Nanoporous ultra-high-entropy alloys containing fourteen elements for water splitting electrocatalysis. *Chem. Sci.* 12 (34), 11306–11315. doi:10.1039/d1sc01981c

Cao, B., Wang, C., Yang, T., and Liu, C. (2020). Cocktail effects in understanding the stability and properties of face-centered-cubic high-entropy alloys at ambient and cryogenic temperatures. *Scr. Mater.* 187, 250–255. doi:10.1016/j.scriptamat.2020.06.008

Chen, J., Zhou, X., Wang, W., Liu, B., Lv, Y., Yang, W., et al. (2018). A review on fundamental of high entropy alloys with promising high–temperature properties. *J. Alloys Compd.* 760, 15–30. doi:10.1016/j.jallcom.2018.05.067

Chen, P-C., Liu, X., Hedrick, J. L., Xie, Z., Wang, S., Lin, Q. Y., et al. (2016). Polyelemental nanoparticle libraries. *Science* 352 (6293), 1565–1569. doi:10.1126/science.aaf8402

Chen, Z., Qing, H., Zhou, K., Sun, D., and Wu, R. (2020). Metal-organic framework-derived nanocomposites for electrocatalytic hydrogen evolution reaction. *Prog. Mater. Sci.* 108, 100618. doi:10.1016/j.pmatsci.2019.100618

Courtney, T. H. (1995). Process modeling of mechanical alloying (overview). *Mater. Trans. JIM* 36 (2), 110–122. doi:10.2320/matertrans1989.36.110

Da Silva, C. M., Amara, H., Fossard, F., Girard, A., Loiseau, A., and Huc, V. (2022). Colloidal synthesis of nanoparticles: From bimetallic to high entropy alloys. *Nanoscale* 14 (27), 9832–9841. doi:10.1039/d2nr02478k

Dąbrowa, J., Kucza, W., Cieślak, G., Kulik, T., Danielewski, M., and Yeh, J. W. (2016). Interdiffusion in the fcc-structured al-co-cr-fe-ni high entropy alloys: Experimental studies and numerical simulations. *J. Alloys Compd.* 674, 455–462. doi:10.1016/j.jallcom.2016.03.046

Dawood, F., Anda, M., and Shafiullah, G. (2020). Hydrogen production for energy: An overview. *Int. J. Hydrogen Energy* 45 (7), 3847–3869. doi:10.1016/j.ijhydene.2019.12.059

Dudina, D. V., Bokhonov, B. B., and Olevsky, E. A. (2019). Fabrication of porous materials by spark plasma sintering: A review. *Materials* 12 (3), 541. doi:10.3390/ma12030541

Fan, L., Ji, Y., Wang, G., Chen, J., Chen, K., Liu, X., et al. (2022). High entropy alloy electrocatalytic electrode toward alkaline glycerol valorization coupling with acidic hydrogen production. *J. Am. Chem. Soc.* 144 (16), 7224–7235. doi:10.1021/jacs.1c13740

Feng, D., Dong, Y., Nie, P., Zhang, L., and Qiao, Z. A. (2022). Conicumgzn high entropy alloy nanoparticles embedded onto graphene sheets via anchoring and alloying strategy as efficient electrocatalysts for hydrogen evolution reaction. *Chem. Eng. J.* 430, 132883. doi:10.1016/j.cej.2021.132883

Feng, G., Ning, F., Song, J., Shang, H., Zhang, K., Ding, Z., et al. (2021). Sub-2 nm ultrasmall high-entropy alloy nanoparticles for extremely superior electrocatalytic hydrogen evolution. *J. Am. Chem. Soc.* 143 (41), 17117–17127. doi:10.1021/jacs.1c07643

Fu, Y., Li, J., Luo, H., Du, C., and Li, X. (2021). Recent advances on environmental corrosion behavior and mechanism of high-entropy alloys. *J. Mater. Sci. Technol.* 80, 217–233. doi:10.1016/j.jmst.2020.11.044

Gao, S., Hao, S., Huang, Z., Yuan, Y., Han, S., Lei, L., et al. (2020). Synthesis of high-entropy alloy nanoparticles on supports by the fast moving bed pyrolysis. *Nat. Commun.* 11 (1), 2016. doi:10.1038/s41467-020-15934-1

Garzón-Manjón, A., Meyer, H., Grochla, D., Loffler, T., Schuhmann, W., Ludwig, A., et al. (2018). Controlling the amorphous and crystalline state of multinary alloy nanoparticles in an ionic liquid. *Nanomaterials* 8 (11), 903. doi:10.3390/nano8110903

George, E. P., Curtin, W., and Tasan, C. C. (2020). High entropy alloys: A focused review of mechanical properties and deformation mechanisms. *Acta Mater.* 188, 435–474. doi:10.1016/j.actamat.2019.12.015

George, E. P., Raabe, D., and Ritchie, R. O. (2019). High-entropy alloys. *Nat. Rev. Mater.* 4 (8), 515–534. doi:10.1038/s41578-019-0121-4

Glasscott, M. W., Pendergast, A. D., Goines, S., Bishop, A. R., Hoang, A. T., Renault, C., et al. (2019). Electrosynthesis of high-entropy metallic glass nanoparticles for designer, multi-functional electrocatalysis. *Nat. Commun.* 10 (1), 2650–2658. doi:10.1038/s41467-019-10303-z

Guillon, O., Gonzalez-Julian, J., Dargatz, B., Kessel, T., Schierning, G., Rathel, J., et al. (2014). Field-assisted sintering technology/spark plasma sintering: Mechanisms, materials, and technology developments. *Adv. Eng. Mater.* 16 (7), 830–849. doi:10.1002/adem.201300409

Gupta, G., Tyagi, R., Rajput, S., Saxena, P., Vashisth, A., and Mehndiratta, S. (2021). Pvd based thin film deposition methods and characterization/property of different compositional coatings-a critical analysis. *Mater. Today Proc.* 38, 259–264. doi:10.1016/j.matpr.2020.07.132

Han, C., Fang, Q., Shi, Y., Tor, S. B., Chua, C. K., and Zhou, K. (2020). Recent advances on high-entropy alloys for 3d printing. *Adv. Mater.* 32 (26), 1903855. doi:10.1002/adma.201903855

Howarth, R. W., and Jacobson, M. Z. (2021). How green is blue hydrogen? *Energy Sci. Eng.* 9 (10), 1676–1687. doi:10.1002/ese3.956

Hu, J., Shen, H., Jiang, M., Gong, H., Xiao, H., Liu, Z., et al. (2019). A dft study of hydrogen storage in high-entropy alloy tizrhfscmo. *Nanomaterials* 9 (3), 461. doi:10.3390/nano9030461

Hu, Z-Y., Zhang, Z-H., Cheng, X-W., Wang, F. C., and Li, S. L. (2020). A review of multi-physical fields induced phenomena and effects in spark plasma sintering: Fundamentals and applications. *Mater. Des.* 191, 108662. doi:10.1016/j.matdes.2020.108662

Huang, E-W., and Liaw, P. K. (2019). High-temperature materials for structural applications: New perspectives on high-entropy alloys, bulk metallic glasses, and nanomaterials. *MRS Bull.* 44 (11), 847–853. doi:10.1557/mrs.2019.257

Hungria, T., Galy, J., and Castro, A. (2009). Spark plasma sintering as a useful technique to the nanostructuration of piezo-ferroelectric materials. *Adv. Eng. Mater.* 11 (8), 615–631. doi:10.1002/adem.200900052

Hussain, I., Lamiel, C., Ahmad, M., Chen, Y., Shuang, S., Javed, M. S., et al. (2021). High entropy alloys as electrode material for supercapacitors: A review. *J. Energy Storage* 44, 103405. doi:10.1016/j.est.2021.103405

Hydrogen Council (2020). *Path to hydrogen competitiveness: A cost perspective*. Belgium: Hydrogen Council.

Jia, Z., Yang, T., Sun, L., Zhao, Y., Li, W., Luan, J., et al. (2020). A novel multinary intermetallic as an active electrocatalyst for hydrogen evolution. *Adv. Mater.* 32 (21), 2000385. doi:10.1002/adma.202000385

Jiang, R., Da, Y., Han, X., Chen, Y., Deng, Y., and Hu, W. (2021). Ultrafast synthesis for functional nanomaterials. *Cell. Rep. Phys. Sci.* 2 (1), 100302. doi:10.1016/j.xcrp.2020.100302

Jien-Wei, Y. (2006). Recent progress in high entropy alloys. *Ann. Chim. Sci. Mat.* 31 (6), 633–648. doi:10.3166/acsm.31.633-648

Kessel, H., Hennicke, J., Kirchner, R., and Kessel, T. (2010). *Rapid sintering of novel materials by fast/sps—further development to the point of an industrial production process with high cost efficiency*. FCT Systeme GmbH, Geinberg, 96528.

Koch, C. (1998). Intermetallic matrix composites prepared by mechanical alloying—A review. *Mater. Sci. Eng. A* 244 (1), 39–48. doi:10.1016/s0921-5093(97)00824-1

Kovač, A., Paranos, M., and Marciuš, D. (2021). Hydrogen in energy transition: A review. *Int. J. Hydrogen Energy* 46 (16), 10016–10035. doi:10.1016/j.ijhydene.2020.11.256

Kulkarni, K., and Chauhan, G. P. S. (2015). Investigations of quaternary interdiffusion in a constituent system of high entropy alloys. *AIP Adv.* 5 (9), 097162. doi:10.1063/1.4931806

Li, H., Lai, J., Li, Z., and Wang, L. (2021a). Multi-sites electrocatalysis in high-entropy alloys. *Adv. Funct. Mater.* 31 (47), 2106715. doi:10.1002/adfm.202106715

Li, H., Zhu, H., Zhang, S., Zhang, N., Du, M., and Chai, Y. (2020a). Nano high-entropy materials: Synthesis strategies and catalytic applications. *Small Struct.* 1 (2), 2000033. doi:10.1002/sstr.202000033

Li, K., and Chen, W. (2021). Recent progress in high-entropy alloys for catalysts: Synthesis, applications, and prospects. *Mater. Today Energy* 20, 100638. doi:10.1016/j.mtener.2021.100638

Li, S., Tang, X., Jia, H., Li, H., Xie, G., Liu, X., et al. (2020b). Nanoporous high-entropy alloys with low Pt loadings for high-performance electrochemical oxygen reduction. *J. Catal.* 383, 164–171. doi:10.1016/j.jcat.2020.01.024

Li, W., Xie, D., Li, D., Zhang, Y., Gao, Y., and Liaw, P. K. (2021b). Mechanical behavior of high-entropy alloys. *Prog. Mater. Sci.* 118, 100777. doi:10.1016/j.pmatsci.2021.100777

Li, Z., Pradeep, K. G., Deng, Y., Raabe, D., and Tasan, C. C. (2016). Metastable high-entropy dual-phase alloys overcome the strength–ductility trade-off. *Nature* 534 (7606), 227–230. doi:10.1038/nature17981

Li, Z., Zhao, S., Ritchie, R. O., and Meyers, M. A. (2019). Mechanical properties of high-entropy alloys with emphasis on face-centered cubic alloys. *Prog. Mater. Sci.* 102, 296–345. doi:10.1016/j.pmatsci.2018.12.003

Lin, H. J., Lu, Y. S., Zhang, L. T., Liu, H. Z., Edalati, K., and Révész, Á. (2022). Recent advances in metastable alloys for hydrogen storage: A review. *Rare Met.* 41 (6), 1797–1817. doi:10.1007/s12598-021-01917-8

Liu, D., Liu, H., Ning, S., and Chu, Y. (2020). Chrysanthemum-like high-entropy diboride nanoflowers: A new class of high-entropy nanomaterials. *J. Adv. Ceram.* 9 (3), 339–348. doi:10.1007/s40145-020-0373-x

Liu, J., Yu, H., Chen, C., Weng, F., and Dai, J. (2017). Research and development status of laser cladding on magnesium alloys: A review. *Opt. Lasers Eng.* 93, 195–210. doi:10.1016/j.optlaseng.2017.02.007

Liu, M., Zhang, Z., Okejiri, F., Yang, S., Zhou, S., and Dai, S. (2019). Entropy-maximized synthesis of multimetallic nanoparticle catalysts via a ultrasonication-assisted wet chemistry method under ambient conditions. *Adv. Mater. Interfaces* 6 (7), 1900015. doi:10.1002/admi.201900015

Liu, Y., Ding, Y., Yang, L., Sun, R., Zhang, T., and Yang, X. (2021). Research and progress of laser cladding on engineering alloys: A review. *J. Manuf. Process.* 66, 341–363. doi:10.1016/j.jmapro.2021.03.061

Lu, Y., Xu, S., Zhang, L., Hu, Q., Song, J., Zhang, F., et al. (2022). The characteristics of excellent electrocatalytic hydrogen evolution for feconi based high entropy alloys. *Sustain. Mater. Technol.* 33, e00455. doi:10.1016/j.susmat.2022.e00455

Ma, P., Zhao, M., Zhang, L., Wang, H., Gu, J., Sun, Y., et al. (2020). Self-supported high-entropy alloy electrocatalyst for highly efficient h2 evolution in acid condition. *J. Materiomics* 6 (4), 736–742. doi:10.1016/j.jmat.2020.06.001

Mao, A., Ding, P., Quan, F., Zhang, T., Ran, X., Li, Y., et al. (2018). Effect of aluminum element on microstructure evolution and properties of multicomponent al-co-cr-cu-fe-ni nanoparticles. *J. Alloys Compd.* 735, 1167–1175. doi:10.1016/j.jallcom.2017.11.233

Marques, F., Balcerzak, M., Winkelmann, F., Zepon, G., and Felderhoff, M. (2021). Review and outlook on high-entropy alloys for hydrogen storage. *Energy and Environ. Sci.* 14 (10), 5191–5227. doi:10.1039/d1ee01543e

Matizamhuka, W. (2016). Spark plasma sintering (sps)-an advanced sintering technique for structural nanocomposite materials. *J. South. Afr. Inst. Min. Metallurgy* 116 (12), 1171–1180. doi:10.17159/2411-9717/2016/v116n12a12

Miracle, D. B., and Senkov, O. N. (2017). A critical review of high entropy alloys and related concepts. *Acta Mater.* 122, 448–511. doi:10.1016/j.actamat.2016.08.081

Mogale, N. F., and Matizamhuka, W. R. (2020). Spark plasma sintering of titanium aluminides: A progress review on processing, structure-property relations, alloy development and challenges. *Metals* 10 (8), 1080. doi:10.3390/met10081080

Moghaddam, A. O., Shaburova, N. A., Samodurova, M. N., Abdollahzadeh, A., and Trofimov, E. A. (2021). Additive manufacturing of high entropy alloys: A practical review. *J. Mater. Sci. Technol.* 77, 131–162. doi:10.1016/j.jmst.2020.11.029

Munir, Z., Anselmi-Tamburini, U., and Ohyanagi, M. (2006). The effect of electric field and pressure on the synthesis and consolidation of materials: A review of the spark plasma sintering method. *J. Mater. Sci.* 41 (3), 763–777. doi:10.1007/s10853-006-6555-2

Murty, B., and Ranganathan, S. (1998). Novel materials synthesis by mechanical alloying/milling. *Int. Mater. Rev.* 43 (3), 101–141. doi:10.1179/imr.1998.43.3.101

Nagesha, K., Rajanish, M., and Shivappa, D. (2013). A review on mechanical alloying. *change* 3.

Okulov, A. V., Joo, S-H., Kim, H. S., Kato, H., and Okulov, I. V. (2020). Nanoporous high-entropy alloy by liquid metal dealloying. *Metals* 10 (10), 1396. doi:10.3390/met10101396

Pinto, G., Silva, F., Porteiro, J., Miguez, J., Baptista, A., and Fernandes, L. (2018). A critical review on the numerical simulation related to physical vapour deposition. *Procedia Manuf.* 17, 860–869. doi:10.1016/j.promfg.2018.10.138

Porodko, O., Fabián, M., Kolev, H., Lisnichuk, M., Zukalova, M., Vinarcikova, M., et al. (2022). A novel high entropy spinel-type aluminate mal2o4 (m= zn, mg, cu, co) and its lithiated oxyfluoride and oxychloride derivatives prepared by one-step mechanosynthesis. *Z. für Phys. Chem.* 236 (6-8), 713–726. doi:10.1515/zpch-2021-3106

Qiu, H-J., Fang, G., Gao, J., Wen, Y., Lv, J., Li, H., et al. (2019). Noble metal-free nanoporous high-entropy alloys as highly efficient electrocatalysts for oxygen evolution reaction. *ACS Mater. Lett.* 1 (5), 526–533. doi:10.1021/acsmaterialslett.9b00414

Ranganathan, S. (2003). Alloyed pleasures: Multimetallic cocktails. *Curr. Sci.* 85 (10), 1404–1406.

Reichelt, K., and Jiang, X. (1990). The preparation of thin films by physical vapour deposition methods. *Thin Solid Films* 191 (1), 91–126. doi:10.1016/0040-6090(90)90277-k

Saheb, N., Iqbal, Z., Khalil, A., Hakeem, A. S., Al Aqeeli, N., Laoui, T., et al. (2012). Spark plasma sintering of metals and metal matrix nanocomposites: A review. *J. Nanomater.* 2012, 1–13. doi:10.1155/2012/983470

Santo, L. (2008). Laser cladding of metals: A review. *Int. J. Surf. Sci. Eng.* 2 (5), 327–336. doi:10.1504/ijsurfse.2008.021345

Sathiyamoorthi, P., and Kim, H. S. (2022). High-entropy alloys with heterogeneous microstructure: Processing and mechanical properties. *Prog. Mater. Sci.* 123, 100709. doi:10.1016/j.pmatsci.2020.100709

Schneider, J. M., Rohde, S., Sproul, W. D., and Matthews, A. (2000). Recent developments in plasma assisted physical vapour deposition. *J. Phys. D Appl. Phys.* 33 (18), R173–R186. doi:10.1088/0022-3727/33/18/201

Schuh, B., Mendez-Martin, F., Völker, B., George, E., Clemens, H., Pippan, R., et al. (2015). Mechanical properties, microstructure and thermal stability of a nanocrystalline cocrfemnni high-entropy alloy after severe plastic deformation. *Acta Mater.* 96, 258–268. doi:10.1016/j.actamat.2015.06.025

Senkov, O. N., Miracle, D. B., Chaput, K. J., and Couzinie, J. P. (2018). Development and exploration of refractory high entropy alloys—A review. *J. Mater. Res.* 33 (19), 3092–3128. doi:10.1557/jmr.2018.153

Siddiqui, A. A., and Dubey, A. K. (2021). Recent trends in laser cladding and surface alloying. *Opt. Laser Technol.* 134, 106619. doi:10.1016/j.optlastec.2020.106619

Singh, M. P., and Srivastava, C. (2015). Synthesis and electron microscopy of high entropy alloy nanoparticles. *Mater. Lett.* 160, 419–422. doi:10.1016/j.matlet.2015.08.032

Singh, S., Goyal, D. K., Kumar, P., and Bansal, A. (2020). Laser cladding technique for erosive wear applications: A review. *Mater. Res. Express* 7 (1), 012007. doi:10.1088/2053-1591/ab6894

Song, J-Y., Kim, C., Kim, M., Cho, K. M., Gereige, I., Jung, W. B., et al. (2021). Generation of high-density nanoparticles in the carbothermal shock method. *Sci. Adv.* 7 (48), eabk2984. doi:10.1126/sciadv.abk2984

Stepanov, N., Yurchenko, N. Y., Zherebtsov, S., Tikhonovsky, M., and Salishchev, G. (2018). Aging behavior of the hfnbtatizr high entropy alloy. *Mater. Lett.* 211, 87–90. doi:10.1016/j.matlet.2017.09.094

Stuart, B. W., and Stan, G. E. (2021). Physical vapour deposited biomedical coatings. *Coatings* 11, 619. doi:10.3390/coatings11060619

Sun, L., Yuan, G., Gao, L., Yang, J., Chhowalla, M., Gharahcheshmeh, M. H., et al. (2021). Chemical vapour deposition. *Nat. Rev. Methods Prim.* 1 (1), 5–20. doi:10.1038/s43586-020-00005-y

Sundaresan, R., and Froes, F. (1987). Mechanical alloying. *Jom* 39 (8), 22–27. doi:10.1007/bf03258604

Suryanarayana, C. (2001). Mechanical alloying and milling. *Prog. Mater. Sci.* 46 (1-2), 1–184. doi:10.1016/s0079-6425(99)00010-9

Suryanarayana, C. (2019). Mechanical alloying: A novel technique to synthesize advanced materials. *Research* 2019, 4219812. doi:10.34133/2019/4219812

Taha, M. A., Youness, R. A., and Zawrah, M. F. (2019). Review on nanocomposites fabricated by mechanical alloying. *Int. J. Minerals, Metallurgy, Mater.* 26 (9), 1047–1058. doi:10.1007/s12613-019-1827-4

Talluri, B., Aparna, M. L., Sreenivasulu, N., Bhattacharya, S. S., and Thomas, T. (2021). High entropy spinel metal oxide (CoCrFeMnNi) 3O4 nanoparticles as a high-performance supercapacitor electrode material. *J. Energy Storage* 42, 103004. doi:10.1016/j.est.2021.103004

Tamanna, N., Crouch, R., and Naher, S. (2019). Progress in numerical simulation of the laser cladding process. *Opt. Lasers Eng.* 122, 151–163. doi:10.1016/j.optlaseng.2019.05.026

Tomboc, G. M., Kwon, T., Joo, J., and Lee, K. (2020). High entropy alloy electrocatalysts: A critical assessment of fabrication and performance. *J. Mater. Chem. A* 8 (30), 14844–14862. doi:10.1039/d0ta05176d

Tomilin, I., and Kaloshkin, S. (2015). High entropy alloys'—'semi-impossible'regular solid solutions? *Mater. Sci. Technol.* 31 (10), 1231–1234. doi:10.1179/1743284715y.0000000028

Tsai, K-Y., Tsai, M-H., and Yeh, J-W. (2013). Sluggish diffusion in co–cr–fe–mn–ni high-entropy alloys. *Acta Mater.* 61 (13), 4887–4897. doi:10.1016/j.actamat.2013.04.058

Vaidya, M., Muralikrishna, G. M., and Murty, B. S. (2019). High-entropy alloys by mechanical alloying: A review. *J. Mater. Res.* 34 (5), 664–686. doi:10.1557/jmr.2019.37

Verma, V., Tripathi, A., and Kulkarni, K. N. (2017). On interdiffusion in fenicocrmn high entropy alloy. *J. Phase Equilibria Diffusion* 38 (4), 445–456. doi:10.1007/s11669-017-0579-y

Vu, T. D., Chen, Z., Zeng, X., Jiang, M., Liu, S., Gao, Y., et al. (2019). Physical vapour deposition of vanadium dioxide for thermochromic smart window applications. *J. Mater. Chem. C* 7 (8), 2121–2145. doi:10.1039/c8tc05014g

Waag, F., Li, Y., Ziefuß, A. R., Bertin, E., Kamp, M., Duppel, V., et al. (2019). Kinetically-controlled laser-synthesis of colloidal high-entropy alloy nanoparticles. *RSC Adv.* 9 (32), 18547–18558. doi:10.1039/c9ra03254a

Wang, H., Wang, H., Zhang, S., Zhang, Y., Xia, K., Yin, Z., et al. (2022a). Carbothermal shock enabled facile and fast growth of carbon nanotubes in a second. *Nano Res.* 15 (3), 2576–2581. doi:10.1007/s12274-021-3762-8

Wang, K-L., Zhu, Y-M., Zhang, Q-B., and Sun, M. L. (1997). Effect of rare Earth cerium on the microstructure and corrosion resistance of laser cladded nickel-base alloy coatings. *J. Mater. Process. Technol.* 63 (1-3), 563–567. doi:10.1016/s0924-0136(96)02684-2

Wang, Q., Wang, W., Li, Y., Tan, L., and Yang, K. (2021a). Biofunctional magnesium coating of implant materials by physical vapour deposition. *Biomater. Transl.* 2 (3), 248–256. doi:10.12336/biomatertransl.2021.03.007

Wang, R., Huang, J., Zhang, X., Zhang, Z., Gao, T., Xu, L., et al. (2022b). Two-dimensional high-entropy metal phosphorus trichalcogenides for enhanced hydrogen evolution reaction. *ACS Nano* 16 (3), 3593–3603. doi:10.1021/acsnano.2c01064

Wang, X., Guo, W., and Fu, Y. (2021b). High-entropy alloys: Emerging materials for advanced functional applications. *J. Mater. Chem. A* 9 (2), 663–701. doi:10.1039/d0ta09601f

Wang, X., Dong, Q., Qiao, H., Huang, Z., Saray, M. T., Zhong, G., et al. (2020). Continuous synthesis of hollow high-entropy nanoparticles for energy and catalysis applications. *Adv. Mater.* 32 (46), 2002853. doi:10.1002/adma.202002853

Wang, Z., Guo, S., and Liu, C. T. (2014). Phase selection in high-entropy alloys: From nonequilibrium to equilibrium. *Jom* 66 (10), 1966–1972. doi:10.1007/s11837-014-0953-8

Weng, F., Chen, C., and Yu, H. (2014). Research status of laser cladding on titanium and its alloys: A review. *Mater. Des.* 58, 412–425. doi:10.1016/j.matdes.2014.01.077

Xu, X., Du, Y., Wang, C., Guo, Y., Zou, J., Zhou, K., et al. (2020). High-entropy alloy nanoparticles on aligned electronspun carbon nanofibers for supercapacitors. *J. Alloys Compd.* 822, 153642. doi:10.1016/j.jallcom.2020.153642

Yan, W., Jiang, H., Yi, W., Zhao, C., Xia, Y., Cong, H., et al. (2022). High-entropy-alloy nanoparticles synthesized by laser metallurgy using a multivariate MOF. *Mater. Chem. Front.* 6, 2796–2802. doi:10.1039/d2qm00588c

Yang, T., Zhao, Y., Tong, Y., Jiao, Z. B., Wei, J., Cai, J. X., et al. (2018). Multicomponent intermetallic nanoparticles and superb mechanical behaviors of complex alloys. *Science* 362 (6417), 933–937. doi:10.1126/science.aas8815

Yao, L., Wu, Q., Zhang, P., Zhang, J., Wang, D., Li, Y., et al. (2018a). Scalable 2d hierarchical porous carbon nanosheets for flexible supercapacitors with ultrahigh energy density. *Adv. Mater.* 30 (11), 1706054. doi:10.1002/adma.201706054

Yao, R. Q., Zhou, Y. T., Shi, H., Wan, W., Zhang, Q., Gu, L., et al. (2021). Nanoporous surface high-entropy alloys as highly efficient multisite electrocatalysts for nonacidic hydrogen evolution reaction. *Adv. Funct. Mater.* 31 (10), 2009613. doi:10.1002/adfm.202009613

Yao, Y., Huang, Z., Xie, P., Lacey, S. D., Jacob, R. J., Xie, H., et al. (2018b). Carbothermal shock synthesis of high-entropy-alloy nanoparticles. *Science* 359 (6383), 1489–1494. doi:10.1126/science.aan5412

Yu, M., Wang, K., and Vredenburg, H. (2021). Insights into low-carbon hydrogen production methods: Green, blue and aqua hydrogen. *Int. J. Hydrogen Energy* 46 (41), 21261–21273. doi:10.1016/j.ijhydene.2021.04.016

Yue, M., Lambert, H., Pahon, E., Roche, R., Jemei, S., and Hissel, D. (2021). Hydrogen energy systems: A critical review of technologies, applications, trends and challenges. *Renew. Sustain. energy Rev.* 146, 111180. doi:10.1016/j.rser.2021.111180

Yurlova, M., Demenyuk, V., Lebedeva, L. Y., Dudina, D. V., Grigoryev, E. G., and Olevsky, E. A. (2014). Electric pulse consolidation: An alternative to spark plasma sintering. *J. Mater. Sci.* 49 (3), 952–985. doi:10.1007/s10853-013-7805-8

Zhang, D., Shi, Y., Zhao, H., Qi, W., Chen, X., Zhan, T., et al. (2021). The facile oil-phase synthesis of a multi-site synergistic high-entropy alloy to promote the alkaline hydrogen evolution reaction. *J. Mater. Chem. A* 9 (2), 889–893. doi:10.1039/d0ta10574k

Zhang, G., Ming, K., Kang, J., Huang, Q., Zhang, Z., Zheng, X., et al. (2018). High entropy alloy as a highly active and stable electrocatalyst for hydrogen evolution reaction. *Electrochimica Acta* 279, 19–23. doi:10.1016/j.electacta.2018.05.035

Zhang, H., Pan, Y., and He, Y-Z. (2011). Synthesis and characterization of feconicrcu high-entropy alloy coating by laser cladding. *Mater. Des.* 32 (4), 1910–1915. doi:10.1016/j.matdes.2010.12.001

Zhivulin, V. E., Trofimov, E. A., Gudkova, S. A., Pashkeev, I. Y., Punda, A. Y., Gavrilyak, M., et al. (2021). Polysubstituted high-entropy [land](cr0. 2mn0. 2fe0. 2co0. 2ni0. 2) o3 perovskites: Correlation of the electrical and magnetic properties. *Nanomaterials* 11 (4), 1014. doi:10.3390/nano11041014

Zhu, L., Xue, P., Lan, Q., Meng, G., Ren, Y., Yang, Z., et al. (2021). Recent research and development status of laser cladding: A review. *Opt. Laser Technol.* 138, 106915. doi:10.1016/j.optlastec.2021.106915

frontiers | Frontiers in Energy Research

TYPE Review
PUBLISHED 01 June 2023
DOI 10.3389/fenrg.2023.1124288

OPEN ACCESS

EDITED BY
Muhammad Wakil Shahzad,
Northumbria University, United Kingdom

REVIEWED BY
Feng Wu,
Guangdong Polytechnic Normal University, China
Tolutope Oluwasegun Siyanbola,
Covenant University, Nigeria

*CORRESPONDENCE
Modupeola Dada,
dadadupeola@gmail.com

RECEIVED 15 December 2022
ACCEPTED 04 May 2023
PUBLISHED 01 June 2023

CITATION
Dada M, Popoola P, Alao A, Olalere F, Mtileni E, Lindokuhle N and Shamaine M (2023), Functional materials for solar thermophotovoltaic devices in energy conversion applications: a review. *Front. Energy Res.* 11:1124288. doi: 10.3389/fenrg.2023.1124288

Functional materials for solar thermophotovoltaic devices in energy conversion applications: a review

Modupeola Dada*, Patricia Popoola, Alice Alao, Folasayo Olalere, Evlly Mtileni, Ntanzi Lindokuhle and Makinita Shamaine

Chemical, Metallurgical and Materials Engineering, Tshwane University of Technology, Pretoria, South Africa

Fossil fuels are now used to meet over 80% of the world's energy demands, but they have the disadvantages of being unsustainable economically and polluting the environment. Solar energy is also one of the most desired alternative forms of renewable energy due to the quantity of direct sunlight among these sources. Due to the difficulties with solar cells, less than 1% of this energy is harvested and transformed into electricity. Notably, solar thermal and photovoltaic systems are the traditional methods for converting solar energy into electricity. It can be challenging to turn the solar energy captured by these systems into power. In contrast to conventional conversion methods, which involve converting solar energy directly into electricity, this article conducts a thorough investigation of solar thermophotovoltaic devices and the high-tech materials used in solar thermophotovoltaic systems as a solution to the conversion challenges.

KEYWORDS

solar energy, thermophotovoltaic devices, energy conversion applications, renewable energy sources, functional material

Introduction

In 2019, the global energy consumption growth rate declined by +0.6% compared to its ever-increasing trend, contributing to slow economic growth. Consumption in Algeria and Indonesia was dynamic; however, consumption in South Africa, Saudi Arabia, and Nigeria continued to increase (Xu G. et al., 2020; Zhou et al., 2020). Generally, energy consumption is a socio-economic human need, and the energy demand is met by fossil fuels such as carbon and hydrogen compounds, from which petroleum, natural gas, and coal are derived (Sharma and Ghoshal, 2015; Pareek et al., 2020). Coal was one of the first fossil fuels used for steam engines, transportation, and the production of steel, while petroleum was used for fuel in combustion engines and lighting paraffin lamps, and natural gas was used for cooking and to generate electricity (Kalair et al., 2021; Welsby et al., 2021). Nonetheless, the adverse effects of these fossil fuels include, but are not limited to, the emission of nitrous oxide (N_2O) and carbon monoxide (CO). Inhalation of CO causes dizziness and headaches that may lead to death (Vohra et al., 2021; Abbasi et al., 2022). N_2O, on the other hand, generates ground-level ozone, which is harmful to crops and the respiratory system. Moreover, oil and coal contain sulfur, which, in contact with moisture, forms sulfuric acid, resulting in very damaging acid rain (Guenet et al., 2021; Qasim et al., 2021). Greenhouse gases are also one of the most destructive emissions of fossil fuels, causing global warming and disrupting the

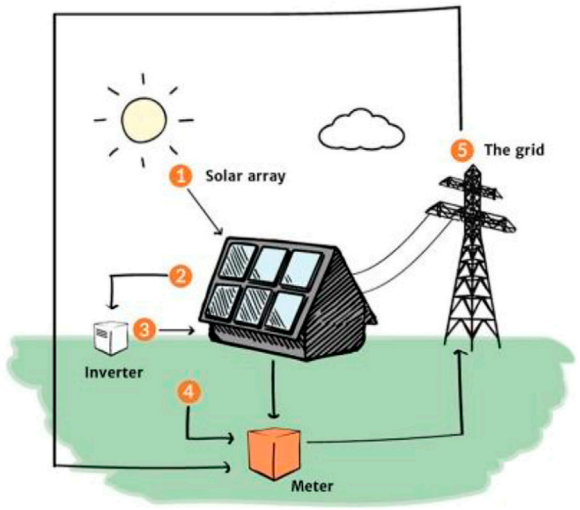

FIGURE 1
Solar energy.

surface temperature of the Earth from sustaining life; consequently, alternative energy sources have been developed (Malhotra, 2020; Shen et al., 2020). This study reviews the innovation in renewable energy sources that are cleaner, more accessible, and derived from natural sources. These sources include wind, geothermal, hydrogen, hydroelectric, biomass, ocean, and solar energy.

Solar energy

The primary source of solar energy, which travels at 3.0×10^8 m per second, is the Sun. The Sun, made up of helium gas and hydrogen, makes this energy in its core through fusion (Kalogirou, 2013; Gong et al., 2019). Fusion involves hydrogen isotopes, and with the transformation of matter, it comes together to form helium atoms, and this transformed matter is given off as radiant energy by the Sun (Okutsu et al., 2021; Kenjo et al., 2022). Radiant energy emitted from the Sun reaches the Earth surface in tiny portions, approximately 1.7 × 1018 W, and these rations are enough to supply the energy needed on Earth (Sisay, 2022). The Sun supplies energy to different parts of the Earth in small fractions per time, making it necessary to capture the solar energy through solar collectors before transforming it into electricity, as shown in Figure 1 (Panwar et al., 2011; Zhang L. et al., 2021).

Conversion of solar energy into electricity

A solar cell built from semiconductor materials is one device that is electronically a collector to convert solar energy into electricity (Fukuda et al., 2020; Kim J. Y. et al., 2020). The material used for solar cells must absorb sunlight, which raises electrons in the light to higher-energy states, and then the high-energy electron moves from the cell to an external circuit (Fonash, 2012; Burlingame et al., 2020). Urbanization is constantly increasing global electricity consumption, and like other types of energy, the need to reduce the price of electricity increases its supply, performance, and storage, making solar cell devices a fundamental solution (Asongu et al., 2020; Zhang et al., 2022). Solar thermal systems and photovoltaics are two methods of converting solar energy into electricity (Pasupathi et al., 2020; Rashidi et al., 2020). Solar thermal systems comprise concentrated solar power, which uses solar energy to generate electricity (Javadi et al., 2020; Osorio et al., 2022). The process involves using a solar collector with a mirrored surface to direct sunlight into a standby receiver, which, in turn, heats a liquid. The heated liquid produces steam, which produces electricity (Peuser et al., 2013; Ndukwu et al., 2021). The photovoltaic process of generating electricity involves the use of solar cells made up of silicon, which supplies electricity when the radiant energy from sunlight strikes the cell, triggering the electrons in the cell to move, and this movement of electrons jerks an electric current, switching from solar energy to electricity (Grätzel, 2005; Prabhu and ValanArasu, 2020).

Limitations to the conversion methods

There is an absolute theoretical Shockley–Queisser (SQ) limitation to the efficiency of conventional solar cells (Shockley and Queisser, 1961; Markvart, 2022). The conversion of solar energy to electricity, as shown in Figure 2 by solar cells is established by the photoelectric effect, which is an interaction between the transformed matter and the electromagnetic wave (Guillemoles et al., 2019; Ehrler et al., 2020). During their study, Shockley and Queisser (1961) realized there was a mismatch between the emission angles and absorption; therefore, they proposed that the Sun and solar cells act as black bodies. To this effect, a single layer of solar cells consisting of silicon was detailed through emission angle restrictions, photon recycling, and optical concentration to having an upper limit of a little above 32% for a 1.1eV gap (Lu et al., 2021; Chen et al., 2022).

The SQ limit defines 32%–33.6% as the maximum solar energy conversion efficiency achievable for any solar cell material (Xiang et al., 2019; Kim S. et al., 2020). This limitation, which was developed in 1961, is applicable to the principle of detailed balancing, which equates the photon flux that goes into the solar cell device with the electron or photon flux that goes out of it at different open-circuit conditions (Rühle, 2016; Green and Ho-Baillie, 2019).

Exploring solutions to the theoretical limitations

In recent times, possible ways of increasing the efficiency of solar cells above the absolute limit have been found, namely, by adding multiple layers of solar cells, which increases the incident intensity, the current density, and the voltage (Kim J. Y. et al., 2020;

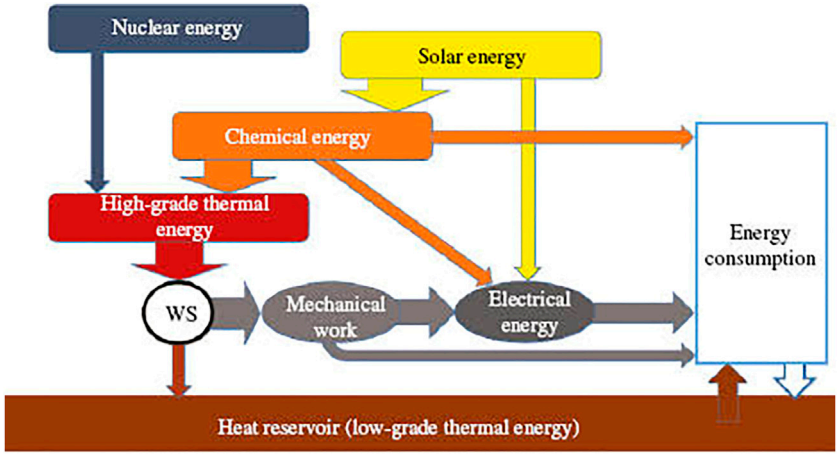

FIGURE 2
Schematic representation of the thermophotovoltaic process.

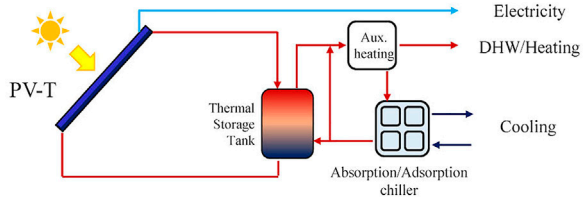

FIGURE 3
Electric power through solar thermophotovoltaic devices.

Park, 2020). Angle restriction filters can also be used to reduce the existing recombination current; multiple semiconductors with several bandgaps can also be used to decrease thermal losses and increase efficiency (Beard et al., 2013; Tennyson et al., 2019). Axelevitch (2018) reviewed the ways of improving the efficiency of single-junction solar cells, with specific attention given to solar cells enhanced with the plasmon. The author described using multi-junction solar cells, down-conversion solar cells, up-conversion solar cells, multiple exciton generation solar cells, solar cells with intermediate bands, and hot carrier solar cells as enhancement mechanisms of solar cells from the SQ limitations (Krügener et al., 2021; Yao and Hou, 2022). The possibility of using nano-structures made up of gold or silver nanoparticles was also discussed, concluding that the combination of an up-converter and a plasmon is a promising solution to the SQ limitation (Chen et al., 2021; Singh and Jen, 2021). The plasmon with extreme energy photons will generate multiple charged carriers under the absorption of one photon, while the up-converter uses the wavelength photons to increase the efficiency of solar cells (Gerislioglu et al., 2019; Huang et al., 2021). Nonetheless, a preferred alternative for exceeding the SQ limitations is the conversion of solar energy to heat first before generating electrical power through solar thermophotovoltaic devices, as shown in Figure 3.

Solar thermophotovoltaics and their devices

There are several technological options for converting primary energy into electricity. A few of them may be converted directly (for example, PV and fuel cells), but the vast majority require the intermediary creation of heat, which is then converted into electricity using a heat engine (Snyder and Toberer, 2008; Shi et al., 2020). Consequently, many other types of heat engines have been invented, but only those based on solid state devices (thermoelectrics and thermionics) have been widely employed, particularly in the energy and aerospace sectors (Mahan and Sales, 1997; Chen et al., 2003), while the dynamic systems (Rankine, Stirling, and Brayton) are still under development until they demonstrate high levels of reliability.

In thermoelectrics, thermal energy is directly converted into electrical energy via thermoelectric modules, which are solid state devices (Snyder and Ursell, 2003; Pei et al., 2012). The "Seebeck effect," which is the appearance of an electrical voltage induced by a temperature gradient across a material, lies at the heart of the conversion process. The inverse of this is the "Peltier effect," which causes a temperature gradient to form when voltage is applied (Tritt, 2011; Pourkiaei et al., 2019). As a result, the performance of the thermoelectric (TE) device is directly dependent on the temperature gradient (DT), the thermoelectric figure of merit (ZT), and the material parameter (Jia et al., 2021; Mao et al., 2021). The thermoelectric efficiency is defined for power generation by combining the Carnot efficiency (DT/Thot) (Zou et al., 2020; Zhang Z. et al., 2021). To increase this efficiency, high ZT values and a significant temperature differential across the thermoelectric material are required (Yang et al., 2021). Mahan and Sofo (1996) studied the electronic structure required to provide a high figure of merit in thermoelectrics, and it was discovered that a delta-shaped transport distribution maximizes thermoelectric properties. Their result indicates that for maximum thermoelectric efficiency, a narrow distribution of the energy of the electrons involved in the transport process is required.

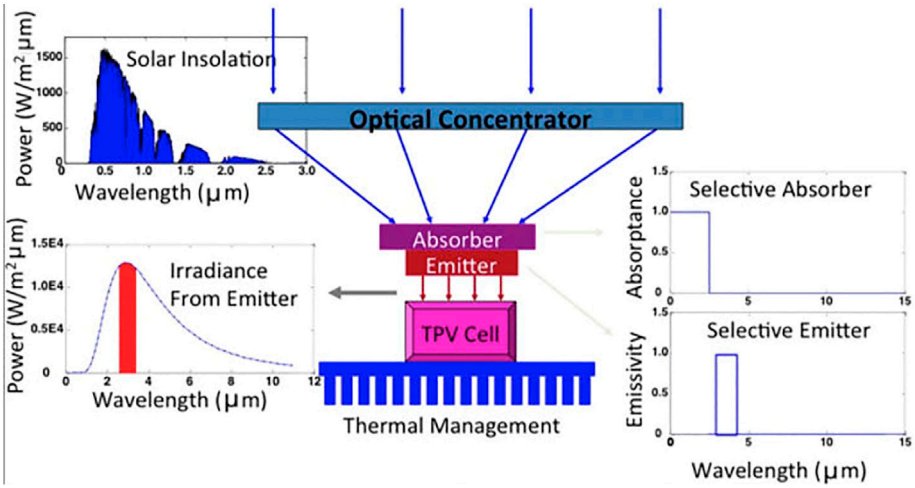

FIGURE 4
Thermal management process.

Nonetheless, according to Sootsman et al. (2009), current thermoelectric devices have a ZT of 0.8 and function at only around 5%–6% efficiency. By raising ZT by a factor of 4 and depending on DT, the estimated efficiency rises to 30%. However, the difficulty in developing high-ZT thermoelectric materials is attaining high electronic conductivity (s), high thermoelectric power (S), and low thermal conductivity (k) in the same solid. These characteristics are governed by the specifics of the electronic structure and the dispersion of charge carriers (electrons or holes) and so cannot be controlled independently. Dresselhaus et al. (2007) discovered a simultaneous increase in power factor and decrease in thermal conductivity using nanocomposites when compared to alloy samples of the same chemical makeup; Nandihalli et al. (2020) studied polymer-based thermoelectric nanocomposites; the level of material performance for output power factor PF = σS^2 and energy conversion efficiency was determined through the dimensionless figure of merit ZT = $\sigma S^2 T/k$ ($\sigma, S, T, and\ K$ are the electrical conductivity, Seebeck coefficient, temperature, and thermal conductivity, respectively). The authors concluded that the trade-off relationships between conductivity and Seebeck coefficient in polymer-based materials, as well as in inorganic thermoelectric (TE) materials, limit the ability to improve TE performance. These issues can be solved, however, by modifying the interfaces between the polymer and inorganic or organic additives. As a result, a suitable manufacturing process is required, in which interfacial density and defects at the interface of nanocomposites may be regulated in order to enhance electrical conductivity and the Seebeck coefficient at the same time. Therefore, significant interest from researchers in developing advanced thermoelectric properties through organic and inorganic nanomaterial-based hybrid nanocomposites has gained popularity among researchers (Bisht et al., 2021).

Compared to thermoelectrics, thermionic energy converters are power generators and their thermal management process is shown in Figure 4. The thermionic converter uses heat as its source of energy and transfers energy through mechanical work at no point during its operation. As a result, it is classified as a fuel cell or a photovoltaic cell (Herring and Nichols, 1949; Schwede et al., 2010).

Thermophotovoltaics (TPV) is a solid state alternative to thermoelectric and thermionic converters, which is very efficient. The two most prevalent methods for harnessing solar energy are photovoltaic, in which sunlight directly excites electron–hole pairs in a semiconductor, and the solar-thermal technique, in which sunlight powers a mechanical heat engine (Daneshvar et al., 2015; Burger et al., 2020). Photovoltaic systems directly convert solar radiation into electricity and are used to generate power from solar energy. Another approach uses a solar collector to convert Sun photons to thermal energy, which is then used in a thermal engine to generate electricity (Joshi et al., 2009; Lupangu and Bansal, 2017).

Photovoltaic power generation is intermittent and only efficiently utilizes a fraction of the Sun spectrum, but the inherent irreversibilities of tiny heat engines make the solar-thermal technique best suited for utility-scale power facilities. As a result, hybrid solutions for solar power generation are becoming increasingly important. Solar thermophotovoltaics (STPV) can also be referred to as systems that collect and re-emit solar light as heat radiation before directing it to photovoltaic cells (Hosenuzzaman et al., 2015; Das et al., 2018). With the STPV system, optimization may involve selecting an emitter spectrum and reflecting the unused portion of the radiation from the receiver back to the emitter surface. STPV systems' primary features are modularity, portability, the absence of moving parts, pollution-free operation, great efficiency, and high-power densities. Typically, the goal is to enhance photovoltaic conversion efficiency by matching the spectrum of the light to the bandgap of the cell (Davies and Luque, 1994; Wang et al., 2019). Solar thermophotovoltaics promise to leverage the benefits of both optimal approaches by converting sunlight into thermal emission tuned to energies that are directly above the photovoltaic bandgap. This is achieved by using a hot absorber–emitter with high efficiency and harnessing the entire solar spectrum, scalability and compactness due to their solid state nature, and dispatchability due to the ability to store energy using

thermal or chemical means (Kohiyama et al., 2016; Chen et al., 2020).

STPV systems have a variety of possible applications, including electrical and thermal energy supply, grid-independent storage appliances, waste-heat recovery, and space and aerospace power applications. However, at high working temperatures, effective sunlight collection in the absorber and spectrum control in the emitter are extremely difficult (Datas and Martí, 2017; Gupta et al., 2018); because of this limitation, earlier experimental demonstrations have had a conversion efficiency of approximately or below 1%. Hence, a number of factors influence solar thermophotovoltaic efficiency, including the sunlight concentration ratio, absorber/emitter temperature/efficiency, photon recycling efficiency, and TPV cell characteristics (Bitnar et al., 2013; Zhou et al., 2016).

In a study of STPV systems, a newly developed Fresnel lens was used, and the calculated system efficiency with a tungsten emitter achieved 35%. The system comprised a solar concentrator, an absorber emitter, a spectrum filter, PV cell arrays, a bottom reflector, and a cooling system. A parabolic reflector was utilized as the concentrator in this case. The emitter might be composed of grayscale or spectrum-selective material. Forty GaSb cells were linked in series and positioned on the cooling system's inner surface. The bottom surface totally reflected heat radiation, ensuring that it was absorbed completely by the cells (Zenker et al., 2001; Khvostikov et al., 2007). The solar collector collects the Sun's rays, which subsequently radiate to the absorber surface area. The absorber was a critical component of the STPV system, acting as a spectrum-selective surface that transforms solar light into thermal energy. This surface increases solar energy absorption in the visible and near-infrared ranges while minimizing heat emission in the infrared region (Chaudhuri, 1992; Nam et al., 2014).

Hence, the absorber surface must function at elevated temperatures with a high energy density to achieve thermal stability. Another selective surface that radiates heat energy toward the PV cell is the emitter. According to the SQ limit, a single-junction solar PV has a significant limitation in utilizing solar energy because photons with less than the required energy to generate electron–hole pairs are practically useless, while photons with more energy than the bandgap result in excess energy at the PV surface and reduce efficiency (Mojiri et al., 2013; Abbas et al., 2022). As a result, by customizing the bandgap, emitters give the most efficient spectrum for the PV cell.

Another innovative STPV system offers electrical energy that is passed via the solid oxide electrolyzer cell (SOEC) to create hydrogen. The ultimate purpose of an electrolyzer cell is to create hydrogen from the intake water. Heat and power are required for the electrolyzer cell to perform this feat. Thus, a steam electrolyzer that runs at high temperatures is an effective way to significantly cut energy use (Charache et al., 1999; Dashiell et al., 2006). Consequently, the efficiency of numerous intermediary energy conversion processes is critical to the performance of STPV. The absorber converts optically focused sunlight into heat, the absorber temperature increases, heat conducts to the emitter, and the hot emitter thermally radiates toward the photovoltaic cell, where radiation is eventually harnessed to excite charge carriers and create electricity (Kohiyama et al., 2020; Hou et al., 2023).

The overall efficiency η stpv can be expressed as a product of the optical efficiency of concentrating sunlight (η o), the thermal efficiency of converting and delivering sunlight as heat to the emitter (η t), and the efficiency of generating electrical power from the thermal emission (η tpv) (Tervo et al., 2020):

$$\eta\,\mathrm{stpv} = \eta\,\mathrm{o}\,\eta\,\mathrm{t}\,\eta\,\mathrm{tpv}.$$

The TPV efficiency η tpv hinges on the spectral properties and temperature of the emitter. A spectrally selective emitter should have a high emittance for energies above the photovoltaic bandgap (Eg) and a low emittance for energies below the bandgap. To excite enough thermal modes for substantial emission above the bandgap, the emitter temperature should ideally be high enough that Planck's blackbody peak coincides with the bandgap; in other words, by Wien's displacement law (Tian et al., 2021)

$$T_e^{opt} \approx 2336\,[\mathrm{K\,eV} - 1] \cdot \mathrm{Eg}.$$

The emitter's high-temperature operation faces two major obstacles to a successful STPV power conversion: efficiently collecting sunlight to meet T_e^{opt} and preserving spectral selectivity at raised temperatures. For the absorber, one approach to effectively enhance the intrinsic solar absorptivity of materials is to use macrocavity geometries. Because of the high aspect ratio of the cavity needed to enhance absorption, this approach typically requires high levels of optical concentration to reach T_e^{opt}. A high optical concentration necessitates sophisticated systems with poor optical efficiencies (η o $\approx$ 65%). Tungsten has poor inherent spectrum selectivity as an emitter at T_e^{opt} because its emissivity at low photon energies (<Eg) increases with temperature, accompanied by an increase in electrical resistance. Ultimately, depending on the intrinsic spectral properties of materials for their absorber–emitter performance is limited with experimental STPV conversion efficiencies. Hence, to improve the performance of the absorber–emitter, the design of structured surfaces with spectral properties approaching those of ideal STPV components is achieved with simulation studies using realistic nanophotonic surfaces, which predict STPV efficiencies exceeding 40% (Bhatt et al., 2020).

Solar thermal generators, which offer very high energetically dense thermal storage, are an eventual alternative to solar PV because an STPV system requires a broadband absorber capable of absorbing the entire solar spectrum, a narrowband emitter capable of converting the absorber's absorbed energy in the form of heat to photons in a narrowband spectrum just above the bandgap of the PV cell, and a low bandgap PV cell capable of effectively generating electron–hole pairs while avoiding thermalization losses (Xu Y. et al., 2020).

The broadband absorber and narrow band emitter create an intermediate structure that may be built with metamaterials and their two-dimensional metasurface equivalents (Liu et al., 2019). Metasurfaces have the special benefit of being compact and having a high absorptance. To produce strong absorptance across a wide range of incidence angles, both the absorber and the emitter should be angle-insensitive (Anggraini et al., 2022). The major goal in both circumstances is to maximize the absorptance profile since, according to Kirchhoff's Law, absorptance equals emittance in thermodynamic equilibrium; furthermore, because the STPV system must function under high-temperature settings, the materials used to construct the absorbers and emitters are

carefully chosen from a limited number of refractory materials (Azzali et al., 2021; Bendelala and Cheknane, 2022). Nevertheless, oxidation is a significant issue when employing refractory materials (Rana et al., 2021). Most refractory metals with high melting points oxidize at significantly lower temperatures and pressures. Tungsten (W), rhenium (Re), tantalum (Ta), and titanium nitride (TiN) are refractory metals with extremely high melting temperatures of 3695.15 K, 3458.15 K, 3290.15 K, and 3203.15 K, respectively. Ongoing research on absorbers, emitters, and STPV systems in general is hampered by non-planar three-dimensional (3D) or multilayer designs and reduced efficiency (Tong, 2018). Fabrication of 3D designs is inherently complex for the primary lens (or mirror), the absorber, the PV cell, and a photon recuperator mechanism, which are the key components of TPV systems (Palfinger, 2006).

Hence, the TPV efficiency is optimized by optimizing three parameters: absorber, PV cell temperatures, and cell voltage. When photons of above-bandgap energy released by the heat emitter are absorbed by the PV cell, the photovoltaic effect produces electron-hole pairs (EHPs) (i.e., photogeneration) (Zou et al., 2020; Ren et al., 2021; Zheng et al., 2021). When EHPs in a PV cell are recombined, photons with energies larger than the bandgap are released (i.e., radiative recombination). The above-bandgap spectral radiation released by the PV cell quantum efficiency (Qe) is mostly the result of radiative recombination (Prentice, 1999). Although Qe comprises a free carrier and lattice emission in the PV cell, its contributions are unimportant to photogeneration or radiative recombination. The photocurrent flows through the external circuit as EHPs produced by photogeneration and radiative recombination undergo charge separation and migrate to electrodes (Sahoo and Mishra, 2018). Charge carriers that are lost due to recombination (non-radiative, radiative, and surface recombination) are unable to contribute to photocurrent production. Internal quantum efficiency is defined as the ratio of the number of created EHPs that may be employed for photocurrent production to the number of absorbed photons (Goodnick and Honsberg, 2022).

Advanced NF-TPV device ideas, particularly hybrid devices with NF-TPV integrated with a thermionic device or light-emitting diode and NF-TPV devices with multi-junction PV cells, are gaining research interest (Song et al., 2022). The trade-off between resistance and shading losses in the frontside is mitigated by serial integration of thermionic and thermophotovoltaic devices as a means of resolving the difficulties in an NF-TPV device. The near-field thermophotovoltaic (nTiPV) device with a thermionic cathode [i.e., LaB6] and an anode [i.e., BaF2] is positioned on the emitter and PV cell sides of the NF-TPV device, respectively (Datas and Vaillon, 2021). Electrons are emitted from the heated cathode and transmitted to the anode through the thermionic effect in nTiPV devices, along with photons. Electrons passing through the anode and reaching the top side of the PV cell negate the accumulated holes caused by the photovoltaic effect (Qiu et al., 2022). As a result, an electrical connection is created via the vacuum, eliminating the necessity for a frontside contact electrode. Additionally, electrons arriving at the PV cell's backside electrode are given to the emitter cathode, releasing the extra-potential of thermionic and photovoltaic effects. The elimination of the trade-off between series resistance and shading losses opens the door to significantly improved performance, even for scaled NF-TPV devices (Song et al., 2022). The space charge effect creates an electrostatic potential within the vacuum gap, acting as a potential barrier to thermionic transfer. When the vacuum gap approaches the near-field regime, not only is photon transport accelerated but also thermionic electron transport since the electric potential barrier is reduced (Khalid et al., 2016; Xiao et al., 2017).

As a result, with no frontside contact electrode, increased photocurrent from evanescent modes may be successfully transported to the emitter side cathode. At a realizable vacuum gap of 100 nm and an emitter temperature of 1000 K, the power density of the nTiPV device was 3.7 times and 10.7 times higher than that of the NF-TPV device in the same operation condition with 'ideal (i.e., series resistance is 0 mΩ)' and 'realistic (i.e., series resistance is 10 mΩ)' conditions, respectively. With a 1-cm^2 macro-scale device area with the same vacuum gap and emitter temperature parameters, the nTiPV device had a power density of 6.73 W/cm2 and 18% conversion efficiency (Jang et al., 2016). As a result of the trade-off between resistive and shading losses, the nTiPV device may be promising for the macro-size application of NF-TPV conversion. Fabrication of the anode and cathode with sufficiently low work-functions, which is required for improved thermionic emission in the near-field domain, still remains a problem for the specified application (Song et al., 2022).

In contrast to PV cells, a light-emitting diode (LED) produces luminescence by radiative recombination of bias-driven injected charge carriers. If the TPV device's passive emitter is replaced with an active emitter, such as an LED, the PV cells' above-bandgap absorption can be boosted due to the electroluminescence created by the LED. A PV-LED hybrid device of this type is known as a thermophotonics (TPX) device. If the nearfield idea is implemented in the TPX device, it is evident that the evanescent mode will improve both PV and LED performances, resulting in a better power density. This gadget works by driving the LED with a portion of the electricity provided by the PV cell (Sadi et al., 2020).

A near-field TPV (nTPX) device used AlGaAs ternary semiconductors in both the PV cell and the LED. Using rigorous balancing analysis, they simulated the photon flow that conveys chemical potential and the non-radiative recombination rate. When the LED and PV cell temperatures were 600 and 300 K, respectively, at the 10-nm vacuum gap, their nTPX device could create 9.6 W/cm^2 of electrical power with a conversion efficiency of 9.8%. With the same temperature difference, the suggested nTPX device exceeded the record-high power output density and conversion efficiency of a conduction-based thermoelectric generator. A TPX device's performance is generally more sensitive to emitter side temperature (i.e., LED temperature) than a TPV device. First and foremost, bandgap alignment between the LED and PV cells is required for high-performance TPX devices. Since the bandgap energy depends on the temperature, the performance of TPX devices could be degraded even if the temperature of the LED slightly deviates from the optimum point. In addition, because parameters of the non-radiative recombination rate, such as Auger and SRH recombination lifetimes (?Auger and ?SRH) and intrinsic carrier concentration (??), are also functions of the temperature, the increase in LED temperature can result in

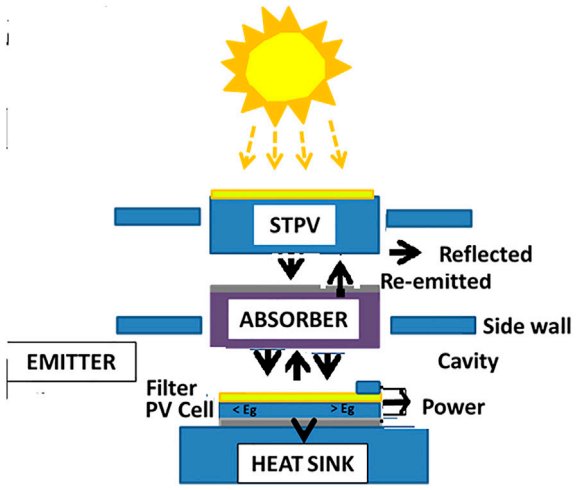

FIGURE 5
STPV and its energy flow flowchart.

detrimental effects on the TPX performance; in other words, as the LED temperature increases, ?Auger and ?SRH decrease and ?? increases (Legendre and Chapuis, 2022).

High-tech materials for solar thermophotovoltaic devices

Conventional photovoltaic materials convert solar energy directly to electricity; hence, they undergo theoretical limitations. However, ways of increasing the overall efficiency are to convert solar energy first to heat and then use the heat to generate electrical energy (Nevala et al., 2019, Hassan et al., 2020). Table 1 shows the solar thermophotovoltaic devices and the devices used for this application are referred to as solar thermophotovolataics (STPV). Devices used for this application are referred to as solar thermophotovoltaics (STPV), with the flowchart shown in Figure 5. STPV pairs low-efficiency conventional solar cells with an added layer of high-tech material that helps in multiplying the SQ limitation, making it possible for the cells to generate more power (Alam and Khan, 2019; Wong et al., 2020). The device works on the principle of dispersing waste solar energy as heat inside the solar cell, a by-product of the nuclear/chemical reactions or mechanical work (Jayawardena et al., 2020; Gong et al., 2021). The heat is then absorbed by the transitional component at temperatures that will allow this component to produce thermal radiation. The configurations of the cell and the high-tech materials used in the devices are fine-tuned to the right wavelengths for the cell to capture light, which improves its efficiency (Guillemoles et al., 2019).

According to Jayawardena et al. (2020), perovskite cells mixed with lead–tin as an absorber can achieve a fill factor above 80% by post-treating the absorber with guanidinium bromide. The authors showed that the post-treatments were favorable in aligning the cathode and anode interfaces, thus enabling a bipolar extraction, which resulted in the device having an area of 0.43 cm^2, a fill factor above 80% and 14.4% power conversion efficiency. Rau et al. (2005) proposed using fluorescent collectors with photonic structures, which act as an omnidirectional spectral band stop-filter, to enhance the efficiency of photovoltaic solar cells, and they concluded that the combination of fluorescent collectors with photonic structures can close the theoretical SQ limitation while saving about 99% of the solar cell material. Thus, the authors recommended more research should be focused on the potential of two- to three-dimensional photonic structures used with fluorescent collectors. Briggs et al. (2013) developed an up-converter solar cell using thermodynamics to exceed the SQ limitation. The results showed that the efficiency of the solar cell increased from 28% to 34% with an increase in the up-converter quantum yield and capacity. Jia et al. (2016) reported the use of silicon nanocrystals built into the dielectric matrix as a promising

TABLE 1 Literature review on solar thermophotovoltaic devices.

Solar thermophotovoltaic (STPV) device	Experimental approach	Findings	Efficiency improvement	References
STPV with a carbon nanotube absorber with a 1D Si/SiO_2 photonic crystal emitter	Physical and chemical vapor deposition	Device is compact and planar than conventional devices	3.2%	Lenert et al. (2014), Fink et al. (1998), Wu et al. (2021), and (Wu et al. (2023)
STPV with a multi-walled carbon nanotube absorber and 1D Si/SiO_2 PhC emitter and the InGaAsSb PV cell	Mathematical modelling and experimental procedures via electrolysis	Overall efficiency of the device is 34% more than conventional devices	17%	Daneshpour and Mehrpooya (2018)
Solid oxide electrolysis cells	Thermodynamic modelling and experimental procedures via electrolysis	The model has a better performance than low-temperature systems	14%	Ferrero et al. (2013)
STPV using simulated solar energy	Thermodynamic modelling and experimental procedures via electrolysis	Temperature stability, no heat exchange of fluids, and easy to fabricate	6.2%	Ungaro et al. (2015)
STPV with a micro-textured absorber and nanostructure multilayer metal-dielectric-coated selective emitter	Thermodynamic modelling and experimental procedures via electrolysis	The highest STPV system efficiency so far	8.4%	Bhatt et al. (2020)
STPV and phase-change materials (PCMs)	Theoretical analysis	Cost reduction and high efficiency	-35%	Datas et al. (2013)

high-tech material for solar cells. Conversely, the material did not exceed the SQ limitation; therefore, the authors investigated the maximum efficiency of the material, and they stated that the practical limit of the solar cell's efficiency was 32%. Based on these results, they made suggestions for further studies to figure out the reason for the limitation and the proposed solution for improving the performance of the cell.

Trupke et al. (2002) tried generating a multiple electron–hole pair, a down-conversion high-energy photon, in enhancing the efficiency of solar cells. The authors detailed that there was an increment in the efficiency of the solar cell from 30.9% to 39.63%. They investigated the reason why intermediate-band solar cells could not exceed the SQ limitation, and they realized that the restriction was attributed to the radiative recombination through the intermediate band, yet they stated that suppressing the radiative recombination by introducing a quantum ratchet to the intermediate band can enhance the solar cell efficiency; therefore, the authors recommended using quantum ratchets as a more effective alternative to single-gap solar cells. On the other hand, Wang et al. (2013) used carrier transport and photon recycling simulation to figure out the reasons why thin-film GaAs solar cells did not exceed the SQ limitation by studying a single-junction thin-film solar cell and the influence of the design parameters. The authors concluded that an increment in efficiency will occur via enhancements on the backside mirror reflectivity above 95%, thus naming the series resistance and the back mirror reflectivity as the two important factors to focus on when creating high-efficiency thin-film solar cells, while Schaller et al. (2006) showed that charge carriers in large portions can enhance the performance of solar cells by increasing the photon to exciton conversion by 700%.

Xu et al. (2015) used nanostructured solar cells as photovoltaic devices, which under a 1.5 solar illumination showed a maximum efficiency of about 42%. However, they reported that the device did not exceed the theoretical limit for planar devices with optical concentrations, even though it exceeded the SQ limitations for non-planar devices. The authors attributed the failure to reach the SQ limitations to the principle of detailed balance with good knowledge of the absorption in the device structure. They recommended that nanostructured devices should be developed with limited absorption at wavelengths and angles very different from the incident illumination. More so, the improvement of the devices should come from the open-circuit voltage with non-radiative recombination and good-quality surface passivation. Mann et al. (2016) showed that large absorption of the cross sections is not responsible for the enhancements of solar cells using nanophotonic materials for photovoltaics; however, increasing the directivity bounds, which consist of the nanoscale concentrations in macroscopic solar cells, and the maintenance of high short-circuit currents are the significant voltage enhancement factors. Bierman et al. (2016) developed a high-tech nanophotonic crystal that was used to emit the desired wavelengths of light when heated while integrated into a system vertically aligned with carbon nanotubes, which serve as absorbers while operating at about 1,000 °C. When the crystal was heated, it continued to give out light that matches the band of wavelengths that the solar cell uses to convert to electric current. The carbon nanotube enables all the energy of the photons to get converted to heat, which, in turn, re-emits light that matches the solar cell's peak efficiency through the nanophotonic crystal. The authors, using an absorber, solar stimulator, photovoltaic receiver, and filter all in one device, argue that a device coupled with a thermal storage system could provide continuous on-demand electrical power. They recommended further studies on increasing the current laboratory size of the device for commercial purposes (Chan et al., 2013; Davids et al., 2020).

Future recommendations

The literature has shown that converting solar energy into heat and then from heat into electricity is an efficient way of exceeding the SQ limitation. This knowledge has sparked significant interest in using solar thermophotovoltaic devices, where photons from a hot emitter are used to transverse a vacuum gap that is absorbed by the solar cell and used to generate electricity. Nonetheless, recent reports have shown that the temperature of the emitter is still too low to give off a photon flux sufficient for the photovoltaic cell, thus limiting the service life of these devices. New approaches use thermophotovoltaic energy conversion mechanisms such as photon-assisted tunneling with a bipolar grating-coupled complementary metal–oxide–silicon tunnel diode or a micro thermophotovoltaic generator, and these are recommended solutions to increase the efficiency. Solar thermophotovoltaic devices lack suitable structural designs that overcome the thermal losses experienced with current fabrication techniques, which can be improved. Thus, further studies need to be conducted to enhance current designs. The real implementation of an NF-TPV device is extremely challenging because it requires maintaining a high-temperature difference in the sub-micron gap between the low-bandgap PV cell and the emitter. In addition, the temperature of the PV cell should be kept near room temperature to prevent performance degradation. Therefore, a thermally isolated emitter would be desirable for a real system. Furthermore, innovative materials that can be used as absorbers, and emitters should be explored for long-term thermal stability. Ways to reduce the cost of setting up the existing thermophotovoltaic systems are few, and cheaper alternatives should also be investigated.

Conclusion

In this paper, we discussed how the world's demand for energy consumption led to the development of fossil fuels; however, economical sustainability and environmental pollution have created a need for cleaner energy sources. Solar energy was outlined as a preferred alternative source of renewable energy attributed to its availability and sustainability; however, the efficiency of this source of energy in its conversion mechanism to electrical power is limited. Therefore, we presented a literature review on different solar thermophotovoltaic devices, materials, and methods researchers have used in exceeding the theoretical limitations, and future recommendations and solutions were shown. Surveying the studies presented, it is clear that nanomaterials as advanced functional materials can enhance the efficiency of solar thermophotovoltaic

devices. In general, solar energy is a significant source for fulfilling the required energy demands.

Author contributions

MD: conceptualization, writing, and editing of the manuscript. PP: supervision, writing, and editing of the manuscript. EM: writing and editing of the manuscript. NL: writing and editing of the manuscript. MS: writing and editing of the manuscript. AA: writing and editing of the manuscript. FO: review, writing, and editing of the manuscript. All authors contributed to the article and approved the submitted version.

Acknowledgments

The authors would like to thank the Surface Engineering Research Laboratory, Durban University of Technology, and the Tshwane University of Technology, Pretoria, South Africa, for their scientific and technical support.

Conflict of interest

The authors declare that the research was conducted in the absence of any commercial or financial relationships that could be construed as a potential conflict of interest.

Publisher's note

All claims expressed in this article are solely those of the authors and do not necessarily represent those of their affiliated organizations, or those of the publisher, the editors, and the reviewers. Any product that may be evaluated in this article, or claim that may be made by its manufacturer, is not guaranteed or endorsed by the publisher.

References

Abbas, M. A., Kim, J., Rana, A. S., Kim, I., Rehman, B., Ahmad, Z., et al. (2022). Nanostructured chromium-based broadband absorbers and emitters to realize thermally stable solar thermophotovoltaic systems. *Nanoscale* 14 (17), 6425–6436. doi:10.1039/d1nr08400c

Abbasi, K. R., Shahbaz, M., Zhang, J., Irfan, M., and Alvarado, R. (2022). Analyze the environmental sustainability factors of China: The role of fossil fuel energy and renewable energy. *Renew. Energy* 187, 390–402. doi:10.1016/j.renene.2022.01.066

Alam, M. A., and Khan, M. R. (2019). Shockley–Queisser triangle predicts the thermodynamic efficiency limits of arbitrarily complex multijunction bifacial solar cells. *Proc. Natl. Acad. Sci.* 116 (48), 23966–23971. doi:10.1073/pnas.1910745116

Anggraini, L., Tarigan, H. J., and Simatupang, J. W. (2022). Metamaterial and metasurface based emitters for solar thermal photovoltaic applications: Analytical review. *Bull. Electr. Eng. Inf.* 11 (6), 3249–3257. doi:10.11591/eei.v11i6.3588

Asongu, S. A., Agboola, M. O., Alola, A. A., and Bekun, F. V. (2020). The criticality of growth, urbanization, electricity and fossil fuel consumption to environment sustainability in Africa. *Sci. Total Environ.* 712, 136376. doi:10.1016/j.scitotenv.2019.136376

Axelevitch, A. (2018). Photovoltaic efficiency improvement: Limits and possibilities. *Sci. Revs Chem. Commun.* 8 (1), 115.

Azzali, N., Meucci, M., Di Rosa, D., Mercatelli, L., Silvestroni, L., Sciti, D., et al. (2021). Spectral emittance of ceramics for high temperature solar receivers. *Sol. Energy* 222, 74–83. doi:10.1016/j.solener.2021.05.019

Beard, H., Cholleti, A., Pearlman, D., Sherman, W., and Loving, K. A. (2013). Applying physics-based scoring to calculate free energies of binding for single amino acid mutations in protein-protein complexes. *PloS one* 8 (12), e82849.

Bendelala, F., and Cheknane, A. (2022). A transparent metasurface absorber/emitter with high solar thermal transfer efficiency for combined solar/thermal conversion application. *Plasmonics* 17 (3), 921–929. doi:10.1007/s11468-021-01580-w

Bhatt, R., Kravchenko, I., and Gupta, M. (2020). High-efficiency solar thermophotovoltaic system using a nanostructure-based selective emitter. *Sol. Energy* 197, 538–545. doi:10.1016/j.solener.2020.01.029

Bierman, D. M., Lenert, A., Chan, W. R., Bhatia, B., Celanović, I., Soljačić, M., et al. (2016). Enhanced photovoltaic energy conversion using thermally based spectral shaping. *Nat. Energy* 1 (6), 16068–16077. doi:10.1038/nenergy.2016.68

Bisht, N., More, P., Khanna, P. K., Abolhassani, R., Mishra, Y. K., and Madsen, M. (2021). Progress of hybrid nanocomposite materials for thermoelectric applications. *Mater. Adv.* 2 (6), 1927–1956. doi:10.1039/d0ma01030h

Bitnar, B., Durisch, W., and Holzner, R. (2013). Thermophotovoltaics on the move to applications. *Appl. Energy* 105, 430–438. doi:10.1016/j.apenergy.2012.12.067

Briggs, J. A., Atre, A. C., and Dionne, J. A. (2013). Narrow-bandwidth solar upconversion: Case studies of existing systems and generalized fundamental limits. *J. Appl. Phys.* 113 (12), 124509. doi:10.1063/1.4796092

Burger, T., Sempere, C., Roy-Layinde, B., and Lenert, A. (2020). Present efficiencies and future opportunities in thermophotovoltaics. *Joule* 4 (8), 1660–1680. doi:10.1016/j.joule.2020.06.021

Burlingame, Q., Ball, M., and Loo, Y. L. (2020). It's time to focus on organic solar cell stability. *Nat. Energy* 5 (12), 947–949. doi:10.1038/s41560-020-00732-2

Chan, W. R., Bermel, P., Pilawa-Podgurski, R. C., Marton, C. H., Jensen, K. F., Senkevich, J. J., et al. (2013). Toward high-energy-density, high-efficiency, and moderate-temperature chip-scale thermophotovoltaics. *Proc. Natl. Acad. Sci.* 110 (14), 5309–5314. doi:10.1073/pnas.1301004110

Charache, G. W., Baldasaro, P. F., Danielson, L. R., DePoy, D. M., Freeman, M. J., Wang, C. A., et al. (1999). InGaAsSb thermophotovoltaic diode: Physics evaluation. *J. Appl. Phys.* 85 (4), 2247–2252. doi:10.1063/1.369533

Chaudhuri, T. K. (1992). A solar thermophotovoltaic converter using Pbs photovoltaic cells. *Int. J. Energy Res.* 16 (6), 481–487. doi:10.1002/er.4440160605

Chen, G., Dresselhaus, M. S., Dresselhaus, G., Fleurial, J. P., and Caillat, T. (2003). Recent developments in thermoelectric materials. *Int. Mater. Rev.* 48 (1), 45–66. doi:10.1179/095066003225010182

Chen, J., Jia, D., Johansson, E. M., Hagfeldt, A., and Zhang, X. (2021). Emerging perovskite quantum dot solar cells: Feasible approaches to boost performance. *Energy & Environ. Sci.* 14 (1), 224–261. doi:10.1039/d0ee02900a

Chen, M., Yan, H., Zhou, P., and Chen, X. (2020). Performance analysis of solar thermophotovoltaic system with selective absorber/emitter. *J. Quantitative Spectrosc. Radiat. Transf.* 253, 107163. doi:10.1016/j.jqsrt.2020.107163

Chen, Y., Jia, B., Guan, X., Han, L., Wu, L., Guan, P., et al. (2022). Design and analysis of III-V two-dimensional van der Waals heterostructures for ultra-thin solar cells. *Appl. Surf. Sci.* 586, 152799. doi:10.1016/j.apsusc.2022.152799

Daneshpour, R., and Mehrpooya, M. (2018). Design and optimization of a combined solar thermophotovoltaic power generation and solid oxide electrolyser for hydrogen production. *Energy Convers. Manag.* 176, 274–286. doi:10.1016/j.enconman.2018.09.033

Daneshvar, H., Prinja, R., and Kherani, N. P. (2015). Thermophotovoltaics: Fundamentals, challenges and prospects. *Appl. Energy* 159, 560–575. doi:10.1016/j.apenergy.2015.08.064

Das, U. K., Tey, K. S., Seyedmahmoudian, M., Mekhilef, S., Idris, M. Y. I., Van Deventer, W., et al. (2018). Forecasting of photovoltaic power generation and model optimization: A review. *Renew. Sustain. Energy Rev.* 81, 912–928. doi:10.1016/j.rser.2017.08.017

Dashiell, M. W., Beausang, J. F., Ehsani, H., Nichols, G. J., Depoy, D. M., Danielson, L. R., et al. (2006). Quaternary InGaAsSb thermophotovoltaic diodes. *IEEE Trans. Electron Devices* 53 (12), 2879–2891. doi:10.1109/ted.2006.885087

Datas, A., Chubb, D. L., and Veeraragavan, A. (2013). Steady state analysis of a storage integrated solar thermophotovoltaic (SISTPV) system. *Sol. energy* 96, 33–45. doi:10.1016/j.solener.2013.07.002

Datas, A., and Martí, A. (2017). Thermophotovoltaic energy in space applications: Review and future potential. *Sol. Energy Mater. Sol. Cells* 161, 285–296. doi:10.1016/j.solmat.2016.12.007

Datas, A., and Vaillon, R. (2021). "Thermophotovoltaic energy conversion," in *Ultra-high temperature thermal energy storage, transfer and conversion* (Sawston, Cambridge: Woodhead Publishing), 285–308.

Davids, P. S., Kirsch, J., Starbuck, A., Jarecki, R., Shank, J., and Peters, D. (2020). Electrical power generation from moderate-temperature radiative thermal sources. *Science* 367 (6484), 1341–1345. doi:10.1126/science.aba2089

Davies, P. A., and Luque, A. (1994). Solar thermophotovoltaics: Brief review and a new look. *Sol. energy Mater. Sol. cells* 33 (1), 11–22. doi:10.1016/0927-0248(94)90284-4

Dresselhaus, M. S., Chen, G., Tang, M. Y., Yang, R. G., Lee, H., Wang, D. Z., et al. (2007). New directions for low dimensional thermoelectric materials. *Adv. Mater.* 19 (8), 1043–1053. doi:10.1002/chin.200726202

Ehrler, B., Alarcón-Lladó, E., Tabernig, S. W., Veeken, T., Garnett, E. C., and Polman, A. (2020). *Photovoltaics reaching for the shockley–queisser limit*. Washington, D.C: ACS Publishing.

Ferrero, D., Lanzini, A., Santarelli, M., and Leone, P. (2013). A comparative assessment on hydrogen production from low-and high-temperature electrolysis. *Int. J. hydrogen energy* 38 (9), 3523–3536. doi:10.1016/j.ijhydene.2013.01.065

Fink, Y., Winn, J. N., Fan, S., Chen, C., Michel, J., Joannopoulos, J. D., et al. (1998). A dielectric omnidirectional reflector. *Science* 282 (5394), 1679–1682. doi:10.1126/science.282.5394.1679

Fonash, S. (2012). *Solar cell device physics*. New York: Academic press.

Fukuda, K., Yu, K., and Someya, T. (2020). The future of flexible organic solar cells. *Adv. Energy Mater.* 10 (25), 2000765. doi:10.1002/aenm.202000765

Gerislioglu, B., Ahmadivand, A., and Adam, J. (2019). Infrared plasmonic photodetectors: The emergence of high photon yield toroidal metadevices. *Mater. Today Chem.* 14, 100206. doi:10.1016/j.mtchem.2019.100206

Gong, J., Li, C., and Wasielewski, M. R. (2019). Advances in solar energy conversion. *Chem. Soc. Rev.* 48 (7), 1862–1864. doi:10.1039/c9cs90020a

Gong, Y., Qiu, R., Niu, C., Fu, J., Jedlicka, E., Giridharagopal, R., et al. (2021). Ag incorporation with controlled grain growth enables 12.5% efficient kesterite solar cell with open circuit voltage reached 64.2% Shockley–Queisser limit. *Adv. Funct. Mater.* 31 (24), 2101927. doi:10.1002/adfm.202101927

Goodnick, S. M., and Honsberg, C. (2022). "Solar cells," in *Springer handbook of semiconductor devices*. Nature Switzerland, Springer, Cham publishing, 699–745.

Grätzel, M. (2005). Solar energy conversion by dye-sensitized photovoltaic cells. *Inorg. Chem.* 44 (20), 6841–6851. doi:10.1021/ic0508371

Green, M. A., and Ho-Baillie, A. W. (2019). Pushing to the limit: Radiative efficiencies of recent mainstream and emerging solar cells. *ACS Energy Lett.* 4 (7), 1639–1644. doi:10.1021/acsenergylett.9b01128

Guenet, B., Gabrielle, B., Chenu, C., Arrouays, D., Balesdent, J., Bernoux, M., et al. (2021). Can N_2O emissions offset the benefits from soil organic carbon storage. *Glob. Change Biol.* 27 (2), 237–256. doi:10.1111/gcb.15342

Guillemoles, J. F., Kirchartz, T., Cahen, D., and Rau, U. (2019). Guide for the perplexed to the Shockley–Queisser model for solar cells. *Nat. photonics* 13 (8), 501–505. doi:10.1038/s41566-019-0479-2

Gupta, M. C., Ungaro, C., Foley IV, J. J., and Gray, S. K. (2018). Optical nanostructures design, fabrication, and applications for solar/thermal energy conversion. *Sol. Energy* 165, 100–114. doi:10.1016/j.solener.2018.01.010

Hassan, H., Yousef, M. S., Fathy, M., and Ahmed, M. S. (2020). Impact of condenser heat transfer on energy and exergy performance of active single slope solar still under hot climate conditions. *Solar Energy* 204, 79–89.

Herring, C., and Nichols, M. H. (1949). Thermionic emission. *Rev. Mod. Phys.* 21 (2), 185–270. doi:10.1103/revmodphys.21.185

Hosenuzzaman, M., Rahim, N. A., Selvaraj, J., Hasanuzzaman, M., Malek, A. A., and Nahar, A. (2015). Global prospects, progress, policies, and environmental impact of solar photovoltaic power generation. *Renew. Sustain. energy Rev.* 41, 284–297. doi:10.1016/j.rser.2014.08.046

Hou, G., Lin, Z., Wang, Q., Zhu, Y., Xu, J., and Chen, K. (2023). Integrated silicon-based spectral reshaping intermediate structures for high performance solar thermophotovoltaics. *Sol. Energy* 249, 227–232. doi:10.1016/j.solener.2022.11.026

Huang, J., Ojambati, O. S., Chikkaraddy, R., Sokołowski, K., Wan, Q., Durkan, C., et al. (2021). Plasmon-induced trap state emission from single quantum dots. *Phys. Rev. Lett.* 126 (4), 047402. doi:10.1103/physrevlett.126.047402

Jang, Y. H., Jang, Y. J., Kim, S., Quan, L. N., Chung, K., and Kim, D. H. (2016). Plasmonic solar cells: From rational design to mechanism overview. *Chem. Rev.* 116 (24), 14982–15034. doi:10.1021/acs.chemrev.6b00302

Javadi, F. S., Metselaar, H. S. C., and Ganesan, P. (2020). Performance improvement of solar thermal systems integrated with phase change materials (PCM), a review. *Sol. Energy* 206, 330–352. doi:10.1016/j.solener.2020.05.106

Jayawardena, K. D. G. I., Bandara, R. M. I., Monti, M., Butler-Caddle, E., Pichler, T., Shiozawa, H., et al. (2020). Approaching the Shockley–Queisser limit for fill factors in lead–tin mixed perovskite photovoltaics. *J. Mater. Chem. A* 8 (2), 693–705. doi:10.1039/c9ta10543c

Jia, N., Cao, J., Tan, X. Y., Dong, J., Liu, H., Tan, C. K. I., et al. (2021). Thermoelectric materials and transport physics. *Mater. Today Phys.* 21, 100519. doi:10.1016/j.mtphys.2021.100519

Jia, X., Puthen-Veettil, B., Xia, H., Yang, T. C. J., Lin, Z., Zhang, T., et al. (2016). All-silicon tandem solar cells: Practical limits for energy conversion and possible routes for improvement. *J. Appl. Phys.* 119 (23), 233102. doi:10.1063/1.4954003

Joshi, A. S., Dincer, I., and Reddy, B. V. (2009). Performance analysis of photovoltaic systems: A review. *Renew. Sustain. Energy Rev.* 13 (8), 1884–1897. doi:10.1016/j.rser.2009.01.009

Kalair, A., Abas, N., Saleem, M. S., Kalair, A. R., and Khan, N. (2021). Role of energy storage systems in energy transition from fossil fuels to renewables. *Energy Storage* 3 (1), e135. doi:10.1002/est2.135

Kalogirou, S. A. (2013). *Solar energy engineering: Processes and systems*. Cambridge, Massachusetts: Academic Press.

Kenjo, S., Ogino, Y., Mukai, K., Bakr, M., Yagi, J., and Konishi, S. (2022). Employing of ZrCo as a fuel source in a discharge-type fusion neutron source operated in self-sufficient mode. *Int. J. Hydrogen Energy* 47 (5), 3054–3062. doi:10.1016/j.ijhydene.2021.10.250

Khalid, K. A. A., Leong, T. J., and Mohamed, K. (2016). Review on thermionic energy converters. *IEEE Trans. electron devices* 63 (6), 2231–2241. doi:10.1109/ted.2016.2556751

Khvostikov, V. P., Gazaryan, P. Y., Khvostikova, O. A., Potapovich, N. S., Sorokina, S. V., Malevskaya, A. V., et al. (2007). GaSb Applications for solar thermophotovoltaic conversion. *AIP Conf. Proc.* 890 (1), 139–148.

Kim, J. Y., Lee, J. W., Jung, H. S., Shin, H., and Park, N. G. (2020). High-efficiency perovskite solar cells. *Chem. Rev.* 120 (15), 7867–7918. doi:10.1021/acs.chemrev.0c00107

Kim, S., Márquez, J. A., Unold, T., and Walsh, A. (2020). Upper limit to the photovoltaic efficiency of imperfect crystals from first principles. *Energy & Environ. Sci.* 13 (5), 1481–1491. doi:10.1039/d0ee00291g

Kohiyama, A., Shimizu, M., Konno, K., Furuhashi, T., and Yugami, H. (2020). Effective photon recycling in solar thermophotovoltaics using a confined cuboid emitter. *Opt. Express* 28 (26), 38567–38578. doi:10.1364/oe.412764

Kohiyama, A., Shimizu, M., and Yugami, H. (2016). Unidirectional radiative heat transfer with a spectrally selective planar absorber/emitter for high-efficiency solar thermophotovoltaic systems. *Appl. Phys. Express* 9 (11), 112302. doi:10.7567/apex.9.112302

Krügener, J., Rienäcker, M., Schäfer, S., Sanchez, M., Wolter, S., Brendel, R., et al. (2021). Photonic crystals for highly efficient silicon single junction solar cells. *Sol. Energy Mater. Sol. Cells* 233, 111337. doi:10.1016/j.solmat.2021.111337

Legendre, J., and Chapuis, P. O. (2022). GaAs-based near-field thermophotonic devices: Approaching the idealized case with one-dimensional PN junctions. *Sol. Energy Mater. Sol. Cells* 238, 111594. doi:10.1016/j.solmat.2022.111594

Lenert, A., Bierman, D. M., Nam, Y., Chan, W. R., Celanović, I., Soljačić, M., et al. (2014). A nanophotonic solar thermophotovoltaic device. *Nat. Nanotechnol.* 9 (2), 126–130. doi:10.1038/nnano.2013.286

Liu, G., Liu, X., Chen, J., Li, Y., Shi, L., Fu, G., et al. (2019). Near-unity, full-spectrum, nanoscale solar absorbers and near-perfect blackbody emitters. *Sol. Energy Mater. Sol. Cells* 190, 20–29. doi:10.1016/j.solmat.2018.10.011

Lu, Y., Li, K., Yang, X., Lu, S., Li, S., Zheng, J., et al. (2021). HTL-free Sb2 (S, Se) 3 solar cells with an optimal detailed balance band gap. *ACS Appl. Mater. Interfaces* 13 (39), 46858–46865. doi:10.1021/acsami.1c10758

Lupangu, C., and Bansal, R. C. (2017). A review of technical issues on the development of solar photovoltaic systems. *Renew. Sustain. Energy Rev.* 73, 950–965. doi:10.1016/j.rser.2017.02.003

Mahan, G. D., and Sofo, J. O. (1996). The best thermoelectric. *Proc. Natl. Acad. Sci.* 93 (15), 7436–7439. doi:10.1073/pnas.93.15.7436

Mahan, G., Sales, B., and Sharp, J. (1997). Thermoelectric materials: New approaches to an old problem. *Phys. Today* 50 (3), 42–47. doi:10.1063/1.881752

Malhotra, R. (2020). *Fossil energy*. New York: Springer.

Mann, S. A., Grote, R. R., Osgood, R. M., Jr, Alù, A., and Garnett, E. C. (2016). Opportunities and limitations for nanophotonic structures to exceed the Shockley–Queisser limit. *ACS Nano* 10 (9), 8620–8631. doi:10.1021/acsnano.6b03950

Mao, J., Chen, G., and Ren, Z. (2021). Thermoelectric cooling materials. *Nat. Mater.* 20 (4), 454–461. doi:10.1038/s41563-020-00852-w

Markvart, T. (2022). Shockley: Queisser detailed balance limit after 60 years. *Wiley Interdiscip. Rev. Energy Environ.* 11 (4), e430. doi:10.1002/wene.430

Mojiri, A., Taylor, R., Thomsen, E., and Rosengarten, G. (2013). Spectral beam splitting for efficient conversion of solar energy—a review. *Renew. Sustain. Energy Rev.* 28, 654–663. doi:10.1016/j.rser.2013.08.026

Nam, Y., Yeng, Y. X., Lenert, A., Bermel, P., Celanovic, I., Soljačić, M., et al. (2014). Solar thermophotovoltaic energy conversion systems with two-dimensional tantalum photonic crystal absorbers and emitters. *Sol. Energy Mater. Sol. Cells* 122, 287–296. doi:10.1016/j.solmat.2013.12.012

Nandihalli, N., Liu, C. J., and Mori, T. (2020). Polymer based thermoelectric nanocomposite materials and devices: Fabrication and characteristics. *Nano Energy* 78, 105186. doi:10.1016/j.nanoen.2020.105186

Ndukwu, M. C., Bennamoun, L., and Simo-Tagne, M. (2021). Reviewing the exergy analysis of solar thermal systems integrated with phase change materials. *Energies* 14 (3), 724. doi:10.3390/en14030724

Nevala, S. M., Hamuyuni, J., Junnila, T., Sirviö, T., Eisert, S., Wilson, B. P., et al. (2019). Electro-hydraulic fragmentation vs conventional crushing of photovoltaic panels–Impact on recycling. *Waste Manag.* 87, 43–50. doi:10.1016/j.wasman.2019.01.039

Okutsu, K., Yamashita, T., Kino, Y., Nakashima, R., Miyashita, K., Yasuda, K., et al. (2021). Design for detecting recycling muon after muon-catalyzed fusion reaction in solid hydrogen isotope target. *Fusion Eng. Des.* 170, 112712. doi:10.1016/j.fusengdes.2021.112712

Osorio, J. D., Wang, Z., Karniadakis, G., Cai, S., Chryssostomidis, C., Panwar, M., et al. (2022). Forecasting solar-thermal systems performance under transient operation using a data-driven machine learning approach based on the deep operator network architecture. *Energy Convers. Manag.* 252, 115063. doi:10.1016/j.enconman.2021.115063

Palfinger, G. (2006). *Low dimensional Si/SiGe structures deposited by UHV-CVD for thermophotovoltaics (Doctoral dissertation)*. Switzerland.

Panwar, N. L., Kaushik, S. C., and Kothari, S. (2011). Role of renewable energy sources in environmental protection: A review. *Renew. Sustain. energy Rev.* 15 (3), 1513–1524. doi:10.1016/j.rser.2010.11.037

Pareek, A., Dom, R., Gupta, J., Chandran, J., Adepu, V., and Borse, P. H. (2020). Insights into renewable hydrogen energy: Recent advances and prospects. *Mater. Sci. Energy Technol.* 3, 319–327. doi:10.1016/j.mset.2019.12.002

Park, N. G. (2020). Research direction toward scalable, stable, and high efficiency perovskite solar cells. *Adv. Energy Mater.* 10 (13), 1903106. doi:10.1002/aenm.201903106

Pasupathi, M. K., Alagar, K., Mm, M., and Aritra, G. (2020). Characterization of hybrid-nano/paraffin organic phase change material for thermal energy storage applications in solar thermal systems. *Energies* 13 (19), 5079. doi:10.3390/en13195079

Pei, Y., Wang, H., and Snyder, G. J. (2012). Band engineering of thermoelectric materials. *Adv. Mater.* 24 (46), 6125–6135. doi:10.1002/adma.201202919

Peuser, F. A., Remmers, K. H., and Schnauss, M. (2013). *Solar thermal systems: Successful planning and construction*. Beuth Verlag Germany: Routledge.

Pourkiaei, S. M., Ahmadi, M. H., Sadeghzadeh, M., Moosavi, S., Pourfayaz, F., Chen, L., et al. (2019). Thermoelectric cooler and thermoelectric generator devices: A review of present and potential applications, modeling and materials. *Energy* 186, 115849. doi:10.1016/j.energy.2019.07.179

Prabhu, B., and ValanArasu, A. (2020). Stability analysis of TiO2-Ag nanocomposite particles dispersed paraffin wax as energy storage material for solar thermal systems. *Renew. Energy* 152, 358–367. doi:10.1016/j.renene.2020.01.043

Prentice, J. S. C. (1999). Optical generation rate of electron-hole pairs in multilayer thin-film photovoltaic cells. *J. Phys. D Appl. Phys.* 32 (17), 2146–2150. doi:10.1088/0022-3727/32/17/302

Qasim, W., Xia, L., Lin, S., Wan, L., Zhao, Y., and Butterbach-Bahl, K. (2021). Global greenhouse vegetable production systems are hotspots of soil N_2O emissions and nitrogen leaching: A meta-analysis. *Environ. Pollut.* 272, 116372. doi:10.1016/j.envpol.2020.116372

Qiu, H., Xu, H., Ni, M., and Xiao, G. (2022). Photo-thermo-electric modeling of photon-enhanced thermionic emission with concentrated solar power. *Sol. Energy Mater. Sol. Cells* 246, 111922. doi:10.1016/j.solmat.2022.111922

Rana, A. S., Zubair, M., Danner, A., and Mehmood, M. Q. (2021). Revisiting tantalum based nanostructures for efficient harvesting of solar radiation in STPV systems. *Nano Energy* 80, 105520. doi:10.1016/j.nanoen.2020.105520

Rashidi, S., Yang, L., Khoosh-Ahang, A., Jing, D., and Mahian, O. (2020). Entropy generation analysis of different solar thermal systems. *Environ. Sci. Pollut. Res.* 27, 20699–20724. doi:10.1007/s11356-020-08472-2

Rau, U., Einsele, F., and Glaeser, G. C. (2005). Efficiency limits of photovoltaic fluorescent collectors. *Appl. Phys. Lett.* 87 (17), 171101. doi:10.1063/1.2112196

Ren, L., Yu, A., Wang, W., Guo, D., Jia, M., Guo, P., et al. (2021). Pn junction based direct-current triboelectric nanogenerator by conjunction of tribovoltaic effect and photovoltaic effect. *Nano Lett.* 21 (23), 10099–10106. doi:10.1021/acs.nanolett.1c03922

Rühle, S. (2016). Tabulated values of the Shockley–Queisser limit for single junction solar cells. *Sol. energy* 130, 139–147. doi:10.1016/j.solener.2016.02.015

Sadi, T., Radevici, I., and Oksanen, J. (2020). Thermophotonic cooling with light-emitting diodes. *Nat. Photonics* 14 (4), 205–214. doi:10.1038/s41566-020-0600-6

Sahoo, G. S., and Mishra, G. P. (2018). Design and modeling of an SJ infrared solar cell approaching upper limit of theoretical efficiency. *Int. J. Mod. Phys. B* 32 (02), 1850014. doi:10.1142/s0217979218500145

Schaller, R. D., Sykora, M., Pietryga, J. M., and Klimov, V. I. (2006). Seven excitons at a cost of one: Redefining the limits for conversion efficiency of photons into charge carriers. *Nano Lett.* 6 (3), 424–429. doi:10.1021/nl052276g

Schwede, J. W., Bargatin, I., Riley, D. C., Hardin, B. E., Rosenthal, S. J., Sun, Y., et al. (2010). Photon-enhanced thermionic emission for solar concentrator systems. *Nat. Mater.* 9 (9), 762–767. doi:10.1038/nmat2814

Sharma, S., and Ghoshal, S. K. (2015). Hydrogen the future transportation fuel: From production to applications. *Renew. Sustain. energy Rev.* 43, 1151–1158. doi:10.1016/j.rser.2014.11.093

Shen, M., Huang, W., Chen, M., Song, B., Zeng, G., and Zhang, Y. (2020). (Micro) plastic crisis: Un-ignorable contribution to global greenhouse gas emissions and climate change. *J. Clean. Prod.* 254, 120138. doi:10.1016/j.jclepro.2020.120138

Shi, X. L., Zou, J., and Chen, Z. G. (2020). Advanced thermoelectric design: From materials and structures to devices. *Chem. Rev.* 120 (15), 7399–7515. doi:10.1021/acs.chemrev.0c00026

Shockley, W., and Queisser, H. J. (1961). Detailed balance limit of efficiency of p-n junction solar cells. *J. Appl. Phys.* 32 (3), 510–519. doi:10.1063/1.1736034

Singh, A. K., and Jen, T. C. (2021). "Introduction to nanomaterials and their applications in optoelectronics," in *Nanomaterials for optoelectronic applications* (Canada: Apple Academic Press), 1–75.

Sisay, T. (2022). *Solar irradiance modeling using feed-forward neural network and multiple linear regression over bahir dar*. Doctoral dissertation. Debreberhan, Ethiopia: Debreberhan University.

Snyder, G. J., and Toberer, E. S. (2008). Complex thermoelectric materials. *Nat. Mater.* 7 (2), 105–114. doi:10.1038/nmat2090

Snyder, G. J., and Ursell, T. S. (2003). Thermoelectric efficiency and compatibility. *Phys. Rev. Lett.* 91 (14), 148301. doi:10.1103/physrevlett.91.148301

Song, J., Han, J., Choi, M., and Lee, B. J. (2022). Modeling and experiments of near-field thermophotovoltaic conversion: A review. *Sol. Energy Mater. Sol. Cells* 238, 111556. doi:10.1016/j.solmat.2021.111556

Sootsman, J. R., Chung, D. Y., and Kanatzidis, M. G. (2009). New and old concepts in thermoelectric materials. *Angew. Chem. Int. Ed.* 48 (46), 8616–8639. doi:10.1002/anie.200900598

Tennyson, E. M., Doherty, T. A., and Stranks, S. D. (2019). Heterogeneity at multiple length scales in halide perovskite semiconductors. *Nat. Rev. Mater.* 4 (9), 573–587. doi:10.1038/s41578-019-0125-0

Tervo, E. J., Callahan, W. A., Toberer, E. S., Steiner, M. A., and Ferguson, A. J. (2020). Solar thermoradiative-photovoltaic energy conversion. *Cell Rep. Phys. Sci.* 1 (12), 100258. doi:10.1016/j.xcrp.2020.100258

Tian, Y., Liu, X., Ghanekar, A., and Zheng, Y. (2021). Scalable-manufactured metal–insulator–metal based selective solar absorbers with excellent high-temperature insensitivity. *Appl. Energy* 281, 116055. doi:10.1016/j.apenergy.2020.116055

Tong, X. C. (2018). *Functional metamaterials and metadevices*, 110. Bolingbrook, IL: Springer.

Tritt, T. M. (2011). Thermoelectric phenomena, materials, and applications. *Annu. Rev. Mater. Res.* 41, 433–448. doi:10.1146/annurev-matsci-062910-100453

Trupke, T., Green, M. A., and Würfel, P. (2002). Improving solar cell efficiencies by down-conversion of high-energy photons. *J. Appl. Phys.* 92 (3), 1668–1674. doi:10.1063/1.1492021

Ungaro, C., Gray, S. K., and Gupta, M. C. (2015). Solar thermophotovoltaic system using nanostructures. *Opt. express* 23 (19), A1149–A1156. doi:10.1364/oe.23.0a1149

Vohra, K., Vodonos, A., Schwartz, J., Marais, E. A., Sulprizio, M. P., and Mickley, L. J. (2021). Global mortality from outdoor fine particle pollution generated by fossil fuel combustion: Results from GEOS-Chem. *GEOS-Chem. Environ. Res.* 195, 110754. doi:10.1016/j.envres.2021.110754

Wang, X., Khan, M. R., Gray, J. L., Alam, M. A., and Lundstrom, M. S. (2013). Design of GaAs solar cells operating close to the Shockley–Queisser limit. *IEEE J. Photovoltaics* 3 (2), 737–744. doi:10.1109/jphotov.2013.2241594

Wang, Y., Liu, H., and Zhu, J. (2019). Solar thermophotovoltaics: Progress, challenges, and opportunities. *Apl. Mater.* 7 (8), 080906. doi:10.1063/1.5114829

Welsby, D., Price, J., Pye, S., and Ekins, P. (2021). Unextractable fossil fuels in a 1.5° C world. *Nature* 597 (7875), 230–234. doi:10.1038/s41586-021-03821-8

Wong, J., Omelchenko, S. T., and Atwater, H. A. (2020). Impact of semiconductor band tails and band filling on photovoltaic efficiency limits. *ACS Energy Lett.* 6 (1), 52–57. doi:10.1021/acsenergylett.0c02362

Wu, F., Liu, T., and Xiao, S. (2023). Polarization-sensitive photonic bandgaps in hybrid one-dimensional photonic crystals composed of all-dielectric elliptical metamaterials and isotropic dielectrics. *Appl. Opt.* 62 (3), 706–713. doi:10.1364/ao.480083

Wu, F., Wu, X., Xiao, S., Liu, G., and Li, H. (2021). Broadband wide-angle multilayer absorber based on a broadband omnidirectional optical Tamm state. *Opt. Express* 29 (15), 23976–23987. doi:10.1364/oe.434181

Xiang, C., Zhao, X., Tan, L., Ye, J., Wu, S., Zhang, S., et al. (2019). A solar tube: Efficiently converting sunlight into electricity and heat. *Nano Energy* 55, 269–276. doi:10.1016/j.nanoen.2018.10.077

Xiao, G., Zheng, G., Qiu, M., Li, Q., Li, D., and Ni, M. (2017). Thermionic energy conversion for concentrating solar power. *Appl. Energy* 208, 1318–1342. doi:10.1016/j.apenergy.2017.09.021

Xu, G., Schwarz, P., and Yang, H. (2020). Adjusting energy consumption structure to achieve China's CO2 emissions peak. *Renew. Sustain. Energy Rev.* 122, 109737. doi:10.1016/j.rser.2020.109737

Xu, Y., Gong, T., and Munday, J. N. (2015). The generalized Shockley-Queisser limit for nanostructured solar cells. *Sci. Rep.* 5 (1), 13536–13539. doi:10.1038/srep13536

Xu, Y., Wang, J., Yu, F., Guo, Z., Cheng, H., Yin, J., et al. (2020). Flexible and efficient solar thermal generators based on polypyrrole coated natural latex foam for multimedia purification. *ACS Sustain. Chem. Eng.* 8 (32), 12053–12062. doi:10.1021/acssuschemeng.0c03164

Yang, S., Qiu, P., Chen, L., and Shi, X. (2021). Recent developments in flexible thermoelectric devices. *Small Sci.* 1 (7), 2100005. doi:10.1002/smsc.202100005

Yao, H., and Hou, J. (2022). Recent advances in single-junction organic solar cells. *Angew. Chem.* 134 (37), e202209021. doi:10.1002/anie.202209021

Zenker, M., Heinzel, A., Stollwerck, G., Ferber, J., and Luther, J. (2001). Efficiency and power density potential of combustion-driven thermophotovoltaic systems using GaSb photovoltaic cells. *IEEE Trans. Electron Devices* 48 (2), 367–376. doi:10.1109/16.902740

Zhang, L., Shi, X. L., Yang, Y. L., and Chen, Z. G. (2021). Flexible thermoelectric materials and devices: From materials to applications. *Mater. Today* 46, 62–108. doi:10.1016/j.mattod.2021.02.016

Zhang, X., Han, L., Wei, H., Tan, X., Zhou, W., Li, W., et al. (2022). Linking urbanization and air quality together: A review and a perspective on the future sustainable urban development. *J. Clean. Prod.* 346, 130988. doi:10.1016/j.jclepro.2022.130988

Zhang, Z., Ding, T., Zhou, Q., Sun, Y., Qu, M., Zeng, Z., et al. (2021). A review of technologies and applications on versatile energy storage systems. *Renew. Sustain. Energy Rev.* 148, 111263. doi:10.1016/j.rser.2021.111263

Zheng, M., Lin, S., Tang, Z., Feng, Y., and Wang, Z. L. (2021). Photovoltaic effect and tribovoltaic effect at liquid-semiconductor interface. *Nano Energy* 83, 105810. doi:10.1016/j.nanoen.2021.105810

Zhou, W., Chen, Q., Luo, D., Jiang, R., and Chen, J. (2020). Global energy consumption analysis based on the three-dimensional network model. *IEEE Access* 8, 76313–76332. doi:10.1109/access.2020.2989186

Zhou, Z., Sakr, E., Sun, Y., and Bermel, P. (2016). Solar thermophotovoltaics: Reshaping the solar spectrum. *Nanophotonics* 5 (1), 1–21. doi:10.1515/nanoph-2016-0011

Zou, H., Dai, G., Wang, A. C., Li, X., Zhang, S. L., Ding, W., et al. (2020). Alternating current photovoltaic effect. *Adv. Mater.* 32 (11), 2001532. doi:10.1002/adma.202001532

frontiers | Frontiers in Energy Research

TYPE Original Research
PUBLISHED 27 July 2023
DOI 10.3389/fenrg.2023.1186095

OPEN ACCESS

EDITED BY
Athanasios I. Papadopoulos,
Centre for Research and Technology Hellas (CERTH), Greece

REVIEWED BY
Giovanni Bracco,
Polytechnic University of Turin, Italy
Alexios-Spyridon Kyriakides,
Centre for Research and Technology Hellas (CERTH), Greece

*CORRESPONDENCE
Ameh A. Attabo,
ameh.attabo@stu.cu.edu.ng
Oluseyi O. Ajayi,
oluseyi.ajayi@covenantuniversity.edu.ng

RECEIVED 14 March 2023
ACCEPTED 11 July 2023
PUBLISHED 27 July 2023

CITATION
Attabo AA, Ajayi OO, Oyedepo SO and Afolalu SA (2023), Assessment of the wind energy potential and economic viability of selected sites along Nigeria's coastal and offshore locations.
Front. Energy Res. 11:1186095.
doi: 10.3389/fenrg.2023.1186095

Assessment of the wind energy potential and economic viability of selected sites along Nigeria's coastal and offshore locations

Ameh A. Attabo[1]*, Oluseyi O. Ajayi[1]*, Sunday O. Oyedepo[1] and Sunday A. Afolalu[2,3]

[1]Mechanical Engineering Department, Covenant University, Ota, Nigeria, [2]Mechanical & Mechatronics Engineering Department, Afe Babalola University, Ado, Nigeria, [3]Mechanical Engineering Science Department, University of Johannesburg, Johannesburg, South Africa

Wind energy is a promising sector in the power generation industry because it is renewable and globally available. In this research work, the wind energy potential and the economic viability of using wind turbines to generate electricity in some selected sites along Nigeria's coastline and offshore locations were evaluated. Using the statistical two-parameter Weibull probability density function method, wind speed data retrieved from an indigenous oceanography company and global information system (GIS) were analyzed for wind energy harvest. The energy output, unit cost of electricity generated by three commercially available wind turbine models (3 MW, 4 MW, and 6 MW), net present value (NPV), and payback period were evaluated. Levelized cost of electricity (LCOE) sensitivity to the discount rate, foundation cost, and turbine lifespan were also examined. The findings from the study showed that the offshore sites have four times greater wind power potential than the coastal sites. The offshore sites can be categorized as "class IIIb" wind sites, making the locations suitable for wind energy harvest. The techno-economic analysis showed that the net gains from investing in a 60-MW wind farm in the region can be as high as $62,000,000.00, while the project payback time can be as low as 5.74 years. Two of the offshore sites are recommended for the development of an offshore wind farm in the country because of their relatively low LCOE (0.04 $/kWh), higher NPV, and lower investment payback time. The Vesta-117 model wind turbine is the most suitable wind turbine system and recommended for use in the region because of its low cut-in speed (3 m/s). Sensitivity analysis showed that the LCOE of offshore-01 was reduced by 31% when the lifespan of the V117 turbine was increased from 20 to 25 years. The results also showed that reductions in the discount rate and foundation cost positively affect the LCOE.

KEYWORDS

wind energy, resource assessment, Nigeria offshore, energy output, net present value, simple payback time, levelized cost of electricity

1 Introduction

Due to the growing population and knowledge of sustainable development and environmental protection, the use of renewable energy sources has received considerable attention during the last few decades. Wind energy, one of the most well-known renewable energy sources, has been widely used in various parts of the world. Wind power is virtually

limitless, clean, and environmentally friendly. Countries like China, the United States of America, Germany, Denmark, Spain, and India are constantly increasing their installed wind power capacities on an annual basis. The increasing level of growth and development of wind energy technology is made possible by the efforts of researchers across the globe. These efforts are geared toward seeking ways to improve the system's generation capacity by enhancing the aerodynamic performance of the blade shape; for example, Göçmen and Özerdem (2012) optimized for the noise emission reduction, Zhang et al. (2018) demonstrated power-trade-off for aeroacoustics, and Ajayi et al. (2019) improved the startup capacity of low-speed wind turbines. Other efforts are also focused on the proper understanding and analysis of the flow dynamics around wind turbine rotors, especially at the wakes, as it concerns the wind farm layout design (Fan et al., 2023).

Adopting wind energy for power generation, however, requires the knowledge of its resource availability in a particular space and time. This is because wind power potentials are location-specific due to the nonlinearity of its availability in space and time (Ajayi et al., 2014). Hence, before the commitment of huge investment associated with renewable energy projects, resource evaluation to determine the feasibility of the project is considered the first step. Most important also is the economic–environmental viability of the project. Based on this, several researchers focused on the first step of resource assessment of siting wind energy and other renewable energy projects in a place to determine the potential and economic viability of such projects. For instance, Kohole et al. (2023) examined the wind energy potential, as well as electricity and hydrogen generation, for the cities of Kousseri, Kaele, Maroua, Mokolo, Mora, and Yagoua in the far northern region of Cameroon using wind speed data recorded at heights of 10 m, 40 m, and 70 m. The Enercon E-48/800 turbine has the highest capacity factor in all of the locations studied, with the energy cost ranging from 0.0578 $/kWh in Kousseri to 0.0838 $/kWh in Mora. If the power plants that burn oil or natural gas as fuel are replaced with wind turbines, CO_2 emission will be reduced by up to 885.36 tons or 641.60 tons in the far northern region of Cameroon. Asamoah et al. (2023) examined the financial, technical, and environmental impact assessment of a 50-MW wind farm in four locations in Ghana, using the net present value as the main financial metric to analyze the profitability of the projects. The study established that a potential utility-scale wind project is feasible in all locations. To fulfill energy demands in Thailand, Khan et al. (2022) used the Wind Atlas Analysis and Application Program (WAsP) to simulate the wind potential in the northern part of the country; the cities studied are Lamphun, Chiang Rai, Mae Hong Son, Mae Sariang, Phayao, Thung Chang, and Theon. The results from the study recommended two out of seven cities to be viable for the establishment of wind farms because the two cities (Phayao and Mae Sariang) have wind power densities higher than 400 W/m^2.

Many studies have also used the global information system (GIS) method to estimate the wind potential in other countries, most especially where physical data collection may not be feasible. For example, Harrucksteiner et al. (2022) employed a GIS-based technique to assess the suitability of using renewable energy generators in some sites in Mongolia; thereafter, an energy tool was deployed to calculate the technical and economic potential obtainable from these locations. The study estimated that the combined technical wind and solar potential is 7.25 TW, of which 2.13 TW can be generated from wind turbines. Tuy et al. (2022) used WRF and Sentinel-1 level 2 to predict offshore wind potential in Cambodia. Martinez and Iglesias (2021) employed a multiparameter analysis for a case study to discern the effects of specific elements on the levelized cost of electricity (LCOE) of floating wind farms located in the Mediterranean Sea. Assumptions were formulated as functions of site-specific variables (distance to shore, water depth, and annual energy production). Shu et al. (2022) worked on optimizing offshore wind farm output using a non-centralized approach. The study evaluated a wind farm comprising 36 wind turbines.

1.1 The case for Nigeria

Currently, Nigeria does not produce a relatively large amount of wind energy; however, the demand for energy occasioned by increased population and industrialization has pushed the limits for the country to critically examine sites suitable for wind energy harvest. At the end of 2021, Nigerian power plants have an installed capacity of 13.5 GW, with natural gas plants accounting for 84.6%, large hydro plants accounting for approximately 14.5%, off-grid small hydro plants accounting for 0.7%, and off-grid distributed PV accounting for 0.2%, and an onshore wind project in Kastina has an installed capacity of 10.2 MW (Climatescope, 2021). With an optimistic gross domestic product (GDP) growth rate of 11.5%, the Energy Commission of Nigeria (ECN) conducted an energy demand and supply study, taking into account economic vision, demography, available energy resources, and modern developmental path. The result shows that Nigeria would need 31,210 MW of energy per day (Ale and Adeyemi, 2022). Furthermore, a 2022 USAID report estimated that there are more than 20 million homes without electricity in Nigeria, and the power plants generate a daily average of 4,100 MW of energy per day between 2020 and 2021 (USAID, 2022). This suggests that there is a significant energy deficit which is responsible for load shedding, power outages, and low voltage in the supply of electricity experienced in most parts of the country (Salakhetdinov and Agyeno, 2020; Chanchangi et al., 2022). This has been a deep concern to both the government and the people of Nigeria for many years. One of the actions taken by the federal government to finding a long-term answer to this problem is the adoption of the National Renewable Energy Action Plans (NREAP) which targets that Nigeria should generate at least 30% of their energy from renewable energy sources before 2030 (NREAP, 2015).

Considering the energy deficit in Nigeria, some studies have reported that the use of wind energy is marginal and can be used for water pumping and electricity generation. For instance, Ayodele et al. (2018) carried out a study using 16 years of wind data obtained from NIMET for a techno-economic analysis of wind energy to pump water in some selected communities in Oyo State, Nigeria. The results from the study showed that the wind power densities in the communities range from 165.75 to 207.2 W/m^2. The Polaris P50 wind turbine was selected as the most suitable wind turbine, with a rated power and wind speed of 50 kW and 9 m/s, respectively. Amole et al. (2023) carried out a comparative analysis of using a hybrid energy system (PV and grid connection) in a rural location in

South West Nigeria. The study examined the monthly grid purchase, unmet electric load, and net present cost of energy. Recommendation from the studies encouraged the use of a PV–grid system, achieving an LCOE as low as USD $ 0.1904. Oladigbolu et al. (2021) used Homer software to analyze hybrid power-generating systems comprising solar PV, wind turbines, and diesel generator to supply power to a rural healthcare facility. The results also showed that the optimized solution is environmentally friendly, with an acceptable carbon dioxide emission of 1,304 kg/year. The emission rate was approximately 80% less than when only fossil fuel was used in the location.

To estimate wind characteristics, variation pattern, wind power potential, and the performance of various estimation tools in Nigeria, Ben et al. (2021) evaluated 10 years of daily mean wind speed data from 13 cities in Central and Southern Nigeria using six different methods of estimating Weibull parameters (graphical, empirical methods of Justus and Lysten, method of moment, maximum likelihood method, and energy pattern factor). They reported that the cities in the southern and central parts of the country have power classes ranging between 1 and 4. Ozioko et al. (2022) evaluated the impact of wind energy penetration on the Nigerian power grid, especially when replacing the conventional fossil fired generator with doubly-fed induction generator (DFIG)-based wind turbine generators. Their study focused on the connection of power generated from wind turbines to the national grid and not on actual wind power generation or assessment.

1.2 Present study

Although there are some wind power classification studies across Nigeria, all the existing studies have focused mainly on onshore sites (Fatigun, et al., 2017; Ben et al., 2021; Richard and Eseosa, 2022). Those that assessed and exposed the potential and economic viability of wind power variability along the coastal and offshore locations are scanty or non-existent. At best, what exist are mere mentions of the possible potential capacity of generating wind power around coastal and offshore locations without any efforts geared toward its assessment and econometrics (Ajayi et al., 2014; Olaofe, 2017). Therefore, the aim of this paper is to evaluate and showcase the wind energy potential of some sites around the coastal and offshore locations in Nigeria using *in-situ* and GIS-retrieved wind data to determine prospective sites for the adoption of wind energy generation in the region. The econometrics of using commercially available wind turbines to generate power at the sites was also considered. The result from this study may draw public attention to the untapped renewable energy source along some coastal towns and offshore locations in the country; it will also serve as a tool for the federal government and other stakeholders in the decision-making process of investing in wind energy projects around the selected sites.

2 Data collection

The wind speed data for the selected locations were obtained from Ines Oceanography Resources (a marine data acquisition firm), covering a 10-year period between 2010 and 2019. Wind data were captured at a height of 10 m above the ground using a cup-generator anemometer; other parameters such as atmospheric pressure and dominant wind direction were also measured. The satellite data used to estimate wind energy in this study were obtained from the National Centers for Environmental Prediction (NCEP) Climate Forecast System Reanalysis (CFSR) platform based in the United States of America. Satellite observations were used in radiance form and were bias-corrected with "spin up" runs at full resolution, taking into account variable CO_2 concentrations. The coordinates of the six locations are given in Table 1, and Figure 1 shows the map of the location of the selected sites. The four offshore sites were tagged "offshore-01 to offshore-04" because these locations are arbitrary locations selected off the shores of Nigeria and within 50 km from the country's shoreline. Figure 1 displays the map locations of the two coastal and four offshore sites.

TABLE 1 Coordinates of the selected coastal and offshore locations.

S/N	Site	Latitude (N°)	Longitude (E°)
1	Apapa Port	6° 25′51.17″	3° 21′14.47″
2	Brass River estuary	4° 18′45.32″	6° 14′11.64″
3	Offshore-01	5°27′50.4″	5°00′00.0
4	Offshore-02	6°24′02.5″	3°45′00.0″
5	Offshore-03	6°24′02.5″	4°03′45.0″
6	Offshore-04	6°05′18.5″	4°22′30.0″

3 Methods of analysis

3.1 Power law

The wind speed measurements were adjusted to the requisite turbine hub height because the heights of the meteorological towers were significantly lower than the turbine hub heights; hence, all the wind speed data from the sites were adjusted to 100 m in this study. The hub height of 100 m was chosen to enable an unbiased comparison for the various sites as the average heights of selected turbines also fall within this range. Previous research showed that wind shear decreases with height, causing wind speeds to increase with height, h, depending on the ground friction coefficient α (Crippa et al., 2021). The wind speed at the hub height can be calculated using the following expression (Sasser et al., 2022):

$$v_2 = v_1\left(\frac{h_2}{h_1}\right)^{\alpha}, \tag{1}$$

where v_2 is the wind speed at the hub height; v_1 is the wind speed at the meteorological mast height; α is the surface roughness coefficient; h_1 is the metrological mast height; and h_2 is the turbine hub height. According to the existing literature, the surface roughness coefficient for various terrains ranges between 0.1 and 0.4, with the smoother terrains having lower magnitudes while the higher range is for rougher terrains. The surface roughness coefficient is calculated using Eq. 2 (Adaramola et al., 2014):

FIGURE 1
Nigeria shoreline map showing coastal and offshore locations of interest.

$$\alpha = 0.37 - 0.0881 \ln v_1. \quad (2)$$

3.2 Weibull distribution function

The prediction of wind energy is relatively complex because wind is a variable resource (Imani et al., 2021). In most cases, the prediction of wind speed is carried out using probability distribution functions, and various models have been used in previous works to predict wind speed with various accuracies (Shu et al., 2015). However, the Weibull and Rayleigh probability distributions have been found to provide a fitting representation of the variation of the mean wind speed (Al-Mhairat and Al-Quraan, 2022; Sumair et al., 2022). Thus, this study employed the Weibull probability distribution function to classify and analyze the wind characteristics of the sites.

Eq. 3 gives the expression for the Weibull probability distribution function (Jabbar, 2021):

$$f(v) = \left(\frac{k}{c}\right)\left(\frac{v}{c}\right)^{k-1} \exp\left[-\left(\frac{v}{k}\right)^{k}\right] \ (v > 0; k > c, c > 0), \quad (3)$$

where $f(v)$ is the probability of observed wind speed v. k and c are known as the Weibull shape parameter and Weibull scale parameter, respectively. The scale parameter c is measured in m/s and describes the abscissa scale of the data distribution plot; a higher value of c indicates a higher wind energy potential in that location. The dimensionless shape parameter k, on the other hand, determines the width of the data distribution plot, which reflects the maximum wind distribution.

The moment method was used to calculate both the k and c parameters.

The mean wind speed (v_m) and variance (σ^2) of the wind data are determined using Eqs 4, 5 (Usta, 2016):

$$v_m = \frac{1}{n}\left[\sum_{i=1}^{n} v_i\right], \quad (4)$$

$$\sigma^2 = \frac{1}{n-1}\sum_{i=1}^{n} (v_i - v_m)^2, \quad (5)$$

while the Weibull parameters (k and c) are estimated using Eq. 6, 7, respectively:

$$k = \left(\frac{\sigma}{V_m}\right)^{-1.086} \quad (1 \le k \le 10), \quad (6)$$

$$c = \frac{v_m}{\Gamma\left(1 + 1/k\right)}. \quad (7)$$

The gamma function is estimated using the standard Eq. 8:

$$\Gamma(x) = \int_0^{\infty} t^{x-1} \exp(-t) dt. \quad (8)$$

3.3 Wind turbine operating probability

There are two important wind speed parameters to consider when estimating wind power potentials: the cut-in and cut-out wind speeds (Klerk and Venter, 2017). The cut-in wind speed is the minimum wind speed required for turbines to generate usable power, whereas the cut-out wind speed is the wind speed at which turbines will be shut down to prevent damage. The cut-in speed for most available wind turbines is in the range of 3–5 m/s, while the cut-out speed can be as high as 25 m/s (Mansi and Aydin, 2022). As a result, wind speed frequencies occurring in the range of "cut-in and cut-out" wind speeds are valuable for the accurate assessment of the operability and economic feasibility of offshore wind turbines in the region. Therefore, the operating probability of the turbines is calculated using the cumulative Weibull distribution function, as shown in Eq. 9 (Ahmed, 2018):

$$P(V_1 < v < V_2) = \exp\left[-\left(\frac{V_1}{c}\right)^k\right] - \exp\left[-\left(\frac{V_2}{c}\right)^k\right], \quad (9)$$

where V_1 and V_2 represent the cut-in and cut-out wind speeds of the turbines, respectively.

3.4 Most probable wind speed and wind speed carrying maximum energy

The peak of the Weibull probability distribution function represents the most probable wind speed, while the wind speed carrying the most energy is the speed at which the most power is generated based on the available wind profile. The most probable wind speed (V_{mp}) and wind speed carrying maximum energy (V_{maxE}) are calculated using Eqs 10, 11, respectively. To improve the overall efficiency of wind farms, it is recommended that the rated wind speed and wind speed carrying maximum energy should be as close as possible, since a wind turbine generator produces maximum power at its rated wind speed (Oyewole et al., 2019).

$$V_{mp} = c\left(1 - \frac{1}{k}\right)^{1/k}, \quad (10)$$

$$V_{maxE} = c\left(1 + \frac{2}{k}\right)^{1/k}. \quad (11)$$

3.5 Wind power density

The wind power density (WPD) is an indicator that has been widely adopted to demonstrate the capacity of wind resources at a specific site (Li et al., 2022). The WPD from the Weibull distribution parameters is estimated using Eq. 12 (Sumair, 2021):

$$WPD = \int_0^\infty \frac{1}{2}\rho v^3 f(v)dv = \frac{1}{2}\rho c^3 \Gamma\left(1 + \frac{3}{k}\right), \quad (12)$$

where ρ is the air density (kg/m^3) and c and k are the Weibull scale and shape factors mentioned previously.

3.6 Annual energy yield

The annual energy yield from the wind turbines is calculated by multiplying the probability of having that speed in a year with the power output of the turbine at a certain speed. Eq. 13 (Ahmed, 2018) is used for the calculation of the annual energy yield from each site.

$$E_a = 8760 \times \sum_{V_1}^{V_2} f(v)P_e(v), \quad (13)$$

where $P_e(v)$ is the power output at speed v and $f(v)$ is the probability of having v.

3.7 Capacity factor

The ratio of the average output power to the rated output power is referred to as the capacity factor (CF). The annual CF is given by Eq. 14 (Mattar and Guzman-Ibarra, 2017):

$$CF = \frac{E_a}{P_{rated} \times 8760}, \quad (14)$$

where P_{rated} is the turbine rated power output.

3.8 Levelized cost of electricity

The LCOE is estimated using Eq. 15 (Chancham and Gagnon, 2017):

$$LCOE = \frac{CRF}{8760P_{rated}C_f}\left(C_I + C_{om(esc)}\right) \quad \frac{cost}{kWh}, \quad (15)$$

where C_I is the total investment cost; $8760P_{rated}C_f$ is the annual energy output from the wind turbine in kWh; CRF is the capital recovery factor which is the equivalent of the annual revenue throughout the lifetime of the wind turbines; and $C_{om(esc)}$ is the annual operations and maintenance cost escalated as given in Eqs 16, 17 (Martinez and Iglesias, 2022).

$$CRF = \frac{(1+dr)^n dr}{(1+dr)^n - 1}, \quad (16)$$

$$C_{om(esc)} = \frac{\frac{C_{om}}{dr - e_{om}}\left[1 - \left(\frac{1+e_{om}}{1+dr}\right)^n\right]cost}{year}, \quad (17)$$

where C_{om}, e_{om}, n, and dr represent the operations and maintenance cost for the first year, escalation of operations and maintenance, useful lifetime of the turbine, and discount rate, respectively. The discount rate can be corrected for the inflation rate (r) and inflation escalation rate (e) using Eqs. 18, 19:

$$e_a = \{(1+e)(1+r)\} - 1, \quad (18)$$

where the apparent escalation rate is designated as e_a, and the discount rate can be calculated as follows:

$$dr = \frac{(1+i)}{(1+e_a)} - 1, \quad (19)$$

where i is the interest rate.

3.9 Net present value

The net present value (NPV) uses the time value of the money concept to convert future cash flow into a present value at a certain discount rate. Mathematically, the present value of future cash flow is calculated using Eq. 20 (Schweizer et al., 2016; Jang et al., 2022):

$$PV = A_a\left[\frac{(1 - (1/dr)^n)}{dr}\right], \quad (20)$$

where PV is the present value of the recurring annuity, A_a. dr is the discount rate, and n is the number of years in the future. In this study, n was set at 20 years as most wind turbines have an estimated lifespan ranging between 20 and 25 years.

3.10 Simple payback time

The simple payback time is a technique for analyzing energy costs that determines how long it will take for energy savings

TABLE 2 Specifications of the wind turbines employed in this study (Vestas Americas, 2014; 2017; and Siemens-Gemesa, 2016).

Specifications	Vesta V90-3.0 MW	Vesta V117-4.0 MW	Siemens SWT-6.0-154 6.0 MW
Rated power	3 MW	4 MW	6 MW
Rotor diameter	90 m	117 m	154 m
Swept area	6,362.0 m^2	10,751.3 m^2	18,600.0 m^2
Cut-in wind speed	4.0 m/s	3.0 m/s	4.0 m/s
Cut-out wind speed	25 m/s	25.0 m/s	25.0 m/s
Rated wind speed	15.0 m/s	14.0 m/s	13.0 m/s
Blade speed range	8.4–18.6 rpm	4–11.3 rpm	5–11 rpm
Number of blades	3	3	3

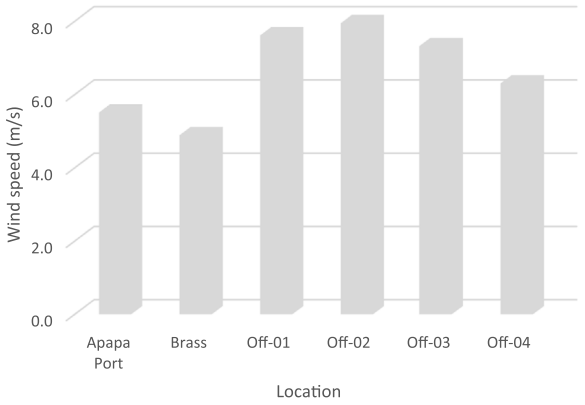

FIGURE 2
Mean wind speeds along the selected Nigerian coastal and offshore locations.

(profit for the farm) to equal the project's initial investment cost (Dai et al., 2022). When determining the wind farm's viability, the payback period is calculated by contrasting the initial investment cost with the project's yearly returns. The more cost-effective the investment, the shorter the payback period. Eq. 21 is used for the calculation of the simple payback time (Ramadhan, 2021).

$$SPT = \frac{C_I}{E_a \times \frac{P_r}{kWh} - C_I - FCR - AOM}, \tag{21}$$

where SPT is the simple payback time in years; C_I is the total investment cost; E_a is energy produced annually (kWh/year); P_r/kWh is the price of energy or price obtained for energy generated; FCR is the fixed charge rate per year; and AOM is the annual operations and maintenance cost per year.

3.11 Cost estimation methods

Due to the difficulty in obtaining the exact costs for the wind farm component at various stages of the project, cost parameters for foundation costs, electrical grid connections, and operations and maintenance costs were estimated.

3.11.1 Foundation cost

A cost function for offshore wind turbine foundations was developed and expressed as a linear function in terms of water depth (Srensen and Larsen, 2021). Eq. 22 provides the relationship between the foundation cost and water depth.

$$c_f = 14557 \times d + 270667, \tag{22}$$

where C_f and d denote the foundation cost ($/MW) and water depth (m), respectively.

3.11.2 Electrical cost

Moller et al. (2012) developed a cost function for estimating electrical expenditures, as shown in Eq. 23, which expressed the cost in terms of the shortest land and subsea distances to the offshore turbines.

$$C_E = \frac{(0.38d_s + 0.4d_l + 76.6) \times 10^6}{200}, \tag{23}$$

where d_s denotes the shortest subsea distance (km), the shortest land distance (km) is denoted as d_l, and C_E is the electrical cost in $/MW. In this study, two types of cable lengths are considered, viz., land cables that are required to connect the OWF to the high-voltage national grid and subsea cables that are required to connect the OWF to the shoreline.

3.11.3 Operations and maintenance costs

The cost function used is expressed in terms of distance to the port, as shown in Eq. 24 (Jacquemin et al., 2011; Rinaldi et al., 2021):

$$C_{om} = 0.29d_p^2 + 159d_p + 50415, \tag{24}$$

where C_{om} represents the operations and maintenance cost ($/MW) and d_p denotes the shortest distance from the harbor or service port (km) to the OWT.

3.12 Selection of reference wind turbines and wind farm layout

For the econometric assessment, three wind turbines with different power ratings (3, 4, and 6 MW) were analyzed, and

10.3389/fenrg.2023.1186095

TABLE 3 Turbine selection parameter for some selected locations in the Nigeria shoreline.

Location	k	c (m/s)	v_{mp}	v_{Emax}
Apapa Port	8.18	5.81	5.72	5.96
Brass River estuary	7.84	5.17	5.08	5.32
Offshore-01	5.91	8.18	7.92	8.59
Offshore-02	5.94	8.53	8.27	8.96
Offshore-03	5.78	7.90	7.64	8.31
Offshore-04	5.72	8.72	8.44	9.19

their economic viabilities were evaluated. The three turbines used for the assessment are V90 (3.0 MW) and Vesta V117 (4.0 MW) manufactured by Vesta and SWT-6.0-154 (6 MW) manufactured by Siemens. Table 2 shows the technical specification of the selected wind turbines.

For each of the sites in this study, a 60-MW wind farm was simulated using the aforementioned three models of wind turbines. For the 3.0-MW wind farm, 20 wind turbines were positioned at least 4 rotor diameters apart from one another (Noel et al., 2022) in the x- and y-planes (using a 5 row by 4 column matrix). Successive turbine rows were offset to the previous rows to minimize the wake effect from upstream turbines. Wind farm simulation for the 4-MW and 6-MW wind farms was carried out using 15 units (i.e., 5 rows by 3 columns) and 10 units (i.e., 5 rows by 2 columns) of wind turbines, respectively, instead of 20 units as used in the case of the 3-MW wind farm setup.

4 Results and discussion

4.1 Wind potentials

The wind potential in the region was assessed by evaluating the average wind speed, power density, and wind directions for each site. Figure 2 shows the 10-year mean wind speeds for coastal and offshore sites interpolated to a hub height of 100 m. Brass had the least magnitude in terms of the annual mean wind speed profile of 4.89 m/s, and offshore-02 had the highest speed of 7.95 m/s. Offshore-01 and offshore-03 (7.61 m/s and 7.32 m/s, respectively) also had an impressive average wind speed compared with the wind data of the other sites. The wind speed in Brass is in the range of 3.02 m/s–6.52 m/s (mean 4.89 m/s), while offshore-02 has a range between 6.91 m/s and 8.25 m/s (mean 7.95 m/s).

Examining the variation in wind speed across the years (Figure 3) shows that there was a decrease in the values of the wind speed profiles across the years for offshore-04, Apapa, and offshore-01. Offshore-04 had an approximately 15% decline in wind speeds when comparing the most recent years with preceding years. However, Brass and offshore-02 and -03 were observed to have a slight increase (less than 5% increase) in their mean wind speed in 2019 when compared to the preceding years.

4.2 Weibull analysis for shoreline sites

The indicators required for the generation of wind energy were deduced using the Weibull (moment method) and are presented in Table 3. The highest annual scale parameter of 8.72 m/s was observed at offshore-04, while the least value of 5.17 m/s was recorded in Brass; the values for Apapa, offshore-01, -02, and -03 are 5.81 m/s, 8.18 m/s, 8.53 m/s, and 7.90 m/s, respectively. The annual most probable wind speeds for the sites ranges from 5.08 m/s to 8.44 m/s. The estimated values for k across all the sites in the region were in the range of $5.7 \leq k \leq 8.18$ m/s. These high values of k ($k \geq 2$) indicate a data spread similar to the normal distribution (Kumar and Gaddada, 2015) and also show that the data have a narrow data spread. In some cases, a relatively high k factor is desirable at higher mean speeds (Thambain and Storm, 2012), which is an indication that the data spread is concentrated at a higher modal wind speed.

The result of the most probable wind speed (V_{mp}) is slightly lower than the wind speed carrying maximum wind energy (i.e., maximum likelihood wind speeds) at all the sites. Similar to the other parameters previously considered, the highest V_{Emax} was noticed at offshore-04 (9.19 m/s), which is closely followed by offshore-02 with 8.96 m/s and Brass with the lowest value of 5.32 m/s.

4.3 Wind power density

The WPD is a function of the mean wind speed in that location, as shown in Figure 4. The WPD ranges from 62 W/m^2 to 361 W/m^2, with offshore-04 having the highest wind power density of 361 W/m^2, closely followed by offshore-02 with a potential of 337 W/m^2. The Brass River estuary has the lowest WPD of 62 W/m^2.

4.4 Wind energy cumulative distribution and probability density functions for shoreline sites

The cumulative distribution function (CDF) and probability density function (PDF) for the six sites studied in Nigeria are shown in Figures 5, 6, respectively. Apapa Port and Brass had a steeper slope for the CDF and PDF than the four offshore locations. This is an indication that the coastal sites (Apapa and Brass) follow the same cumulative distribution pattern, while the four offshore sites have a wider spread. The steep CDF plots at these locations indicate that the energy produced over the period is contained within a narrower range, resulting in a plot that is slightly inclined to the left side of the graph. Offshore-01 to offshore-04 have higher potentials; hence, the shape of their CDFs is tilted to the right, indicating a higher energy potential. The PDF plots of both the coastal locations showed high peaks, inferring that the majority of the data were densely packed around the mean values. For Apapa and Brass, 80% of the WPD ranged between 75 and 110 W/m^2, while 50% of the data series ranged between 80 and 105 W/m^2. At offshore-01, 80% of the data series ranged from 220 W/m^2 to 330 W/m^2, while up to 50% of the data series ranged from 250 W/m^2 to 305 W/m^2. Offshore-04

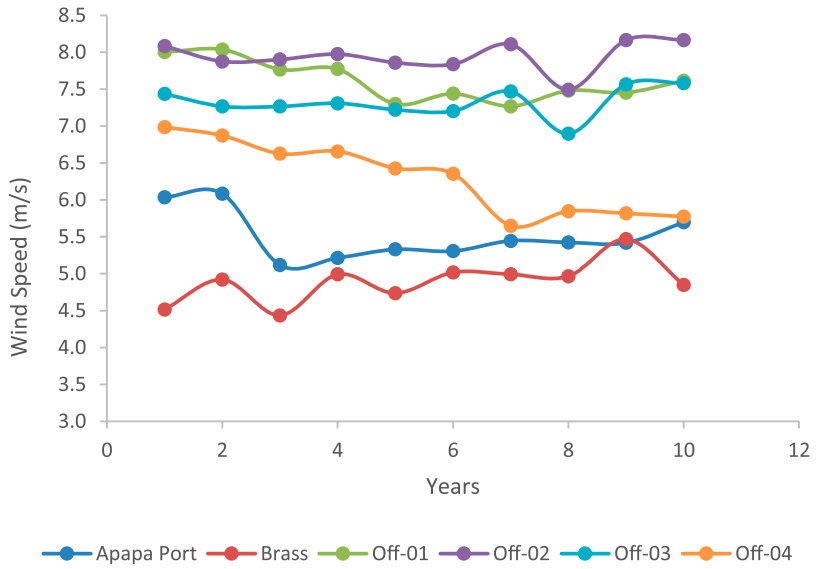

FIGURE 3
Annual variations in wind speeds of some sites along the Nigerian shoreline and offshore location.

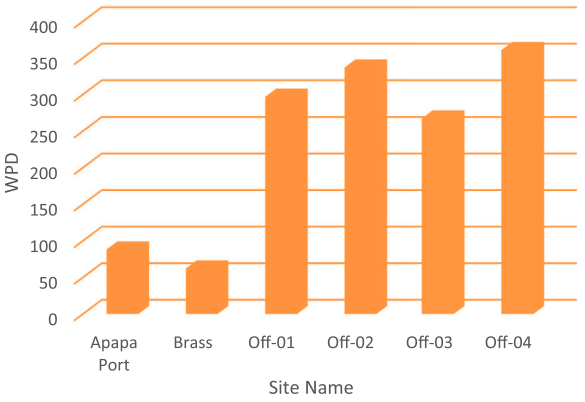

FIGURE 4
Mean WPD for some Nigerian sites along the shoreline.

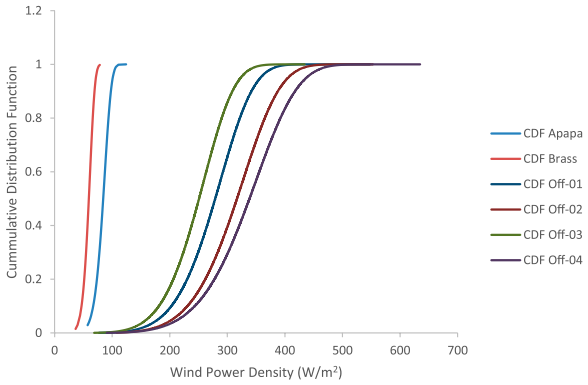

FIGURE 5
Wind energy CDF for some Nigerian sites along the shoreline.

had a higher wind energy potential than the other sites, resulting in a plot that is slightly skewed to the right.

4.5 Prevailing wind directions at the sites

In this study, wind roses were developed from the wind speeds and directions for all the locations for a period of 10 years, and the details are shown in Figures 7, 8. The wind rose for Apapa (Figure 7A) reveals that 202.50 (i.e., the south-south-western direction) was the dominant direction, with frequencies of 36.47% for the various wind speed ranges. In this direction, the most likely wind speed magnitude is 4.65 m/s (29% occurrence). The fetch area for the Brass River estuary (Figure 7B) is also from the south-south-west direction, with wind magnitudes ranging from 3.6 to 5.7 m/s occurring approximately 26% of the time and wind speeds greater than 5.7 m/s occurring only 2% of the time. The wind direction from the south-western directions had a 25% prevalence, while other directions in Brass had less than 12% occurrence.

The wind rose for the four offshore sites is illustrated in Figure 8, and it was observed that the plots look similar. The similarity is in the fact that the surface roughness scale is the same and there is little or no interference to the wind flow in the sites. The similarity in their wind rose plot could be attributed to the fact that there is no obstruction or vegetation to deflect the wind direction in the offshore regions. Even though the wind rose plot was similar at the offshore sites, the magnitude of the wind speeds varies; for example, offshore-02 had a higher speed in the

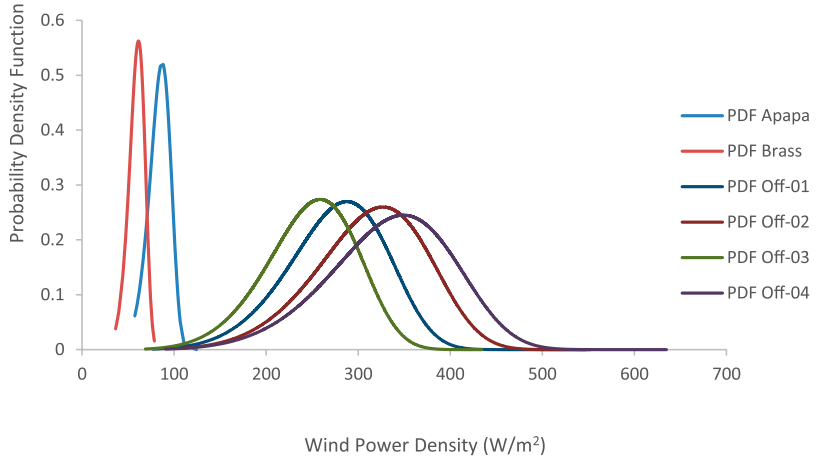

FIGURE 6
Wind energy PDF for some Nigerian sites along the shoreline.

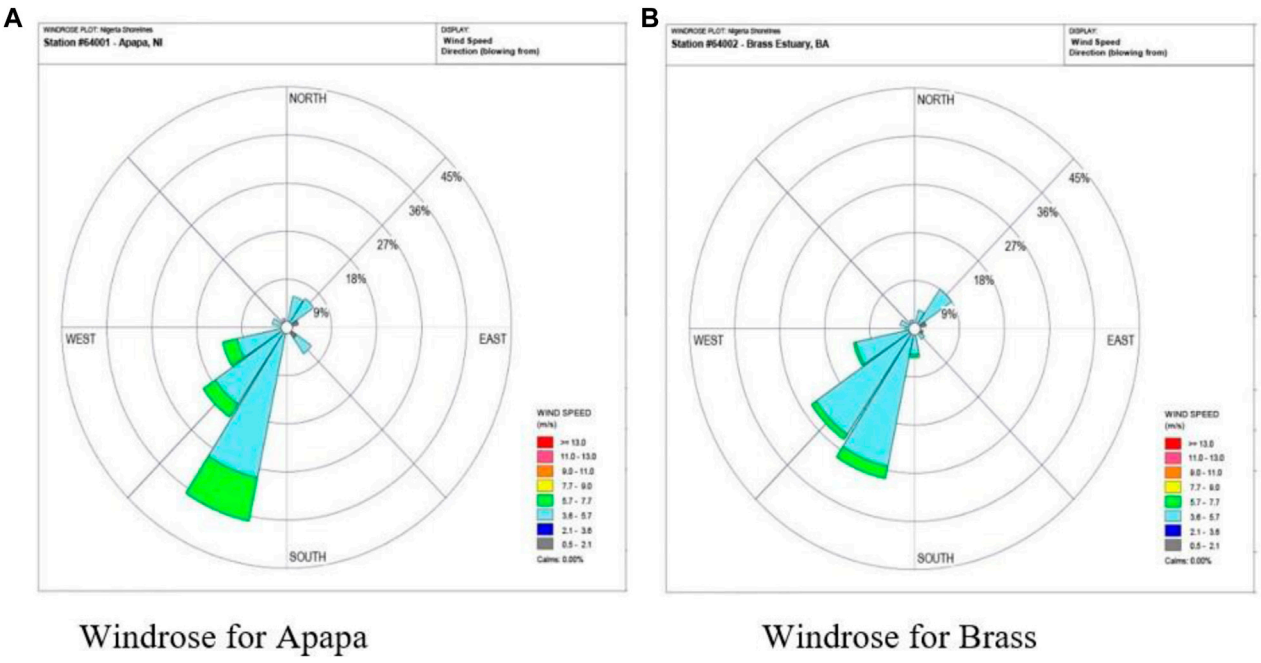

FIGURE 7
Wind roses for the coastal sites. Wind roses for **(A)** Apapa Port; **(B)** Brass River estuary.

prevailing direction. The wind rose plots of the offshore sites show a slightly different behavior from the coastal regions; the most prevalent wind direction for the offshore locations was from the south-western direction with an occurrence for 36% and wind speed >5.7 m/s. Winds from the SSW and WSW directions prevailed for 13.7% and 7.95% of the time, respectively; while a period of no wind was observed in these sites across the years for 3.7% of the time. The most variability in the direction of the winds was observed in the offshore areas, and this also comes with greater mean wind speeds.

4.6 Econometrics of 60-MW offshore wind farms

The annual energy produced (AEP) from the various sites is plotted and shown in Figure 9. It shows that the AEP ranges from 29 GWh at Brass using the Siemens SWT 6 model to 223 GWh at offshore-04 using the Vesta V117 model. Regardless of the location, the Vesta V117 wind turbine model generated the highest amount of electricity, while the Siemens SWT 6 model generated the least amount of electricity for this region. This is

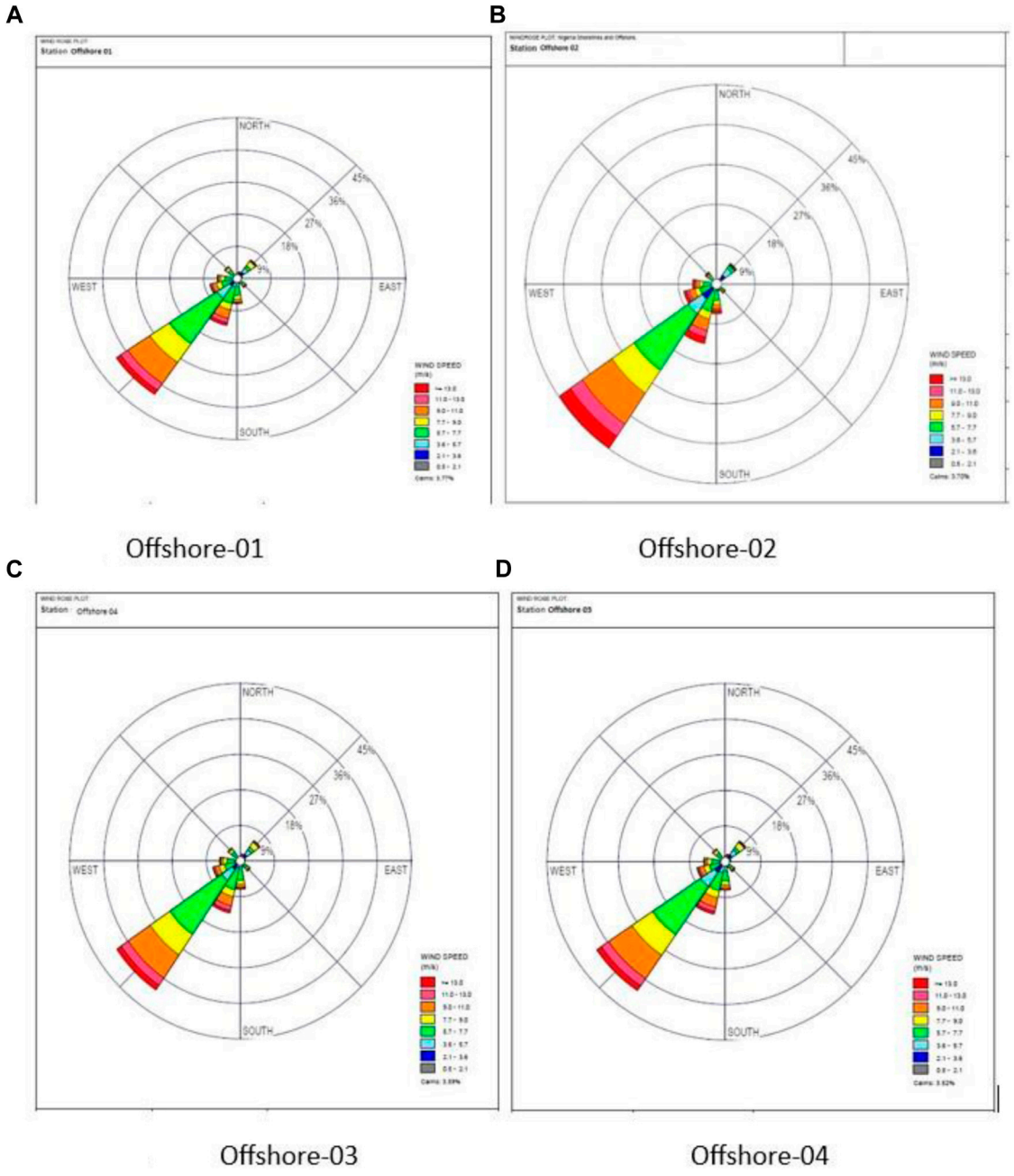

FIGURE 8
Wind roses for the offshore sites. **(A)** Offshore-01; **(B)** offshore-02; **(C)** offshore-03; **(D)** offshore-04.

due to the lower cut-in speed of the Vesta V117 model than that of both the SWT 6 and V3000 models. The difference of 1 m/s in the cut-in speeds at Apapa resulted in approximately a 3% improvement in the AEP, which shows that there is a geometric relationship between the wind speed and energy harvested from the wind turbine.

The capacity factors (Cfs) for the selected wind turbine models are shown in Table 4; the Vesta V117 model has the highest value among the models considered for all the sites, for the same reason given for the AEP previously. There was a close correlation between the turbine performance when comparing the AEP and Cf as both variables are dependent on the wind speed potential at the given site.

The turbine operating probability denotes the percentage of time that a practical turbine installed at the given wind speed regime can operate in a year, and it is the percentage of time in a year that a practical turbine installed at the given wind speed regime can operate. Eq. 3.10 is used to calculate the operating probability of wind turbines at each location. Using the most prevailing cut-in speeds of available commercial wind turbines, three different cut-in speeds (3 m/s, 3.5 m/s, and 4 m/s) were evaluated in this study, but the value of

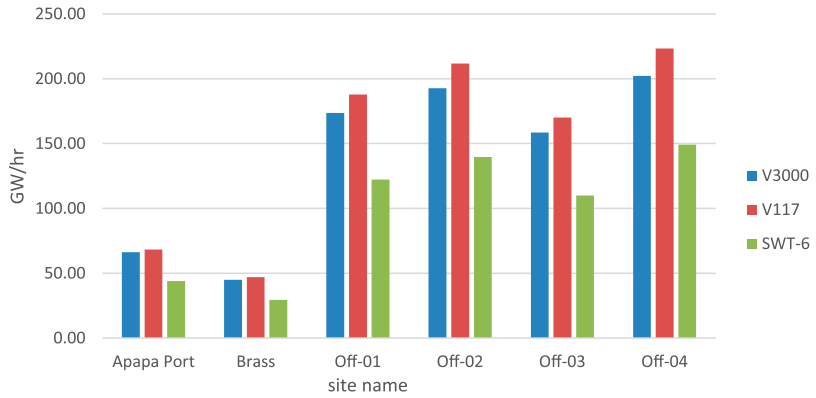

FIGURE 9
Annual energy produced from the various sites studied.

TABLE 4 Capacity factor for the three turbine models and turbine operating probabilities at the selected coastal sites.

Site name	Capacity factor (%)			Turbine operability at different cut-in speeds		
	V3000	V117	SWT-6	3.0 (m/s)	3.5 (m/s)	4.0 (m/s)
Apapa Port	12.61	12.99	8.38	95.38	88.33	74.54
Brass River estuary	8.55	8.92	5.60	87.51	82.24	62.36
Offshore-01	33.05	35.73	23.27	96.74	96.36	95.59
Offshore-02	36.65	40.27	26.56	96.80	96.51	95.92
Offshore-03	30.17	32.36	20.90	96.64	96.12	95.11
Offshore-04	38.48	42.49	28.38	96.13	94.97	92.82

the cut-out wind speed was set at 25 m/s (because most wind turbines have a cut-out speed of 25 m/s). Table 4 also summarizes the operating probabilities for various cases. In general, as the cut-in speed increases, the operating probability at each site decreases. As a result, the operating probability is sensitive and inversely related to the cut-in speed at a specific wind energy-generating site. Offshore-02 had the highest operating probability, up to 96.8%. Brass, on the other hand, has the lowest operating probability of the six sites studied. Based on the wind regime at the site, a Vesta V117-4.0 MW wind turbine with a capacity of 4 MW and a cut-in wind speed of 3 m/s will operate 96.1% of the time at offshore-04, while the same turbine will operate 95.38% of the time at Apapa Port.

4.7 Cost of electricity

For the estimation of the levelized cost of electricity generated by each commercial wind turbine in the region, the following assumptions were considered.

1. The interest rate (r) and inflation rate (i) were taken to be 15% and 10.4%, respectively. These are the prevailing rates retrieved from the Central Bank of Nigeria.
2. Each wind turbine is assumed to produce the same amount of energy each year during its useful lifetime.
3. The lifetime (n) of each wind turbine was set at 20 years.

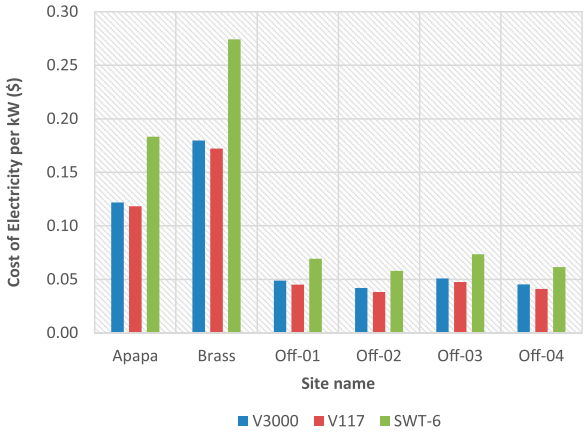

FIGURE 10
Levelized cost of electricity in US dollars.

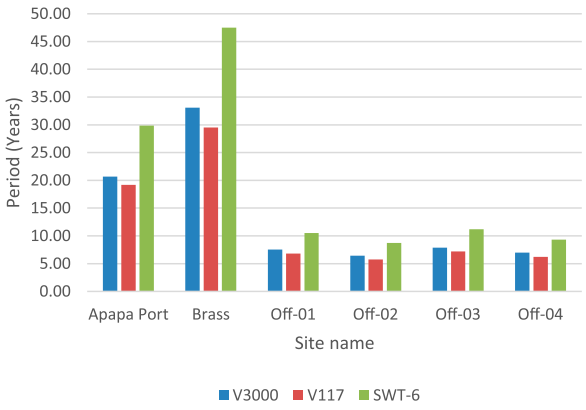

FIGURE 11
Simple payback time for the various sites.

4. The annual maintenance and operations costs are assumed to be 3% of the wind turbine installation system's initial capital cost. This figure is based on the result of research work carried out by Wiser et al. (2019).

The estimated cost of electricity (i.e., LCOE) generated by the selected wind turbines at each location is shown in Figure 10 ($/kWh) based on the aforementioned assumptions. The least cost of unit energy per kWh was obtained as 0.04 $/kWh at offshore-02 using the V3000 and V117 wind turbine generators (WTGs), while similar cost of generating electricity was obtained at offshore-04 using the V117 WTG. It can be further observed that the highest cost of electricity is obtained by the SWT-6 model WTG, with the cost ranging between 0.06 $/kWh (offshore-02 and -04) and 0.27 $/kWh (Brass). Even though the WPD at offshore-04 was greater than that at offshore-02, the later had a lower cost of generating electricity because of other factors like distance to the shore and foundation depths.

4.8 Simple payback time for the studied sites in Nigeria

The simple payback time (SPT) analysis for the sites is shown in Figure 11, and the result shows that the offshore sites have shorter payback periods, which is because of the higher wind speeds observed at these locations. For the V117 model, 83% of the sites have repayment times of less than 20 years, and the repayment times for the best performing site is approximately 5.74 years which is very impressive as this repayment time is less than 30% of the turbine's useful life. Using the V3000 model shows that the shortest time in which the money for the investment could be recovered is 6.41 years, while Brass (at the coastline) had the longest repayment time (33.09 years). The SPT for the SWT-6 model had the longest repayment time in all the sites; however, all the offshore sites evaluated had repayment time <11.2 years. This is an indication that the WTGs will pay off the cost of the project shortly after they are at half of their useful life, which is a good index for profitability. The two coastal sites had a payback time greater than 20 years, which is due to wind dampening as a result of buildings and other vegetations around the sites.

TABLE 5 Net present value for some Nigerian coastal and offshore sites.

Site name	Farm NPV ($)		
	V3000	V117	SWT-6
Apapa Port	−46,247,910	−43,037,658	−59,161,882
Brass River estuary	−61,978,047	−58,797,092	−69,904,421
Offshore-01	28,233,970	40,458,235	−5,947,115
Offshore-02	46,807,939	62,545,496	11,191,639
Offshore-03	21,691,845	31,922,653	−10,712,827
Offshore-04	40,571,237	57,988,649	5,287,665

4.9 Net present value (NPV) for the studied coastal and offshore sites

Table 5 shows the net present value for the coastal and offshore sites studied; the NPV with negative values are sites that might run at loss, while a positive value in the NPV indicates that if the parameters remain the same, a wind farm situated in these locations will be profitable. Considering the V117 1 and V3000 wind turbines, the NPV for all the offshore sites in this region returned with positive values, an indication that the probability of making profit from these sites using the wind turbine generator models used in this work is high; therefore, the establishment of wind farms in these locations is highly recommended. For example, the net gains from using the V177 model at offshore site-02 could be as high as $62,000,000.00. For SWT-6, four out of the six sites considered returned with a negative value when using these WTGS; however, offshore-02 and 04 were still profitable with net gains higher than $5,000,000 from the investments.

4.10 Sensitivity analysis

Three variables were chosen as sensitive variables to examine their impact on the LCOE of offshore wind projects in Nigeria, viz., discount rate, useful project life, and percentage change in foundation cost were evaluated as sensitivity parameters using offshore-01 as a representative site. By changing the discount rate from 2% to 16% as shown in Figure 12, it was observed that changes in the discount rate have significant impact on the LCOE of the site; an increase in the discount rate causes an increase in LCOE, while a decrease in the discount rate causes a decrease in LCOE. In the case of the V3000 WTG, increasing the discount rate by 2% (from 8% −10%) resulted in an increase of approximately 18% in

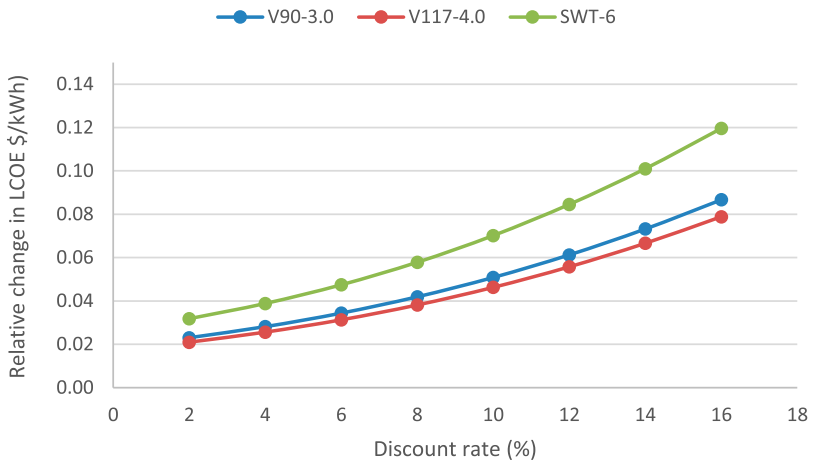

FIGURE 12
Effect of varying discount rates on the LCOE.

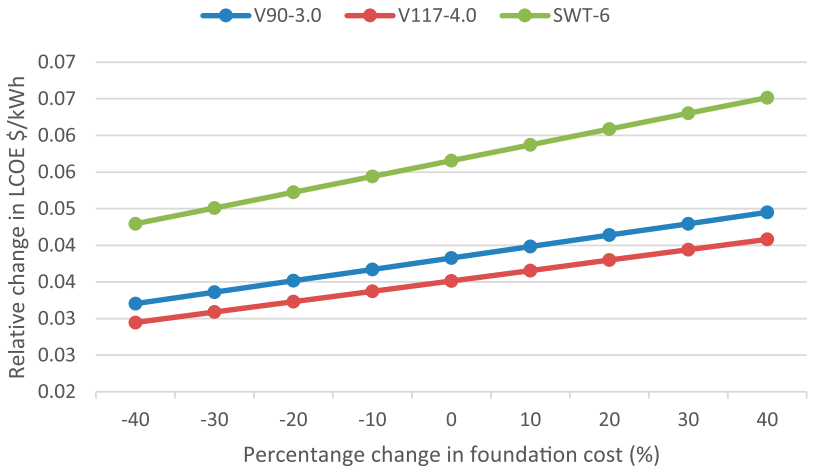

FIGURE 13
Effect of varying foundation costs on the LCOE.

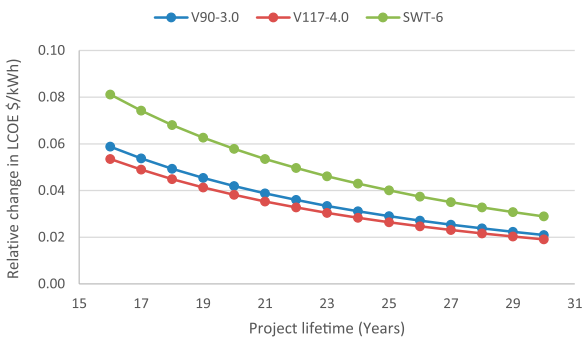

FIGURE 14
Effect of turbine lifetime on the LCOE.

the unit cost of electricity. Figure 13 shows the effect of foundation cost on the LCOE. If the cost of the foundation is increased from 10% to 20% of the initial cost for the SWT-6 wind turbine, the LCOE will increase from 0.060 $/kWh to 0.063 $/kWh (a 4% increase in the cost of electricity).

The effect of changing the project's lifespan from 16 to 30 years is shown in Figure 14. It was observed that increasing the turbine lifespan lowers the cost of energy production; on the contrary, shortening the turbine lifetime significantly increases the LCOE. The LCOE was reduced by 31% when the lifespan of the V117 turbine was increased from 20 to 25 years, demonstrating that extending the turbine lifespan has a significant favorable impact on the LCOE. This explains why a well-maintained wind turbine has minimal unplanned shutdowns, and the turbulence effect is preferable from an economic standpoint.

5 Conclusion

The first step in the development of a wind farm project is the wind energy resource assessment. It serves as a tool for the selection of the most viable sites by examining the sites to determine if there is enough wind potential, and it also provides a basis for the selection of a suitable wind turbine for the location. The study findings can be summarized as follows:

1. In terms of the WPD, all the offshore sites outperformed the coastal sites; for example, the WPD at offshore-04 is four times greater than the potential at Apapa Port. The highest potential in the coastal region was observed at Apapa with a WPD of 88 W/m^2, while the offshore-04 had the highest potential when considering offshore sites (361 W/m^2).
2. According to the International Electrotechnical Commission (IEC) classification 61400, the offshore sites evaluated in this study can be categorized as "class IIIb" sites. This means that the sites are moderately suitable for the harvest of wind energy, and if harnessed, it could supplement the energy deficit in the country and reduce the country's carbon footprint.
3. All the sites have their most prominent wind from the south-south-western direction, i.e., between the 191.25 and 213.75 segments, although the magnitude of the occurrences varies from site to site (between 41% and 19%). Offshore regions showed the greatest wind direction variability, which was accompanied by higher mean wind speeds.
4. The result from the study also shows that the Vesta V-117 model (4-MW offshore wind turbine model) is best suited for energy generation in the region compared to the other two wind turbines considered. The outstanding performance of the V-117 model at a lower mean speed is due to its relatively lower cut-in speed.
5. The net gains from investing in a 60-MW wind farm in the region can be as high as $62,000,000.00, while the project payback time can be as low as 5.74 years.
6. The LCOE of the offshore site showed that irrespective of the type of the turbine used, the cost of electricity from the offshore site was less than 0.07 $/kWh, which is less than the country's current electricity tariff (0.075 $/kWh).
7. The offshore sites have great potential for energy harvesting even with an 8% discount rate used in this work. If the federal government of Nigeria decreases the discount rate on wind energy projects or grants tax waivers for offshore wind projects, the viability of these projects will be increased.

Data availability statement

The raw data supporting the conclusion of this article will be made available by the authors, without undue reservation.

Author contributions

AA and OA carried out conceptualization and drafting of the research work. SO and SA carried out proof reading and editing of the report. All authors contributed to the article and approved the submitted version.

Acknowledgments

The authors thank Afe Babalola University, Ado-Ekiti (ABUAD), for the financial support offered to publish this research.

Conflict of interest

The authors declare that the research was conducted in the absence of any commercial or financial relationships that could be construed as a potential conflict of interest.

Publisher's note

References

Adaramola, M., Agelin-Chaab, M., and Paul, S. S. (2014). Assessment of wind power generation along the coast of Ghana. *A Journal of Energy Conversion and Management* 77, 61–69. doi:10.1016/j.enconman.2013.09.005

Ahmed, A. S. (2018). Wind resource assessment and economics of electric generation at four locations in Sinai Peninsula, Egypt. *J. Clean. Prod.* 183, 1170–1183. doi:10.1016/j.jclepro.2018.02.182

Ajayi, O. O., Fagbenle, R. O., James, K., JuliusNdambuki, M., Omole, D. O., and Badejo, A. A. (2014). Wind energy study and energy cost of wind electricity generation in Nigeria: Past and recent results and a case study for South West Nigeria. *Energies* 7 (12), 8508–8534. doi:10.3390/en7128508

Ajayi, O. O. (2009). Assessment of utilization of wind energy resources in Nigeria. *Energy Policy* 37 (2), 750–753. doi:10.1016/j.enpol.2008.10.020

AjayiOjoVasel, O. O. O. A., and Vasel, A. (2019). On the need for the development of low wind speed turbine generator system. *IOP Conf. Ser. Earth Environ. Sci.* 331, 1–12. 012062. doi:10.1088/1755-1315/331/1/012062

Al-Mhairat, B., and Al-Quraan, A. (2022). Assessment of wind energy resources in Jordan using different optimization techniques. *Processes* 10 (1), 105. doi:10.3390/pr10010105

Ale, T., and Adeyemi, A. (2022). Electricity demand pattern and supply availability on Nigeria grid system. *J. Appl. Sci. Process Eng.* 9 (1), 1042–1053. doi:10.33736/jaspe.4264.2022

Amole, A. O., Oladipo, S., Olabode, O. E., Makinde, K. A., and Gbadega, P. (2023). Analysis of grid/solar photovoltaic power generation for improved village energy supply: A case of ikose in Oyo state Nigeria. *Renew. Energy Focus* 44, 186–211. doi:10.1016/j.ref.2023.01.002

Asamoah, S. S., Parbey, J., Yankey, I. K., and Awuah, A. (2023). Techno-economic assessment of a central grid-connected wind farm in Ghana using RETScreen® expert. *Heliyon* 9, e12902. doi:10.1016/j.heliyon.2023.e12902

Ayodele, T. R., Ogunjuyigbe, A. S. O., and Amusan, T. O. (2018). Techno-economic analysis of utilizing wind energy for water pumping in some selected communities of Oyo State, Nigeria. *Renew. Sustain. Energy Rev.* 91, 335–343. doi:10.1016/j.rser.2018.03.026

Ben, U. C., Akpan, A. E., Mbonu, C. C., and Ufuafuonye, C. H. (2021). Integrated technical analysis of wind speed data for wind energy potential assessment in parts of southern and central Nigeria. *Clean. Eng. Technol.* 2, 100049. doi:10.1016/j.clet.2021.100049

Chancham, C., Waewsak, J., and Gagnon, Y. (2017). Offshore wind resource assessment and wind power plant optimization in the Gulf of Thailand. *Energy* 1139, 706–731. doi:10.1016/j.energy.2017.08.026

Chanchangi, Y., Adu, F., Ghosh, A., Sundaram, S., and Mallick, T. (2022). Nigeria's energy review: Focusing on solar energy potential and penetration. *Environ. Dev. Sustain.* 25, 5755–5796. doi:10.1007/s10668-022-02308-4

Climatscope-BloombergNEF Nigeria energy (2021). Climatscope-BloombergNEF Nigeria energy report. Available at: https://global-climatescope.org/markets/ng/.

Crippa, P., Alifa, M., Bolster, D., Genton, M. G., and Castruccio, S. (2021). A temporal model for vertical extrapolation of wind speed and wind energy assessment. *Appl. Energy* 301, 117378. doi:10.1016/j.apenergy.2021.117378

Dai, H., Li, N., Wang, Y., and Zhao, X. (2022). "March). The analysis of three main investment criteria: NPV IRR and Payback Period," in 2022 7th International Conference on Financial Innovation and Economic Development (ICFIED 2022), Harbin, China, January21-23, 2022 (Amsterdam, Netherlands: Atlantis Press), 185–189.

Fan, Z., Li, S., Gao, Z., Zhang, L., Zheng, X., Zhu, W., et al. (2023). On the importance of wind turbine wake boundary to wind energy and environmental impact. *Energy Convers. Manag.* 277, 116664. doi:10.1016/j.enconman.2023.116664

Fatigun, A. T., Akoshile, C. O., Ajibola, T. B., and Salau, R. O. (2017). Evaluation of wind energy potential of Ikeja, Southwest, Nigeria using two-parameter weibull distribution function. *Evaluation* 7 (09).

Göçmen, T., and Özerdem, B. (2012). Airfoil optimization for noise emission problem and aerodynamic performance criterion on small scale wind turbines. *Energy* 46 (1), 62–71. doi:10.1016/j.energy.2012.05.036

Harrucksteiner, A., Thakur, J., Franke, K., and Sensfuß, F. (2023). A geospatial assessment of the techno-economic wind and solar potential of Mongolia. *Sustain. Energy Technol. Assessments* 55, 102889. doi:10.1016/j.seta.2022.102889

Imani, M., Fakour, H., Lan, W. H., Kao, H. C., Lee, C. M., Hsiao, Y. S., et al. (2021). Application of rough and fuzzy set theory for prediction of stochastic wind speed data using long short-term memory. *Atmosphere* 12 (7), 924. doi:10.3390/atmos12070924

Jabbar, R. I. (2021). Statistical analysis of wind speed data and assessment of wind power density using weibull distribution function (case study: Four regions in Iraq). *J. Phys. Conf. Ser.* 1804 (1), 012010. IOP Publishing. doi:10.1088/1742-6596/1804/1/012010

Jacquemin, J., Butterworth, D., Garret, C., Baldock, N., and Henderson, A. (2011). *Inventory of location specific wind energy cost*. Bristol, United Kingdom: Garrad Hassan Partners, 58.

Jang, D., Kim, K., Kim, K. H., and Kang, S. (2022). Techno-economic analysis and Monte Carlo simulation for green hydrogen production using offshore wind power plant. *Energy Convers. Manag.* 263, 115695. doi:10.1016/j.enconman.2022.115695

Khan, T., Theppaya, T., and Taweekun, J. (2022). Wind resource assessment of northern part of Thailand. *Ain Shams Eng. J.* 14, 102025. doi:10.1016/j.asej.2022.102025

Klerk, M. G. D., and Venter, W. C. (2017). Power calculation accuracy as a function of wind data resolution. *J. energy South. Afr.* 28 (2), 1–14. doi:10.17159/2413-3051/2017/v28i2a1656

Koholé, Y. W., Fohagui, F. C. V., Djiela, R. H. T., and Tchuen, G. (2023). Wind energy potential assessment for co-generation of electricity and hydrogen in the far North region of Cameroon. *Energy Convers. Manag.* 279, 116765. doi:10.1016/j.enconman.2023.116765

Li, M., Cao, S., Zhu, X., and Xu, Y. (2022). Techno-economic analysis of the transition towards the large-scale hybrid wind-tidal supported coastal zero-energy communities. *Appl. Energy* 316, 119118. doi:10.1016/j.apenergy.2022.119118

Mansi, A., and Aydin, D. (2022). The impact of trailing edge flap on the aerodynamic performance of small-scale horizontal axis wind turbine. *Energy Convers. Manag.* 256, 115396. doi:10.1016/j.enconman.2022.115396

Martinez, A., and Iglesias, G. (2022). Mapping of the levelised cost of energy for floating offshore wind in the European Atlantic. *Renew. Sustain. Energy Rev.* 154, 111889. doi:10.1016/j.rser.2021.111889

Martinez, A., and Iglesias, G. (2021). Multi-parameter analysis and mapping of the levelised cost of energy from floating offshore wind in the Mediterranean Sea. *Energy Convers. Manag.* 243, 114416. doi:10.1016/j.enconman.2021.114416

Mattar, C., and Guzman-Ibarra, M. C. (2017). A techno-economic assessment of offshore wind energy in Chile. *Energy* 133, 191–205. doi:10.1016/j.energy.2017.05.099

Moller, B., Hong, L., Lonsing, R., and Hvelplund, F. (2012). Evaluation of offshore wind resources by scale of development. *Energy* 48 (3), 314–322. doi:10.1016/j.energy.2012.01.029

National Renewable Energy Action Plans (2015). *A policy document by ministry of power federal republic of Nigeria*. Nigeria: Energypedia, 5–9.

Noel, W., Weis, T. M., Yu, Q., Leach, A., and Fleck, B. A. (2022). Mapping the evolution of Canada's wind energy fleet. *Renew. Sustain. Energy Rev.* 167, 112690. doi:10.1016/j.rser.2022.112690

Oladigbolu, J. O., Al-Turki, Y. A., and Olatomiwa, L. (2021). Comparative study and sensitivity analysis of a standalone hybrid energy system for electrification of rural healthcare facility in Nigeria. *Alexandria Eng. J.* 60 (6), 5547–5565. doi:10.1016/j.aej.2021.04.042

Olaofe, Z. O. (2017). Assessment of the offshore wind speed distributions at selected stations in the south-west coast, Nigeria. *Int. J. Renew. Energy Res.* 7 (2), 565–577. doi:10.20508/ijrer.v7i2.5439.g7031

Oyewole, J. A., Aweda, F. O., and Oni, D. (2019). Comparison of three numerical methods for estimating weibull parameters using weibull distribution model in Nigeria. *Niger. J. Basic Appl. Sci.* 27 (2), 08–15. doi:10.4314/njbas.v27i2.2

Ozioko, I. O., Ugwuanyi, N. S., Ekwue, A. O., and Odeh, C. I. (2022). Wind energy penetration impact on active power flow in developing grids. *Sci. Afr.* 18, e01422. doi:10.1016/j.sciaf.2022.e01422

Ramadhan, R., and Farizal, F. (2021). Feasibility analysis of renewable energy alternative selection in rural areas using zero energy building concept. *J. Phys. Conf. Ser.* 1858 (1), 012089. IOP Publishing. doi:10.1088/1742-6596/1858/1/012089April

Richard, M. O. N., and Eseosa, O. (2022). Evaluation of wind energy potentials in some selected areas in the six geo-political regions in Nigeria. *J. Altern. Renew. Energy Sources* 8 (1), 20–37. doi:10.46610/joares.2022.v08i01.004

Rinaldi, G., Garcia-Teruel, A., Jeffrey, H., Thies, P. R., and Johanning, L. (2021). Incorporating stochastic operation and maintenance models into the techno-economic analysis of floating offshore wind farms. *Appl. Energy* 301, 117420. doi:10.1016/j.apenergy.2021.117420

Salakhetdinov, E., and Agyeno, O. (2020). Achieving energy security in africa: Prospects of nuclear energy development in south Africa and Nigeria. *Afr. J. Sci. Technol. Innovation Dev.* 14 (1), 22–30. doi:10.1080/20421338.2020.1799538

Sasser, C., Yu, M., and Delgado, R. (2022). Improvement of wind power prediction from meteorological characterization with machine learning models. *Renew. Energy* 183, 491–501. doi:10.1016/j.renene.2021.10.034

Schweizer, J., Antonini, A., Govoni, L., Gottardi, G., Archetti, R., Supino, E., et al. (2016). Investigating the potential and feasibility of an offshore wind farm in the Northern Adriatic Sea. *Appl. Energy* 177, 449–463. doi:10.1016/j.apenergy.2016.05.114

Siemens-Gemesa (2016). Siemens SWT 6.0-154; 6 MW Offshore Wind Turbine data sheet. Available at: http://www.seimensgemesa.com.

Shu, T., Song, D., and Joo, Y. H. (2022). Non-centralised coordinated optimisation for maximising offshore wind farm power via a sparse communication architecture. *Appl. Energy* 324, 119705. doi:10.1016/j.apenergy.2022.119705

Shu, Z. R., Li, Q. S., and Chan, P. W. (2015). Investigation of offshore wind energy potential in Hong Kong based on Weibull distribution function. *Appl. Energy* 156, 362–373. doi:10.1016/j.apenergy.2015.07.027

Sørensen, J. N., and Larsen, G. C. (2021). A minimalistic prediction model to determine energy production and costs of offshore wind farms. *Energies* 14, 448. doi:10.3390/en14020448

Sumair, M., Aized, T., Bhutta, M. M. A., Siddiqui, F. A., Tehreem, L., and Chaudhry, A. (2022). Method of Four Moments Mixture-A new approach for parametric estimation of Weibull Probability Distribution for wind potential estimation applications. *Renew. Energy* 191, 291–304. doi:10.1016/j.renene.2022.04.054

Sumair, M., Aized, T., Gardezi, S. A. R., Ur Rehman, S. U., and Rehman, S. M. S. (2021). Wind potential estimation and proposed energy production in Southern Punjab using Weibull probability density function and surface measured data. *Energy Explor. Exploitation* 39 (6), 2150–2168. doi:10.1177/0144598720920748

Thambain, M., and Storm, B. (2012)"Implications of the Weibull k factor in resource assessment," in 2nd Latin American Congress of Wind Engineering, National University of La Plata, Argentina, December 5–7, 2012.

Tuy, S., Lee, H. S., and Chreng, K. (2022). Integrated assessment of offshore wind power potential using Weather Research and Forecast (WRF) downscaling with Sentinel-1 satellite imagery, optimal sites, annual energy production and equivalent CO2 reduction. *Renew. Sustain. Energy Rev.* 163, 112501. doi:10.1016/j.rser.2022.112501

United States Agency for International development (2022). Power africa project. Available at: www.usaid.gov/powerafrica.

Usta, I. (2016). An innovative estimation method regarding Weibull parameters for wind energy applications. Energy 106, 301–314. doi:10.1016/j.energy.2016.03.068

Vestas Americas (2014). Vesta V90-3 MW Offshore Wind Turbine data sheet. Available at: http://www.vestas.com.

Vestas Americas (2017). Vesta V117- 4 MW Offshore Wind Turbine data sheet. Available at: http://www.vestas.com.

Wiser, R., Bolinger, M., and Lantz, E. (2019). Assessing wind power operating costs in the United States: Results from a survey of wind industry experts. *Renew. Energy Focus* 30, 46–57. doi:10.1016/j.ref.2019.05.003

Zhang, S., Luo, K., Yuan, R., Wang, Q., Wang, J., Zhang, L., et al. (2018). Influences of operating parameters on the aerodynamics and aeroacoustics of a horizontal-axis wind turbine. *Energy* 160, 597–611. doi:10.1016/j.energy.2018.07.048

frontiers | Frontiers in Energy Research

TYPE Original Research
PUBLISHED 26 September 2023
DOI 10.3389/fenrg.2023.1240473

OPEN ACCESS

EDITED BY
Olusegun David Samuel,
Federal University of Petroleum Resource Effurun, Nigeria

REVIEWED BY
Andrea Toscani,
University of Parma, Italy
Kenneth E. Okedu,
Melbourne Institute of Technology, Australia

*CORRESPONDENCE
Xiaoguang Kong,
kongxiaoguang@syuct.edu.cn

RECEIVED 15 June 2023
ACCEPTED 12 September 2023
PUBLISHED 26 September 2023

CITATION
Kong X, Zhang Y and Xu G (2023), Optimal design and control of permanent magnet assisted dual rotor motor.
Front. Energy Res. 11:1240473.
doi: 10.3389/fenrg.2023.1240473

Optimal design and control of permanent magnet assisted dual rotor motor

Xiaoguang Kong*, Yaowen Zhang and Gepeng Xu

School of Information Engineering, Shenyang University of Chemical Technology, Shenyang, China

As high-performance motors, permanent magnet motors are widely used in a wide range of applications. It has become a consensus to mine reluctance torque in permanent magnet motors. The combination of permanent magnet motors and reluctance motors to generate higher output torque is one of the hotspots in motor research. A dual-rotor motor can be formed by connecting a coaxial connector or a concentric end disk, which can make the motor generate higher torque. However, although the motor torque has been improved, the cogging torque still affects the output torque of the motor. This paper describes a method to reduce the cogging torque of the permanent magnet rotor of the permanent magnet-assisted double rotor motor. By analyzing the motor power equation, it is concluded that the pole arc coefficient, the thickness of the magnetic steel, the length of the air gap, and the slot width of the stator have four influences on the teeth. For the parameters of the slot torque, the upper and lower limits of the parameter value are obtained according to the size of the motor. A certain parameter is taken as a fixed value, and the remaining parameters are uniformly valued. Use parametric scanning to determine the optimal value range of the parameter, and use Maxwell for parameterization. Simulation and analysis show that the cogging torque of the motor is reduced by 90% and the torque ripple is reduced by 50%. In order to simplify the motor control system, this paper designs a fuzzy controller based on granular functions, and the fuzzy rules of the fuzzy controller are to perform feature sampling and fit the response function, eliminating fuzzification and defuzzification, improving the response speed of fuzzy control, and simplifying the control system.

KEYWORDS

dual rotor, permanent magnet synchronous motor, cogging torque, parameter scan, granular function

1 Introduction

The advantages of permanent synchronous motors include their small size, light size, minimal loss, outstanding performance, and wide range of applications (Wang and Leng, 2018). They are widely used for various occasions and equipment. However, due to the high price and limited supply of rare earth magnets, the development of high-performance motors without rare earths has gradually attracted great attention. Reducing the use of permanent magnets in permanent magnet motors and using synchronous reluctance motors without permanent magnets are feasible alternatives. The synchronous reluctance motor has a reliable mechanical design, a low cost, and a multi-barrier construction that can efficiently

enhance the output torque, but its applicability is also constrained by its drawbacks of poor torque density and low factor (Hofmann and Sanders, 2000).

The two ideal properties of a motor are high torque density and high efficiency (Agbo et al., 2021). Due to its high torque density and high space efficiency, the double-rotor motor has always been a research focus for scientists. In recent years, in order to further improve the motor efficiency and torque density, scientists from different countries have developed various types of double rotor motors, such as double rotor permanent magnet motors with different pole topologies (NS) (Qu and Lipo, 2003) and double rotor disc motors with modified stator core yoke (Liu and Li, 2022), steel sheets instead of part of the permanent magnets reduce the Manufacturing cost of the double rotor axial flux motor (Diao et al., 2023), and there is also a concentric switched double-rotor reluctance motor that integrates two rotors and two stators into a compact and robust structure (Aravind et al., 2011; Al-Ani, 2021), and a switched double-rotor reluctance motor with magnetic isolation ring (Shirzad, 2023), and yokeless double-rotor mutual coupling switched reluctance motor (Fu et al., 2023); magnetic field modulation brushless double-rotor machine (Bai et al., 2015), double-rotor in-wheel motor with multiple operating modes (Li et al., 2023) Permanent magnet reluctance dual rotor motor (Li et al., 2017), and so on. In general, it is mainly divided into permanent magnet double rotor motors and reluctance double rotor motors. In this paper, combining the advantages of a permanent magnet motor and a reluctance motor, a permanent magnet-assisted dual-rotor motor is proposed.

In order to achieve the goals of high torque density and wide constant-speed operating range, a permanent magnet assisted dual-rotor motor is proposed in this paper, which adopts a dual-rotor radial flux configuration, combining the synchronous reluctance rotor and the permanent magnet rotor with rare earth permanent magnets to form a single motor entity, the design can control reluctance torque and permanent magnet torque more flexibly, since the cogging torque determines the torque ripple, and the torque ripple affects the quality of the output torque, therefore the goal of the permanent magnet synchronous motorization of the outer rotor is to reduce the cogging torque, according to the definition of the cogging torque, determine the parameters that affect the cogging torque, such as the pole arc coefficient, considering that the parameters have little influence on each other, the parameter sweep method can be used. The range of parameter optimization is given according to the size constraints of the motor, and the cogging torque of the permanent magnet rotor is optimized. Through the simulation analysis of the optimized motor model, the effectiveness of this optimization scheme is verified. Finally, the permanent magnet-assisted dual-rotor motor designed in this paper has the characteristics of a magnetic isolation ring. The motor is split into internal and external parts for control. The internal and external motor control systems share a speed loop and are equipped with hysteresis controllers, respectively. The internal and external motors use torque ratios for current distribution and introduce granular functions to improve the constant fuzzy speed loop, which simplifies the control system and improves the rapidity and robustness of motor response.

2 Motor preliminary design

2.1 Motor topology

The outer rotor of a permanent magnet assisted dual rotor motor is a surface-mounted permanent rotor, which shares several characteristics with permanent magnet dual rotor motors. The distinction is that the permanent magnet synchronous motor and the synchronous reluctance motor are integrated into a single motor, and the synchronous reluctance rotor is used to replace the internal permanent magnet rotor (Yunyun et al., 2012). The two rotors share a shaft and rotate at the same mechanical speed. The stator winding adopts the ring winding method, and the magnetomotive force direction of the stator winding of the outer motor is opposite that of the stator winding of the inner motor. In order to achieve magnetic insulation between the inner stator and the outer stator, a magnetic insulator used as a barrier ring is used in the middle of the stator yoke. The insulator is made of brass. Figure 1 is a three-dimensional diagram of the motor. The parameters of the motor are shown in Table 1.

In order to ensure that the motor outputs ideal torque, the internal synchronous reluctance rotor should be properly designed. The typical number of rotor poles of a synchronous reluctance motor is four, but this requires the external surface-mounted permanent magnet rotor to also maintain a four-pole topology. This design method will cause the external permanent magnet rotor yoke to become thicker, and with added weight comes reduced performance. The external surface-mounted permanent magnet rotor is more suitable for the application of multi-rotor pole topology to reduce the thickness of the yoke and the weight of the motor, but this type of topology is not the best design for synchronous reluctance motors because, because of the multi-pole structure, the pole speed of the magnetization inductor of the synchronous reluctance rotor will decrease, and the performance

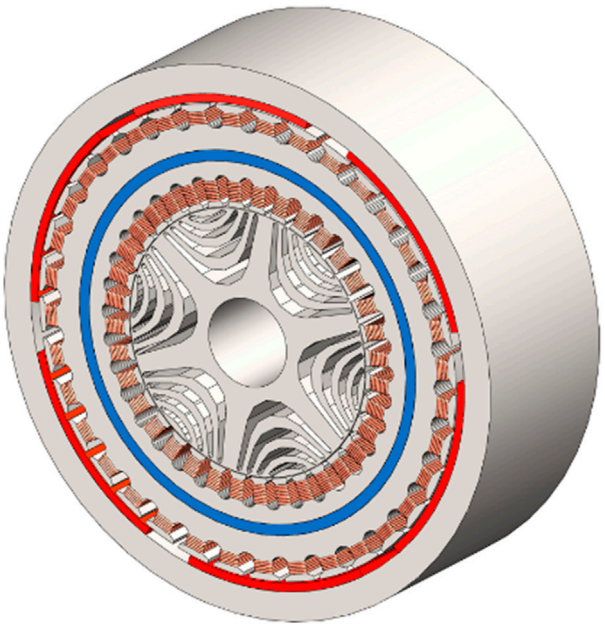

FIGURE 1
3D model of motor.

TABLE 1 Main parameters of the motor.

Parameter	Data	
	Internal motor	External motor
Rotor pole number	6	6
Number of stator slots	36	36
Stator radius/mm	48.65	63.95
Outer radius of rotor/mm	36	74.65
Inner radius of rotor/mm	12	66.65
Air gap length/mm	0.35	0.5
Length of iron core/mm	70	70
Power rating/kw	1	2
Speed/rpm	1,600	1,600

of the synchronous reluctance rotor will also decrease under the condition of a high pole number. Therefore, the number of rotor poles selected for this type of motor is six, and the number of poles of the inner and outer rotors is the same, so as to balance the low number of magnetic poles of the synchronous reluctance rotor and the high number of magnetic poles of the surface-mounted permanent magnet rotor.

The design of the synchronous reluctance rotor flux barrier focuses on the number and position of each flux barrier layer. Generally, for the inner rotor synchronous reluctance motor, the torque ripple decreases with the increase of the number of flux barriers, but due to the limitations of the manufacturing process, the rotor flux barriers are generally set to 4 layers in the design of the synchronous reluctance motor (Jurca and Martis, 2017), so the number of rotor magnetic barriers in this paper is also set to 4 layers.

Different windings, cogging slots, permanent magnet arrangements, and reluctance rotor magnetic barrier shapes of permanent magnet-assisted dual-rotor motors have various topological structures. The permanent magnet rotor can not only be installed on the surface but also be buried in the ground, and the shape of the magnetic barrier of the reluctance rotor can also be LAL, ARC, segmented rectangle, etc. Figure 2 shows the permanent magnet rotor and a few examples of magnetic choke rotors.

2.2 Motor power equation

2.2.1 External permanent magnet motor

The rated output power of the motor is the product of the number of phases, voltage, and current of the motor. There must be conversion efficiency in power conversion, and the stator waveform of the motor is a rectangular wave rather than a sine wave in most cases. Therefore, it is necessary to multiply the motor efficiency coefficient η and the shape coefficient k_p, Therefore, after ignoring the loss caused by the external stator winding impedance and leakage inductance, the output power of the external permanent magnet motor P_{spm} can be expressed as:

$$P_{spm} = \eta m k_p E_{pk} I_{pk} \tag{1}$$

Among them, η is the motor efficiency; m is the number of phases; k_p is the power form factor; E_{pk} is the peak value of the back electromotive force of the single-phase winding; I_{pk} is the peak value of the stator phase current. Since the stator current vector is aligned with the back EMF vector, the d-axis current is 0, and the value of k_p can be set to 0.5.

The peak value of the back electromotive force of the external permanent magnet motor can be expressed as the product of the peak value of the air gap flux density, the effective length of the winding, and the speed at which the winding cuts the magnetic induction line, $E = BLV$. Among them, the peak value of the air gap magnetic field can be expressed by $B_{gl.p}$, and the effective length of the winding can be expressed as the product of the number of turns N_t of each phase winding, the winding coefficient K_w and the axial length L_e, since the length of the air gap is very short, for an external rotor motor, the linear velocity of a point on the outer diameter of the stator can be used to represent the linear velocity of a certain point in the air gap, so the linear velocity of a certain point in the air gap can be calculated by the formula $v = 2\pi rn$ express, for an external rotor motor, the formula should be expressed as $v = 2\pi \frac{D_{os}}{2} (\frac{f_e}{p})$, so the peak value of the back electromotive force of the external permanent magnet rotor E_{pk} can be expressed as:

$$E_{pk} = B_{gl.p} * K_w N_t L_e * 2\pi \frac{D_{os}}{2} \left(\frac{f_e}{p}\right) = \pi K_w N_t B_{gl.p} \left(\frac{f_e}{p}\right) D_{os} L_e \tag{2}$$

Among them, K_w is the winding coefficient; N_t is the number of winding turns per phase; $B_{gl.p}$ is the peak value of the surface-mounted permanent magnet rotor side air gap flux density; f_e is the power supply frequency; p is the number of pole pairs; D_{os} is the permanent The outer diameter of the stator of the magneto; L_e is the axial length of the motor core, v is the linear velocity of a certain point in the air gap, r is the radius of the motor, and n is the speed of the motor.

Use the electrical load value $A_{sp.rms}$ on the rotor side to represent the peak value of the stator phase current I_{pk}, $A_{sp.rms} D_{os} \pi$ represents the current effective value of the electrical load, $\frac{A_{sp.rms} D_{os} \pi}{m}$ represents the effective value of current that each phase needs to provide to the load, $\frac{A_{sp.rms} D_{os} \pi}{m N_t}$ represents the effective value of current that each turn of wire needs to provide to the load, and the current peak value needs to be multiplied by the coefficient $\sqrt{2}$, so the peak value of the stator phase current can be expressed as $\sqrt{2}\ \frac{A_{sp.rms} D_{os} \pi}{m N_t}$, after adjusting the parameter position, peak current I_{pk} can be obtained:

$$I_{pk} = \frac{\sqrt{2} D_{os} \pi}{m N_t} A_{sp.rms} \tag{3}$$

Substituting parameters in Eqs 2, 3 into Eq. 1, the output power of the motor can be expressed as:

$$P_{spm} = \frac{\sqrt{2}\pi^2}{2} K_w \eta \left(\frac{f_e}{p}\right) B_{gl.p} A_{sp.rms} D_{os}^2 L_e \tag{4}$$

2.2.2 Internal reluctance motor

The stator winding must supply the d-axis and q-axis current components to generate the reluctance torque, so in the expression, the formula needs to be multiplied by an included angle coefficient $\cos \gamma$. The constraint equation of the synchronous reluctance rotor can be compared to the constraint equation of the permanent magnet synchronous motor. The difference is that the

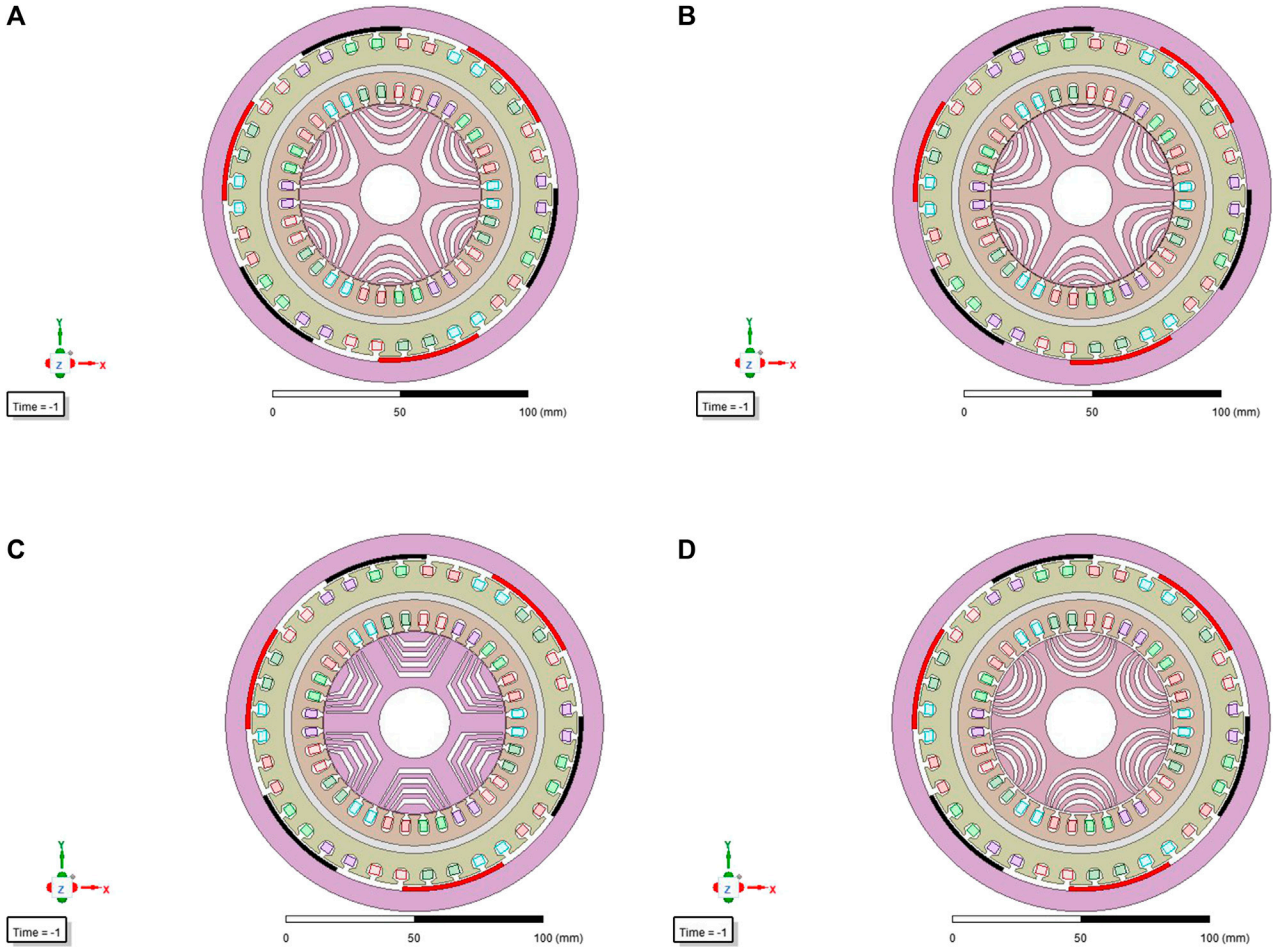

FIGURE 2
Other types of permanent magnet assisted reluctance dual-rotor motor topology: **(A)** Hyperbolic magnetic barrier, **(B)** Plug-in permanent magnet, **(C)** Segmented magnetic barrier, **(D)** ARC barrier.

TABLE 2 Optimize the parameter range.

Parameter	The lower limit	The upper limit
Polar arc coefficient	0.6	0.76
Stator slot width/mm	1.2	3
Permanent magnet thickness/mm	1	2.6
Air gap length/mm	0.2	1.6

synchronous reluctance rotor does not have a permanent magnet that generates back electromotive force. As a result, the synchronous reluctance rotor's output power P_{syr} can be stated as:

$$P_{syr} = \frac{\sqrt{2}\pi^2}{2} K_w \eta \left(\frac{f_e}{p}\right) \cos\gamma B_{g1.R} A_{sR.rms} D_{is}^2 L_e \tag{5}$$

Among them, $\cos\gamma$ is the power factor of the inner rotor motor, γ is the angle between the q-axis component and the stator current; $B_{g1.R}$ is the peak value of the air gap magnetic flux density of the synchronous reluctance rotor side; $A_{sR.rms}$ is the electrical load value on the rotor side of the synchronous reluctance; D_{is} is the inner diameter of the stator of the synchronous reluctance motor.

2.2.3 Double rotor motor

By combining the constraint equations of the external permanent magnet motor and the internal reluctance motor, the complete constraint equation of the dual-rotor motor can be derived, the output power P_{total} is expressed as:

$$P_{total} = \frac{\sqrt{2}\pi^2}{2} K_w \eta \left(\frac{f_e}{p}\right) L_e \left[B_{g1.R} A_{sR.rms} D_{is}^2 \cos\gamma + B_{g1.p} A_{sp.rms} D_{os}^2\right] \tag{6}$$

Since the inner and outer motor stator windings of the motor are connected in series, the winding currents are equal, so it can be obtained:

$$\frac{A_{sp.rms} D_{os} \pi}{m N_t} = \frac{A_{sR.rms} D_{is} \pi}{m N_t} \tag{7}$$

A simple transformation can be obtained

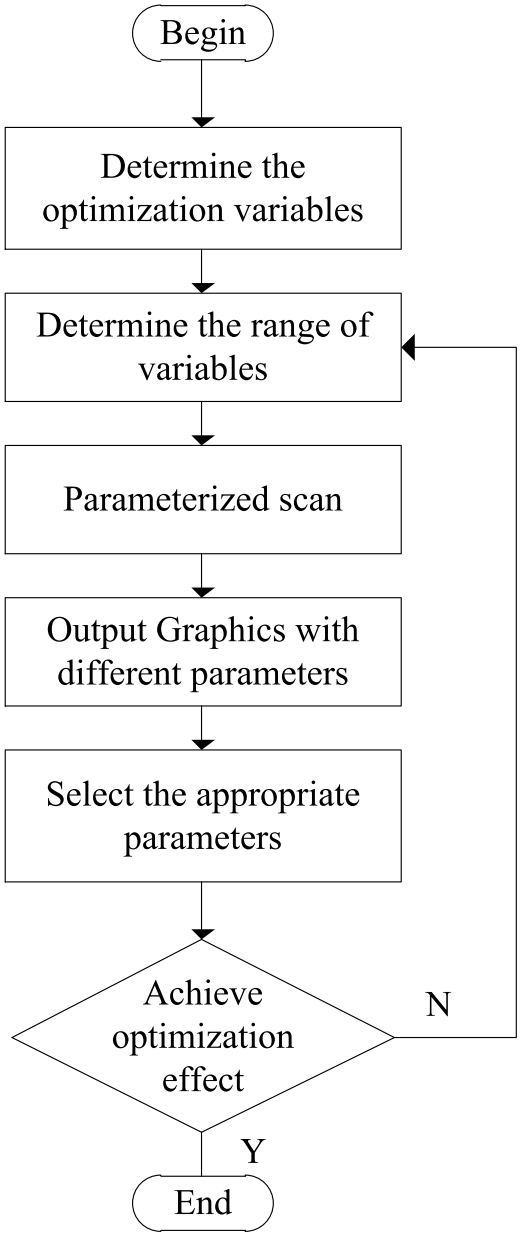

FIGURE 3
Flow chart of cogging torque optimization scheme.

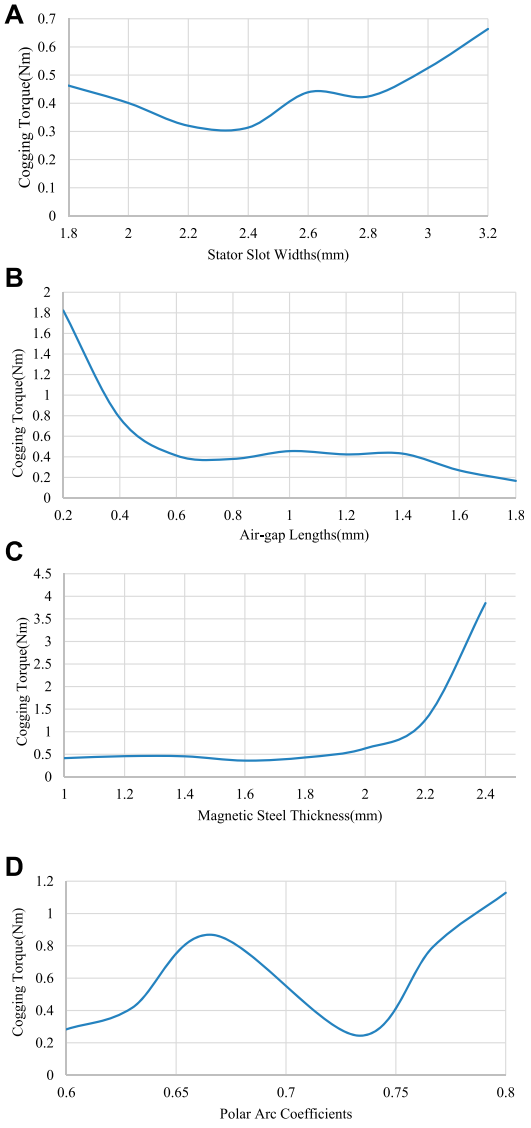

FIGURE 4
The maximum value of cogging torque when each parameter changes: **(A)** Maximum cogging torque at different stator slot widths, **(B)** Maximum cogging torque at different air-gap lengths, **(C)** Maximum cogging torque at different magnet thicknesses, **(D)** Maximum cogging torque at different polar arc coefficients.

$$A_{sp.rms}D_{os} = A_{sR.rms}D_{is} \tag{8}$$

The relationship between the load on the inner rotor side and the outer rotor side can be expressed by the ratio of the inner diameter of the inner motor to the outer diameter of the outer motor:

$$A_{sR.rms} = \frac{D_{is}}{D_{os}}A_{sR.rms} \tag{9}$$

Putting Formula (9) into Formula (6), after simplification, motor total power P_{total} can be expressed as:

$$P_{total} = \frac{\sqrt{2}\pi^2}{2}K_w\eta\left(\frac{f_e}{p}\right)\left[B_{g1.R}\cos\gamma + B_{g1.P}\frac{D_{os}}{D_{is}}\right]A_{sR.rms}D_{is}^2L_e \tag{10}$$

3 Cogging torque optimization

3.1 Cogging torque and optimization method

A major contributor to torque ripple in permanent magnet motors is the cogging torque (Wang et al., 2011). In order to reduce the influence of the cogging torque on the surface-mount permanent magnet motor, Patel (2023) recommended slotting to reduce the gear toque by 48.78%. Rashid and Mohammed (2023) proposed a sawtooth moment mitigation method based on the radial slits of the pole pieces. Won et al. (2023) used neural network prediction to achieve the purpose of reducing cogging torque. Wang et al. (2023) adopted the method of combining in-phase unit (IPU) grouping and slotting angle

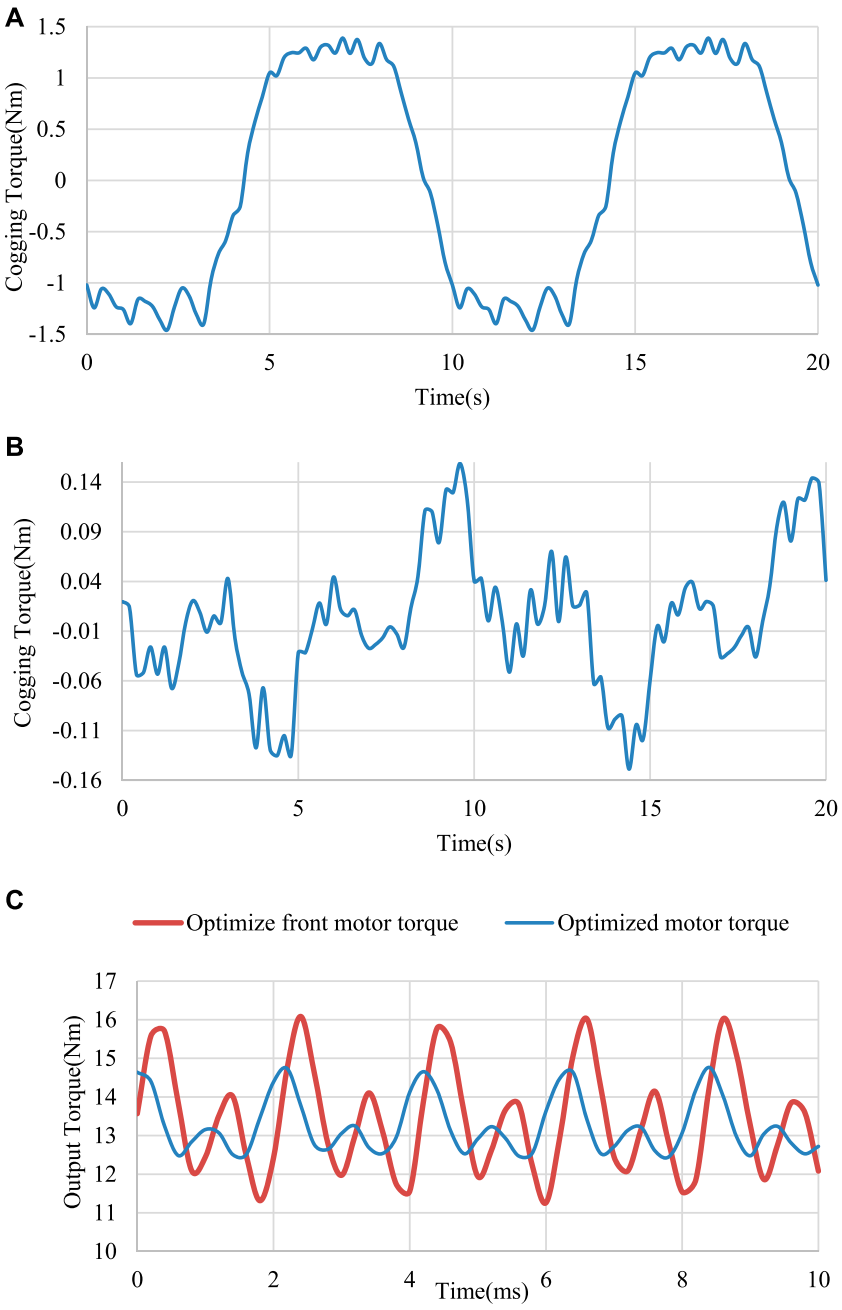

FIGURE 5
Waveform comparison before and after optimization: **(A)** Cogging torque waveform before optimization, **(B)** Cogging torque waveform after optimization, **(C)** Output torque waveform before and after optimization.

offset so that the main harmonic component of the sawtooth torque is cancelled to achieve the purpose of reducing the cogging torque.

This paper chooses to determine the factors affecting cogging torque from the definition of cogging torque. Cogging torque T_{cog} is defined as the negative derivative of the magnetic energy w with respect to the position angle α when de-energized. The expression can be derived as follows:

$$T_{cog}(\alpha) = \frac{\pi z L_e}{4u_0}\left(R_2^2 - R_1^2\right)\sum_{n=1}^{\infty} nG_n B_{rn}\, sin(nz\alpha) \tag{11}$$

In the formula, R_1 is outside armature diameter of external motor, R_2 is stator inner diameter of external motor, z is number of stator slots, α is the relative position angle between the stator and rotor, u_0 is vacuum permeability.

B_{rn} is the Fourier coefficient of the residual flux density squared along the circumference of permanent magnets, and the formula is as follows:

$$B_{rn} = \frac{2}{n\pi} B_r^2 \sin n\alpha_p \pi \tag{12}$$

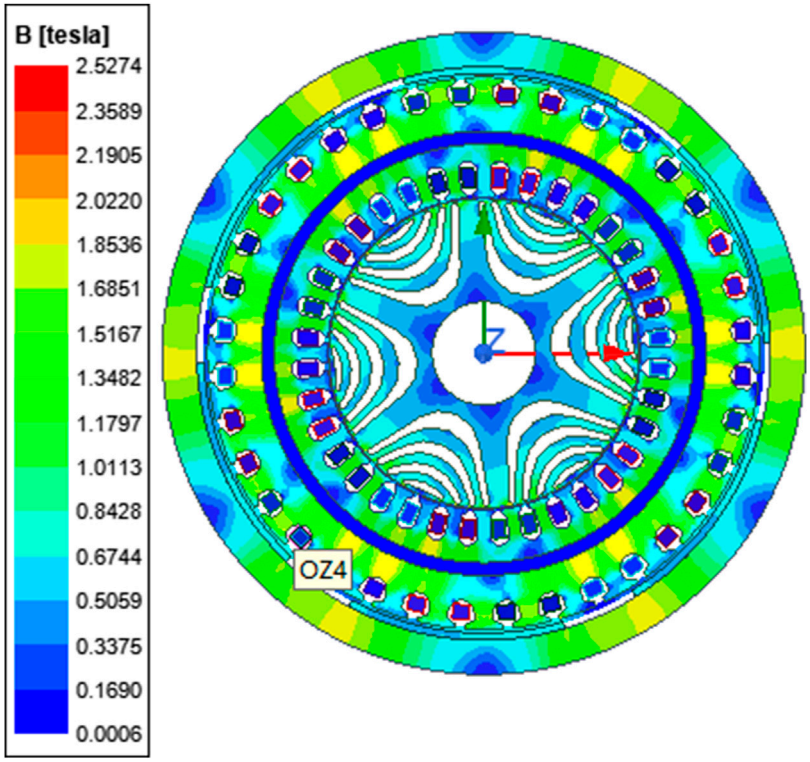

FIGURE 6
Motor magnetic field density map.

In the formula, B_r is the residual flux density in a permanent magnet, α_p is polar arc coefficient of permanent magnetic pole.

G_n is the Fourier coefficient of the square relative permeability of the air-gap and the formula is as follows:

$$G_n = \sum_{n=1}^{\infty} \frac{2}{n\pi} \left(\frac{h_m}{h_m + \delta} \right)^2 \sin\left(n\pi - \frac{nz\theta_s}{2} \right) \tag{13}$$

In the formula, δ is air gap length, h_m is the thickness of the permanent magnet along the magnetization direction, θ_s is the corresponding radian value of the width of the stator groove.

3.2 Determine optimization variables and parameter ranges

It can be seen from the above formula that the slot opening angle width, magnetic steel angle width, magnetic steel thickness, and air gap length all have a great influence on the cogging torque. Therefore, these four parameters are selected as the cogging torque optimization parameters in this paper to study their effect on cogging torque. Table 2 lists the optimized variable parameter ranges.

3.3 Parameter optimization

In order to explore the law of cogging torque weakening caused by different design variables, each design variable is parameterized in the optimization process, and one parameter is selected as a variable. The upper and lower limits are given as shown in Table 2. Other parameters are constants; after obtaining the waveforms of the cogging torque in various situations, select the maximum value to draw the trend of the cogging torque changing with the parameters, and select the optimal parameters for simulation verification in Maxwell. If the optimal effect meets expectations, the optimization is complete. If the effect is not as expected, it is necessary to change the upper and lower limits of the parameters or to optimize the parameters. The specific optimization scheme flow chart is shown in Figure 3. As we can see in Figure 4, the optimal values of the four parameters can be easily found according to the graph.

3.4 Optimization results

During the cogging torque parameterization, different degrees of attenuation can be demonstrated by using different methods and changing the parameter range. It can be seen from Figure 4 that when the pole arc coefficient is between 0.72 and 0.74 and the thickness of the magnetic steel is between 1.6 mm and 1.8 mm, the calculated cogging torque is relatively lower. Considering that increasing the air gap will reduce the output torque of the motor, the length of the air gap should be kept between 0.6 mm and 1 mm. The cogging torque waveform before and after adjustment is shown in Figure 5. The cogging torque is reduced from 1.5 Nm to 0.15 Nm, and the optimized output torque waveform is more stable, the torque ripple is lower, and the optimization effect is more obvious.

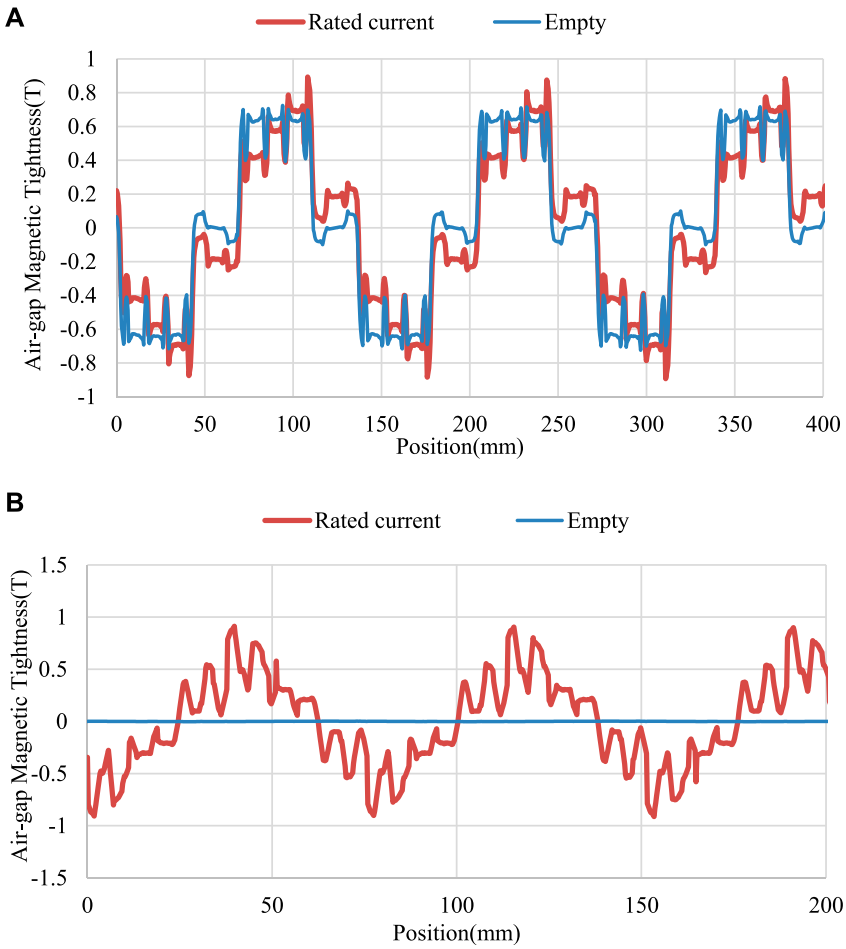

FIGURE 7
Air gap magnetic: **(A)** Outer motor air gap flux density and **(B)** Inner motor air gap flux density.

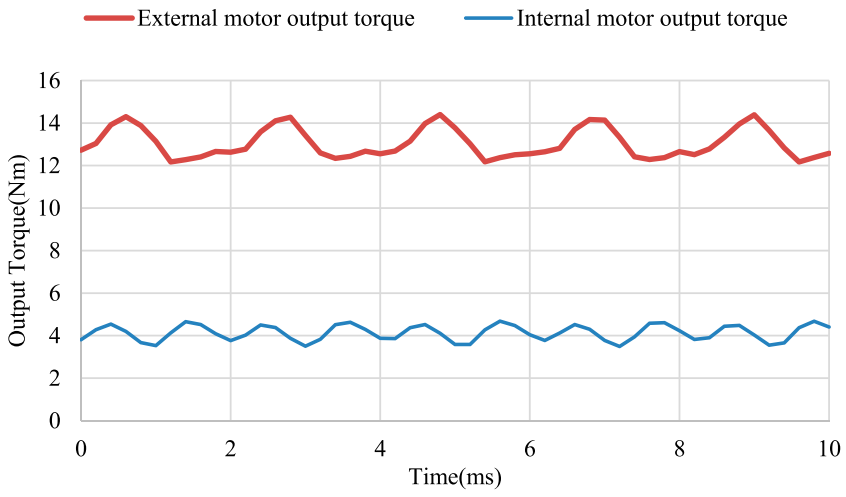

FIGURE 8
Output torque waveform of internal and external motors.

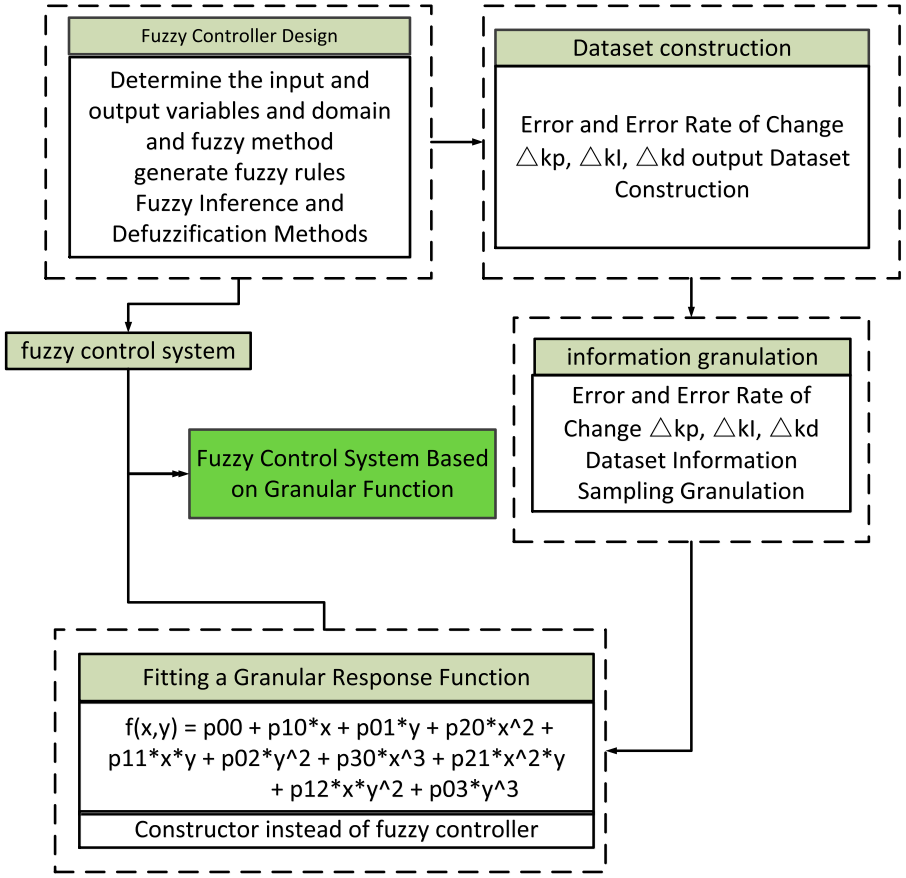

FIGURE 9
Construction process of granular function optimization fuzzy controller.

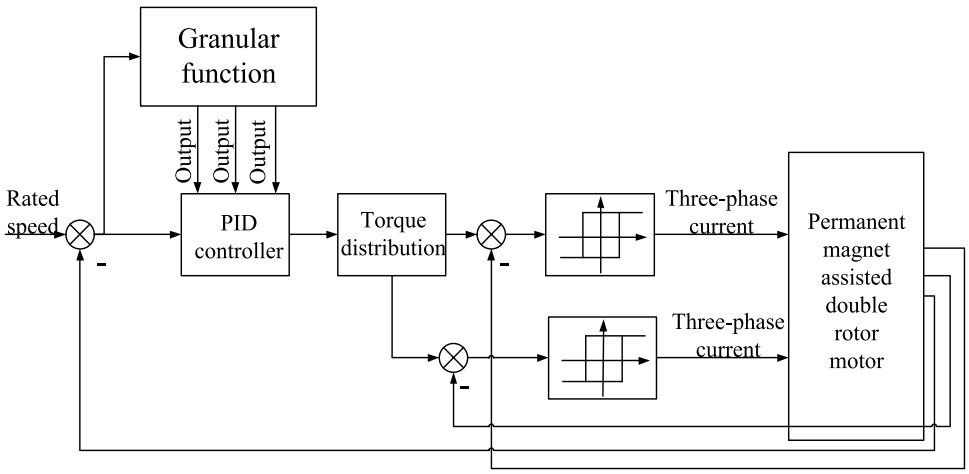

FIGURE 10
Control system block diagram.

4 Electromagnetic characteristic analysis

4.1 Magnetic flux density

After the optimization is completed, use the finite element software Maxwell to establish a two-dimensional model of the motor, set the rated current on the inner and outer stator windings, and obtain the magnetic flux density cloud diagram of the permanent magnet assisted dual-rotor motor with load through finite element simulation. As shown in Figure 6, the maximum value of the magnetic flux density appears at the position of the inner and outer stator yoke, which is about 1.8T, which does not exceed the design limit of 2T and meets the motor operation specification.

4.2 Air gap magnetic density

The air-gap magnetic field density is an important indicator of motor design. Figure 7 is the air-gap flux density curve of the internal and external motors under no-load and rated current. The amplitude of the air-gap flux density reflects the magnetic field strength and torque density of the motor, it can be seen that the waveform is closer to a sine wave. From the comparison of the two curves, we can see that the air gap flux density curve of the inner motor is more reasonable than the sinusoidal distribution of the outer motor, indicating that the inner motor can meet the requirements of torque output and power density. The peak values of the air gap magnetic density of the outer motor and the inner motor are 0.8T and 1 T, respectively, which generally meet the design requirements.

4.3 Output torque

Since the motor has a double-air-gap structure, its total output torque is the sum of the output torques of the inner and outer motors, and the torque output waveforms of the inner and outer motors are shown in Figure 8. According to the output torque results, the output torque of the inner rotor synchronous reluctance motor is about 4 Nm, and the torque ripple is about 28.8%. The output torque of the outer rotor permanent magnet synchronous motor is about 13 Nm, and the torque ripple is about 17.1%, which verifies the effectiveness of the optimized design, and the quality of the motor output torque has been significantly improved.

5 Design of control system for dual rotor motor

5.1 Motor mathematical model

The dual-rotor motor is composed of inner rotor, outer rotor, permanent magnet, magnetic isolation ring and other parts. It has the characteristics of strong coupling and nonlinearity. For the convenience of analysis, the assumptions are as follows: 1) Neglect eddy current and hysteresis loss; 2) Excitation current There is no response time; 3) The stator windings are star-connected, and the stator windings are connected in parallel. According to the above assumptions, it can be obtained that the dual-rotor motor can be split into a permanent magnet synchronous motor and a synchronous reluctance motor, and after transformation by clark and park the voltage equation of the motor under the dq axis.

$$\begin{bmatrix} u_{d1} \\ u_{q1} \end{bmatrix} = \begin{bmatrix} \cos\theta_1 & \cos\left(\theta_1 - \frac{2\pi}{3}\right) & \cos\left(\theta_1 - \frac{4\pi}{3}\right) \\ -\sin\theta_1 & -\sin\left(\theta_1 - \frac{2\pi}{3}\right) & -\sin\left(\theta_1 - \frac{4\pi}{3}\right) \end{bmatrix} \begin{bmatrix} U_{A1} \\ U_{B1} \\ U_{C1} \end{bmatrix} \quad (14)$$

$$\begin{bmatrix} u_{d2} \\ u_{q2} \end{bmatrix} = \begin{bmatrix} \cos\theta_2 & \cos\left(\theta_2 - \frac{2\pi}{3}\right) & \cos\left(\theta_2 - \frac{4\pi}{3}\right) \\ -\sin\theta_2 & -\sin\left(\theta_2 - \frac{2\pi}{3}\right) & -\sin\left(\theta_2 - \frac{4\pi}{3}\right) \end{bmatrix} \begin{bmatrix} U_{A2} \\ U_{B2} \\ U_{C2} \end{bmatrix} \quad (15)$$

Since the double-rotor motor is divided into two parts, the inner rotor and the outer rotor, the electromagnetic torque of the motor is expressed as the permanent magnet torque of the outer motor and the reluctance torque of the inner motor, and the sum of the inner and outer torques is the total electromagnetic torque of the motor.

$$T_e = T_{e1} + T_{e2} = \frac{3}{2} p_1 \left(L_{d1} - L_{q1}\right) i_{d1} i_{q1} + \frac{3}{2} p_2 i_{q2} \psi_f \quad (16)$$

$$T_e - T_L = J\frac{d\omega}{dt} + B\omega \quad (17)$$

In these formulas, p_x is the logarithm of the motor poles, U_{Ax} U_{Bx} U_{Cx} is the motor stator three-phase current, i_{dx} i_{qx} is current of dq axial, u_{dx} u_{qx} is voltage of dq axial, θ_x is angle from abc axial to dq axial, T_{ex} is the electromagnetic torque of a motor, T_L is a load torque, B is the damping coefficient, ω is the mechanical speed of a motor, J is the moment of inertia of the motor, ψ_f is the permanent magnet linkage of a motor. x equals to 1 is the reluctance part of the motor, x equals to 2 is the permanent magnet portion of the motor.

5.2 Vector control

Vector control is based on the control idea of a DC motor, converts the three-phase current into excitation current and torque current, and realizes indirect control of the motor by changing the magnitude of the excitation current and torque current, that is, by controlling the axis current of the motor to achieve the purpose of controlling the motor. At present, the commonly used vector control methods of permanent magnet synchronous motors include $i_d = 0$ control, $\cos\varphi = 1$ control, maximum torque-current ratio control and flux weakening control; vector control methods of synchronous reluctance motor include maximum torque-to-current ratio control, maximum power factor control, maximum torque change rate control, and so on. The external motor of the double-rotor motor is a surface-mounted permanent magnet synchronous motor, and the $i_d = 0$ control is equivalent to the maximum torque-to-current ratio control, therefore, the inner and outer motors of the dual-rotor motor in this paper are controlled by the maximum torque-current ratio, which simplifies the control system.

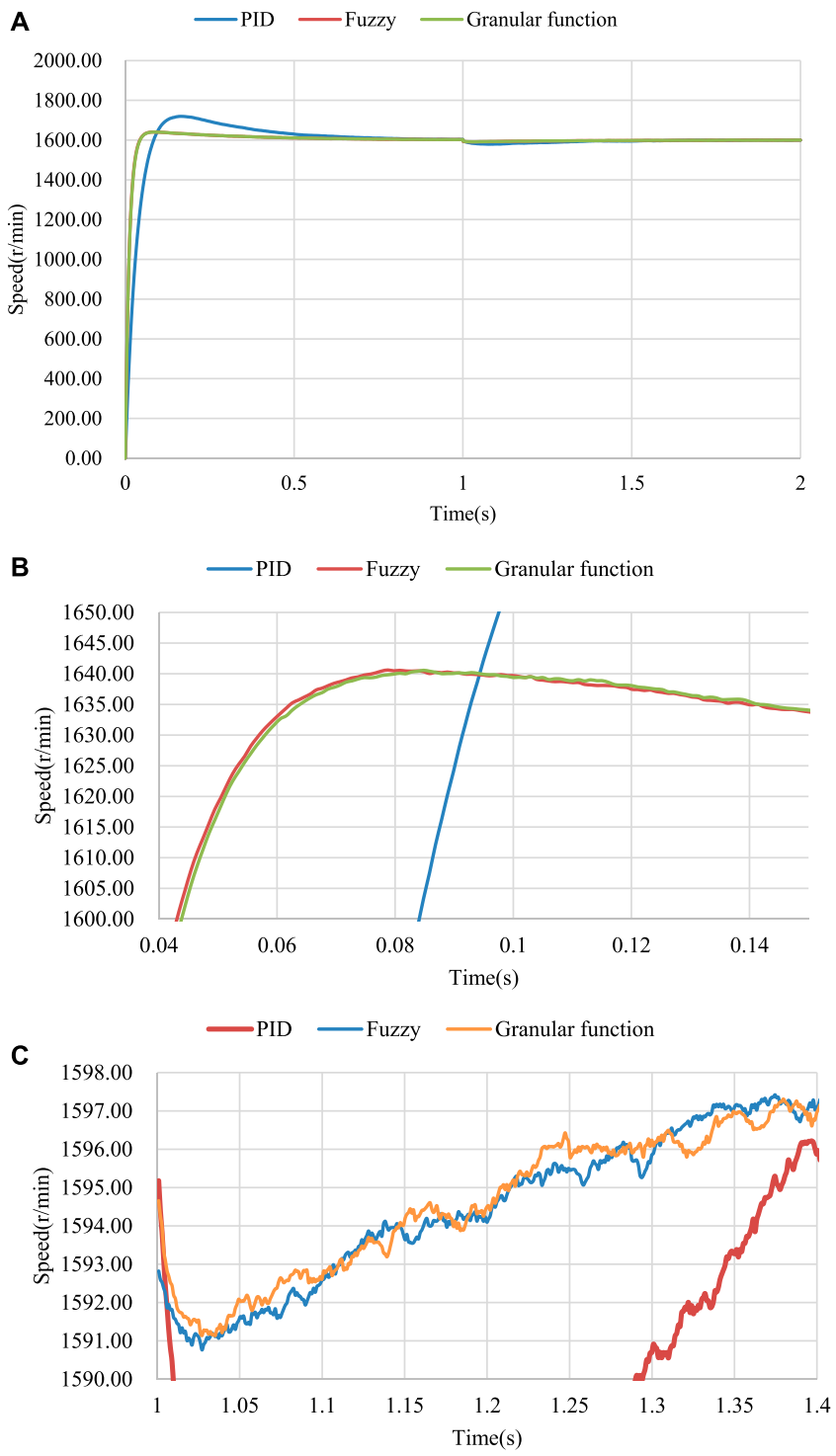

FIGURE 11
Motor output waveform: **(A)** The output waveforms of different control modes, **(B)** Partial enlarged view of the speed increase process. **(C)** Partial enlarged view of the speed drop process after.

5.3 Torque distribution

Due to the existence of the magnetic isolation ring, the dual-rotor motor can be equivalent to a surface-mounted permanent magnet synchronous motor and a synchronous reluctance motor. Conventional control requires two sets of controllers that interact with each other. In order to solve this problem, torque distribution is introduced. Torque distribution is used to fix the ratio of the output torque of the internal and external motors, distribute the torque current of the internal and external motors, and simplify the control system.

5.4 Controller design

5.4.1 Current controller design

The current controller in this design adopts the mode of hysteresis control, also called bang-bang control, which has the characteristics of real-time control, fast reaction, and strong robustness. The implementation method is to change the switching state of the inverter by comparing the given current value with the detected current value, and then output the actual current in the shape of a sawtooth wave. Although there are certain errors, this current control method is simple and easy to implement and does not rely on motor parameters.

5.4.2 Speed controller design

The speed control of this design adopts the granular function instead of the fuzzy controller. The granular function is based on the theory of granular computing. Granular computing (GrC) is usually defined in an informal way as a general computing theory that can be used effectively. To build an efficient computational model for complex applications with large amounts of data, information, and knowledge (Bargiela and Pedrycz, 2008), the granular function shifts from a machine-centered approach to a human-centered approach. It is one of the trends in granular computing research (Yao, 2010), and fuzzy set theory is an application of granular computing (Zarandi Baghini et al., 2023). The construction of granular functions in fuzzy control is divided into steps such as information sampling, information granulation, and fitting. Using granular functions instead of fuzzy controllers can save steps such as fuzzification and defuzzification. The construction process of a granular computing fuzzy controller is shown in Figure 9.

5.5 System simulation and analysis

5.5.1 Control system block diagram

According to the description of the fuzzy control optimized by the above granular function, a dual-rotor motor control system frame can be built as shown in Figure 10. The control system is composed of a traditional PID controller, a granular function optimization module, a torque distribution module, a current hysteresis controller, and a motor body.

5.5.2 Simulation result analysis

As shown in Figure 11, the highest speed for fuzzy control and granular function control is about 1,640 r/min, and after changing the load, fuzzy control and granular function control motors drop to 1,591 r/min. It can be concluded that the granular function is comparable to the fuzzy control in terms of control performance, but the granular function removes the complicated fuzzification and defuzzification processes, only needs one response function, and the simulation time is less than one-tenth of the fuzzy control.

6 Conclusion

This paper aims to address the problem that the cogging torque of a dual-rotor motor connected by concentric end disks affects the motor's output torque. By deriving the motor power equation constraints, the fixed-value scanning method is used for optimization analysis. After optimization, the motor cogging torque was reduced from 1.5 Nm to 0.15 Nm, a reduction of 90%; the external rotor torque ripple was reduced by 50%; the torque output waveform was improved; and the optimized electromagnetic performance was verified. Finally, in order to simplify the motor control system, this paper uses granular functions to improve the fuzzy controller, performs feature sampling on fuzzy rules, and uses response functions to replace the fuzzy controller, omitting the fuzzification and defuzzification links. Simulation shows that after granular function optimization, the response speed of the system is significantly improved.

Data availability statement

The original contributions presented in the study are included in the article/Supplementary Materials, further inquiries can be directed to the corresponding author.

Author contributions

YZ and GX wrote and typed the manuscript, and XK provided writing guidance, checking and correction.

Funding

This work is supported in part by the National Natural Science Foundation of China under grant 51877139 and the Basic Scientific Research Project of Liaoning Provincial Department of Education of China under grant LJKMZ20220778.

Conflict of interest

The authors declare that the research was conducted in the absence of any commercial or financial relationships that could be construed as a potential conflict of interest.

Publisher's note

Supplementary material

The Supplementary Material for this article can be found online at: https://www.frontiersin.org/articles/10.3389/fenrg.2023.1240473/full#supplementary-material

References

Agbo, S., Samuel, O. D., Amosun, S. T., Oyejide, O. J., Fayomi, O. S. I., Bamisaye, O. S., et al. (2021). Development of a solar energy-powered surface water pump. *IOP Publ.* 1107 (1), 012002. doi:10.1088/1757-899X/1107/1/012002

Al-Ani, M. (2021). Multi-physics design and analyses of dual rotor synchronous reluctance machine. *eTransportation* 8, 100113. doi:10.1016/j.etran.2021.100113

Aravind, C. V., Norhisam, M., Aris, I., Marhaban, M. H., Ahmad, D., and Nirei, M. (2011). "Double-rotor switched reluctance machine (DRSRM): fundamentals and magnetic circuit analysis," in 2011 IEEE Student Conference on Research and Development (IEEE), 294–299.

Bai, J., Zheng, P., Cheng, L., Zhang, S., Liu, J., and Liu, Z. (2015). A new magnetic-field-modulated brushless double-rotor machine. *IEEE Trans. Magnetics* 51 (11), 1–4. doi:10.1109/tmag.2015.2445917

Bargiela, A., and Pedrycz, W. (2008). Toward a theory of granular computing for human-centered information processing. *IEEE Trans. Fuzzy Syst.* 16 (2), 320–330. doi:10.1109/tfuzz.2007.905912

Diao, C., Zhao, W., Ding, H., and Wang, X. (2023). *Design and analysis of low-cost double rotor axial flux permanent magnet synchronous motor*.

Fu, D., Lv, Z., Si, H., Liu, Y., and Wu, X. (2023). *Analysis and comparison of novel yokeless double rotor mutually coupled switched reluctance motor*.

Hofmann, H., and Sanders, S. R. (2000). High-speed synchronous reluctance machine with minimized rotor losses. *IEEE Trans. Industry Appl.* 36 (2), 531–539. doi:10.1109/28.833771

Jurca, F., and Martis, C. (2017). "Analysis of outer rotor synchronous reluctance motor for low-speed applications[C]," in 2017 19th International Conference on Electrical Drives and Power Electronics (EDPE), Dubrovnik, Croatia, 04-06 October 2017 (IEEE), 242–247.

Li, J., Wang, J., Liu, J., and Ren, C. (2023). Coordinated control strategy for drive mode switching of double rotor in-wheel motor based on MPC and control allocation. *World Electr. Veh. J.* 14 (5), 132. doi:10.3390/wevj14050132

Li, Y., Bobba, D., and Sarlioglu, B. (2017). Design and optimization of a novel dual-rotor hybrid PM machine for traction application. *IEEE Trans. Industrial Electron.* 65 (2), 1762–1771. doi:10.1109/tie.2017.2739686

Liu, Y., and Li, J. (2022). Research on concentrated winding counter-rotating double rotor disk motor. *Mech. Des. Manuf.* (03), 110–113. doi:10.19356/j.cnki.1001-3997.20211115.003

Patel, A. N. (2023). *Slot opening displacement technique for cogging torque reduction of axial flux brushless DC motor for electric two-wheeler application*.

Qu, R., and Lipo, T. A. (2003). Dual-rotor, radial-flux, toroidally wound, permanent-magnet machines. *IEEE Trans. industry Appl.* 39 (6), 1665–1673. doi:10.1109/tia.2003.818968

Rashid, M. K., and Mohammed, A. M. (2023). A reduction method of cogging torque for magnetic gears. *Iran. J. Electr. Electron. Eng.* 19 (2), 2752. doi:10.22068/IJEEE.19.2.2752

Shirzad, E. (2023). *Calculation of flux density in air-gap for reluctance motor with two ports (Double-Stator, double-rotor) by fourier series*.

Wang, D., Wang, X., Qiao, D., Pei, Y., and Jung, S. Y. (2011). Reducing cogging torque in surface-mounted permanent-magnet motors by nonuniformly distributed teeth method. *IEEE Trans. Magnetics* 47 (9), 2231–2239. doi:10.1109/tmag.2011.2144612

Wang, H., and Leng, J. (2018). "Summary on development of permanent magnet synchronous motor," in 2018 Chinese Control And Decision Conference (CCDC) (IEEE), 689–693.

Wang, L., Lu, S., Chen, Y., and Wang, S. (2023). An in-phase unit slot-opening shift method for cogging torque reduction in interior permanent magnet machine. *Mathematics* 11 (7), 1735. doi:10.3390/math11071735

Won, Y. J., Kim, J. H., Park, S. H., Lee, J. H., An, S. M., Kim, D. Y., et al. (2023). Transfer learning-based design method for cogging torque reduction in PMSM with step-skew considering 3-D leakage flux. *IEEE Trans. Magnetics*, 1. doi:10.1109/tmag.2023.3294601

Yao, J. (2010). Novel developments in granular computing: applications for advanced human reasoning and soft computation: applications for advanced human reasoning and soft computation. *IGI Glob*.

Yunyun, C., Li, Q., Xiaoyong, Z., Hua, W., and Wang, Z. (2012). Electromagnetic performance analysis of double-rotor stator permanent magnet motor for hybrid electric vehicle. *IEEE Trans. Magnetics* 48 (11), 4204–4207. doi:10.1109/tmag.2012.2206374

Zarandi Baghini, A., Babaei, H., Tabatabaei Mirhosseini, R., and Torkzadeh Tabrizi, L. (2023). New approach based on fuzzy hypergraphs in granular computing (an application to the urban vulnerability assessment). *Int. J. Nonlinear Analysis Appl.* doi:10.21203/rs.3.rs-1167172/v1

Frontiers in
Energy Research

Advances and innovation in sustainable, reliable and affordable energy

Explores sustainable and environmental developments in energy. It focuses on technological advances supporting Sustainable Development Goal 7: access to affordable, reliable, sustainable and modern energy for all.

Discover the latest Research Topics

See more →

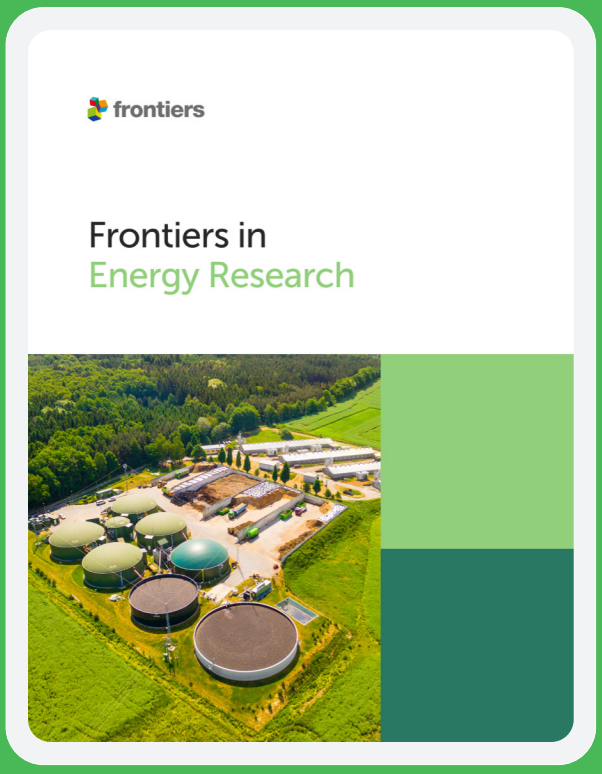

Frontiers

Avenue du Tribunal-Fédéral 34
1005 Lausanne, Switzerland
frontiersin.org

Contact us

+41 (0)21 510 17 00
frontiersin.org/about/contact